Transactions of the ASME

Journal of Applied Mechanics

Published Quarterly by The American Society of Mechanical Engineers

VOLUME 50 • NUMBER 3 • SEPTEMBER 1983

The Journal of Applied Mechanics (ISSN 0021-8936) is published quarterly for $72 per year by The American Society of Mechanical Engineers, 345 East 47th Street, New York, NY 10017. Second class postage paid at New York, NY and additional mailing offices. POSTMASTER: Send address changes to The Journal of Applied Mechanics, c/o THE AMERICAN SOCIETY OF MECHANICAL ENGINEERS, P.O. Box 3199, Grand Central Station, New York, NY 10163. **CHANGES OF ADDRESS** must be received at Society headquarters seven weeks before they are to be effective. Please send old label and new address.

PRICES: To members, $36.00, annually; to nonmembers, $72.00. Single copies, $24.00 each. Add $6.00 for postage to countries outside the United States and Canada.

INDEXED by the Engineering Index, Inc.

(Contents continued on Inside Back Cover)

CONTENTS (CONTINUED)

BRIEF NOTES

DISCUSSION

BOOK REVIEWS

ERRATA

Analysis of Composite Materials—A Survey

Z. Hashin
Nathan Cummings Professor of Mechanics of Solids,
Department of Solid Mechanics, Materials and Structures,
Tel Aviv University,
Tel Aviv, Israel
Fellow ASME

The purpose of the present survey is to review the analysis of composite materials from the applied mechanics and engineering science point of view. The subjects under consideration will be analysis of the following properties of various kinds of composite materials: elasticity, thermal expansion, moisture swelling, viscoelasticity, conductivity (which includes, by mathematical analogy, dielectrics, magnetics, and diffusion) static strength, and fatigue failure.

*"Where order in variety we see
And where, though all things differ, all agree"*

Alexander Pope

1 Introduction

Composite materials consist of two or more different materials that form regions large enough to be regarded as continua and which are usually firmly bonded together at the interface. Many natural and artificial materials are of this nature, such as: reinforced rubber, filled polymers, mortar and concrete, alloys, porous and cracked media, aligned and chopped fiber composites, polycrystalline aggregates (metals), etc.

Analytical determination of the properties of composite materials originates with some of the most illustrious names in science. J. C. Maxwell in 1873 and Lord Rayleigh in 1892 computed the effective conductivity of composites consisting of a matrix and certain distributions of spherical particles (see Part 6). Analysis of mechanical properties apparently originated with a famous paper by Albert Einstein in 1906 in which he computed the effective viscosity of a fluid containing a small amount of rigid spherical particles. Until about 1960, work was primarily concerned with macroscopically isotropic composites, in particular, matrix/particle composites and also polycrystalline aggregates. During this period the primary motivation was scientific. While the composite materials investigated were of technological importance, a technology of composite materials did not as yet exist. Such a technology began to emerge about 1960 with the advent of modern fiber composites consisting of very stiff and strong aligned fibers (glass, boron, carbon, graphite) in a polymeric matrix and later also in a light weight metal matrix.

The engineering significance of reliable analysis of properties is quite different for particulate composites and for fiber composites. For the former, such capability is desirable, while for the latter it is crucial. The reason is that the range of realizable properties and the ability to control the internal geometry are quite different in the two cases. For example: the effective Young's modulus of an isotropic composite consisting of matrix and very much stiffer and stronger spherical type particles will depend primarily on volume fractions and can be increased in practice only up to about four–five times the matrix modulus. The strength of such a composite is only of the order of the matrix strength and may even be lower. The effect of stiffening and strengthening increases if particles have elongated shapes but at the price of lowering the maximum attainable particle volume fraction.

A unidirectional fiber composite is highly anisotropic and therefore has many more stiffness and strength parameters than a particulate composite. Stiffness and strength in the fiber direction are of fiber value order, and thus very high. Stiffnesses and strengths transverse to the fiber direction are of matrix order, similar to those of a particulate composite, and thus much lower. Carbon and graphite are themselves significantly anisotropic, their elastic properties being defined by five numbers instead of the usual two for an isotropic material. Furthermore, matrix properties may be strongly influenced by environmental changes such as heating, cooling, and moisture absorption. All of this creates an enormous variety of properties, of much wider range than for a particulate composite.

The generally low values of stiffness and strength transversely to the fibers provide the motivation for *laminate* construction consisting of thin unidirectional layers with different reinforcement directions. The laminates are formed into laminated structures. The layer thicknesses, fiber directions, choice of fibers, and matrix are at the designers disposal and should, ideally, be chosen from the point of view of optimization of an important quantity such as weight or price. The design of such structures is an integrated process leading from constituents to structure in the sequence:

Contributed by the Applied Mechanics Division for publication in the JOURNAL OF APPLIED MECHANICS.

Discussion on this paper should be addressed to the Editorial Department, ASME, United Engineering Center, 345 East 47th Street, New York, N.Y. 10017, and will be accepted until two months after final publication of the paper itself in the JOURNAL OF APPLIED MECHANICS. Manuscript received by ASME Applied Mechanics Division, February, 1983.

FIBERS AND MATRIX → UNIDIRECTIONAL COMPOSITE → LAMINATE → LAMINATED STRUCTURE.

Traditionally, material properties have been obtained by experiment and material improvement has been achieved empirically and qualitatively. The structural designer had at his disposal a limited number of material options provided by the materials developer. This situation is entirely different for fiber composite structures. The only constituents that are materials in the traditional sense are fibers and matrix. Everything following in the sequence, including the unidirectional material, is of such immense variety that analysis, rather than experimentation, is the practical procedure to obtain properties. Thus, the relevant methods are those of applied mechanics rather than those of materials science.

The purpose of the present survey is to present analysis of composite materials from the applied mechanics and engineering science point of view, and thus as a subject that is based on principles and rational methods and not on empiricism and speculation. The subjects under consideration will be analysis of the following properties of various kinds of composite materials: elasticity, thermal expansion, moisture swelling, viscoelasticity, conductivity (which includes, by mathematical analogy, dielectrics, magnetics, and diffusion) static strength, and fatigue failure. Relevant comprehensive literature expositions are Hashin [1] and Christensen [2] which will be referred to frequently. Important subject omissions are elastodynamic behavior and plasticity, this for reasons of space limitation. Surveys of these subjects may be found in [2]. Analysis of laminates is not included since this is a well understood subject and it has been described in several textbooks, except for the problem of laminate failure which will be briefly discussed.

2 General Considerations

There are two kinds of information that determine the properties of a composite material: the internal phase geometry, i.e., the phase interface geometry and the physical properties of the phases, i.e., their constitutive relations. Of these, the former is far more difficult to classify than the latter. In reality the internal geometry of every composite material is to a certain extent random. In a general two phase material (for reasons of simplicity the discussion will be concerned with two phases. The case of more phases will only be considered as needed) the phase regions are of arbitrary unspecified shapes. When one phase is in the form of *particles* embedded in the second *matrix* phase the material is called a *particulate composite*. The internal geometry may be three or two dimensional. The latter case implies cylindrical specimens where each cross section has the same plane geometry. If nothing else is specified this is called a *fibrous material*, which is the two-dimensional case of a general two phase material. The two-dimensional analogue of a particulate composite is a *fiber composite*, the particles being aligned cylinders.

It is necessary to explain what is meant by a composite *material* in distinction from a composite body. In the former it is possible to define *representative volume elements* (RVE) Fig. 1, which are large compared to typical phase region dimensions (e.g., fiber diameters and spacings). From a practical point of view, a necessary characteristic of a composite material is *statistical homogeneity* (SH). A strict statistical definition of this concept must be expressed in terms of n-point probabilities and ensemble averages, see e.g., [3, 4]. Suffice it to say for present purposes that in a SH composite all global geometrical characteristics such as volume fractions, two-point correlations, etc. are the same in any RVE, irrespective of its position.

The effective properties of a composite material define the relations between averages of field variables such as stress and strain when their space variation is statistically homogeneous. For a strict definition of statistical homogeneity of such fields the reader is again referred to [4]. It may be said, somewhat loosely, that statistically homogeneous fields are statistically indistinguishable within different RVE in a heterogeneous body. By this is implied that their statistical moments such as average, variance, etc. are the same when taken over any RVE within the heterogeneous body. In particular, statistical homogeneity implies that body averages and RVE averages are the same.

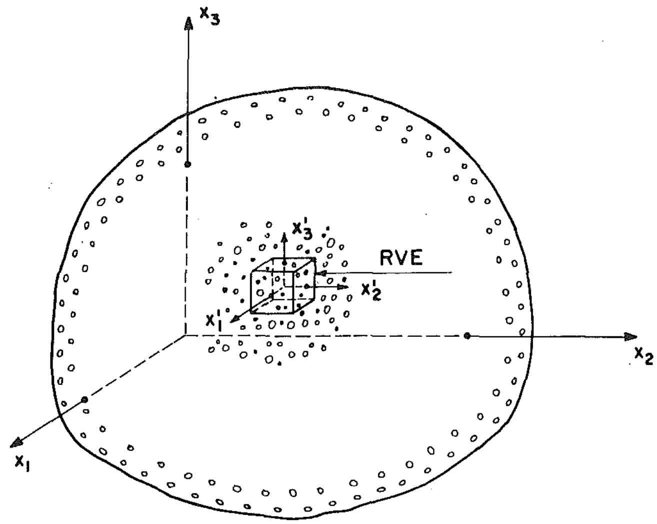

Fig. 1 Representative volume element

To produce a SH field in a composite it is expedient to apply boundary conditions that produce homogeneous fields in an homogeneous body. Such boundary conditions will consequently be called homogeneous (not to be confused with the concept of homogeneous boundary conditions in the theory of differential equations). For elastic bodies, homogeneous boundary conditions are either one of

$$u_i(S) = \epsilon^0_{ij} x_j \quad (a) \qquad T_i(S) = \sigma^0_{ij} n_j \quad (b) \tag{2.1}$$

where ϵ^0_{ij} are constant strains and σ^0_{ij} are constant stresses.

For heat (or electrical) conduction such boundary conditions are

$$\varphi(S) = -H^0_i x_i \quad (a) \qquad q_n(S) = q^0_i n_i \quad (b) \tag{2.2}$$

where φ is temperature or potential, H^0_i are constants (components of gradient), q^0_i are constant fluxes, and q_n is the normal flux component. Other cases of homogeneous boundary conditions will be given as needed.

The fundamental postulate of the theory of (elastic) heterogeneous media states, Hashin [1]: *"The stress and strain fields in a large SH heterogeneous body subjected to homogeneous boundary conditions are SH, except in a boundary layer near the external surface."* The postulate applies in obvious fashion to other physical properties.

The effective elastic properties are defined by the linearity relations

$$\bar{\sigma}_{ij} = C^*_{ijkl} \bar{\epsilon}_{kl} \quad (a) \qquad \bar{\epsilon}_{ij} = S^*_{ijkl} \bar{\sigma}_{kl} \quad (b) \tag{2.3}$$

where C^*_{ijkl} are *effective elastic moduli* and S^*_{ijkl} are *effective elastic compliances*, connected by the usual reciprocity relation and having the usual symmetries, and overbars denote here and from now on, averages over RVE. When (2.1*a*) is prescribed, it follows by the average strain theorem, [1], that $\bar{\epsilon}_{ij} = \epsilon^0_{ij}$. Thus to determine C^*_{ijkl} the average stress $\bar{\sigma}_{ij}$ must be computed subject to (2.1*a*). Conversely, when (2.1*b*) is prescribed, then from the average stress theorem, [1], $\bar{\sigma}_{ij} = \sigma^0_{ij}$. Thus to find S^*_{ijkl} the average strain $\bar{\epsilon}_{ij}$ must be computed subject to (2.1*b*).

Everything is analogous for conductivity. The *effective conductivity* tensor μ^*_{ij} and the *effective resistivity* tensor ρ^*_{ij} are defined by

$$\bar{q}_i = \mu^*_{ij}\bar{H}_j \quad \bar{H}_i = \rho^*_{ij}\bar{q}_j \tag{2.4}$$

where $H_i = -\varphi_{,i}$. The tensors μ^*_{ij} and ρ^*_{ij} are reciprocal and are determined analogously to effective elastic properties. The averages $\bar{H}_i$ and $\bar{q}_i$ are given by H^0_i and q^0_i in (2.2) from conductivity average theorems, [1].

The computation of effective properties in terms of averages will be called the *direct approach*. In general it requires determination of the appropriate fields in the phases as defined by the field equations, interface continuity conditions, and external homogeneous boundary conditions, in order to compute the required averages. The interface conditions are, for solid mechanics,

$$u^{(1)}_i = u^{(2)}_i; \quad T^{(1)}_i = T^{(2)}_i \quad \text{on} \quad S_{12} \tag{2.5}$$

and for conductivity

$$\varphi^{(1)} = \varphi^{(2)}; \quad q^{(1)}_n = q^{(2)}_n \quad \text{on} \quad S_{12} \tag{2.6}$$

It follows that effective physical properties are in general functions of all the details of the constituent interface geometry. Actual direct computation is an extremely difficult problem, primarily because of the necessity to satisfy (2.5) or (2.6), and it must be restricted to simple models not only because of mathematical difficulties but also because the actual details of the interface geometry are never known.

An alternative definition of effective physical properties can be given in terms of energy expressions. This is based on the average theorem of virtual work, [1], which when specialized to heterogeneous elastic bodies with homogeneous boundary conditions states

$$\begin{aligned} U^\epsilon &= \frac{1}{2} C^*_{ijkl}\bar{\epsilon}_{ij}\bar{\epsilon}_{kl} V = W^\epsilon V \qquad (a) \\ U^\sigma &= \frac{1}{2} S^*_{ijkl}\bar{\sigma}_{ij}\bar{\sigma}_{kl} V = W^\sigma V \qquad (b) \end{aligned} \tag{2.7}$$

where U^ϵ is strain energy, U^σ is stress energy (this replaces the expression strain energy in terms of stresses), V is the volume, W is elastic energy per unit volume RVE, equation (2.7*a*) is associated with (2.1*a*), and (2.7*b*) is associated with (2.1*b*).

Similarly for conduction with homogeneous boundary conditions

$$\begin{aligned} Q^H &= \frac{1}{2}\mu^*_{ij}\bar{H}_i\bar{H}_j V \qquad (a) \\ Q^q &= \frac{1}{2}\rho^*_{ij}\bar{q}_i\bar{q}_j V \qquad (b) \end{aligned} \tag{2.8}$$

where Q is $1/2\int q_i(\mathbf{x})H_i(\mathbf{x})dV$, are associated with (2.2 *a*,*b*), respectively.

It is of interest to note that in the early stages of the theory of composite materials, effective elastic moduli were defined in terms of energy by expressions of type (2.7), following Einstein's pioneering paper on viscosity of dilute suspensions, [5]. The equivalence of the average and energy definitions of effective elastic moduli (2.3) and (2.7) was apparently only recognized in 1963, independently, by Hill [6] and by Hashin [3]. On the other hand, early work on effective conductivity employed the average definition (2.4).

The primary importance of (2.8) is in that such energy expressions can be bounded from above and below by extremum principles. Bounding requires construction of admissible fields that are much easier to construct than actual solutions. By judicious choice of boundary conditions, energy expressions can be expressed in terms of a single property, e.g., effective elastic modulus. Bounding of strain energy yields an upper bound on effective modulus. Bounding of stress energy yields an upper bound on the effective compliance, and thus on the reciprocal of the effective modulus, and consequently a lower bound on the effective modulus. Similar considerations apply for conduction.

Everything said so far has merely been concerned with effective properties. In the context of homogeneous media the analogous subject would be homogeneous material properties, which are of course measured in the laboratory using specimens with internal homogeneous fields. Indeed equations (2.3), (2.4), (2.7), and (2.8) have completely analogous homogeneous material counterparts in terms of field quantities "at a point." The question that now arises is: what is a suitable macrodescription of a heterogeneous material body when it is subjected to arbitrary boundary conditions and thus the internal fields are no longer statistically homogeneous? It is instructive to recall how this problem is resolved in the case of "homogeneous" continua. It is always assumed that such continua retain their properties regardless of specimen size, thus also for infinitesimal elements. This permits establishment of field equations in terms of field derivatives. However, all real materials have microstructure. Metals, for example, are actually polycrystalline aggregates and are thus heterogeneous materials. Therefore the differential element of the theory of elasticity is in reality a RVE, which is composed of a sufficiently large number of crystals, and whose effective elastic moduli are the elastic moduli of the theory of elasticity. Since the RVE is not infinitesimal it emerges that the classical theory of elasticity is an approximation that results in a macrodescription of a polycrystalline aggregate when the RVE size is "sufficiently small" in relation to the body dimensions.

The simplest point of view would be to adopt the same approximation for a composite material body. This would imply that the classical field equations of elasticity, conductivity, or other are *assumed* valid for the composite material body with effective properties replacing the usual homogeneous properties. Such an approach may be called the *classical approximation* and will now be discussed within the frame of more general theory. It is first necessary to define appropriate field variables for construction of field equations which are to describe a composite material as some equivalent continuum. The usual choice is *moving averages* over RVE or *ensemble averages*. A moving average of a function, e.g., displacement, is defined as

$$\bar{u}_i(\mathbf{x}) = \frac{1}{\Delta V}\int u'_i(\mathbf{x},\mathbf{x}')\,d\mathbf{x}' \tag{2.9}$$

where $\mathbf{x}$ is a position vector to a reference point in the RVE (e.g., centroid) defining its location, x'_i is a local coordinate system originating at $\mathbf{x}$ (Fig. 1) and the integration is over RVE.

The moving average concept is tied to the concept of geometrical scaling of a composite material which is indispensable for its representation as some equivalent continuum. The typical dimensions of phase regions, e.g., particle diameters, single crystal dimensions, are defined as the MICRO scale. The dimensions of the RVE are defined as the MINI scale and the dimensions of the composite material body as the MACRO scale. The equivalent continuum is a meaningful representation of a heterogeneous body only if

$$\text{MICRO} << \text{MINI} << \text{MACRO} \tag{2.10}$$

This will be referred to as the *MMM principle*. Displacements $u'_i(\mathbf{x},\mathbf{x}')$, strains $\epsilon'_{ij}(\mathbf{x},\mathbf{x}')$, and stresses $\sigma'_{ij}(\mathbf{x},\mathbf{x})$ within the phases are called microvariables while moving averages should by the same token be called minivariables. Accordingly computation of effective physical properties on the basis of phase geometry is frequently called *micromechanics*. It has been suggested that analysis of a composite as if it were some continuum, thus in terms of minivariables, should be called *minimechanics*, [7].

It is easily shown that moving averaging and differentiation are commutative (see e.g., [1]). Thus for example

$$\overline{\frac{\partial u_i'}{\partial x_j'}} = \frac{\partial \bar{u}_i}{\partial x_j} \tag{2.11}$$

This leads at once to the conclusion that

$$\overline{\epsilon_{ij}'(\mathbf{x}',\mathbf{x})} = \bar{\epsilon}_{ij}(\mathbf{x}) \tag{2.12}$$

$$\overline{\frac{\partial \sigma_{ij}'}{\partial x_j'}} = 0 = \frac{\partial \bar{\sigma}_{ij}}{\partial x_j} \tag{2.13}$$

Another point of view is based on the ensemble average. This average is based on the concept of an ensemble of composite specimens that have certain common characteristics such as: phase properties, phase volume fractions, and certain statistical moments of spatial variation of properties. The ensemble average of u_i is defined by

$$< u_i > (\mathbf{x}) = \frac{1}{N} \sum_{n=1}^{n=N} u_{in}(\mathbf{x}) \tag{2.14}$$

where there are N members of the ensemble. The operations of ensemble averaging and differentiation are commutative. Therefore (2.12) and (2.13) are also valid for ensemble averages; see e.g. [4].

In the case of SH fields, the moving average and the ensemble average are constants. It is also quite evident that they are equal, which is known as an ergodic hypothesis. The fundamental problem is the relation between moving averages or ensemble averages of statistically nonhomogeneous stress and strain. It is remarkable that the answer to this question has been given for both kinds of averages almost at the same time and that the relations are the same (Beran and McCoy [8]–ensemble average, Levin [9]–moving average), thus

$$\bar{\sigma}_{ij}(\mathbf{x}) = \int L^*_{ijkl}(\mathbf{x},\mathbf{x}')\bar{\epsilon}_{kl}(\mathbf{x}')d\mathbf{x}' \tag{2.15}$$

This important result shows that space variable averages are defined by what is called today a *nonlocal theory*. It is, however, not a practical result since the two point tensor $\mathbf{L}^*$ depends on phase properties and phase geometry in unknown fashion. For similar developments for conductivity of heterogeneous media see Beran, [10].

It is of interest to note that multipolar or strain gradient theories are special cases of nonlocal theory. This is seen from series expansion around $\mathbf{x}$, [8], from which it follows that (2.15) can be approximated by

$$\bar{\sigma}_{ij} = C^*_{ijkl}\bar{\epsilon}_{kl} + D^*{}_{ijklm}\bar{\epsilon}_{kl,m} + E^*_{ijklmn}\bar{\epsilon}_{kl,mn} + \ . \ . \ . \tag{2.16}$$

If only the first term in the right side of (2.16) is retained then

$$\bar{\sigma}_{ij}(\mathbf{x}) = C^*_{ijkl}\bar{\epsilon}_{kl}(\mathbf{x}) \tag{2.17}$$

which implies that variable averages are related just as constant averages in (2.3). The relations (2.11)–(2.13), and (2.17) are equivalent to classical elasticity equations where the displacements are moving or ensemble averages and the elastic properties are effective. Therefore, equation (2.17) is the essence of the classical approximation for heterogeneous media introduced in the foregoing. Classical approximations for other kinds of physical behavior are defined analogously. On the basis of accumulated experience with composite materials and heterogeneous media it appears that this simplest approximation is adequate for most engineering problems. The situation is different for dynamic problems with very high frequencies of vibration, thus very small wavelengths, and for very high stress and strain gradients, e.g., at crack tips.

This survey will be almost exclusively concerned with classical effective properties that define the classical approximation. The following discussions of analytical treatments will be divided, if possible, into three categories: (*a*) direct approach, (*b*) variational approach, and (*c*) approximations. Direct approach implies exact calculation of effective properties for some geometrical model of a composite material. The value of such results obviously depends on the realism of the model used but the number of choices that permit exact analysis is not large. Exact analysis implies that the microfields that are averaged satisfy the phase governing differential equations, the phase interface conditions, and the external boundary conditions on the composite. However, the latter need not be satisfied precisely but only in a suitable average sense (recall the boundary layer in the fundamental postulate of the theory of heterogeneous media). It frequently happens that effective properties computed for a certain model agree well with experimental data although the *details* of phase geometry of the model and the tested specimen are different. From this it should not be concluded that the model microfields are in similar agreement with specimen microfields, because effective properties are defined in terms of averages and functions that have the same averages can be very different in detail.

The variational approach is in a certain sense more powerful than the direct approach since it leads to bounds on effective properties when exact calculation is not possible. In particular, it is the only approach that can give results for irregular phase geometry in terms of partial information. The practical importance of the bounds obtained depends on their proximity.

Approximations are by their nature of unlimited variety. The most primitive approach is to postulate "semiempirical" expressions without the benefit of a model or theory. Such expressions will inevitably contain an undetermined parameter to be fitted to the experimental data. However, other experimental data will generally require a different value of the parameter and so measurement of the effective property has been replaced by measurement of a parameter, for no good reason. In more sophisticated and sometimes very ingenious versions, models of composite materials are analyzed on the basis of assumptions that are in principle incorrect, with the hope that the error introduced is not large. Only this kind of approximations will be discussed in the present survey and it will be endeavored to point out their relations to exact procedures. While approximations are unavoidable and often very valuable in the development of a complex subject of practical importance they should always be viewed with caution and should never displace available exact results.

3 Elastic Properties

3.1 Statistically Isotropic Composites

3.1.1 Introduction. A composite is statistically isotropic when its effective stress strain relation is independent of the choice of coordinate system. Important cases are: random mixture of two phases, matrix containing spherical type particles or randomly oriented elongated particles (e.g., short fibers), porous media, etc. It is of interest to note that a polycrystalline aggregate with randomly oriented crystals is a statistically isotropic composite with an infinite number of anisotropic phases. This will be discussed in Section 3.1.5. It follows just as for homogeneous elastic materials that in the isotropic case (2.3) reduce to the usual forms

$$\bar{\sigma}_{ij} = \lambda^*\bar{\epsilon}_{kk}\delta_{ij} + 2G^*\bar{\epsilon}_{ij} \tag{3.1.1}$$

or

$$\bar{\sigma} = 3K^*\bar{\epsilon} \quad (a) \quad \bar{s}_{ij} = 2G^*\bar{e}_{ij} \quad (b) \tag{3.1.2}$$

where K^* = effective bulk modulus; G^* = effective shear modulus; $\bar{\sigma}$, $\bar{\epsilon}$ = isotropic part of average stress, strain; and

$\bar{s}_{ij}, \bar{e}_{ij}$ = deviatoric part of average stress, strain. Other effective elastic properties such as E^* and ν^* are defined in the usual way. All of the interrelations of isotropic elastic moduli remain valid for effective elastic moduli.

3.1.2 Direct Approach. Central to the direct approach for two phase composites with isotropic phases are the elementary relations

$$K^* = K_1 + (K_2 - K_1)\frac{\bar{\epsilon}^{(2)}}{\bar{\epsilon}}v_2 \quad (a)$$
$$G^* = G_1 + (G_2 - G_1)\frac{\bar{e}_{ij}^{(2)}}{\bar{e}_{ij}}v_2 \quad (b) \qquad (3.1.3)$$

(*no sum on ij* in (*b*)), where 1, 2 indicate the phases, $\bar{\epsilon}^{(2)}$ and $\bar{e}_{ij}^{(2)}$ are averages of $\epsilon(\mathbf{x})$ and $e_{ij}(\mathbf{x})$ over phase 2, and v is volume fraction. The averages $\bar{\epsilon}$ and $\bar{e}_{ij}$ are induced by homogeneous boundary conditions of type (2.1*a*)

$$u_i(S) = \bar{\epsilon}x_i \quad \text{or} \quad u_i(S) = \bar{e}_{ij}x_j \qquad (3.1.4)$$

which arise from the decomposition $\bar{\epsilon}_{ij} = \bar{\epsilon}\delta_{ij} + \bar{e}_{ij}$. Relations of type (3.1.3) can also be written in terms of stress averages over one phase, see e.g., [1, 6].

The simplest case is dilute concentration of spherical or ellipsoidal particles of material 2 in matrix 1. The definition of "dilute" is that the state of strain in any one particle in the composite body under homogeneous boundary conditions is not affected by all the other particles. Thus the strain is that of a single particle in an infinite body and this happens to be uniform for an ellipsoid with far field homogeneous strain, Eshelby [11]. Thus for spherical particles it follows very simply from spherical particle strain expressions and (3.1.3) that

$$K^* = K_1 + (K_2 - K_1)\frac{3K_1 + 4G_1}{3K_2 + 4G_1}c \qquad (a)$$
$$G^* = G_1 + (G_2 - G_1)\frac{5(3K_1 + 4G_1)}{9K_1 + 8G_1 + 6_1(K_1 + 2G_1)G_2/G_1}c \qquad (b) \qquad (3.1.5)$$

given independently in [11-13]. Here 1 indicates matrix, 2 = spherical particles, and $c = v_2 << 1$. Results for randomly oriented ellipsoidal particles were given in [11]. The special cases of elongated ellipsoids (short fibers) and platelets have been discussed in [2].

Dilute concentration results may be viewed as the first two terms of a power series in particle volume fraction c. In this representation an effective property M^* may be written as

$$\frac{M^*}{M_1} = 1 + a_1c + a_2c^2 + \ldots \qquad (3.1.6)$$

Dilute concentration results such as (3.1.5) determine the coefficient a_1. Evaluation of a_2 as a much more difficult problem which has been resolved by Batchelor and Green [15] for identical rigid spheres embedded in incompressible elastic matrix (in the context of their treatment of effective viscosity of a rigid spheres suspension). Chen and Acrivos [14] have extended the analysis to the considerably more difficult case of any linear isotropic elastic spheres and matrix. The analyses require proper summation of the effects of all sphere doublets and unlike a_1, a_2 depends on particle statistics. For randomly and isotropically distributed identical rigid spheres in incompressible matrix the analysis of [15] provides the estimate $a_2 = 5.2 \pm 0.3$ while according to [14] $a_2 = 5.01$ in this case.

The case of finite concentration of spherical particles is an extremely difficult problem since computation of effective moduli requires a detailed elastic field analysis subject to interface continuity conditions (2.5) on *all* spherical surfaces. It appears that only one rigorous treatment for a special

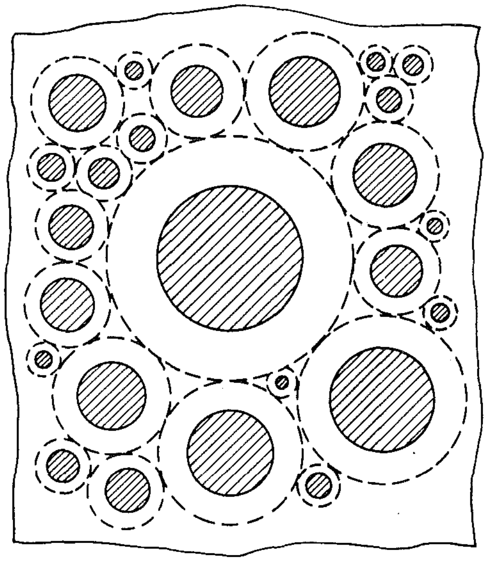

Fig. 2 Composite spheres assemblage; composite cylinders assemblage

arrangement of spheres called the *composite spheres assemblage* is available and this only for the effective bulk modulus. A composite sphere is defined by an isotropic sphere 2 enclosed in an isotropic concentric shell 1, Fig. 2. If the external boundary $r = b$ is subjected to purely radial displacement $u_r(b) = \epsilon^0 b$, the radial stress on the boundary is written $\sigma_{rr}(b) = 3K_s^*\epsilon^0$ where K_s^* follows from the analysis of this elementary, radially symmetric, elasticity problem and is a function of core and shell elastic moduli and of a/b. It is seen that to an external observer the composite sphere behaves just as a homogeneous sphere of radius b with bulk modulus K_s^*. If a homogeneous isotropic body with bulk modulus K_s^* is subjected to homogeneous isotropic strain $\epsilon^0\delta_{ij}$, the displacement and traction on any internal spherical surface with radius b are purely radial and are precisely those on the composite sphere boundary given in the foregoing. It follows that such a sphere can be replaced by the composite sphere without perturbing the homogeneous isotropic state of stress and strain in the body. Therefore such replacements can be performed again and again with composite spheres of different sizes as long as the spheres all have the same K_s^* which is certainly the case if in all composite spheres the ratio a/b and the constituent properties are the same. It may be rigorously shown that if the body is filled out with composite spheres, which diminish to infinitesimal size, then in the limit as the remaining volume goes to zero the effective bulk modulus of this composite material converges to the bulk modulus K_s^*. This model is called the composite spheres assemblage, Fig. 2. Its bulk modulus is given, Hashin [16], by

$$K^* = K_1 + (K_2 - K_1)\frac{(3K_1 + 4G_1)v_2}{3K_2 + 4G_1 - 3(K_2 - K_1)v_2}$$
$$= K_1 + \frac{v_2}{1/(K_2 - K_1) + 3v_1/(3K_1 + 4G_1)} \qquad (3.1.7)$$

where 1 indicates matrix and 2 indicates particles. The result (3.1.7) is easily generalized to the case of hollow spheres, reference [17], which is of practical importance for hollow microsphere reinforcement.

The basis for the results established so far is special internal geometry which permits exact analysis. Another class of exact solutions is based on special relations among the constituent properties. One of these cases is a two-phase material of arbitrary phase geometry where the shear moduli of the two phases are equal. In this case (3.1.7) is the exact solution for this case, Hill [6].

Another case is a weakly inhomogeneous medium which is defined by small deviation of local space variable moduli from their averages. Then, for any number of phases,

$$K^* = \bar{K} + \frac{\overline{K'^2}}{\bar{K} + 4\bar{G}/3} \tag{3.1.8}$$

where $\overline{K'^2}$ is the variance of K, Molyneux and Beran [18], which for two phases is given by $(K_2 - K_1)^2 v_1 v_2$. Then (3.1.8) can be interpreted as the beginning of a series expansion in $(K_2 - K_1)/\bar{K}$.

Finally, the isotropic version of (2.15) and (2.16) will be briefly discussed. In the case of statistical isotropy the two-point tensor L^*_{ijkl} appearing in (2.15) is statistically isotropic. Even in this simplest case this tensor is expressed in terms of six scalars which are unknown function of $r = |\mathbf{x} - \mathbf{x}'|$, of the phase geometry and the phase properties. This should be contrasted with (3.1.2) which require only two material constants. It has been shown, reference [8], that in the isotropic version of (2.16) D^*_{ijklm} vanish and the stress-strain relation reduces to that of first strain gradient theory, requiring classical elastic moduli K^*, G^*, and two effective material length parameters, l_1 and l_2. The latter have been computed, Beran and McCoy [8], for weakly non-homogeneous media in terms of two-point correlations of the space variable local elastic moduli. It appears that this is the only calculation of higher order elastic constants of heterogeneous media available in the literature.

3.1.3 Variational Bounding. When a composite material is statistically isotropic, the strain and stress energies (2.7) can be expressed in terms of (3.1.2) in the convenient forms

$$W^\epsilon = \frac{1}{2}(9K^*\bar{\epsilon}^2 + 2G^*\bar{e}_{ij}\bar{e}_{ij})$$
$$W^\sigma = \frac{1}{2}(\bar{\sigma}^2/K^* + \bar{s}_{ij}\bar{s}_{ij}/2G^*) \tag{3.1.9}$$

Appropriate homogeneous boundary conditions to obtain energy expressions with K^* only are

$$u_i(S) = \bar{\epsilon}x_i \quad T_i(S) = \bar{\sigma}n_i \tag{3.1.10}$$

To obtain energy expressions with G^* only

$$u_i(S) = \bar{e}_{ij}x_j \quad T_i(S) = \bar{s}_{ij}n_j \tag{3.1.11}$$

In the following, lower and upper bounds on some effective property M^* will be denoted $M^*_{(-)}, M^*_{(+)}$ implying that

$$M^*_{(-)} \le M^* \le M^*_{(+)} \tag{3.1.12}$$

For arbitrary internal phase geometry with isotropic phases the extremum principles of minimum potential and minimum complementary energy have been used with admissible linear displacement fields or with admissible constant stress to obtain the elementary bounds, Paul [19]

$$K^*_{(-)} = [\Sigma v_n/K_n]^{-1} = \frac{\overline{1}}{K} \quad (a)$$
$$K^*_{(+)} = \Sigma K_n v_n = \bar{K} \quad (b) \tag{3.1.13}$$

$$G^*_{(-)} = [\Sigma v_n/G_n]^{-1} = \frac{\overline{1}}{G} \quad (a)$$
$$G^*_{(+)} = \Sigma G_n v_n = \bar{G} \quad (b) \tag{3.1.14}$$

where n labels the phases. Averages such as $\bar{K}$ and $\bar{G}$ are (unfortunately) sometimes called "rules of mixture." It follows from the usual relation of Young's modulus E to K and G that

$$E^*_{(\pm)} = \frac{9K^*_{(\pm)}G^*_{(\pm)}}{3K^*_{(\pm)} + G^*_{(\pm)}} \tag{3.1.15}$$

for *any* bounds on K^* and G^*. Similar bounds for effective Poisson's ratio ν^* cannot be established.

For most applications, the bounds (3.1.13) and (3.1.14) are not close enough. Improved bounds for arbitrary statistically isotropic phase geometry have been derived, Hashin and Shtrikman [20], on the basis of new variational principles in terms of the elastic polarization tensor established in [21]. For two-phase media these results are:

$$K^*_{(-)} = K_1 + \frac{v_2}{1/(K_2 - K_1) + 3v_1/(3K_1 + 4G_1)} \quad (a)$$
$$K^*_{(+)} = K_2 + \frac{v_1}{1/(K_1 - K_2) + 3v_2/(3K_2 + 4G_2)} \quad (b) \tag{3.1.16}$$

$$G^*_{(-)} = G_1 + \frac{v_2}{1/(G_2 - G_1) + 6v_1(K_1 + 2G_1)/5G_1(3K_1 + 4G_1)} \quad (a)$$
$$G^*_{(+)} = G_2 + \frac{v_1}{(1/(G_1 - G_2) + 6v_2(K_2 + 2G_2)/5G_2(3K_2 + 4G_2)} \quad (b) \tag{3.1.17}$$

when

$$K_1 < K_2 \quad G_1 < G_2 \tag{3.1.18}$$

Bounds for any number of isotropic phases were also given in [20].

The original derivation of the bounds, reference [20], included some mathematical liberties. These were first removed in [22] by application of Fourier transform methods. Walpole [23] elegantly rederived the bounds by Green's function and potential methods using the classical extremum principles with the polarization concept in a manner indicated by Hill, reference [24]. He also generalized the bounds by removal of the restriction (3.1.18). Other elegant and interesting derivations and generalizations were given by Korringa [25], Willis [26, 27], Kröner [28], who introduced the notion of odd and even order bounds ((3.1.13) and (3.1.14) are first (odd) order and (3.1.16) and (3.1.17) are second (even) order), and Wu and McCullough [29].

Comparison of (3.1.16*a*) with (3.1.7) reveals the remarkable fact that they are the same. Since (3.1.7) is an exact result and since (3.1.16*a*) is a general lower bound in terms of phase volume fraction, it follows that (3.1.16*a*) is the *best possible lower bound in terms of volume fractions.* Similarly, (3.1.16*b*) is the *best possible upper bound* since it is at once interpreted as an exact result for a composite spheres assemblage with particles 1 of volume fraction v_1 and matrix 2. It has never been shown that (3.1.17) are also best possible in terms of volume fractions but they well may be. The bounds are generally in good agreement with experimental data. A recent particularly careful experimental investigation is given in [30] also citing other experimental investigations.

The bounds are of practical value for phase stiffness mutual ratios up to about 10. They obviously cannot provide good estimates for extreme phase stiffness ratios such as one rigid phase or an empty phase (porous medium). Since the only geometrical information entering is volume fractions, the bounds cannot distinguish between phases in the form of matrix or particles. Evidently, of two composites with same phases and volume fractions, one having very stiff matrix and the other very stiff particles – the first is much stiffer than the second, but both of them must obey the same bounds. Thus in the extreme case of one infinitely rigid phase, the upper bounds become infinite while in the other extreme case of an empty phase the lower bounds vanish.

To improve the bounds it is necessary to incorporate additional geometrical information. One way of doing this is in terms of higher order statistical information. The volume fractions of a statistically homogeneous material can be interpreted as one-point probabilities. Therefore it is plausible to try to incorporate additional geometrical information in terms of two-point, three-point . . . probabilities. This can be done in terms of the classical extremum principles, reference [4], or in terms of the polarization principles [27, 28], which have been used to derive (3.1.16) and (3.1.17). Kröner [34] has given results for so-called "perfectly disordered" materials, defined as composites in which properties of a phase are not correlated with properties of adjacent phases and thus the two-point probabilities become delta functions. This however, is not a realistic concept since it implies that phase regions are points or that the microscale in the MMM principle has been lost. For discussion of various statistical bounds derived see [4, 31, 32]. For discussion of the pertinent Russian literature see [33].

The improvement of bounds in terms of statistical information poses some intrinsic problems. Experimental determination of the required probability functions is an involved and time-consuming task and it is certainly easier to determine the effective moduli experimentally. Furthermore, the ususal multipoint probability functions cannot in general distinguish between matrix and particle phases. Therefore, they are not very useful for the case of one phase much stiffer than the other because the bounds will be far apart for the same reasons given previously in relation to bounds (3.1.16) and (3.1.17).

A different way to obtain improved bounds is to abandon general phase geometry and to construct bounds for a specific model. A case in point is the effective shear modulus of the composite spheres assemblage model discussed in the foregoing in the bulk modulus context. Since a sheared composite sphere does not behave as some equivalent homogeneous sphere, the replacement scheme employed for effective bulk modulus fails. However, solutions for a sheared composite sphere can be interpreted as admissible fields for the principles of minimum potential and minimum complementary energy. This gives the following upper bound for the case of particles stiffer than matrix, Hashin [16, 87].

$$G^*_{(+)} = G_1\left[1+\frac{c}{1/(\gamma-1)+A(1-c)-c(1-c^{2/3})/(Bc^{7/3}+C)}\right] \tag{3.1.19}$$

where c is particle volume fraction and

$$\gamma = G_2/G_1$$

$$A=\frac{2(4-5\nu_1)}{15(1-\nu_1)}$$

$$B=\frac{10(1-\nu_1)}{21}\cdot\frac{(7-10\nu_2)(7+5\nu_1)-\gamma(7-10\nu_1)(7+5\nu_2)}{4(7-10\nu_2)+\gamma(7+5\nu_2)}$$

$$C=\frac{10}{21}(7-10\nu_1)(1-\nu_1)$$

while the lower bound remains (3.1.17*a*). These bounds are much more restrictive than (3.1.17) (of course, at the price of very special geometry) and are close even for high particle/matrix stiffness ratio. The bounds coincide for small c (to yield (3.1.5*b*)) and also for c very close to 1.

3.1.4 Approximations. A well-known approximation for effective properties of particulate composites is the so-called Self Consistent Scheme (SCS). It is best discussed in terms of the relations (3.1.3) and in this sense it is a method to estimate the particle phase strain average. A typical particle is assumed to have spherical or ellipsoidal shape. In the most commonly used version of the method it is assumed that any

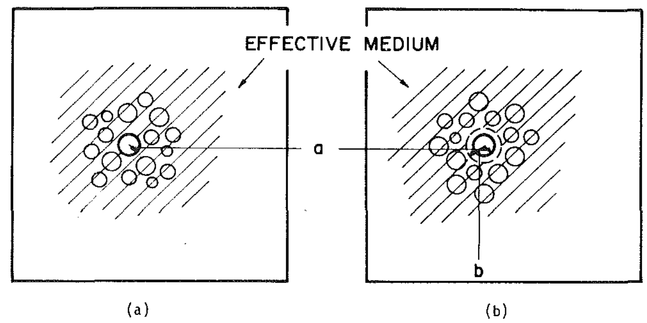

Fig. 3 Self-consistent scheme; (*a*) first version, and (*b*) generalized version

particle is embedded in a homogeneous body which has the unknown properties K^* and G^* and is subject to boundary conditions of type (3.1.4) at infinity, Fig. 3(*a*). This defines a boundary value problem which can be solved for an arbitrary ellipsoidal particle, Eshelby [11], resulting in uniform strain in the particle that is a function of K^* and G^*. Inserting the average particle strain into (3.1.3) results in two simultaneous algebraic equations for K^* and G^*. It appears that the method originates with Bruggeman [120] in the context of conductivity (see Section 6.4) who named it effective medium theory. We shall call this the first version of the SCS. There is, however, no compelling reason to embed the particle directly in the effective medium. We may imagine the particle to be embedded in a matrix shell which is embedded in the effective medium. We shall call this the generalized SCS. Obviously, the mathematics is now more difficult since it is necessary to solve a three-phase inclusion boundary value problem to obtain the particle strain. For this reason the generalized version has been carried out only for spherical surrounded by concentric spherical matrix shell.

The first version has been applied for spherical particles by Budiansky [35] and by Hill [36]. The final results as given by the latter are

$$\begin{aligned}\frac{v_1}{K^*-K_2}+\frac{v_2}{K^*-K_1}&=\frac{3}{3K^*+4G^*}\\ \frac{v_1}{G^*-G_2}+\frac{v_2}{G^*-G_1}&=\frac{6(K^*+2G^*)}{5G^*(3K^*+4G^*)}\end{aligned} \tag{3.1.20}$$

The method has been extended to randomly oriented ellipsoidal particles by Wu [37].

The essential problem with this simple method is that it violates the MMM principle. The inclusion boundary value problem defines variable elastic fields in the equivalent body. As has been explained in Part 2, the treatment of such a case requires micro, mini, and macroscales. In the simplest version, named the classical approximation, classical elasticity formulations can be used to obtain moving averages (or ensemble averages), thus minivariables. The solution of the particle boundary value problem in the SCS version requires satisfaction of displacement and traction continuity condition at particle-equivalent body interface. Thus microvariables (particle) are equated to minivariables (effective material) which is clearly meaningless, since the latter are averages of the former. Such a procedure would only be permissible for a particle whose size is of RVE order. To put it figuratively: the SCS assumes that a tree sees the forest – but a tree sees only other trees.

It may be shown that K^* and G^* as defined by (3.1.20) are always between the bounds (3.1.16) and (3.1.17). If plotted as functions of particle volume fraction they are tangent to the lower bounds at $v_2=0$ and tangent to the upper bounds at $v_2=1$. For particles much stiffer than matrix, equation (3.1.20) overestimates the effective moduli while for particles much more compliant than matrix, the effective moduli are underestimated. Indeed, for rigid particles (3.1.20) predicts infinite effective moduli for $v_2 = 0.50$ and for voids-zero effective moduli for $v_2 = 0.50$. These results are unreasonable. Furthermore, equation (3.1.20) are invariant to phase property interchange while a particulate composite must certainly be strongly biased to such interchange since stiff matrix defines a much stiffer composite than stiff particles. It must be concluded that this version of the SCS should be considered with caution. But it should be noted that there are cases when no other method is available, e.g., short randomly oriented fibers which can be represented as elongated prolate spheroids, or platelets, which can be regarded as flat oblate spheroids and are thus special cases of the treatment in [37].

In the generalized version a composite sphere consisting of a particle with radius a and a concentric matrix shell with radius b is embedded in the effective medium, Fig. 3(*b*). The ratio $\eta = a/b$ is now an unknown parameter which (arbitrarily) was assigned the value 1 in the first version. In most work with the generalized version it was assumed that $\eta^3 = v_2$ implying that volume fractions in the composite sphere are the same as in the composite. The first attempt appears to be due to Kerner [38] who made a number of unnecessary assumptions, obtained the correct result for K^* and an incorrect result for G^*. Interestingly enough, the result for K^* is the same as the composite spheres assemblage result (3.1.9). (The mathematical reasons for this are known but unpublished.) He obtained for G^* the lower bound (3.1.17*a*) but this result is incorrect since he made the assumption that in the three phase boundary value problem, Fig. 3, in shear, the state of strain in the particle is a uniform shear. Another incorrect analysis to obtain G^* was given by Van der Poel [39], who employed an inadmissible elasticity solution for the matrix shell. The correct solution for G^* was given by Smith [40] and an improved version by Christensen and Lo [41]. It is a complicated implicit result but is easily evaluated numerically. It is interesting to note that this G^* result is in between the shear modulus bounds for the composite spheres assemblage, (3.1.17*a*) and (3.1.19), and tangent to the bounds at both extremities of particle volume concentration $v_2 = 0,1$.

The generalized SCS appears to be a more realistic approximation than the first SCS version since the matrix shell mitigates the problem of satisfaction of interface conditions and results are no longer unbiased to phase interchange. Intuitively, it appears that in any embedding approximation the best results will be achieved when a typical "building block" of the composite material will be embedded. An element consisting of particle and surrounding matrix is such a building block but a particle is obviously not. However, the choice of η for a spherical composite element is not obvious. For G^*, Christensen and Lo [41] have interpreted the result as an approximate value for the composite spheres assemblage where of course $\eta^3 = v_2$. The case of arbitrary η has been considered in [42], in the context of conductivity, and it has been shown that the range $v_2 \leq \eta^3 \leq 1$ defines a family of nonintersecting curves which densely cover the region between the composite spheres assemblage result or best possible lower bound and the first SCS version.

A method that is related in spirit to the SCS is the so-called differential scheme, Boucher [43], McLaughlin [44]. It appears that this method also was first conceived by Bruggeman (see Section 6.4). It is essentially assumed that addition of a small amount of particles to a composite will increase the effective modulus by a dilute concentration-type expression with current effective modulus $M^*(v_2)$ replacing matrix modulus. This approximation again assumes that particles see an effective material and thus also violates the MMM principle.

In many composites of interest the particles are very elongated and can thus not be approximated by spheres. A case in point is randomly oriented fibers in a matrix, a material that is of significant modern technological importance and is called a chopped fiber composite. A reasonable approximate treatment for very long fibers is due to Christensen and Waals [45]. It essentially consists of orientation averaging of the effective properties of a randomly oriented composite cylinder. The results are actually upper bounds and are in reasonably good agreement with experimental data. If the fibers are short the only result available is the SCS treatment in [37], but this will probably considerably overestimate effective moduli for such large stiffness ratios as encountered for glass/polymer systems.

3.1.5 Polycrystalline Aggregates. Metals consist of irregularly shaped anisotropic crystalline grains whose principal crystallographic axes are mostly randomly oriented in space. Consequently, the material is statistically isotropic. If the elastic moduli of all single crystals are referred to one fixed system of axes the polycrystalline aggregate (PA) is described as a composite with an infinite number of anisotropic phases, each phase being defined by orientation of crystallographic axes of its member crystalline grains.

The problem of determination of the effective elastic moduli of a PA is one of long standing. Voigt [46] has analyzed the problem by assuming uniform strain in all crystals and Reuss [47], by assuming uniform stress in all crystals. Hill [48], in a pioneering paper, has shown on the basis of the classical extremum principles of elasticity, that the results are upper and lower bounds, respectively. To the writer's knowledge this paper has initiated the notion of bounding of effective moduli. These so-called Voigt and Reuss bounds are the analogues of (3.1.13) and (3.1.14).

Hashin and Shtrikman [49] have employed their variational principles [21] to develop a method for bounding of PA effective moduli and gave explicit results for cubic crystals. These are a considerable improvement of the Voigt-Reuss-Hill bounds. The method has been employed by Peselnick and Meister [50], Watt [51], and Watt and Peselnick [52], to construct bounds for hexagonal, triclinic, tetragonal, and monoclinic crystals. Hashin [53] has given bounds for a PA consisting of two different kinds of cubic crystals. It has been argued [4, p. 229], that the derivation of the bounds by this method implies the assumption that a certain integral vanishes. It has been shown in [53] that this assumption does not enter if the grains are "equiaxed" i.e., have no preferred dimension. Furthermore, Walpole's [54] elegant rederivation of the bounds based on Green's functions and potential theory also reaffirms the rigorous validity of the bounds.

Hershey [55] and Kröner [56] have used the self-consistent scheme with the assumption that a single crystal can be approximated by an anisotropic sphere embedded in the effective isotropic medium. This is the first SCS version and obviously the only one applicable in this case. Here the single crystal is the typical building block.

3.2 Fiber Composites

3.2.1 General. The composite material under consideration consists of aligned parallel fibers which are embedded in a matrix. Material specimens are generally cylindrical with fibers in generator direction x_1, Fig. 4. The phase geometry is defined by any transverse plane cut and is thus two-dimensional. The material is in a certain sense the two-dimensional analogue of a particulate composite. A more general two-dimensional material is a *fibrous composite* where the phases have cylindrical shape but are not necessarily in the form of matrix and fibers. This is the two-dimensional analogue of the general two-phase material. The most commonly used fibers are glass, carbon, and graphite. Their cross-sectional diameters are of the order of 0.01 mm and they are randomly located in the transverse plane. The composite is consequently *statistically transversely isotropic* which implies

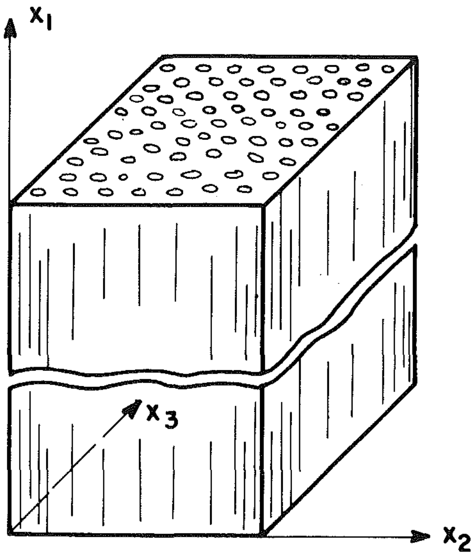

Fig. 4 Unidirectional fiber composite

that the effective stress strain-relations are invariant with respect to any rotation of the x_2, and x_3 axes about x_1. Such stress-strain relations are well known and may be written as

$$\bar{\sigma}_{11} = n^*\bar{\epsilon}_{11} + l^*\bar{\epsilon}_{22} + l^*\bar{\epsilon}_{33}$$
$$\bar{\sigma}_{22} = l^*\bar{\epsilon}_{11} + (k^* + G_T^*)\bar{\epsilon}_{22} + (k^* - G_T^*)\bar{\epsilon}_{33} \tag{3.2.1}$$
$$\bar{\sigma}_{33} = l^*\bar{\epsilon}_{11} + (k^* - G_T^*)\bar{\epsilon}_{22} + (k^* + G_T^*)\bar{\epsilon}_{33}$$

$$\bar{\sigma}_{12} = 2G_L^*\bar{\epsilon}_{12} \quad \bar{\sigma}_{23} = 2G_T^*\bar{\epsilon}_{23} \quad \bar{\sigma}_{13} = 2G_L^*\bar{\epsilon}_{13} \tag{3.2.2}$$

$$\bar{\epsilon}_{11} = \frac{\bar{\sigma}_{11}}{E_L^*} - \frac{\nu_L^*}{E_L^*}\bar{\sigma}_{22} - \frac{\nu_L^*}{E_L^*}\bar{\sigma}_{33}$$

$$\bar{\epsilon}_{22} = -\frac{\nu_L^*}{E_L^*}\bar{\sigma}_{11} + \frac{\bar{\sigma}_{22}}{E_T^*} - \frac{\nu_T^*}{E_T^*}\bar{\sigma}_{33} \tag{3.2.3}$$

$$\bar{\epsilon}_{33} = -\frac{\nu_L^*}{E_L^*}\bar{\sigma}_{11} - \frac{\nu_T^*}{E_T^*}\bar{\sigma}_{22} + \frac{\bar{\sigma}_{33}}{E_T^*}$$

where

k^* = transverse bulk modulus,
G_T^* = transverse shear modulus,
G_L^* = longitudinal shear modulus,
E_L^* = longitudinal Young's modulus,
E_T^* = transverse Young's modulus,
ν_L^* = longitudinal Poisson's ratio,
ν_T^* = transverse Poisson's ratio.

There are five independent effective elastic moduli and there are thus interrelations among the ones appearing in (3.2.1)-(3.2.3), see [1,58]. Two of these are:

$$G_T^* = \frac{E_T^*}{2(1+\nu_T^*)} \qquad (a)$$
$$\tag{3.2.4}$$
$$4/E_T^* = 1/G_T^* + 1/k^* + 4\nu_L^{*2}/E_L^* \qquad (b)$$

It has been shown in a general sense [1], that for isotropic or transversely isotropic constituents all effective property computations are defined by two-dimensional elasticity problems; antiplane strain for G_L^* and generalized plane strain for all others.

Hill [57], has shown that for any two-phase fibrous cylinder the effective properties n^*, l^*, k^*, E_L^*, and ν_L^* are interconnected. Two of such relations are:

$$E_L^* = \bar{E} + \frac{4(\nu_2-\nu_1)^2}{(1/k_2 - 1/k_1)^2}\left(\overline{\frac{1}{k}} - \frac{1}{k^*}\right)$$
$$\tag{3.2.5}$$
$$\nu_L^* = \bar{\nu} - \frac{\nu_2-\nu_1}{1/k_2 - 1/k_1}\left(\overline{\frac{1}{k}} - \frac{1}{k^*}\right)$$

Here an overbar denotes averages in the sense $\bar{E} = E_1 v_1 + E_2 v_2$. The relations are valid for isotropic and for transversely isotropic phases. They imply that a two-phase transversely isotropic fibrous material has only three independent effective elastic properties.

3.2.2 Direct Approach. To compute the effective elastic moduli it is best to proceed as follows: homogeneous boundary conditions (2.1*a*) are imposed on a fiber-reinforced cylinder with $\epsilon_{22}^0 = \epsilon_{33}^0 = \epsilon^0$, all others vanish. Then from (3.2.1) $\bar{\sigma}_{22} = \bar{\sigma}_{33} = 2k^*\epsilon^0$. Once k^* has been computed E_L^* and ν_L^* are known from (3.2.5) and l^* and n^* follow from moduli interrelations. To compute G_T^*, equation (2.1*a*) are applied with $\epsilon_{23}^0 \neq 0$, all others vanish. This defines G_T^* by $\bar{\sigma}_{23} = 2G_T^*\epsilon_{23}^0$ and it is required to solve a shearing plane strain boundary value problem. Similarly, G_L^* is defined by $\bar{\sigma}_{12} = 2G_L^*\epsilon_{12}^0$ when ϵ_{12}^0 is the only nonvanishing average strain and the boundary value problem that must be solved is now antiplane.

For purposes of computation, some model of a fiber composite must be assumed. It appears that the only models for which exact analyses are available are the *composite cylinder assemblage* (CCA) for which simple closed-form analytical results are available and periodic arrays of identical fibers which must, however, be analyzed numerically. The CCA model is the two-dimensional analogue of the composite spheres assemblage model, Section 3.1.2., Fig. 2. The basic element is a long composite cylinder consisting of inner circular fiber and outer concentric matrix shell. For certain kinds of boundary deformations or loadings the composite cylinder is externally indistinguishable from some homogeneous transversely isotropic cylinder. Such boundary conditions are: radial displacement and stress in the transverse plane, uniform extension in axial direction, and uniform longitudinal shearing displacement and traction on the boundary. This, however, is not so for boundary conditions equivalent to transverse shear or to transverse uniaxial stress. It follows that a composite cylinder can be replaced by an equivalent homogeneous cylinder with regard to elastic properties k^*, E_L^*, ν_L^*, n^*, l^*, and G_L^* but not with regard to properties G_T^*, E_T^* and ν_T^*. The CCA is constructed by filling out a homogeneous transversely isotropic cylinder of arbitrary transverse section with composite cylinders of different radii in which the fiber volume fraction and constituent properties are the same. It can then be shown that, in the limit, k^*, E_L^*, ν_L^*, n^*, l^*, and G_L^* of the assemblage are those of one composite cylinder. For details see [1]. In view of what has been said in the foregoing it is sufficient to determine k^* and G_L^* and all others of the preceding group follow. Results of interest are

$$k^* = \frac{k_1(k_2+G_1)v_1 + k_2(k_1+G_1)v_2}{(k_2+G_1)v_1 + (k_1+G_1)v_2} \tag{3.2.6}$$

$$= k_1 + \frac{v_2}{1/(k_2-k_1) + v_1/(k_1+G_1)}$$

$$E_L^* = E_1 v_1 + E_2 v_2 + \frac{4(\nu_2-\nu_1)^2 v_1 v_2}{v_1/k_2 + v_2/k_1 + 1/G_1} \tag{3.2.7}$$

$$\nu_L^* = \nu_1 v_1 + \nu_2 v_2 + \frac{(\nu_2-\nu_1)(1/k_1 - 1/k_2)v_1 v_2}{v_1/k_2 + v_2/k_1 + 1/G_1} \tag{3.2.8}$$

$$G_L^* = G_1\frac{G_1 v_1 + G_2(1+v_2)}{G_1(1+v_2) + G_2 v_1} \tag{3.2.9}$$

$$= G_1 + \frac{v_2}{1/(G_2-G_1) + v_1/2G_1}$$

where 1 is matrix and 2 is fibers. These results were first given by Hashin and Rosen [58], with (3.2.7) and (3.2.8) in different more complicated form. The method is easily extended to hollow fibers [1, 58]. It is of interest to note that for the usual case of fibers which are considerably stiffer than the matrix the third term in the right side of (3.2.10) is negligible which leads to the well-known result

$$E_L^* = E_1 v_1 + E_2 v_2 \tag{3.2.10}$$

This can be derived by elementary means and is also rigorously true for any fiber (or fibrous) geometry if Poisson's ratios of phases are equal.

The effective properties G_T^*, E_T^*, and ν_T^* can unfortunately not be derived by such a simple method and expressions are not available. However, close bounds have been established as will be discussed in the following.

Most of numerical analyses of effective elastic properties have been carried out for square or hexagonal periodic arrays of identical circular fibers, mostly by finite element and by finite different methods; see e.g., references [59–61]. The boundary conditions on a typical repeating element of the array can be established by symmetry considerations and thus the numerical analysis can be confined to a single repeating element. Effective properties are then found by numerical averaging. It should be pointed out that the square array is not a suitable model for glass, carbon, and graphite fibers since the model is not transversely isotropic but tetragonal. The square array is conceivably applicable to boron/aluminum composites in which fibers are arranged in patterns that resemble such arrays. It is, however, not applicable to any type of boron tapes or prepregs. The reason is that these are thin unidirectionally reinforced layers whose thickness is of the order of the diameter of *one* boron fiber and can therefore not be considered composite *materials* (remember the MMM principle).

The hexagonal array is a more suitable model since it is transversely isotropic. (All elastic materials of hexagonal symmetry are also transversely isotropic, see e.g., Love [62].) Comparison of effective elastic moduli results for hexagonal arrays with the CCA results (3.2.6)–(3.2.9) reveals the remarkable fact that they are numerically extremely close, up to fiber volume fractions of 70 percent [1], to all practical purposes. Such a remarkable agreement between two entirely different models leads one to the speculation that as long as the fibers are circular and are not in contact the actual locations of fibers and their diameter variations do not have significant effect on the effective moduli. If this is so the simple results (3.2.6)–(3.2.9) should apply for all such fiber composites.

The results discussed so far are for isotropic fibers and matrix. However, carbon and graphite fibers are very anisotropic. This anisotropy is due to the rope-like microstructure of these fibers which are composed of long ribbons of graphite crystallites. Since the microstructure is axially symmetric these fibers have transversely isotropic properties. Their stress strain relations are thus of form (3.2.1)–(3.2.3) with elastic properties k, G_T, G_L, E_L, E_T, ν_L, ν_T. A simple scheme to transform results and analysis procedures for isotropic fibers and matrix into corresponding results and procedures for transversely isotropic fibers (and matrix – if desired) has been given in [1, 63]. This is here summarized

Effective Property	Isotropic Phase Modulus	Transversely Isotropic Replacement	
	$k=\lambda+G$	k	
	G	G_T	
$k^*, G_T^*, E_T^*, \nu_T^*$	E	$G_T(3-G_T/k)$	(3.2.11)
	ν	$\frac{1}{2}(1-G_T/k)$	
G_L^*	G	G_L	(3.2.12)

E_L^* and ν_L^* can now be obtained from (3.2.5) where ν and k of fibers must be interpreted as ν_L and k of transversely isotropic fibers.

3.2.3 Variational Bounding. The development of variational bounding methods for fiber composites has many similarities to such development for statistically isotropic composites. The classical principles of minimum potential and complementary energy in conjunction with linear admissible displacement fields and constant stress fields easily yield Voigt and Reuss type bounds, the analogues of (3.1.13) and (3.1.14), for all of the effective moduli, Hill [57], see also [1]. These bounds are, however, not of practical value for the fiber composites used in practice. It has proved possible to established closer bounds in terms of volume fractions only. These bounds happen to be also CCA effective moduli expressions. In order to present them there is introduced for (3.2.6)–(3.2.9) the notation $k^*(1,2)$, $E_L^*(1,2)$, $\nu_L^*(1,2)$, $G_L^*(1,2)$ where 1,2 denote the phases. In addition denote

$$G_T^*(1,2) = G_1 + \frac{v_2}{1/(G_2-G_1)+v_1(k_1+2G_1)/2G_1(k_1+G_1)} \tag{3.2.13}$$

Then all lower bounds are given by $k^*(1,2)$, $E_L^*(1,2)$ etc. and all upper bounds are given by $k^*(2,1)$, $E_L^*(2,1)$ etc. (However, $\nu_L^*(1,2)$ and $\nu_L^*(2,1)$ may be either lower or upper. See [1,57] for criteria). All of the bounds except for G_T^* are at once recognized to be best possible in terms of volume fractions since they coincide with exact results for the CCA model. The bounds are the fibrous material counterpart of the bounds (3.1.16) and (3.1.17). Bounds for k^*, E_L^*, and ν_L^* have been given by Hill [57] and bounds for k^*, G_T^*, and G_L^* by Hashin [22]. The bounds are easily transformed to apply for transversely isotropic fibers by use of (3.2.11) and (3.2.12). Details are given in [63].

With respect to practical significance of the bounds, it is noted that E_L^* bounds are always extremely close, thus demonstrating that (3.2.10) is valid for any fiber composite or fibrous material. The ν_L^* bounds are useful estimates (about 15 percent margin). The margin between the other bounds depends strongly on fiber/matrix stiffness ratio. For glass/polymer and boron/polymer composites the bounds are too far apart. For carbon, graphite/polymer they are close enough to be regarded as results (for arbitrary fiber geometry!) [63].

It will be recalled that G_T^* of the CCA model could not be obtained by a direct approach. However, it can be bounded by use of the classical extremum principles of elasticity. Admissible fields are displacements and stresses in a sheared composite cylinder. Details are given in [1,58]. The results will be written for transversely isotropic fibers 2 and for isotropic matrix 1. In view of (3.2.11), equation (3.2.13) becomes

$$G_T^*(1,2) = G_1 + \frac{v_2}{1/(G_{T2}-G_1)+v_1(k_1+G_1)/2G_1(k_1+G_1)}$$

Then

$$G_{T(-)}^* = G_T^*(1,2)$$
$$G_{T(+)}^* = G_1\left\{1+\frac{(1+\beta_1)v_2}{\rho-v_2[1+3\beta_1^2 v_1^2/(\alpha v_2^3+1)]}\right\} \tag{3.2.15}$$

when

$$G_1 > G_{T2} \quad k_1 < k_2.$$

$$G_{T(-)}^* = G_1\left\{1+\frac{(1+\beta_1)v_2}{\rho-v_2[1+3\beta_1^2 v_1^2/\alpha v_2^3-\beta_1)]}\right\}$$
$$G_{T(-)}^* = G_T^*(1,2) \tag{3.2.16}$$

when

$$G_1 > G_{T2} \quad k_1 > k_2.$$

Here

$$\alpha=(\beta_1-\gamma\beta_2)/(1+\gamma\beta_2) \quad \rho=(\gamma+\beta_1)/(\gamma-1)$$
$$\beta_1=1/(3-4\nu_1) \quad \beta_2=k_2/(k_2+2G_{T2}) \qquad (3.2.17)$$
$$\gamma=G_{T2}/G_1$$

The bounds (3.2.15) are applicable for fiber composites with fibers stiffer than matrix, thus all composites with polymeric matrix. The bounds (3.2.16) are applicable for the case of matrix stiffer than fibers, and thus for all cases of carbon and graphite fibers in aluminum or other metallic matrix (note that while E_L of carbon and graphite fibers is larger than E of aluminum, the fiber moduli k and G_T are smaller than those of aluminum).

Bounds on E_T^* are simply obtained from (3.2.4b) as follows:

$$\frac{4}{E^*_{T(\pm)}}=\frac{1}{G^*_{T(\pm)}}+\frac{1}{k^*}+\frac{4\nu_L^{*2}}{E_L^*} \qquad (3.2.18)$$

3.2.4 Approximations. Different methods of approximation of varying degrees of sophistication have been devised over the years to determine the effective elastic properties of fiber composites. For the case of continuous fibers the exact methods discussed in Sections 3.2.2 and 3.2.3 are of sufficient accuracy and reliability to render such approximations obsolete. The purpose of the present discussion is to assess the status of some approximations that are still being used, in relation to the exact results given.

The self-consistent scheme (SCS) can be readily applied to fiber composites, similarly to its application to two-phase particulate composites. In the first version a circular fiber is regarded as being embedded directly in the equivalent transversely isotropic material. This yields algebraic equations for determination of all five effective moduli, Hill [64]. The results are in between the arbitrary phase geometry bounds tangent to the lower bounds (upper bounds) at fiber volume fraction zero (one). The results considerably overestimate the actual effective moduli. The first SCS version has also been applied to the case of unidirectional short fibers by considering them as elongated ellipsoids [65]. In the generalized version a composite cylinder in which fiber and matrix volume fractions are those of the composite is embedded in the equivalent transversely isotropic material. This has been done by Hermans [66] for the case $\eta^2=(a/b)^2=v_2$ and is the analogue of Kerners approach [38], see Section 3.1.4. The results for k^*, E_L^*, ν_L^*, and G_L^* are precisely the exact CCA results (3.2.9)–(3.2.12) (this was not noted by Hermans). The G_T^* expression obtained is the lower bound (3.2.17) but this result is incorrect [1, 2], since not all of the fiber/matrix and continuity conditions are satisfied by the analysis. It is curiously the same mistake made by Kerner in analysis of G^* of a particulate composite. The correct result for G_T^* in this context has been given by Christensen and Lo [2, 41]. It is algebraically lengthy but easily amenable to numerical evaluation. The case of unspecified η has been discussed in [1].

A method in which fiber/matrix interface conditions are approximately satisfied (in a force resultant sense) has been devised by Aboudi [173] and has been employed for analysis of aligned short fiber composites, assuming square fiber cross sections.

In some engineering circles, semiempirical so-called "Halpin-Tsai equations" [67], are sometimes used. These consist of the weighted average (3.2.10) for E_L^* (this is universally accepted), a similar weighted average for ν_L^* (this is not a good approximation), the CCA result (3.2.9) for G_L^*, the lower bound (3.2.13) for G_T^* (taken from Hermans' paper, discussed above) and an empirical expression for E_T^*. There seems to be no obvious reason for adopting such an approach.

3.3 Cracked Materials. An interesting and important heterogeneous medium is an elastic body containing many cracks. This heterogeneous material is unlike any discussed before since the empty phase comprising the cracks has zero volume fraction. The stiffness reduction produced by the cracks is due to the stress singularities at the crack tips. Because of these the stress energy for prescribed surface fractions is increased by a finite amount relative to the stress energy of the body without cracks. Thus the cracks increase the compliances and therefore decrease the stiffnesses.

It may be shown that when a cracked elastic body is subjected to boundary condition (2.1b), the effective elastic compliances S^*_{ijkl} are defined by

$$S^*_{ijkl}\sigma^0_{kl}=S_{ijkl}\sigma^0_{kl}+\gamma_{ij}$$
$$\gamma_{ij}=\frac{1}{2V}\sum^m\int_{S_m}([u_i]n_j+[u_j]n_i)dS \qquad (3.3.1)$$

where S_{ijkl} are matrix compliances, $[u_i]$ are displacement jumps across the crack faces, and the summation extends over all cracks. The matrix compliances S_{ijkl} may be isotropic or anisotropic. The symmetry of S^*_{ijkl} is defined by crack arrangement. Thus for randomly oriented cracks in an isotropic matrix the effective compliance tensor is isotropic while for cracks aligned in one direction it is orthotropic. In the former case (3.3.1) reduce to

$$\frac{1}{K^*}=\frac{1}{K}+\frac{2}{\sigma^0}\gamma_{ii}$$
$$\frac{1}{G^*}=\frac{1}{G}+\frac{2}{\sigma^0_{12}}\gamma_{12} \qquad (3.3.2)$$

An alternative important definition of effective compliances is provided by the energy relation

$$U^\sigma=U_0^\sigma+\Sigma\Delta U_m \qquad (3.3.3)$$

where

$$U^\sigma=\frac{1}{2}S^*_{ijkl}\sigma^0_{ij}\sigma^0_{kl}V$$
$$U_0^\sigma=\frac{1}{2}S_{ijkl}\sigma^0_{ij}\sigma^0_{kl}V \qquad (3.3.4)$$

and ΔU_m is the energy increase due to the mth crack in the presence of all others. This quantity can be expressed in terms of the crack stress intensity factor(s) (SIF), if known. In the case of isolated cracks this is a useful procedure since the SIF are simple known expressions. In the case of interacting cracks, however, the SIF become unknown functions of the mth crack length and of the entire crack geometry and ΔU_m, in the presence of other cracks, must be found in terms of an integral of growing mth crack length, a somewhat hopeless undertaking.

The simplest case is small density which is the analogue of dilute concentration discussed in the foregoing. It is assumed that the SIF and displacement jumps of each are given accurately by those of one crack in an infinite medium. The problem then becomes very simple. All results involve the crack density parameter α which is given by

$$\alpha=\begin{cases}\dfrac{1}{A}\Sigma a_m^2 & \text{plane cracks}\\[2ex] \dfrac{1}{V}\Sigma a_m b_m^2 & \text{elliptical cracks}\end{cases} \qquad (3.3.5)$$

where a_m is half crack length and A the area of the plane specimen in the former case, while a_m, b_m are the axes of the elliptical crack and V the volume in the latter case. All small crack density results are of the form

$$S^*_{ijkl} = S_{ijkl} + \alpha\Gamma_{ijkl} \qquad (3.3.6)$$

where Γ_{ijkl} depend on matrix properties and crack geometry. The first low crack density result given appears to be due to Bristow [68] who considered the case of randomly oriented line cracks. Walsh [69] computed the effective moduli for small density of randomly oriented elliptical cracks. Aligned circular cracks in an isotropic body were treated by Piau [70] in terms of long wave scattering (this is an unduly complicated method. The static method outlined in the foregoing is much simpler and gives the same results). Results for aligned line cracks in orthotropic bodies were given by Gottesman [71, 72]. The only exact direct result for arbitrary crack density appears to be due to Delameter, Herrmann, and Barnett [73] who computed the elastic properties of a sheet containing a periodic rectangular array of identical line cracks by an analytical/numerical procedure.

The self-consistent scheme approximation is readily adaptable to the present problem. The energy change due to any one crack is estimated by assuming that the crack is situated in the effective medium. The results are then given by (3.3.6) replacing in the Γ_{ijkl} functions matrix compliances by effective compliances. The SCS generally underestimates the stiffness of cracked materials. The SCS has been applied to the case of randomly oriented elliptical cracks by Budiansky and O'Connell [74] and to the case of circular cracks aligned in planes by Hoenig [75]. An SCS treatment for a plane orthotropic body with line cracks distributed parallel to the two axes of orthotropy has been given in [76].

Variational methods to obtain bounds have been recently initiated. Willis [77] has obtained bounds for the compliances of a material containing aligned penny-shaped cracks which are identical to the small density results for that case. Gottesman [71] and Gottesman, Hashin, and Brull [72] have employed the classical variational principles to obtain bounds in terms of admissible fields which are elasticity solutions for subregions of the cracked body, each containing one crack.

This concludes the discussion of elastic behavior. There are many important aspects that could not be included here. For excellent recent expositions see Willis [27], which also includes wave propagation, McCoy [30], which emphasizes statistical treatment, and Walpole [78]. See also Watt [177].

4 Thermal Expansion and Moisture Swelling

4.1 General. The effective thermal expansion coefficients of a composite material are defined similarly to those of a homogeneous material. A large composite material body with no load on the boundary is subjected to uniform temperature rise φ. It may be trivially shown, from steady state heat conduction, that if φ = const. on the boundary, this is also true throughout the composite. The resulting average strains are then expressed as

$$\bar{\epsilon}_{ij} = \alpha^*_{ij}\varphi \qquad (4.1.1)$$

and α^*_{ij} are defined as the effective thermal expansion coefficients. Since the body is not loaded the average stresses vanish but not the microstresses. For further general discussion of the subject see [1].

The fundamental result in theory of thermal expansion of two-phase composites is due to Levin [79] and extended by Rosen and Hashin [82] to generally anisotropic composites and phases in the forms.

$$\alpha^*_{ij} = \bar{\alpha}_{ij} + (\alpha^{(2)}_{kl} - \alpha^{(1)}_{kl})P_{klrs}(S^*_{rsij} - \bar{S}_{rsij}) \qquad (4.1.2)$$
$$= \alpha^{(1)}_{ij} + (\alpha^{(2)}_{kl} - \alpha^{(1)}_{kl})P_{klrs}(S^*_{rsij} - S^{(1)}_{rsij})$$

where

$$P_{klrs}(S^{(2)}_{rsij} - S^{(1)}_{rsij}) = I_{ijkl}$$

Here $\bar{\alpha}_{ij}$ and $\bar{S}_{ijkl}$ are the averages of the composites' thermal expansion coefficients and compliances, respectively, and I_{ijkl} is the fourth-rank symmetric unit tensor. The result (4.1.2) uniquely determines α^*_{ij} in terms of phase properties and effective compliances S^*_{ijkl} for the most general kind of thermoelastic two-phase composite. It has been derived by application of the theorem of virtual work. The derivation is restricted to the case of two phases.

For temperature dependence, equation (4.1.2) remains valid with all temperature dependent properties taken at final temperature (secant properties).

An interesting general result is obtained for a porous or cracked body. If the matrix is given the index 1 then

$$\alpha^*_{ij} = \alpha^{(1)}_{ij} \qquad (4.1.3)$$

for *any pore or crack geometry*. This may be deduced from (4.1.2) and also simply from first principles.

The case of moisture swelling is very similar. Moisture absorption is characterized by the specific moisture concentration c which is the moisture absorbed by unit mass of the material. In a homogeneous anisotropic body the stress-free moisture-swelling strains are given by

$$\epsilon_{ij} = \beta_{ij}c \qquad (4.1.4)$$

where β_{ij} are the swelling coefficients. If the body is isotropic $\beta_{ij} = \beta\delta_{ij}$. If there are, in addition, mechanical strains produced by stresses, the simplest assumption is to superpose them on the swelling strains thus obtaining the complete analogue of uncoupled thermoelasticity. The analogy extends to all governing equations with α_{ij} replaced by β_{ij}. In composites there are certain differences between thermal expansion and moisture swelling. When the boundary of a composite is subjected to a constant humidity environment moisture will seep in through the boundary until a steady state of constant c is achieved but this will take much longer (days) than for temperature where steady state is achieved after very short time. Furthermore, in most applications, one is concerned with a polymeric matrix that absorbs moisture, containing particles or fibers that do not. Thus these particles or fibers act as insulators and their swelling coefficients are zero. It follows from (4.1.2) that the effective swelling coefficients β^*_{ij}, are given by

$$\beta^*_{ij} = \beta^{(1)}_{ij} - \beta^{(1)}_{kl}P_{klrs}(S^*_{rsij} - S^{(1)}_{rsij}) \qquad (4.1.5)$$

where 1 indicates absorbing phase.

Finally it is noted that expressions for effective specific heats c^*_v, at constant volume, and c^*_p, at constant pressure, for two-phase materials have been obtained in [82]. To practical purposes they are given by the volume fraction-weighted averages of the corresponding phase specific heats.

4.2 Statistically Isotropic Composites. For a two-phase material with isotropic phases all tensors in (4.1.3) become isotropic. This leads to the simple result

$$\alpha^* = \alpha_1 + \frac{\alpha_2 - \alpha_1}{1/K_2 - 1/K_1}(1/K^* - 1/K_1) \qquad (4.2.1)$$

where K^* is the effective bulk modulus and K_1 and K_2 are the phase bulk moduli. This fundamental result has been given in [79] and also, independently, in [80–82]. Introducing the exact composite spheres assemblage result (3.1.7) into (4.2.1) it follows that for that model

$$\alpha^* = \alpha_1 v_1 + \alpha_2 v_2 + \frac{4(K_2 - K_1)(\alpha_2 - \alpha_1)G_1 v_1 v_2}{3K_1K_2 + 4G_1(K_1 v_1 + K_2 v_2)} \qquad (4.2.2)$$

Arbitrary phase geometry bounds for α^* which are best possible are easily established. The key to the procedure is the result (3.1.13*a*) from which it follows that (4.2.1) is a monotonic function of K^*, thus replacement of K^* by a bound in (4.2.1) produces a bound on α^*. Introducing the bounds (3.1.16) into (4.2.1) and denoting the result (4.2.2) as $\alpha^*(1,2)$ yields the best possible bounds

$$\alpha^*(1,2) \le \alpha^* \le \alpha^*(2,1) \qquad (4.2.3)$$

when

$$(K_2 - K_1)(\alpha_2 - \alpha_1) < 0 \ (a) \quad K_1 < K_2; \quad G_1 < G_2 \ (b) \qquad (4.2.4)$$

Most materials obey (4.2.4*a*). If, however, this inequality reverses then the bounds (4.2.3) also reverse.

All results are applicable to moisture swelling. β^* is obtained by setting $\alpha_2 = 0$ and replacing α_1 by β_1, the swelling coefficient of the absorbent phase.

4.3 Fiber Composites. A statistically transversely isotropic fiber composite has two expansion coefficients, α_L^* in fiber direction and α_T^* transverse to the fibers. If fibers and matrix are isotropic it follows from (4.1.3) that

$$\alpha_L^* = \alpha_1 + \frac{\alpha_2 - \alpha_1}{1/K_2 - 1/K_1}\left[\frac{3(1-2\nu_L^*)}{\mathrm{E}_L^*} - \frac{1}{K_1}\right]$$

$$\alpha_T^* = \alpha_1 + \frac{\alpha_2 - \alpha_1}{1/K_2 - 1/K_1}\left[\frac{3}{2k^*} - \frac{3(1-2\nu_L^*)\nu_L^*}{\mathrm{E}_L^*} - \frac{1}{K_1}\right]$$

These results were implicitly given in [79] and explicitly in [82]. A detailed derivation is given in [1].

To obtain the thermal expansion coefficients for the CCA model the results (3.2.9)–(3.2.11) are introduced into (4.3.1). For numerical treatment the numerical results for effective moduli are introduced into (4.3.1). (Unfortunately, expensive numerical analyses of effective thermal expansion coefficients, ignoring (4.3.1), still persist.) The results (4.3.1) also apply to aligned short fiber composites in terms of their effective elastic properties. They are also easily generalized to transversely isotropic phases, [63], thus for carbon and graphite fibers.

Moisture swelling is of particular importance for fiber composites. Again the results are obtained by setting $\alpha_2 = 0$ and $\alpha_1 = \beta_1$. This yields from (4.3.1) the longitudinal and transverse swelling coefficients β_L^* and β_T^*.

4.4 Approximations. In view of the unique relations (4.1.3), (4.2.1), and (4.3.1) between effective thermal expansion coefficients and effective elastic properties approximate treatments to obtain the former are redundant and should be confined to effective elastic properties.

5 Viscoelastic Properties

5.1 General. Study of viscoelastic behavior of composite materials is of interest primarily because of the considerable number of composites that have a polymeric matrix. This is the case for most fiber composites, the most common polymer being epoxy for unidirectional fiber composites, polyimide for elevated temperature applications, and polyesters for chopped fiber composites. Because of the time-dependent properties of the polymer the composite will also exhibit time dependence. This implies that deformations grow (creep), stresses relax in time, and amplitudes of vibration are attenuated. The significance of such effects is magnified at elevated temperatures. For a review article on the subject see [83]. A comprehensive detailed treatment emphasizing fiber composites is contained in [1].

Analysis of properties of viscoelastic composites is closely related to analysis of elastic composites. When a viscoelastic composite is subjected to homogeneous boundary conditions $u_i(S) = \epsilon_{ij}^0 x_j H(t)$ or $T_i(S) = \sigma_{ij}^0 n_j H(t)$, where $H(t)$ is the Heaviside step function, the average strains are $\epsilon_{ij}^0 H(t)$ in the former case and the average stresses are $\sigma_{ij}^0 H(t)$ in the latter case. It follows from linearity that in these cases

$$\begin{aligned}\bar{\sigma}_{ij}(t) &= C_{ijkl}^*(t)\,\epsilon_{kl}^0 \\ \bar{\epsilon}_{ij}(t) &= S_{ijkl}^*(t)\,\sigma_{kl}^0\end{aligned} \qquad (5.1.1)$$

Then $C_{ijkl}^*(t)$ is defined as the effective relaxation moduli tensor and $S_{ijkl}^*(t)$ is the effective creep compliance tensor. These relations assume the usual hereditary form of viscoelastic stress-strain relations when strain and stress averages are general time functions. When the composite is statistically isotropic the effective stress-strain relations reduce to the usual isotropic forms in terms of effective bulk relaxation modulus $K^*(t)$, shear relaxation modulus $G^*(t)$, bulk creep compliance $I^*(t)$, and shear creep compliance $J^*(t)$.

If the problem of determination of internal fields in a viscoelastic composite subjected to homogeneous boundary conditions is formulated and the Laplace Transform (LT) is applied to all equations, the LT problem is entirely analogous to the corresponding problem of an elastic composite. Elastic phase moduli C_{ijkl} are replaced by transform domain (TD) moduli $p\hat{C}_{ijkl}(p)$ where p is the transform variable and lower denotes LT. There then emerges a correspondence principle for quasi-static properties of viscoelastic composites, Hashin, [84]: "*The effective TD moduli/compliances of a viscoelastic composite are obtained by replacement of phase elastic moduli by corresponding phase TD moduli in the expressions for effective elastic moduli/compliances of an elastic composite with identical phase geometry.*" In symbols: let expressions for effective elastic properties be written

$$\begin{aligned}{}^eC_{ijkl}^* &= F_{ijkl}[{}^e\mathbf{C}^{(1)}, {}^e\mathbf{C}^{(2)}, \ldots, \{g\}] \\ {}^eS_{ijkl}^* &= f_{ijkl}[{}^e\mathbf{C}^{(1)}, {}^e\mathbf{C}^{(2)}, \ldots, \{g\}]\end{aligned} \qquad (5.1.2)$$

where, the left e superscript denotes elastic property, ${}^e\mathbf{C}^{(m)}$ denote phase elastic moduli, and $\{g\}$ denotes geometry. Then

$$\begin{aligned}p\hat{C}_{ijkl}^*(p) &= F_{ijkl}[p\hat{\mathbf{C}}^{(1)}(p),\ p\hat{\mathbf{C}}^{(2)}(p), \ldots, \{g\}] \\ p\hat{S}_{ijkl}^*(p) &= f_{ijkl}[p\hat{\mathbf{C}}^{(1)}(p),\ p\hat{\mathbf{C}}^{(2)}(p), \ldots, \{g\}]\end{aligned} \qquad (5.1.3)$$

Equations (5.1.3) reduce the determination of quasi-static effective elastic properties to LT inversion, provided that expressions for effective elastic properties are known. It should be noted that in the present context the presence of an elastic phase in the composite implies that its properties are left unchanged in the replacement scheme (the TD moduli of an elastic material are its elastic moduli).

It has been shown [85, 1] that the values of effective viscoelastic properties at times 0, ∞ are given by the simple scheme

$$\begin{aligned}C_{ijkl}^*({}^0_\infty) &= F_{ijkl}[\mathbf{C}^{(1)}({}^0_\infty),\ \mathbf{C}^{(2)}({}^0_\infty), \ldots, \{g\}] \\ S_{ijkl}^*({}^0_\infty) &= f_{ijkl}[\mathbf{C}^{(1)}({}^0_\infty),\ \mathbf{C}^{(2)}({}^0_\infty), \ldots, \{g\}]\end{aligned} \qquad (5.1.4)$$

which implies that initial (final) values of effective relaxation moduli and creep compliances are determined by associated effective elastic moduli and compliances in terms of initial (final) values of viscoelastic phase properties. It has been argued [83], that relations of type (5.1.9) could be used to approximate effective viscoelastic properties for the whole time range, but such "quasi-elastic" approximation must be regarded with caution.

Relaxation moduli and creep compliances are necessary information for quasi-static analysis of viscoelastic materials. In the important case of steady state vibrations another set of viscoelastic properties called *complex moduli* are indispensable. For homogeneous viscoelastic materials the complex moduli are defined by the coefficients of linear relations between stress and strain amplitudes in steady state vibrations; see e.g., Christensen [86]. For composite materials the analogous definition is in terms of linear relations between averages of stress and strain amplitudes. This raises a problem, for the spatial variation of stress and strain in a composite material in a state of vibration can never be SH since oscillatory stress and strain in homogeneous bodies can never be spatially uniform. In the simplest approach a classical approximation of type (2.17) is adopted. Then the effective complex moduli are defined for sinusoidally space variable average (moving or ensemble) strain and stress as follows: If

$$\bar{\epsilon}_{ij}(\mathbf{x},t) = \tilde{\bar{\epsilon}}_{ij}(\mathbf{x})e^{\iota\omega t} \quad \bar{\sigma}_{ij}(\mathbf{x},t) = \tilde{\bar{\sigma}}_{ij}(\mathbf{x})e^{\iota\omega t} \tag{5.1.5}$$

Then

$$\tilde{\bar{\sigma}}_{ij}(\mathbf{x}) = \tilde{C}^*_{ijkl}(\iota\omega)\tilde{\bar{\epsilon}}_{kl}(\mathbf{x}) \quad \tilde{\bar{\epsilon}}_{ij}(\mathbf{x}) = \tilde{S}^*_{ijkl}(\iota\omega)\tilde{\bar{\sigma}}_{kl}(\mathbf{x}) \tag{5.1.6}$$

where $\tilde{C}^*_{ijkl}$ and $\tilde{S}^*_{ijkl}$ are effective complex moduli and compliances, respectively, $\iota = \sqrt{-1}$, and ω is the frequency of vibration. For statistical isotropy (5.1.6) reduce to

$$\tilde{\bar{\sigma}} = 3\tilde{K}^*(\iota\omega)\tilde{\bar{\epsilon}} \quad \tilde{\bar{s}}_{ij} = 2\tilde{G}^*(\rho\omega)\tilde{\bar{e}}_{ij} \tag{5.1.7}$$

where the stress and strain amplitude are the usual isotropic and deviatoric parts. It is customary to separate complex moduli into real and imaginary parts. Thus

$$\begin{aligned} \tilde{K}^*(\iota\omega) &= K^*(\omega) + \iota K^{*\,\prime\prime}(\omega) \\ \tilde{G}(\iota\omega) &= G^{*\,\prime}(\omega) + \iota G^{*\,\prime\prime}(\omega) \end{aligned} \tag{5.1.8}$$

Loss tangents are defined by

$$\tan\delta^*_K = K^{*\,\prime\prime}/K^{*\,\prime} \quad \tan\delta^*_G = G^{*\,\prime\prime}/G^{*\,\prime} \tag{5.1.9}$$

All of (5.1.5)-(5.1.9) are analogous to corresponding relations for homogeneous materials, thus for viscoelastic phases of a composite material.

The effective complex moduli are related to effective elastic moduli by the correspondence principle for complex moduli of composites, Hashin [87]: *"The effective complex moduli (compliances) of a viscoelastic composite are obtained by replacement of phase elastic moduli by corresponding phase complex moduli in the expressions for the effective elastic moduli (compliances) of a composite with identical phase geometry."* In symbols

$$\begin{aligned} \tilde{C}^*_{ijkl}(\iota\omega) &= F_{ijkl}[\mathbf{C}^{(1)}(\iota\omega), \quad \mathbf{C}^{(2)}(\iota\omega), \ldots, \{g\}] \\ \tilde{S}^*_{ijkl}(\iota\omega) &= f_{ijkl}[\mathbf{C}^{(1)}(\iota\omega), \quad \mathbf{C}^{(2)}(\iota\omega), \ldots, \{g\}] \end{aligned} \tag{5.1.10}$$

where the functions on the right sides are the same as in (5.1.4) and $\mathbf{C}^{(1)}(\iota\omega)$, $\mathbf{C}^{(2)}(\iota\omega)$, . . . denote the phase complex moduli.

The evaluation of (5.1.10) can be greatly simplified when the phase loss tangents are small, which is usually the case [1, 87]. In this event

$$\begin{aligned} C^{*\prime}_{ijkl}(\omega) &= F_{ijkl}[\mathbf{C}^{(1)\,\prime}(\omega), \mathbf{C}^{(2)\,\prime}(\omega), \ldots, \{g\}] \\ S^{*\prime}_{ijkl}(\omega) &= f_{ijkl}[\mathbf{C}^{(1)\,\prime}(\omega), \mathbf{C}^{(2)\,\prime}(\omega), \ldots, \{g\}] \end{aligned} \tag{5.1.11}$$

while imaginary parts are given in terms of derivatives of (5.1.11) with respect to the components of real parts of phase complex moduli, [87]. Examples will be given in the following.

Viscoelastic properties of polymers are strongly temperature dependent and thus also the effective viscoelastic properties of composites with polymeric constituents (generally the matrix). It has been pointed out by Schapery [83], that the results given here can be modified for temperature dependence by means of a correspondence principle when the composite consists of a thermorheologically simple phase and an elastic phase. It is also possible to obtain thermoviscoelastic expansion coefficients in this case [83]. This method fails, however, for composites consisting of thermorheologically simple phases with different time shifts.

5.2. Statistically Isotropic Composites

5.2.1 Direct Approach. The most important case is a viscoelastic matrix containing elastic particles. It can mostly be assumed that the matrix is viscoelastic in shear only and thus has an elastic bulk modulus K_1, shear relaxation modulus $G_1(t)$, and shear creep compliance $J_1(t)$. Available elastic results can be converted into corresponding viscoelastic results. As an example for various approaches the expression for elastic bulk modulus of the composite spheres assemblage is considered to obtain $K^*(t)$ of the corresponding viscoelastic case. According to (5.1.3), (3.1.7) converts into [84]:

$$p\hat{K}^*(p) = K_1 + (K_2 - K_1)\frac{[3K_1 + 4p\hat{G}_1(p)]v_2}{3K_2 + 4p\hat{G}_1(p) - 3(K_2 - K_1)v_2} \tag{5.2.1}$$

If $G_1(t)$ is known only numerically (5.2.1) can be converted into an integral equation in the time domain that must be solved numerically for $K^*(t)$. One possibility to obtain analytical solutions is to represent the shear stress-strain relation of the matrix by a suitable spring-dashpot model whose differential equation is

$$P(D)s_{ij} = Q(D)e_{ij} \quad D = \frac{d}{dt} \tag{5.2.2}$$

where P and Q are polynomials in D. Simple examples are the Maxwell model and "standard solids." It follows from LT of (5.2.2) that

$$p\hat{G}(p) = Q(p)/2P(p) \tag{5.2.3}$$

Introducing this into (5.2.1) the result can be inverted to obtain $K^*(t)$. Finally, the theorems (5.1.4) can be utilized to obtain $K^*(0)$ and $K^*(\infty)$. The former is merely the elastic result (3.1.7) with $G_1(0)$ and the latter becomes upon assuming very small $G_1(\infty)$

$$K^*(\infty) = (v_1/K_1 + v_2/K_2)^{-1} \tag{5.2.4}$$

which interestingly is the lower bound (3.1.13*a*). For the extreme cases of rigid particles (5.2.1) can be inverted in general fashion for the whole time domain

$$K^*(t) = \left[K_1 + \frac{4}{3}G_1(t)v_2\right]/v_1 \tag{5.2.5}$$

for cavities

$$I^*(t) = \left[1/3K_1 + \frac{3}{4}J_1(t)v_2\right]v_1 \tag{5.2.6}$$

Such simple results are of course exceptional.

The case of shear is much more difficult since an exact result for G^* of an elastic particulate composite for the entire range of volume fractions is not available. The dilute concentration result (3.1.5*b*) can be transformed to viscoelasticity but this is only of academic interest. There is one general result for incompressible viscoelastic matrix containing either rigid particles or voids. It has been shown [84] that in these cases

$$\frac{G^*(t)}{G_1(t)} = \frac{J_1(t)}{J^*(t)} = \frac{{}^eG^*}{{}^eG_1} = \psi \tag{5.2.7}$$

where the extreme right is the ratio between effective elastic shear modulus and matrix shear modulus for same composite with elastic incompressible matrix containing rigid particles or voids.

Effective complex moduli are easily obtained by utilization of (5.1.10). Assuming again elastic particles 2 and matrix 1 viscoelastic in shear only (5.1.10) reduce to

$$\begin{aligned} \tilde{K}^*(\iota\omega) &= F_K[K_1, \tilde{G}_1(\iota\omega), K_2 G_2; \{g\}] \\ \tilde{G}^*(\iota\omega) &= F_G[K_1, \tilde{G}_1(\iota\omega), K_2, G_2, \{g\}] \end{aligned} \tag{5.2.8}$$

where F_K and F_G denote expressions for effective elastic moduli. Define the matrix loss tangent by

$$\tan\delta = G_1''(\omega)/G_1'(\omega) \tag{5.2.9}$$

It has been shown [87], that for small $\tan\delta$ (smaller than 0.1, which is usually the case) (5.2.8) can be accurately approximated by

$$G^{*\prime}(\omega)=F_G[K_1,G_1'(\omega),K_2,G_2,\{g\}]$$
$$G^{*\prime\prime}(\omega)=G_1''\partial F_G/\partial G_1' \tag{5.2.10}$$

with a similar approximation for K^*. The relations (5.2.8) are easily applied to (3.1.7) to obtain the complex bulk modulus for the CCA model. Details are given in [1]. For complex shear modulus of viscoelastic matrix with rigid particles or voids

$$\tilde{G}^*(\iota\omega)/\tilde{G}_1(\iota\omega)=\psi$$

which implies

$$G^{*\prime}(\omega)=\psi G_1'(\omega)$$
$$G^{*\prime\prime}(\omega)=\psi G_2'(\omega) \tag{5.2.11}$$
$$\tan\delta_{G^*}=\tan\delta_{G_1}$$

where ψ is given by (5.2.7). Thus the shear loss tangent of viscoelastic incompressible matrix is not changed by rigid particles or voids.

5.2.3 Variational Bounding. Unfortunately the variational bounding methods that are so powerful for elastic composites are only of limited usefulness for viscoelastic composites. In view of the mathematical analogy between elasticity problems and Laplace transformed quasi-static viscoelastic problems, all bounds on effective elastic moduli convert into bounds on Laplace Transforms of effective viscoelastic properties. However, a bound on Laplace Transform does not convert into a bound on the transformed function.

One special situation where elastic property bounds are easily converted is a viscoelastic incompressible matrix with rigid particles or voids, discussed in the foregoing (5.2.7). Suppose that in the elastic case, bounds are defined by

$$\psi_{(-)}{}^eG_1\le{}^eG^*\le\psi_{(+)}{}^eG_1$$

It follows that

$$\psi_{(-)}G_1(t)\le G^*(t)\le\psi_{(+)}G_1(t) \tag{5.2.12}$$

Another special situation is for times 0, ∞ when in view of (5.1.4) all elasticity bounds convert into bounds in terms of viscoelastic properties at times 0, ∞.

Bounding methods for effective complex moduli have been given by Christensen [88] and Roscoe [89, 90]. Of special interest are the general relations between effective moduli and effective complex moduli bounds derived in [90]. However, because of the complicated relations between real and imaginary parts of complex moduli and compliances such bounds are only rarely of practical value. In the case of small loss tangents, which is the usual situation in practice, it follows from the reasoning leading to (5.1.11) that all effective elastic moduli bounds convert in bounds for real parts of effective complex moduli by replacing phase moduli in elasticity bound expressions by corresponding real parts of phase complex moduli. The situation for bounds on imaginary parts is more complicated. Such bounds can be established by methods used for the analogous problem of lossy dielectrics; see Section 6.3.

5.2.4 Approximations. In view of the correspondence principles, any approximation for an effective elastic modulus can be interpreted as an approximation for the LT of an effective relaxation modulus or for an effective complex modulus. In the first case inversion into the time domain is required, which may be very difficult. It is also quite possible that the inversion will aggravate the inaccuracies introduced by the approximation. In the second case the separation into real and imaginary parts may introduce additional approximations.

Laws and McLaughlin [91] have used the first version of the SCS to estimate viscoelastic properties of a particulate composite based on a time domain analysis. It would seem preferable to use the generalized SCS version. The required analysis for shear modulus would of course be very difficult and it appears that no attempt in this direction has been made.

An important viscoelastic composite is a chopped fiber composite, e.g., glass fibers in polymeric matrix. As has been mentioned before, the only available analytical approach for effective modulus is the first version of the SCS [37].

5.3 Fiber Composites. The case of interest is a unidirectional fiber composite consisting of viscoelastic matrix and elastic fibers. The effective stress-strain relaxation type relations are described by the viscoelastic hereditary analogue of (3.2.1) and (3.2.2) in terms of relaxation moduli $n^*(t)$, $l^*(t)$, $k^*(t)$, $G_L^*(t)$, and $G_T^*(t)$. This defines time-dependent stress in terms of given strain history. For creep, thus time-dependent strain in terms of given stress history, it is necessary to use the viscoelastic analogue of the elastic strain-stress relations (3.2.3) in terms of creep compliances $e_L^*(t)$, $e_T^*(t)$, $c_L^*(t)$, $c_T^*(t)$, $g_L^*(t)$, and $g_T^*(t)$ which are the viscoelastic analogues of the elastic compliances $1/E_L^*$, $1/E_T^*$, $-\nu_L^*/E_L^*$, $-\nu_T^*/E_T^*$, $1/G_L^*$ and $1/G_T^*$, respectively. All of the interrelations between elastic properties now apply in transform space and thus become quite complicated in the time domain.

Results and methods discussed in Sections 5.1. and 5.2 are all applicable to fiber composites. In the direct approach the CCA results (3.2.6)–(3.2.9), if necessary modified for anisotropic fibers, can be interpreted as Laplace Transforms of effective viscoelastic properties. Assuming matrix viscoelastic in shear, only elastic matrix properties G_1, k_1, and ν_1 are replaced by $p\hat{G}_1$ and by

$$p\hat{k}_1=K_1+p\hat{G}_1/3$$
$$\nu_1(p)=(3K_1-2p\hat{G}_1)/2(3K_1+p\hat{G}_1) \tag{5.3.1}$$

Some simple results obtained in this fashion are

$$E_L^*(t)=E_1(t)v_1+E_2v_2 \quad e_L^*(t)=e_1(t)v_1+v_2/E_2 \tag{5.3.2}$$

where $E_1(t)$ and $e_1(t)$ are matrix Young's relaxation modulus and creep compliance, respectively. Since $E_2>>E_1(t)$ the time-dependent part of these expressions is generally negligible and thus for practical purposes the fiber composite is elastic in fiber direction.

For fibers with shear modulus infinitely larger than matrix shear modulus (not carbon, graphite)

$$G_L^*=G_1(t)\frac{1+v_2}{1-v_2} \quad g_L^*(t)=g_1(t)\frac{1-v_2}{1+v_2} \tag{5.3.3}$$

where $g_1(t)$ is matrix shear creep compliance.

Other results are not as simple. For detailed analysis see [1]. Some important general conclusions are that the time dependence of $n^*(t)$, $l^*(t)$, $k^*(t)$, and $c_L^*(t)$ is weak. Such results may be conveniently obtained by using the final and initial value theorems (5.1.4). The situation with respect to $G_T^*(t)$, $g_T^*(t)$, $E_T^*(t)$, $\nu_T^*(t)$, and $c_T^*(t)$ is much more complicated since only bounds are available for their elastic counterparts. If elastic bounds are close, any of them that is analytically sufficiently simple can be regarded as an approximate result and utilized with the correspondence principle to (it is hoped) obtain the corresponding viscoelastic results. This is the situation for carbon or graphite reinforced polymers where the bounds on G_T^* and E_T^* are extremely close, [63].

6 Conduction

6.1 General. The subject under consideration is steady state conduction through a composite material to be charaterized by an effective conductivity tensor. General aspects of the problem have already been discussed in Part 2. While the present discussion will be in the context of thermal conduction it should be realized that the problems of thermal conduction, electrostatics, magnetostatics, and diffusion are mathematically analogous. Therefore everything said applies to all of these. A list of analogous quantities is given in the following.

Physical Subject	φ	$\mathbf{H} = -\nabla\varphi$	μ	$\mathbf{q}$
thermal conduction	temperature	gradient	thermal conductivity	heat flux
electrical conduction	potential	intensity	electrical conductivity	current density
electrostatics	potential	intensity	permittivity	electric induction
magnetostatics	potential	intensity	magnetic permeability	magnetic induction
diffusion	concentration	gradient	diffusivity	

The subject of diffusion is of particular current interest for composite materials in the context of moisture absorption.

It is helpful to realize that there is a strong conceptual relation between the problems of effective elastic properties and of effective conductivity. Every theorem and result in one area has its counterpart in the other. The conceptual relation between elasticity and conduction is summarized in the following table:

	Elasticity		Conduction
u_i	= displacement	φ	= temperature
ϵ_{ij}	= strain	$-\varphi,_i$	= gradient
σ_{ij}	= stress	q_i	= flux
T_i	= traction	q_n	= normal flux component
C_{ijkl}	= elastic moduli	μ_{ij}	= conductivities
S_{ijkl}	= compliances	ρ_{ij}	= resistivities
	rigid phase		superconductor
	empty phase		insulator

All of the methods, models, and results for elastic composites have their conductivity counterparts. The mathematics of the conductivity problems is considerably simpler than that of the elasticity problems since vectors take the place of second rank tensors and the scalar Laplace equation takes the place of the vectorial elasticity displacement equations.

6.2 Statistically Isotropic Composites

6.2.1 Direct Approach. When the composite is statistically isotropic the effective conductivity and resistivity tensors appearing in (2.4) assume the form

$$\mu^*_{ij} = \mu^*\delta_{ij} \quad \rho^*_{ij} = \rho^*\delta_{ij} \quad \mu^*\rho^* = 1 \tag{6.2.1}$$

Let a two-phase composite material body be subjected to the homogeneous boundary condition (2.2*a*). Then μ^* can be expressed in the form

$$\mu^* = \mu_1 + (\mu_2 - \mu_1)(\bar{H}_i^{(2)}/H_i^0)v_2 \quad \text{(no sum on } i\text{)} \tag{6.2.2}$$

which is the counterpart of (3.1.3). An analogous definition can be given in terms of flux averages, see e.g., reference [42].

Equation (6.2.2) is the basis for dilute concentration results for ellipsoidal or spherical particles 2 embedded in a matrix 1. The temperature gradient in an ellipsoidal inclusion when the far temperature field is linear is uniform and is a function of ellipsoidal axes, μ_1 and μ_2 and orientation of the ellipsoid. Thus (6.2.2) is easily evaluated for randomly oriented ellipsoids by suitable averaging. The special case of spherical particles appears to be, historically, the first exact solution for an effective property of a composite material, Maxwell [92]. For discussion of various dilute concentration results see [93].

The problem of determination of the second term in a concentration expansion of type (3.1.6) has been treated by Jeffrey [94] on the basis of the Batchelor-Green method [15] and by McCoy and Beran [95]. For randomly distributed identical spheres the analysis of [94] gives a_2 as a function of μ_2/μ_1. The largest value of a_2 is $a_2(\infty) = 4.51$.

The composite spheres assemblage (CSA) model is easily analyzed for conductivity, [96]. The result is

$$\mu^* = \mu_1 + \frac{v_2}{1/(\mu_2 - \mu_1) + v_1/3\mu} \tag{6.2.3}$$

Another model which has been treated is a cubical array of equal spheres in matrix, Rayleigh [97], refined by Meredith and Tobias [98], McPhedran and McKenzie [99], and Bergman, [100]. It is interesting to note that the results for this model and for the CSA (6.2.3) are numerically very close, up to 40 percent particle volume fractions [101], where they begin to diverge. (Note that a cubical array is isotropic for conductivity but not for elasticity.) This divergence is easily understood since in the cubical array, particle volume fractions cannot exceed 52 pecent, i.e., close packing, while in the CSA model 100 percent volume fraction of particles is theoretically possible. Up to 40 percent volume fraction the results agree very well with experimental data [101]. It may be recalled that a similar situation has been encountered with respect to fiber composite elastic moduli for hexagonal array and composite cylinder assemblage results. As in that case it may be conjectured that the effective conductivity of a statistically isotropic particle composite depends primarily on volume fractions and only insignificantly on the statistics of sphere size and locations as long as the spheres are "not close."

The statistical approach for conductivity in particular and for heterogeneous media in general originates with a pioneering paper by Brown [102] in which it was shown that μ^* for a two phase medium is given by the series.

$$\frac{\mu^*}{\bar{\mu}} = 1 - \frac{1}{3}\left(\frac{\mu_2 - \mu_1}{\bar{\mu}}\right)^2 v_1 v_2 + \left(\frac{1}{9}v_1 v_2^2 - \frac{1}{3}v_1^2 v_2 + v_1^2 J\right)\left(\frac{\mu_2 - \mu_1}{\bar{\mu}}\right)^3 + \ldots \tag{6.2.4}$$

where λ is a complicated integral involving three and two-point probability functions of the phase geometry. It is seen that the first two terms define the case of weak inhomogeneity. This has been directly derived by Beran and Molyneux [103], on the basis of statistical field analysis of the weakly inhomogeneous case. For further aspects of statistical analysis see Beran [4, 104].

6.2.2 Variational Bounding. The basis for variational bounding of conductivity is the definition (2.8) of conductivity which for statistically isotropic composites assumes the form

$$Q^H = \frac{1}{2}\mu^*\bar{H}_i\bar{H}_i V \quad Q^q = \frac{1}{2\mu^*}\bar{q}_i\bar{q}_i V \tag{6.2.5}$$

Application of the classical variational principles for steady state conductivity (these are the counterparts of the principles of minimum potential and complementary energies of elasticity) in conjunction with linear admissible temperature or constant admissible fluxes easily yields the elementary bounds

$$\frac{\bar{1}}{\mu} \leq \mu^* \leq \bar{\mu} \tag{6.2.6}$$

These were first derived by Wiener [105] by very complex methods.

Improved bounds in terms of volume fractions have been derived by Hashin and Shtrikman [96], on the basis of variational principles involving the polarization vector. These bounds are:

$$\begin{aligned} \mu^*_{(-)} &= \mu_1 + \frac{v_2}{1/(\mu_2-\mu_1)+v_1/3\mu_1} \quad (a) \\ \mu^*_{(+)} &= \mu_2 + \frac{v_1}{1/(\mu_1-\mu_2)+v_2/3\mu_2} \quad (b) \\ \mu_2 &> \mu_1 \end{aligned} \tag{6.2.7}$$

It is seen that (6.2.7*a*) is the same as the CSA result (6.2.3) and therefore (6.2.7*b*) coincides with a CSA result where the particles are of material 1 and the matrix of material 2. Therefore the bounds (6.2.7) are *best possible in terms of volume fractions* and their improvement requires additional geometric information. Bounds have also been given in [96] for any number of phases. It is of interest to note that if the bounds (6.2.7) are expanded in series such as (6.2.4) the first two terms are identically equal to the first two terms of (6.2.4). An interesting derivation of the bounds (6.2.7) has been given by Bergman [106].

Various bounds in terms of additional statistical information have been derived. For discussion see [32, 104]. Prager [107] has shown that a known value for effective conductivity can be used to obtain better bounds than (6.2.7) for another two-phase material with the same phase geometry but different phase properties.

The bounds (6.2.7) are not useful when one of the phases is highly conducting relative to the other. Unfortunately, all of the improved bounds in terms of higher order statistical information such as three-point correlations do not provide a practical answer to this problem because the statistical information is more difficult to measure than the effective property. Even such improved bounds are not close enough since statistical description in terms of the usual *n*-point probabilities or correlations cannot dectect which phase is matrix and which phase is particles. This topological distinction is, however, of primary importance for the case under consideration.

If a random two-phase composite contains a small amount of highly conducting phase 2 the chances are that this will be in the form of particles. Then μ^* will be governed by the poorly conducting matrix 1 and will be close to the lower bound. If the relative volume of phase 2 is increased it will at some volume fraction start to form a continuous skeleton and thus μ^* will increase dramatically, almost discontinuously, and will become close to the upper bound. This phenomenon is called *percolation* and its initiation is called percolation threshold. Discussion of this important phenomenon is not within the scope of the present survey. For literature and discussion see, e.g., reference [108].

6.3 Anisotropic and Fiber Composites. For a transversely isotropic fiber composite the conductivity effective constitutive relations (2.4) assume the form

$$\bar{q}_1 = \mu^*_L \bar{H}_1 \quad \bar{q}_2 = \mu^*_T H_2 \quad \bar{q}_3 = \mu^*_T \bar{H}_3 \tag{6.3.1}$$

where x_1 is fiber direction, μ^*_L is effective longitudinal conductivity, and μ^*_T is effective transverse conductivity.

It is easily shown, e.g., reference [42], that

$$\mu^*_L = \mu_1 v_1 + \mu_2 v_2 \tag{6.3.2}$$

for any cylindrical fibrous phase geometry. The problem of μ^*_T determination requires the solution of a plane potential problem with interface conditions (2.6) in the transverse plane and plane homogeneous boundary conditions of type (2.2). Examination of the governing equations reveals that this problem is entirely analogous to the longitudinal shearing problem which must be solved to determine the longitudinal shear modulus G^*_L, Section 3.2.5. This may be called the longitudinal shearing-transverse conduction analogy. It follows that [1], if

$$G^*_L = F(G_1, G_2, \{g\}) \tag{6.3.3}$$

then

$$\mu^*_T = F(\mu_1, \mu_2, \{g\}) \tag{6.3.4}$$

where $\{g\}$ denotes interface geometry. This analogy is also valid for numerical analysis results as has been noted for the case of square arrays of circular fibers by Springer and Tsai [109]. It then follows [1, 110] from (3.2.9) that for the composite cylinder assemblage model

$$\mu^*_T = \mu_1 + \frac{v_2}{1/(\mu_2-\mu_1)+v_1/2\mu_1} \tag{6.3.5}$$

Keller [111] has shown that for a periodic fiber composite with two axes of symmetry (e.g., a rectangular array of circular fibers) the two effective conductivities in the principal transverse directions obey a simple relation. For the case of a square array with equal conductivity μ^*_T in these two directions this relation assumes the form

$$\mu^*_T(\mu_1, \mu_2)\mu^*_T(\mu_2, \mu_1) = \mu_1 \mu_2 \tag{6.3.6}$$

If μ^*_T is insensitive to interchange of phase 1 with phase 2 this yields the simple result

$$\mu^*_T = \sqrt{\mu_1 \mu_2} \tag{6.3.7}$$

Some geometries for which (6.3.7) is valid are alternating patterns of equal squares (checkerboard) and regular hexagons. Keller stated that (6.3.7) is also valid for statistically transversely isotropic fibrous material of random geometry which is insensitive to phase interchange. Such a situation occurs for completely random mixtures of cylindrical phases of 0.50 volume fraction each. Keller's conjecture was proved by Mendelson [112]. However, all of these results are not of much practical value for fiber composites.

The longitudinal shearing-transverse conductivity analogy implies that all shear modulus bounds convert directly into transverse conductivity bounds. It follows that the best possible bounds transform into similar bounds for any transversely isotropic fibrous material. Thus [1, 110]

$$\begin{aligned} \mu^*_{T(-)} &= \mu_1 + \frac{v_2}{1/(\mu_2-\mu_1)+v_1/2\mu_1} \\ \mu^*_{T(+)} &= \mu_2 + \frac{v_1}{1/(\mu_1-\mu_2)+v_2/2\mu_2} \end{aligned} \tag{6.3.8}$$

If the phases are transversely isotropic, μ_1 and μ_2 are their transverse conductivities.

Bounds on μ^*_T in terms of statistical information (three-point correlation functions) were given by Beran and Silnutzer [113] and Hori and Yonezawa [114]. Prager type bounds (in terms of known conductivity for certain specified values of phase conductivities) by Schulgasser [115, 116] who also discussed statistical bounds. Bounds for transversely isotropic composites consisting of matrix with aligned spheroidal particles or circular cracks have been derived by Willis [26].

6.4 Lossy Dielectrics. When a lossy dielectric is subjected to sinusoidally alternating potential the induction and intensity vectors are not in phase. If the phase induction is $\mathbf{D}e^{\iota\omega t}$ and the intensity is $e^{\iota\omega t}$ then these are related by

$$\mathbf{D} = \bar{\mu}(\iota\omega)H \tag{6.4.1}$$

where

$$\tilde{\mu}(\iota\omega) = \mu'(\omega) - \iota\mu''(\omega) \tag{6.4.2}$$

It is seen by comparison with viscoelastic vibrations, Section 5.1, that (6.4.2) is the analogue of the complex modulus. Here μ' is called the dielectric constant, μ'' which is customarily taken as negative – the loss factor, while the loss tangent is defined by

$$\tan\delta = \mu''/\mu' \tag{6.4.3}$$

A composite material consisting of lossy dielectric phases has an effective complex dielectric constant or permittivity

$$\tilde{\mu}^*(\iota\omega) = \mu^{*\prime}(\omega) - \iota\mu^{*\prime\prime}(\omega) \tag{6.4.4}$$

which relates average induction amplitude to average intensity amplitude. It follows just as in viscoelasticity that if the permittivity for nonlossy phases is

$$\mu^* = F(\mu_1, \mu_2, \ldots \{g\}) \tag{6.4.5}$$

then the complex permittivity is

$$\tilde{\mu}^*(\iota\omega) = F[\tilde{\mu}_1(\iota\omega), \tilde{\mu}_2(\iota\omega), \ldots \{g\}] \tag{6.4.6}$$

where $\{g\}$ denotes the phase geometry. This is the complete analogue of the complex moduli correspondence principle (5.1.10) and permits conversion of any effective permittivity result into a complex permittivity result. If the phase loss tangents are small, equation (6.4.6) converts into

$$\begin{aligned} &\mu^{*\prime}(\omega) = F[\mu_1'(\omega), \mu_2'(\omega), \ldots \{g\}] \quad (a) \\ &\mu^{*\prime\prime}(\omega) = \mu_1'' \frac{\partial F}{\partial \mu_1'} + \mu_2'' \frac{\partial F}{\partial \mu_2'} + \ldots \quad (b) \end{aligned} \tag{6.4.7}$$

All of these results have been given by Schulgasser and Hashin [117]. It follows for example that the CSA result (6.2.3) converts at once into a corresponding result for $\mu^{*\prime}$ while $\mu^{*\prime\prime}$ must be found in terms of the derivatives of (6.2.3) with respect to μ_1' and μ_2'.

The bounds (6.2.7) convert into best possible bounds for $\mu^{*\prime}$ for any statistically isotropic two-phase geometry. The situation with respect to $\mu^{*\prime\prime}$ bounds is much more complicated. Such bounds have been derived in [117] for small loss tangent. Bounds for $\mu^{*\prime}$ and $\mu^{*\prime\prime}$ without this simplification have also been derived by Milton [118] and Bergman [119].

6.5 Approximations. Many approximations have been derived over the years. For comprehensive discussion see Boettcher [93] and Landauer [108]. The CSA result (6.2.3) has been derived as an approximation by a number of scientists in the 19th Century, Mossotti in 1850, Clausius in 1879, Lorentz in 1868, and Lorenz in 1880. For historical details see [108]. The self-consistent scheme has been applied in the versions discussed in Section 3.1.4. In the first version, in which a sphere is directly embedded in the effective medium, by Bruggeman [120]. This is sometimes called symmetric effective medium theory in the conductivity context. The result is

$$\frac{\mu_1 - \mu^*}{\mu_1 + 2\mu^*} v_1 + \frac{\mu_2 - \mu^*}{\mu_2 + 2\mu^*} v_2 = 0 \tag{6.5.1}$$

This appears to be the initiation of the SCS to composite materials. Similar results have been obtained by Landauer [121].

The generalized SCS with $\eta^3 = v_2$ (see Section 3.1.4) has been applied by Kerner [122] with some unnecessary assumptions. The result is again (6.2.3). The case of arbitrary η has been investigated by Hashin [42]. It was shown that η is restricted to the range $v_2 \le \eta^3 \le 1$ and that the results corresponding to this range define a family of nonintersecting curves that densely cover the region between (6.1.7*a*) and (6.4.1). It is not clear which member of this family of SCS results is to be preferred.

The differential scheme discussed in Section 3.1.4. has been applied to the present problem by Bruggeman [120] and this appears to be the origination of the method.

7 Failure

7.1 Introduction. The problem of the analysis of failure of composite materials is by an order of magnitude more difficult than the problem of physical property prediction which has been discussed until now. When a composite specimen is subjected to increasing load and/or temperature, microfailures will develop at some stage. These may be in the form of matrix cracks, fiber ruptures, interface separation, and local plastification. As loading continues they will multiply and ultimately merge to produce catastrophic failure. The failure process described cannot be followed analytically since: (*a*) knowledge of microfailure criteria is incomplete; (*b*) the stresses and strains that produce microfailures cannot be analytically obtained since they are strongly dependent on the details of microstructure, which are not known; and (*c*) even if a model of microstructure is assumed, stress analysis in the presence of interacting microfailures is a prohibitively difficult problem. While the problem of microfield determination also arises in property analysis, its implications are different in that context since effective properties are relations between *averages* and thus errors in details are not necessarily significant. Furthermore, the powerful variational bounding method, which can be applied with incomplete definition of microstructure, is not available for the failure problem.

In spite of these difficulties, much valuable work has been done in failure prediction but the treatment must necessarily be qualitative rather than quantitative, in a "strength of materials" rather than "theory of elasticity" spirit. The present discussion will not in any sense aim at reviewing the immense existing body of literature but will emphasize available analytical ideas and guidelines. Almost everything said is concerned with fiber composites. Static and fatigue failure of unidirectional fiber composites are discussed from the point of view that they are the building blocks of laminates. Finally, static and fatigue failure of laminates are discussed in one Section.

7.2 Static Failure: One Stress Component. In "homogeneous" materials it is customary to determine failure when only one stress component, e.g., uniaxial stress, is active, experimentally, and to construct failure criteria for combined stress in terms of one-dimensional ultimate stresses. An excellent review of the subject has been given by Paul [123]. A similar point of view may be adopted for composite materials and this will be discussed in the next section. In this section we consider the important subject of the relation of one-dimensional average ultimate failure stresses to the microstructure and to the constituent properties.

Very little analytical work has been done for the case of statistically isotropic composites, e.g., a matrix reinforced with particles. The analytical difficulties are quite staggering since it is first necessary to obtain the stress fields, which by itself is an intractable problem, and to utilize these to draw conclusions about progressive and ultimate failure. In the case when the matrix can be regarded as ideally plastic and the particles as rigid, limit analysis methods are, in principle, applicable. However, the construction of nontrivial admissible stress or velocity fields is an extremely difficult problem. Drucker [124] has shown that when it is possible to pass a principal shear plane without intersecting particles through the matrix, a highly theoretical state of affairs, the limit load is equal to that of a specimen without particles. It may also be easily shown that when there is no such geometrical restriction the matrix limit load is a lower bound on the composite limit load. For a porous material Hashin [110] has shown that limit stress for uniaxial stress or shear stress is bounded from above by $\sigma_0(1-c)$ where σ_0 is matrix limit stress and c is the pores volume fraction. The result for shear is analogous.

Experimental evidence shows that reinforcement of a compliant and weak matrix with stiff and strong "equiaxed" particles does not materially improve the strength and may even decrease it. Substantial increase in strength is obtained when the particles are elongated and randomly oriented. An important example is a chopped fiber or whisker-reinforced composite. However, any reliable analytical treatment of strength does not appear to be available.

In the case of a unidirectional fiber composite the following failure stresses are of interest: σ_L^+ = tensile strength in fiber direction, σ_L^- = compressive strength in fiber direction, σ_T^+ = tensile strength transverse to fibers, σ_T^- = compressive strength transverse to fibers, τ_L = longitudinal shear strength (σ_{12} or σ_{13}), and τ_T = transverse shear strength (σ_{23}).

A great deal of work has been done in the context of σ_L^+. The oldest approach consists of the assertion

$$\sigma_L^+ = \sigma_{Lf} v_f + \sigma_m v_m \tag{7.2.1}$$

where σ_{Lf} is fiber tensile strength, σ_m is matrix tensile strength, and v_f and v_m are the volume fractions. This would be rigorously correct if fibers and matrix reached their respective failure stresses simultaneously and the Poisson's ratios of the two constituents were equal. The last requirement is practically unimportant and the first one is numerically unimportant if $\sigma_{Lf} >> \sigma_m$. The failure mode for which (7.2.1) is applicable is a more or less plane transverse fracture of a tension specimen. For further discussion and results in this context see Kelly [125].

The most stringent underlying condition (7.2.1) is the tacit assumption that σ_{Lf} is a fixed definite number. However, fiber strengths are often considerably scattered and are also functions of fiber length. A well-known analysis of tensile strength taking this into account has been given by Rosen [126]. The failure mechanism underlying this work is progressive random fiber ruptures. The strength of the broken parts is modified since the length has changed. In addition, the buildup of shear stress at a broken end diminishes fiber longitudinal stress in the shear region thus further reducing fiber-effective length. A fiber's carrying capacity is exhausted when its length has diminished to the point where it cannot transfer appreciable longitudinal stress (at which point it acts essentially as a particle). The failure mode consists of cumulative rupture of fibers resulting in a jagged and irregular fracture surface. This approach to predict tensile strength in fiber direction has been extended and further developed in numerous papers, Rosen and Zweben [127, 128], Hedgepeth and Van Dyke [129], and in particular, the statistical analyses by Phoenix [130, 131] and associates.

The failure mode in compression in fiber direction essentially consists of fiber buckling within the matrix. This has been experimentally verified and an approximate two-dimensional analysis to determine this buckling load has been given by Rosen [132] and Schuerch [133]. The result is

$$\sigma_L^- = G_m(1-v_f) \tag{7.2.2}$$

where G_m is isotropic matrix shear modulus.

Whatever results are available for longitudinal strength are made possible by the simple cylindrical geometry of fibers and matrix. In the case of transverse strength the situation is as difficult as for a particulate composite since the internal stress fields are unattainable. Attempts to represent the composite by a periodic array and to draw conclusions from the stress fields in this case do not appear useful since the actual stress fields will have vastly different local peaks. Limit analysis methods have been employed by Hashin [134] to repeat Drucker's argument that when a shear plane can be passed through the matrix without cutting fibers the limit stress is equal to the matrix limit stress. Bounds on limit shear stresses have been obtained by Shu and Rosen [135] and by McLaughlin [136–138]. All of these results are not of much practical value for they apply only to ideally plastic matrix and rigid fibers. The only fiber composite for which this has any relevance is boron/aluminum. Graphite and carbon fibers are transversely much less stiff than aluminum, and polymers are certainly not ideally plastic. Experience shows that the transverse tensile and shear strengths are of the order of matrix strength and quite lower than this in the case of carbon and graphite/aluminum. For review articles on the problems discussed here see Rosen [139], Chamis [140], and Phoenix [131].

7.3 Static Failure: Combined Stress. Unidirectional fiber composites are primarily utilized in the form of laminates consisting of differently oriented parallel layers or laminae. The simplest state of stress in any lamina is plane. At laminate free edges the internal state of stress is generally three dimensional. It is therefore necessary to establish failure criteria for combined states of stress. It is generally assumed that the failure criterion can be expressed in terms of average stress components. It is in principle possible to use failure criteria in terms of strains but this is less convenient and this subject will not be considered here. For discussion, see Wu [141].

It is generally assumed that failure criteria are quadratic polynomials in stress. It should be emphasized that this is an assumption of convenience and curve fitting nature, although the quadratic nature of stress energy has led to attempts of physical interpretation of the quadratic approximation. The coefficients in the stress polynomial must be determined in terms of simple failure information, preferably single-component ultimate stresses. In one of the first contributions to the subject Tsai [142] assumed that Hill's [143] yield criterion for orthotropic plastic materials could be used as a failure criterion. Hoffman [144] added linear terms for the purpose of accounting for different tensile and compressive ultimate stresses. The problem with these criteria is that they imply that isotropic stress cannot produce failure which is incorrect for an anisotropic material. This was corrected by Tsai and Wu [145] who represented the failure criterion of any anisotropic material as a general quadratic in the stresses

$$F_{ijkl}\sigma_{ij}\sigma_{kl} + F_{ij}\sigma_{ij} = 1 \tag{7.3.1}$$

where F_{ijkl} and F_{ij} are coefficients to be determined. Similar criteria have been proposed in the Russian literature; see e.g, Wu [141]. It is customary to abbreviate the coefficient indices according to the scheme $11 \equiv 1$, $22 \equiv 2$, $33 \equiv 3$, $13 \equiv 4$, $23 \equiv 5$, and $12 \equiv 6$. If the indices denote the material axes of a fiber composite with x_1 in fiber direction, terms with odd powers in shear stresses must be rejected since the material is insensitive to change of sign of shear stress. For transverse isotropy the surviving coefficients are

$$\begin{aligned} &F_{11} = 1/\sigma_L^+\sigma_L^- && F_1 = 1/\sigma_L^+ - 1/\sigma_L^- \\ &F_{22} = F_{33} = 1/\sigma_T^+\sigma_T^- && F_2 = F_3 = 1/\sigma_T^+ - 1/\sigma_T^- \\ &F_{44} = F_{66} = 1/\tau_L^2 && F_{55} = 1/\tau_T^2 \\ &F_{23} = 2/\sigma_T^+\sigma_T^- - 1/\tau_T^2 \end{aligned} \tag{7.3.2}$$

and F_{12}. This coefficient must be found from a biaxial failure experiment involving σ_{11} and σ_{22}. Since, however, the material has different strengths in tension and compression there are four different failure pairs σ_{11}, σ_{22} and therefore F_{12} has four different values F_{12}^{++}, F_{12}^{+-}, F_{12}^{-+}, and F_{12}^{--}. This contradicts the basic assumption underlying (7.3.1) that the failure criterion can be described by a single continuous polynomial. Another problem with (7.3.1) is that it does not predict the failure *mode* of the composite. For further discussion of these aspects see [146].

These problems can be avoided if the different failure modes of the fiber composite and the primary stresses contributing to them are identified and each mode is modeled separately by a quadratic. The principal modes are: tensile fiber mode described by fiber rupture; compressive fiber mode described by fiber buckling; tensile matrix mode described by plane failure surface parallel to fibers with $\sigma_{22}+\sigma_{33}>0$ and compressive matrix mode with $\sigma_{22}+\sigma_{33}<0$. Experimental evidence for some of these modes, obtained with off-axis specimens of various composites has been described in [147–149]. Quadratic failure criteria corresponding to these various modes are, Hashin [146]:

Tensile Fiber Mode

$$(\sigma_{11}/\sigma_L^+)^2+(\sigma_{12}^2+\sigma_{13}^2)/\tau_L^2=1 \quad \sigma_{11}>0 \tag{7.3.3}$$

Compressive Fiber Mode

$$\sigma_{11}=-\sigma_L^- \quad \sigma_{11}<0 \tag{7.3.4}$$

Tensile Matrix Mode

$$\sigma_{22}+\sigma_{33}>0$$

$$(\sigma_{22}+\sigma_{33})^2/\sigma_T^{+2}+(\sigma_{23}^2-\sigma_{22}\sigma_{33})/\tau_T^2+(\sigma_{12}^2+\sigma_{13}^2)/\tau_L^2=1 \tag{7.3.5}$$

Compressive Matrix Mode

$$\sigma_{22}+\sigma_{33}<0$$

$$(\sigma_{22}+\sigma_{33})[(\sigma_T^-/2\tau_T)^2-1]/\sigma_T^-+(\sigma_{22}+\sigma_{33})^2/4\tau_T^2$$
$$+(\sigma_{22}^2-\sigma_{22}\sigma_{33})/\tau_T^2+(\sigma_{12}^2+\sigma_{13}^2)/\tau_L^2=1 \tag{7.3.6}$$

Denoting the left sides of the four failure criteria by $F_i(\sigma)$ failure for a given stress state is identified by the one for which $F_i(\sigma)=1$ while for the remaining ones $F_j(\sigma)<1$. This procedure also identifies the failure mode of the composite which is of significant importance for design considerations and finite element analysis of progressing structural failure.

There is much need for critical comparative experimental examination of the various failure criteria proposed. A significant problem is the incorporation of scatter of test data into the failure criteria. A tentative approach to this problem has been proposed in [150].

7.4 Fatigue Failure of Unidirectional Fiber Composites. The subject of concern is failure of unidirectional fiber composites under cyclic average stress. Any such cyclic stress component is characterized by the maximum amplitude σ_{ij}^2, the minimum amplitude σ_{ij}^1, and the cycling frequency. Alternatively, it is customary to use the quantities: mean stress $\sigma_{ij}^m=1/2(\sigma_{ij}^2+\sigma_{ij}^1)$, alternating stress $\sigma_{ij}^a=1/2(\sigma_{ij}^2-\sigma_{ij}^1)$, and stress ratio $R=\sigma_{ij}^1/\sigma_{ij}^2$. Tensile-tensile cycling is characterized by $0<R<1$, tensile-compressive by $R<1$, and compressive-compressive by $R>1$. Cycling at maximum amplitude which is smaller than the static ultimate stress will produce failure after N cycles, generally called fatigue lifetime. The lifetime is a function of the two amplitudes and of the frequency. It is however frequently a weak function of the latter for a range of frequencies of practical interest and therefore this effect will be disregarded.

In the basic case of constant amplitude cycling the plot of lifetime N, generally plotted as log N, versus maximum stress amplitude is known as the *S-N* curve. Because of the large scatter, N is a random variable for any given stress amplitude. The probability distribution function of N may be described by the log-normal or by the Weibull distribution. The elementary *S-N* curve is described in terms of the mean or the median of log N. More sophisticated, *P-S-N* curves, are defined parametrically in terms of probability of failure. Since the unidirectional fiber composite is anisotropic there are different *S-N* curves in different directions. In analogy with static failure stresses defined in Section 7.2 one may define the *S-N* curves $\sigma_L(R,N)$, $\sigma_T(R,N)$, $\tau_L(R,N)$, and $\tau_T(R,N)$ as basic fatigue failure information. The problem of predicting such *S-N* curves on the basis of microstructural progressive failure is exceedingly difficult, much more so than the corresponding static failure problem, and therefore no attempt will be made to discuss whatever scant literature there is available on this subject.

The two major problems in analysis of fatigue failure of unidirectional fiber composites are:

1. Establishment of fatigue failure criteria for combined cyclic stress.
2. Prediction of lifetime under variable amplitude cycling.

The first problem is of particular significance for fiber composites since they are generally used as laminates; see Section 7.3. The second problem is known as the cumulative damage problem and has been the subject of much investigation in the context of metals. It is of great practical importance since cyclic loadings in practice are generally of variable amplitude.

Development of failure criteria for cyclic combined stress is quite similar to treatment for static failure criteria. In the general case of three-dimensional cyclic stress there are the 12 stress amplitudes σ_{ij}^1 and σ_{ij}^2. In the event that the stresses do not cycle in phase there are also in addition five mutual phase lags. A failure criterion is defined as a functional relationship of these 17 variables that produces failure after a specified number of cycles N. This defines a family of failure criteria with parameter N. For discussion see [150]. Here we shall be concerned only with the simple but practically important case when all stresses cycle in phase and all R ratios of the stress components are the same. Then the failure criteria family becomes

$$F(\sigma_{ij},R,N)=1 \tag{7.4.1}$$

where σ_{ij} implies maximum amplitude. For $R=1$ or for $N=0$, equation (7.4.1) reduces to the static failure criterion.

Fatigue failure testing of off-axis coupons reveals that in tensile-tensile fatigue there are two distinct failure modes, (*a*) fiber mode defined by fiber rupture, and (*b*) matrix mode delivered by a sudden crack along fibers. This phenomenon has been described by Hashin and Rotem [147] for glass/epoxy. The same failure modes occur for graphite/epoxy, Awerbuch and Hahn, [151]. The situation for tensile-compressive and compressive-compressive cycling is less understood; see e.g., reference [150] for discussion. The metal fatigue phenomenon of slow propagation of one dominant crack does not occur in unidirectional fiber composites. In the fiber mode, failure occurs after accumulation of many microcracks or other flaws producing an irregular rupture surface. In the matrix mode, one crack propagates instantaneously along the fibers producing a plane fracture surface [147, 151]. The failure modes described are of phenomenological nature. A discussion of failure modes in terms of micromechanisms has been given by Talreja [152].

Adopting again the point of view that fiber and matrix modes should be modeled separately, exploiting the transverse isotropy of the unidirectional composite, and using a quadratic approximation, it has been shown, Hashin [150], that for fully reversed cycling, $R=-1$, the failure criteria are:

Fiber Mode

$$(\sigma_{11}/\sigma_L)^2+(\sigma_{12}^2+\sigma_{13}^2)/\tau_L^2=1 \tag{7.4.2}$$

Matrix Mode

$$[(\sigma_{22}+\sigma_{33})/\sigma_T]^2+(\sigma_{23}^2-\sigma_{22}\sigma_{33})/\tau_T^2+(\sigma_{12}^2+\sigma_{13}^2)/\tau_L^2=1 \tag{7.4.3}$$

where $\sigma_L=\sigma_L(-1,N)$, $\sigma_T=\sigma_T(-1,N)$, $\tau_L=\tau_L(-1,N)$, and $\tau_T=\tau_T(-1,N)$ are the *S-N* relations for fully reversed cycling of stress in fiber direction, stress normal to fiber direction, longitudinal and transverse shear stress, respectively, and x_1 is fiber direction. In the important case of plane cyclic stress in the x_1x_2 plane, which is appropriate for a fiber composite lamina, equations (7.4.2) and (7.4.3) reduce to

Fiber Mode

$$(\sigma_{11}/\sigma_L)^2 + (\sigma_{12}/\tau_L)^2 = 1$$

Matrix Mode (7.4.4)

$$(\sigma_{22}/\sigma_T)^2 + (\sigma_{12}/\tau_L)^2 = 1$$

When the cycling also has mean stress, additional coefficients appear in the failure criteria which must be determined by test data for two combined cyclic stresses. However, the results (7.4.4) are in reasonable agreement with tensile-tensile off-axis test data, $R = 0.1$, reference [147].

There is much need for systematic experimental work to investigate failure modes in tensile-compressive and compressive-compressive cycling. Unfortunately, most of experimental work is concerned with laminates. A very significant problem is the large scatter of fatigue test data. The failure criteria discussed in the foregoing as well as all others used in the literature are of deterministic nature. It is customary to interpret them in a mean sense but there is no firm foundation for this assumption. A fatigue failure criterion should predict probability of failure or at least-means and variances of failure loads. A tentative approach to this problem has been outlined in [150].

Next the cumulative damage problem is considered. The goal is to predict lifetime under specified cyclic loading program. Since such lifetime is a random variable the problem is of statistical nature. In spite of the large amount of work done for metals the problem is still unresolved in that case. Much less is known in the case of fiber composites. There have been two major approaches for metals. In the first, test data information for simple cyclic loading, such as *S-N* data, are used to predict lifetimes for complicated cyclic loadings. The most well-known result in this context is the simple Palmgren-Miner rule, which is, however, unreliable. In the second approach it is attempted to predict the growth of a single dominant crack under cyclic loading program. This approach is not applicable to unidirectional fiber composites since, as has been explained previously, slow growth of one dominant crack does not occur.

Most of fiber composite work within the first approach has been based on the concept of residual strength degradation. This concept also called "wearout" appears to have been introduced to composites by Halpin and associates; see, e.g., reference [153]. The residual strength $\sigma_r(n)$ is defined as static strength after n elapsed cycles. It is obviously a monotonically decreasing function of n and is chosen as the damage parameter. Fatigue failure is assumed to occur when $\sigma_r(n)$ becomes equal to the maximum stress amplitude. A recent paper by Yang and Jones [154] gives a statistical treatment for two-stage cyclic loading in terms of this approach which is in reasonable agreement with some of the test data obtained in [155] and also contains a summary of previous work. The main difficulties with this interesting approach are: (*a*) it requires a statistical functional relationship of σ_r not only of n but also of previous cyclic loading history, and (*b*) in many cases σ_r degradation until failure is insignificant. (This has been sometimes called "sudden death.")

Another possible approach is a general cumulative damage theory proposed by Hashin and Rotem [156] which has recently been generalized to a statistical theory [157]. In this approach damage due to a cyclic loading program is characterized by the residual lifetime under subsequent constant amplitude cycling.

In conclusion it should be pointed out that the problems of failure criterion and cumulative damage which have been discussed separately are in reality inseparable since the state of stress in a lamina within a laminate is at least plane and therefore cumulative damage theory under combined stress is required.

There is obvious need for systematic experimental work for unidirectional composites. Unfortunately, most of experimental investigation has been done for laminates thus introducing major additional complexity as will become apparent in the next section.

7.5 Failure of Laminates. In conclusion, the important problem of laminate failure under static or cyclic loading will be briefly discussed. A fiber composite laminate consists of thin, parallel, unidirectionally reinforced layers, often called laminae, which are firmly bonded together. The heterogeneity is produced by the different fiber orientations of the layers. Additional heterogeneity may be introduced when the laminate consist of different composites, in which case the laminate is called hybrid. It is usually assumed that the laminae can be represented as homogeneous anisotropic with the effective properties of the unidirectional material. The analysis of elastic and other physical properties of laminates in terms of lamina properties is well understood and is not incorporated in this survey.

Unfortunately, however, analytical determination of static or fatigue failure characteristics of laminates is a very difficult problem which cannot be considered resolved at the present time. The simplest case is a symmetric laminate (the midplane is a geometrical and material plane of symmetry) which is loaded by membrane forces in its plane. In this case the laminae are in states of plane stress while at the edges, however, the state of stress is three dimensional and certain of its components may be singular. For such laminates consisting of polymer fiber composites, under static or cyclic load, there are two major failure processes: (1) *The intralaminar process:* intralaminar cracks accumulate in fiber or in matrix modes. In the former case the cracks are short, rupturing fibers and debonding fiber matrix interfaces and are randomly located. In the latter case cracks run parallel to fibers from edge to edge. Reifsnider [158] has shown experimentally the occurrence of periodic matrix-mode crack patterns (named Characteristic Damage States) and has given a simple analytical method to predict such crack patterns. (2) *The interlaminar process:* the high edge stresses, interlaminar shear, and tension open up an interlaminar edge crack which may split the laminate. For static load this is a short-time phenomenon while for cyclic load the interlaminar crack may grow slowly with cycling, not unlike a metal fatigue crack. Interaction between these two processes occurs to some extent. Adjacent intralaminar cracks may produce interlaminar debonding and interlaminar cracks may branch out to become intralaminar. For further discussion of such effects see Reifsnider et al. [159].

Analytical prediction is concerned with initiation, development, and termination of the failure process. The most common approach for prediction of initiation of the intralaminar process is to obtain the plane stress fields in the laminae, away from the edges, by conventional methods of linear elastic laminate stress analysis. Laminae nonlinearity may also be incorporated, Hahn [160] for nonlinearity in shear only, Hashin et al. [161] for nonlinear interaction of shear and transverse stress. The failure criteria for unidirectional material discussed in the foregoing are then examined for all laminae stresses and initial failure is characterized by first compliance with a failure criterion. This defines the failed lamina and its failure mode. Such an approach has been employed by Rotem and Hashin [162] for fatigue failure of angle plies. Not surprisingly, the predicted fatigue strength is often less than the experimental result. This and other aspects of fatigue of laminates have also been discussed in a survey article by Hahn, reference [163].

Analysis of failure in terms of intralaminar crack accumulation by fracture mechanics methods (assuming that it is legitimate to consider the cracks as if in homogeneous anisotropic laminae) appears to be too difficult an undertaking at the present time. Consequently, the approach generally adopted is to represent lamina damage accumulation in terms of in situ stiffness reduction. This produces redistribution of laminae stresses. New initial failure may be predicted until the load-carrying capacity of the laminate is exhausted. The most primitive approach is to assume that lamina fiber-mode failure implies zero stiffness in fiber direction and lamina matrix-mode failure implies zero transverse and shear stiffness. Ultimate failure is mostly identified with fiber-mode failure of primary load-carrying laminae. This approach is sometimes called the Ply Discount Method and may also be applied to the case of cyclic load in terms of laminae *S-N* curves and the fatigue failure criteria (7.4.4).

The prediction capability of this procedure evidently depends on the accuracy of lamina stiffness-reduction evaluation. One approach is to determine in situ stiffness reduction analytically in terms of crack patterns. This is an important subject in the stage of development. Another approach is to determine such stiffness reduction in terms of measurement of laminate stiffness reduction via the known relations between laminae and laminate stiffnesses; see e.g., O'Brien and Reifsnider [164], Rotem [165]. But the crucial question regarding both approaches is: to what extent is lamina damage accumulation independent of the laminate stacking sequence, or at least of the fiber orientation of its immediate neighboring laminae? While a definitive answer to this question does not seem available at this time it is of interest to note that fatigue failure prediction of laminates based on the experimental stiffness reduction method, Rotem [165], is in good agreement with test data.

The source of interlaminar failure is a theoretically singular state of edge stress, i.e., a very high state of stress of unknown magnitude. The prediction of interlaminar crack opening is thus a fracture mechanics problem the solution to which requires: (1) the mathematical nature of the edge singularity; (2) a criterion of crack criticality for static load; and (3) a crack growth law for cyclic load. With respect to (1), the first edge stress analysis was performed, numerically, by Pipes and Pagano [166] and many others have followed. See a recent review article by Soni and Pagano [167]. The possibility of edge stress singularity had already been surmised in [166] but numerical methods cannot uncover it. The analytical nature of edge singularities and of boundary layer edge fields has been established by Wang and Choi for mechanically loaded laminates [168] and for moisture swelling of laminates [169]. Problems (2) and (3) must be considered unresolved at the present time. Consequently edge delamination studies have frequently been based on application of failure criteria to edge stresses averaged over a small distance from the edge, Herakovich [170, 171].

This concludes the brief discussion of laminate failure. A recent comprehensive survey has been given by Rosen [172]. The present underlying point of view is that laminate failure must be understood in terms of failure of laminae. To descend to the fiber/matrix scale will result in hopeless difficulties. On the other hand, to explore laminate strength in terms of laminate coupon testing is an equally hopeless undertaking since from this point of view laminates are an infinite set of materials.

Conclusion

This survey has been written with the aim of presenting analysis of mechanical and materials as a discipline within the engineering sciences. Several important subjects have not been covered. One of these is plasticity of composite materials which is of particular importance in the context of metal matrix fiber composites. Much work on this subject has been done by Dvorak and associates and a brief survey has been given in [2]. See also recent analyses by Min [175] and Aboudi [176]. A related problem is plasticity of a polycrystalline aggregate which has received repeated attention, in particular by Budiansky and Wu, Hill, Hutchinson and Lin. The older literature has been discussed in [3]. A second important subject is dynamic behavior and wave propagation in composites. There exists a considerable literature on the subject in the contexts of particulate composites and layered media which by itself would require a substantial survey effort. Recent surveys have been given in [27, 174].

The subjects of strength and failure of composite materials are of special nature. Engineering design requirements have motivated an immense literature much of which is confined to unpublished reports. At the same time the problems are of such difficulty that an analytical definition and/or solution has not been achieved in many cases and therefore much of the available work is of semiempirical nature. The many important problems that require analytical solution continue to be a primary challenge in composite materials research.

Acknowledgment

Support by Naval Air Systems Command, Washington D.C. and Office of Naval Research, Arlington Va. under contract N00014-78-C-0544 is gratefully acknowledged.

References

1 Hashin, Z., *Theory of Fiber Reinforced Materials*, NASA CR-1974, 1972.

2 Christensen, R. M., *Mechanics of Composite Materials*, Wiley-Interscience, New York, 1979.

3 Hashin, Z., "Theory of Mechanical Behavior of Heterogeneous Media," *Applied Mechanics Reviews*, Vol. 17, 1964, pp. 1-9.

4 Beran, M. J., *Statistical Continuum Theories*, Wiley, New York, 1968.

5 Einstein, A., "Eine Neue Bestimmung der Moleküldimensionen," *Annalen der Physik*, Vol. 19, 1906, pp. 289-306, Vol. 34, 1911, pp. 591-592 (errata). English translation in *Investigations on the Theory of Brownian Motion*, Dover, 1956, pp. 36-62.

6 Hill, R., "Elastic Properties of Reinforced Solids: Some Theoretical Principles," *Journal of the Mechanics and Physics of Solids*, Vol. 11, 1963, pp. 357-372.

7 Herrmann, G., in an oral presentation in 1967 of Herrmann, G., and Achenbach, J. D., "Wave Propagation in Laminated and Fiber-Reinforced Composites," in *Mechanics of Composite Materials*, Pergamon Press, 1970, pp. 337-360.

8 Beran, M. J., and McCoy, J. J., "Mean Field Variations in a Statistical Sample of Heterogeneous Linearly Elastic Solids," *International Journal of Solids and Structures*, Vol. 6, 1970, pp. 1035-1054.

9 Levin, V. M., "The Relation Between Mathematical Expectation of Stress and Strain Tensors in Elastic Microheterogeneous Media," *Prikladnaya Matematika y Mekhanika* (English translation from Russian), Vol. 35, 1971, pp. 694-701.

10 Beran, M. J., "Application of Statistical Theories for the Determination of Thermal, Electrical and Magnetic Properties of Heterogeneous Materials," in *Composite Materials*, Vol. 2, Sendeckyj, G. P., ed., Academic Press, New York, 1974, pp. 209-249.

11 Eshelby, J. D., "The Determination of the Field of an Ellipsoidal Inclusion and Related Problems," *Proceedings of the Royal Society*, London, Vol. *A*, No. 241, 1957, pp. 376-396.

12 Dewey, J. M., "The Elastic Constants of Materials Loaded With Non-rigid Fillers," *Journal of Applied Physics*, Vol. 18, 1947, pp. 578-581.

13 Hashin, Z., "The Moduli of an Elastic Solid Containing Spherical Particles of Another Elastic Material," in *Nonhomogeneity in Elasticity and Plasticity*, Olszak, W. ed., Pergamon Press, 1959, pp. 463-478.

14 Chen, H. S., and Acrivos, A., "The Effective Elastic Moduli of Composite Materials Containing Spherical Particles at Non-Dilute Concentrations," *International Journal of Solids and Structures*, Vol. 14, 1978, pp. 349-364.

15 Batchelor, G. K., and Green, J. T., "The Determination of the Bulk Stress in a Suspension of Spherical Particles to Order c^2," *Journal of Fluid Mechanics*, Vol. 56, 1972, pp. 401-427.

16 Hashin, Z., "The Elastic Moduli of Heterogeneous Materials," ASME Journal of Applied Mechanics, Vol. 29, 1962, pp. 143-150.

17 Lee, K. J., and Westmann, R. A., "Elastic Properties of Hollow-Sphere-Reinforced Composites," *Journal of Composite Materials*, Vol. 4, 1970, pp. 242–253.

18 Molyneux, J., and Beran, M. J., "Statistical Properties of the Stress and Strain Fields in a Medium With Small Random Variations in Elastic Coefficients," *Journal of Mathematics and Mechanics*, Vol. 14, 1965, pp. 337–352.

19 Paul, B., "Prediction of Elastic Constants of Multiphase Materials," *Transactions of the ASME*, Vol. 218, 1960, pp. 36–41.

20 Hashin, Z., and Shtrikman, S., "A Variational Approach to the Theory of the Elastic Behaviour of Multiphase Materials," *Journal of the Mechanics and Physics of Solids*, Vol. 11, 1963, pp. 127–140.

21 Hashin, Z., and Shtrikman, S., "On Some Variational Principles in Anisotropic and Nonhomogeneous and Elasticity," *Journal of the Mechanics and Physics of Solids*, Vol. 10, 1962, pp. 335–342.

22 Hashin, Z., "On Elastic Behaviour of Fibre Reinforced Materials of Arbitrary Transverse Phase Geometry," *Journal of Mechanics and Physics of Solids*, Vol. 13, 1965, pp. 119–134.

23 Walpole, L. J., "On Bounds for the Overall Elastic Moduli of Inhomogeneous Systems—I," *Journal of the Mechanics and Physics of Solids*, Vol. 14, 1966, pp. 151–162.

24 Hill, R., "New Derivations of Some Elastic Extremum Principles," in *Progress in Applied Mechanics*, Prager Anniversary Volume, Macmillan, New York, 1963, pp. 91–106.

25 Korringa, J., "Theory of Elastic Constants of Heterogeneous Media," *Journal of Mathematics and Physics*, Vol. 14, 1973, pp. 509–513.

26 Willis, J. R., "Bounds and Self-Consistent Estimates for the Overall Moduli of Anisotropic Composites," *Journal of the Mechanics and Physics of Solids*, Vol. 25, 1977, pp. 185–202.

27 Willis, J. R., "Variational and Related Methods for the Overall Properties of Composites," in *Advances in Applied Mechanics*, Vol. 21, Yih, C. S., ed., Academic Press, New York, 1981, pp. 1–78.

28 Kröner, E., "Bounds for Effective Elastic Moduli of Disordered Materials," *Journal of the Mechanics and Physics of Solids*, Vol. 25, 1977, pp. 137–155.

29 Wu, C. T. D., and McCullough, R. L., "Constitutive Relationships for Heterogeneous Materials," in *Developments in Composite Materials*, Holister, G. S., ed., 1977, pp. 119–187.

30 Watt, P. J., and O'Connell, R. J., "An Experimental Investigation of the Hashin-Shtrikman Bounds on Two-Phase Aggregate Elastic Properties," *Physics of the Earth and Planetary Interiors*, Vol. 21, 1980, pp. 359–370.

31 McCoy, J. J., "Macroscopic Response of Continua With Random Microstructures," in *Mechanics Today*, Vol. 6, Nemat-Nasser, S., ed., Pergamon Press, 1981, pp. 1–40.

32 Milton, G. W., "Bounds on the Elastic and Transport Properties of Two-Component Composites," *Journal of the Mechanics and Physics of Solids*, Vol. 30, 1982, pp. 177–191.

33 Sendeckyj, G. P., "Elastic Behavior of Composites," in *Composite Materials*, Vol. 2, Sendeckyj, G. P., ed., Academic Press, New York, 1974, pp. 45–83.

34 Kröner, E., "Elastic Moduli of Perfectly Disordered Materials," *Journal of the Mechanics and Physics of Solids*, Vol. 15, 1967, pp. 319–329.

35 Budiansky, B., "On the Elastic Moduli of Some Heterogeneous Materials," *Journal of the Mechanics and Physics of Solids*, Vol. 13, 1965, pp. 223–227.

36 Hill, R., "A Self Consistent Mechanics of Composite Materials," *Journal of the Mechanics and Physics of Solids*, Vol. 13, 1965, pp. 213–222.

37 Wu, T. T., "The Effect of Inclusion Shape on the Elastic Moduli of a Two-Phase Material," *International Journal of Solids and Structures*, Vol. 2, 1966, pp. 1–8.

38 Kerner, E. H., "The Elastic and Thermoelastic Properties of Composite Media," *Proceedings of the Physical Society*, Vol. *B* 69, 1956, pp. 807–808.

39 Van der Poel, C., "On the Rheology of Concentrated Suspensions," *Rheologica Acta*, Vol. 1, 1958, pp. 198–205.

40 Smith, J. C., "Correction and Extension of Van der Poel's Method for Calculating the Shear Modulus of a Particulate Composite," *Journal of Research of the National Bureau of Standards*, Vol. 78*A*, 1974, pp. 355–362.

41 Christensen, R. M., and Lo, K. H., "Solutions for Effective Shear Properties in Three Phase Sphere and Cylinder Models," *Journal of the Mechanics and Physics of Solids*, Vol. 27, 1979, pp. 315–330.

42 Hashin, Z., "Assessment of the Self Consistent Scheme Approximation: Conductivity of Particulate Composites," *Journal of Composite Materials*, Vol. 2, 1968, pp. 284–300.

43 Boucher, S., "On the Effective Moduli of Isotropic Two-Phase Elastic Composites," *Journal of Composite Materials*, Vol. 8, 1974, pp. 82–89.

44 Mclaughlin, R., "A Study of the Differential Scheme for Composite Materials," *International Journal of Engineering Science*, Vol. 15, 1977, pp. 237–244.

45 Christensen, R. M., and Waals, F. M., "Effective Stiffness of Randomly Oriented Fiber-Reinforced Composites," *Journal of Composite Materials*, Vol. 6, 1972, pp. 518–532.

46 Voigt, W., *Lehrbuch der Kristallphysik*, Teubner, Berlin, 1910.

47 Reuss, A., "Berechnung der Fliessgrense von Mischkristallen auf Grund der Plastizitätsbedingung für Einkristalle," *Zeitschrift fur Angewandte Mathematik und Mechanik*, Vol. 9, 1929, pp. 49–58.

48 Hill, R., "The Elastic Behaviour of a Crystalline Aggregate," *Proceedings of the Physical Society*, London, Vol. *A*65, 1952, pp. 349–354.

49 Hashin, Z., and Shtrikman, S., "A Variational Approach to the Theory of the Elastic Behaviour of Polycrystals," *Journal of the Mechanics and Physics of Solids*, Vol. 10, 1962, pp. 343–352.

50 Peselnick, L., and Meister, R., "Variational Method for Determining Effective Moduli of Polycrystals: (*A*) Hexagonal Symmetry, (*B*) Trigonal Symmetry," *Journal of Applied Physics*, Vol. 36, 1965, pp. 2879–2884; also, Vol. 37, 1966, pp. 4121–4125.

51 Watt, P. J., "Hashin-Shtrikman Bounds on the Effective Elastic Moduli of Polycrystals With Orthorhombic Symmetry," *Journal of Applied Physics*, Vol. 50, 1979, pp. 6290–6295; ". . . with Monoclinic Symmetry," Vol. 51, 1980, pp. 1520–1524.

52 Watt, P. J., and Peselnick, L., "Clarification of the Hashin-Shtrikman Bounds on the Effective Elastic Moduli of Polycrystals With Hexagonal, Trigonal and Tetragonal Symmetries," *Journal of Applied Physics*, Vol. 51, 1980, pp. 1525–1531.

53 Hashin, Z., "Elasticity of Random Media," *Transactions of the Society of Rheology*, Vol. 9, 1965, pp. 381–406.

54 Walpole, L. J., "On Bounds for the Overall Elastic Moduli of Inhomogeneous Systems—II," *Journal of the Mechanics and Physics of Solids*, Vol. 14, 1966, pp. 289–301.

55 Hershey, A. V., "The Elasticity of an Isotropic Aggregate of Anisotropic Cubic Crystals," ASME Journal of Applied Mechanics, Vol. 21, 1954, pp. 236–240.

56 Kroner, E., "Berechnung der Elastischen Konstanten des Vielkristalls aus den Konstanten des Einkristalls," *Zeitschrift für Physik*, Vol. 151, 1958, pp. 504–518.

57 Hill, R., "Theory of Mechanical Properties of Fibre-Strengthened Materials—I. Elastic Behaviour," *Journal of the Mechanics and Physics of Solids*, Vol. 12, 1964, pp. 199–212.

58 Hashin, Z., and Rosen, B. W., "The Elastic Moduli of Fiber-Reinforced Materials," ASME Journal of Applied Mechanics, Vol. 31, 1964, pp. 223–232.

59 Pickett, G., and Johnson, M. W., "Analytical Procedures for Predicting the Mechanical Properties of Fiber Reinforced Composites," AFML-TR-65-2200, Air Force Materials Laboratory, Wright Patterson AFB, 1965.

60 Adams, D. F., Doner, D. R., and Thomas, R. L., "Mechanical Behavior of Fiber Reinforced Composite Materials," AFML-TR-67-96, Air Force Materials Laboratory, Wright-Patterson AFB, 1967 (See also *Journal of Composite Materials*, Vol. 1, 1967, pp. 4–17, pp. 152–165.

61 Chen, C. H., and Cheng, S., "Mechanical Properties of Fiber Reinforced Composites," *Journal of Composite Materials*, Vol. 1, 1967, pp. 30–41.

62 Love, A. E. H., *A Mathematical Treatise on the Theory of Elasticity*, Dover, 1944.

63 Hashin, Z., "Analysis of Properties of Fiber Composites With Anisotropic Constituents," ASME Journal of Applied Mechanics, Vol. 46, 1979, pp. 543–550.

64 Hill, R., "Theory of Mechanical Properties of Fibre-Strengthened Materials—III. Self-Consistent Model," *Journal of the Mechanics and Physics of Solids*, Vol. 13, 1965, pp. 189–198.

65 Chu, T. W., Nomura, S., and Taya, M., "A Self Consistent Approach to the Elastic Stiffness of Short-Fiber Composites," *Journal of Composite Materials*, Vol. 14, 1980, pp. 178–188.

66 Hermans, J. J., "The Elastic Properties of Fiber Reinforced Materials When the Fibers are Aligned," *Proceedings Koninklijke Nederlandse Akademie van Wetenschappen*, Series *B*, Vol. 70, 1967, pp. 1–9.

67 Ashton, J. E., Halpin, J. C., and Petit, P. H., *Primer on Composite Materials*, Chapter 5, Technomic, 1969.

68 Bristow, J. R., "Microcracks and the Static and Dynamic Elastic Constants of Annealed and Heavily Cold-Worked Metals," *British Journal of Applied Physics*, Vol. 11, 1960, pp. 81–85.

69 Walsh, J. B., "The Effect of Cracks on the Compressibility of Rock," *Journal of Geophysical Research*, Vol. 70, 1965, pp. 381–389, "The Effect of Cracks on the Uniaxial Elastic Compression of Rocks," ibid, pp. 399–411. "The Effect of Cracks in Rocks on Poisson's Ratio," ibid, pp. 5249–5257.

70 Piau, M., "Crack Induced Anisotropy and Scattering in Stressed Rocks: Effective Moduli and Attenuation," *International Journal of Engineering Science*, Vol. 18, 1980, pp. 549–568.

71 Gottesman, T., "Effective Elastic Moduli of Cracked Materials," Ph.D. Dissertation, Tel-Aviv University, 1980.

72 Gottesman, T., Hashin, Z., and Brull, M. A., "Effective Elastic Moduli of Cracked Fiber Composites," in *Advances in Composite Materials, Proc. ICCM 3*, Bunsell et al. eds., Pergamon Press, 1980, pp. 749–758.

73 Delameter, W. R., Herrmann G., and Barnett, D. M., "Weakening of an Elastic Solid by a Rectangular Array of Cracks," ASME Journal of Applied Mechanics, Vol. 42, 1975, pp. 74–80, Erratum, ibid, Vol. 44, 1977, p. 190.

74 Budiansky, B., and O'Connell, R. J., "Elastic Moduli of a Cracked Solid," *International Journal of Solids and Structures*, Vol. 12, 1976, pp. 81–97.

75 Hoenig, A., "Elastic Moduli of a Non-Randomly Cracked Body," *International Journal of Solids and Structures*, Vol. 15, 1979, pp. 137–154.

76 Hashin, Z., and Derby, E. A., "Evaluation of the Non-Linear Stress Strain Behavior of Sheet Molding Compounds," TFR 6301/1010. 1979, Materials Sciences Corp.

77 Willis, J. R., "A Polarization Approach to the Scattering of Elastic Waves. II. Multiple Scattering from Inclusions," *Journal of Mechanics and Physics of Solids*, Vol. 28, 1980, pp. 307–327.

78 Walpole, L. J., "Elastic Behaviour of Composite Materials: Theoretical Foundations," in *Advances in Applied Mechanics*, Vol. 21, Yih, C. S., ed., Academic Press, New York, 1981, pp. 169–242.

79 Levin, V. M., "On the Coefficients of Thermal Expansion of Heterogeneous Materials," *Mekhanika Tverdogo Tela*, Vol. 1, 1967, pp. 88–94, English translation—*Mechanics of Solids*, Vol. 2, 1967, pp. 58–61.

80 Rosen, B. W., "Thermal Expansion Coefficients of Composite Materials," Ph.D. Dissertation, University of Pennsylvania, 1968.

81 Schapery, R. A., "Thermal Expansion Coefficients of Composite Materials Based on Energy Principles," *Journal of Composite Materials*, Vol. 2, 1968, pp. 380–404.

82 Rosen, B. W., and Hashin, Z., "Effective Thermal Expansion Coefficients and Specific Heats of Composite Materials," *International Journal of Engineering Science*, Vol. 8, 1970, pp. 157–173.

83 Schapery, R. A., "Viscoelastic Behavior and Analysis of Composite Materials," in *Composite Materials*, Vol. 2, Sendeckyj, G. P., ed., Academic Press, New York, 1974, pp. 84–168.

84 Hashin, Z., "Viscoelastic Behavior of Heterogeneous Media," ASME Journal of Applied Mechanics, Vol. 32, 1965, pp. 630–636.

85 Hashin, Z., "Viscoelastic Fiber Reinforced Materials," *AIAA Journal*, Vol. 4, 1966, pp. 1411–1417.

86 Christensen, R. M., *Theory of Viscoelasticity*, Academic Press, New York, 1971.

87 Hashin, Z., "Complex Moduli of Viscoelastic Composites: I. General Theory and Application to Participate Composites," *International Journal of Solids and Structures*, Vol. 6, 1970, pp. 539–552. "II. Fiber Reinforced Materials," ibid., Vol. 6, 1970, pp. 797–807.

88 Christensen, R. M., "Viscoelastic Properties of Heterogeneous Media," *Journal of the Mechanics and Physics of Solids*, Vol. 17, 1969, pp. 23–41.

89 Roscoe, R., "Bounds for the Real and Imaginary Parts of the Dynamic Moduli of Composite Viscoelastic System," *Journal of the Mechanics and Physics of Solids*, Vol. 17, 1969, 17–22.

90 Roscoe, R., "Improved Bounds for Real and Imaginary Parts of Complex Moduli of Isotropic Viscoelastic Composites," *Journal of the Mechanics and Physics of Solids*, Vol. 20, 1972, pp. 91–99.

91 Laws, N., and McLaughlin, R., "Self-Consistent Estimates for the Viscoelastic Creep Compliances of Composite Materials," *Proceedings of the Royal Society*, London, Series *A*, Vol. 359, pp. 251–273.

92 Maxwell, J. C., *Treatise on Electricity and Magnetism*, 1st Ed., Clarendon Press, Oxford, 1873, p. 365.

93 Boettcher, C. J. F., *Theory of Electric Polarization*, Elsevier, 1952.

94 Jeffrey, D. J., "Conduction Through a Random Suspension of Spheres," *Proceedings of the Royal Society*, London, Series *A*, Vol. 335, 1973, pp. 355–367.

95 McCoy, J. J., and Beran, M. J., "On the Effective Thermal Conductivity of a Random Suspension of Spheres," *International Journal of Engineering Science*, Vol. 104, 1976, pp. 7–18.

96 Hashin, Z., and Shtrikman, S., "A Variational Approach to the Theory of the Effective Magnetic Permeability of Multiphase Materials," *Journal of Applied Physics*, Vol. 33, 1962, pp. 1514–1517.

97 Lord Rayleigh, "On the Influence of Obstacles Arranged in Rectangular Order Upon the Properties of a Medium," *Philosophical Magazine*, Vol. 34, 1892, pp. 481–502.

98 Meredith, R. E., and Tobias, C. W., "Resistance to Potential Flow Through a Cubical Array of Spheres," *Journal of Applied Physics*, Vol. 31, 1960, pp. 1270–1275.

99 McPhedran, R. C., and McKenzie, D. R., "The Conductivity of Lattices of Spheres. I. The Simple Cubic Lattice," *Proceedings of the Royal Society*, London, Series *A*, Vol. 359, 1978, pp. 45–63.

100 Bergman, D. J., "The Dielectric Constant of a Simple Cubic Array of Spheres," *Journal of Applied Physics*, Vol. *C* 12, 1979, pp. 4947–

101 Hashin, Z., "Rapporteurs Report," *Proceedings of the 1975 International Conference on Composite Materials, Metallurgical Society of AIME*, 1976, pp. 472–483.

102 Brown, W. F., "Solid Mixture Permittivities," *Journal of Chemical Physics*, Vol. 23, 1955, pp. 1514–1517.

103 Beran, M. J., and Molyneux, J., "Statistical Properties of the Electric Field in a Medium With Small Random Variations in Permittivity," *Il Nuovo Cimento*, Vol. 30, 1963, pp. 1406–1422.

104 Beran, M. J., "Application of Statistical Theories for the Determination of Thermal, Electrical and Magnetic Properties of Heterogeneous Materials," in *Mechanics of Composite Materials*, Vol. 2, of *Composite Materials*, Academic Press, New York, 1974, pp. 209–249.

105 Wiener, O., *Abhandlungen der Mathematisch—Physischen Klasse der Königlichen Sächsischen Gesellschaft der Wissenschaften*, Vol. 32, 1912, p. 509.

106 Bergman, D. J., "The Dielectric Constant of a Composite Material—A Problem in Classical Physics," Physics Reports (Section *C* of Physics Letters), Vol. 43, 1978, pp. 377–407.

107 Prager, S., "Improved Variational Bounds on Some Bulk Properties of a Two-Phase, Random Medium," *Journal of Chemical Physics*, Vol. 50, 1969, pp. 4305–4312.

108 Landauer, R., "Electrical Conductivity in Inhomogeneous Media," in *Electrical, Transport and Optical Properties of Inhomogeneous Media*, American Institute of Physics, 1978, pp. 2–43.

109 Springer, G. S., and Tsai, S. W., "Thermal Conductivities of Unidirectional Materials," *Journal of Composite Materials*, Vol. 1, 1967, pp. 166–173.

110 Hashin, Z., "Theory of Composite Materials," in *Mechanics of Composite Materials*, Pergamon Press, 1970, pp. 201–242.

111 Keller, J. B., "A Theorem on the Conductivity of a Composite Medium," *Journal of Mathematical Physics*, Vol. 5, 1964, pp. 548–549.

112 Mendelson, K. S., "A Theorem on the Conductivity of Two-Dimensional Heterogeneous Medium," *Journal of Applied Physics*, Vol. 46, 1975, pp. 917–918.

113 Beran, M. J., and Silnutzer, N., "Effective Electrical, Thermal and Magnetic Properties of Fiber Reinforced Materials," *Journal of Composite Materials*, Vol. 5, 1971, pp. 246–249.

114 Hori, M., and Yonezawa, F., "Statistical Theory of Effective Electrical, Thermal and Magnetic Properties of Random Heterogeneous Materials. V. One and Two-Dimensional Systems," *Journal of Mathematical Physics*, Vol. 16, 1975, pp. 365–377.

115 Schulgasser, K., "On the Conductivity of Fiber Reinforced Materials," *Journal of Mathematical Physics*, Vol. 17, 1976, pp. 382–387.

116 Schulgasser, K., "Concerning the Effective Transverse Conductivity of a Two-Dimensional Two-Phase Material," *International Journal of Heat and Mass Transfer*, Vol. 20, 1977, pp. 1273–1280.

117 Schulgasser, K., and Hashin, Z., "Bounds for Effective Permittivities of Lossy Dielectric Composites," *Journal of Applied Physics*, Vol. 47, 1975, pp. 424–427.

118 Milton, G. W., "Bounds on the Complex Dielectric Constant of a Composite Material," *Applied Physics Letters*, Vol. 37, 1980, pp. 300–302.

119 Bergman, D. J., "Exactly Solvable Microscopic Geometries and Rigorous Bounds for the Complex Dielectric Constant of a Two-Component Composite Material," *Physical Review Letters*, Vol. 44, 1980, pp. 1285–1287.

120 Bruggeman, D. A. G., "Berechnung verschiedener physikalischer Konstanten von heterogenen Substanzen. I. Dielektrizitätskonstanten und Leitfähigkeiten der Mischkörper aus isotropen Substanzen," *Annalen der Physik*, Vol. 24, 1935, pp. 636–679.

121 Landauer, R., "Electrical Resistance of Binary Mixtures," *Journal of Applied Physics*, Vol. 23, 1952, pp. 779–784.

122 Kerner, E. H., "The Electrical Conductivity of Composite Media," *Proceedings of the Physical Society*, Vol. *B* 69, 1956, pp. 802–807.

123 Paul, B., "Macroscopic Criteria for Plastic Flow and Brittle Fracture," in *Fracture*, Liebowitz, H., ed., Vol. III, Chapter 4, Academic Press, New York, 1968.

124 Drucker, D. C., "On Minimum Weight Design and Strength of Nonhomogeneous Plastic Bodies," in *Nonhomogeneity in Elasticity and Plasticity*, Olszak, W., ed., Pergamon Press, 1959, pp. 139–

125 Kelly, A., *Strong Solids*, Clarendon Press, Oxford, 1966.

126 Rosen, B. W., "Tensile Failure of Fibrous Composites," *Journal of the AIAA*, Vol. 2, 1964, pp. 1985–1991.

127 Zweben, C., and Rosen, B. W., "A Statistical Theory of Material Strength With Application to Composite Materials," *Journal of the Mechanics and Physics of Solids*, Vol. 18, 1970, pp. 180–206.

128 Rosen, B. W., and Zweben, C. H., "Tensile Failure Criteria for Fiber Composite Materials," NASA CR-2057, Aug. 1972.

129 Hedgepeth, J. M., and Van Dyke, P., "Local Stress Concentrations in Imperfect Filamentary Composite Materials," *Journal of Composite Materials*, Vol. 1, 1967, pp. 294–309.

130 Harlow, D. G., and Phoenix, S. L., "The Chain-of-Bundles Probability Model for the Strength of Fibrous Materials, I. Analysis and Conjectures," *Journal of Composite Materials*, Vol. 12, 1978, pp. 195–214. "II. A Numerical Study of Convergence," ibid, Vol. 12, 1978, pp. 314–334.

131 Phoenix, S. L., "Statistical Aspects of Failure of Fibrous Materials," in *Composite Materials: Testing and Design*, STP674 ASTM, 1979, pp. 455–483.

132 Rosen, B. W., "Mechanics of Composite Strengthening," in *Fiber Composite Materials*, American Society for Metals, 1965.

133 Schuerch, H., "Prediction of Compressive Strength in Uniaxial Fiber-Metal Matrix Composites," *Journal of AIAA*, Vol. 4, 1966, 102–106.

134 Hashin, Z., "Transverse Strength" in Dow, N.F., and Rosen, B. W., "Evaluation of Filament Reinforced Composites for Aerospace Structural Applications," NASA CR-207, 1965, pp. 36–43.

135 Shu, L. S., and Rosen, B. W., "Strength of Fiber Reinforced Composites by Limit Analysis Method," *Journal of Composite Materials*, Vol. 1, 1967, pp. 366–381.

136 McLaughlin, P. V., "Limit Behavior of Fibrous Materials," *International Journal of Solids and Structures*, Vol. 6, 1970, pp. 1357–1376.

137 McLaughlin, P. V., "Plastic Limit Behavior and Failure of Filament Reinforced Materials," *International Journal of Solids and Structures*, Vol. 8, 1972, pp. 1299–1318.

138 Majumdar, S., and McLaughlin, P. V., "Upper Bounds to In-Plane Shear Strength of Unidirectional Fiber Composites," ASME Journal of Applied Mechanics, Vol. 40, 1973, pp. 824–825.

139 Rosen, B. W., "Strength of Uniaxial Fibrous Composites," in *Mechanics of Composite Materials*, Pergamon Press, 1970, pp. 621–651.

140 Chamis, C. C., "Micromechanics Strength Theories," in *Fracture and Fatigue*, Vol. 5 of *Composite Materials*, Academic Press, New York, 1974, pp. 93–151.

141 Wu, E. M., "Phenomenological Anisotropic Failure Criterion," in *Mechanics of Composite Materials*, Vol. 2 of *Composite Materials*, Academic Press, New York, 1974, pp. 353–431.

142 Tsai, S. W., "Strength Characteristics of Composite Materials," NASA CR-224, 1965.
143 Hill, R., "A Theory of the Yielding and Plastic Flow of Anisotropic Materials," *Proceedings of the Royal Society*, London, Series *A*, Vol. 193, 1948, pp. 281–290.
144 Hoffman, O., "The Brittle Strength of Orthotropic Materials," *Journal of Composite Materials*, Vol. 1, 1967, pp. 200–206.
145 Tsai, S. W., and Wu, E. M., "A General Theory of Strength for Anisotropic Materials," *Journal of Composite Materials*, Vol. 5, 1971, pp. 58–81.
146 Hashin, Z., "Failure Criteria for Unidirectional Fiber Composites," ASME JOURNAL OF APPLIED MECHANICS, Vol. 47, 1980, pp. 329–334.
147 Hashin, Z., and Rotem, A., "A Fatigue Failure Criterion for Fiber-Reinforced Materials," *Journal of Composite Materials*, Vol. 7, 1973, pp. 448–464.
148 Pipes, R. B., and Cole, B. W., "On the Off-Axis Strength Test for Anisotropic Materials," *Journal of Composite Materials*, Vol. 7, 1973, pp. 246–256.
149 Kim, R. Y., "On the Off-Axis and Angle-Ply Strength of Composites," in *Test Methods and Design Allowables for Fibrous Composites*, ASTM, STP 734, 1981, pp. 281–337.
150 Hashin, Z., "Fatigue Failure Criteria for Undirectional Fiber Composites," ASME JOURNAL OF APPLIED MECHANICS, Vol. 48, 1981, pp. 846–852.
151 Awerbuch, J., and Hahn, H. T., "Off-Axis Fatigue of Graphite/Epoxy Composite," in *Fatigue of Fibrous Composite Materials*, ASTM, STP 723, 1981, pp. 243–273.
152 Talreja, R., "Fatigue of Composite Materials: Damage Mechanisms and Fatigue-Life Diagrams," *Proceedings of the Royal Society*, London, Series *A*, Vol. 378, 1981, pp. 461–475.
153 Halpin, J. C., Jerina, K. L., and Johnson, T. A., "Characterization of Composites for the Purpose of Reliability Evaluation," in *Analysis of the Test Methods for High Modulus Fibers and Composites*, ASTM, STP 521, 1973, pp. 5–64.
154 Yang, J. N., and Jones, D. L., "Load Sequence Effects on the Fatigue of Unnotched Composite Materials," in *Fatigue of Fibrous Composite Materials*, ASTM, STP 723, 1981, pp. 213–231.
155 Broutman, L. J., and Sahu, S., "A New Theory to Predict Cumulative Fatigue Damage in Fiberglass Reinforced Plastics," in *Composite Materials: Testing and Design*, ASTM, STP 497, 1972, pp. 170–188.
156 Hashin, Z., and Rotem, A., "A Cumulative Damage Theory of Fatigue Failure," *Materials Science and Engineering*, Vol. 34, 1978, pp. 147–160.
157 Hashin, Z., "Statistical Cumulative Damage Theory for Fatigue Life Prediction," ASME JOURNAL OF APPLIED MECHANICS, in press.
158 Reifsnider, K. L., "Some Fundamental Aspects of Damage in Composite Laminates," *Proceedings 14th Annual Meeting of Society of Engineering Science*, Bethlehem, Pa., 1977, pp. 373–384.
159 Reifsnider, K. L., Henneke, E. G., Stinchcomb, N. W., and Duke, J. C., "Damage Mechanics and NDE of Composite Laminates," in *Mechanics of Composite Materials: Recent Advances*, Proceedings IUTAM Symposium on Mechanics of Composite Materials, Hashin, Z., and Herakovich, C. T., eds., Pergamon Press, 1983.
160 Hahn, H. T., "Nonlinear Behavior of Laminated Composites," *Journal of Composite Materials*, Vol. 7, 1973, pp. 257–271.
161 Hashin, Z., Bagchi, D., and Rosen, B. W., "Non-Linear Behavior of Fiber Composite Laminates," NASA CR-2313, 1974.
162 Rotem, A., and Hashin, Z., "Fatigue Failure of Angle Ply Laminates," *AIAA Journal*, Vol. 14, 1976, pp. 868–872.
163 Hahn, H. T., "Fatigue Behavior and Life Prediction of Composite Laminates," in *Composite Materials: Testing and Design*, ASTM, STP 674, 1979, pp. 383–417.
164 O'Brien, T. K., and Reifsnider, K. L., "Fatigue Damage Evaluation Through Stiffness Measurements in Boron-Epoxy Laminates," *Journal of Composite Materials*, Vol. 15, 1981, pp. 55–70.
165 Rotem, A., "Fatigue Failure Mechanism of Composite Laminates," in *Mechanics of Composite Materials: Recent Advances*, Proceedings IUTAM Symposium on Mechanics of Composite Materials, Hashin, Z., and Herakovich, C. T., eds., Pergamon Press, 1983.
166 Pipes, R. B., and Pagano, N. J., "Interlaminar Stresses in Composite Laminates Under Uniform Axial Extension," *Journal of Composite Materials*, Vol. 4, 1970, pp. 538–548.
167 Soni, S. R., and Pagano, N. J., "Elastic Response of Composite Laminates," in *Mechanics of Composite Materials: Recent Advances*. Proceedings IUTAM Symposium on Mechanics of Composite Materials, Hashin, Z., and Herakovich, C. T., eds., Pergamon Press, 1983.
168 Wang, S. S., and Choi, I., "Boundary Layer Effects in Composite Laminates," ASME JOURNAL OF APPLIED MECHANICS, Vol. 49, 1982, "Part 1-Free-Edge Singularities," pp. 541–548, "Part 2—Free-Edge Solutions and Basic Characteristics," pp. 549–560.
169 Wang, S. S., and Choi, I., "Influence of Fiber Orientation and Ply Thickness on Hygroscopic Boundary—Layer Stresses in Angle-Ply Composite Laminates," *Journal of Composite Materials*, Vol. 16, 1982, pp. 244–258.
170 Herakovich, C. T., Nagarkar, A., and O'Brien, D. A., "Failure Analysis of Composite Laminates With Free Edges," in *Modern Developments in Composite Materials and Structures*, ASME, 1979, pp. 53–66.
171 Herakovich, C. T., "On the Relationship Between Engineering Properties and Delamination of Composite Materials," *Journal of Composite Materials*, Vol. 15, 1981, pp. 336–348.
172 Rosen, B. W., "Failure of Fiber Composite Laminates," in *Mechanics of Composite Materials: Recent Advances*, Proceedings IUTAM Symposium on Mechanics of Composite Materials, Hashin, Z., and Herakovich, C. T., eds., Pergamon Press, 1983.
173 Aboudi, J., "The Effective Moduli of Short-Fiber Composites," *International Journal of Solids and Structures*, in press, 1983.
174 Kennett, B. L. N., "Elastic Wave Propagation in Stratified Media," in *Advances in Applied Mathematics*, Vol. 21, Yih, C. S., ed., Academic Press, New York, 1981, pp. 80–167.
175 Min, B. K., "A Plane Stress Formulation for Elastic Plastic Deformation of Unidirectional Composites," *Journal of the Mechanics and Physics of Solids*, Vol. 29, 1981, p. 327–352.
176 Aboudi, J., "Effective Behavior of Inelastic Fiber-Reinforced Composites," *International Journal of Engineering Sciences*, in press.
177 Watt, P. J., "The Elastic Properties of Composite Materials," *Reviews of Geophysics and Space Physics*, Vol. 14, 1976, pp. 541–563.

Forced Oscillations in a Two-Layer Fluid of Finite Depth

R. K. Manna
Department of Applied Mathematics,
Calcutta University,
92, Acharyya Prafulla Chandra Road,
Calcutta - 700 009, India

An initial value investigation is made of the development of surface and internal wave motions generated by an oscillatory pressure distribution on the surface of a fluid that is composed of two layers of limited depths and of different densities. The displacement functions both on the free surface and on the interface are obtained with the help of generalized Fourier transformation. The method for the asymptotic evolution of the wave integrals is based on Bleistein's method. The behavior of the solutions is examined for large values of time and distance. It is found that there are two classes of waves—the first corresponds to the usual surface waves with a changed amplitude and the second arises entirely due to stratification. Some interesting features of the wave system have also been studied.

1 Introduction

The waves generated by an oscillatory pressure distribution on the surface of a homogeneous fluid has been discussed by Miles [1] in case of an infinite depth and by Debnath [2] in a finite uniform depth. The problem in a stratifed fluid has been studied by Debnath [3] for an oscillatory pressure distribution acting on the interface, while Pramanik [4] and many others examined the wave pattern due to a moving oscillatory surface pressure in a layered fluid. But none of the previous authors made studies on the wave train in the case of a two-layer fluid of limited depth. The aim of the present paper is to show the wave pattern due to an oscillatory pressure distribution on the surface of a two-layer fluid of finite depth.

We consider the initial value problem of waves due to an oscillatory pressure distribution on the surface of a fluid of constant density ρ_1 and of finite depth h_1 which lies over another liquid of constant density $\rho_2(\rho_2>\rho_1)$, and of finite uniform depth h_2. The integral representations of the displacements of both the free surface and the interface are obtained with the help of generalized Fourier transformation method. The integrals are evaluated for large values of time and distance by a method due to Bleistein [6]. The ultimate wave system both on the free surface and on the interface are found to consist of two distinct components. The first component corresponds to the ultimate surface wave for the homogeneous case with, however, a changed amplitude, and the second arises entirely due to stratification. Another interesting fact follows from our investigation regarding the positions of the resulting wave system. It is found that there exits two moving points both on the free surface and on the interface such that in the region left to the first point, both the waves exist in the region in between the points only one wave exists, and in region to the right there is no wave.

2 Formulation of the Problem

We consider the two-dimensional linearized problem of wave propagation in an inviscid, incompressible two-fluid system as one of constant density ρ_1 of uniform depth h_1 that floats over another liquid of density $\rho_2(\rho_2>\rho_1)$ of finite depth h_2. It is convenient to assume that the x-z plane be undisturbed horizontal interface and Y-axis vertically positive upward; and the origin of rectangular Cartesian coordinates is taken on the interface $y = 0$. Waves are generated in the system by the continuous action of a pressure distribution $f(x)$ exp $(i\omega t)$ which is suddenly applied to the free surface at time $t = 0$. We assume that $y = h_1 + \eta_1(x,t)$ and $y = \eta_2(x,t)$ are the equations of the free surface and the interface, respectively, and g is the acceleration due to gravity. Let $\varphi_1(x, y,t)$ and $\varphi_2(x,y,t)$ be the velocity potentials for the upper and lower liquids, respectively. Then the linearized equations of motion and the boundary conditions are

$$\nabla \varphi_1^2=0;\ (-\infty<x<\infty,\ 0\le y<h_1,\ t\ge 0) \tag{1}$$

$$\left.\begin{aligned}
&\frac{\partial\varphi_1}{\partial t}+g\eta_1+\frac{f(x)}{\rho_1}e^{i\omega t}=0 && (2)\\
&\frac{\partial\varphi_1}{\partial y}=\frac{\partial\eta_1}{\partial t} && (3)\\
&\nabla^2\varphi_2=0;\quad(-h_2<y\le 0) && (4)
\end{aligned}\right\}\ \text{at}\quad y=h_1$$

Interfacial conditions are

$$\left.\begin{aligned}
&\rho_1\left(\frac{\partial\varphi_1}{\partial t}+g\eta_2\right)=\rho_2\left(\frac{\partial\varphi_2}{\partial t}+g\eta_2\right) && (5)\\
&\frac{\partial\varphi_1}{\partial y}=\frac{\partial\varphi_2}{\partial y}=\frac{\partial\eta_2}{\partial t} && (6)
\end{aligned}\right\}\ \text{at}\quad y=0$$

Contributed by the Applied Mechanics Division for publication in the JOURNAL OF APPLIED MECHANICS.

Discussion on this paper should be addressed to the Editorial Department, ASME, United Engineering Center, 345 East 47th Street, New York, N.Y. 10017, and will be accepted until two months after final publication of the paper itself in the JOURNAL OF APPLIED MECHANICS. Manuscript received by ASME Applied Mechanics Division August, 1982; final revision, February, 1983.

Initial conditions are

$$\left.\begin{aligned}\varphi_1(x,y,0)=\varphi_2(x,y,0)=0\\ \eta_1(x,0)=\eta_2(x,0)=0\end{aligned}\right\} \tag{7}$$

The boundary conditions at the rigid bottom surface is given by

$$\frac{\partial \varphi_2}{\partial y}=0; \quad \text{at} \quad y=-h_2 \tag{8}$$

Solution to the Problem

The applied pressure $f(x)e^{i\omega t}$ is assumed to be a generalized function in the sense of reference [5]. To solve the preceding system of equation (1)–(8) we introduce Fourier transformations of the functions in x as follows:

$$\bar{\varphi}_1(\kappa,y,t)=\frac{1}{\sqrt{2\pi}}\int_{-\infty}^{\infty}\varphi_1(x,y,t)e^{-i\kappa x}dx \qquad \text{etc.}$$

The solutions of the transformed equations (1) and (4) subject to the transformed conditions (7) and (8) are

$$\varphi_1=A(\kappa,t)\cosh|\kappa|y+B(\kappa,t)\sinh|\kappa|y \tag{9}$$

$$\varphi_2=C(\kappa,t)\cosh|\kappa|(y+h_2) \tag{10}$$

where the constants A, B, and C are the functions of x and t. Transformed condition (6) together with (9) and (10) gives

$$B=C\sinh|\kappa|h_2 \tag{11}$$

Transformed equations of (2) and (3) with the help of (9) gives

$$\frac{\partial^2 A}{\partial t^2}+\frac{\partial^2 B}{\partial t^2}\tanh|\kappa|h_1+g|\kappa|(A\tanh|\kappa|h_1+B)+\frac{i\omega\bar{f}(\kappa)\operatorname{sech}|\kappa|h_1e^{i\omega t}}{\rho_1}=0 \tag{12}$$

Transformed equation of (5) and (6) with the help of (10) and (11) gives

$$\rho_1\frac{\partial^2 A}{\partial t^2}+g|\kappa|(\rho_1-\rho_2)B=\rho_2\coth|\kappa|h_2\frac{\partial^2 B}{\partial t^2} \tag{13}$$

(12) and (13) at once gives

$$\frac{\partial^4 A}{\partial t^4}+g|\kappa|\frac{\rho_2(1+\tanh|\kappa|h_1\coth|\kappa|h_2)}{\rho_1\tanh|\kappa|h_1+\rho_2\coth|\kappa|h_2}\frac{\partial^2 A}{\partial t^2}+(g|\kappa|)^2\frac{(\rho_2-\rho_1)\tanh|\kappa|h_1}{\rho_1\tanh|\kappa|h_1+\rho_2\coth|\kappa|h_2}A$$
$$+\frac{i\omega\bar{f}(\kappa)\operatorname{sech}|\kappa|h_1\{(\rho_1-\rho_2)g|\kappa|+\rho_2\omega^2\coth|\kappa|h_2\}e^{i\omega t}}{\rho_1\{\rho_1\tanh|\kappa|h_1+\rho_2\coth|\kappa|h_2\}}=0 \tag{14}$$

Solution of (14) is

$$A=\sum_{l=1}^{2}\sum_{m=1}^{2}A_{lm}(\kappa)e^{i[(-1)^{m-1}\sigma_l]t}+P(\kappa)e^{i\omega t} \tag{15}$$

where the larger and the smaller roots of (14) are

$$\sigma_1{}^2=\frac{g|\kappa|}{2g_3(\kappa)}\{g_1(\kappa)+g_2(\kappa)\}$$

$$\sigma_2{}^2=\frac{g|\kappa|}{2g_3(\kappa)}\{g_1(\kappa)-g_2(\kappa)\} \tag{16}$$

and

$$P(\kappa)=\frac{i\omega\bar{f}(\kappa)\operatorname{sech}|\kappa|h_1\{\rho_2\omega^2\coth|\kappa|h_2+g|\kappa|(\rho_1-\rho_2)\}}{\rho_1(\sigma_2{}^2-\sigma_1{}^2)g_3(\kappa)}\left[\frac{1}{\sigma_1{}^2-\omega^2}-\frac{1}{\sigma_2{}^2-\omega^2}\right] \tag{17}$$

$$g_1(\kappa)=\rho_2(1+\tanh|\kappa|h_1\coth|\kappa|h_2)$$

$$g_2(\kappa)=\{g_1^2(\kappa)-4(\rho_2-\rho_1)g_3(\kappa)\tanh|\kappa|h_1\}^{1/2}$$

$$g_3(\kappa)=\rho_1\tanh|\kappa|h_1+\rho_2\coth|\kappa|h_2$$

Using the transformed conditions (7) and (8) the constant A_{lm} ($l=1$, 2; $m=1$, 2) are to be determined in the following form:

$$2\sigma_lA_{lm}(\kappa)=\frac{i\bar{f}(\kappa)\operatorname{sech}|\kappa|h_1}{H_1g_3(\kappa)}\left[\frac{H_2(a_{lm}^2-\omega^2)}{\sigma_2{}^2-\sigma_1{}^2}\cdot\frac{1}{\sigma_l-(-1)^{m-1}\omega}-\frac{H_2\{\sigma_l+(-1)^{m-1}\omega\}}{\sigma_2{}^2-\sigma_1{}^2}\right.$$
$$\left.+(-1)^{m-l}\left\{\rho_2\coth|\kappa|h_2\left[a_{lm}^2-\left\{(-1)^{m-1}\sigma_l+\omega\right\}\omega\right]-\frac{J_1(\kappa)}{g_3(\kappa)}\right\}\right]$$

where

$$H_1=\rho_1(\sigma_2{}^2-\sigma_1{}^2)$$

$$H_2=\omega\{(\rho_2-\rho_1)g|\kappa|-\rho_2\omega^2\coth|\kappa|h_2\}$$

$$J_1(\kappa)=g|\kappa|\{(\rho_1{}^2-\rho_1\rho_2+\rho_2{}^2\coth^2|\kappa|h_2)\tanh|\kappa|h_1+\rho_1\rho_2\coth|\kappa|h_2\}$$

$a_{lm}=\sigma_2$; $(l=1)$

$a_{lm}=\sigma_1$; $(l=2)$; $g_3(\kappa)$ already defined.

The surface displacement η_1 is now obtained after Fourier inversion:

$$\left.\begin{aligned}\eta_1=&\int_0^\infty\frac{F_1(\kappa,\sigma_1)}{\sigma_1-\omega}e^{i(\kappa x+\sigma_1t)}dk+\int_0^\infty\frac{F_1(-\kappa,\sigma_1)}{\sigma_1-\omega}e^{i(\sigma_1t-\kappa x)}dk\\
&+\int_0^\infty\frac{F_1(\kappa,-\sigma_1)}{\sigma_1+\omega}e^{i(\kappa x-\sigma_1t)}dk+\int_0^\infty\frac{F_1(-\kappa,-\sigma_1)}{\sigma_1+\omega}e^{-i(\sigma_1t+\kappa x)}dk\\
&-\int_0^\infty\frac{F_1(\kappa,\omega)}{\sigma_1-\omega}e^{i(\omega t+\kappa x)}dk-\int_0^\infty\frac{F_1(-\kappa,\omega)}{\sigma_1-\omega}e^{i(\omega t-\kappa x)}dk\\
&-\int_0^\infty\frac{F_1(\kappa,\omega)}{\sigma_1+\omega}e^{i(\omega t+\kappa x)}dk-\int_0^\infty\frac{F_1(-\kappa,\omega)}{\sigma_1+\omega}e^{i(\omega t-\kappa x)}dk\\
&+\int_0^\infty\frac{F_2(\kappa,\sigma_2)}{\sigma_2-\omega}e^{i(\sigma_2t+\kappa x)}dk+\int_0^\infty\frac{F_2(-\kappa,\sigma_2)}{\sigma_2-\omega}e^{i(\sigma_2t-\kappa x)}dk\\
&+\int_0^\infty\frac{F_2(\kappa,-\sigma_2)}{\sigma_2+\omega}e^{i(\kappa x-\sigma_2t)}dk+\int_0^\infty\frac{F_2(-\kappa,-\sigma_2)}{\sigma_2+\omega}e^{-i(\kappa x+\sigma_2t)}dk\\
&-\int_0^\infty\frac{F_2(\kappa,\omega)}{\sigma_2-\omega}e^{i(\omega t+\kappa x)}dk-\int_0^\infty\frac{F_2(-\kappa,\omega)}{\sigma_2-\omega}e^{i(\omega t-\kappa x)}dk\\
&-\int_0^\infty\frac{F_2(\kappa,\omega)}{\sigma_2+\omega}e^{i(\omega t+\kappa x)}dk-\int_0^\infty\frac{F_2(-\kappa,\omega)}{\sigma_2+\omega}e^{i(\omega t-\kappa x)}dk\\
&-\frac{1}{\sqrt{2\pi}\rho_1g}\int_{-\infty}^{\infty}\bar{f}(\kappa)e^{i(\omega t+\kappa x)}dk-\frac{\rho_2\omega^2}{\sqrt{2\pi}\rho_1g^2|\kappa|}\\
&\int_{-\infty}^{\infty}\frac{\bar{f}(\kappa)\coth|\kappa|h_2\sinh|\kappa|h_1e^{i(\omega t+\kappa x)}dk}{(\rho_1-\rho_2)\sinh|\kappa|h_1+\rho_2\coth|\kappa|h_2\cosh|\kappa|h_1}\end{aligned}\right\} \tag{18}$$

where

$$F_1(\kappa,\sigma)=R_1(\kappa,\sigma)N_1(\kappa,\sigma)$$

$$F_2(\kappa,\sigma)=R_2(\kappa,\sigma)N_1(\kappa,\sigma)$$

$$R_1(\kappa,\sigma)=\frac{\bar{f}(\kappa)\mathrm{sech}|\kappa|h_1}{2\sqrt{2\pi}\,g\sigma_1 H_1 g_3(\kappa)}\left[\frac{H_2(\sigma_2{}^2-\omega^2)}{\sigma_2{}^2-\sigma^2}-\frac{H_2(\sigma^2-\omega^2)}{\sigma_2{}^2-\sigma_1{}^2}\right.$$
$$\left.-(\sigma-\omega)\left\{\rho_2\coth|\kappa|h_2[\omega(\sigma+\omega)-\sigma_2{}^2]+\frac{J_1(\kappa)}{g_3(\kappa)}\right\}\right]$$
$$R_2(\kappa,\sigma)=\frac{\bar{f}(\kappa)\mathrm{sech}|\kappa|h_1}{2\sqrt{2\pi}\,g\sigma_1 H_1 g_3(\kappa)}\left[-\frac{H_2(\sigma_1{}^2-\omega^2)}{\sigma_1{}^2-\sigma^2}-\frac{H_2(\sigma^2-\omega^2)}{\sigma_2{}^2-\sigma_1{}^2}\right.$$
$$\left.+(\sigma-\omega)\left\{\rho_2\coth|\kappa|h_2[\omega(\sigma+\omega)-\sigma_1{}^2]+\frac{J_1(\kappa)}{g_3(\kappa)}\right\}\right]$$
$$N_1(\kappa,\sigma)=\left\{\cosh|\kappa|h_1\right.$$
$$\left.-\frac{\rho_2\coth|\kappa|h_2\sinh^2|\kappa|h_1}{(\rho_1-\rho_2)\sinh|\kappa|h_1+\rho_2\coth|\kappa|h_2\cosh|\kappa|h_1}\right\}\sigma$$
$$+\frac{\omega^2\sigma\sinh|\kappa|h_1(\rho_1\sinh|\kappa|h_1+\rho_2\coth|\kappa|h_2\cosh|\kappa|h_1)}{g|\kappa|\{(\rho_1-\rho_2)\sinh|\kappa|h_1+\rho_2\coth|\kappa|h_2\cosh|\kappa|h_1\}}$$
$H_1, H_2, J_1(\kappa)$ and $g_3(\kappa)$ are already defined.

Similarly displacement of η_2 can be deduced in the following form:

$$\left.\begin{aligned}
(\rho_1-\rho_2)\eta_2=&\int_0^\infty\frac{F_3(\kappa,\sigma_1)}{\sigma_1-\omega}e^{i(\sigma_1t+\kappa x)}dk\\
&+\int_0^\infty\frac{F_3(-\kappa,\sigma_1)}{\sigma_1-\omega}e^{i(\sigma_1t-\kappa x)}dk+\int_0^\infty\frac{F_3(\kappa,-\sigma_1)}{\sigma_1+\omega}e^{i(x\kappa-\sigma_1t)}dk\\
&+\int_0^\infty\frac{F_3(-\kappa,-\sigma_1)}{\sigma_1+\omega}e^{-i(\sigma_1t+\kappa x)}dk-\int_0^\infty\frac{F_3(\kappa,\omega)}{\sigma_1-\omega}e^{i(\omega t+\kappa x)}dk\\
&-\int_0^\infty\frac{F_3(-\kappa,\omega)}{\sigma_1-\omega}e^{i(\omega t-\kappa x)}dk-\int_0^\infty\frac{F_3(\kappa,\omega)}{\sigma_1+\omega}e^{i(\omega t+\kappa x)}dk\\
&-\int_0^\infty\frac{F_3(-\kappa,\omega)}{\sigma_1+\omega}e^{i(\omega t-\kappa x)}dk+\int_0^\infty\frac{F_4(\kappa,\sigma_2)}{\sigma_2-\omega}e^{i(\sigma_2t+\kappa x)}dk\\
&+\int_0^\infty\frac{F_4(-\kappa,\sigma_2)}{\sigma_2-\omega}e^{i(\sigma_2t-\kappa x)}dk+\int_0^\infty\frac{F_4(\kappa,-\sigma_2)}{\sigma_2+\omega}e^{i(\kappa x-\sigma_2t)}dk\\
&+\int_0^\infty\frac{F_4(-\kappa,-\sigma_2)}{\sigma_2+\omega}e^{-i(\sigma_2t+\kappa x)}dk-\int_0^\infty\frac{F_4(\kappa,\omega)}{\sigma_2-\omega}e^{i(\omega t+\kappa x)}dk\\
&-\int_0^\infty\frac{F_4(-\kappa,\omega)}{\sigma_2-\omega}e^{i(\omega t-\kappa x)}dk-\int_0^\infty\frac{F_4(\kappa,\omega)}{\sigma_2+\omega}e^{i(\omega t+\kappa x)}dk\\
&-\frac{F_4(-\kappa,\omega)}{\sigma_2+\omega}e^{i(\omega t-\kappa x)}dk-\frac{\omega^2\rho_2}{\sqrt{2\pi}\rho_1g^2|\kappa|}\\
&\int_{-\infty}^\infty\frac{\bar{f}(\kappa)\coth|\kappa|h_2e^{i(\omega t+\kappa x)}dk}{(\rho_1-\rho_2)\sinh|\kappa|h_1+\rho_2\coth|\kappa|h_2\cosh|\kappa|h_1}
\end{aligned}\right\}\tag{19}$$

where

$$F_3(\kappa,\sigma)=R_1(\kappa,\sigma)N_2(\kappa,\sigma)$$
$$F_4(\kappa,\sigma)=R_2(\kappa,\sigma)N_2(\kappa,\sigma)$$

$N_2(\kappa,\sigma)$

$$=\left\{\rho_1+\frac{\rho_2{}^2\coth^2|\kappa|h_2\sinh|\kappa|h_1}{(\rho_1-\rho_2)\sinh|\kappa|h_1+\rho_2\coth|\kappa|h_2\cosh|\kappa|h_1}\right\}\sigma$$
$$-\frac{\rho_2\omega^2\sigma\coth|\kappa|h_2(\rho_1\sinh|\kappa|h_1+\rho_2\coth|\kappa|h_2\cosh|\kappa|h_1)}{g|\kappa|\{(\rho_1-\rho_2)\sinh|\kappa|h_1+\rho_2\coth|\kappa|h_2\cosh|\kappa|h_1\}}$$

$R_1(\kappa,\sigma)$ and $R_2(\kappa,\sigma)$ defined earlier.

3 Asymptotic Analysis of Unsteady State

In this section we will study the unsteady wave motion for large values of t and $|x|$. The dominant contribution to this asymptotic analysis comes from the poles and the stationary points of the integrals in (18) and (19). Integrals in (18) and (19) contain either a pole or a stationary point or none for each of the integrals, excepting the second and tenth integrals which have both the pole and the stationary point. These integrals are to be evaluated by a method due to Bleistein [6], so that the result remains valid even when the pole and the stationary point coincide.

Now the expression in (16) for $\sigma_1{}^2$ and $\sigma_2{}^2$ have been written in a simpler form by Mahanti [7].

Following them we write

$$\left.\begin{aligned}\sigma_1{}^2&=g|\kappa|\tanh|\kappa|(h-h_0)\\ \sigma_2{}^2&=g|\kappa|\tanh|\kappa|h_0\end{aligned}\right\}\tag{20}$$

where $h=h_1+h_2$ and $0<h_0<h_1$.

First we confine our attention to the waves along the positive x-axis direction. Let the stationary points and the poles for the second and the tenth integrals in (18) be denoted by α_0, α and β_0, β, respectively, which are the solutions to

$$\left.\begin{aligned}\sigma_j'&=x/t\\ \sigma_j&=\omega\end{aligned}\right.\ ;\quad j=1,2$$

where σ' denotes the differentiation of σ with respect to k. It may be pointed out that the stationary points α_0 and β_0 exists only when $\sqrt{g(h-h_0)}>x/t$ and $\sqrt{gh_0}>x/t$.

Following Bleistein we first evaluate the second integral in (18). For this we make a change of variables of integration by the relation.

$$(\sigma_1-\omega)t/x-(\kappa-\alpha)=-\left(\frac{1}{2}z^2+a_1z\right)\tag{21}$$

where a_1 is a parameter inserted to determine the distance between α and α_0. Here we note that $z=0$ corresponds a pole $k=\alpha$. Then the second integral in (18) reduces to

$$\int_0^\infty\left[\frac{F_1(-\kappa,\sigma_1)}{\sigma_1-\omega}\frac{dk}{dz}\right]e^{i(\sigma_1t-\kappa x)}dz=e^{i\left(\omega t-\alpha x+\frac{1}{2}xa_1^2\right)}$$
$$\int_0^\infty\left[\frac{F_1(-\kappa,\sigma_1)}{\sigma_1-\omega}\frac{dk}{dz}\right]e^{-\frac{1}{2}ix(z+a_1)^2}dz\tag{22}$$

where

$$a_1=(\alpha-\alpha_0)\{t/x\cdot|\sigma_1''(\alpha_0)|\}^{1/2}$$

Since $z=0$ is a simple pole of the integrand, we may write

$$\frac{F_1(-\kappa,\sigma_1)}{\sigma_1-\omega}\frac{dk}{dz}=\frac{A_1}{z}+\sum_{n=0}^\infty B_n(z+a_1)^n$$

Now it immediately follows that

$$A_1=\frac{F_1(-\alpha,\omega)}{\sigma_1'(\alpha)}$$
$$B_0=\frac{A_1}{a_1}+\frac{F_1(-\alpha_0,\omega)}{\sigma_1(\alpha_0)+\omega}\left[\frac{x/t}{|\sigma_1''(\alpha_0)|}\right]^{1/2}$$

For $x\to\infty$ by Watson's lemma the expression in (22) reduces to

$$e^{i\left(\omega t-\alpha x+\frac{1}{2}xa_1^2\right)}\left[A_1\int_{-\infty}^\infty\frac{e^{-\frac{1}{2}ixz^2}}{z-a_1}dz+B_0\int_{-\infty}^\infty e^{-\frac{1}{2}ixz^2}dz\right.$$
$$=-\pi(1+i)A\,\mathrm{sgn}(\alpha-\alpha_0)\mathrm{cis}\left(x\frac{a_1{}^2}{2}\right)e^{i(\omega t-\alpha x)}$$

$$+B_0\sqrt{\frac{\pi}{x}}\,(1-i)e^{i\left(\omega t-\alpha x+\frac{1}{2}x a_1^2\right)} \tag{23}$$

where cis $x=c(x)+is(x)$

$$\left[c(x), s(x) = \frac{1}{\sqrt{2\pi}}\int_0^x \frac{1}{\sqrt{x}}[\cos x, \sin x]dx\right]$$

The main contribution of the third and the eleventh integrals in (18) to the asymptotic analysis comes from the stationary points α_0 and β_0, respectively. To evaluate such integrals we use Kelvin's method [8] of stationary phase. For example, this method gives

$$\int_0^\infty \frac{F_1(\kappa,-\sigma_1)}{\sigma_1+\omega}e^{i(\kappa x-\sigma_1 t)}dk$$

$$\approx\left[\frac{2\pi}{t|\sigma_1''(\alpha_0)|}\right]^{1/2}\frac{F_1(\alpha_0,-\omega)}{\sigma_1(\alpha_0)+\omega}e^{i\{x\alpha_0-\sigma_1(\alpha_0)t+\pi/4\}}$$

To estimate the polar contribution of the other integrals in (18) we take the help of Lighthill's [5] method. For example, for large x this method gives

$$\int_0^\infty \frac{F_1(\kappa,\sigma_1)}{\sigma_1-\omega}e^{i\kappa x}dk\approx\pi i\frac{F_1(\alpha_1\omega)}{\sigma_1'(\alpha)}e^{i\alpha x}$$

Collecting all the results so obtained we finally derive the following uniformly valied asymptotic estimate for η_1:

$$\eta_1=\pi\frac{F_1(-\alpha,\omega)}{\sigma_1'(\alpha)}\left[i-(1+i)\operatorname{sgn}(\alpha-\alpha_0)\operatorname{cis}\left(\frac{x\alpha_1^2}{2}\right)\right]$$

$$H\left(\sqrt{g(h-h_0)}>\frac{x}{t}\right)e^{i(\omega t-\alpha x)}$$

$$+\left[\frac{2\pi}{t|\sigma_1''(\alpha_0)|}\right]^{1/2}\frac{F_1(\alpha_0,-\omega)}{\sigma_1(\alpha_0)+\omega}e^{i\{x\alpha_0-\sigma_1(\alpha_0)t+\pi/4\}}$$

$$+B_0\sqrt{\frac{\pi}{x}}\,(1-i)H\left(\sqrt{g(h-h_0)}>\frac{x}{t}\right)e^{i\left(\omega t-\alpha x+\frac{1}{2}xa_1^2\right)}$$

$$+\pi\frac{F_2(-\beta,\omega)}{\sigma_2'(\beta)}\left[i-(1+i)\operatorname{sgn}(\beta-\beta_0)\operatorname{cis}\left(x\frac{a_2^2}{2}\right)\right]$$

$$H\left(\sqrt{gh_0}>\frac{x}{t}\right)e^{i(\omega t-\beta x)}$$

$$+\left[\frac{2\pi}{t|\sigma_2''(\beta_0)|}\right]^{1/2}\frac{F_2(\beta_0,-\omega)}{\sigma_2(\beta_0)+\omega}e^{i\{x\beta_0-\sigma_2(\beta_0)t+\pi/4\}}$$

$$+B_0'\sqrt{\frac{\pi}{x}}\,(1-i)H\left(\sqrt{gh_0}>\frac{x}{t}\right)e^{i\left(\omega t-\beta x+\frac{1}{2}xa_2^2\right)} \tag{24}$$

where a_2 is determined the distance between β_0 and β; B_0' denotes the similar quantity as B_0 and H is the HEAVISIDE step function. Similarly we get the expression for η_2:

$$(\rho_1-\rho_2)\eta_2=\pi\frac{F_3(-\alpha,\omega)}{\sigma_1'(\alpha)}\left[i-(1+i)\operatorname{sgn}(\alpha-\alpha_0)\operatorname{cis}\left(x\frac{a_1^2}{2}\right)\right]$$

$$H\left(\sqrt{g(h-h_0)}>\frac{x}{t}\right)e^{i(\omega t-\alpha x)}$$

$$+\left[\frac{2\pi}{t|\sigma_1''(\alpha_0)|}\right]^{1/2}\frac{F_3(\alpha_0,-\omega)}{\sigma_1(\alpha_0)+\omega}e^{i\{x\alpha_0-\sigma_1(\alpha_0)t+\pi/4\}}$$

$$+D_0\sqrt{\frac{\pi}{x}}\,(1-i)H\left(\sqrt{g(h-h_0)}>\frac{x}{t}\right)e^{i\left(\omega t-\alpha x+\frac{1}{2}xa_1^2\right)}$$

$$+\pi\frac{F_4(-\beta,\omega)}{\sigma_2'(\beta)}\left[i-(1+i)\operatorname{sgn}(\beta-\beta_0)\operatorname{cis}\left(x\frac{a_2^2}{2}\right)\right]$$

$$H\left(\sqrt{gh_0}>\frac{x}{t}\right)e^{i(\omega t-\beta x)}$$

$$+\left[\frac{2\pi}{t|\sigma_2''(\beta_0)|}\right]^{1/2}\frac{F_4(\beta_0,-\omega)}{\sigma_2(\beta_0)+\omega}e^{i\{x\beta_0-\sigma_2(\beta_0)t+\pi/4\}}$$

$$+D_0'\sqrt{\frac{\pi}{x}}\,(1-i)H\left(\sqrt{gh_0}>\frac{x}{t}\right)e^{i\left(\omega t-\beta x+\frac{1}{2}xa_2^2\right)} \tag{25}$$

where D_0 and D_0' denote the similar expression as B_0 and B_0'.

Thus we get an asymptotic estimate of the surface waves and the waves at the interface which are valied for all values of the parameters of the problem.

The wave motion represented in (24) and (25) consists of a system of decaying dispersive waves superposed on a non-decaying traveling wave represented by the first and the fourth terms both in (24) and (25) on the right-hand side of these equations. The traveling waves have a slowly varying amplitude and move with velocities ω/α and ω/β, respectively.

4 Steady State

In this portion we will consider the important limiting case $t>>1$. For large time and distance the transient part in (24) and (25) dies out and the motion reduces to a steady state wave motion. To derive this steady state wave motion we note that for large argument

$$\operatorname{cis}\left(\frac{xa_1^2}{2}\right)\approx\frac{1}{2}(1+i)$$

Then the steady state wave is given by

$$\left.\begin{aligned}\eta_1&=2\pi i\frac{F_1(-\alpha,\omega)}{\sigma_1'(\alpha)}e^{i(\omega t-\alpha x)}\\&+2\pi i\frac{F_2(-\beta,\omega)}{\sigma_2'(\beta)}e^{i(\omega t-\beta x)}\\&=\eta_1'+\eta_1''\end{aligned}\right\}\begin{aligned}&\text{for }\alpha_0>\alpha\\&\beta_0>\beta\end{aligned}$$

$$\left.=0\right\}\begin{aligned}&\beta_0<\alpha\\&\beta_0<\beta\end{aligned} \tag{26}$$

and

$$\left.\begin{aligned}(\rho_1-\rho_2)\eta_2&=2\pi i\frac{F_3(-\alpha,\omega)}{\sigma_1'(\alpha)}e^{i(\omega t-\alpha x)}\\&+2\pi i\frac{F_4(-\beta,\omega)}{\sigma_2'(\beta)}e^{i(\omega t-\beta x)}\\&=\eta_2'+\eta_2''\end{aligned}\right\}\begin{aligned}&\text{for }\alpha_0>\alpha\\&\beta_0>\beta\end{aligned}$$

$$\left.=0\right\}\begin{aligned}&\beta_0<\alpha\\&\beta_0<\beta\end{aligned} \tag{27}$$

In the same way we can deduce the expressions of the waves propagating along the negative x-axis direction as follows:

$$\left.\begin{aligned}\eta_1&=2\pi i\frac{F_1(\alpha,\omega)}{\sigma_1'(\alpha)}e^{i(\omega t+\alpha x)}\\&+2\pi i\frac{F_2(\beta,\omega)}{\sigma_2'(\beta)}e^{i(\omega t+\beta x)}\end{aligned}\right\}\begin{aligned}&\text{for }\alpha_0>\alpha\\&\beta_0>\beta\end{aligned}$$

$$\left.=0\right\}\begin{aligned}&\beta_0<\alpha\\&\beta_0<\beta\end{aligned}$$

and

$$
\left.\begin{aligned}
(\rho_1-\rho_2)\eta_2 &= 2\pi i\frac{F_3(\alpha,\omega)}{\sigma_1'(\alpha)}e^{i(\omega t+\alpha x)} \\
&+ 2\pi i\frac{F_4(\beta,\omega)}{\sigma_2'(\beta)}e^{i(\omega t+\beta x)}
\end{aligned}\right\}\begin{aligned}&\text{for } \alpha_0>\alpha\\ &\beta_0>\beta\end{aligned}
$$

$$
=0 \quad \left.\right\}\begin{aligned}&\beta_0<\alpha\\ &\beta_0<\beta\end{aligned}
$$

Expressions (26) and (27) reveals that both η_1 and η_2 consists of two distinct components of progressive waves. The first component corresponds to the usual surface waves with a changed amplitude and the second component arises entirely due to stratification.

Now we turn our attention to find the physical meaning of the condition that existence of the system of waves depends on the relative magnitudes of α_0, β_0, α, and β. The precise condition for this occurrence of $\alpha = \alpha_0$ and $\beta = \beta_0$ are

$$
\left.\begin{aligned}\sigma_j &= \omega\\ \sigma_j' &= \frac{x}{t}\end{aligned}\right\}; \quad j=1,2 \tag{28}
$$

for substituting $\kappa h_0 = \lambda$ and introducing two dimensionless parameters

$$
u=\frac{\omega\sqrt{h_0}}{\sqrt{g}}, \quad v=\frac{x}{t}\frac{1}{\sqrt{gh_0}}.
$$

Conditions (28) can be written for $j = 1$ in the following form:

$$
\left.\begin{aligned}
u &= \left\{\lambda\tanh\lambda\left(\frac{h}{h_0}-1\right)\right\}^{1/2}\\
v &= \frac{1}{2}\,\frac{\tanh\lambda\left(\frac{h}{h_0}-1\right)+\left(\frac{h}{h_0}-1\right)\lambda\,\mathrm{sech}^2\lambda\left(\frac{h}{h_0}-1\right)}{\left\{\lambda\tanh\lambda\left(\frac{h}{h_0}-1\right)\right\}^{1/2}}
\end{aligned}\right\};
$$

$$
0<\lambda<\infty \tag{29}
$$

and for $j=2$

$$
\left.\begin{aligned}
u &= \{\lambda\tanh\lambda\}^{1/2}\\
v &= \frac{1}{2}\,\frac{\tanh\lambda+\lambda\,\mathrm{sech}^2\lambda}{\{\lambda\tanh\lambda\}^{1/2}}
\end{aligned}\right\}; \quad 0<\lambda<\infty \tag{30}
$$

Since $\sigma_1{}^2 > \sigma_2{}^2$ it immediately follows from (20) that

$$
\frac{h}{h_0}>2 \tag{31}
$$

Equations (29) and (30) under condition (31) are the parametric equations of the two curves I, II in the (u, v) plane as shown in Fig. 1. It is easy to see that for points (v, v) below curve I, $\alpha < \alpha_0$, and for points (u, v) below curve II, $\beta < \beta_0$. We also note that the curves intersect at a point for certain values of the parameter, u, say $u = u_0$. Now let us fix ω, h_0, t and increase x from zero, then for $u < u_0$ we meet first the curve II and then the curve I and the reverse takes place for $u > u_0$. Physically this means that on the water surface there are two moving points x_1 and x_2 say, so that the whole region is divided into three subregions in each of which the wave pattern is different.

The following statements regarding the existence of the steady state waves (η_{1s}) in different regions can be verified:

Case I: $u<u_0$

for $x_2<x$; $\eta_{1s}=\eta_1'+\eta_1''$

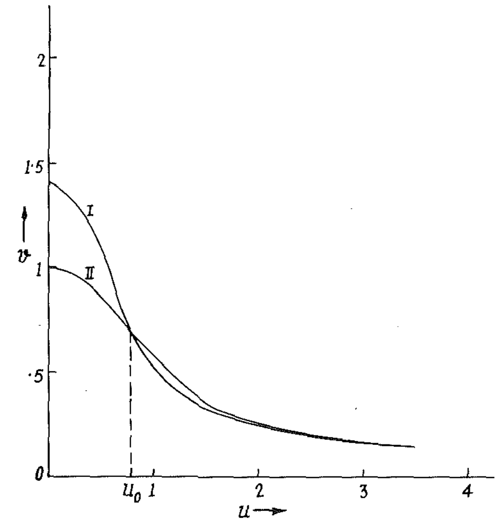

Fig. 1 The curves $\alpha = \alpha_0$ and $\beta = \beta_0 (h/h_0 = 3)$

$x_2<x<x_1$; $\eta_{1s}=\eta_1'$

$x_1<x$; $\eta_{1s}=0$

Case II: $u=u_0$

for $x_1=x_2$

$x<x_1$; $\eta_{1s}=\eta_1'+\eta_1''$

$x>x_1$; $\eta_{1s}=0$

Case III: $u>u_0$

for $x_1<x$; $\eta_{1s}=\eta_1'+\eta_1''$

$x_1<x<x_2$; $\eta_{1s}=\eta_1'$

$x_2<x$; $\eta_{1s}=0$

Our conclusions are based on the particular value of the parameter h/h_0. However, it is easy to see for other values of h/h_0 the qualitative nature of the solution will not change.

Thus our method of investigation gives important information regarding the position of the waves with respect to the source and the two moving lines. It is interesting to note that the two moving points change their relative positions for different values of the parameter u. Similar situation arises at the surface of separation of the two liquids.

Acknowledgments

The author is grateful to Dr. A. K. Pramanik of Calcutta University for his help and guidance during the preparation of this paper.

References

1 Miles, J. W., "Transient Gravity Wave Response to an Oscillatory Pressure," *J. Fluid Mech.*, Vol. 13, 1962, p. 145.

2 Debnath, L., "On the Transient Development of Surface Waves," *Z. Math. Phys.*, Vol. 19, 1968, p. 948.

3 Debnath, L., "Transient Development of Internal Waves in Stratified Ocean," *I. J. Pure and Appl. Math.*, Vol. 1, No. 3, 1970, p. 372.

4 Pramanik, A. K., "Waves Due to a Moving Oscillatory Surface Pressure in a Stratified Fluid," ASME JOURNAL OF APPLIED MECHANICS, Vol. 41, 1974, pp. 571–574.

5 Lighthill, M. J., *An Introduction to Fourier Analysis and Generalised Function*, Cambridge University Press, 1958.

6 Bleistein, N., *Comm. Pure Appl. Math.*, Vol. 19, 1966, p. 353.

7 Mahanti, N. C., "Oscillations Modes in Superposed Fluid," ASME JOURNAL OF APPLIED MECHANICS, Vol. 45, 1978, pp.

8 Stocker, J. J., *Water Waves*, Interscience, 1957.

A. Solan
Professor.
Mem. ASME

S. Olek
Graduate Assistant.

M. Toren
Adjunct Senior Lecturer.

Faculty of Mechanical Engineering,
Technion - Israel Institute of Technology,
Haifa, Israel 32 000

Rotating Compressible Flow Over an Infinite Disk

The laminar boundary layer in rotating compressible flow over an infinite rotating disk is considered for various ratios of disk-to-infinity rotation rates and temperatures. It is shown that a similarity solution exists for $T_d/T_\infty < (\Omega_d/\Omega_\infty)^2$ and linearized solutions near this limit are presented. Numerical solutions for flow and temperature are given for representative values of the parameters, near and far from the limit.

Introduction

In this paper we consider the laminar boundary layer of a rotating compressible flow over a rotating infinite disk, driven either by a difference in rotation rates, or a difference in temperatures, or by both.

In the analysis of rotating flow, similarity solutions for infinite disks with simple boundary conditions serve as a basis for the qualitative understanding of the flow, or as a reference for seminumerical work for complex geometry or boundary conditions. The incompressible rotating flow without heat transfer, with various ratios of rotation between disk and fluid Ω_d/Ω_∞ is well known, both for the linear (Ekman layer) and the nonlinear case (e.g., [1]). Heat transfer in incompressible flow over a rotating disk was first studied for a stationary fluid (e.g., [2]), and has been reexamined by many authors, most recently by Vira and Fan [3], who extended the solution to a range of Ω_d/Ω_∞ from 0 to 1. Compressible flow over a rotating disk with a temperature difference between disk and fluid was treated by Riley for a stationary fluid ($\Omega_\infty/\Omega_d=0$)[4] and for rigid body rotation ($\Omega_d/\Omega_\infty=1$)[5]. Recently, some authors have examined compressible flow in an enclosed geometry, driven by small differences of velocity or temperature at the boundaries (e.g., [6, 7]). These studies, which considered very high angular velocities and emphasized the complex interaction of different regions in a closed geometry, were limited to small (linear) perturbations about an isothermal rigid body rotation. Here we consider the simple geometry of an infinite disk and only a moderate angular velocity, but allow the ratio of angular velocities of disk and fluid (both in the same sense) and the ratio of their temperatures to be arbitrary, i.e., not necessarily close to unity. We limit ourselves to cases in which a thermal boundary layer exists, i.e., when the axial velocity is directed toward the disk, maintaining a balance between convection and diffusion. The direction of the axial velocity is determined by the combined effect of the difference in angular velocities and temperature: when the disk rotates faster than the fluid it causes a radial outflow near the disk and an axial inflow toward it. Conversely, if the disk rotates slower than the fluid there is a radial inflow near the disk and an axial flow away from it. Similarly, cooling the disk causes the fluid near it to be more dense and thus drives the fluid radially outward with an axial inflow, similar to a fast disk, and, conversely, heating causes radial inflow and axial outflow, similar to a slow disk. Thus the four combinations of boundary conditions are: (*a*) disk faster and colder than fluid, (*b*) disk faster and warmer, (*c*) disk slower and colder, and (*d*) disk slower and warmer. In case (*a*) both mechanisms act in the same sense, resulting in an axial inflow. In cases (*b*) and (*c*) the mechanisms are opposed, so that a boundary layer will exist only for disk temperatures below a limiting value determined by the rotation ratio. In fact, one result of the present work is to find this limiting temperature. In case (*d*) both mechanisms act in the same sense resulting in an axial outflow and no thermal boundary layer exists. This case will not be treated here.

In the following we will formulate the coupled problem of flow and heat transfer in the boundary layer. We will show that the limit of existence of a similarity solution is $(T_d/T_\infty)_{\text{limit}}=(\Omega_d/\Omega_\infty)^2$, and will present analytical linearized solutions near this (nonlinear) limit, and numerical solutions away from it. The fully linear compressible and incompressible solutions will be obtained as special cases. The analogous problem of flow near the edge of a finite disk was treated in our previous paper [8]. The main result of the present paper is an extension of the similarity solutions for a rotating disk in compressible flow [4, 5] to rotation and temperature ratios that are not close to unity.

Contributed by the Applied Mechanics Division for publication in the JOURNAL OF APPLIED MECHANICS.

Discussion on this paper should be addressed to the Editorial Department, ASME, United Engineering Center, 345 East 47th Street, New York, N.Y. 10017, and will be accepted until two months after final publication of the paper itself in the JOURNAL OF APPLIED MECHANICS. Manuscript received by ASME Applied Mechanics Division, July 1981; final revision, March 1983.

Analysis

Consider a perfect gas rotating with constant angular velocity Ω_∞ over an infinite disk rotating with angular velocity Ω_d about an axis normal to its plane, $z=0$. The temperature

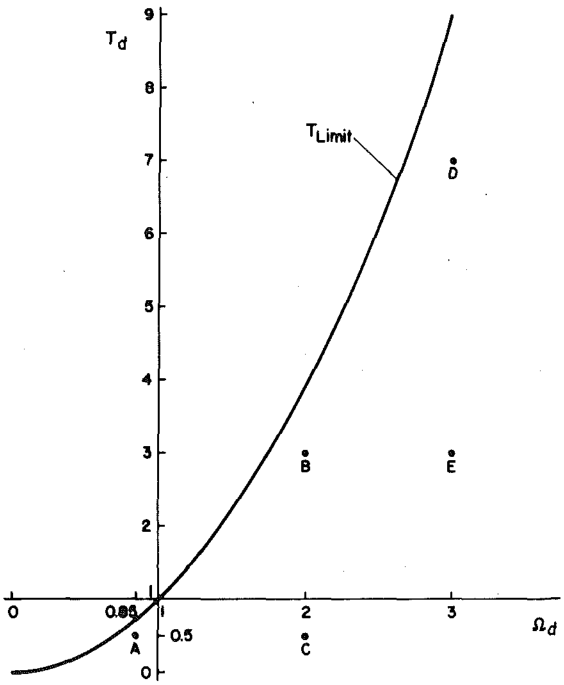

Fig. 1 Limit of existence of boundary layer. *A* to *E* are parameter values used in numerical computations (Figs. 3(*a*-*d*)).

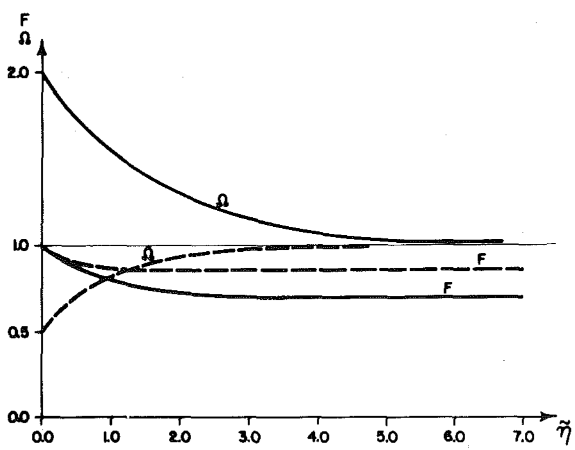

Fig. 2 Outer layer solution $\Omega_d = 2$____; $\Omega_d = 0.5$ ----

of the fluid at infinity is T_∞ and that of the disk T_d. The dimensional boundary layer equations in a stationary frame of reference are:

$$\frac{\partial}{\partial r}(\rho r u) + \frac{\partial}{\partial z}(\rho r w) = 0 \tag{1}$$

$$\rho\left(u\frac{\partial u}{\partial r} + w\frac{\partial u}{\partial z} - \frac{v^2}{r}\right) = -\frac{\partial p}{\partial r} + \frac{\partial}{\partial z}\left(\mu\frac{\partial u}{\partial z}\right) \tag{2}$$

$$\rho\left(u\frac{\partial v}{\partial r} + w\frac{\partial v}{\partial z} + \frac{uv}{r}\right) = \frac{\partial}{\partial z}\left(\mu\frac{\partial v}{\partial z}\right) \tag{3}$$

$$\frac{\partial p}{\partial z} = 0 \tag{4}$$

$$\rho c_p\left(u\frac{\partial T}{\partial r} + w\frac{\partial T}{\partial z}\right) = \frac{\partial}{\partial z}\left(k\frac{\partial T}{\partial z}\right) \tag{5}$$

$$p = \rho R T \tag{6}$$

The boundary conditions are

$$z=0: \quad u=w=0 \quad v=\Omega_d r \quad T=T_d$$
$$z\to\infty: \quad u\to 0 \quad v\to\Omega_\infty r \quad T\to T_\infty \tag{7}$$

All variables have their usual meaning. Our attention is limited to values of r such that $\sqrt{\mu_\infty/(\rho_1(r)\Omega_\infty)} < r < \sqrt{c_p T_\infty/\Omega_\infty}$, i.e., the local Ekman number $\mu_\infty/\rho_1(r)\Omega_\infty r^2)$ is sufficiently small so that the flow is confined to a boundary layer, and the local Mach number $\Omega_\infty r/\sqrt{c_p T_\infty}$ is sufficiently small so that dissipation and pressure work may be neglected. Here $\rho_1(r)$ is the density outside the boundary layer. We introduce a new variable $Z = \int_0^z dz \rho(r,z)/\rho_1(r)$ and a stream function ψ such that $ru = \partial\psi/\partial Z$ and $\rho r w/\rho_1 = \partial\psi/\partial r + (\partial\psi/\partial Z)(\partial Z/\partial r)$ and assume $\mu \propto T$. Then, with the pressure gradient in the boundary layer imposed by its free-stream value $\partial p/\partial r = \rho_1(r) r\Omega_\infty^2$, we obtain

$$\frac{1}{r}\frac{\partial\psi}{\partial Z}\frac{\partial}{\partial r}\left(\frac{1}{r}\frac{\partial\psi}{\partial Z}\right) - \frac{1}{r}\frac{\partial\psi}{\partial r}\frac{\partial}{\partial Z}\left(\frac{1}{r}\frac{\partial\psi}{\partial Z}\right) - \frac{v^2}{r} = -\frac{T}{T_\infty}r\Omega_\infty^2 + \nu_1\frac{\partial^2}{\partial Z^2}\left(\frac{1}{r}\frac{\partial\psi}{\partial Z}\right) \tag{8}$$

$$\frac{1}{r}\frac{\partial\psi}{\partial Z}\frac{\partial v}{\partial r} - \frac{1}{r}\frac{\partial\psi}{\partial r}\frac{\partial v}{\partial Z} + \frac{1}{r^2}\frac{\partial\psi}{\partial Z}v = \nu_1\frac{\partial^2 v}{\partial Z^2} \tag{9}$$

$$\frac{1}{r}\frac{\partial\psi}{\partial Z}\frac{\partial T}{\partial r} - \frac{1}{r}\frac{\partial\psi}{\partial r}\frac{\partial T}{\partial Z} = \frac{\nu_1}{Pr}\frac{\partial^2 T}{\partial Z^2} \tag{10}$$

These equations are similar to those for incompressible flow, except for the T term in (8), and the fact that $\nu_1(r) = \mu_\infty/\rho_1(r)$ is a function of radius. The equations are identical to those of Riley, but for the boundary conditions (reference [4] considered $\Omega_\infty = 0$ and reference [5] considered $\Omega_\infty = \Omega_d$). Following [5] we introduce a similarity assumption

$$\eta = \sqrt{\Omega_\infty/(2\nu_1)}\ Z, \quad \psi = r^2\Omega_\infty\sqrt{2\nu_1/\Omega_\infty}F(\eta) \tag{11}$$

$$v = r\Omega_\infty[1+G(\eta)], \quad T = T_\infty[1+\theta(\eta)] \tag{12}$$

The resulting equations are

$$F'^2 - 2FF'' - G^2 - 2G = -\theta + \tfrac{1}{2}F''' \tag{13}$$

$$2F'G - 2FG' + 2F' = \tfrac{1}{2}G'' \tag{14}$$

$$-2F\theta' = \frac{1}{2Pr}\theta'' \tag{15}$$

with the boundary conditions

$$\eta=0: \quad F=F'=0 \quad G=G_d \quad \theta=\theta_d$$
$$(\text{or } \Omega=\Omega_d \quad T=T_d) \tag{16}$$
$$\eta\to\infty: \quad F'\to 0 \quad G\to 0 \quad \theta\to 0$$
$$(\text{or } \Omega\to 1 \quad T\to 1)$$

(From here on we will use either G and θ or $\Omega = 1+G$, $T = 1+\theta$, where Ω and T now denote dimensionless variables.) These equations will be solved numerically for various values of G_d, θ_d.

Limit of Existence of Solution. As pointed out in the foregoing, a boundary layer always exists when $G_d > 0$, $\theta_d < 0$, does not exist when $G_d < 0$, $\theta_d > 0$, and otherwise exists only when $\theta_d < \theta_{\text{limit}}$ (Fig. 1). We will now show that $\theta_{\text{limit}} = G_d^2 + 2G_d$ (i.e., $T_{\text{limit}} = \Omega_d^2$). For that we assume $G_d = 0(1)$ arbitrary (i.e., $\Omega_d - 1$ is not assumed small) and

$$\theta_d = G_d^2 + 2G_d - \epsilon \quad (T_d = \Omega_d^2 - \epsilon) \tag{17}$$

where $\epsilon << 1$ is positive. Following Riley [5] we assume a two-layer solution. In the inner layer $\eta = 0(1)$ we assume

$$F = \epsilon \hat{F}(\eta), \quad G = G_d - \epsilon \hat{G}(\eta), \quad \theta = 2G_d + G_d^2 - \epsilon \hat{\theta}(\eta) \quad (18)$$

with the boundary conditions

$$\hat{F}(0) = \hat{F}'(0) = 0 \quad \hat{G}(0) = 0 \quad \hat{\theta}(0) = 1 \quad (19)$$

where the remaining boundary conditions will be satisfied by matching with the outer layer. Substituting (18) into (13)–(15) and linearizing with respect to ϵ, we obtain

$$2\Omega_d \hat{G} = \hat{\theta} + \frac{1}{2}\hat{F}''', \quad -2\Omega_d \hat{F}' = \frac{1}{2}\hat{G}'', \quad \hat{\theta}'' = 0 \quad (20)$$

The solution is

$$\hat{F} = \frac{1}{4\sqrt{2}\Omega_d^{3/2}}[1 - e^{-\sqrt{2\Omega_d}\eta}(\cos\sqrt{2\Omega_d}\eta + \sin\sqrt{2\Omega_d}\eta)],$$

$$\hat{G} = \frac{1}{2\Omega_d}(1 - e^{-\sqrt{2\Omega_d}\eta}\cos\sqrt{2\Omega_d}\eta), \quad \hat{\theta} = 1 \quad (21)$$

In the outer layer we rescale

$$\tilde{\eta} = \frac{\epsilon}{\sqrt{2}\Omega_d^{3/2}}\eta \quad (22)$$

$$F = \frac{\epsilon}{4\sqrt{2}\Omega_d^{3/2}}\tilde{F} \quad (23)$$

$$G = \tilde{G} \quad \theta = \tilde{\theta} \quad (\text{or } \tilde{\Omega} = 1 + \tilde{G}, \quad \tilde{T} = 1 + \tilde{\theta}) \quad (24)$$

to obtain the equations

$$\tilde{\Omega}^2 = \tilde{T}, \quad \tilde{\Omega}\tilde{F}' - \tilde{F}\tilde{\Omega}' = \tilde{\Omega}'',$$
$$-\tilde{F}\tilde{T}' = \frac{1}{Pr}\tilde{T}'' \quad (' \equiv d/d\tilde{\eta}) \quad (25)$$

$$\tilde{\eta} = 0: \quad \tilde{F} = 1 \quad \tilde{\Omega} = \tilde{\Omega}_d \quad \tilde{T} = \tilde{\Omega}_d^2$$
$$\tilde{\eta} \to \infty: \quad \tilde{\Omega} \to 1 \quad \tilde{T} \to 1 \quad (26)$$

The nonlinear coupled system of equations (25) and (26) with the two parameters Ω_d, Pr must be solved numerically. In the special case $Pr = 1$ the temperature can be eliminated to yield

$$\tilde{\Omega}\tilde{F}' - \tilde{F}\tilde{\Omega}' = \tilde{M}\tilde{\Omega}'', \quad \tilde{\Omega}'^2 + \tilde{\Omega}^2\tilde{F}' = 0 \quad (27)$$

This has been solved numerically for representative values of $\tilde{\Omega}_d$ both larger and smaller than unity (Fig. 2) (The solution for $Pr \neq 1$ is not presented here, for conciseness).

Thus, a two-layer solution to the problem defined in equation (17) with arbitrary G_d (i.e., Ω_d) and $\epsilon << 1$ has been found, provided that $\epsilon > 0$. It can be seen that as $\epsilon \to 0$, the outer layer expands to infinity, i.e., the boundary layer solution ceases to exist. This proves that solutions exist for $\theta_d < \theta_{\text{limit}} = G_d^2 + 2G_d (T_d < T_{\text{limit}} = \Omega_d^2)$. It is interesting to compare this with the analogous condition for the existence of the asymptotic similarity solution for the thermal boundary layer in compressible flow over the *edge* of a finite disk [8]. For the disk edge problem the condition is (in the present notation) $\theta_d > \theta_{\text{limit}} = G_d^2 + 2G_d$.[1] Clearly, the edge boundary layer solution exists when the disk is *warmer* than the equilibrium value, whereas at the center ("infinite disk") the solution exists when the disk is *colder*. In both cases these are the conditions for axial flow *toward* the disk.[2]

[1] In further analysis of reference [8], it has been found that the existence condition stated on p. 253, first column, last paragraph, is necessary, but not sufficient. The condition should read $0 < v_{w,eq} < 2$, which is in the present notation $\theta_d > G_d^2 + 2G_d$. The upper limit for $v_{w,eq}$ results from discarding solutions in which the equivalent incompressible boundary layer is detached.

[2] A numerical computation of a series expansion of the edge problem in powers of the distance from the edge, shows that the compressible boundary layer exists down to about 0.7 of the disk radius.

The following two special cases reduce to those discussed by others:

Fully Linear Case (Compressible). Consider $G_d << 1$, $\theta_d << 1$, i.e., small perturbation (velocity *and* temperature) about isothermal solid body rotation. The limit of existence of a boundary layer solution is now $\theta_d < \theta_{\text{limit}} = 2G_d$. The inner solution is now obtained by substituting $\Omega_d = 1$ and $\epsilon = G_d - \frac{1}{2}\theta_d$ in (18) and (21), to yield

$$F = \frac{1}{2\sqrt{2}}\left(G_d - \frac{1}{2}\theta_d\right)[1 - e^{-\sqrt{2}\eta}(\cos\sqrt{2}\ \eta + \sin\sqrt{2}\ \eta)]$$

$$G = \left(G_d - \frac{1}{2}\theta_d\right)e^{-\sqrt{2}\eta}\cos\sqrt{2}\ \eta + \frac{1}{2}\theta_d, \quad \theta = \theta_d \quad (28)$$

The outer solution, defined by the linearized form of equations (25) and (26), can now be written in closed form

$$F = \frac{1}{2\sqrt{2}}\left(G_d - \frac{1}{2}\theta_d\right)$$

$$G = \frac{1}{2}\theta_d e^{-Pr(G_d - \frac{1}{2}\theta_d)\sqrt{2}\eta}, \quad \theta = 2G \quad (29)$$

The inner layer is a superposition of an Ekman layer driven by a velocity perturbation in isothermal flow and a Riley layer driven by a temperature perturbation in solid body rotation. Note that the inner layer adjusts the azimuthal velocity to a value determined by the temperature. The outer layer, which exists only in the case of temperature driving, depends on the axial flow due to the combined effect of both driving terms. This fully linear problem is equivalent to that discussed by Brouwers [6] for the case of low angular velocity, without dissipation or pressure work (our $G - \frac{1}{2}\theta$ is equivalent to χ in [6]).

Incompressible Flow. The incompressible flow is obtained from the governing equations with the changes $\rho = \text{const.}$, $\mu = \text{const.}$, $Z = z$, and with the dimensionless temperature redefined as $\theta(\eta) = (T - T_\infty)/(T_d - T_\infty)$. The flow problem F, G is then the well-known solution of Rogers and Lance [1], which, recomputed, can be substituted in the energy equation to obtain θ or $\theta'(0)$. Unlike the compressible case in which the Prandtl number of gases is of order unity, the incompressible case may also be applied to liquids with a much wider range of Prandtl number, or to the analogous mass transfer problem, with the Prandtl number replaced by the Schmidt number. Three limiting cases can be solved explicitly:

(*a*) $Pr << 1$

$$\theta(\eta) = \exp(-4PrF(\infty)\eta), \quad \theta'(0) = -4PrF(\infty) \quad (30)$$

(*b*) $Pr >> 1$

$$\theta(\eta) = 1 - \int_0^{a\eta}\exp(-\xi^3)d\xi/\Gamma\left(\frac{4}{3}\right),$$

$$\theta'(0) = -a/\Gamma\left(\frac{4}{3}\right), \quad a = [2PrF''(0)/3]^{1/3} \quad (31)$$

These expressions are of the same form as in [2], except for the values of $F(\infty)$, $F''(0)$, which here are functions of Ω_d. Essentially similar results were obtained by [3].

(*c*) $\Omega_d = 1 - \epsilon$. The flow is an Ekman layer $F(\eta) = \epsilon/2\sqrt{2}[1 - e^{-\sqrt{2}\eta}(\cos\sqrt{2}\ \eta + \sin\sqrt{2}\ \eta)]$, yielding for $Pr = 0(1)$

$$\theta(\eta) = 1 - \int_0^\eta \exp\left(-4Pr\int_0^\xi F(\zeta)d\zeta\right)d\xi/$$
$$\int_0^\infty \exp\left(-4Pr\int_0^\xi F(\zeta)d\zeta\right)d\xi$$

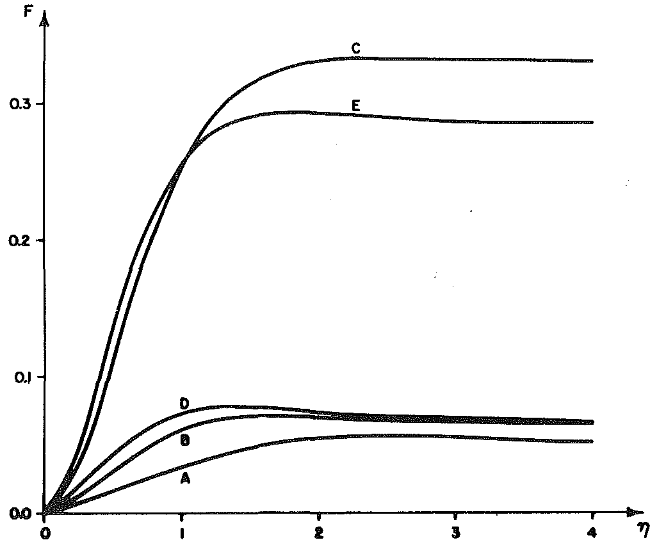

Fig. 3(*a*) Axial velocity

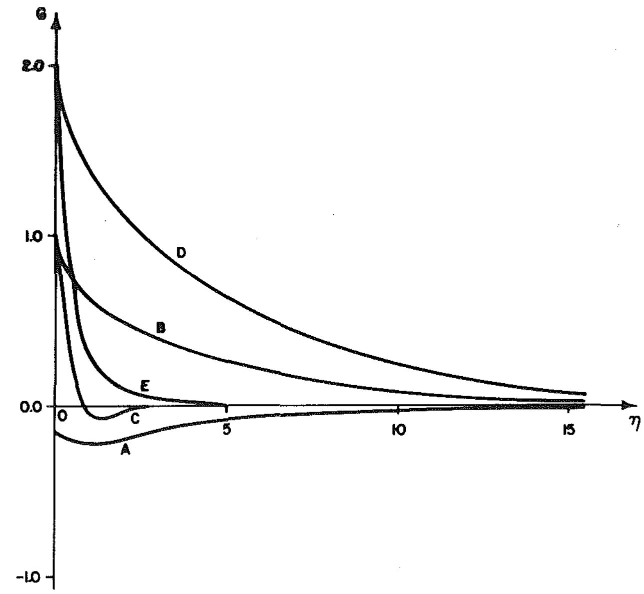

Fig. 3(*c*) Azimuthal velocity

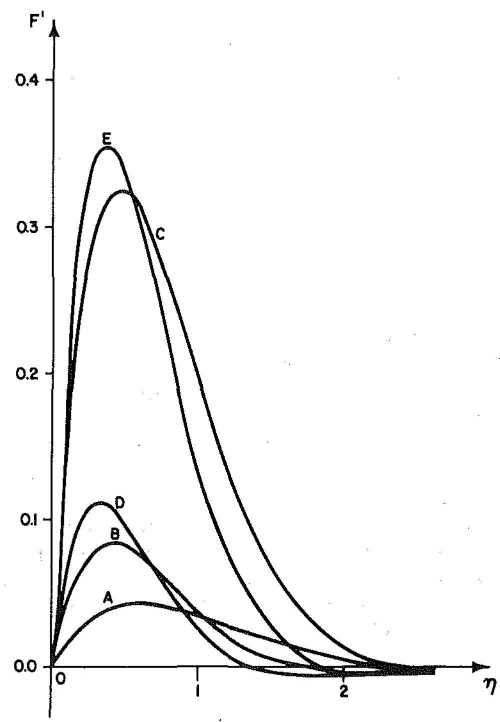

Fig. 3(*b*) Radial velocity

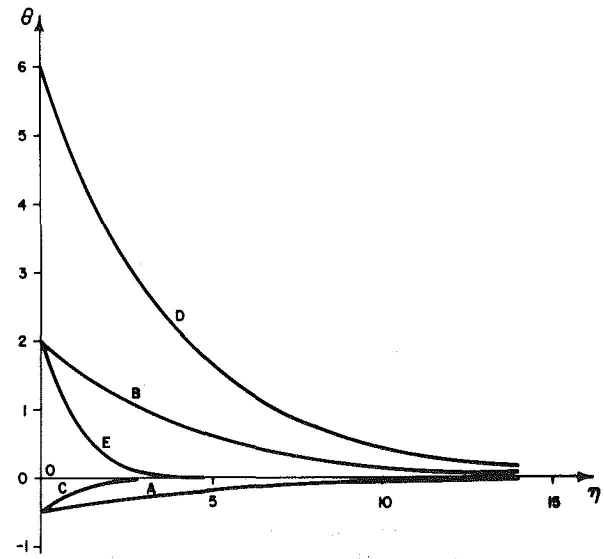

Fig. 3(*d*) Temperature

Fig. 3 Numerical solution, *A* to *E* as in Fig. 1.

$$\theta'(0) = -1/\int_0^\infty \exp\left(-4Pr\int_0^\xi F(\zeta)d\zeta\right)\mathrm{d}\xi \cong -\sqrt{2}Pr\epsilon. \quad (32)$$

Numerical Results and Discussion

The nonlinear set of equations (13)-(16) was solved numerically for five representative values of the velocity and temperature ratios, shown as points A,B,C,D, and E in Fig. 1. Note that A,B, and D are close to the limit of existence of the boundary layer solution and should approach the linearized limit discussed in equations (17)-(27). At A both G_d and θ_d are small (equations (28) and (29)), whereas at B, D, G_d and θ_d are finite, only their difference being small.

Figures 3(*a-d*) show $F(\eta)$, $F'(\eta)$, $G(\eta)$, and $\theta(\eta)$ for the five cases for $Pr=1$. As expected, in Figs. 3(*a*) and 3(*b*) (axial and radial velocities) the results for A, B and D are close, and the values for C and E are significantly larger, in agreement with the fact that these points are much farther away from the limit curve. The difference from D to E is similar to that from B to C (or from A to C is similar to that from B to E).

Figures 3(*c*) and 3(*d*) (azimuthal velocity and temperature) again show the expected trends between the different points, though here the maximum values of the variables, at the disk surface are prescribed by the boundary conditions. Note that the thickness of the boundary layers of G and θ increases as the parameters approach the limit curve, e.g., compare E and D or C and B in Fig. 3(*c*), or E and B or C and A in Fig. 3(*d*).

Figures 4(*a-c*) show numerically computed values of $F''(0)$, $G'(0)$, and $\theta'(0)$, i.e., shear stress and temperature gradient at the disk surface, as functions of T_d,Ω_d. Also shown are the curves obtained from the limiting solutions for small $\epsilon = \Omega_d^2 -$

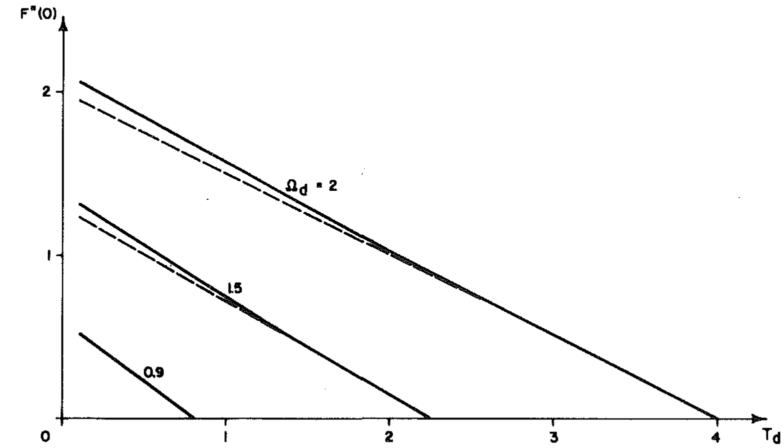

Fig. 4(*a*) Radial velocity gradient

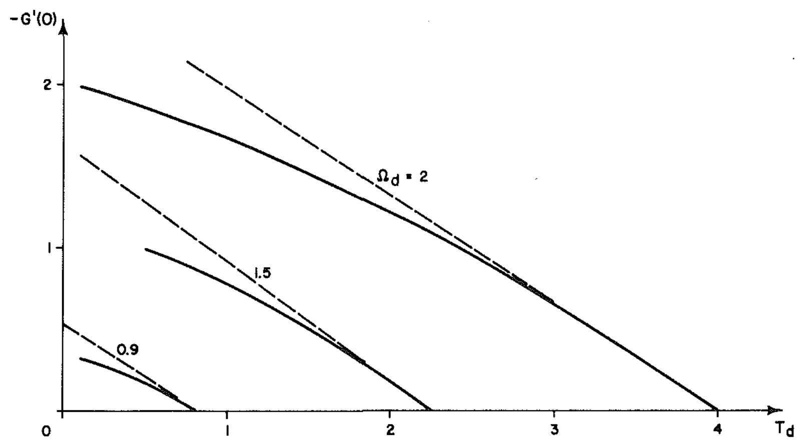

Fig. 4(*b*) Azimuthal velocity gradient

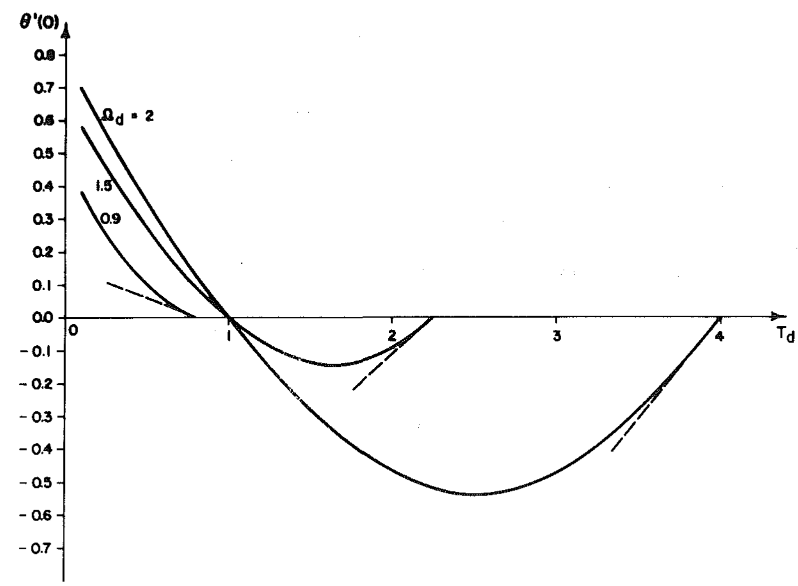

Fig. 4(*c*) Temperature gradient

Fig. 4 Gradients at the wall. ____ Numerical results ---- asymptotic analysis.

T_d. It may be seen that the numerical results of the fully nonlinear problem approach the predicted limits as the parameter values approach the limit curve, viz., the values of $F''(0)$, $G'(0)$, $\theta'(0)$ vanish at the predicted points, and the slopes of the curves near the vanishing points coincide with the slopes predicted from the linearized theory (17)–(27):

$$F''(0) \sim \frac{d^2\hat{F}(\eta)}{d\eta^2}\bigg|_0 = \frac{\epsilon}{\sqrt{2\Omega_d}}$$

$$G'(0) \sim -\epsilon\frac{d\hat{G}(\eta)}{d\eta}\bigg|_0 + \frac{d\tilde{\eta}}{d\eta}\frac{d\tilde{G}}{d\tilde{\eta}}\bigg|_0$$

$$= \frac{-\epsilon}{\sqrt{2\Omega_d}} + \frac{\epsilon}{\sqrt{2}\Omega_d^{3/2}}\tilde{G}'(0) \qquad (33)$$

$$\theta'(0) \sim \frac{d\tilde{\eta}}{d\eta}\frac{d\tilde{\theta}}{d\tilde{\eta}}\bigg|_0 = \frac{\sqrt{2}}{\sqrt{\Omega_d}}\epsilon\tilde{G}'(0)$$

where $\tilde{G}'(0) = \tilde{\Omega}'(0)$ is the value obtained from the numerical solution to equation (27). Note that for $F''(0)$ and $G'(0)$ the linearized values hold over a fairly wide range. In Fig. 4(c) for $\theta'(0)$, the curves pass through (1, 0) since in the absence of dissipation and pressure work, the flow is isothermal for $T_d = 1$.

All the preceding results were obtained for $Pr = 1$. To check the influence of the Prandtl number, two numerical runs: $\Omega_d = 3$, $T_d = 1.5$, and $\Omega_d = 0.65$, $T_d = 0.25$ were repeated for $Pr = 0.7$ and $Pr = 1$ (not shown here). The effect of the Prandtl number is, in this range, quite small.

Acknowledgment

This work was supported by the Fund for the Promotion of Research at Technion (Grant 030-278). The first author wishes to acknowledge the hospitality of the Department of Mechanical and Aerospace Engineering, Rutgers University, during 1981–82, where the final work on this paper was completed.

References

1 Rogers, M. H., and Lance, G. N., "The Rotationally Symmetric Flow of a Viscous Fluid in the Presence of a Rotating Disk," *Journal of Fluid Mechanics*, Vol. 7, 1960, pp. 617–631.

2 Sparrow, E. M., and Gregg, J. L., "Heat Transfer From a Rotating Disk to Fluids of any Prandtl Number," ASME *Journal of Heat Transfer*, Vol. 81, 1959, pp. 249–251.

3 Vira, N. R., and Fan, D. N., "Temperature Distribution in Generalized Von Karman Rotating-Disk Flows," *Numerical Heat Transfer*, Vol. 3, 1980, pp. 483–497.

4 Riley, N., "The Heat Transfer From a Rotating Disk," *Quarterly Journal of Mechanics and Applied Mathematics*, Vol. 17, 1964, pp. 331–349.

5 Riley, N., "Thermally Induced Boundary-Layer Flows in a Rotating Environment," *Journal of Fluid Mechanics*, Vol. 29, 1967, pp. 241–257.

6 Brouwers, J. J. H., "On Compressible Flow in a Rotating Cylinder," *Journal of Engineering Mathematics*, Vol. 12, 1978, pp. 265–285.

7 Wood, H. G., and Morton, J. B., "Onsager's Pancake Approximation for the Fluid Dynamics of a Gas Centrifuge," *Journal of Fluid Mechanics*, Vol. 101, 1980, pp. 1–31.

8 Toren, M., and Solan, A., "Rotating Compressible Flow Over the Edge of a Finite Disk," ASME Journal of Applied Mechanics, Vol. 48, 1981, pp. 249–254.

The Effect of Viscosity on the Forced Vibrations of a Fluid-Filled Elastic Shell

T. C. Su
Associate Professor,
Department of Ocean Engineering,
Florida Atlantic University,
Boca Raton, Fla. 33431
Mem. ASME

The effect of viscosity on the axisymmetric, forced vibrations of a fluid-filled, elastic, spherical shell is studied analytically. Necessary theory, using boundary layer approximation for the fluid as developed in a previous paper for free vibrations, has been extended to incorporate an external forcing excitation. Shell response, fluid loading, and energy dissipation rate are computed for radial, tangential, and combined force excitations. The essential feature of the modal and the total responses is determined by resonant frequencies and various vibration-absorbing frequencies. Frequency spectra for such frequencies, as well as various response curves, are presented in dimensionless forms to illustrate the characteristics of the solution.

1 Introduction

Based on the classical bending theory for shell motion and with a boundary layer approximation employed for the fluid medium, the governing equations for the free, axisymmetric vibrations of an elastic spherical shell containing a compressible viscous fluid have been previously derived [1]. To examine the effect of viscosity on the axisymmetric forced vibrations of a fluid-filled elastic shell in vacuo, the present paper incorporates an additional term corresponding to the external forcing excitation. In the following sections, expressions are given for the normal and tangential shell displacements, the pressure and shear stress on the shell surface, and the energy dissipation rate associated with shell vibration of a general harmonic excitation. From these, resonant frequencies and various vibration-absorbing frequencies are defined for radial, tangential, and combined form excitations, respectively. Computed frequency spectra for these frequencies, as well as various response curves are presented including the limiting cases of the inviscid fluid and the thin shell. Characteristics of these frequencies and response curves are established. It is also found that while the energy is usually dissipated through viscous action, there exist nondissipating modes in which little energy dissipation occurs according to the boundary layer theory. The existence of these nondissipating modes in the vibration of fluid-filled spherical shells may have some implications in the study of head and eye injuries, in fluid dampers for space applications, in spherical acoustic resonators for absorption studies, and in some topics of earth dynamics.

Contributed by the Applied Mechanics Division and presented at the 1983 ASME Applied Mechanics, Bioengineering, and Fluids Engineering Conference, Houston, Texas, June 20–22, 1983 of THE AMERICAN SOCIETY OF MECHANICAL ENGINEERING.

Discussion on this paper should be addressed to the Editorial Department, ASME, United Engineering Center, 345 East 47th Street, New York, N.Y. 10017, and will be accepted until two months after final publication of the paper itself in the JOURNAL OF APPLIED MECHANICS. Manuscript received by ASME Applied Mechanics Division, October, 1982; final revision, November, 1982. Paper No. 83-APM-34.

Copies will be available until February, 1984.

2 Dynamic Responses

Based on classical bending theory of spherical shells, the mode shapes of the kth modes for axisymmetric, torsionless vibration of the shell may be expressed by the Legendre polynomial P_k (cos θ) and its derivatives $(d/d\theta)P_k$ (cos θ). Assuming the Reynolds number for the motion in question is very large, the analysis of the forced vibrations of an elastic spherical shell containing a compressible viscous fluid, carried out in light of boundary layer theory, yields the following response expressions [2]:

$$\frac{W}{h}=\sum_{k=0}^{\infty}\bar{W}_kP_k(\chi)e^{i\Omega t};\quad \frac{V}{h}=\sum_{k=1}^{\infty}\bar{V}_k\frac{dP_k(\chi)}{d\theta}e^{i\Omega t};\qquad (1,2)$$

$$\frac{p_s}{\rho_sc_s^2}=\sum_{k=0}^{\infty}\bar{p}_kP_k(\chi)e^{i\Omega t}$$

$$=-\frac{\rho}{\rho_s}\frac{h}{R}\left(\frac{\Omega R}{c_s}\right)^2\sum_{k=0}^{\infty}\bar{P}_kP_k(\chi)e^{i\Omega t};\qquad (3)$$

$$\frac{\tau_s}{\rho_sc_s^2}=\sum_{k=1}^{\infty}\bar{\tau}_k\frac{dP_k(\chi)}{d\theta}e^{i\Omega t}$$

$$=i^{3/2}\frac{\rho}{\rho_s}\frac{h}{R}\left(\frac{\nu}{Rc_s}\right)^{1/2}\left(\frac{\Omega R}{c_s}\right)^{3/2}\sum_{k=1}^{\infty}\bar{T}_k\frac{dP_k(\chi)}{d\theta}e^{i\Omega t},\ (4)$$

$$\frac{\bar{e}}{\rho_s c_s{}^3 R^2} = \sum_{k=1}^{\infty} \bar{e}_k$$

$$= \sum_{k=1}^{\infty} \sqrt{2}\pi \frac{\rho}{\rho_s} \left(\frac{h}{R}\right)^2 \left(\frac{\nu}{Rc_s}\right)^{1/2} \left(\frac{\Omega R}{c_s}\right)^{5/2} \frac{k(k+1)}{2k+1} |\bar{T}_k|^2. \quad (5)$$

In these expressions, W and V are the radial and tangential displacement of the shell, respectively; p_s and τ_s are the pressure and the shear stress on the shell surface, respectively, and $\bar{e}$ is the time-averaged energy dissipation rate associated with shell vibration. Further, h and R are the thickness and radius of the shell, respectively, $c_s = (E/\rho_s)^{1/2}$, E is the Young's modulus of the shell material, ρ_s is the density of the shell material, Ω is the frequency of vibration, ρ and ν are the density and kinematic viscosity of the fluid, respectively, t is the time, $i = (-1)^{1/2}$, θ is the meridional angle, $\chi = \cos\theta$, and $P_k(\chi)$ is the Legendre polynomial of degree k. $\bar{W}_k$, $\bar{V}_k$, $\bar{P}_k$, and $\bar{T}_k$ are the corresponding response functions of the kth mode for the normal and tangential shell displacements and for the pressure and shear stress on the shell surface, respectively. Here, $\bar{T}_k$ characterizes the behavior of the energy dissipation rate. These response functions are defined as follows for $k \geq 1$:

$$\bar{W}_k = \Delta^{-1}\Big\{\eta_r\Big[\Big(\frac{\Omega R}{c_s}\Big)^2 - \Big(\frac{\bar{\omega}_k R}{c_s}\Big)^2 + \Lambda_1\Big(\frac{\Omega R}{c_s}\Big)^2\Big]$$

$$-\eta_\theta k(k+1)\Big[-C_k\Big(\frac{\hat{\omega}_k R}{c_s}\Big)^2 + \Big(\frac{\Omega R}{c_s}\Big)^2 \Lambda_1 J\Big]\Big\}, \quad (6)$$

$$\bar{V}_k = \Delta^{-1}\Big\{\eta_r\Big[-C_k\Big(\frac{\hat{\omega}_k R}{c_s}\Big)^2 + \Lambda_1\Big(\frac{\Omega R}{c_s}\Big)^2 J\Big]$$

$$+\eta_\theta\Big[\Big(\frac{\bar{\omega}'_k R}{c_s}\Big)^2 - \Big(\frac{\Omega R}{c_s}\Big)^2 - \Big(\frac{\Omega R}{c_s}\Big)^2 (1+m_k)\gamma J$$

$$-\Lambda_1 k(k+1)\Big(\frac{\Omega R}{c_s}\Big)^2 J^2\Big]\Big\}, \quad (7)$$

$$\bar{T}_k = \Delta^{-1}\Big\{\eta_r\Big[C_k\Big(\frac{\hat{\omega}_k R}{c_s}\Big)^2 + \Big[\Big(\frac{\Omega R}{c_s}\Big)^2 - \Big(\frac{\bar{\omega}_k R}{c_s}\Big)^2\Big]J\Big]$$

$$+\eta_\theta\Big[-\Big(\frac{\bar{\omega}'_k R}{c_s}\Big)^2 + \Big(\frac{\Omega R}{c_s}\Big)^2 + \Big(\frac{\Omega R}{c_s}\Big)^2 (1+m_k)\gamma J$$

$$+C_k k(k+1)\Big(\frac{\hat{\omega}_k R}{c_s}\Big)^2 J\Big]\Big\} \quad (8)$$

and

$$\bar{P}_k = J\Delta^{-1}\Big\{\eta_r\Big[\Big(\frac{\Omega R}{c_s}\Big)^2 - \Big(\frac{\bar{\omega}_k R}{c_s}\Big)^2 + \Lambda_1\Big(\frac{\Omega R}{c_s}\Big)^2\Big]$$

$$+\eta_r G\Big[C_k\Big(\frac{\hat{\omega}_k R}{c_s}\Big)^2 + J\Big[\Big(\frac{\Omega R}{c_s}\Big)^2 - \Big(\frac{\bar{\omega}_k R}{c_s}\Big)^2\Big]\Big]$$

$$+\eta_\theta\Big[-k(k+1)\Big[-C_k\Big(\frac{\hat{\omega}_k R}{c_s}\Big)^2 + \Lambda_1\Big(\frac{\Omega R}{c_s}\Big)^2 J\Big]$$

$$-G\Big[\Big(\frac{\bar{\omega}'_k R}{c_s}\Big)^2 - \Big(\frac{\Omega R}{c_s}\Big)^2 - \Big(\frac{\Omega R}{c_s}\Big)^2 (1+m_k)\gamma J$$

$$-C_k k(k+1)\Big(\frac{\hat{\omega}_k R}{c_s}\Big)^2 J\Big]\Big]\Big\}. \quad (9)$$

Here

$$\eta_r = \frac{f_{r,k}}{\rho_s c_s{}^2}\left(\frac{R}{h}\right)^2 \quad \text{and} \quad \eta_\theta = \frac{f_{\theta,k}}{\rho_s c_s{}^2}\left(\frac{R}{h}\right)^2 \quad (10)$$

with

$$f_{r,k} = \frac{2k+1}{2}\int_{-1}^{1} F_r P_k(\chi)d\chi, \text{ and } f_{\theta,k}$$

$$= \frac{2k+1}{2k(k+1)}\int_{-1}^{1} F_\theta \frac{d}{d\theta} P_k(\chi)d\chi, \quad (11)$$

and F_r and F_θ are the amplitude of the applied radial load $F_r e^{i\Omega t}$ and the amplitude of the applied tangential load $F_\theta e^{i\Omega t}$, respectively. Also, C_k and C'_k are constants defined in reference [1], m_k is the ratio of the generalized masses associated with two mode shapes as defined in reference [1], and ω'_k and ω_k are the in vacuo natural frequencies. In terms of m_k, ω'_k and ω_k, the following notations are defined;

$$\bar{\omega}_k{}^2 = (m_k \omega_k{}^2 + \omega'^2_k)/(1+m_k), \quad (12)$$

$$\hat{\omega}_k{}^2 = (\omega'_k{}^2 - \omega_k{}^2)/(1+m_k), \quad (13)$$

and

$$\bar{\omega}'_k{}^2 = (m_k \omega'_k{}^2 + \omega_k{}^2)/(1+m_k), \quad (14)$$

In addition,

$$\Lambda_1 = (1-i)\frac{\sqrt{2}}{2}\frac{R}{h}\frac{\rho}{\rho_s}\left(\frac{\nu}{Rc_s}\right)^{1/2}\left(\frac{\Omega R}{c_s}\right)^{-1/2}, \quad (15)$$

$$G = (1-i)\frac{\sqrt{2}}{2}k(k+1)\left(\frac{\nu}{Rc_s}\right)^{1/2}\left(\frac{\Omega R}{c_s}\right)^{-1/2}, \quad (16)$$

$$J = j_k\Big(\frac{\Omega R}{c}\Big)\Big/ j'_k\Big(\frac{\Omega R}{c}\Big)\Big/\Big(\frac{\Omega R}{c}\Big), \quad (17)$$

and

$$\gamma = \frac{2}{(2k+1)}\frac{R}{h}\frac{1}{M_k}\frac{\rho}{\rho_s}. \quad (18)$$

Here c is the speed of sound in the fluid, M_k is defined in reference [1], the $j_k(\Omega R/c)$ are spherical Bessel functions of the first kind, and $j'_k(z) = dj_k(z)/dz$.

The Δ in equations (6)–(9) is a function of forcing frequency Ω with

$$\Delta = \Big[\Big(\frac{\Omega R}{c_s}\Big)^2 - \Big(\frac{\omega_k R}{c_s}\Big)^2\Big]\Big[\Big(\frac{\Omega R}{c_s}\Big)^2 - \Big(\frac{\omega'_k R}{c_s}\Big)^2\Big]$$

$$+\gamma\Big(\frac{\Omega R}{c_s}\Big)^2 (m_k+1)\Big[\Big(\frac{\Omega R}{c_s}\Big)^2 - \Big(\frac{\bar{\omega}_k R}{c_s}\Big)^2\Big]J$$

$$+\Lambda_1\Big(\frac{\Omega R}{c_s}\Big)^2\Big[\Big(\frac{\Omega R}{c_s}\Big)^2 - \Big(\frac{\omega'_k R}{c_s}\Big)^2\Big]$$

$$+\Lambda_1 k(k+1)\Big(\frac{\Omega R}{c_s}\Big)^2\Big\{2C_k\Big(\frac{\hat{\omega}_k R}{c_s}\Big)^2 J + \Big[\Big(\frac{\Omega R}{c_s}\Big)^2$$

$$-\Big(\frac{\bar{\omega}_k R}{c_s}\Big)^2\Big]J^2\Big\} + \Lambda_1\gamma\Big(\frac{\Omega R}{c_s}\Big)^4 (1+m_k)J \quad (19)$$

The frequency equation for the free vibration problem can be obtained by setting $\Delta = 0$.

For the breathing mode, $k = 0$, the relevant response functions are

$$\bar{W}_0 = -\frac{2\eta_r}{M'_0}\Big[\Big(\frac{\omega'_0 R}{c_s}\Big)^2 - \Big(\frac{\Omega R}{c_s}\Big)^2$$

$$-2\frac{R}{h}\frac{1}{M_0'}\frac{\rho}{\rho_s}J\Big(\frac{\Omega R}{c_s}\Big)^2\Big]^{-1} \quad \text{and} \quad \bar{P}_0 = J\bar{W}_0,$$

in which M'_0 is also defined in reference [1]. The effect of fluid viscosity disappears, as would be expected for the vibration of zeroth mode.

3 Responses to Radial Loading

3.1 Critical Frequencies. Following (6)–(9), the critical

Table 1 Response characteristics $k \geq 1$

			Response function		Forcing frequencies	
			$\Omega \to \Omega_{\text{nat.}}$	$\Omega \to \Omega_{\text{rigid}} \neq \bar{\omega}_k$	$\Omega \to \Omega_{\text{rigid}} = \bar{\omega}_k$	Other vibration absorbing frequencies
(a) Radial loading	Inviscid	$\bar{W}_k$	∞	$0(\gamma^{-1}J^{-1}) \to 0$	0	$\Omega = \bar{\omega}_k$
		$\bar{V}_k$	∞	$0(\gamma^{-1}J^{-1}) \to 0$	$0(1)$	none
		$\bar{P}_k$	∞	$0(\gamma^{-1})$	$0(\gamma^{-1})$	$\Omega = \bar{\omega}_k$ or $J = 0$
	Viscous	$\bar{W}_k$	$0(1/\Lambda_1)$	$0(\Lambda_1^{-1}J^{-2}) \to 0$	$0(J^{-1}) \to 0$	$0(\Lambda_1)$ as $\Omega \to \bar{\omega}_k$
		$\bar{V}_k$	$0(1/\Lambda_1)$	$0(J^{-1}) \to 0$	$0(\gamma^{-1})$	none
		$\bar{T}_k$	$0(1/\Lambda_1)$	$0(\Lambda_1^{-1}J^{-1}) \to 0$	$0(\Lambda_1^{-1}J^{-1}\gamma^{-1}) \to 0$	roots of (20)
		$\bar{P}_k$	$0(1/\Lambda_1)$	$0(\gamma^{-1})$	$0(\gamma^{-1})$	$J = 0$; $0(\Lambda_1)$ if $\Omega \to \bar{\omega}_k$ and $J \sim 0(1)$
(b) Tangential loading	Inviscid	$\bar{W}_k$	∞	$0(\gamma^{-1}J^{-1}) \to 0$	$0(1)$	none
		$\bar{V}_k$	∞	$0(1)$	$0(\gamma J) \to \infty$	roots of (22)
		$\bar{P}_k$	∞	$0(\gamma^{-1})$	$0(J) \to \infty$	$J = 0$
	Viscous	$\bar{W}_k$	$0(1/\Lambda_1)$	$0(J^{-1}) \to 0$	$0(\gamma^{-1})$	none
		$\bar{V}_k$	$0(1/\Lambda_1)$	$0(1)$	$0(J\gamma^{-1}) \to \infty$	$0(\Lambda_1)$ if (22) is satisfied
		$\bar{T}_k$	$0(1/\Lambda_1)$	$0(\gamma\Lambda_1^{-1}J^{-1}) \to 0$	$0(\Lambda_1^{-1}) >> 1$	roots of (23)
		$\bar{P}_k$	$0(1/\Lambda_1)$	$0(1)$	$0(\gamma^{-1}J) \to \infty$	$J = 0$
(c) Combined loading	Inviscid	$\bar{W}_k$	∞	$0(\gamma^{-1}J^{-1}) \to 0$	$0(1)$	root of (25)
		$\bar{V}_k$	∞	$0(1)$	$0(\gamma J) \to \infty$	roots of (26)
		$\bar{P}_k$	∞	$0(\gamma^{-1})$	$0(J) \to \infty$	$J = 0$ or root of (25)
	Viscous	$\bar{W}_k$	$0(1/\Lambda_1)$	$0(J^{-1}) \to 0$	$0(\gamma^{-1})$	$0(\Lambda_1)$ if (25) is satisfied
		$\bar{V}_k$	$0(1/\Lambda_1)$	$0(1)$	$0(\gamma^{-1}J) \to \infty$	$0(\Lambda_1)$ if (26) is satisfied
		$\bar{T}_k$	$0(1/\Lambda_1)$	$0(\gamma\Lambda_1^{-1}J^{-1}) \to 0$	$0(\Lambda_1{}^{-1}) >> 1$	roots of (27)
		$\bar{P}_k$	$0(1/\Lambda_1)$	$0(1)$	$0(\gamma^{-1}J) \to \infty$	$J = 0$; $0(\Lambda_1)$ if (25) is satisfied

frequencies, at which the peak response or vibration-absorbing phenomena [3] is expected to occur, are defined in Table 1. In Table 1, $\Omega_{\text{nat.}}$ is defined as the root of $\Delta = 0$, with Δ defined in (19) and Ω_{rigid} is a root of $J^{-1} = 0$ corresponds to Rayleigh's rigid shell mode [4]. Critical frequencies are computed in the following and presented in form of frequency spectrum. All spectra plotted in this paper are discrete, i.e., only those points corresponding to integral values of the mode number k are physically meaningful. Figure 1 plots the in vacuo natural frequencies ω_k and ω_k', together with frequencies $\bar{\omega}_k$, $\hat{\omega}_k$, and $\bar{\omega}_k'$ defined in (12)–(14). This figure demonstrates the well-known feature of the in vacuo natural frequency. The membrane mode ω_k' is almost independent of h/R; in the bending modes, ω_k is sensitive to changes in h/R for large k due to the bending effect. Figure 1 reveals that $\bar{\omega}_k$ and $\hat{\omega}_k$ are close to ω_k' and therefore are also insensitive to change in h/R. $\bar{\omega}_k'$, however is h/R-dependent and becomes a constant function of k for very thin shells.

For the fluid-filled shells, the peak response is generally expected as the forcing frequency Ω approaches the natural frequency $\Omega_{\text{nat.}}$ To illustrate the characteristics of the solution, computations were carried out with $c_s = 4968$ m/s, $c = 1326$ m/s, $\rho_s = 7852$ kg/m^3, $\rho = 897$ kg/m^3, $\nu = 1.672 \times 10^{-3}$ m^2/s, $R = 0.3048$ m, and the Poisson's ratio of 0.3, corresponding to a petroleum (crude oil) - filled steel shell. Therefore, the dimensionless input parameters are $c/c_s = 0.267$, $\rho/\rho_s = 0.114$, and $(\nu/Rc_s)^{1/2} = 1.05 \times 10^{-3}$. Selection of petroleum (crude oil) and a small size shell is intended to emphasize the effect of viscosity. Since the effect of viscosity appears through $(\nu/Rc_s)^{1/2}$, the viscous effect becomes less pronounced as R increases or ν decreases. Figure 2 plots the spectrum of the circular component of $\Omega_{\text{nat.}}$ corresponding to a petroleum-filled steel shell with $h/R = 0.03$. Also plotted are the roots of $J^{-1} = 0$ and $J = 0$, with J defined according to (17), and the roots of

$$C_k \hat{\omega}_k{}^2 + (\Omega^2 - \bar{\omega}_k{}^2)J = 0. \tag{20}$$

The roots of $J^{-1} = 0$ corresponds to Rayleigh's rigid shell mode (i.e., $\Omega = \Omega_{\text{rigid}}$), whereas the roots of $J = 0$ correspond to the modes with vanishing fluid pressure on shell surface. The roots of (20) are the nondissipating modes under radial loading. From Fig. 2, the natural frequencies follow very closely either those of a fluid-filled rigid shell or the in vacuo natural frequencies.

The roots of $\Delta = 0$, $J = 0$, $J^{-1} = 0$, and (20) are also studied, for a petroleum-filled steel shell with $h/R = 0.0003$. In this case the natural frequencies follow very closely either $\bar{\omega}_k$, 0 or the roots of $J = 0$. For thin shell limit, γ in (18) approaches ∞, and for Δ defined in (19) to become zero, either J, Ω, or $(\Omega - \bar{\omega}_k)$ must vanish. The spectra of $J = 0$, $J^{-1} = 0$ are independent of h/R.

The nondissipating modes, shown as broken lines in Fig. 2 are insensitive to changes in h/R. Because all parameters involved in (20) are insensitive to changes in h/R, the roots are also unaffected.

The peak response usually occurs as $\Omega \to \Omega_{\text{nat.}}$, but the occurrence of the vibration-absorbing phenomena may depend on the type of response and form of forcing. Under radial loading, the modal responses of the normal shell displacement $\bar{W}_k$, tangential shell displacement $\bar{V}_k$, shear stress $\bar{\tau}_k$ on the shell surface, and the energy dissipation rate associated with shell vibration $\bar{e}_k$ vanish as $\Omega \to \Omega_{\text{rigid}}$ (i.e., $J^{-1} = 0$). If $\Omega \to \Omega_{\text{rigid}}$ and $\Omega_{\text{rigid}} = \bar{\omega}_k$, then $\bar{V}_k \sim 0(1)$. As $\Omega \to \bar{\omega}_k$ (Fig. 1), the normal shell displacement $\bar{W}_k$ and the pressure on the shell surface $\bar{p}_k$ vanish for inviscid fluids and are vanishingly small for fluids with small viscosity.

3.2 Response Curves. The response to radial loading are computed for a concentrated force:

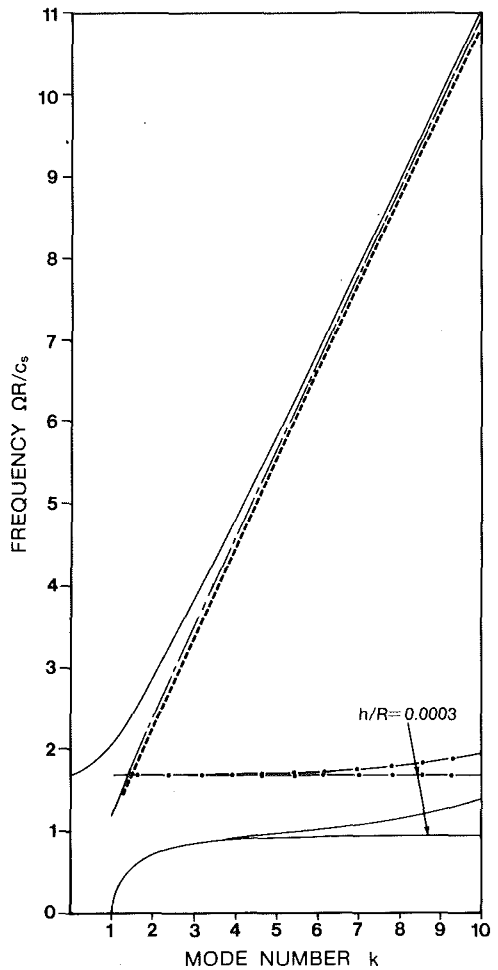

Fig. 1 Natural frequencies of a steel shell in vacuo with h/R = 0.03 or 0.0003 (____ for $\omega_k R/c_s$ and $\omega_k' R/c_s$, __ . __ for $\bar{\omega}_k R/c_s$, ····· for $\hat{\omega}_k R/c_s$, and ___ . ___ $\omega_k' R/c_s$)

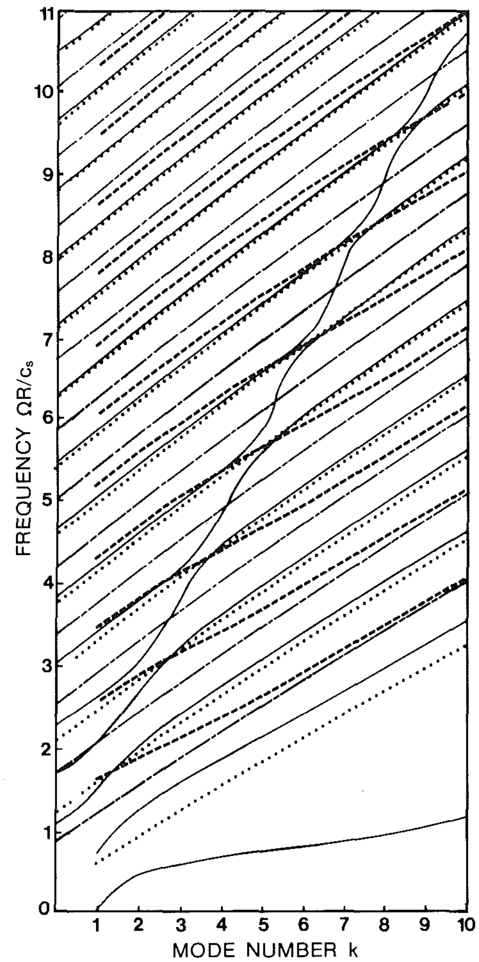

Fig. 2 Critical frequencies of a petroleum-filled steel shell with h/R = 0.03 (____ for natural frequencies, – – – for the roots of (20), ___ . ___ for roots of J = 0, and . . . . . for roots of J^{-1} = 0)

$$\hat{F}_r = F_r e^{i\Omega t} = P\delta(\chi - 1)e^{i\Omega t}. \tag{21}$$

The dimensionless frequencies $\Omega R/c_s$, in increments of 0.05, ranging from 0.05 to 6.0. The static case $\Omega = 0$ is excluded. The force at the apex equals $2\pi R^2 P e^{i\Omega t}$.

The amplitudes of modal responses $\bar{W}_k$, $\bar{V}_k$, $\bar{p}_k$, $\bar{\tau}_k$, and $\bar{e}_k$ versus forcing frequencies are presented in Fig. 3 for mode number $k = 2$. In graphical presentations, parameters are normalized as described in Table 2. Peak responses are observed for all these response functions at and only at the immediate neighborhood of the natural frequencies for each mode. The response curves of $\bar{\tau}_k$ and $\bar{e}_k$ are similar, because both are characterized by the same response function $\bar{T}_k$. As $\Omega \to \Omega_{\text{rigid}}$, vibration-absorbing phenomena are observed for $\bar{W}_k$ and $\bar{V}_k$, and to a less obvious extent for $\bar{\tau}_k$ and $\bar{e}_k$, because as $\Omega \to \Omega_{\text{rigid}}$, $J \to \infty$ and $\bar{T}_k \sim 0\ (\Lambda_1^{-1} J^{-1}) \to 0$. Thus, while $\bar{T}_k \to 0$ as $J \to \infty$, it remains an order of $(1/\Lambda_1)$ higher than $\bar{W}_k$ and $\bar{V}_k$, which are of the order of $(1/J)$. The response curve is a continuous plot with a frequency increment of 0.05. The curve may not be able to resolve the vibration-absorbing phenomenon for $\bar{\tau}_k$ and $\bar{e}_k$ near Ω_{rigid}. Other vibration-absorbing frequencies occurring at $\Omega = \bar{\omega}_k$ for $\bar{W}_k$ and $\bar{p}_k$ are easily noted. The additional vibration-absorbing frequencies of $\bar{p}_k$ at $J(\Omega) = 0$ can also be easily identified. For $\bar{p}_k$ of very thin shells, the vibration-absorbing mode $J = 0$ may be so close to the natural frequency that the vibration-absorbing effect will be dominant in the vicinity of resonance. Consequently, the response curve behaves as a

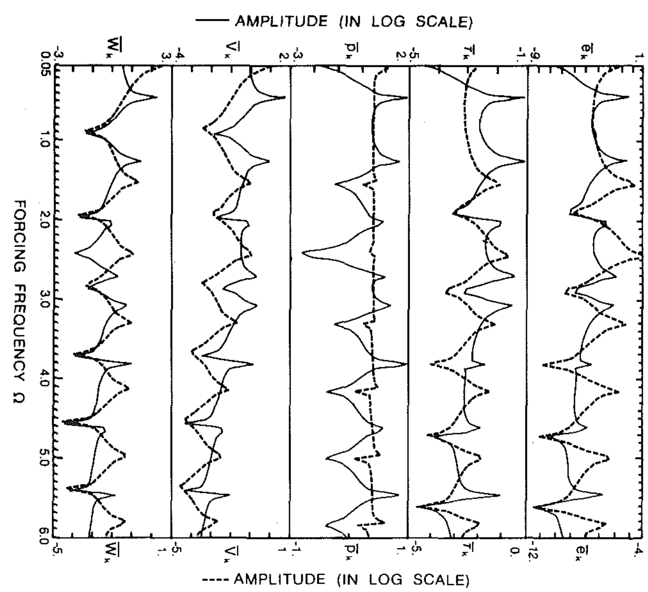

Fig. 3 The amplitudes of modal responses to radial loading for a petroleum-filled shell (k = 2), ____ h/R = 0.03, and ····· h/R = 0.0003

gentle, almost flat, curve; peak and zero responses occur within a narrow band in the thin shell limit. In addition to rigid modes, nondissipating phenomena occur as Ω satisfies equation (20). Those nondissipating modes appear to exhibit a

Table 2 Normalized parameters used in the graphed presentation

Original form		Abbreviation
$\Omega R/c_s$		Ω
$\dfrac{\bar{W}_k}{h}\left[\dfrac{P}{\rho_s c_s^2}\left(\dfrac{R}{h}\right)^2\right]^{-1}$,	$\dfrac{W}{h}\left[\dfrac{P}{\rho_s c_s^2}\left(\dfrac{R}{h}\right)^2\right]^{-1}$	$\bar{W}_k, W$
$\dfrac{\bar{V}_k}{h}\left[\dfrac{P}{\rho_s c_s^2}\left(\dfrac{R}{h}\right)^2\right]^{-1}$,	$\dfrac{V}{h}\left[\dfrac{P}{\rho_s c_s^2}\left(\dfrac{R}{h}\right)^2\right]^{-1}$	$\bar{V}_k, V$
$\dfrac{\bar{p}_k}{P}, \dfrac{p_s}{P}, \dfrac{\bar{\tau}_k}{P}, \dfrac{\tau_s}{P}$		$\bar{p}_k, p_s, \bar{\tau}_k, \tau_s$
$\dfrac{\bar{e}_k}{\rho_s c_s^3 R^2}\left[\dfrac{P}{\rho_s c_s^2}\left(\dfrac{R}{h}\right)\right]^{-2}$		$\bar{e}_k$
$\dfrac{E_{11}}{\rho_s c_s^3 R^2}\left[\dfrac{P}{\rho_s c_s^2}\left(\dfrac{R}{h}\right)\right]^{-2}$,	$\dfrac{E_{10}}{\rho_s c_s^3 R^2}\left[\dfrac{P}{\rho_s c_s^2}\left(\dfrac{R}{h}\right)\right]^{-2}$	E_{11}, E_{10}

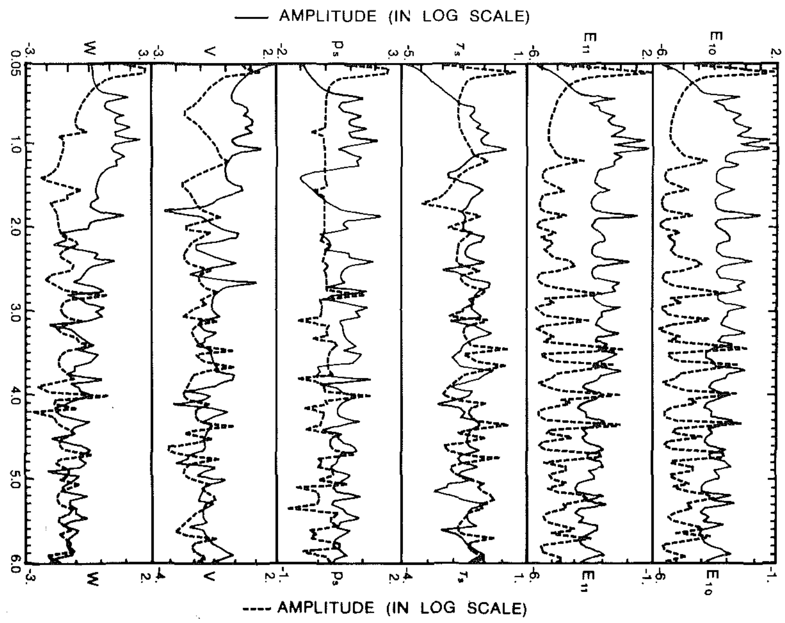

Fig. 4 Total response to radial loading at θ = 90 deg; ——— h/R = 0.03 and ----- h/R = 0.0003

larger band width than the rigid modes. The amplitudes of responses $\bar{W}_k$, $\bar{V}_k$, and $\bar{p}_k$ for the inviscid fluid problem are indiscernible from those of the viscous fluid case given in Fig. 3. The expressions of the response functions (6)–(9), clearly indicate that the contribution of the viscous effect for shell displacements and pressure on the shell surface is of small order, except in the vicinity of the order of $(\nu/Rc_s)^{1/2}$ of frequencies of peak responses and zero responses, which cannot be resolved with an increment of $\Omega R/c_s$ equal to 0.05. Figures plotted with enlarged scales, as given in Fig. 8 of reference [2], show a typical effect of damping on vibratory response. Viscosity reduces the peak response and the resonant frequency.

The total response could be obtained by proper superpositioning. Figure 4 plots the following parameters for the viscous fluid problem: the amplitudes of the total radial displacement W; the total tangential displacement V; the radiated pressure p_s; the shear stress τ_s at the equator (θ = 90 deg) of the shell surface; and the rate of total energy dissipated, E_{11} and E_{10}; E_{11} and E_{10} are evaluated by superimposing the 11 and 10 modes, respectively. Peak responses are observed in the immediate neighborhood of the natural frequencies. A comparison of the E_{11} and E_{10} plots indicates that the use of 11 modes to obtain the total response of a point load excitation is adequate, except for the case in which the frequency is close to one of the natural frequencies associated with the tenth mode.

The detailed study of the phase lag of modal responses is presented in [2]. For mode number k = 2 for the inviscid fluid, the phase lag is either zero or $-\pi$. For the response function $\bar{W}_k$, the phase lag equals $-\pi$ for low-frequency excitations. As the frequency increases, a phase change takes place, with the phase lag switching between 0 and $-\pi$, when $\Omega = \Omega_{\text{nat.}}$, $\Omega = \Omega_{\text{rigid}}$ or $\Omega = \bar{\omega}_k$. The phase lag of $\bar{V}_k$ follows the same rule, except that no phase shift takes place at $\Omega = \bar{\omega}_k$. Thus, for $\Omega < \bar{\omega}_k$, $\bar{W}_k$ and $\bar{V}_k$ are in phase, while for $\Omega > \bar{\omega}_k$, $\bar{W}_k$ and $\bar{V}_k$ are 180 deg out of phase. The phase lag of $\bar{p}_k$ is zero for low frequencies. As Ω is increased, the phase shift takes place at $\Omega = \Omega_{\text{nat.}}$, zeroes at J, and at $\Omega = \bar{\omega}_k$. As to the corresponding phase response for the viscous fluid problem, the phase lag for $\bar{W}_k$ has changed little compared to the inviscid case. A noticeable change in the phase lag for $\bar{V}_k$ takes place as Ω becomes greater than the first resonant frequency above $\bar{\omega}_k$. When $\Omega > \bar{\omega}_k$, the phase responses within the narrow band width between $\Omega_{\text{nat.}}$ and Ω_{rigid} are complicated. The resolution of plots in [2] is insufficient. In the domain of $\Omega > \bar{\omega}_k$, aside from those narrow band widths, the phase lags shift from $-\pi$ to $+\pi$ as a result of viscosity.

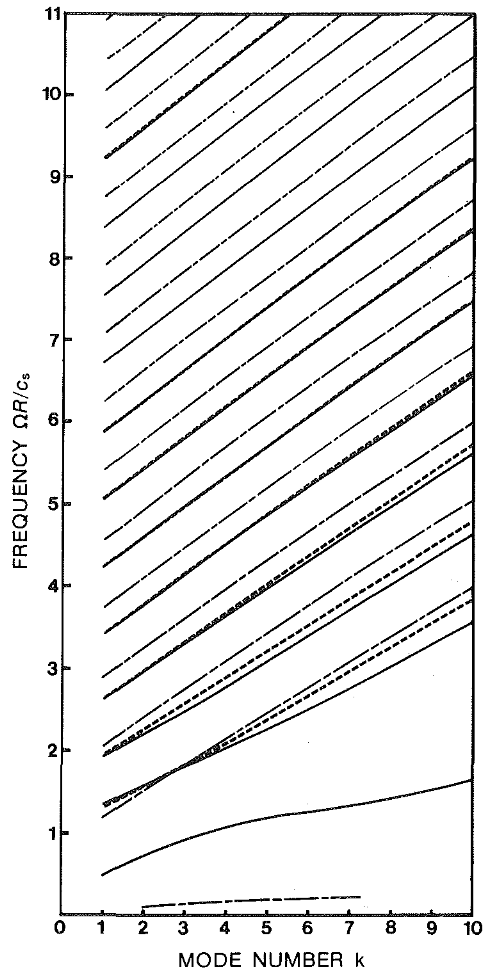

Fig. 5 Additional critical frequencies of petroleum-filled steel shell for tangential loading, _____ roots of (22) (h/R = 0.03), ___ . ___ (h/R = 0.0003), and ····· roots of (23) (h/R = 0.03)

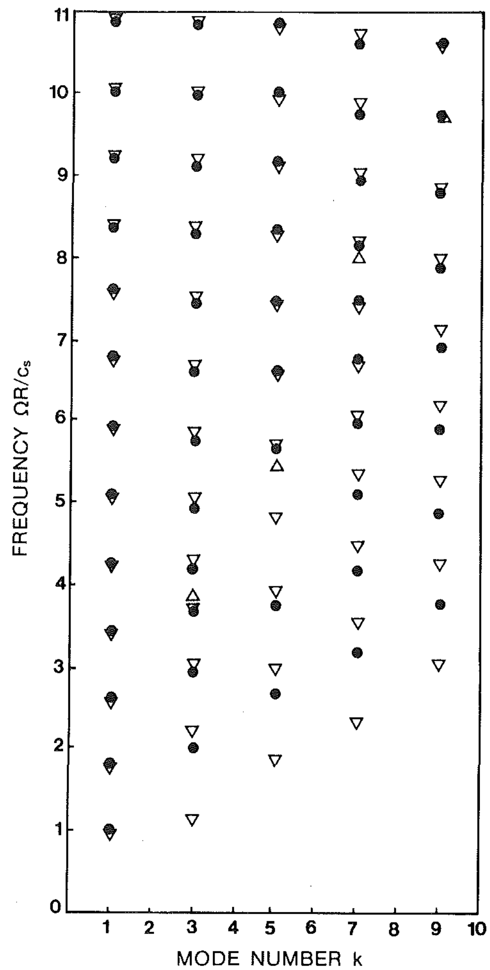

Fig. 7 Critical frequencies of a petroleum-filled steel shell under a combined loading, "Δ," root of (25), "∇" root of (26), and "." root of (27). Only odd modes solution are presented.

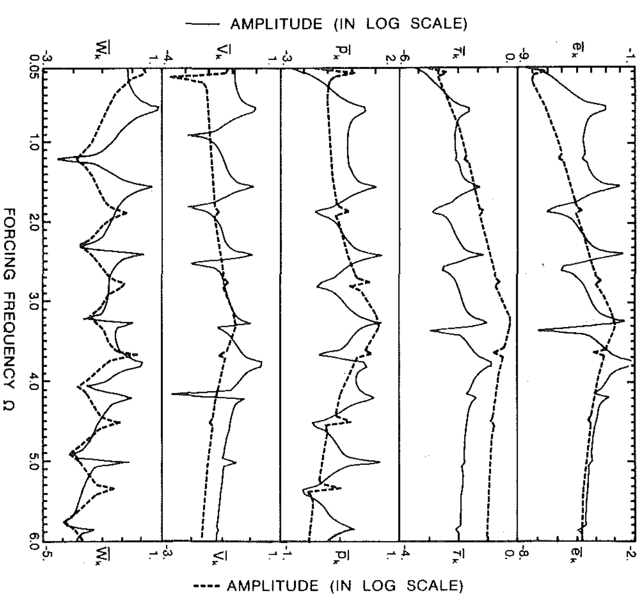

Fig. 6 The responses of the third mode to tangential loading for a petroleum-filled shell, _____ h/R = 0.03, and ····· h/R = 0.0003

4 Responses to Tangential Loading

4.1 Critical Frequencies. The peak responses are expected to occur as $\Omega \rightarrow \Omega_{\text{nat.}}$. In addition, for tangential shell displacement $\bar{V}_k$, fluid loading $\bar{p}_k$, and $\bar{\tau}_k$, and energy dissipation rate $\bar{e}_k$, peak responses may also occur as $\Omega \rightarrow \Omega_{\text{rigid}}$ if $\Omega_{\text{rigid}} = \bar{\omega}_k$.

The vibration-absorbing phenomena for $\bar{W}_k$ occur only as $\Omega \rightarrow \Omega_{\text{rigid}} \neq \bar{\omega}_k$. For $\bar{V}_k$, the vibration-absorbing frequency is given by the roots of

$$\bar{\omega}_k'^2 - \Omega^2[1+(1+m_k)\gamma J]=0 \qquad (22)$$

Figure 5 plots these roots in solid lines and dash-dot lines for petroleum-filled shells with $h/R = 0.03$ and 0.0003, respectively. Except for the lowest branch, the solid lines follow the roots of $J^{-1} = 0$, whereas the dash-dot lines follow the roots of $J = 0$. This is easily explained by expression (22).

The vibration-absorbing phenomena for $\bar{p}_k$ can only occur at roots of $J = 0$. In addition, the nondissipating mode also occurs only when the forcing frequency equals the frequency defined by

$$-\bar{\omega}_k'^2+\Omega^2+\Omega^2\gamma J(1+m_k)+C_k k(k+1)\hat{\omega}_k{}^2 J=0 \qquad (23)$$

These roots are also shown in Fig. 5 in dashed lines for a shell with $h/R = 0.03$. For higher Ω, the dashed lines merge into solid lines. The nondissipating mode for very thin shells follows the root of $J = 0$ as expression (23) shows.

4.2 Response Curves. The responses to tangential loading are computed for a circumferential line force:

$$\hat{F}_\theta = F_\theta e^{i\Omega t} = -P\delta(\chi)e^{i\Omega t}. \qquad (24)$$

The total force at the equator equals $-2\pi R^2 P e^{i\Omega t}$.

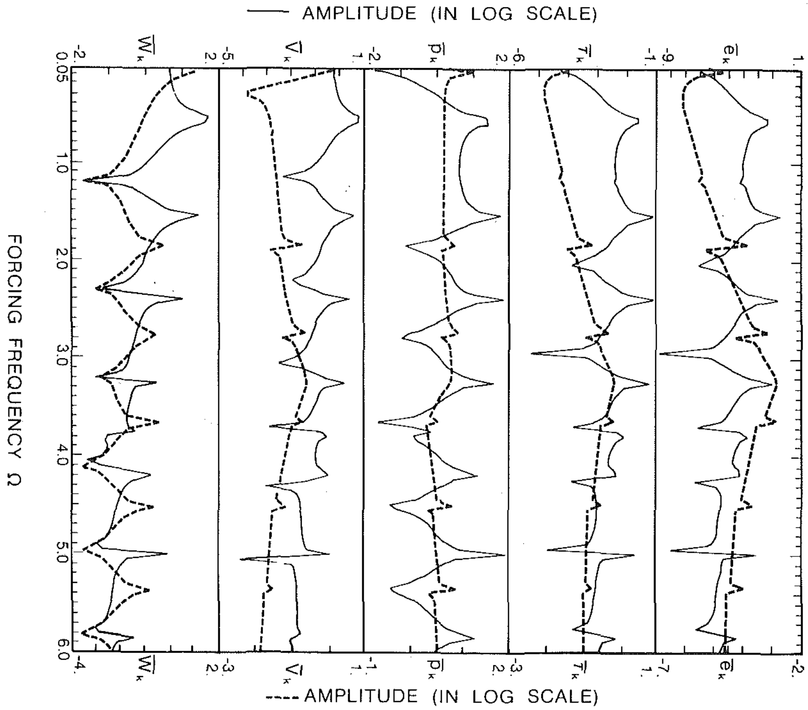

Fig. 8 Third mode responses to combined loading for a petroleum-filled shell, _____ h/R = 0.03, and ----- h/R = 0.0003

The amplitudes of modal responses $\bar{W}_k$, $\bar{V}_k$, $\bar{p}_k$, $\bar{\tau}_k$, and $\bar{e}_k$ versus forcing frequencies are presented in Fig. 6 for mode number $k = 3$. Peak responses are observed for all response functions at and only at the immediate neighborhood of the natural frequency for each mode, except those for $\bar{W}_k$ with $h/R = 0.0003$, as $\Omega R/c_s$ approaches 3.271913. For the case of viscous fluid, this resonant frequency is associated with a large damping component of 0.234651, so that the peak response is smoothed out by viscous damping.

As $\Omega \rightarrow \Omega_{\text{rigid}}$, vibration-absorbing phenomena are observed for $\bar{W}_k$. For $\bar{\tau}_k$ and $\bar{e}_k$, the vibration-absorbing phenomena as $\Omega \rightarrow \Omega_{\text{rigid}}$ are not noticeable in the plot, because $\bar{T}_k \sim 0(1/\Lambda_1/J)$. Although $\bar{T}_k$ approaches zero as $J \rightarrow \infty$, it is of $0(1/\Lambda_1)$ higher than $\bar{W}_k$. The response curve is a continuous plot with a frequency increment of 0.05 and is not expected to resolve the vibration-absorbing phenomena of band width in the order of Λ_1 for $\bar{\tau}_k$ and $\bar{e}_k$ near Ω_{rigid}. Other vibration-absorbing frequencies such as zeroes of J for $\bar{p}_k$, roots of (22) for $\bar{V}_k$ and roots of (23) for $\bar{T}_k$ are easily noted in the figure.

While the vibration-absorbing frequencies for $\bar{W}_k$ and $\bar{p}_k$, which occur at Ω_{rigid} and zeroes of J, respectively, are independent of h/R (Fig. 6), the vibration-absorbing frequencies for $\bar{V}_k$, $\bar{\tau}_k$ and $\bar{e}_k$ are thickness-dependent. For very thin shells, γ in (22) and (23) become very large. The zeroes of (22) and (23) are expected to be very close to the zeroes of J. Thus, in the thin shell limit, the vibration-absorbing frequencies for $\bar{V}_k$, $\bar{\tau}_k$ and $\bar{e}_k$ become close to those for $\bar{p}_k$, as confirmed by Fig. 6. In addition, both the peak and zero responses of $\bar{V}_k$, $\bar{p}_k$, $\bar{\tau}_k$ and $\bar{e}_k$ approach zeroes of J in the thin shell limit. They appear as narrowly banded perturbations on a base curve, which gently peaks near ω_k'.

The corresponding phase lag is also studied [2]. The phase lag of modal response for the inviscid fluid are either zero or π. A phase shift takes place, from zero to π or vice versa, when a resonant frequency or vibration-absorbing frequency is encountered. Again, for the thin shell limit, both resonant frequency and the vibration-absorbing frequency of $\bar{V}_k$ and $\bar{p}_k$ approach the zero of J. The effect of the phase shift is cancelled in a narrow frequency band and is not resolvable.

Viscosity significantly alters the corresponding phase responses for the viscous fluid problem. At low frequencies, the phase lag of $\bar{\tau}_k$ starts from $-\pi/4$ for $k = 3$. The phase shifts as a resonant frequency or a vibration-absorbing frequency is encountered. As pointed out in the discussion of amplitude response of $\bar{V}_k$, $\bar{p}_k$, and $\bar{\tau}_k$ the response amplitude versus frequency in the thin shell limit appears to form a response curve with peaks near the in vacuo frequencies ω_k and ω_k'. The overall phase pattern seems to respond to this general feature with the group phase shift taking place near ω_k and ω_k'.

As to the total responses to tangential loading, peak responses are observed in the immediate neighborhood of the natural frequencies for W and to a lesser extent for V, p_s, τ_s, and E for very thin shells. Because the resonant and the vibration-absorbing frequencies are very close in the thin shell limit for V, p_s, and τ_s, the response curve behaves as a gentle curve with peaks near ω_k' of odd k.

5 Responses to Combined Loading

The responses to combined loading are computed for a concentrated force of (21) and a line force of (24). The force at the apex and the force at the equator are $2\pi R^2 P\exp(i\Omega t)$ and $-2\pi R^2 P\exp(i\Omega t)$, respectively. The net force is zero. Under this loading, even mode responses are the same as those given in Section 3 for radial loading.

Peak responses are generally expected to occur in the neighborhood of the natural frequency for each mode. Peak responses for $\bar{\tau}_k$ and $\bar{e}_k$ may also occur as $\Omega \rightarrow \Omega_{\text{rigid}} = \bar{\omega}_k$. As $\Omega \rightarrow \Omega_{\text{rigid}} \neq \bar{\omega}_k$, zero responses for $\bar{W}_k$, $\bar{\tau}_k$, and $\bar{e}_k$ are expected. Zero response occurs for $\bar{p}_k$ if $J = 0$. In addition, both $\bar{W}_k$ and $\bar{p}_k$ are of the order of Λ_1 if the following relationship is satisfied.

$$[\Omega^2 - \bar{\omega}_k{}^2 + \eta k(k+1)\ C_k \hat{\omega}_k{}^2] = 0 \tag{25}$$

in which $\eta = \eta_\theta/\eta_r$. One root of (25) exists for each mode. The solutions for the odd mode are represented by triangles (Δ) in Fig. 7. Also shown in Fig. 7 are the roots of

$$\{-C_k\hat{\omega}_k{}^2+\eta[\bar{\omega}_k'^2-\Omega^2-\Omega^2(1+m_k)\gamma J]\}=0 \qquad (26)$$

as inverted triangles (∇) and

$$[-C_k\hat{\omega}_k{}^2-(\Omega^2-\bar{\omega}_k{}^2)J]+\eta[\bar{\omega}_k'^2-\Omega^2 -\Omega^2\gamma J(1+m_k)-C_k k(k+1)\hat{\omega}_k{}^2 J]=0 \qquad (27)$$

as solid circles (•) for odd modes in which $\bar{V}_k$ and $\bar{e}_k$ (or $\bar{\tau}_k$) are expected to become vanishingly small. Petroleum-filled shell with $h/R = 0.03$ is assumed. The roots of (27) follow those of $J^{-1} = 0$, for higher frequency excitations and broken lines in Fig. 2 for lower frequencies. The roots of (26) follow those of $J^{-1} = 0$. The h/R has little effect on roots of (25), whereas the root of (26) and (27) will follow those of $J = 0$ in the limit of very thin shells.

The amplitudes of modal responses are shown in Fig. 8 for combined loading. Locations of critical frequencies are readily noted. The peak and zero responses of $\bar{V}_k$, $\bar{p}_k$, $\bar{\tau}_k$, and $\bar{e}_k$ are narrowly banded in the thin shell limit. They appear as perturbations on a base curve which gently peaks near ω_k and ω_k'. The overall phase pattern seems to respond to this general feature with the group phase shift that takes place near ω_k and ω_k'. Because the resonant and the vibration-absorbing frequencies are very close in the thin shell limit for V, p_s, and τ_s, the total response curve behaves as a gentle curve with peaks near ω_k' of odd k [2].

6 Summary

To clarify the effect of viscosity on fluid-structure interaction, axisymmetric vibrations of a compressible fluid contained in a spherical elastic shell under harmonic excitation has been investigated on the basis of boundary layer theory.

An expression for the response to a general harmonic excitation is obtained. From this, the response of the shell, the fluid loading, and the energy dissipation rate are examined for radial, tangential, and combined force excitations. Various limiting cases are studied, including the inviscid fluid limit and the thin shell limit.

The essential feature of the modal and the total response is determined by resonant frequencies and various vibration-absorbing frequencies. Characteristics of these frequencies and response curves are established. These characteristics may have some implications in applications related to the vibration of spherical shells containing viscous fluid.

References

1 Su, T. C., "The Effects of Viscosity on Free Oscillations of Fluid-Filled Spherical Shells," *Journal of Sound and Vibration*, Vol. 74, No. 2, Jan. 1981, pp. 205–220.

2 Su, T. C., "The Effects of Viscosity on the Dynamic Response of a Fluid-Filled Elastic Shell," Texas Engineering Experiment Station Report No. COE-244, Sept. 1981.

3 Timoshenko, S., *Vibration Problems in Engineering*, 2nd Ed., D. Van Nostrand, New York, 1947, pp. 240–252.

4 Rayleigh, L., "On the Vibrations of a Gas Contained Within a Rigid Spherical Envelope," *Proceedings of London Mathematical Society*, Vol. 4, 1872, pp. 93–103.

R. C. Benson
Associate Professor,
Department of Mechanical Engineering,
University of Rochester,
Rochester, N.Y. 14627
Mem. ASME

Observations on the Steady-State Solution of an Extremely Flexible Spinning Disk With a Transverse Load

The steady deflection of a transversely loaded, extremely flexible, spinning disk is studied. Membrane theory is used to predict the shapes and locations of waves that dominate the response. It is found that waves in disconnected regions are possible. Some results are presented to show how disk stiffness moderates the membrane waves, the most important result being an upper bound on the highest ordered wave of significant amplitude. A hybrid system of differential equations and boundary conditions is developed to replace the pure membrane formulation that is singular, and the full fourth-order plate formulation that is numerically sensitive. The hybrid formulation retains the salient features of the flexible disk response and facilitates calculations for very small disk stiffnesses.

1 Introduction

It is the purpose of this paper to examine the steady-state, transverse deflections of the most flexible spinning disks, such as computer "floppy" disks. Attention is focused on the near-membrane problem, which is a disk with extremely small but nonzero intrinsic stiffness. Solutions are difficult to obtain because, as shown by Benson and Bogy [1], the pure membrane problem is singular. Higher ordered plate terms may be retained in the analysis; however, the leading terms in the governing differential equations may be so small, and render the problem so delicate, that numerical convergence is impossible to achieve. Most numerical results in the spinning disk literature are for stiffnesses more appropriate to circular saw blades rather than computer floppy disks.

Following the problem formulation of Section 2, the near-membrane is examined from three different viewpoints; pure membrane theory in Section 3, full fourth-order plate theory in Section 5, and a hybrid second-order approach in Section 4. The membrane equations of Section 3 are used to predict the dominant part of the flexible disk response. Despite the singularity of this formulation, much can be deduced about the eventual solution when the small stiffness is reintroduced. It is found that the flexible disk will always have an annulus adjacent to the rim which supports steady, transverse waves along characteristic arcs. Depending on the clamping geometry and material selection, there may sometimes appear a second wave-supporting annulus, disconnected from the first, which is adjacent to the clamp.

In Section 4, nonsingular, second-order differential equations are derived which retain the small disk stiffness only in combination with a parameter that grows large. The choice of appropriate boundary conditions is discussed. These equations may be solved numerically for exceedingly small stiffnesses and give promising results. These are used to illustrate the results of Section 5 in which bounds on dominant waves are established. An examination of the terms of the fourth-order plate equations shows that disk stiffness moderates the membrane waves, particularly in setting an upper bound on the highest ordered wave of significant amplitude.

Reference [1], and the thesis by Benson [2] are the primary references for this work. The other spinning disk references cited here are representative of an extensive literature, and are chosen for their quality and historical importance. The Simmonds paper [3] is concerned with free vibrations in a spinning membrane and has closed-form solutions in terms of hypergeometric functions. Eversman and Dodson [4] examine free vibrations in a spinning disk. They numerically calculate frequencies of free vibration for low-ordered modes and a wide range of disk stiffnesses. The Greenberg [5] and Adams [6] papers are representative of more modern works specifically directed toward floppy disk design. They take into account read/write head interactions and hydrodynamic effects from the surrounding air.

2 Problem Formulation

Figure 1 shows the geometry of the spinning disk. It is clamped at radius a, free at radius b, and has a small thickness $h << b$. The disk is homogeneous, isotropic, elastic with Young's modulus E, Poisson's ratio ν, and mass density ρ. q is a steady transverse load and Ω is the angular velocity. r and ϕ are space-fixed polar coordinates. The problem is non-dimensionalized by taking

Contributed by the Applied Mechanics Division for publication in the JOURNAL OF APPLIED MECHANICS.

Discussion on this paper should be addressed to the Editorial Department, ASME, United Engineering Center, 345 East 47th Street, New York, N.Y. 10017, and will be accepted until two months after final publication of the paper itself in the JOURNAL OF APPLIED MECHANICS. Manuscript received by ASME Applied Mechanics Division, July, 1982; final revision, December, 1982.

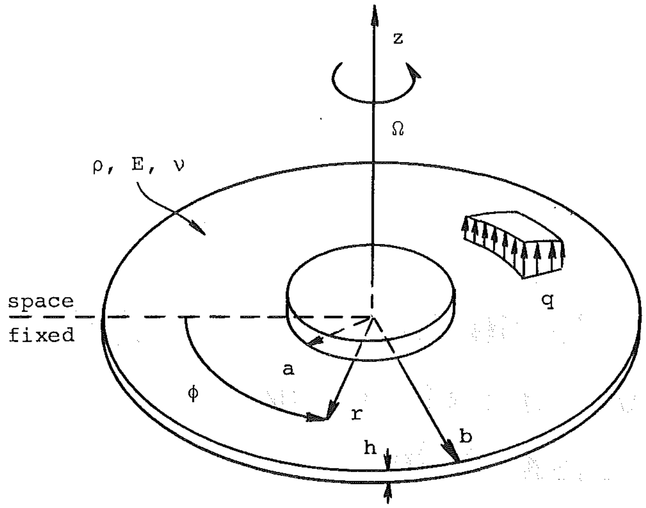

Fig. 1 Disk geometry

$$w = u/b, \quad \zeta = r/b, \quad \kappa = a/b, \quad Q = 8q/[\rho\Omega^2 b^2(3+\nu)],$$
$$\alpha = 8D/[\rho\Omega^2 b^4(3+\nu)],$$
$$\beta = \left(\frac{1-\nu}{3+\nu}\right)\left[\frac{(3+\nu)-(1+\nu)\kappa^2}{(1+\nu)+(1-\nu)\kappa^2}\right]\kappa^2, \tag{1}$$

where u is the physical transverse deflection of the disk, and $D = Eh^3/[12(1-\nu^2)]$ is the plate bending rigidity. Thus, in the context of classical plate theory, the differential equation for steady transverse deflection is [6]

$$Q = \alpha\left[\frac{\partial^2}{\partial\zeta^2} + \frac{1}{\zeta}\frac{\partial}{\partial\zeta} + \frac{1}{\zeta^2}\frac{\partial^2}{\partial\phi^2}\right]^2 w$$
$$+ \frac{1}{\zeta}\frac{\partial}{\partial\zeta}\left\{\zeta\left[(\zeta^2-1)+\beta\left(1-\frac{1}{\zeta^2}\right)\right]\frac{\partial w}{\partial\zeta}\right\}$$
$$+ \frac{1}{\zeta^2}\left[(3\zeta^2-1)+\beta\left(1+\frac{1}{\zeta^2}\right)\right]\frac{\partial^2 w}{\partial\phi^2}. \tag{2}$$

Associated with this are the boundary conditions of zero deflection and slope at the clamp, $\zeta = \kappa$

$$w = 0, \quad \frac{\partial w}{\partial\zeta} = 0, \tag{3),(4}$$

and zero moment and equivalent shear at the rim, $\zeta = 1$

$$\frac{\partial^2 w}{\partial\zeta^2} + \nu\frac{\partial w}{\partial\zeta} + \nu\frac{\partial^2 w}{\partial\phi^2} = 0, \tag{5}$$

$$\frac{\partial^3 w}{\partial\zeta^3} + (2-\nu)\frac{\partial^3 w}{\partial\zeta\partial\phi^2} + \frac{\partial^2 w}{\partial\zeta^2} - \frac{\partial w}{\partial\zeta} - (3-\nu)\frac{\partial^2 w}{\partial\phi^2} = 0. \tag{6}$$

Periodicity in ϕ is also required

$$w(\zeta,\phi) = w(\zeta,\phi+2\pi). \tag{7}$$

The disk response, as governed by (2) consists of two parts. There is a fourth-order, biharmonic, "plate" part, preceeded by the parameter α, and a second-order "membrane" part which is modified by the parameter β. Here, α will be referred to as the "spin stiffness" since it is a relative measure of the contribution of plate effects versus membrane effects due to spin. Interest is on those systems that are predominantly membrane-like, with spin stiffnesses on the order of 10^{-4}.

The "membrane parameter" β combines the effects of the clamping radius κ and Poisson's ratio ν into one number that enters into the governing partial differential equation. Some of the referenced articles [1–3] treat the simplified case of a complete disk with a partial clamp that restrains transverse deflections only. For that system $\kappa > 0$ for the application of the boundary conditions, but $\beta \equiv 0$ in the partial differential

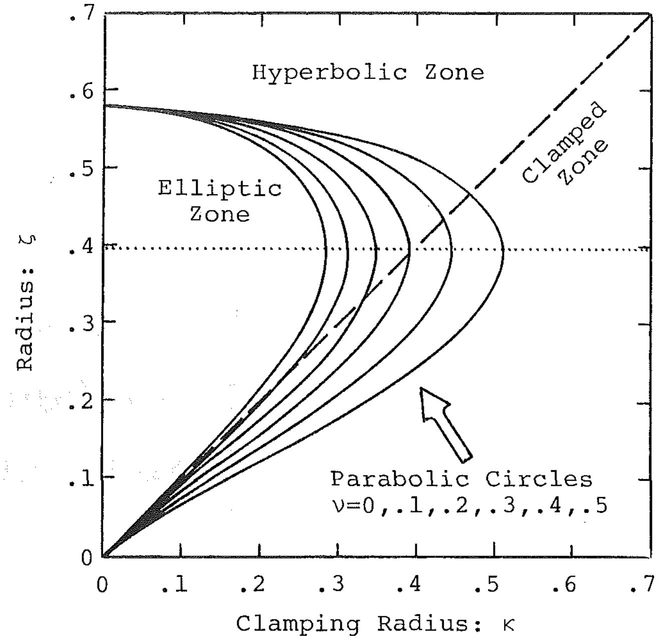

Fig. 2 Membrane response zones

equation, equation $(1)_6$ not withstanding. Others admit a full clamp [4–6], in which case β may be as large as 1/3 for a thin annular disk, $\kappa \to 1$ with a small Poisson's ratio, $\nu \to 0$. Most geometries will have β in the range $0 \leq \beta \leq 0.2$.

3 Membrane Operator

The dominating membrane operator of equation (2) is examined

$$L_\beta[w] = \left[(\zeta^2-1)+\beta\left(1-\frac{1}{\zeta^2}\right)\right]\frac{\partial^2 w}{\partial\zeta^2}$$
$$+ \left[\left(3\zeta-\frac{1}{\zeta}\right)+\beta\left(\frac{1}{\zeta}+\frac{1}{\zeta^3}\right)\right]\frac{\partial w}{\partial\zeta}$$
$$+ \left[\left(3-\frac{1}{\zeta^2}\right)+\beta\left(\frac{1}{\zeta^2}+\frac{1}{\zeta^4}\right)\right]\frac{\partial^2 w}{\partial\phi^2} \tag{8}$$

with emphasis on the influence of the membrane parameter β. L_β is classified as elliptic, parabolic, or hyperbolic, if the product of the coefficients of the second-order derivatives is positive, zero, or negative, respectively [7]. This leads to the following divisions in the membrane

Parabolic: $\zeta = 1$,

$$\zeta = +\left\{\left(\frac{1-\beta}{6}\right) \mp \left[\left(\frac{1-\beta}{6}\right)^2 - \frac{\beta}{3}\right]^{1/2}\right\}^{1/2} \equiv \zeta_1, \zeta_2;$$

Elliptic: $\zeta_1 < \zeta < \zeta_2$;

Hyperbolic: $0 \leq \zeta < \zeta_1, \quad \zeta_2 < \zeta < 1.$ (9)

These results are graphed in Fig. 2, using the more meaningful parameters κ and ν in place of β. The curves mark the radii of the parabolic transition circles where the membrane switches from elliptic to hyperbolic behavior. A horizontal dotted lined separates the ζ_1 branch from the ζ_2 branch, and a diagonal dashed line shows the radius of the clamp. It is seen that the membrane can support two hyperbolic regions separated by an elliptic annulus. For most applications, elliptic behavior is desired as transverse deflections die out away from a load. In hyperbolic zones a load causes waves to form along characteristic arcs [7]. The greatest elliptic area occurs for $\beta = 0$, $\zeta_1 = 0$, $\zeta_2 = 1/\sqrt{3} \approx 0.577$,

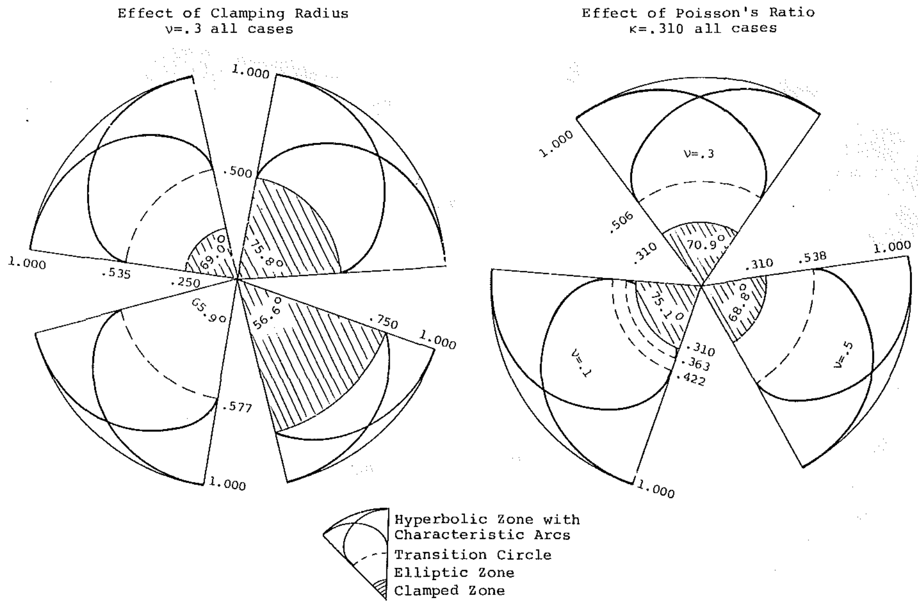

Fig. 3 Membrane zones

reproducing the geometry of reference [1]. For $\beta = 7-4\sqrt{3} \approx 0.0718$, $\zeta_1 = \zeta_2 = [(2/\sqrt{3})-1]^{1/2} \approx 0.393$, and the elliptic annulus vanishes altogether. For many disks the clamp will extend sufficiently far to obscure the first or both of the parabolic circles at ζ_1 and ζ_2.

The characteristic arcs of the hyperbolic regions are given by $\psi(\zeta,\phi)=$constant, and satisfy the first-order, nonlinear partial differential equation

$$\left[(\zeta^2-1)+\beta\left(1-\frac{1}{\zeta^2}\right)\right]\left(\frac{\partial\psi}{\partial\zeta}\right)^2 + \left[\left(3-\frac{1}{\zeta^2}\right)+\beta\left(\frac{1}{\zeta^2}+\frac{1}{\zeta^4}\right)\right]\left(\frac{\partial\psi}{\partial\phi}\right)^2 = 0. \tag{10}$$

The solution to the equation has the separable form $\psi(\zeta,\phi) = \pm\phi + f(\zeta)$, with

$$\frac{df}{d\zeta} = \frac{1}{\zeta}\left[\frac{(3\zeta^2-1)+\beta(1+\zeta^{-2})}{(1-\zeta^2)+\beta(\zeta^{-2}-1)}\right]^{1/2}. \tag{11}$$

The value of $f(\zeta)$ in the split hyperbolic zones is found by integrating within the limits $\kappa \le \zeta \le \zeta_1$ and $\zeta_2 \le \zeta \le 1$. This was performed numerically, after first treating the square-root singularity at $\zeta = 1$, and example results are shown in Fig. 3. Only one example exhibits the inner hyperbolic annulus, and it exists for a very narrow band $(\zeta_1 - \kappa = 0.053)$ near the clamp, and for an unusually small Poisson's ratio $(\nu = 0.1)$. One may conclude that the inner hyperbolic annulus will rarely appear and, when it does, will not support large amplitudes waves, due to the adjacency of the clamp. The β effect is more important to the ever-present outer hyperbolic annulus. Since it may be wide, and is adjacent to the free edge, waves of significant amplitude may be generated. In terms of the component parameters of β, we see in Fig. 3 that the area of the outer hyperbolic annulus increases as κ increases to ζ_2. The area of the hyperbolic annulus is also increased for decreased Poisson's ratio.

4 A Nonsingular Second-Order Formulation for the Spinning Disk Problem

Returning to the full fourth-order problem, if we assume the separable form

$$w(\zeta,\phi) = \sum_{n=0}^{\infty} z_n(\zeta)e^{in\phi}, \tag{12}$$

$$Q(\zeta,\phi) = \sum_{n=0}^{\infty} Q_n(\zeta)e^{in\phi}, \tag{13}$$

we obtain a set of radial ordinary differential equations and boundary conditions

$$\begin{aligned} Q_n = {} & \alpha z_n'''' + \alpha\frac{2}{\zeta}z_n''' \\ & + \left[(\zeta^2-1)+\beta\left(1-\frac{1}{\zeta^2}\right)-\alpha(1+2n^2)\frac{1}{\zeta^2}\right]z_n'' \\ & + \left[\left(3\zeta-\frac{1}{\zeta}\right)+\beta\left(\frac{1}{\zeta}+\frac{1}{\zeta^3}\right)+\alpha(1+2n^2)\frac{1}{\zeta^3}\right]z_n' \\ & - n^2\left[\left(3-\frac{1}{\zeta^2}\right)+\beta\left(\frac{1}{\zeta^2}+\frac{1}{\zeta^4}\right)+\alpha(4-n^2)\frac{1}{\zeta^4}\right]z_n, \end{aligned} \tag{14}$$

$$z_n(\kappa)=0, \quad z_n'(\kappa)=0, \tag{15),(16}$$

$$z_n''(1)+\nu z_n'(1)-\nu n^2 z_n(1)=0, \tag{17}$$

$$\begin{aligned} & z_n'''(1)+z_n''(1)-z_n'(1) \\ & \quad -n^2[(2-\nu)z_n'(1)-(3-\nu)z_n(1)]=0, \\ & \quad n-0,1,2,\ldots\ . \end{aligned} \tag{18}$$

Here a prime denotes differentiation with respect to ζ. The form of (12) satisfies the periodicity requirement, and n denotes the number of equally spaced nodal diameters $z_n \cdot \exp(in\phi)$ possesses. In this paper we will focus on the case of a single concentrated load at radius $\zeta = \xi$, for which Q_n is expressed in terms of the Dirac delta function

$$Q_n(\zeta;\xi) = \frac{\delta(\zeta-\xi)}{\pi\xi}\begin{Bmatrix} 1 & ; n>0 \\ 1/2 & ; n=0 \end{Bmatrix}. \tag{19}$$

The resulting radial modes $z_n(\zeta;\xi)$ when substituted into (12) comprise the Green's function for the spinning disk. For the pure membrane problem, differential equation (14) is reduced to the second order by taking α identically zero, and replacing boundary conditions (15)–(18) with

$$z_n(\kappa)=0, \quad |z_n(1)|<\infty. \tag{20),(21}$$

This problem has been shown to be singular [1] as it admits modes of finite amplitude at arbitrarily large orders of n.

One can, of course, work with the full fourth-order formulation, but this is unsatisfactory for numerical solution of the near-membrane case. An obvious problem of accuracy

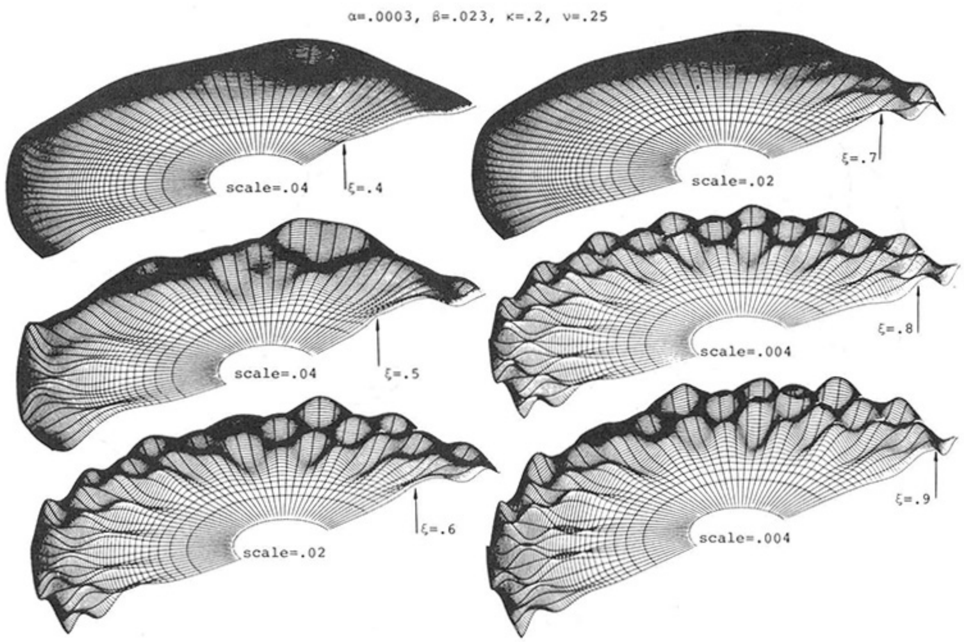

Fig. 4 Disk deflections

occurs because the coefficients on the highest two derivatives in equation (14) are only $0(\alpha)^1$, and this are dwarfed by the coefficients of the second and first derivatives which are $0(1+\alpha n^2)$, and the coefficient of the zeroth derivative which is $0[n^2(1+\alpha n^2)]$. Simultaneously it becomes very difficult to satisfy boundary conditions (16)–(18) which are lost for $\alpha=0$. A further difficulty arises due to the nature of the radial modes $z_n(\zeta;\xi)$ which are wavelike when ξ falls in the hyperbolic region of the disk.[2] This is a consequence of using polar coordinates that cut across characteristic wave fronts. In order to "see" the radial mode waves, numerical step sizes must be kept quite small, say no more than $(1-\kappa)/100$. This mandates calculation of z_n to many significant digits so that finite difference calculations for z_n' through z_n'''' will be accurate. Roundoff error increases with the order of the derivative, and it is illustrative to note that 32-place accuracy was required in reference [2] to solve for the deflections of disks with $\alpha=0.001$. Smaller values of α could not be accommodated.

It becomes desirable then to find an alternative to both the singular, second-order, membrane formulation, and the numerically "noisy," fourth-order, plate formulation. A promising hybrid approach arises from the observation that, while α is small, αn^2 need not be, and αn^4 can be quite large. By neglecting terms of $0(\alpha)$, but not terms of $0(\alpha n^2)$ in equation (14), a set of second-order, Sturm-Louiville, differential equations is produced

$$Q_n=\frac{1}{\zeta}\frac{d}{d\zeta}\left\{\zeta\left[(\zeta^2-1)+\beta\left(1-\frac{1}{\zeta^2}\right)-\alpha(1+2n^2)\frac{1}{\zeta^2}\right]\frac{dz_n}{d\zeta}\right\}$$
$$-n^2\left[\left(3-\frac{1}{\zeta^2}\right)+\beta\left(\frac{1}{\zeta^2}+\frac{1}{\zeta^4}\right)+\alpha(4-n^2)\frac{1}{\zeta^4}\right]z_n,$$
$$n=0,1,2,\ \ldots\ . \tag{22}$$

Of the two boundary conditions needed to accompany (22), one is obviously the zero displacement equation (15), but it is not clear what the second equation must be. The choice is made on the basis of the following heuristic arguments[3].

It is supposed that the second boundary condition derives from one of the equations (16)–(18), and (21). The membrane boundedness condition (21) is ruled out because equation (22) is not singular at $\zeta=1$. The zero slope condition (16) is eliminated as this leads to perfectly flat disk displacements in the region $\kappa\le\zeta\le\xi$. If, for large n^2, we treat boundary conditions (17) and (18) as we did the differential equation (14), we obtain the approximate expressions

$$z_n(1)=0,\quad z_n'(1)=\frac{3-\nu}{2-\nu}\,z_n(1). \tag{23),(24}$$

Of these only equation (24) has an appropriate form for the circumferential waves that form at the rim of the disk.

Thus equation (24) is tentatively included with (15) and (22) to form a "hybrid" set of equations for transverse disk deflection. As a test, calculations were made for the near membrane system with $\alpha=0.0003$, $\beta=0.023$, $\nu=0.25$, $\kappa=0.2$, and concentrated loads at $\xi=0.4,\ 0.5,\ \ldots\ ,0.9$. This approximates a Mylar computer floppy disk [2]. A central difference numerical scheme was employed for the calculation of $z_n(\zeta;\xi)$, with unequal step sizes used to concentrate nodes in the wavelike outer region of the disk. The results are shown in Fig. 4, with transverse displacements multiplied by a scale to improve legibility. It is encouraging to note that the membrane behavior predicted in Section 3 seems to be properly exhibited. Deflections in the elliptic zone are minimal in all cases, and when the load is applied on the hyperbolic side of the transition circle ($\zeta_2=0.548$) waves are formed along fronts resembling characteristic arcs.

Another available test of the hybrid equations is to compare results with the membrane results for axisymmetric loading, $Q_n=0$, $n=1,2,3,\ \ldots$ The $n=0$ equations are the only ones for which closed-form solutions are available, and it is interesting to note that, despite the apparent inappropriateness of (24) for $n=0$, the smallness of α is sufficient to bring the hybrid solution for z_0 into close agreement with the pure membrane solution. The respective solutions (deflection under a ring load at ($\zeta=\xi$) are

[1] I.e., on the order of magnitude of α.

[2] Strictly speaking, the leading biharmonic operator in equation (4) makes the disk problem everywhere elliptic. Nevertheless, the membrane operator dominates the response for small α, and it is convenient to retain the labels "hyperbolic" and "elliptic" to describe the same regions in the disk as they would in the pure membrane.

[3] Methods of singular perturbation hold promise, but so far have not been fruitful [8].

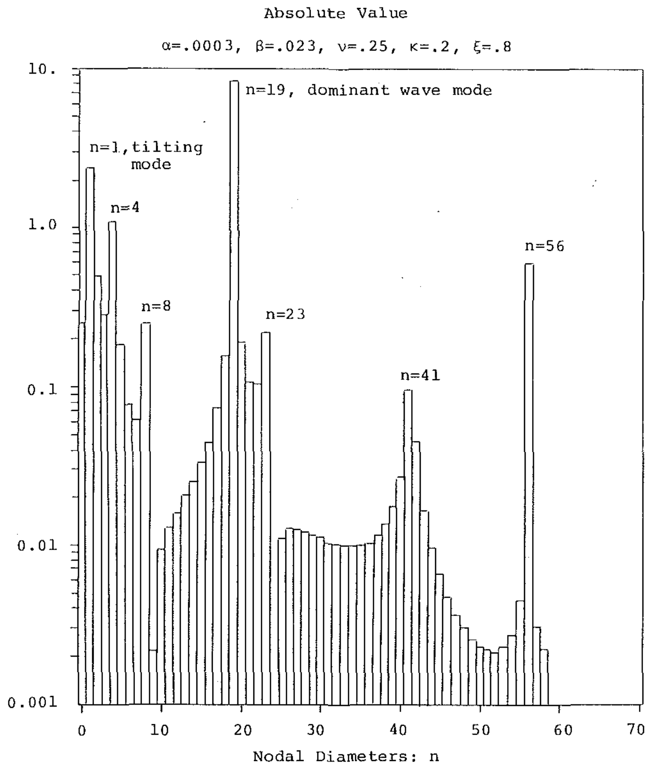

Fig. 5 Magnitudes of the radial modes at the rim

Hybrid Equations

$$z_0 = \frac{-C}{(4\pi)(1+\beta+2\gamma)} ln\left(\frac{1+\gamma-\zeta^2}{1+\gamma-\kappa^2}\cdot\frac{\beta+\gamma+\kappa^2}{\beta+\gamma+\zeta^2}\right)$$

$$+\frac{1}{(4\pi)(1+\beta+2\gamma)}\left\{\begin{array}{l} 0; \quad \zeta\le\xi \\ ln\left(\frac{1+\gamma-\zeta^2}{1+\gamma+\xi^2}\cdot\frac{\beta+\gamma+\xi^2}{\beta+\gamma+\zeta^2}\right); \ \zeta\ge\xi \end{array}\right\}, \tag{25}$$

Membrane

$$z_0 = \frac{1}{(4\pi)(1+\beta)}\left\{\begin{array}{l} ln\left(\frac{1-\kappa^2}{1-\zeta^2}\cdot\frac{\beta+\zeta^2}{\beta+\kappa^2}\right); \zeta\le\xi \\ ln\left(\frac{1-\kappa^2}{1-\xi^2}\cdot\frac{\beta+\xi^2}{\beta+\kappa^2}\right); \zeta\ge\xi \end{array}\right\}, \tag{26}$$

where

$$\gamma=\frac{\alpha}{1+\beta}, \quad C=\frac{g(\xi)}{g(\kappa)},$$

$$g(\xi)=1+\frac{\gamma}{1+\gamma+\beta}$$

$$+\frac{\gamma}{2}\left(\frac{3-\nu}{2-\nu}\right)ln\left(\frac{\gamma}{1+\gamma-\kappa^2}\cdot\frac{\beta+\gamma+\xi^2}{\beta+\gamma+1}\right). \tag{27}$$

Boundary condition (24) is retrieved in (25) for a very narrow band near the rim, and it is the only one of the considered boundary conditions that gives this match.

The desired capability to make calculations for extremely small spin stiffnesses was achieved. One test case was run for $\alpha=10^{-5}$ which is well below the value of most computer floppy disks. Contrariwise, the hybrid equations should not be used for stiffnesses much larger than treated here. This hinders comparison with full fourth-order results in a mutually compatible stiffness range. A "nearest neighbor" is given in reference [2] for the system $\alpha=0.001$, $\beta\equiv 0$, $\nu=0.23$, $\kappa=0.2$, and $\xi=0.8$. Results generated by the hybrid equations showed generally good agreement except for a noticeable z_5 hybrid mode not seen in reference results. This points out a problem in making numerical calculations for the near-membrane problem. As it is almost singular, the near-membrane is extremely sensitive to small parameter changes and numerical roundoff errors. The mismatched z_5 hybrid mode could be artificially made to rise and fall in amplitude with very small changes in the system parameters. More will be said about this in the next section. For design applications the stability of the solution will be greatly improved by the presence of an external damping mechanism (e.g., air) as used by Greenberg [5] and Adams [6].

5 Dominant Wave Modes and Solution Sensitivity

In this section an examination is made of the modes z_n which dominate the disk response. Sensitivity to small parameter changes is also discussed. The discussion focuses on the full fourth-order system of equations although it is convenient to use the numerical results of the preceding section for illustrative purposes.

As noted in [1] and seen again in Fig. 4, loading in the hyperbolic zone causes a dominant wave with $n\ge 2$ to stand out. For the disks loaded at $\xi=0.6$, 0.8, and 0.9, the respective dominant waves are z_{18}, z_{19}, and z_{19}. For $\xi=0.7$, modes z_{17} to z_{23} are present in about equal magnitudes, leading to destructive interferance and the relatively flat geometry seen in the figure. To illustrate the pattern of modal influence, the amplitudes of rim displacements $|z_n(1)|$, $n=0,1,2,\ldots$, are plotted in Fig. 5 for the $\xi=0.8$ case. The dominant $n=19$ mode stands out, as do other local peaks at $n=4$, 8, 23, 41, and 56. Higher ordered amplitudes, $|z_n(1)|$, $n\ge 59$, including a final peak $|z_{74}(1)|=0.000143$ are too small to be shown on the graph. For $n\ge 75$ there is monotonic decrease of $z_n(\zeta)$ for all ζ. A large tilting mode $n=1$ is also present. Observe that the larger modes occur for scattered and sometimes large values of n. This lack of monotonicity is due to the awkwardness of having to form characteristic wave fronts from modes that are intrinisically polar. If the concentrated load is in the elliptic region of the disk and characteristic waves are not formed, then convergence is far more rapid and uniform.

For the example system of Fig. 5, and for other hyperbolic loading cases, there is a general trend for the radial modes to acquire zeroes (nodal circles)

$$z_n(\zeta)=0; \quad \kappa\le\zeta<1 \tag{28}$$

as n gets larger. After a point the trend is reversed and the modes become less wavelike and show most deflection in the vicinity of the load. This sequence is illustrated in Fig. 6 for some of the larger modes from Fig. 5. Another pattern, which is observed, is a sign reversal near the index of the larger modes. For each of the modes z_1, z_4, z_8, z_{19}, z_{41}, and z_{56}, the next mode had a similar shape with the same number of nodes, but opposite sign and lesser magnitude. For the local peak at z_{23} the sign change occurred with the preceding mode. From z_{75} on, there were no sign changes and no nodes.

Much of this behavior can be explained through an examination of the last term in equation (14)

$$n^2\left[\left(3-\frac{1}{\zeta^2}\right)+\beta\left(\frac{1}{\zeta^2}+\frac{1}{\zeta^4}\right)+\alpha(4-n^2)\frac{1}{\zeta^4}\right]z_n. \tag{29}$$

For most ζ the coefficient of z_n grows as n^4 and will eventually come to dominate the rest of equation (14). Thus at any distance from a load the balance of equation (14) will require

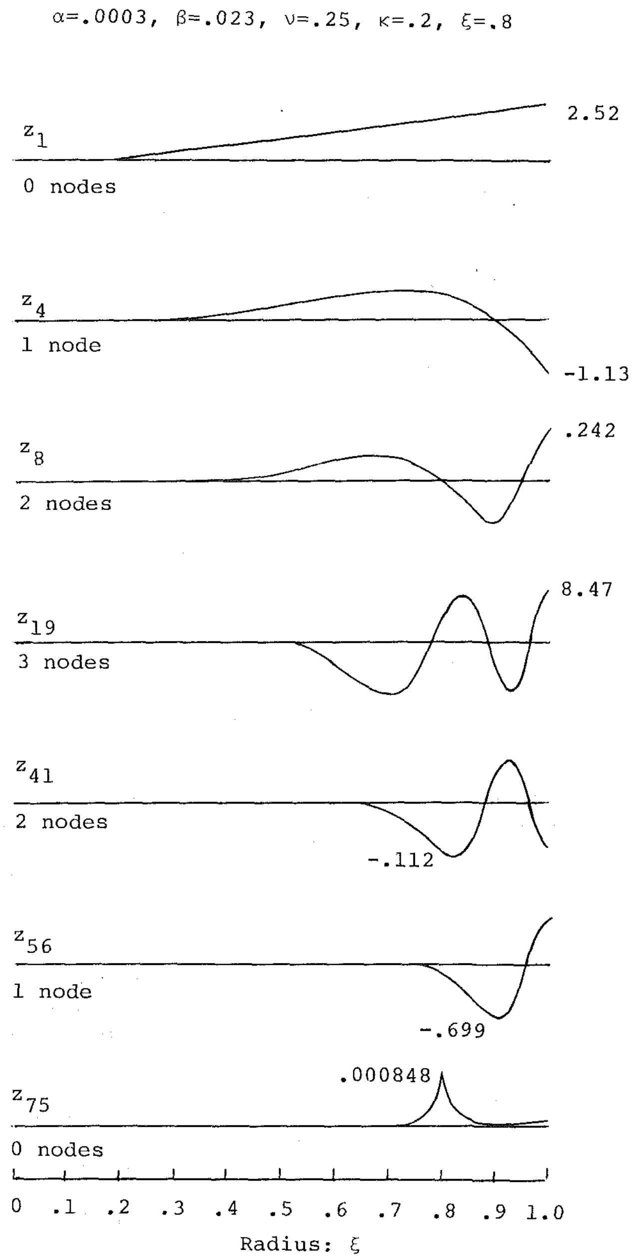

Fig. 6 Selected radial modes

very small values of z_n. This is typified by z_{75} in Fig. 6. It is possible however that if the quantity in brackets in (29) is near zero, the effect can be negated and quite a different solution may be possible. We can solve for the index n_0 which causes the brackets to be zero

$$n_0 = \left\{ \frac{1}{\alpha} \left[(3\zeta^4 - \zeta^2) + \beta(\zeta^2 + 1) + 4\alpha \right] \right\}^{1/2} . \tag{30}$$

This in itself does not explain why specific modes are large. That would probably require an eigenfunction study to see where the nodal diameters and nodal circles lie, in relationship to (30). Still, equation (30) can be used to set some limits on the large modes.

First it will be noted that if the quantity in brackets in (30) is less than zero there will be no index n_0 which causes (29) to vanish. This occurs for ζ approximately between the transition circle radii ζ_1 and ζ_2 of equation (9). The presence of the small quantity 4α in the polynomial perturbs the roots slightly. Thus we may conclude that for large n, z_n will have no significant magnitude in the elliptic portion of the disk. This is borne out in Fig. 6. Secondly, it is observed that the largest possible solution to (30) occurs for $\zeta = 1$

$$n_0 \Big|_{\zeta=1} = \left[\frac{2(1+\beta)+4\alpha}{\alpha} \right]^{1/2} \equiv N. \tag{31}$$

From this we conclude that z_n with $n > N$ will be small compared to other modes with $n < N$. It has further been the author's experience with numerical results that for small α, the sequence $z_n(\zeta)$, $n = N, N+1, N+2, \ldots$ is positive and converges monotonically for all $\kappa \leq \zeta < 1$. For the example results of Fig. 5 and 6, $N = 83$.

Note that had we taken $\alpha \equiv 0$ then N would be infinite, and membrane waves of finite amplitude would be possible for infinitely many nodal diameters n. This reinforces the demonstration of membrane singularity in reference [1]. Physically, as n becomes larger and wavelengths become shorter, even the floppiest disks, $0 < \alpha << 1$, will come to resist being bent into infinitely tight waves.

The floppy disk is extremely sensitive to perturbations in material and geometric parameters. Typically a parameter change, such as setting $\beta \equiv 0$ to model a partial clamp, causes the amplitudes of the radial modes to rise and fall without necessarily changing the wave numbers n of the important modes. It can then occur that a secondary wave mode and a primary wave mode, such as z_{41} and z_{19} in Fig. 5, may switch roles for a dramatic change in the appearance of the disk. It may also happen that the dominant wave mode switches its sign while remaining the dominant mode. While an exhaustive sensitivity study was not undertaken, it was generally found that the disk is highly sensitive to changes in α, β, κ, and ξ near the transition circle. The disk seemed less sensitive to changes in ν and ξ not near the transition circle.

6 Summary

The steady-state response of a spinning disk with a transverse load has been studied near the singular limit of zero spin stiffness. The near-membrane is shown to support one and sometimes two annuli of wavelike deflections. An intervening region of exponentially decaying deflections disappears as the clamping radius is increased. A nonsingular second-order differential equation is presented for the solution of radial modes when spin stiffnesses are extremely small. This makes possible numerical calculations that would be extremely difficult if the full system of equations was used. The choice of appropriate boundary conditions for the reduced differential equation is discussed and supported through heuristic arguments and numerical results. Dominant wave modes in the spinning disk are examined and limits are established concerning the region where large deflections may occur, and the greatest number of nodal diameters a large wave may possess.

References

1 Benson, R. C., and Bogy, D. B., "Deflection of a Very Flexible Spinning Disk Due to a Stationary Transverse Load," ASME Journal of Applied Mechanics, Vol. 45, Sept. 1978, pp. 636–642.

2 Benson, R. C., "Deflection of a Transversely Loaded Spinning Disk," Ph.D Thesis, Department of Mechanical Engineering, University of California, Berkeley, Nov. 1977.

3 Simmonds, J. G., "The Transverse Vibrations of a Flat Spinning Membrane," *Journal of the Aeronautical Sciences*, Vol. 29, No. 1, Jan. 1962, pp. 16–18.

4 Eversman, W., and Dodson, R. O., "Free Vibration of a Centrally Clamped Spinning Circular Disk," *AIAA Journal*, Vol. 7, No. 10, Oct. 1969, pp. 2010–2012.

5 Greenberg, H. J., "Flexible Disk—Read/Write Head Interface," *IEEE Trans. Magnetics*, Vol. MAG-14, No. 5, Sept. 1978, pp. 336–338.

6 Adams, G. G., "Analysis of the Flexible Disk/Head Interface," ASME *Journal of Lubrication Technology*, Vol. 102, No. 1, Jan. 1980, pp. 86–90.

7 Garabedian, P. R., *Partial Differential Equations*, Wiley, New York, 1964.

8 Erdelyi, A., *Asymptotic Expansions*, Dover, New York, 1956.

Nonlinear Shell Dynamics—Intrinsic and Semi-Intrinsic Approaches

A. Libai
Professor,
Department of Aeronautical Engineering,
Technion - Israel Institute of Technology,
Haifa 32000, Israel

The intrinsic approach to the nonlinear dynamics of shells, which was introduced in [6], is reviewed and extended by the addition of appropriate initial and boundary conditions of the dynamic and kinematic types to the field equations. The alternative semi-intrinsic velocity approaches (where the velocity components supply the connection between the equations of motion and the time rates of the metric and curvature) are also presented. Both linear and rotational velocity forms are included. The relative merits of these approaches to shell dynamics are discussed and compared with extrinsic approaches.

1 Introduction

The field equations of the nonlinear statics of thin shells can be formulated in terms of several alternative sets of field variables. The most important are:

(*a*) **Displacement Form.** Here, the three components of the displacement are used. A convenient approach is to resolve the vector and the corresponding equations of motion in the direction of the base vectors and normal ("basic triad") of the *undeformed* references surface [1].

(*b*) **Finite Rotation Form.** The basic geometric quantities are the components of a "rotation vector" which rotates the basic triad from the undeformed to the deformed configuration. Corresponding static quantities can be the components of a stress function vector. It is most suitable for cases of very large rotations [9, 11].

(*c*) **Intrinsic Form.** Here, the basic variables are the metric and curvature tensors of the deformed reference surface. These are usually represented incrementally by extensional and bending strains. The force resultants are occasionally substituted for the extensional strains as field variables since the latter are ill behaved in cases of almost-inextensional deformations. In special variants of this approach the number of variables can be reduced through the introduction of stress and curvature potential functions. An example is quasi-shallow shell theory [3, Part 3]. The inherent advantages of the intrinsic approach are offset to some extent by difficulties encountered in the formulation of kinematic boundary conditions. For representative formulations see [4, section 2], [2, 5].

(*d*) **Mixed Forms.** The most important case is that of (strictly) shallow shell theory which utilizes the displacement in the Cartesian z direction together with a stress function. Another variant is the Donnell-Mushtari-Vlasov theory which utilizes the displacement in the direction of the normal to the undeformed reference surface together with a stress function. For discussions, see [10], [3, part 3].

Corresponding formulations for nonlinear shell dynamics are seemingly restricted by the need for an inertial frame of reference for the acceleration terms. Many computer codes for shells indeed follow this approach by rotating the equations to a global inertial coordinate system which may be a Cartesian system [7], the undeformed system, or a stepwise updated system. A dynamic formulation in terms of the components of the rotation vector and force resultants is available but is rather complicated. For the utilization of the Cartesian displacement in the dynamics of shallow shells, see [8].

In a recent paper, this author presented the field equations of the nonlinear dynamics of doubly curved shells in an *intrinsic* form [6]. The basic variables in the formulation were, as in the corresponding static form, the metric and curvature tensors of the evolving reference surface with their time derivatives. An auxiliary curvature-rate potential function was also introduced—which led to a substantial simplification. However, the formulation was incomplete in the sense that initial and boundary conditions for the field equations were not included.

The first part of this paper completes the formulation of the problem of the intrinsic dynamics of shells by presenting and discussing appropriate initial and boundary conditions for the field equations. It will be seen that some of the difficulties, which are encountered in the static case, of satisfying kinematic boundary conditions, disappear in the dynamic case. Also, most of the classical boundary conditions of shell theory can be entirely in terms of intrinsic quantities, so that the dynamic intrinsic approach is, in fact, a promising method of attack on the dynamics of doubly curved shells with *either* kinematic or dynamic boundary conditions.

The dynamic intrinsic approach is restricted to shells whose evolving reference surfaces are nondevelopable. It is also

Contributed by the Applied Mechanics Division for publication in the Journal of Applied Mechanics.

Discussion on this paper should be addressed to the Editorial Department, ASME, United Engineering Center, 345 East 47th Street, New York, N.Y. 10017, and will be accepted until two months after final publication of the paper itself in the Journal of Applied Mechanics. Manuscript received by ASME Applied Mechanics Division, May, 1982; final revision, January, 1983.

awkward to implement in some cases of mixed kinematic-dynamic boundary data. For these and other cases, the alternative velocity forms are available. They utilize the components of either the rotational or the linear velocity as auxiliary variables, connecting the equations of motion to the metric and curvature time rates. The loss of some of the advantages of the full intrinsic method is compensated for by wider applicability and convenience. As in the full intrinsic form, the position/displacement vector is excluded from the formulation, but the inclusion of the velocity vector (linear or rotational) suggests that they be classified as semi-intrinsic. An early linear-velocity variant was introduced in [12]. Since then, the ingredients appeared in other publications [13, part 2]. A recent paper [15] presents a detailed study of the rotational velocity approach as an initial value problem in the Cauchy sense. For more material, see Chapter 3 of [14]. The velocity forms are summarily presented in Part 3 of this paper. Part 4 discusses the relative merits of the foregoing approaches to shell dynamics. In the Appendix, the rather trivial example of "rod" dynamics illustrates the concepts of the intrinsic approach. Throughout the paper, only Kirchhoff motion is considered.

2 Dynamic Intrinsic Form

Field Equations. In this section, the field equations for intrinsic shell dynamics, introduced in [6] are presented in compact form together with basic notations.

$\mathbf{R}(u^\alpha, t)$ denotes the position vector of the evolving reference surface of a shell with base vectors $\mathbf{R}_{,\alpha}$ and unit normal $\mathbf{n}$. The comma (,) denotes partial differentiation with respect to convected surface coordinates u^α. Let

$$a_{\alpha\beta} = \mathbf{R}_{,\alpha} \cdot \mathbf{R}_{,\beta} \quad b_{\alpha\beta} = \mathbf{n} \cdot \mathbf{R}_{,\alpha\beta} \tag{1}$$

denote the metric and curvature tensors of the surface, respectively. Other commonly used surface quantities are the permutation tensor $\epsilon_{\alpha\beta}$, Gaussian curvature K, $a = \det(a_{\alpha\beta})$, and of the time t. Time derivatives ("rates") are denoted by a super dot. Thus $\dot{\mathbf{R}}$ is the velocity, $\ddot{\mathbf{R}}$ is the acceleration, while and of the time t. Time derivatives ("rates") are denoted by a super dot. Thus $\dot{\mathbf{R}}$ is the velocity, $\ddot{\mathbf{R}}$ is the acceleration, while $\dot{a}_{\alpha\beta}$ $\dot{b}_{\alpha\beta}$ are the metric and curvature rates, respectively. An additional kinematic quantity Ω is appended to the basic kinematic variables. It serves as a "curvature rate-potential function" and simplifies the transition from the equations of motion to the kinematics.

Considering now the dynamic quantities, the stress resultant vector $\mathbf{T}^\alpha$ and equations of motion are, respectively,

$$\mathbf{T}^\alpha = n^{\alpha\beta}\mathbf{R}_{,\beta} + m^{\beta\alpha}|_\beta \mathbf{n} \tag{2}$$

$$\mathbf{T}^\alpha|_\alpha + \mathbf{q} = \rho\ddot{\mathbf{R}} \tag{3}$$

Here, $n_{\alpha\beta}$ and $m^{\alpha\beta}$ are force and couple stress resultants, respectively, $\mathbf{q} = (q^\alpha \mathbf{R}_{,\alpha} + q\,\mathbf{n})$ is the loading/unit area, ρ is the shell mass/unit area, and the bar denotes covariant differentiation. All are referred to $\mathbf{R}$. Other auxiliary quantities are used for economy in notations and in order to avoid bulky equations. These are of no basic importance and are identified by asterisks (*) when introduced.

In terms of preceding definitions and notations, the field equations for the intrinsic problem are:

Motion:

$$A_{\alpha\beta} = \left[\frac{1}{\rho} (n^{\lambda}_{\cdot\alpha}|_\lambda - b_{\alpha\gamma} m^{\lambda\gamma}|_\lambda + q_\alpha) \right]\Big|_\beta - \frac{1}{\rho} b_{\alpha\beta}(n^{\lambda\gamma} b_{\lambda\gamma} + m^{\lambda\gamma}|_{\lambda\gamma} + q) \tag*{(4)$^{(*)}$}$$

$$\ddot{a}_{\alpha\beta} = A_{\alpha\beta} + A_{\beta\alpha} + 2d^{\lambda}_{\cdot\alpha} d_{\lambda\beta} + 2\omega_\alpha\omega_\beta \tag{5}$$

$$(\sqrt{a}\Omega)^{\cdot} = \frac{1}{2}(A_{12} - A_{21}) \tag{6}$$

Kinematics:

$$d_{\alpha\beta} = \frac{1}{2}\dot{a}_{\alpha\beta} + \epsilon_{\alpha\beta}\Omega \tag*{(7)$^{(*)}$}$$

$$\omega_\alpha = K^{-1}\epsilon^{\beta\mu}\epsilon^{\lambda\nu} b_{\alpha\beta} d_{\mu\nu}|_\lambda \tag*{(8)$^{(*)}$}$$

$$\dot{b}_{\alpha\beta} = \frac{1}{2}(-\omega_\alpha|_\beta + b^{\lambda}{}_{\beta} d_{\lambda\alpha}) \tag{9}$$

Conservation:

$$(\sqrt{a}\rho^{\cdot}) = 0 \tag{10}$$

Constitutive:

$$n^{\alpha\beta} = \hat{n}^{\alpha\beta}(a_{\gamma\delta};\quad b_{\gamma\delta}) \tag{11}$$

$$m^{\alpha\beta} = \hat{m}^{\alpha\beta}(a_{\gamma\delta};\quad b_{\gamma\delta}) \tag{12}$$

The latter can be any specified algorithm that converts strain measures (and possibly their time derivatives) into force and couple resultants. For elastic, isotropic, small-strain theory, those commonly used in shell analysis (for example, 8.9–8.10 of [3] or 89 of [1]) should be satisfactory.

The equations are set in a form that is convenient for stepwise time integration [6]. An integration cycle goes through the sequence (4)–(12), with the geometry taken from the previous cycle and updated after equation (9). The $d_{\alpha\beta}$ and ω_α for equation (5) are also taken from the previous cycle, but subcycling between (5) and (7)–(8) can be performed for better accuracy. Symmetrization of (9) is advisable.

A useful adjunct to the set of intrinsic field equations are expressions for the time derivatives of the basic triad of $\mathbf{R}$:

$$\dot{\mathbf{R}}_{,\alpha} = d^{\beta}_{\cdot\alpha}\mathbf{R}_{,\beta} - \omega_\alpha\mathbf{n} \tag{13a}$$

$$\dot{\mathbf{n}} = \omega^\alpha \mathbf{R}_{,\alpha} \tag{13b}$$

These equations although not needed for the integration process itself, are useful for the establishing of kinematic initial and boundary conditions.

Finally, it should be noted that to preserve simplicity, the equations of motion do not utilize the refined symmetrizing processes which are common in modern shell theory. Should one want to utilize this refinement, then the substitution

$$n^{\alpha\beta} = n^{(\alpha\beta)} - b^{\alpha}{}_{\lambda} m^{(\lambda\beta)} \quad m^{(\alpha\beta)} = \frac{1}{2}(m^{\alpha\beta} + m^{\beta\alpha})$$

can be made. Here, $n^{(\alpha\beta)}$ and $m^{(\alpha\beta)}$ are symmetrized stress resultants. Other symmetrizations such as (65) or (74) of [1] may also be useful.

Initial Conditions. The intrinsic shell equations represented by equations (4)–(12) require the specification, at an *initial state* of the shell ($t = t_0$), of 10 kinematic ($b^0_{\alpha\beta}$, $a^0_{\alpha\beta}$, $\dot{a}^0_{\alpha\beta}$, Ω_0) and seven dynamic (ρ_0, $n^{\alpha\beta}_0$, $m^{\alpha\beta}_0$) quantities. The increase in the number of kinematic variables and correspondingly in time integrations (only *six* independent kinematic quantities are specified at the initial state of a body in motion) implies that the initial kinematic quantities should be so interconnected as to satisfy compatibility at the initial state. These would be the Gauss and Codazzi equations (2.20 and 2.22 of [3]) and a rate of compatibility equation (15*a* of [6]).

There is no need for additional compatibility requirements during the integration, since the intrinsic set is internally compatible.

A shell dynamics problem is normally specified at the initial state in terms of the position vector

$$\mathbf{R}(u^\alpha, t = t_0) = \mathbf{R}_0(u^\alpha) \tag{14a}$$

and velocity vector

$$\dot{\mathbf{R}}(u^\alpha, t = t_0) = \dot{\mathbf{R}}_0(u^\alpha) \tag{14b}$$

of its reference surface.

In addition, an *undeformed state* (which need not coincide with $\mathbf{R}_0$)

$$\mathbf{R}=\mathbf{r}(u^\alpha) \tag{14c}$$

is usually (but not always) specified together with its mass/area ρ_r. The force and couple resultants of the initial state are then obtainable from the constitutive laws by utilizing the incremental metric and curvature tensors from $\mathbf{r}$ to $\mathbf{R}_0$, whereas the initial mass/area ρ_0 is obtainable from equation (10) which implies that $\rho\sqrt{a}$ is constant.

The derivation of the initial intrinsic kinematic set from the data of (14) is performed as follows:

(*a*) $a^0_{\alpha\beta}$ and $b^0_{\alpha\beta}$ are calculated by using equation (1).

(*b*) $d^0_{\alpha\beta}$ is obtained from equation (13).

(*c*) the $\dot{a}^0_{\alpha\beta}$ and Ω_0 are then calculated through the use of equation (7).

Since the set is derived from *real* position and velocity vectors, it automatically satisfies all the compatibility requirements. However, there may exist cases where the initial data is supplied directly. Under such circumstances, initial compatibility must be carefully checked. An example is the experimental acquisition of the strains and strain rates of the initial state.

Boundary Conditions. The boundary of the shell at the initial state is defined by a sectionally smooth curve $L_0{:}u^\alpha = f^\alpha(S_0)$ on $\mathbf{R}_0$, where S_0 is arc length. This curve is mapped into the boundary curve $L{:}u^\alpha = f^\alpha(S_0)$ on $\mathbf{R}$, with arc length S. The arc lengths are connected by the extension ratio λ which is expressed in terms of the metric of $\mathbf{R}$:

$$\lambda = 1+\epsilon_S = \frac{dS}{dS_0} = (a_{\alpha\beta} f^\alpha,_{S_0} f^\beta,_{S_0})^{1/2} \tag{16}$$

Occasionally it may be specified as boundary data, such as when the shell is bounded by an inextensional ring ($\lambda = 1$).

Let the unit tangent and unit normal to L (in the tangent planes of $\mathbf{R}$) be defined, respectively, by

$$\left.\begin{aligned} \boldsymbol{\tau} &= \tau^\alpha \mathbf{R}_{,\alpha} \quad & \tau^\alpha &= \lambda^{-1} f^\alpha,_{S_0} \\ \boldsymbol{\nu} &= \nu_\alpha \mathbf{R}^\alpha_{,} \quad & \nu_\alpha &= \epsilon_{\alpha\beta}\tau^\beta \end{aligned}\right\} \tag{17}$$

The unit vectors $\boldsymbol{\tau}$, $\boldsymbol{\nu}$, and $\mathbf{n}$ form a basic triad along L.

Boundary data are directed quantities that are specified along L. The crucial test for possible use in intrinsic theory is that the data be specified in terms of the triad of L. This will be assumed in the sequel. If the data is specified in terms of the L_0 triad, then displacement [1] or finite rotation [9, 11] approaches would be more appropriate to use.

Dynamic quantities on the shell boundary are forces and moments per unit length of L. These are related to the interior variables as follows:

$$\left.\begin{aligned} &N = n^{\alpha\beta}\nu_\alpha\nu_\beta && \text{normal force} \\ &T = n^{\alpha\beta}\nu_\alpha\tau_\beta && \text{tangential force} \\ &Q = m^{\alpha\beta}|_\alpha \nu_\beta + (m^{\alpha\beta}\nu_\alpha\tau_\beta),_s && \text{effective transverse shear} \\ &M = m^{\alpha\beta}\nu_\alpha\nu_\beta && \text{bending moment.} \end{aligned}\right\} \tag{18}$$

It is noted that dynamic boundary data is usually expressed in terms of the intrinsic variables and can be accommodated within intrinsic theories. For more details on dynamic boundary conditions in nonlinear shell theory see, for example, [2–4].

Kinematic rotational data in a nonlinear problem for a shell of the Love-Kirchhoff type is restricted by the requirement that only rotations around the tangents $\boldsymbol{\tau}$ of L may be specified. Considering the fact that $\boldsymbol{\tau}$ changes with time, the common possibility is to specify the angular velocity ω around $\boldsymbol{\tau}$. The relation with the interior variables is

$$\omega^\alpha \nu_\alpha = \omega(S_0 t) \tag{19}$$

It follows from equations (7) and (8) that the specification of ω as boundary data is suitable for use in the intrinsic theory.

If, in addition, $L \equiv L_0$ (held boundary) then $\boldsymbol{\tau} = \boldsymbol{\tau}_0$, and the *total rotation* around $\boldsymbol{\tau}$

$$\phi = \int_{t_0}^{t} \omega\, dt \tag{19a}$$

becomes intrinsic too.

"Linear" kinematic data would be the specification along the boundary L of the velocity vector

$$\dot{\mathbf{R}} = \mathbf{F}(S_0,t) = F^\alpha \mathbf{R}_{,\alpha} + F\mathbf{n} \tag{20}$$

where F^α,F are specified as functions of S_0 and t. Although $\dot{\mathbf{R}}$ is not an intrinsic quantity, its space and time derivatives can be converted into intrinsic boundary conditions. The procedure is as follows: First, equation (20) is differentiated with respect to time. Using equation (13), the result is:

$$\ddot{\mathbf{R}} = \dot{\mathbf{F}} = (\dot{F}^\alpha + d^\alpha_{\cdot\beta}F^\beta + \omega^\alpha F)\mathbf{R}_{,\alpha} + (\dot{F} - \omega_\alpha F^\alpha)\,\mathbf{n} \tag{21}$$

Substitution of $\ddot{\mathbf{R}}$ into the equation of motion (3) results in a dynamic vectorial boundary condition along L:

$$\mathbf{T}^\alpha|_\alpha = \rho\,\dot{\mathbf{F}} - \mathbf{q} \tag{22}$$

which implies three component conditions:

$$(n^{\beta\alpha}|_\beta - b^\alpha{}_\beta m^{\lambda\beta}|_\lambda) = \rho(\dot{F}^\alpha + d^\alpha_{\cdot\beta}F^\beta + \omega^\alpha F) - q^\alpha \tag{22a}$$

$$n^{\alpha\beta}b_{\alpha\beta} + m^{\alpha\beta}|_{\alpha\beta} = \dot{F} - \omega_\alpha F^\alpha - q \tag{22b}$$

The latter equations are (essentially) conditions on the surface derivatives of the stress resultants at the boundary in terms of the supplied data F^α, F, q^α, q, and the additional kinematic quantities which are obtained from equations (7) and (8). It is expressed in terms of the intrinsic quantities.

The question may arise whether relevant boundary data was or was not lost by converting condition (20) into condition (22). Indeed, by differentiating (20) with respect to S_0, another seemingly separate condition could be arrived at.

$$\begin{aligned} \mathbf{F},_{S_0} = \lambda\dot{\mathbf{R}}_{,\alpha}\tau^\alpha &= [F^\alpha,_{S_0} + \lambda(\Gamma^\alpha_{\beta\lambda}F^\lambda - b^\alpha{}_\beta F)\tau^\beta]\mathbf{R}_{,\alpha} \\ &\quad + (F,_{S_0} + \lambda b_{\alpha\beta}F^\alpha\tau^\beta)\mathbf{n} \end{aligned} \tag{23}$$

When this is combined with (13), the resulting component conditions are

$$\lambda(d^\alpha_{\cdot\beta} + b^\alpha{}_\beta F - \Gamma^\alpha_{\beta\lambda}F^\lambda)\tau^\beta = F^\alpha,_{S_0} \tag{23a}$$

$$\lambda(\omega_\beta + b_{\alpha\beta}F^\alpha)\tau^\beta = -F,_{S_0} \tag{23b}$$

The requirements set by equations (23) are, however, superfluous. A simplifed explanation is as follows: The field equations of motion are an internally compatible set which is expressed (essentially) in terms of $\dot{\mathbf{R}}_{,t\alpha}$. The conditions needed for the retrieval of $\dot{\mathbf{R}}$ (to within a constant) are the specification of $\dot{\mathbf{R}}_{,t}$ on L and that of $\dot{\mathbf{R}}_{,S}$ at $t = t_0$. However, the second data is automatically available from the *initial conditions*. Hence, only $\dot{\mathbf{R}}_{,t}$ is needed to complete the data (represented by equations 22) and the specification of $R_{,S}$ for all t (represented by equations 23) is, indeed, superfluous. (See Appendix for illustration.) Nevertheless, the latter may be useful for *numerical processes* where the use of overlapping boundary data in addition to the initial data may be helpful to avoid error accumulation.

The methods of treating dynamic, rotational kinematic, and linear kinematic boundary data clearly show that many types of boundary conditions can be cast in terms of the intrinsic variables, provided that the data can be related to the basic triad along L. Homogeneous boundary data is included in this category, as are the *classical* boundary conditions of shell theory.

Some of the more important cases are given in the following:

(*a*) Free boundary: The requirement is that all the dynamic quantities should vanish on L.

$$N=T=Q=M=0 \tag{24}$$

(*b*) Clamped (fixed) boundary: Here, the boundary is both held (**F** = 0) and prevented from rotating (ω =0). Hence:

$$n^{\beta\alpha}|_{\beta}-b^{\alpha}{}_{\beta}m^{\lambda\beta}|_{\lambda}=-q^{\alpha} \tag{25}$$

$$n^{\alpha\beta}b_{\alpha\beta}+m^{\alpha\beta}|_{\alpha\beta}=-q \tag{26}$$

$$\omega_{\alpha}\nu^{\alpha}=0 \tag{27}$$

(*c*) Simply supported (and held) boundary: This is similar to the preceding case except that (27) is replaced with

$$M=0 \tag{28}$$

(*d*) Held boundary with rotational elastic restraint: This is similar to (*b*) except that (27) is replaced with

$$\int_{t_0}^{t}\omega^{\alpha}\nu_{\alpha}\,dt=kM \tag{29}$$

where k is the spring constant.

Uniform Loadings. These are defined as surface loadings such that $1/\rho\,\mathbf{q}$ is independent of the surface variables u^{α} (but may depend on time). The most important are those generated by uniform parallel acceleration fields–such as *gravity*.

In the case of uniform loadings, the term $1/\rho\,\mathbf{q}$ drops out of the equations of motion (4)–(6) which then become homogeneous. These loadings do not affect the deformation of the shell, *unless* linear kinematic conditions are imposed in the form of equation (22).

In many physical applications uniform loadings are related to fixed directions in space. The implication is that **q** in (22) is *extrinsic* so that problems of this type cannot be conveniently solved by intrinsic methods. A major exception occurs in the case of the *held* boundary (**F** = 0). Here $\boldsymbol{\tau}=\tau_0$ and $\boldsymbol{\nu}$, **n** are completely determined by the angle of rotation ϕ of equation (19*a*):

$$\mathbf{n}=\mathbf{n}_0\,\mathrm{Cos}+\boldsymbol{\nu}_0\,\mathrm{Sin}\phi$$

$$\boldsymbol{\nu}=-\mathbf{n}_0\,\mathrm{Sin}\phi+\boldsymbol{\nu}_0\,\mathrm{Cos}\phi \tag{30}$$

Thus, any loading vector **q** defined with respect to L_0 is also intrinsically defined with respect to L, so that a shell with held boundaries subjected to uniform loadings can be treated by intrinsic methods.

3 Velocity (Semi-Intrinsic) Forms

Rotational Velocity Form. Here the components (ω_{α},Ω) of the rotational velocity vector are used, *together* with the metric, to bridge the gap between the equations of motion and the kinematics. It is strongly related to the dynamic intrinsic form—which may be considered as a further development of it.

The basic equations stem from representations of the velocity and acceleration gradient vectors. The first is equation (13*a*) and the second is

$$\ddot{\mathbf{R}}_{,\beta}=A_{\alpha\beta}\mathbf{R}_{,}{}^{\alpha}+B_{\beta}\mathbf{n} \tag{31}$$

Both $A_{\alpha\beta}$ and B_{β} can be expressed in terms of the stress-resultants though the equations of motion. The first is equation (4) and the second is

$$B_{\beta}=\left[\frac{1}{\rho}\,(n^{\lambda\gamma}b_{\lambda\gamma}+m^{\lambda\gamma}|_{\lambda\gamma}+q)\right]_{,\beta}+\frac{1}{\rho}\,b_{\alpha\beta}\,(n^{\lambda\alpha}|_{\lambda}-b^{\alpha}{}_{\gamma}m^{\lambda\gamma}|_{\lambda}+q^{\alpha}) \tag{32(*)}$$

The main field equations are obtained by time differentiation of (13) and comparison with (31). The result is equations (5)–(7) for the time rates of $(\dot{a}_{\alpha\beta},\Omega)$ and corresponding equations for the time rates of the ω_{β}:

$$\dot{\omega}_{\beta}=-B_{\beta}+d_{\alpha\beta}\omega^{\alpha} \tag{33}$$

The "rotational velocity form" of shell dynamics consists, therefore, of the following equations in sequential order:

Motion: (4), (32), (5), (6), (33)
Kinematics: (7), (9)
Conservation and Constitutive: (10), (11), (12).

Initial and boundary conditions for this form are the same as those of the dynamic intrinsic form, with the addition of ω_0^{α} which is obtained at the initial state from (13). The preferred mode of solution is again stepwise time integration with geometric updating, subcycling and finite approximation schemes for surface differentiation.

The kinematic quantities at the velocity *or* accleration levels are interrelated by three compatibility conditions that result from the conditions set on vectorial gradients in order that the original vector exist [6]. Thus, if

$$\mathbf{F}_{,\beta}=f_{\alpha\beta}\mathbf{R}_{,}{}^{\alpha}+f_{\beta}\mathbf{n}$$

is a vectorial gradient, then the integrability requirement $\epsilon^{\alpha\beta}\mathbf{F}|_{\alpha\beta}=0$ implies the three conditions

$$\epsilon^{\beta\gamma}(f_{\alpha\beta}|_{\gamma}-b_{\alpha\gamma}f_{\beta})=0 \tag{34}$$

$$\epsilon^{\beta\gamma}(f_{\beta}|_{\gamma}+b^{\alpha}{}_{\gamma}f_{\alpha\beta})=0 \tag{35}$$

The application to the velocity or acceleration gradients is done by identifying $(f_{\alpha\beta},f_{\beta})$ with $(d_{\alpha\beta},\,-\,\omega_{\beta})$ or $(A_{\alpha\beta},B_{\beta})$, respectively.

The compatibility equations are satisfied automatically by the rotational velocity form. The explanation is that $A_{\alpha\beta}$ and B_{β} are defined in terms of the three components of the acceleration vector. The elimination of these components from the equations is equivalent to the compatibility equations, as can be shown by direct calculation.

However, the use of some of the compatibility equations as a substitute to their corresponding equations of motion may lead to useful results. The application of equation (34) to $(d_{\alpha\beta},\,-\,\omega_{\beta})$ and its inversion has led to equation (8) of the dynamic intrinsic form, which has been used *instead* of (33) for shells with $K\neq 0$. In a similar fashion if $b^{\alpha}{}_{\alpha}$ ($\neq$ 0 then application of (35) to $(d_{\alpha\beta},\,-\,\omega_{\beta})$ leads to the expression

$$\Omega=(b_{\alpha}{}^{\alpha})^{-1}\epsilon^{\beta\gamma}\left(-\omega_{\beta}|_{\gamma}+\frac{1}{2}b^{\alpha}{}_{\gamma}\dot{a}_{\alpha\beta}\right) \tag{36}$$

The latter equation can be used instead of equation (6), if so desired. Another useful equation is obtained by applying (7) and ω_{β} to (34). Elimination of Ω from the result leads to

$$\epsilon^{\beta\gamma}\epsilon^{\alpha\delta}\left(\frac{1}{2}\,\dot{a}_{\alpha\beta}|_{\gamma\delta}+b_{\alpha\gamma}\omega_{\beta}|_{\delta}\right)=0$$

The later equation can be helpful for deriving mixed and approximate forms of shell dynamics.

Linear Velocity Form. Here, the three components of $\dot{\mathbf{R}}$ are used as auxiliary variables:

$$\dot{\mathbf{R}}=V^{\alpha}\mathbf{R}_{,\alpha}+V\,\mathbf{n} \tag{37}$$

Space and time differentiations of (37) and the use of (13) yield the relations (see also [13],5.2.5):

$$d^{\alpha}_{\cdot\beta}=V^{\alpha}|_{\beta}-b^{\alpha}{}_{\beta}V \tag{38*}$$

$$\omega_\alpha = -V_{,\alpha} - b_{\alpha\beta} V^\beta \tag{39}^*$$

$$\ddot{\mathbf{R}} = (\dot{V}^\alpha + V\omega^\alpha + d^{\alpha}_{\cdot\beta}\omega^\beta)\mathbf{R}_{,\alpha} + (\dot{V} - V^\alpha \omega_\alpha)\mathbf{n} \tag{40}$$

Introduction of (40) into equation (3) yields the component equations of motion in the form

$$\dot{V}^\alpha = \frac{1}{\rho}(n^{\beta\alpha}|_\beta - b^\alpha{}_\beta m^{\lambda\beta}|_\lambda + q^\alpha) - d^{\alpha}_{\cdot\beta} V^\beta - \omega^\alpha V \tag{41}$$

$$\dot{V} = \frac{1}{\rho}(n^{\alpha\beta} b_{\alpha\beta} + m^{\alpha\beta}|_{\alpha\beta} + q) + V^\alpha \omega_\alpha \tag{42}$$

Also, from equation (7):

$$\dot{a}_{\alpha\beta} = d_{\alpha\beta} + d_{\beta\alpha} \tag{43}$$

The other equations of the system remain unchanged. The "linear velocity form" consists, therefore, of the following equations in sequential order:

Motion: (41), (42)
Kinematics: (38), (39), (43), (9)
Conservation and Constitutive: (10), (11), (12).

The remarks made in previous sections regarding preferred modes of solution apply in this case too. The specification of initial conditions follows directly from (14), (1), and (37).

Boundary conditions of all types can be accommodated as long as they are specified with respect to the triad of L. These include dynamic conditions (N,T,Q,M), kinematic conditions $(V^\alpha \nu_\alpha, V^\alpha \tau_\alpha, V, \omega^\alpha \nu_\alpha)$, or mixed conditions. For example, a "normal diaphragm support" implies the conditions: $N = V^\alpha \tau_\alpha = V = M = 0$. On the other hand, a fixed (in space) diaphragm support is extrinsic and should be treated by a fully Lagrangian displacement or rotation approaches.

4 Discussion

The two forms of the shell equations presented here—intrinsic and semi-intrinsic—are useful in certain types of shell dynamics problems. The relative advantages offered by these approaches are:

(*a*) They are well adapted to cases where the boundary conditions and loading are defined relative to the deformed shell.

(*b*) In numerical solution processes, the time-consuming operation of recalculating the position vector in each integration cycle is bypassed.

(*c*) Shell problems where relatively small strains are superposed on large motion can be dealt with in a natural way without numerical difficulties since the "rigid" component separates out.

(*d*) The equations are defined in terms of the deformation variables. This makes the formulation simple and more direct.

The two main disadvantages are obvious:

(*i*) They are very awkward to use when the data is extrinsic (i.e., defined in terms of fixed directions in space), although some important exceptions exist.

(*ii*) They lose much of their effectiveness when the *position* of the shell is a major objective of the analysis.

A few remarks are in order regarding the relative merits of the various semi-intrinsic and intrinsic forms.

The linear velocity form offers the following advantages:

(*a*) There are no restrictions on the type of shell to be analyzed.

(*b*) Natural, kinematic, and mixed boundary conditions can be accommodated.

(*c*) It can treat problems involving interaction with surrounding media. Usually, normal velocities and loadings are matched between shell and medium, while tangential conditions would range from $q^\alpha = 0$ for a frictionless fluid to match V^α for a fully adherent medium.

The intrinsic approach offers the following useful features:

(*i*) The extensional and bending components of the deformation are separated. Small strain approximations are easier to make and the important inextensional mode of deformation falls out clearly.

(*ii*) The utilization of velocity components in the field equations of the velocity forms leads occasionally to numerical difficulties in cases of small deformations superposed on large velocities. This is largely avoided in the full intrinsic approaches.

The rotational velocity approach occupies an intermediate position between the previous two. It is capable of treating all types of shells and also separates the bending and extensional modes of deformation. Yet, it is awkward in handling some types of mixed boundary data and can still lead to difficulties in some cases of large velocities and small deformations (although less so than the linear velocity approach). It has more time integrations than the other two approaches but compensates for this by needing less surface differentiations at the kinematic level.

A sound approach to the shell problem is to carefully weigh the advantages and drawbacks of the various available means and algorithms for solving the problem at hand. The main objective of this paper is to present the case for including the intrinsic and velocity approaches among these tools, so that they may become the preferred methods for appropriate objectives and data.

Acknowledgment

This study was supported by the Fund for the Promotion of Research at the Technion, Israel Institute of Technology.

References

1 Budiansky, B., "Notes on Nonlinear Shell Theory," ASME Journal of Applied Mechanics, Vol. 35, 1968, pp. 393–401.

2 Danielson, D. A., "Simplifed Intrinsic Equations for Aribtrary Elastic Shells," *International Journal of Engineering Science*, Vol. 8, 1970, pp. 251–259.

3 Koiter, W. T., "On the Nonlinear Theory of Thin Elastic Shells," *Proc. Kon. Ned. Akad. Wet.*, 69*B*, 1966, pp. 1–54.

4 Koiter, W. T., and Simmonds, J. G., "Foundations of Shell Theory," *Proc. 13th Int. Congr. Theor. and Appl. Mech.*, Moscow, 1972. Springer Verlag, 1973, pp. 150–176.

5 Koiter, W. T., "The Instrinsic Equations of Shell Theory With Some Applications," *Mechanics Today*, Vol. 5, Pergamon, 1980, pp. 139–154.

6 Libai, A., "On the Nonlinear Intrinsic Dynamics of Doubly, Curved Shells," ASME Journal of Applied Mechanics, Vol. 48, Dec. 1981, pp. 909–914.

7 Morino, L., Leech, J. W., and Witmer, E. A., "An Improved Numerical Calculation Technique for Large Elasto-Plastic Transient Deformations of Thin Shells," ASME Journal of Applied Mechanics, Vol. 38, 1971, pp. 423–436.

8 Naghdi, P. M., "On the General Problem of Elastokinetics in the Theory of Shallow Shells," *Proc. Symp., The Theory of Thin Elastic Shells*, Delft, 1959, North Holland, 1960, pp. 301–330.

9 Pietraskiewicz, W., "Finite Rotations and Lagrangian Description in the Nonlinear Theory of Shells," *Polish Scientific Publishers*, Warsaw, 1979.

10 Sanders, J. L., Jr., "Nonlinear Theories for Thin Shells," *Q. Appl. Math.*, Vol. 21, 1963, pp. 21–36.

11 Simmonds, J. G., and Danielson, D. A., "Nonlinear Shell Theory With Finite Rotation and Stress-Function Vectors," ASME Journal of Applied Mechanics, Vol. 39, 1972, pp. 1085–1090.

12 Libai, A., "On the Nonlinear Elastokinetics of Shells and Beams," *J. Aero. Sci.*, Vol. 29, 1962, pp. 1190–1195, 1209.

13 Mason, J., *Variational, Incremental and Energy Methods in Solid Mechanics and Shell Theory*, Elsevier, 1980.

14 Libai, A., and Simmonds, J. G., "Nonlinear Elastic Shell Theory," University of Virginia, DAMACS Report 82-04, 1982.

15 Ferrarese, G., "Dinamica dei Continui sottili Bidimensionali: Formulazione Instrinseca del Problema di Cauchy," *Riv. Mat. Univ. Parma*, Vol. 4, No. 5, 1979, pp. 321–335.

APPENDIX

The Longitudinal Dynamics of a Rod

This is the simplest configuration within which the concepts of intrinsic dynamics can be examined.

Denote the longitudinal coordinate of a rod at its unstressed and current states by ξ and x, respectively, with $x = \hat{x}(\xi,t)$. Let N be the longitudinal force, A the cross-section area, E the elastic modulus, ρ the mass/unit length, q the axial load/unit length, and ϵ the strain (that represents the metric). For simplicity, the small strain approximation will be used. With these notations and approximation, the rod equations are:

Motion: $N_{,\xi} + q = \rho\ddot{x}$ $\quad (A.1)$

Kinematics: $\epsilon = x_{,\xi} - 1$ $\quad (A.2)$

Constitutive: $\epsilon = N/EA$ $\quad (A.3)$

Initial conditions: $x,\dot{x}$ supplied at $t=t_0$ for all ξ. $\quad (A.4)$

Boundary conditions: Either N or x (or $\dot{x}$) supplied at

$$\xi = 0,L \quad \text{for all} \quad t \tag{A.5}$$

Here, L is the length of the rod at its undeformed state. In the displacement form, defining $u = x - \xi$ and eliminating the other variables, the field equation becomes

$$u_{,\xi\xi} = {}^{\rho}/_{EA}\,\ddot{u} - q/EA \tag{A.6}$$

with

initial conditions: $u,\dot{u}$ supplied at $t=t_0$

boundary conditions: $u,_{\xi}$ or u supplied at $\xi = 0,L$.

The intrinsic (strain) form, is obtained by differentiating $(A.6)$ with respect to x. The result is

$$\epsilon,_{\xi\xi} = {}^{\rho}/_{EA}\,\ddot{\epsilon} - \frac{1}{EA}q,_{\xi} \tag{A.7}$$

The initial conditions are also obtained by spatial differentiation and are:

$$\epsilon,\dot{\epsilon} \text{ supplied at } t=t_o. \tag{A.8}$$

The dynamic boundary condition is the specification of N at $\xi = 0,L$. To obtain the kinematic boundary condition, it is assumed that either x or $\dot{x}$ are specified at $\xi = 0.L$ for all t, from which $\ddot{x}_{\xi=0} = f_1(t)$ and $\ddot{x}_{\xi=L} = f_2(t)$ are extracted at the boundary. This is introduced into $(A.1)$, and the resulting kinematic condition at $\xi = 0,L$ transforms into:

$$N,_{\xi} = \rho f_i - q = W_i(t) \text{ specified at } \xi = 0,L \tag{A.9}$$

Finally, converting from forces to strains, the boundary conditions become

$$\text{either } \epsilon \text{ or } \epsilon,_{\xi} \text{ are specified at } \xi = 0,L \tag{A.9a}$$

The similarity to the procedure of the intrinsic dynamic approach are obvious. Some of the main points are:

(*a*) Spatial differentiation of the equations of motion.

(*b*) The kinematic boundary conditions are transformed into conditions on the derivatives of th metric.

(*c*) Uniform loadings are represented as boundary data only.

(*d*) Neither position nor velocity appear in the formulation.

(*e*) The original velocity data profile (along the beam at $t = t_0$ and at the boundaries $\xi = 0,L$ for $t \geq t_0$) is retrievable from $\dot{\epsilon}(t = t_0)$, f_1 and f_2 to within the constant $x(\xi = 0,\ t = t_0)$. The latter is, however, immaterial in Newtonian mechanics. It follows that no relevant data is lost in the transformation to intrinsic conditions but the system has been cleared of nonessential data.

S. Kyriakides
Assistant Professor.

E. Arikan
Research Assistant.

Department of Aerospace Engineering and Engineering Mechanics,
The University of Texas at Austin,
Austin, Texas 78712

Postbuckling Behavior of Inelastic Inextensional Rings Under External Pressure

This paper deals with the problem of predicting the postbuckling configuration of a thin, inextensional, inelastic ring under external pressure. Previous work has shown that the postbuckling configuration of such a ring is unstable up to the point where the first two diametrically opposite points on the ring's circumference first come into contact. The presented analysis deals with ring configurations past the first contact. It is shown that the configuration is stable and that for plastic materials, multiple contact points tend to develop. Collapse experiments on thin tubes are consistent with the analytical predictions.

Introduction

A large deflection formulation of thin, inelastic, inextensional rings under external pressure was presented in reference [1]. It was shown that the response of such rings is characterized by a limit load type of instability (Fig. 1). The ring configurations in the unstable regime, beyond the limit load, were obtained through a displacement-controlled numerical procedure. The configurations were successively calculated until the first two diametrically opposite points on the ring circumference touched. A typical collapse sequence followed by such a ring is shown in Fig. 2.

This analysis was motivated by a study of the problem of a propagating buckle [2–4]. In this problem a local damage on a long pipe under external pressure propagates flattening the whole pipe. The lowest pressure at which a buckle will propagate is known as the *Propagation Pressure* (P_p). Thus, a buckle can be initiated at any pressure between the propagation pressure and the buckling pressure of the undisturbed ring. The ring response is also characterized by two such bounding pressures (Fig. 1). The limit load is associated with the buckling pressure and the lowest point on the response with the propagation pressure. More details about this comparison can be found in [2].

The severity to which the pipe is deformed by a propagating buckle depends on the pressure difference between the pressure during the collapse process and the propagation pressure of the pipe. Figure 3 shows four cross sections of a pipe flattened by buckles initiated at different pressures. (From left to right $P/P_p = 1.0, 2.3, 3.0, 3.3$.) The gap between the opposite walls of the collapsed cross section is caused by unloading (spring back). In the loaded condition the sections develop a progressively larger contact area.

It has been observed [5] that for certain combinations of geometric and material parameters the deformation induced by the propagating buckle causes fracture along the sharp corners of the cross section (Fig. 4).

This paper carries the analogy between the ring and the propagating buckle further. The purpose is to develop a simple way of predicting the maximum strain in the collapsed pipe for various geometric and material parameters. Ring

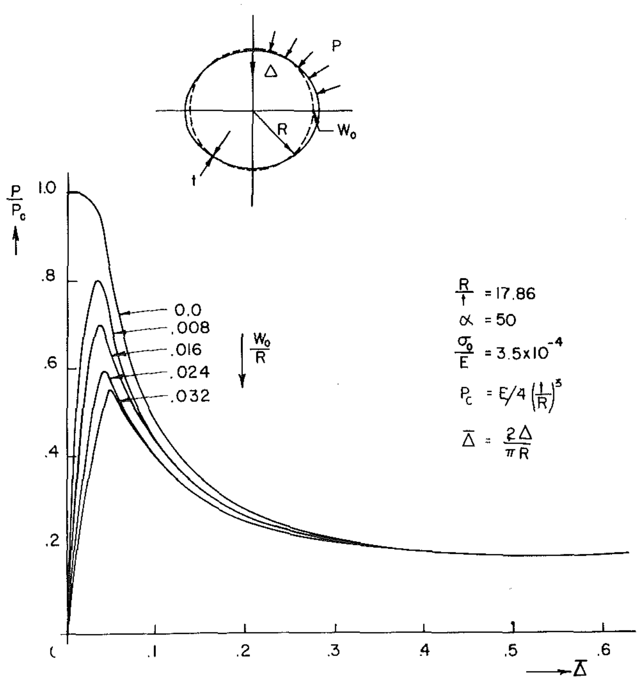

Fig. 1 Large deflection response of inelastic rings

Contributed by the Applied Mechanics Division for presentation at the Winter Annual Meeting, Boston, Mass., November 13–18, 1983 of THE AMERICAN SOCIETY OF MECHANICAL ENGINEERS.

Discussion on this paper should be addressed to the Editorial Department, ASME, United Engineering Center, 345 East 47th Street, New York, N.Y. 10017, and will be accepted until two months after final publication of the paper itself in the JOURNAL OF APPLIED MECHANICS. Manuscript received by ASME Applied Mechanics Division, June, 1982; final revision, January, 1983. Paper No. 83-WA/APM-4.

Copies will be available until July, 1984.

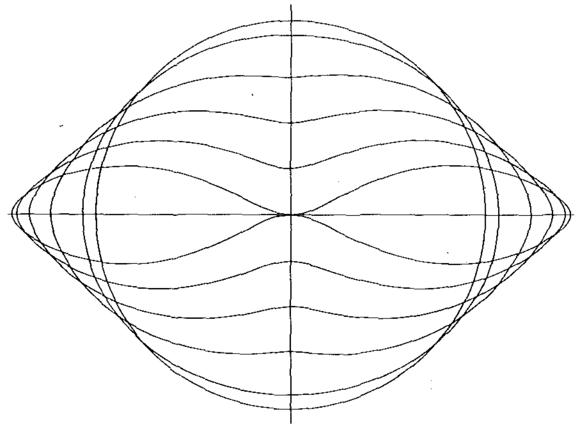

Fig. 2 Collapse sequence of circular ring under external pressure

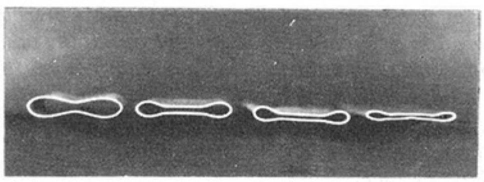

Fig. 3 Cross sections of pipes flattened by propagating buckles initiated at different pressures

configurations beyond the one where two points first touch are examined and the response obtained. The solution procedure is the same as in [1] with obvious modifications to deal with the contact problem that develops. In addition, the constitutive behavior is modified to include elastic unloading necessary for this part of the solution.

The Problem

Consider a circular ring of mean radius R, thickness t, and unit width, under external pressure P. The midsurface of the ring cross section is assumed to be inextensional. The ring material is assumed to be inelastic and the $\sigma-\epsilon$ behavior is idealized by a bilinear strain-hardening material. The equilibrium configurations of the ring during the collapse are to be determined. The nonlinear equations describing the large deflection response of the ring, up to the point of first contact, can be found in [1]. These are solved numerically through a finite difference formulation and a displacement-controlled procedure.

After first contact a new formulation is necessary to deal with the progressive growth of the contact area. In addition, the ring section close to the lift-off point undergoes reverse bending. Since this section has previously been plastically deformed, reverse bending causes unloading.

The contact problem which develops is dealt with by making various simplifying assumptions customary for this type of problem [6–8]. It is assumed that the ring sections in contact are flat and in complete contact up to the point of lift off, at which a concentrated (point) shear force is added to equilibrate the uplifted section (see Fig. 5(b)).

The equilibrium equations have been developed in equations (2) of [1]. The same notation and sign convention will be used here (see Fig. 5(a)). For simplicity, the midsurface of the ring cross section is assumed to remain inextensional. This is a customary assumption but restricts the analysis to relatively thin rings ($D/t>30$). The geometry is also defined in the same way as in [1].

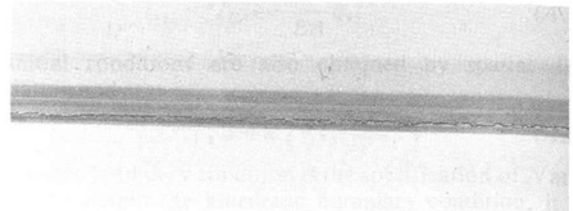

Fig. 4(a)

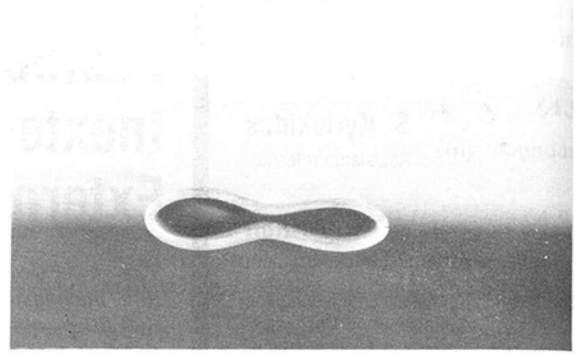

Fig. 4(b)

Fig. 4 Pipe fractured during flattening caused by a propagating buckle

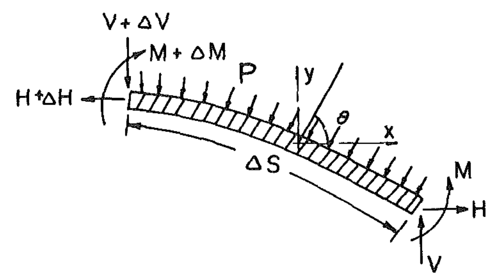

Fig. 5(a) Equilibrium of elemental ring section

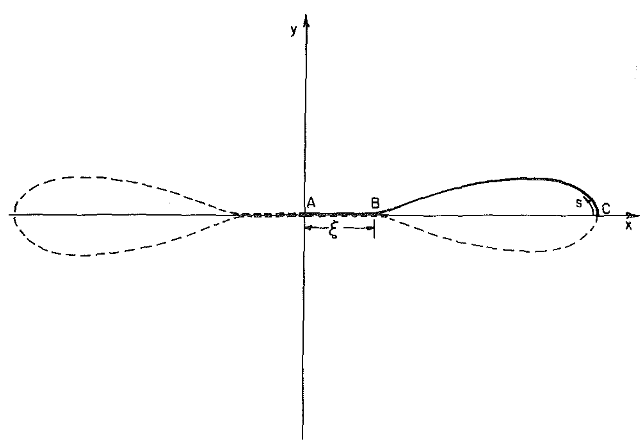

Fig. 5(b) Problem geometry after first touchdown

Fig. 5

Constitutive Behavior

For simplicity only bending stresses will be considered in this formulation. This of course implies that the analysis is restricted to higher values of D/t where the bending stress is much higher than the hoop stress. A simple calculation shows

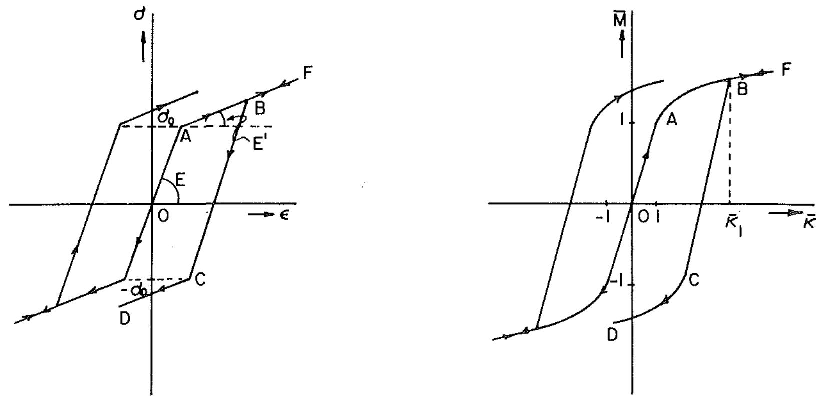

(a) $\sigma-\epsilon$ (b) $\bar{M}-\bar{\kappa}$

Fig. 6 Constitutive relationships

that this assumption is consistent with that of inextentionality (i.e., acceptable for $D/t>30$).

A bilinear approximation to the $\sigma-\epsilon$ relationship of the material (Fig. 6(a)) is used. Let the stress at the outermost fiber at a point on the cross section follow a path as that shown in Fig. 6(a). Both the bilinear elastic (no plastic unloading) as well as the multilinear elastoplastic material will be considered. For the latter case, an intermediate hardening rule is assumed (this can easily be modified to isotropic or kinematic hardening). The corresponding moment-curvature relationships in nondimensional form can be expressed as follows:

(a) **Loading to $\bar{\kappa}_1$**

$$\bar{M}=\bar{\kappa} \qquad \bar{\kappa}<1, \tag{1a}$$

$$\bar{M}=\frac{1}{\alpha}\bar{\kappa}-\frac{1}{2}\left(1-\frac{1}{\alpha}\right)\frac{1}{\bar{\kappa}^2}+\frac{3}{2}\left(1-\frac{1}{\alpha}\right),\ \bar{\kappa}>1. \tag{1b}$$

(b) **Unloading From $\bar{\kappa}_1$**

$$\bar{M}=\bar{\kappa}+\frac{3}{2}\left(1-\frac{1}{\alpha}\right)\left(1-\frac{1}{\bar{\kappa}_1^2}\right)-\left(1-\frac{1}{\alpha}\right)\left(1-\frac{1}{\bar{\kappa}_1^3}\right)\bar{\kappa}_1$$
$$\bar{\kappa}_2<\bar{\kappa}<\bar{\kappa}_1 \tag{1c}$$

$$\bar{M}=\left(1-\frac{1}{\alpha}\right)\left\{-\frac{1}{2}\frac{1}{\bar{\kappa}_1^2}-\frac{\bar{\kappa}_1}{\alpha}+\frac{\bar{\kappa}}{\alpha\left(1-\frac{1}{\alpha}\right)}-\frac{3}{2}\left(1-\frac{1}{\alpha}\right)+\frac{\left(2-\frac{1}{\alpha}\right)^3}{2\left[\bar{\kappa}_1\left(1-\frac{1}{\alpha}\right)-\bar{\kappa}\right]^2}\right\} \qquad \bar{\kappa}<\bar{\kappa}_2 \tag{1d}$$

where

$$\bar{\kappa}_2=\left[-\left(2-\frac{1}{\alpha}\right)+\bar{\kappa}_1\left(1-\frac{1}{\alpha}\right)\right],$$

$$\bar{M}=\frac{6M}{\sigma_0 t^2},\ \bar{\kappa}=\frac{\kappa t E}{2\sigma_0} \quad \text{and} \quad \kappa=\frac{d\theta_0}{dS}-\frac{d\theta}{dS}, \tag{2}$$

Here $d\theta_0/dS$ represents the initial curvature of the unloaded ring and $\alpha=E/E'$ is the ratio of slopes of the bilinear stress-strain representation. Nondimensionalizing all equations appropriately one obtains:

$$\frac{d\bar{H}}{ds}=-\bar{P}\cos\theta,\quad \frac{d\bar{V}}{ds}=-\bar{P}\sin\theta,$$
$$\frac{d\bar{M}}{ds}=\bar{H}\cos\theta+\bar{V}\sin\theta,$$

$$\frac{d\theta}{ds}=\frac{d\theta_0}{ds}-\pi\left(\frac{R}{t}\right)\left(\frac{\sigma_0}{E}\right)\bar{\kappa}(\alpha,\bar{M}), \tag{3}$$
$$\frac{d\bar{P}}{ds}=0,\quad \frac{d\bar{y}}{ds}=\cos\theta,\quad \frac{d\bar{x}}{ds}=-\sin\theta,$$
$$0\le s\le(1-\xi)$$

where $\bar{\kappa}(\alpha,\bar{M})$ is obtained by solving the appropriate, in each case, constitutive equation, i.e., equations ($1a$-d).

All ($\bar{}$) quantities are nondimensionalized as follows:

$$s=2S/\pi R,\ \bar{x}=2x/\pi R,\ \bar{y}=2y/\pi R$$
$$\bar{H}=3\pi HR/\sigma_0 t^2,\ \bar{V}=3\pi VR/\sigma_0 t^2,\ \bar{M}=6M/\sigma_0 t^2, \tag{4}$$
$$\bar{P}=\frac{3}{2}\pi^2\left(\frac{R}{t}\right)^2\left(\frac{P}{\sigma_0}\right).$$

The problem is solved by prescribing the length of the part of the ring that is in contact and then seeking the equilibrium solution. As a result the pressure $\bar{P}$ is an unknown parameter of the problem. Let the length of the ring section in contact be ξ. From Fig. 5 the problem boundary conditions are:

$$\begin{aligned} &\bar{H}(0)=0, && \bar{M}(1-\xi)=\bar{M}_0,\\ &\theta(0)=0, && \theta(1-\xi)=\pi/2,\\ &\bar{y}(0)=0, && \bar{x}(1-\xi)=\xi,\\ & && \bar{y}(1-\xi)=0. \end{aligned} \tag{5}$$

$\bar{M}_0$ is found by solving

$$\bar{\kappa}(\alpha,\bar{M}_0)=\frac{1}{\pi}\left(\frac{t}{R}\right)\left(\frac{E}{\sigma_0}\right)\frac{d\theta_0}{ds}.$$

Equations (3)–(5) can be expressed in vector form as

$$\frac{d\mathbf{u}}{ds}=\mathbf{f}(s,\mathbf{u}),\quad 0\le s\le(1-\xi),$$

where $\quad \mathbf{u}=(\bar{H},\bar{V},\bar{M},\theta,\bar{P},\bar{x},\bar{y}),$ (6)

and

$$\begin{aligned} &u_1(0)=0, && u_3(1-\xi)=\bar{M}_0,\\ &u_4(0)=0, && u_4(1-\xi)=\pi/2,\\ &u_7(0)=0, && u_6(1-\xi)=\xi,\\ & && u_7(1-\xi)=0. \end{aligned}$$

Equations (6) constitute a two-point, nonlinear, boundary value problem which is solved numerically. The interval $s\epsilon[0,1]$ is descretized into $N\,(\sim 51)$ points. ξ is prescribed each time by making it equal to the length of the last m elements. m

is incremented by 1 each time. Equations (6) are expressed in finite difference form. The resulting nonlinear equations are solved using Newton's method.

Solution

(a) Bilinear Elastic Case. First consider a material that follows the same path for both loading as well as unloading (e.g., bilinear elastic (1*a*) and (1*b*)). The collapse process, up to first contact, is the same as in [1]. When contact is established at A, equal and opposite reactive forces develop over the section in contact. This causes a change in the ring response from an unstable one (in some cases, depending on D/t, neutrally stable) to a stable one. Further deformation of the ring is achieved as follows. With all other parameters kept constant, the curvature at point A is gradually reduced to zero. For each value of prescribed curvature the complete ring solution is found. This step was found to be particularly important in the case of relatively thick rings, where the pressure has to be increased substantially, before the curvature at A is reduced to zero. The second step involves gradual increase of the contact length from zero, to a length ξ. These sections are assumed to be flat along the line $y=0$, for all subsequent deformation. Thus the problem domain is reduced to $1-\xi$. The point $(\xi,0)$ represents the lift-off point. The slope and curvature are assumed to be zero and the unknown concentrated shear force at this point is one of the unknowns found by the iterative procedure described in the foregoing. This solution scheme is continued by increasing the value of ξ by $\Delta\xi(=0.02)$. The complete prebuckling and postbuckling load-displacement relationship of the collapsed ring is shown in Fig. 7. After the first touchdown, the load-displacement behavior becomes stable. Although a rather "soft" response is observed at the initial stages of this stable collapse process, this quickly changes to a much "stiffer" one for higher pressures.

The ring collapse configurations past the first contact are shown in Fig. 8(*a*). The area of contact is represented by a straight line along $y=0$. For the case presented, at pressure P_c, about 40 percent of the ring circumference is flat and in contact with the opposite wall.

The moment distribution in the ring quadrant at different stages of contact is shown in Fig. 9. If these are compared with the moment distributions in the ring at first contact $(P/P_c=0.2468)$, it becomes evident that during the collapse process part of the ring unloads to accommodate the reverse bending required by the prescribed displacement field in the area of contact.

(b) Elastoplastic Case. Typical structural metals have elastoplastic material behavior. The analysis was generalized to include such material behavior. For simplicity a multilinear $\sigma-\epsilon$ curve is used (Fig. 6(*a*)) with permanent deformations being assumed to take place during loading. The corresponding moment-curvature relationship at a point (Fig. 6(*b*)) is represented by (1*c*) and (1*d*). These are functions of $\bar{\kappa}_1$, the maximum value of curvature achieved in the monotonic loading branch.

The solution follows the same lines as the nonlinear elastic case discussed earlier i.e., a displacement-controlled procedure is followed where the area of contact is increased step by step and the pressure is treated as one of the problem unknowns found iteratively. The main difference is that during this iterative procedure the moment at every point is compared to the highest moment at the same point in the last converged equilibrium configuration. If the moment is found to decrease then the relationships (1*c*,*d*) are used, with $\bar{\kappa}_1$ being the curvature at that point in the last equilibrium configuration. If the moment is found to increase then (1*a*, 1*b*) continue to be used. If during the iterations a point first

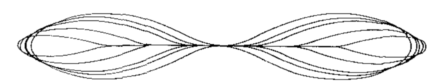

Fig. 8(*a*)

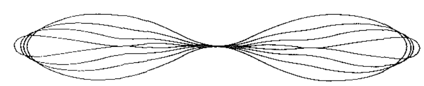

Fig. 8(*b*)

Fig. 8 Ring collapse sequence after first contact

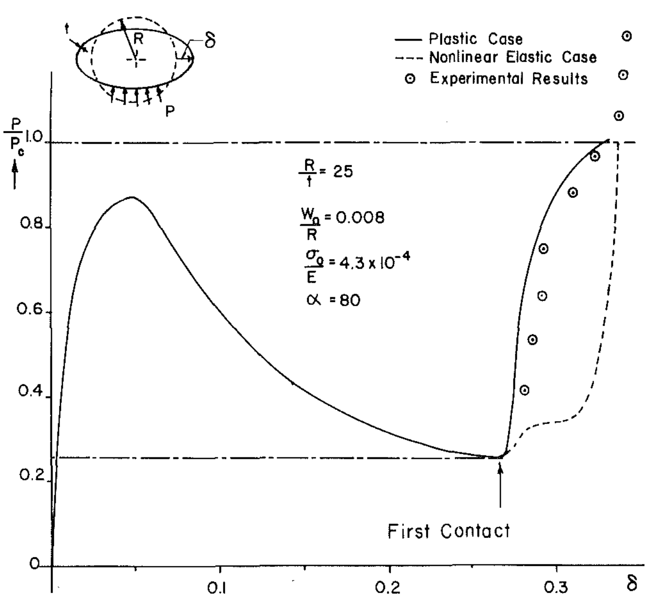

Fig. 7 Complete load-displacement behavior of ring under external pressure

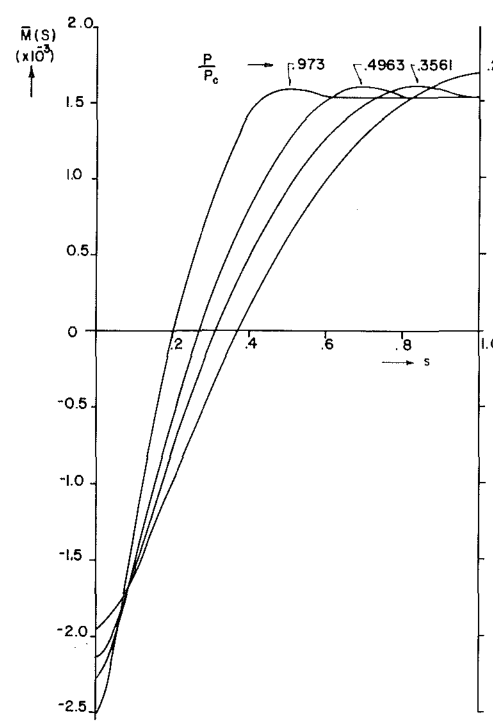

Fig. 9 Moment distribution at different load conditions (nonlinear elastic case)

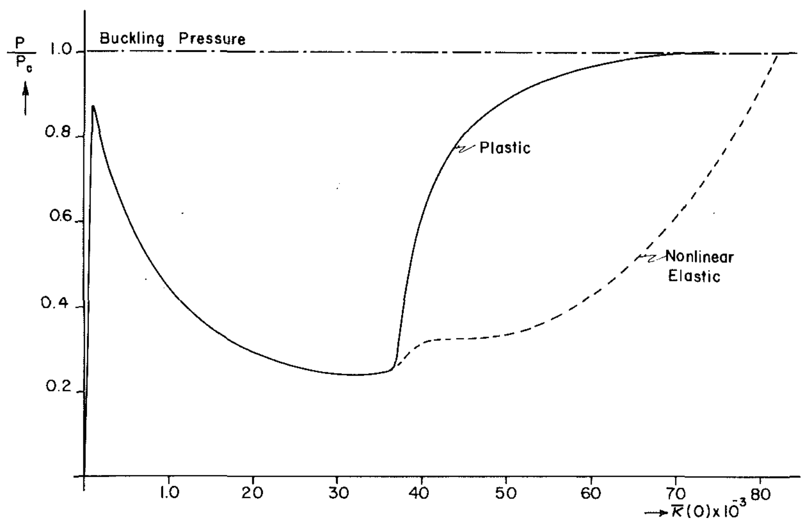

Fig. 10 Maximum strain (curvature) as a function of pressure

unloads along BC and then reloads, it is forced to follow the path CBF (see Fig. 6(b)).

The load-displacement behavior of the ring is also shown in Fig. 7. As in the case of the nonlinear elastic problem the response following first contact is stable. The plastic response is "stiffer" than the nonlinear elastic one, especially at the initial stages of loading. A relative "softening" is observed in the response for pressures close to the buckling pressure. The reason for this should become clear from what follows. Experimental measurements on buckled circular tubes are also included on the same plot for comparison (see the next section). Although not exactly the same as the theoretical predictions, the experimental results exhibit the same behavior as the results predicted by the plastic material and add credibility to most assumptions made in the solution process.

The sequence of cross sections obtained during the collapse process that follows first contact, is shown in Fig. 8(b). This sequence is distinctly different from that obtained for the nonlinear elastic material. In the plastic case a much smaller area of contact develops. At some pressure the middle part of the quadrant sustains bending which leads to the development of a second contact area. The bending of this midsection of the ring is thought to be responsible for the "softening" observed in the response curve for higher pressures. For all cases considered the solution procedure was pursued up to and until the second contact developed. For the sample problem presented second contact occurred very close to $P/P_c = 1$. For other combinations of material and geometric parameters it could occur below or above this value. It was not thought prudent to pursue the solution beyond this point. It is conceivable though, that for different parameters, a third or more contact points would develop. The existence of the second contact area in the problem at hand, is the subject of an experimental investigation presented in the next section.

The purpose of this investigation was to develop a relatively simple model for predicting the maximum strain in the ring during any stage of the postbuckling path. The maximum curvature is plotted as a function of the dimensionless pressure parameter in Fig. 10. (The curvature is maximum at $s = 0$.) A big difference is observed between the results from the two materials with the nonlinear elastic estimate of curvature being much higher than the plastic case.

The moment distributions in the ring before buckling, at the instant of first contact, and at the instant of the second contact, are shown in Fig. 11. The maximum positive value of moment is seen to shift away from $s = 1$ after first contact and is the cause of the severe bending observed in the midsection of the ring circumference, preceding and leading to the second contact point developing in that area. The section in contact is assumed to remain flat and in contact for all subsequent configurations. As a result the moment distribution remains constant and has a value given by the equation:

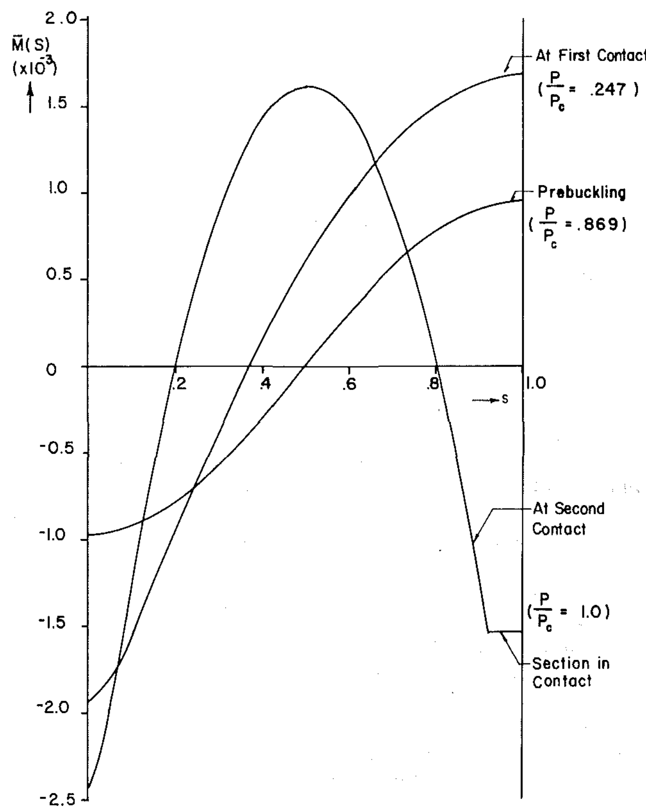

Fig. 11 Moment distribution at different load conditions (plastic case)

$$\bar{\kappa}(\alpha, \bar{M}_0) = \frac{1}{\pi}\left(\frac{t}{R}\right)\left(\frac{E}{\sigma_0}\right)\frac{d\theta_0}{ds}. \qquad (7)$$

Experimental Observations

The existence of more than one contact areas in the cross section of a ring collapsed by external pressure, was first recognized from the preceding analysis. Postmortem examination of many pipes buckled in a previous experimental program [2] showed that some but not conclusive

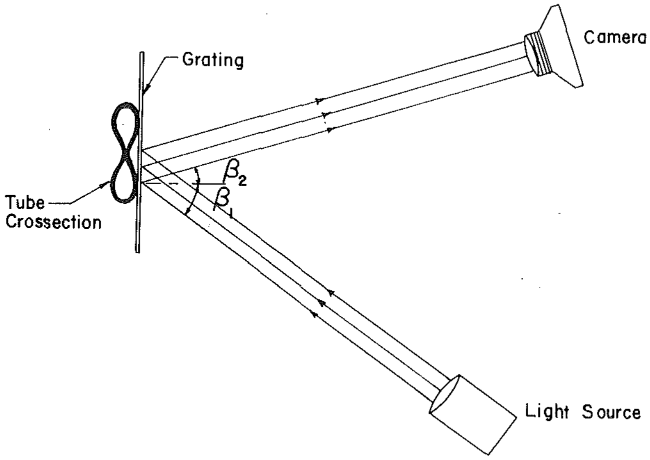

Fig. 12 Schematic of optical setup

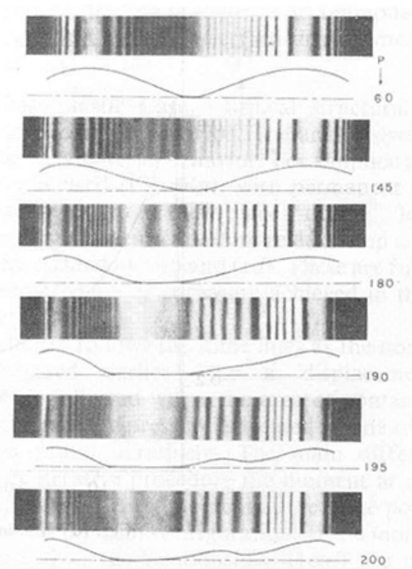

Fig. 13 Shadow moiré patterns and profiles of the tube cross sections at different external pressures

evidence existed for this behavior. As a result, a separate experiment was set up with the specific purpose of obtaining the geometry of the cross sections of rings in the postbuckling regime. The experiments were carried out on aluminum D6061-T6 tubes with diameter (D) of 1.0 in. (25.4 mm) and thickness (t) of 0.020 in. (0.50 mm).

The experimental procedure involved two stages. In the first stage the tube was collapsed from the original round cross section to one that has the typical "dog bone" shape, with just one contact point. As seen from Fig. 2 the postbuckling part of this path is unstable so a volume-controlled propagation procedure was used to flatten the tube. The experimental procedure used is similar to the one described in [2] for determining the propagation pressure of pipes.

The second stage of the experiment involved developing a technique for measuring the deformation of the pipe cross section from this point on. The pipe was already collapsed and as a result any further displacements were relatively small in magnitude. Since the measurements were required to be made while the tube was under pressure, it was necessary to use a noncontacting, remotely controlled measurement technique. The shadow moiré method (parallel illumination-parallel receiving) was chosen (see [9 and 10] for details about the method). A ruled glass plate was placed onto the collapsed pipe in such a way so as to touch it only at two places. It was secured in place with elastic bands so that continuous contact with the tube, as it deformed under pressure, was guaranteed. Subsequently the tube was placed in a transparent pressure vessel and pressurized (water on air). The tube was fixed in space so that no rigid body movements were allowed during pressurization. A collimated light beam from outside the tank was pointed toward the grating and a camera was used as the viewing instrument. The geometric arrangement of the light source, grating, and camera are shown in Fig. 12.

Fringes are formed by interference between the shadow formed by the incoming light beam on the deformed surface and the master grating. This fringe pattern can be related to the out-of-plane displacement of the surface onto which the shadow is cast. As the pressure was raised the geometry of the surface changed. A set of moiré patterns obtained from one such experiment are shown in Fig. 13. The one dimensionality of the problem is demonstrated by the parallelity of the fringes. A digitizer was used to record the position of each fringe. The order of the fringes was decided by monitoring the position of contact between the tube surface and the glass plate (zero-order fringe). Knowing the angles β_1 and β_2, the order of the fringe (n), and the grating pitch (λ), the out-of-plane displacement (w) of the surface was obtained from the expression

$$w = \frac{n\lambda}{\tan\beta_1 + \tan\beta_2}.$$

A digital calculator and a plotter were used to calculate and plot the profiles as obtained from these measurements. The results are shown in Fig. 13. Since only the out-of-plane displacement of one side of the pipe was measured, it was impossible to define the points of contact. In addition, in most experiments carried out, a slight asymmetry in the geometry caused one side to develop the second touchdown before the other. In spite of these differences both the pressure values as well as the profiles demonstrate the validity of the numerical predictions.

In addition to measuring the out-of-plane deformation, the change of length of the maximum diameter of the buckled tube was obtained photographically for different values of pressure. These values, normalized by $P_c (= [E/4(1-\nu^2)](t/R)^3$, are plotted for comparison with the analysis in Fig. 7. The agreement with analysis is quite good.

Conclusions

The complete postbuckling sequence of equilibrium configurations of an inelastic inextensional ring under external pressure has been obtained. The pressure-displacement response is characterized by a limit load that leads to instability and a stable branch that occurs after contact between the ring's opposite surfaces is established. The stable branch of the response and the ring configurations associated with it have been shown to be quite different in nature for the nonlinear elastic and elastoplastic cases. In the latter case multiple contact points were shown to develop. The existence of these was also verified experimentally. The results for the nonlinear elastic case compare well with those of Flaherty et al. [6], where only linearly elastic material was modeled.

Acknowledgment

The authors would like to express deep appreciation for Professor C. D. Babcock's (California Institute of Technology) continuous encouragement and guidance in carrying out the reported work. Special thanks are also due to Mr. P. K. Shaw for helping in the experimental part of the work as well as to Mrs. E. Rich for the excellent typing. The paper was prepared with the support of the U.S. Department of Transportation (Grant No. DTRS5680-C-00010). However any opinions, conclusions, or recommendations expressed herein are those of the authors and do not necessarily reflect the views of DOT.

References

1 Kyriakides, S., and Babcock, C. D., "Large Deflection Collapse Analysis of an Inelastic Inextensioned Ring Under External Pressure," *Int. J. of Solids and Structures*, Vol. 17, No. 10, 1981, pp. 981–993.

2 Kyriakides, S., and Babcock, C. D., "Experimental Determination of the Propagation Pressure of Circular Pipes," ASME *Journal of Pressure Vessel Technology*, Vol. 103, Nov. 1981, pp. 328–336.

3 Palmer, A. C., "Buckle Propagation in Submarine Pipelines," *Nature*, Vol. 254, No. 5495, March 6, 1975, pp. 46–48.

4 Mesloh, R., Johns, T. G., and Sorenson, J. E., "The Propagating Buckle," *BOSS 76, Proceedings, Battelle-Colombus Laboratories*, Vol. 1, 1976, pp. 787–797.

5 Kyriakides, S., and Babcock, C. D., "Prediction of Wet Buckles in Offshore Pipelines," *Proc. of the Marine Tech. '80 Conf.*, Oct. 1980, pp. 439–444.

6 Flaherty, J. E., Keller, J. B., and Rubinow, S. I., "Post Buckling of Elastic Tubes and Rings With Opposite Sides in Contact," *SIAM J. of Applied Mathematics*, Vol. 23, No. 4, Dec. 1972, pp. 446–455.

7 Bonis, M., Ribreau, C., and Verchery, G., "Experimental and Theoretical Study of the Flattening of a Depressed Elastic Tube," *Journal De Mécanique Appliquée*, Vol. 5, No. 2, 1981, pp. 123–144.

8 Wang, C.-Y., and Watson, L. T., "Equilibrium of Heavy Elastic Cylindrical Shells," ASME Journal of Applied Mechanics, Vol. 48, 1981, pp. 582–586.

9 Theocaris, P. S., "Moiré Method in Plates," *Proceed, Int. Assoc. Shell Struct.* (Symposium), Warson North Holland, 1963, pp. 877–889.

10 Chiang, F. P., "Moiré Methods of Strain Analysis," Chapter VI, *Manual on Experimental Stress Analysis, Exp. Mech.*, Aug. 1979, pp. 290–308.

Free Vibration of a Circular Cylindrical Shell Elastically Restrained by Axially Spaced Springs

T. Irie
Professor.

G. Yamada
Associate Professor.

Y. Muramoto
Graduate Student.

Department of Mechanical Engineering,
Hokkaido University,
Kita-13, Nishi-8, Kita-ku,
Sapporo, 060 Japan

An analysis is presented for the free vibration of a circular cylindrical shell restrained by axially spaced elastic springs. The governing equations of vibration of a circular cylindrical shell are written as a coupled set of first-order differential equations by using the transfer matrix of the shell. Once the matrix has been determined, the entire structure matrix is obtained by the product of the transfer matrices and the point matrices at the springs, and the frequency equation is derived with terms of the elements of the structure matrix under the boundary conditions. The method is applied to circular cylindrical shells supported by axially equispaced springs of the same stiffness, and the natural frequencies and the mode shapes of vibration are calculated numerically.

Introduction

This paper presents an analysis of the free vibration of a circular cylindrical shell elastically restrained by several springs uniformly distributed along the circumference of the shell, in which the transfer matrix approach is used. Circular cylindrical shells play an important role in many industrial fields, and therefore a considerable number of papers are available on the vibration of the shells. Leissa [1] collected and reviewed the comprehensive literature dealing with the vibration of shells up to 1972. Since then, Dym [2], Goldman [3], Kumar [4], Chandra and Kumar [5–7], and Chung [8] studied the free vibration of cylindrical shells by analytical solutions of vibration equations. Cunningham and Leanhardt [9], Grief and Chung [10], Sharma [11–13], and Tonin and Bies [14] also analyzed cylindrical shells by the Ritz method; Soedel [15] by the Galerkin method, and Gladwell and Vijay [16], Ramamurti and Pattabiraman [17], and Delpak and Hague [18] by the finite element method. Recently, Ludwig and Krieg [19] have studied cylindrical shells stiffened by a rigid ring at an edge. However, there are no papers dealing with the cylindrical shells reported here.

For the purpose of this study, the equations of free vibration of a circular cylindrical shell based on the Goldenveizer-Novozhilov theory are written in a matrix differential equation of the first order by use of the transfer matrix of the shell. The transfer matrix is expressed con-

Contributed by the Applied Mechanics Division for publication in the JOURNAL OF APPLIED MECHANICS.

Discussion on this paper should be addressed to the Editorial Department, ASME, United Engineering Center, 345 East 47th Street, New York, N.Y. 10017, and will be accepted until two months after final publication of the paper itself in the JOURNAL OF APPLIED MECHANICS. Manuscript received by ASME Applied Mechanics Division, July 1982; final revision, February, 1983.

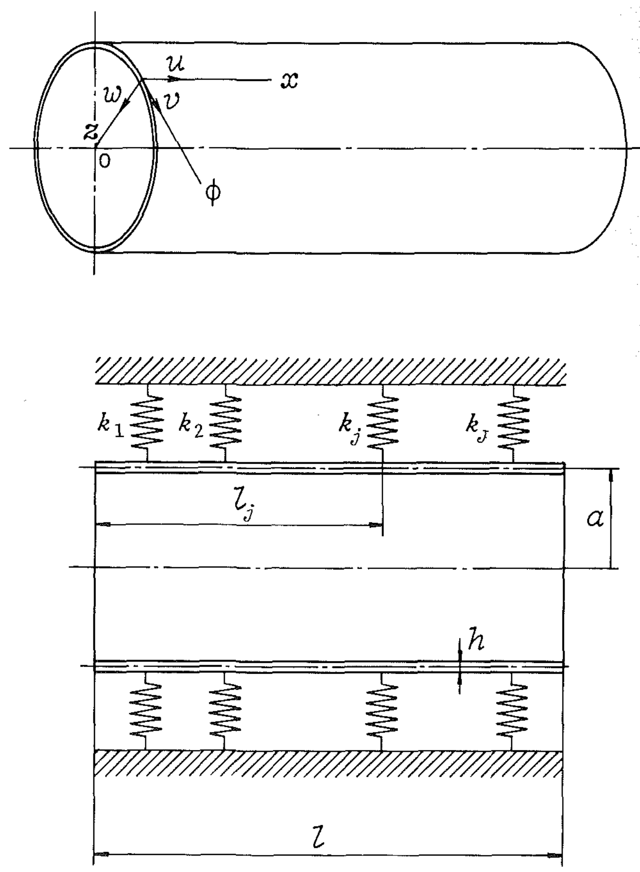

Fig. 1 A circular cylindrical shell elastically restrained by axially spaced springs

veniently by a power series solution to the matrix equation, and the entire structure matrix of the shell is obtained as the product of the transfer matrices and the point matrices at each spring. The frequency equation is derived with only terms of the elements of the structure matrix necessary for the calculation under a given combination of boundary conditions.

By the application of the method, the natural frequencies (the eigenvalues of vibration) and the mode shapes are calculated numerically for circular cylindrical shells elastically supported by axially equispaced springs of the same stiffness, and the results are presented in some figures.

Equations of Vibration and the Solution

Figure 1 shows a circular cylindrical shell elastically restrained by several axially spaced springs. With the axial length of the shell denoted by ℓ, the radius of the neutral surface by a, the cylindrical coordinates (x, φ, z) are taken as shown in the figure. The equatins of free vibration of the shell based on the Goldenveizer-Novozhilov theory are written as [20,21]

$$\frac{\partial N_x}{\partial x}+\frac{\partial N_{\varphi x}}{a\partial\varphi}+\rho h\omega^2 u=0,\quad \frac{\partial N_\varphi}{a\partial\varphi}+\frac{\partial N_{x\varphi}}{\partial x}-\frac{1}{a}Q_\varphi$$

$$+\rho h\omega^2 v=0,\ \frac{\partial Q_x}{\partial x}+\frac{\partial Q_\varphi}{a\partial\varphi}+\frac{1}{a}N_\varphi+\rho h\omega^2 w=0 \qquad (1)$$

where ρ is the mass density, h is the wall thickness, and ω is the angular frequency. The components of the shearing force are given by

$$Q_x=\frac{\partial M_x}{\partial x}+\frac{\partial M_{\varphi x}}{a\partial\varphi},\quad Q_\varphi=\frac{\partial M_\varphi}{a\partial\varphi}-\frac{\partial M_{x\varphi}}{\partial x} \qquad (2)$$

and the Kelvin-Kirchoff membrane force and shearing force, respectively, are

$$R_x=N_{x\varphi}+\frac{1}{a}M_{x\varphi},\quad S_x=Q_x-\frac{\partial M_{x\varphi}}{a\partial\varphi} \qquad (3)$$

The components of the membrane force are given by

$$N_x = D\left\{\frac{\partial u}{\partial x}+\frac{\nu}{a}\left(\frac{\partial v}{\partial\varphi}-w\right)\right\},$$

$$N_\varphi = D\left\{\frac{1}{a}\left(\frac{\partial v}{\partial\varphi}-w\right)+\nu\frac{\partial u}{\partial x}\right\},$$

$$N_{x\varphi} = N_{\varphi x}+\frac{1-\nu}{12}D\frac{h^2}{a^2}\left(\frac{\partial v}{\partial x}+\frac{\partial\psi}{\partial\varphi}\right),$$

$$N_{\varphi x} = \frac{1-\nu}{2}D\left(\frac{\partial u}{a\partial\varphi}+\frac{\partial v}{\partial x}\right) \qquad (4)$$

and those of the moment are

$$M_x = -K\left\{\frac{\partial\psi}{\partial x}+\frac{\nu}{a^2}\left(\frac{\partial v}{\partial\varphi}+\frac{\partial^2 w}{\partial\varphi^2}\right)\right\},$$

$$M_\varphi = -K\left\{\frac{1}{a^2}\left(\frac{\partial v}{\partial\varphi}+\frac{\partial^2 w}{\partial\varphi^2}\right)+\nu\frac{\partial\psi}{\partial x}\right\},$$

$$M_{x\varphi} = -M_{\varphi x}=\frac{K(1-\nu)}{a}\left(\frac{\partial v}{\partial x}+\frac{\partial\psi}{\partial\varphi}\right) \qquad (5)$$

in terms of the displacements u, v, w in the axial, circumferential, and radial directions, respectively, and the slope of the displacement w expressed as $\psi=\partial w/\partial x$. The quantities D and K, respectively, are the extensional and flexural rigidities expressed as $D=Eh/(1-\nu^2)$, $K=Eh^3/12(1-\nu^2)$ in terms of Young's modulus E, Poisson's ratio ν and the wall thickness. For the free vibration of the shell, one may take

$$(u,w)=h(\bar u,\bar w)\cos n\varphi,\quad v=h\bar v\sin n\varphi,\quad \psi=\frac{h}{a}\bar\psi\cos n\varphi,$$

$$(N_x,N_\varphi,Q_x,S_x)=\frac{K}{a^2}(\bar N_x,\bar N_\varphi,\bar Q_x,\bar S_x)\cos n\varphi,$$

$$(N_{x\varphi},N_{\varphi x},Q_\varphi,R_x)=\frac{K}{a^2}(\bar N_{x\varphi},\bar N_{\varphi x},\bar Q_\varphi,\bar R_x)\sin n\varphi,$$

$$(M_x,M_\varphi)=\frac{K}{a}(\bar M_x,\bar M_\varphi)\cos n\varphi,$$

$$(M_{x\varphi},M_{\varphi x})=\frac{K}{a}(\bar M_{x\varphi},\bar M_{\varphi x})\sin n\varphi \qquad (6)$$

where the quantities $\bar u$, $\bar v$, . . . marked with an overscore are the respective dimensionless variables. For simplicity of the analysis, the following dimensionless parameters are also introduced:

$$\xi=\frac{x}{\ell},\quad (\bar\ell,\bar h)=\frac{1}{a}(\ell,h),\quad \lambda^2=\frac{\rho h a^2\omega^2}{D} \qquad (7)$$

Upon eliminating N_φ, $N_{x\varphi}$, $N_{\varphi x}$, Q_x, Q_φ, M_φ, $M_{x\varphi}$, and $M_{\varphi x}$ from (1)–(5), the equations of vibration can be written as the matrix differential equation,

$$\frac{d}{d\xi}\begin{Bmatrix}\bar u\\ \bar v\\ \bar w\\ \bar\psi\\ \bar M_x\\ \bar S_x\\ \bar R_x\\ -\bar N_x\end{Bmatrix}=\bar\ell\begin{bmatrix}0 & u_{12} & u_{13} & 0 & 0 & 0 & 0 & u_{18}\\ u_{21} & 0 & 0 & u_{24} & 0 & 0 & u_{27} & \\ 0 & 0 & 0 & u_{34} & 0 & 0 & & \\ 0 & u_{42} & u_{43} & 0 & u_{45} & & & \\ u_{51} & 0 & 0 & u_{54} & & & & \\ 0 & u_{62} & u_{63} & & & SYM & & \\ 0 & u_{72} & & & & & & \\ u_{81} & & & & & & & \end{bmatrix}\begin{Bmatrix}\bar u\\ \bar v\\ \bar w\\ \bar\psi\\ \bar M_x\\ \bar S_x\\ \bar R_x\\ -\bar N_x\end{Bmatrix} \qquad (8)$$

where

$$u_{12} = u_{42}=-n\nu,\quad u_{13}=\nu,\quad u_{18}=-\bar h/12,$$
$$u_{21} = n/(1+\bar h^2/3),\quad u_{24}=n/(1+3/\bar h^2),$$
$$u_{27} = \bar h/6(1-\nu)(1+\bar h^2/3),$$

$$u_{34} = 1, \quad u_{43} = n^2\nu, \quad u_{45} = -1/\bar{h},$$
$$u_{51} = -u_{54} = 6n^2(1-\nu)/(1+3/\bar{h}^2)/\bar{h},$$
$$U_{62} = -12n(1-\nu^2)(1+n^2\bar{h}^2/12)/\bar{h},$$
$$u_{63} = 12\{(1-\nu^2)(1+n^4\bar{h}^2/12)-\lambda^2\}/\bar{h},$$
$$u_{72} = 12\{n^2(1-\nu^2)(1+\bar{h}^2/12)-\lambda^2\}/\bar{h},$$
$$u_{81} = -12\{n^2(1-\nu)/2(1+3/\bar{h}^2)-\lambda^2\}/\bar{h} \tag{9}$$

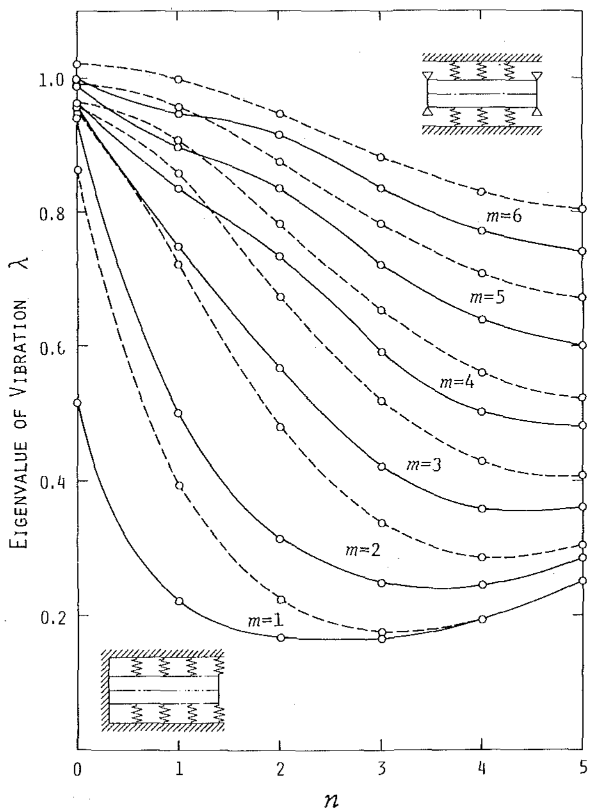

Fig. 2 Eigenvalues of vibration of a free-clamped and a simply supported cylindrical shell versus the circumferential wave number: $\nu = 0.3$, $\bar{\ell} = 3$, $\bar{h} = 0.03$, $J = 4$ **(free-clamped),** $J = 3$ **(simply supported),** $\bar{k}_x = \bar{k}_\varphi = \bar{k}_z = 5$

Equation (8) can be written as

$$\frac{d}{d\xi}\{z(\xi)\} = \bar{\ell}\,[U]\{z(\xi)\} \tag{10}$$

by use of the state vector $\{z(\xi)\} = \{\bar{u}\bar{v}\bar{w}\bar{\psi}\bar{M}_x\bar{S}_x\bar{R}_x - \bar{N}_x\}^T$ and the coefficient matrix $\bar{\ell}\,[U]$ given in (8). The state vector $\{z(\xi)\}$ can be expressed as $\{z(\xi)\} = [T(\xi)]\,\{z(0)\}$ by using the transfer matrix $[T(\xi)]$ of the shell, and the substitution of the expression into (10) yields

$$\frac{d}{d\xi}[T(\xi)] = \bar{\ell}\,[U][T(\xi)] \tag{11}$$

The matrix $[T(\xi)]$ is determined by the power series solution to (11) as follows:

$$[T(\xi)] = e^{\bar{\ell}[U]\xi} = [I] + \frac{1}{1!}[U]\bar{\ell}\xi + \frac{1}{2!}[U]^2\bar{\ell}^2\xi^2 + \ldots \tag{12}$$

The convergent values of the transfer matrix can be obtained by numerical calculation with quadruple precision on a digital computer.

Frequency Equation

Along a circle locating at $\xi = \xi_j$ where the shell is supported by a spring, we have the relation expressed as

$$\{z_{j+1}(\xi_j + 0)\} = [P_j]\{z_j(\xi_j - 0)\} \tag{13}$$

by using the point matrix

$$[P_j] = \begin{bmatrix} 1 & 0 & 0 & 0 & 0 & 0 & 0 & 0 \\ 0 & 1 & 0 & 0 & 0 & 0 & 0 & \\ 0 & 0 & 1 & 0 & 0 & 0 & & \\ 0 & 0 & 0 & 1 & 0 & & & \\ 0 & 0 & 0 & 0 & & & & \\ 0 & 0 & \bar{k}_{z,j} & & & SYM & & \\ 0 & \bar{k}_{\varphi,j} & & & & & & \\ -\bar{k}_{x,j} & & & & & & & \end{bmatrix},$$

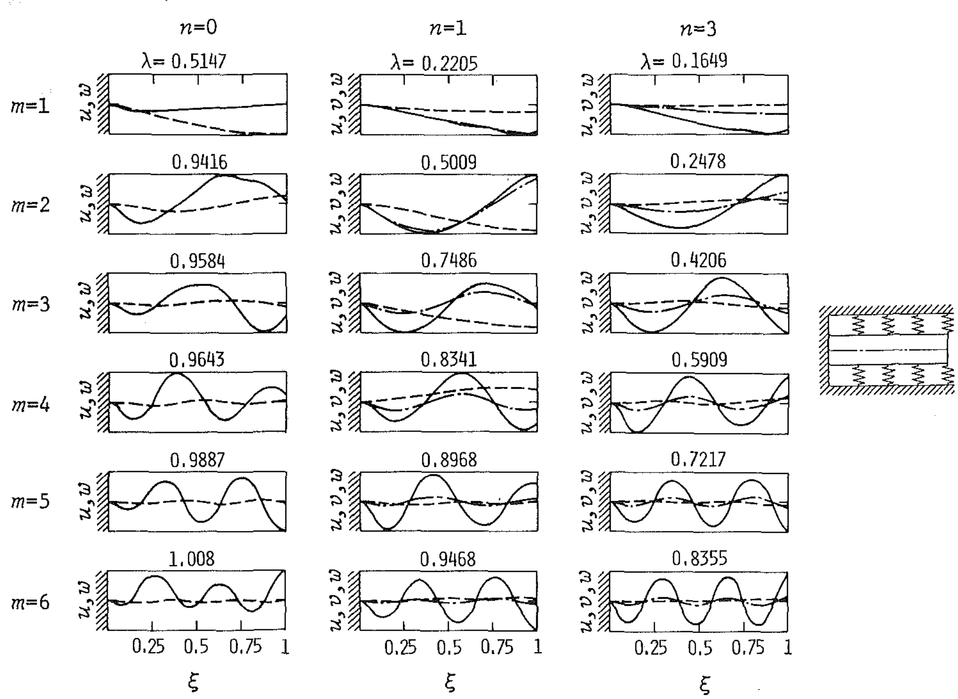

Fig. 3 Eigenvalues of vibration and mode shapes of a free-clamped cylindrical shell elastically restrained by axially equispaced springs: $\nu = 0.3$, $\bar{\ell} = 3$, $\bar{h} = 0.03$, $J = 4$, $\bar{k}_x = \bar{k}_\varphi = \bar{k}_z = 5$, - - - - - $\bar{u}$, — - — $\bar{v}$, ——— $\bar{w}$

$$(\bar{k}_x, \bar{k}_\varphi, \bar{k}_z)_j = \frac{a^2 h}{K}(k_x, k_\varphi, k_z)_j \tag{14}$$

where $k_{x,j}$, $k_{\varphi,j}$, and $k_{z,j}$ are the axial, circumferential, and radial stiffnesses, respectively, of the spring. At an arbitrary circle, the state vector of the shell is expressed as

$$\{z_j(\xi)\} = [T_j(\xi)] \prod_{i=1}^{j-1} [P_i][T_i(\xi_i)]\{z_1(0)\}$$

$$= [\overline{T_j(\xi)}]\{z_1(0)\} \; (\xi_{j-1} \le \xi \le \xi_j) \tag{15}$$

The present method can be applied to cylindrical shells under any combination of boundary conditions. Here, two examples will be explained.

Example 1: A free-clamped cylindrical shell. For a shell with a free and a clamped edge, the boundary conditions are written as

$$u = v = w = 0, \; \psi = 0 \quad \text{at } x = 0$$

$$N_x = R_x = S_x = 0, \; M_x = 0 \quad \text{at } x = \ell \tag{16}$$

The substitution of (15) into (16) yields the frequency equation

$$\overline{\begin{bmatrix} T_{55} & T_{56} & T_{57} & T_{58} \\ T_{65} & T_{66} & T_{67} & T_{68} \\ T_{75} & T_{76} & T_{77} & T_{78} \\ T_{85} & T_{86} & T_{87} & T_{88} \end{bmatrix}}_{(1)} \begin{Bmatrix} \bar{M}_x \\ \bar{S}_x \\ \bar{R}_x \\ -\bar{N}_x \end{Bmatrix}_{(0)} = 0 \tag{17}$$

with only the elements of $[\overline{T(1)}]$ necessary for the calculation.

Since $[U]$ and $[T(\xi)]$ depend on the frequency parameter λ, $[\overline{T(1)}]$ is also a function of λ. The natural frequencies of the shell are determined by calculating the eigenvalues λ of (17), and the mode shapes of vibration are determined by calculating the eigenvectors corresponding to the eigenvalues.

Example 2: A simply supported cylindrical shell. For a shell simply supported (by shear diaphragms [1]) at both edges, the boundary conditions are

$$v = w = 0, \; N_x = 0, \; M_x = 0 \quad \text{at } x = 0, \text{ and } \ell \tag{18}$$

and therefore the frequency equation is expressed as

$$\overline{\begin{bmatrix} T_{21} & T_{24} & T_{26} & T_{27} \\ T_{31} & T_{34} & T_{36} & T_{37} \\ T_{51} & T_{54} & T_{56} & T_{57} \\ T_{81} & T_{84} & T_{86} & T_{87} \end{bmatrix}}_{(1)} \begin{Bmatrix} \bar{u} \\ \bar{\psi} \\ \bar{S}_x \\ \bar{R}_x \end{Bmatrix}_{(0)} = 0 \tag{19}$$

Numerical Calculation and Discussion

In this section, the eigenvalues of vibration λ and the mode shapes are calculated numerically by applying the method for circular cylindrical shells elastically restrained by axially equispaced springs of the same stiffness.

Figure 2 shows the eigenvalues versus the circumferential wave number n for a free-clamped shell (solid lines) and a simply supported shell (broken lines). The eigenvalues change with the variation of the number n, and the minimum values appears in the case of $m=1$ and $n=2$ or 3, where m denotes the axial wave number. Although the eigenvalues of a simply supported shell are larger than those of a free-clamped one, the variation of them is similar to each other.

Figure 3 shows the mode shapes of the free-clamped shell presented in Fig. 2 for the circumferential wave number $n=0$, 1, and 3, where the radial, circumferential, and axial displacements are shown by solid lines, chain lines, and broken lines, respectively. The maximum radial displacement is taken to have unit value at the free edge or at the loop causing the maximum displacement except for the case of

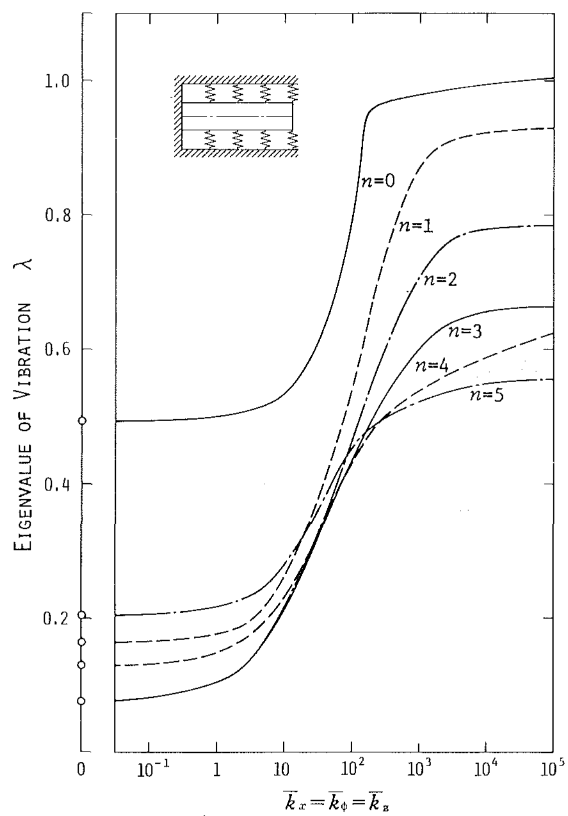

Fig. 4 Eigenvalues of vibration of a free-clamped cylindrical shell versus the stiffness parameter of springs: $\nu=0.3$, $\bar{\ell}=3$, $\bar{h}=0.03$, $J=4$, $m=1$

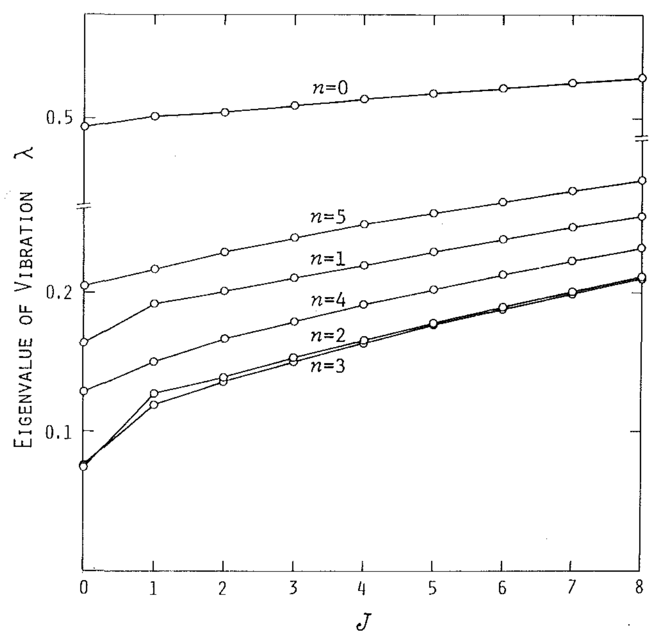

Fig. 5 Eigenvalues of vibration of a free-clamped cylindrical shell versus the number of springs: $\nu=0.3$, $\bar{\ell}=3$, $\bar{h}=0.03$, $\bar{k}_x=\bar{k}_\varphi=\bar{k}_z=5$, $m=1$

$m=1$, $n=0$, in which the axial displacement is extremely larger than the radial one. The vibration of $n=0$ is an axisymmetrical one. With an increase of the circumferential wave number n, the mode shapes come to be similar to those of a cantilever beam.

Figure 4 shows the eigenvalues versus the stiffness parameters $\bar{k}_x=\bar{k}_\varphi=\bar{k}_z$ of springs for the axial wave number $m=1$. The values marked with a small circle on the ordinate represent the eigenvalues of a cylindrical shell without springs. With an increase of the stiffness parameters, the eigenvalues become larger monotonically, although the increasing rate is different depending on the number n.

Figure 5 shows the eigenvalues versus the number J of springs for $m=1$. The values marked with a circle on the ordinate are the same as those presented in Fig. 4. With an increase in number J, the eigenvalues also monotonically increase.

The numerical calculations presented here were carried out on an HITAC M-200H computer of the Hokkaido University Computing Center.

References

1 Leissa, A. W., "Vibration of Shells," NASA SP-288, 1973.

2 Dym, C. L., "Some New Results for the Vibrations of Circular Cylinders," *Journal of Sound and Vibration*, Vol. 29, No. 2, 1973, pp. 189–205.

3 Goldman, R. L., "Mode Shapes and Frequencies of Clamped-Clamped Cylindrical Shells," *AIAA Journal*, Vol. 12, No. 12, 1974, pp. 1755–1756.

4 Kumar, R., "Axially Symmetric Vibrations of Finite Cylindrical Shells of Various Wall Thicknesses-I," *Acustica*, Vol. 34, 1976, pp. 281–288.

5 Chandra, J., and Kumar, R., "Axially Symmetric Vibrations of Finite Cylindrical Shells of Various Wall Thicknesses-II," *Acustica*, Vol. 38, 1977, pp. 24–29.

6 Chandra, J., and Kumar, R., "Flexural Vibrations of Finite Cylindrical Shells of Various Wall Thicknesses-I," *Acustica*, Vol. 38, 1977, pp. 258–263.

7 Chandra, J., and Kumar, R., "Flexural Vibrations of Finite Cylindrical Shells of Various Wall Thicknesses-II," *Acustica*, Vol. 46, 1980, pp. 283–288.

8 Chung, H., "Free Vibration Analysis of Circular Cylindrical Shells," *Journal of Sound and Vibration*, Vol. 74, No. 3, 1981, pp. 331–350.

9 Cunningham, F. M., and Leanhardt, D. E., "Vibration Characteristics of Free Thin Cylindrical Shells," ASME *Journal of Engineering for Industry*, Vol. 96, No. 3, 1974, pp. 1036–1040.

10 Greif, R., and Chung, H., "Vibrations of Constrained Cylindrical Shells," *AIAA Journal*, Vol. 13, No. 9, 1975, pp. 1190–1198.

11 Sharma, C. B., "Calculation of Natural Frequencies of Fixed-Free Circular Cylindrical Shells," *Journal of Sound and Vibration*, Vol. 35, No. 1, 1974, pp. 55–76.

12 Sharma, C. B., "Simple Linear Formulas for Critical Frequencies for Cantilever Circular Cylindrical Shells," *Journal of Sound and Vibration*, Vol. 55, No. 3, 1977, pp. 467–471.

13 Sharma, C. B., "Vibration Characteristics of Thin Circular Cylinders," *Journal of Sound and Vibration*, Vol. 63, No. 4, 1979, pp. 581–592.

14 Tonin, R. F. and Bies, D. A., "Free Vibration of Circular Cylinders of Variable Thickness," *Journal of Sound and Vibration*, Vol. 62, No. 2, 1979, pp. 165–180.

15 Soedel, W., "A New Frequency Formula for Closed Circular Cylindrical Shells for a Large Variety of Boundary Conditions," *Journal of Sound and Vibration*, Vol. 70, No. 3, 1980, pp. 309–317.

16 Gladwell, G. M. L., and Vijay, D. K., "Natural Frequencies of Free Finite-Length Circular Cylinders," *Journal of Sound and Vibration*, Vol. 42, No. 3, 1975, pp. 387–397.

17 Ramamurti, V., and Pattabiraman, J., "Free Vibrations of Circular Cylindrical Shells," *Journal of Sound and Vibration*, Vol. 48, No. 1, 1976, pp. 137–155.

18 Delpak, R., and Hague, W. M., "An Experimental and Theoretical Investigation of the Frequencies and Mode Shapes of Axisymmetric Shell Models," *Journal of Sound and Vibration*, Vol. 72, No. 2, 1980, pp. 235–249.

19 Ludwig, A., and Krieg, R., "An Analytical Quasi-Exact Method for Calculating Eigenvibrations of Thin Circular Cylindrical Shells," *Journal of Sound and Vibration*, Vol. 74, No. 2, 1981, pp. 155–174.

20 Goldenveizer, A. L., *Theory of Thin Shells*, Pergamon Press, New York, 1961.

21 Novozhilov, V. V., "The Theory of Thin Elastic Shells," P. Noordhoff Ltd, Groningen, The Netherlands, 1964.

A. Drescher
Professor,
Department of Civil and Mineral Engineering,
University of Minnesota,
Minneapolis, Minn. 55455

Limit Plasticity Approach to Piping in Bins

The plastic limit analysis method is adopted to derive a criterion for piping in particulate solids discharged from prismatic and cylindrical bins. Plane, rectangular, and circular cross sections of empty channels (pipes) are considered. Utilizing the kinematic approach, various mechanisms of failure of the material surrounding an empty channel are discussed. The geometry of a stable channel is related to the material strength parameters c and ϕ, specific weight γ, and geometry of the bin; safe estimate to the piping criterion is given.

Introduction

This paper deals with stability of vertical empty channels or pipes, forming within particulate solids during discharge from bins. Accordingly, the term piping is used to describe the formation of a stable empty channel.

The phenomenon of piping occurs in plug-flow bins, where a particulate solid exhibits sufficiently high strength to withstand the stresses produced by its weight in a vertical slope surrounding an empty channel [1-4]. If the Mohr–Coulomb strength criterion is assumed, two material parameters, the angle of internal friction ϕ, an the cohesion c, define the strength of the material; and unsupported vertical slope can form only if $c>0$. Although variation of c and ϕ with the depth of bin can be implemented in the analysis presented in the paper, it is assumed throughout that both parameters are constant.

To evaluate stresses around a vertical channel in cylindrical slopes, Jenike and Yen [5] assumed a rigid perfectly plastic model for the particulate material. Using equilibrium equations, the Mohr–Coulomb strength criterion, and utilizing the method of characteristics [6], Jenike and Yen arrived at a formula for the diameter of a stable pipe as a function of c and ϕ. As a criterion for stability, a bounded stress characteristic field was assumed.

In the present paper, another approximate approach is suggested, based on the limit plasticity method. Examples of application of limit analysis for determination of wall pressures in bins are given in [7].

Limit Analysis Method

The method of limit analysis is based on the concept of perfectly plastic material, obeying a flow rule associated with the yield condition [8], for which the lower and upper bounds to the true collapse load can rigorously be proven [8-10]. Numerous experiments performed on cohesionless and cohesive soils indicate that the associated flow rule does not accurately describe the deformation of the material. Nonassociated flow rules have been proposed (cf [8, 13-15]), but in these formulations useful upper and lower limit analysis theorems cannot be proven. However, materials obeying nonassociated flow rules cannot be stronger than one with an associated rule [7]. Thus, the upper limit load for a material with the associated flow rule is also an upper bound to the true load for a particulate solid.

For the considered problem, the collapse load is identified with the material specific weight γ, or, for a given specific weight, the dimensions of a surrounding channel slope at collapse can be found. If the formation of a stable channel within a particulate solid occupying a bin is regarded as undesirable when operating bins, then a safe estimate of the true geometry of the channel at collapse may be found from the upper bound solution, by examining kinematically admissible velocity fields. In fact, if the channel of height determined from a kinematically admissible field will collapse, the height corresponding to the true solution cannot be greater.

Plane and Rectangular Bins

The term rectangular bin is used to describe a container with four vertical flat walls and rectangular cross section of half width B and half length L. The outlet in the flat bottom is also rectangular, and usually extends throughout the bin length. If the length of a rectangular bin is appreciably greater than its width, the bin is called plane. It is assumed that in both types of bins a vertical empty channel may form with rectangular cross section of half width w and half length $s \leqq L$.

Plane Failure. Consider first a plane bin in which the mechanism of failure of a vertical slope extends throughout the whole length L. It may be assumed, then, that plane-strain conditions prevail. Two simple mechanisms of kinematically admissible field of failure, namely sliding and rotation (see Figs. 1(a) and (b)) are considered. For the first mechanism, the relationship between the geometry of the failing portion of the slope and the material parameters is

Contributed by the Applied Mechanics Division for publication in the JOURNAL OF APPLIED MECHANICS.

Discussion on this paper should be addressed to the Editorial Department, ASME, United Engineering Center, 345 East 47th Street, New York, N.Y. 10017, and will be accepted until two months after final publication of the paper itself in the JOURNAL OF APPLIED MECHANICS. Manuscript received by ASME Applied Mechanics Division, October, 1982.

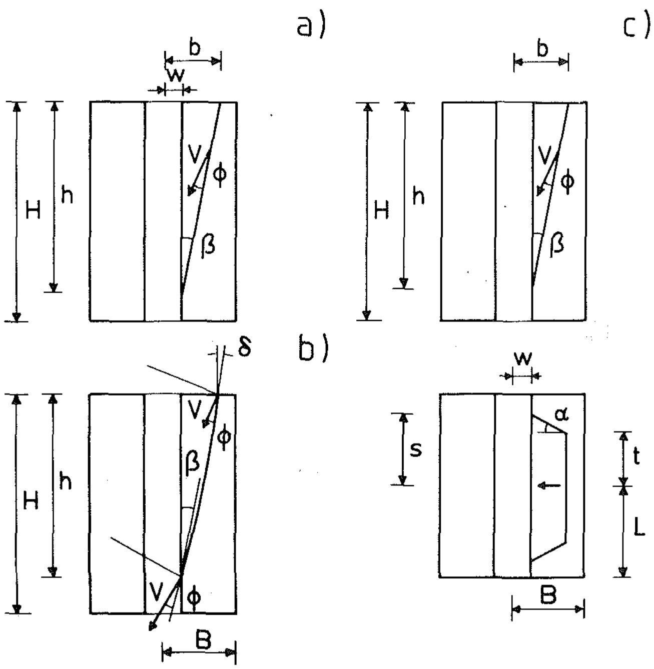

Fig. 1 Mechanisms of failure in a plane and rectangular bin

$$\frac{c}{\gamma H}=\frac{h}{H}\frac{\sin\beta\cos(\beta+\phi)}{2\cos\phi}, \tag{1}$$

Rigid rotation, with angular velocity Ω, of a material obeying the associated flow rule is admissible providing the velocity discontinuity line is a log spiral, with velocity jump increasing exponentially. The resulting expression for $c/\gamma H$ becomes

$$\frac{c}{\gamma H}=\frac{h}{H}\frac{\cos(\theta_3-\beta)}{\sin(\theta_3-\theta_1)\cos\beta}\left(\frac{K_2-K_3-K_4}{K_1}\right), \tag{2}$$

where

$$K_1 = \frac{\cos\phi}{2\tan\phi}[e^{2(\theta_3-\theta_1)\tan\phi}-1],$$

$$K_2 = \frac{e^{-3\theta_1\tan\phi}}{3(9\tan^2\phi+1)}[e^{3\theta_3\tan\phi}(3\tan\phi\cos\theta_3 +\sin\theta_3)-e^{3\theta_1\tan\phi}(3\tan\phi\cos\theta_1+\sin\theta_1)],$$

$$K_3 = \frac{\sin^3\theta_1}{6}\left(\frac{1}{\sin^2\theta_1}-\frac{1}{\sin^2\theta_2}\right),$$

$$K_4 = \frac{e^{3(\theta_3-\theta_1)\tan\phi}}{3}\cos^3\theta_3(\tan\theta_3-\tan\theta_2), \tag{3}$$

and the angles θ_1, θ_2, and θ_3 are defined as

$$\theta_1=\phi+\delta,\quad \theta_2=\theta_1+\epsilon,\quad \theta_3=\theta_1+\omega, \tag{4}$$

with

$$\epsilon=\tan^{-1}\frac{\sin\theta_1\sin\omega\sin\beta}{\cos(\omega+\theta_1-\beta)-\cos\theta_1\sin\omega\sin\beta}, \tag{5}$$

and ω resulting from

$$e^{\omega\tan\phi}[\cos\omega-\tan(\delta+\phi-\beta)\sin\omega]=1. \tag{6}$$

Both mechanisms of failure are well known in the soil slope stability problem. However, the critical height of a failing soil slope is obtained using the fact that it extends horizontally without limit. In the case of a bin, the slope is bounded by the width of bin.

Prismatic Failure. If the length L of a bin is comparable with the width B, plane failure cannot be assumed. A kinematically admissible mechanism is suggested consisting of rigid sliding of a trapezoidal prism, Fig. 1(*c*). The side walls and the bottom wall are the velocity discontinuity surfaces, inclined to the velocity vector V at the angle ϕ. The intersection of the side walls with the upper surface of the slope makes the angle α, given by

$$\sin\alpha=\frac{\sin\phi}{\sin(\beta+\phi)}, \tag{7}$$

and the ratio $c/\gamma H$ is

$$\frac{c}{\gamma H}=\frac{1}{H}\frac{L_1}{(M_1+M_2)}\frac{\cos(\beta+\phi)}{\cos\phi}, \tag{8}$$

where

$$M_1 = (s-t)\frac{h}{\sin\alpha},$$

$$M_2 = (s+t)\frac{h}{\cos\beta},$$

$$L_1 = \frac{1}{3}h^2(t+2s)\tan\beta,$$

$$s = h\tan\alpha\ \tan\beta+t. \tag{9}$$

The preceding mechanism was suggested for failure of buried plates anchoring retaining walls in [12], with erroneous expression for α. It may apply to rectangular bins with the length of the outlet smaller than the length of the bin.

Circular and Square Bins

In cylindrical bins with circular outlets, and in prismatic bins with square outlets, the horizontal cross section of the empty channel is usually circular. The following analysis is limited, therefore, to cylindrical channels only.

Axisymmetric Failure. Axisymmetric mode of failure requires the velocities V of particles to be directed toward the vertical axis of symmetry z. Circumferential strain rates $\dot\epsilon_\theta=V/r\neq 0$ do not allow for development of a conical velocity discontinuity surface with constant velocity jump. Thus, rigid motion mechanism of failure is not admissible. Instead, a continuous, axisymmetric velocity field $V=V(r,z)$ is postulated. To find an axisymmetric velocity field for a dilatant material is difficult, because the volumetric strain-rate rule contains an unknown scalar factor $\lambda\geqq 0$. The problem simplifies if the material is incompressible, and equation $\dot\epsilon_r+\dot\epsilon_\theta+\dot\epsilon_z=0$ is available. Incompressibility is enforced if the angle of internal friction is zero. An example of an axisymmetric velocity field for incompressible material, and the resulting dimensions of a failing slope, are given in the following.

It is assumed that the velocity field $V=V(r,z)$ is bounded by a cylindrical region $R_1<r<R_0$ and $z>0$ (Fig. 2(*a*)), with $V_r=V_z=0$ at the boundaries. The boundary conditions and incompressibility of the material are fulfilled if the velocity field is postulated as

$$V_r = -A(r-R_0)^2 z,$$

$$V_z = A\frac{z^2}{2}\left[2(r-R_0)+\frac{(r-R_0)^2}{r}\right], \tag{10}$$

for $r\leqq R_0$, $z\geqq 0$, where A is an arbitrary positive constant of dimension 1/sec cm^2. A realistic mechanism of failure is obtained if the inner radius of the empty channel $R_1\geqq R_*=R_0/3^{1/2}$. The total rate of energy dissipation, obtained by integration of specific rate of energy over the failing region is

$$D=2\pi c\int_{R_1}^{R_0}\int_0^h(\dot\epsilon_1-\dot\epsilon_2-\dot\epsilon_3)r\ dr\ dz, \tag{11}$$

where

$$\dot{\epsilon}_{1,2} = \frac{A}{2}\left[\frac{(r-R_0)^2 z}{r} \pm \right.$$

$$\left.\sqrt{z^2(r-R_0)^2\left(5-\frac{R_0}{r}\right)^2 + \frac{z^4}{4}\left(3-\frac{R_0{}^2}{r^2}\right)^2 - z^2\left(3-\frac{R_0{}^2}{r^2}\right)(r-R_0)^2 + (r-R_0)^4}\,\right],$$

$$\dot{\epsilon}_3 = \dot{\epsilon}_\theta = -A\frac{(r-R_0)^2 z}{r}. \tag{12}$$

Because analytic integration of (12) is complicated by the terms within the square root, numerical integration giving $f(R_1,R_0,h)$ is recommended, and

$$\frac{c}{\gamma H} = \frac{h^3 R_1(R_1-R_0)^2}{6Hf(R_1,R_0,h)}. \tag{13}$$

Other velocity fields for a frictionless material were recently considered in [16].

Partial Failure. Partial failure mechanism of an axisymmetric slope is probably more realistic than fully axisymmetric one. It also offers the possibility to derive the stability criterion for a material with internal friction. Accordingly, the mechanism similar to that for rectangular bin is assumed (Fig. 2(*b*)). The expression for $c/\gamma H$ at collapse is:

$$\frac{c}{\gamma H} = \frac{1}{H}\,\frac{(L_1-L_2)}{(M_1+M_3)}\,\frac{\cos(\beta+\phi)}{\cos\phi}, \tag{14}$$

where M_1, L_1, and s are given by (9) and

$$M_3 = (s+t)\frac{h}{\cos\beta} - \sqrt{1+\cot^2\beta}\left[R_1{}^2\cos^{-1}\left(\frac{1}{R_1}\sqrt{R_1{}^2-s^2}\right) - s\sqrt{R_1{}^2-s^2}\right], L_2 = \frac{1}{2}hR_1{}^2(\mu-\sin\mu)$$

$$+\frac{1}{3}\tan\beta\left[3R_1{}^3\frac{\mu}{2}\cos\frac{\mu}{2} - s(3R_1{}^2-s^2)\right],$$

$$\mu = 2\sin^{-1}\frac{s}{R_1}. \tag{15}$$

Criterion for piping

As a criterion for piping for a given bin, a relationship between the geometry of a stable channel and the material parameters is postulated. In the adopted kinematic approach the greatest ratio $c/\gamma H$, corresponding to a given width w or radius R_1 of the channel, defines the maximum height of the stable pipe. Because of complexity of some of the derived

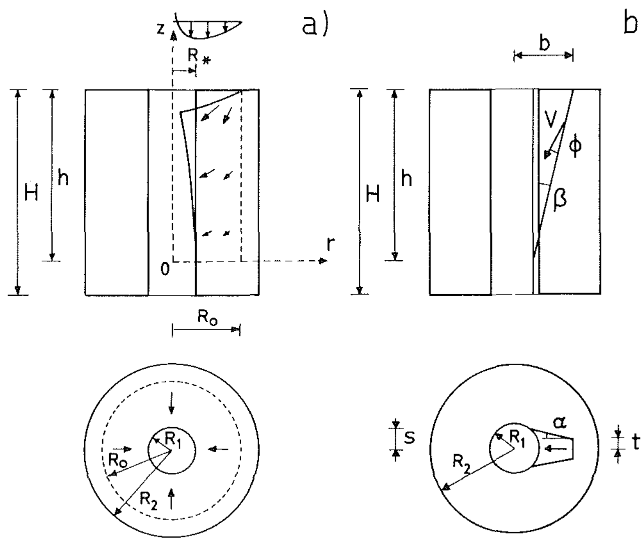

Fig. 2 Axisymmetric and partial failure in a circular bin

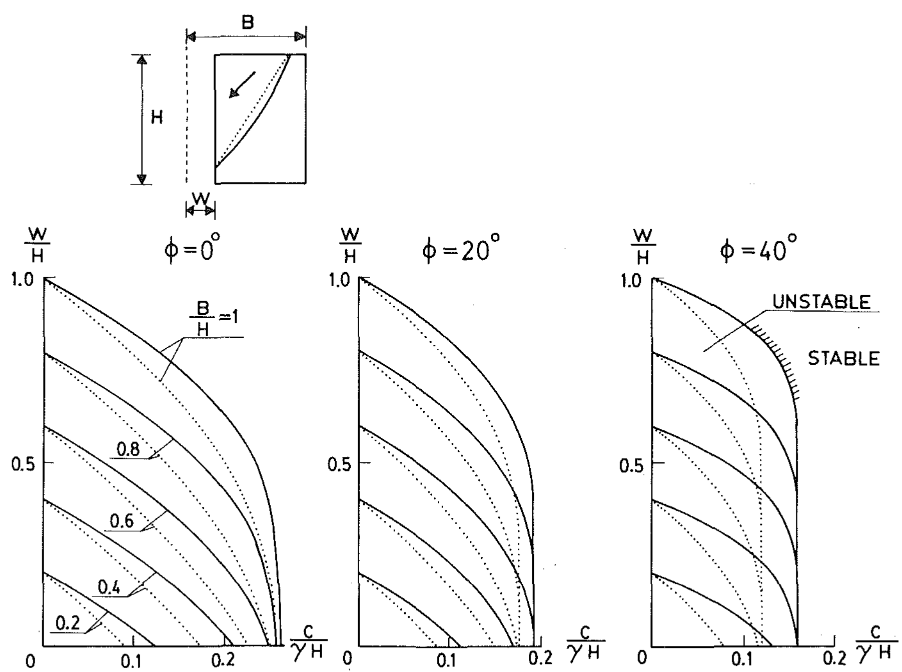

Fig. 3 Regions of stable and unstable empty channel in a plane bin

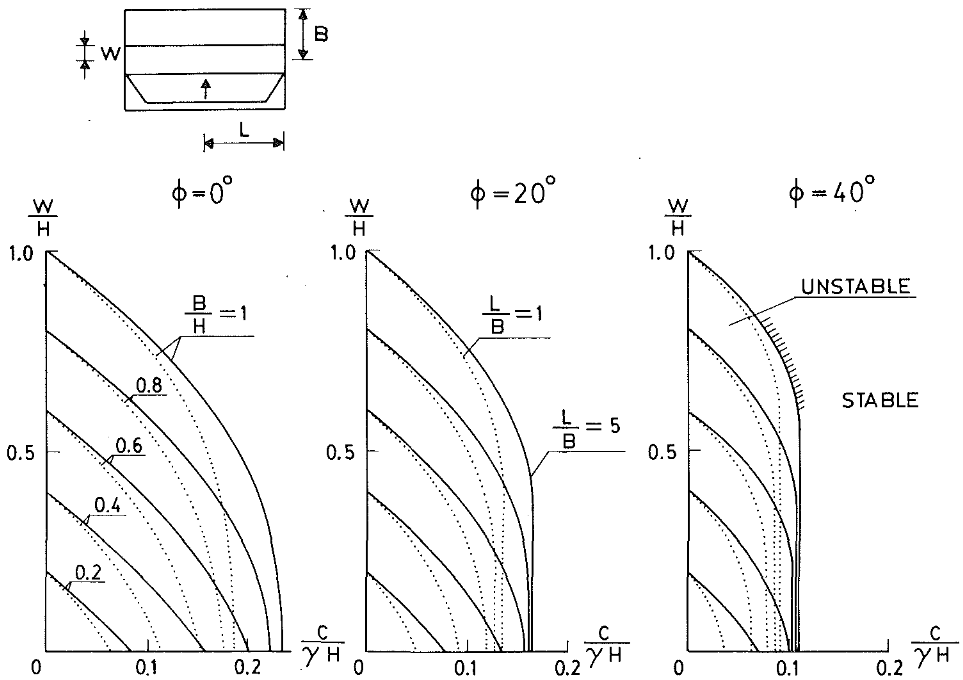

Fig. 4 Regions of stable and unstable empty channel in a rectangular bin

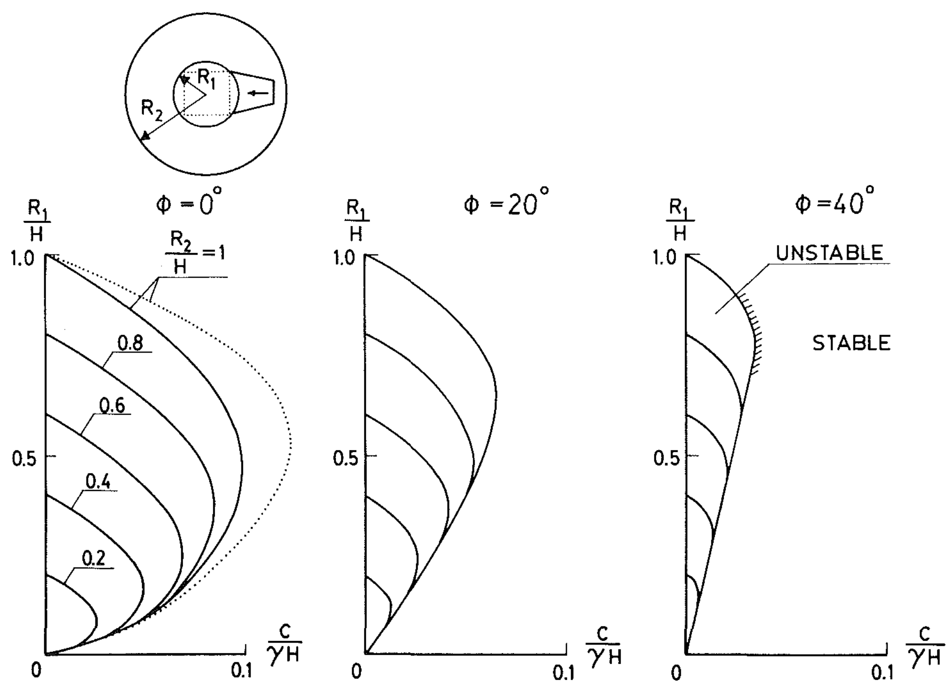

Fig. 5 Regions of stable and unstable empty channel in a cylindrical bin, partial failure

relations, the maxima of the ratio $c/\gamma H$ were found numerically, and the results presented graphically. In Fig. 3 the results for plane bin are shown. Solid lines correspond to the rotational mechanism, dotted lines to rigid sliding. The regions inside the lines define unstable channels; outside the lines the channel may not fail. Figure 4 applies to rectangular bins with outlet extending over the whole length. Two different ratios of the bin cross section L/B = 1,5 were selected. The results for cylindrical bin and partial failure mechanism are depicted in Fig. 5. The dotted line for $\phi=0$ pertains to the square bin with a square outlet inscribed within a circle of the radius R_1. Regions of stable and unstable channels for the axisymmetric failure are shown in Fig. 6. For comparison, the results for circular bin and partial failure are drawn as dotted lines.

Discussion

From the diagrams presented in the preceding section, the width or radius of a stable or unstable channel can be determined, if the material parameters c and ϕ, specific weight γ, and height H of the solid in the bin are known. Assuming that the dimension of the channel cannot be smaller than the dimension of the outlet, the geometry of the outlet

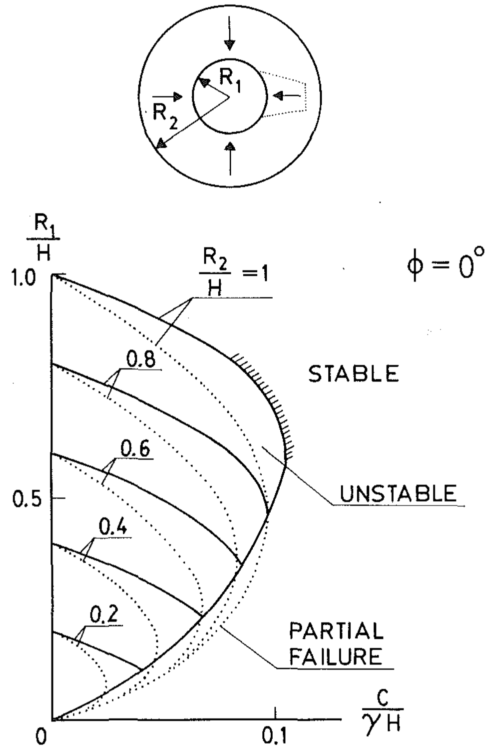

Fig. 6 Regions of stable and unstable empty channel in a cylindrical bin, axisymmetric failure

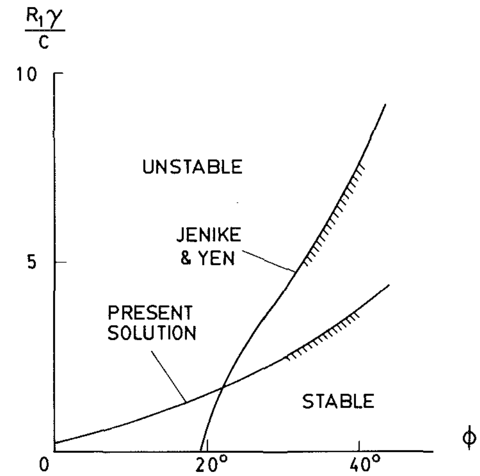

Fig. 7 Regions of stable and unstable empty channel in a tall cylindrical bin

preventing piping can be found. Generally, an increase of ϕ reduces the region of instability. In other words, internal friction increases risk of piping. However, the primary factor responsible for piping is the cohesion c; for $c=0$ piping cannot occur. In circular or square bins small outlets may lead to piping even for very small cohesion. For $\phi=0$ the difference between the axisymmetric and partial failure is small. In all cases, a critical ratio $c/\gamma H$ exists, above which a stable channel may form for any dimension of the outlet. This critical ratio is much higher for plane or rectangular bins (note the difference in the horizontal scale).

It should be remembered, however, that the kinematic approach adopted yields only a bound to the true criterion of piping. Other mechanisms of failure may lead to larger regions of instability. Within the framework of limit analysis any hypothetical mechanism may be suggested, provided its kinematical admissibility is satisfied. Nonetheless, the actual geometry of stable channels cannot be smaller than that resulting from the considered kinematic fields. Thus, the regions denoted in Figs. 3-5 give safe estimates of the geometry of unstable channels.

Although piping in bins is reported in the literature, and taken into account in the design of bins [1-4], the author has been unable to collect quantitative experimental data relevant for comparison with the theoretical solution. In experimental work on flow of particulate solids through bins and hoppers cohesionless materials are favored over cohesive ones.

Finally, it is interesting to compare the present solutions for cylindrical bins with the solution given by Jenike and Yen [5]. The latter applies to tall bins, where stresses do not vary with depth. The criterion for piping can be written as

$$\frac{R_1\gamma}{c} \leqq \frac{1}{2}F(\phi), \tag{16}$$

where $F(\phi)$ is given in [5] in a graphical form, and does not depend on H (see Fig. 9 in [5]). Assuming partial failure, R_2/H and R_1/H close to zero, the function $F(\phi)$ for the present approach was calculated. The results plotted in Fig. 7 indicate an essential discrepancy. The solution suggested in [5] is available for $\phi \geqq 19.5$ deg, whereas in the kinematic approach no limitation applies to ϕ. For higher values of ϕ the present solution gives much lower ratio $R_1\gamma/c$ for collapse, i.e., smaller outlets.

The reason for the discrepancy in the solutions may be explained as follows. The static solution presented in [5] would give a lower bound to the radius R_1 of the channel at collapse providing the solution be statically admissible. However, the boundary conditions at the bin walls are not included in the analysis – the slope is treated as infinitely extending – and static admissibility cannot be claimed.

Acknowledgment

The author is indebted to Dr. H. Haitjema for suggesting partial failure in cylindrical bins. The work reported in this paper has been partly supported by a grant from the University of Minnesota Graduate School.

References

1 Jenike, A. W., "Gravity Flow of Bulk Solids, "Bulletin No. 108, Utah Eng. Exp. St., Univ. of Utah, 1961.

2 Jenike, A. W., "Storage and Flow of Solids," Bulletin No. 123, Utah Eng. Exp. St., Univ. of Utah, 1976.

3 Johanson, J. R., "Effect of Initial Pressures on Flowability of Bins," ASME *Journal of Engineering for Industry*, Vol. 95, 1969, pp. 395-399.

4 Giunta, J. S., "Flow Patterns of Granular Materials in Flat-Bottom Bins," ASME *Journal of Engineering for Industry*, Vol. 95, 1969, pp. 406-413.

5 Jenike, A. W., and Yen, B. C., "Slope Stability in Axial Symmetry," *Proc. 5th Symp. Rock Mech.*, Univ. of Minnesota, 1962, pp. 689-710.

6 Sokolovski, V. V., *Statics of Soil Media*, Butterworths, London 1960.

7 Mroz, Z., and Drescher, A., "Limit Plasticity Approach to Some Cases of Flow of Bulk Solids," ASME *Journal of Engineering for Industry*, Vol. 95, 1969, pp. 357-364.

8 Hill, R., *The Mathematical Theory of Plasticity*, Clarendon Press, Oxford, 1956.

9 Drucker, D. C., and Prager, W., "Soil Mechanics and Plastic Analysis or Limit Design," *Quart. Appl. Math.*, Vol. 10, 1954, pp. 157-165.

10 Chen, W. F., "Soil Mechanics and Theorems of Limit Analysis," *J. Soil Mech. Found. Div. Proc. ASCE*, Vol. 95, 1969, pp. 493-518.

11 Chen, W. F., *Limit Analysis and Soil Plasticity*, Elsevier, Amsterdam, 1975.

12 Izbicki, R. J., and Mroz, Z., *Limit Analysis Methods in Rock and Soil Mechanics (in Polish), PWN*, Warsaw, 1976.

13 Jenike, A. W., and Shield, R. T., "On the Plastic Flow of Coulomb Solids Beyond Original Failure, ASME JOURNAL OF APPLIED MECHANICS, Vol. 27, 1959, pp. 599-602.

14 Radenkovic, D., *Theorie de Charge Limites, Extension a la Mechanique de Sols*, Ecole Polytechnique, Paris 1961.

15 Mroz, Z., *Nonassociated Flow Rules in Description of Plastic Flow of Granular Materials*, CISM Udine, 1974.

16 Britto, A. M., and Kusakabe, O., "Stability of Unsupported Axisymmetric Excavations in Soft Clay, *Geotechnique*, Vol. 32, 1982, pp. 261-270.

E. H. Lee
Life Fellow ASME

R. L. Mallett
Mem. ASME

Department of Mechanical Engineering and Aeronautical Engineering and Mechanics, Rensselaer Polytechnic Institute, Troy, N.Y. 12181

T. B. Wertheimer
MARC Analysis Research Corp., Palo Alto, Calif.

Stress Analysis for Anisotropic Hardening in Finite-Deformation Plasticity

Kinematic hardening represents the anisotropic component of strain hardening by a shift of the center of the yield surface in stress space. The current approach in stress analysis at finite deformation includes rotational effects by using the Jaumann derivatives of the shift and stress tensors. This procedure generates the unexpected result that oscillatory shear stress is predicted for monotonically increasing simple shear strain. A theory is proposed that calls for a modified Jaumann derivative based on the spin of specific material directions associated with the kinematic hardening. This eliminates the spurious oscillation. General anisotropic hardening is shown to require a similar approach.

1 Introduction

In an intriguing paper [1], Nagtegaal and de Jong evaluated the stresses generated by simple shear to large deformation in elastic-plastic and rigid-plastic materials that exhibit anisotropic hardening. In comformity with current practice for finite deformation in the case of kinematic hardening, they used an evolution equation for the back stress or shift tensor α (the current center of the yield surface) which relates the Jaumann derivative of α to the plastic strain rate. This incorporates aspects of finite deformation and ensures objectivity of the evolution equation under rigid-body rotations. For a material that strain hardens monotonically in tension, they obtained the unexpected result that the shear traction grows to a maximum value at a shear strain γ of the order unity and then oscillates with a period of about six as the strain increases.

Study of the analytical structure of the kinematic hardening law shows that, in the case of simple shear, the use of the conventional Jaumann derivative causes the shift tensor α to rotate continuously and this generates oscillations in the stress field. However, the back stress α is a residual stress generated by deformation of the heterogeneous structure of crystallites and hence is embedded in the material. Thus for simple shear, the total angular rotation of α must be limited since in simple shear, as pointed out in the following section, no lines of material elements ever rotate by more than π radians. A modified theory is presented which eliminates this anomaly and yields a monotonically increasing shear traction for the problem under discussion.

Contributed by the Applied Mechanics Division for presentation at the Winter Annual Meeting, Boston, Mass., November 13–18, 1983 of The American Society of Mechanical Engineers.

Discussion of this paper should be addressed to the Editorial Department, ASME, United Engineering Center, 345 East 47th Street, New York, N.Y. 10017, and will be accepted until two months after final publication of the paper itself in the Journal of Applied Mechanics. Manuscript received by ASME Applied Mechanic Division, January, 1982; final revision, December, 1982. Paper No. 83-WA/APM-5.

Copies will be available until July, 1984.

2 The Kinematics of Simple Shear

Using rectangular Cartesian coordinates for the configuration at time t, a simple shear in the x_1 direction is defined, as depicted in Fig. 1, with displacements

$$u_1 = ktx_2, \quad u_2 = u_3 = 0. \tag{1}$$

The corresponding velocity field is

$$v_1 = kx_2, \quad v_2 = v_3 = 0 \tag{2}$$

having the velocity gradient tensor $\mathbf{L}$ with symmetric part $\mathbf{D}$, the rate of deformation, and antisymmetric part $\mathbf{W}$, the spin.

$$\mathbf{L} = \frac{\partial v_i}{\partial x_j} = \begin{bmatrix} 0 & k & 0 \\ 0 & 0 & 0 \\ 0 & 0 & 0 \end{bmatrix},$$

$$\mathbf{D} = \begin{bmatrix} 0 & k/2 & 0 \\ k/2 & 0 & 0 \\ 0 & 0 & 0 \end{bmatrix}, \quad \mathbf{W} = \begin{bmatrix} 0 & k/2 & 0 \\ -k/2 & 0 & 0 \\ 0 & 0 & 0 \end{bmatrix} \tag{3}$$

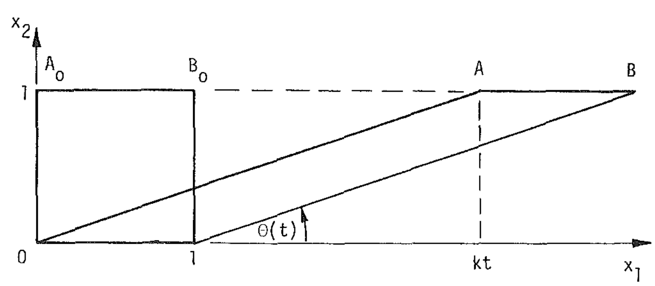

Fig. 1 Simple shear in the x_1 direction

The velocity field is thus steady with constant rate of shear strain $\dot{\gamma} = k$ and constant spin $\mathbf{W}$ with angular speed $k/2$.

Because the velocity field is linear in $\mathbf{x}$, straight material lines remain straight and, for example, the initially square figure illustrated in Fig. 1 is deformed into a sequence of parallelograms. The velocity gradient is uniform over the body so that the angular velocity of any line of particles in the (x_1, x_2) plane depends only on its current orientation angle θ (see Fig. 1) and is given by

$$\dot{\theta} = -k \sin^2\theta \tag{4}$$

It is evident that the line of particles initially on $0A_0$ in Fig. 1 approaches the x_1 axis as $t \to \infty$. Moreover, the largest total rotation of any line of particles is less than π, this bound corresponding to the initial inclination $\theta_0 = \pi - \epsilon$, $0 < \epsilon \to 0$.

Note that the anglular velocity of the material lines $\theta = \pi/4$ or $3\pi/4$, which coincide instantaneously with the principal directions of the deformation rate tensor $\mathbf{D}$, is $k/2$, equal to the spin as it should be. This is also the average of the angular velocities over all directions in the current configuration.

3 The Currently Adopted Kinematic-Hardening Analysis for Finite Strain

The back stress $\boldsymbol{\alpha}$, which prescribes the position of the center of the yield surface in stress space, provides the asymmetry in the yield function between continued and reversed loading needed to incorporate such phenomena as the Bauschinger effect.

For combined kinematic-isotropic hardening [2] with the isotropic-hardening stress measure satisfying a Mises type yield condition, the yield function takes the form

$$\begin{aligned}(s_{ij} - \alpha_{ij})(s_{ij} - \alpha_{ij}) &= (\mathbf{s} - \boldsymbol{\alpha}):(\mathbf{s} - \boldsymbol{\alpha}) \\ &= (\mathbf{s} - \boldsymbol{\alpha})\cdot(\mathbf{s} - \boldsymbol{\alpha}) = 2\sigma_0^2(\bar{\epsilon}^p)/3\end{aligned} \tag{5}$$

where $(\ ):(\ )$ denotes the trace of the matrix product and $(\ )\cdot(\ )$ the dot product in nine-dimensional stress space (it is helpful to keep in mind both of these representations). The matrix or vector $\mathbf{s}$ is the stress deviator and σ_0 is the tensile value of the isotropic part of the yield stress. The latter depends on the history of plastic deformation as expressed through the generalized plastic strain scalar $\bar{\epsilon}^p$ given by the growth law

$$\dot{\bar{\epsilon}}^p = \sqrt{2\mathbf{D}^p:\mathbf{D}^p/3} \tag{6}$$

where $\mathbf{D}^p$ is the plastic strain rate.

The growth of the anistropic part of the yield stress in kinematic hardening is given by the evolution equation for the internal variable $\boldsymbol{\alpha}$

$$\overset{\circ}{\boldsymbol{\alpha}} = \dot{\boldsymbol{\alpha}} - \mathbf{W}\boldsymbol{\alpha} + \boldsymbol{\alpha}\mathbf{W} = C(\bar{\epsilon}^p)\mathbf{D}^p \tag{7}$$

where, for finite-deformation applications, the Jaumann derivative $\overset{\circ}{\boldsymbol{\alpha}}$ is commonly chosen to replace the material derivative $\dot{\boldsymbol{\alpha}}$ used in infinitesimal displacement theory. This ensures that (7) is objective under superposed time-dependent rigid body rotations.

Large shear strains $\gamma = kt$ of the order 10 are considered so that elastic strains can be neglected and rigid-plastic theory adopted. Thus the plastic strain rate equals the total strain rate defined in (3)

$$\mathbf{D}^p = \mathbf{D}. \tag{8}$$

The normality condition associated with the yield function (5) determines the flow rule

$$\mathbf{D}^p \propto (\mathbf{s} - \boldsymbol{\alpha}). \tag{9}$$

Thus with $\mathbf{D}^p$ prescribed by (8) and (3), $\bar{\epsilon}^p(t)$ can be determined by integrating (6), and $\boldsymbol{\alpha}(t)$ by integrating (7) from the initial condition $\boldsymbol{\alpha}(0) = \mathbf{0}$. Equations (9) and (5) then determine $(\mathbf{s} - \boldsymbol{\alpha})$, so that $\mathbf{s}(t)$ can be evaluated.

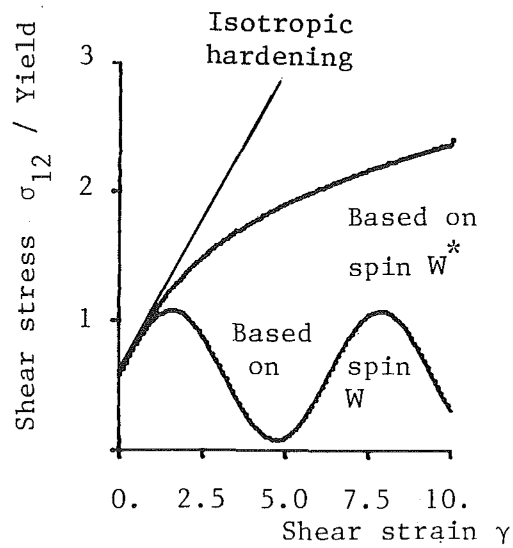

Fig. 2 Shear stress variation

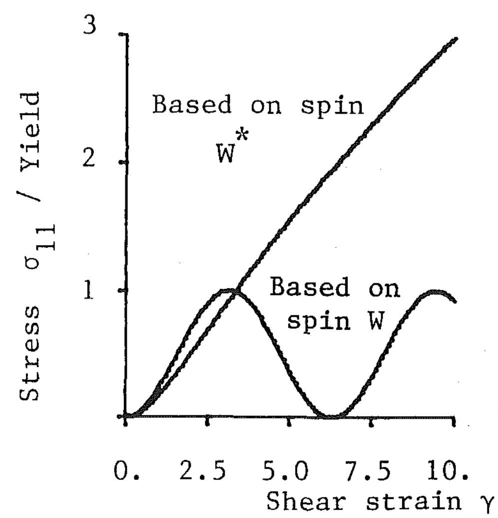

Fig. 3 Normal stress variation

Such an evaluation was presented in [1] and both it and the corresponding elastic-plastic solution resulted in oscillatory stresses. The rigid-plastic case corresponding to purely kinematic hardening (σ_0 constant) and linear hardening in tension (constant tangent modulus $3C/2$) can be evaluated analytically, as pointed out to us by Y. F. Dafalias, to give shear stress

$$\tau = s_{12} = \sigma_0/\sqrt{3} + (C \sin \gamma)/2, \ \gamma = kt \tag{10}$$

and the nonzero normal stress deviator components

$$s_{11} = -s_{22} = C(1 - \cos \gamma)/2. \tag{11}$$

For comparison with the results of a modified theory, these stress variations are shown by the oscillatory curves in Figs. 2 and 3, respectively. The oscillations arise since the spin terms in (7) generate a tensor $\boldsymbol{\alpha}$ which rotates with angular velocity $k/2$ and, because of (5) with constant σ_0, this causes the components of $\boldsymbol{\alpha}$ and hence of $\mathbf{s}$ to oscillate with angular frequency k, and thus with period 2π in $\gamma = kt$.

4 A Modified Constitutive Relation

Constitutive relations for anisotropic hardening were initially developed for infinitesimal displacement theory, so that, for example, the evolution law (7) for α was expressed in [2] as

$$\dot{\alpha} = C(\bar{\epsilon}^p)\mathbf{D}^p \tag{12}$$

where the superimposed dot denotes the material derivative with the time differentiation performed with respect to axes fixed in space. The term on the right-hand side of (12) expresses the influence on the growth of α of the plastic flow currently taking place. However, the effect of the rotation of α due to the deformation of the material in which the back stress is embedded also contributions to the change of α, but this component is neglected in infinitesimal displacement theory in which rotation terms are consistently neglected compared with strain terms. It was pointed out by Rice [3] that, when the tangent modulus is of the order of the stress, such an approximation is not justified, even at small strains, and this is often the case in elastic-plastic theory. Thus, for finite deformation, and possibly even for small deformation, the effect of the rotation of the back stress generated by previous plastic flow must be added to the contribution of the plastic flow currently taking place and thus to the right-hand side of (12).

It should perhaps be pointed out that more elaborate laws than (12) were developed with the same kinematic restriction of neglecting the change in α due to its rotation, and these can be written [1]

$$\dot{\alpha}_{ij} = L_{ijkl} D^p_{kl} \tag{13}$$

in terms of the shift operator $\mathbf{L}$ which could depend on $\mathbf{s}$, α, $\bar{\epsilon}^p$, and other internal variables determined by the history of deformation. These laws were devised to obtain better agreement with experimental measurements, particularly those involving unloading and reversed loading, but obviously made no contribution toward improving the neglect of the rotation influence. Since both laws (12) and (13) are incremental in form, relating increments or rates of α and strain, they could be applied at any instant during the deformation history since the required rate variables already occur there.

As mentioned in the Introduction, the back stress α is embedded in the material as residual stresses generated due to the heterogeneous structure of anisotropic crystallites forming the polycrystalline material. Alternatively this influene can be thought of in terms of dislocations piled up against grain boundaries, or other analogous micromechanisms, the mobility of which depends on the strain rate tensor imposed, both with regard to the asymmetry between continued and reversed straining and to the direction of straining in the material. A study of the micromechanics of the situation, either at the crystallite level, the dislocation level, or at both, may be needed to fully understand this question, but such seems not now to be available. However, information can be gleaned from the macroscopic theory. In particular, the principal component of α having the largest absolute magnitude produces the major influence on the yield surface and hence on the stress field and is carried in the lines of material elements oriented in the corresponding eigenvector direction. Thus rotation of these lines of material elements may be considered to incorporate the major rotational influence of the back stress generated by previous plastic flow.

In the case of simple shear, the principal component α_{33} is zero and since α is a deviator tensor, the other two are equal in magnitude and opposite in sign. Thus the choice of the eigenvalue of largest absolute magnitude is not unique and one must therefore look further into the evolution of α. In the case of kinematic hardening according to (7) or (12), α initially grows parallel to $\mathbf{D}^p$ with the tensile eigenvector at $\theta = \pi/4$ and the compressive one at $\theta = 3\pi/4$. Increments parallel to $\mathbf{D}^p$ are being continually added and for the tensile direction the line of elements that carries the back stress rotates toward the x_1 axis with angular velocity $k/2$ initially and thereafter with ever decreasing speed as is evident from (4). In contrast, material lines instantaneously coincident with the compressive eigenvector initially rotate with increasing angular velocity as they approach the x_2 axis. The increasingly larger angle that the rotated eigenvector makes with the corresponding tensor increments continuously being added (due to the $C\mathbf{D}^p$ term) inhibits the growth of the compressive eigenvector compared with the tensile one. For example, in simple tension or compression the increments sum in fixed directions and generate the maximum kinematic hardening component (see Hill [6], p. 39 for comparison of tension and compression, with shear).

Such considerations suggest that, in the case of simple shear, the rotation of lines of material elements along the tensile eigenvector of α play the major role in determining the influence on the evolution equation for α of the back stress caused by previous plastic flow.

Rotation terms must thus be added to (12) yielding

$$\dot{\alpha} = C(\bar{\epsilon}^p)\mathbf{D}^p + \mathbf{W}^*\alpha - \alpha\mathbf{W}^* \tag{14}$$

where the spin $\mathbf{W}^*$ of the line of material elements considered to carry the back stress is given by the angular velocity (4).

Comparing this with (7), the currently accepted evolution equation for kinematic hardening at finite deformation, shows that (7) is equivalent to assuming that the back stress already generated contributes to $\dot{\alpha}$ according to rotation with constant angular speed $k/2$ (even though it is embedded in material no directed elements of which ever rotate by more than π radians). The nature of the connection between the elements in an elastic-plastic continuum and thus the stresses needed to generate such unlimited rotation of the embedded stress clearly rule out the validity of (7) for ductile metals.

The structure of (14) suggests a modified interpretation by writing it in the form

$$\overset{*}{\alpha} = \dot{\alpha} - \mathbf{W}^*\alpha + \alpha\mathbf{W}^* = C(\bar{\epsilon}^p)\ \mathbf{D}^p \tag{15}$$

where $\overset{*}{\alpha}$ defines a modified Jaumann derivative associated with the spin $\mathbf{W}^*$ of lines of material elements carrying the major influence of the back stress α. It is shown in the Appendix that $\overset{*}{\alpha}$ is objective. In fact it is shown that for a spin $\mathbf{\Omega}(t)$ the modified Jaumann derivative

$$\overset{\Omega}{\alpha} = \dot{\alpha} - \mathbf{\Omega}\alpha + \alpha\mathbf{\Omega} \tag{16}$$

is objective if, under time-dependent rigid body rotation expressed by the rotation matrix $\mathbf{Q}(t)$, $\mathbf{\Omega}$ transforms as

$$\mathbf{\Omega} \rightarrow \dot{\mathbf{Q}}\mathbf{Q}^{-1} + \mathbf{Q}\mathbf{\Omega}\mathbf{Q}^T \tag{17}$$

This expresses a simple geometrical requirement, namely that the time-dependent rotation $\mathbf{Q}(t)$ superimposed on the spin $\mathbf{\Omega}(t)$ adds the current superimposed spin tensor $\dot{\mathbf{Q}}\mathbf{Q}^{-1}$ to the spin $\mathbf{\Omega}$ transformed by the rotation that has taken place. This applies in the case where $\mathbf{\Omega}$ is the spin of lines of material elements in a deforming body. These matters are discussed in more detail in Section 7.

5 Comparison of Solutions

Equation (14) was integrated numerically with the initial condition $\alpha(0) = \mathbf{0}$ and the result was substituted into (5) and (9) to give the stress variations shown in Figs. 2 and 3 for the shear and normal stresses σ_{12} and $\sigma_{11} = -\sigma_{22}$. Purely kinematic hardening was assumed with an initial yield stress $Y = 207$ MPa (30 ksi) and linear tensile hardening with modulus 310 MPa (45 ksi). These values are appropriate to model an aluminum alloy. The rigid-plastic analysis used implies an incompressible medium and thus stresses are determined only to within an arbitrary hydrostatic pressure since it causes no deformation. This pressure was taken to be zero so that the stresses plotted are stress deviators. Figure 2 also includes the stress-strain relation in shear for isotropic hardening corresponding to the same tensile behavior. No normal stresses are generated in this case.

It is seen that all the stress-strain curves have a common tangent at zero strain. The two kinematic hardening solutions remain close to each other for strains up to about 0.5 but at larger strains the stresses predicted on the basis of the conventional Jaumann derivative oscillate while the approach suggested in this paper yields a monotonically increasing shear stress-strain curve, with a tangent modulus that decreases as the strain increases.

The stress fields of the conventional approach and the suggested new one agree for small strains because the eigenvectors of $\mathbf{D}^p$ and α initially coincide so that $\mathbf{W} = \mathbf{W}^*$ as mentioned in Section 2. With increasing strain, the tensile eigenvector of the new solution approaches an asymptote at $\theta \sim 15$ deg. Thus the tensile strain rate in simple shear becomes inclined at some 30 deg to the direction in which the maximum tensile yield stress has been generated by induced anisotropy. This angle has been increasing and is consistent with the lessening of the tangent modulus. Such softening has been termed a rotational Bauschinger effect by Jonas [4]. The oscillations predicted by the solution based on the conventional Jaumann derivative are clearly due to the inappropriate use of the spin $\mathbf{W}$ to express the influence of the back stress already generated (as discussed in the preceding section).

Both [1] and the present paper analyzed purely kinematic hardening without a component of isotropic hardening in order to focus on the effects of anisotropy, although results based on isotropic hardening were presented for comparison. This led to a rather drastic difference in the stress variations given by the two approaches to the kinematic hardening case. A physically more appropriate representation for many materials would be isotropic hardening initially, later accompanied by the growth of a kinematic component. When the conventional Jaumann derivative is used this would introduce an oscillatory component superimposed on a smooth monotonically increasing curve, so that initially a minor ripple with period 2π would appear, insufficient to produce a zero tangent modulus. This could thus be observed without an instability developing.

Recently torsion tests have been carried out to a shear strain of 7 on six different ductile metals (copper, brass, nickel, steel, and two types of iron) [5]. Tests were carried out for a range of strain rates and the strain-rate influence was not so marked as to rule out adequate analysis on the basis of rate-independent theory. In the low strain-rate isothermal range, monotonically increasing stress-strain curves were obtained except for an initial upper yield in the steel and one iron. No indication of a ripple or superimposed oscillation was evident. These results support the concept presented in this paper that the continued rotation of α predicted by the use of the conventional Jaumann derivative has no physical validity.

6 Elastic-Plastic Stress Analysis

Finite-element elastic-plastic computer programs are available for kinematic hardening and have been considered applicable for stress and deformation analysis at finite deformation since they use the (conventional) Jaumann derivative of stress to account for rotational effects. They were shown in [1] to predict stress oscillations in simple shear. In view of the rigid-plastic solutions discussed in the preceding section, use of the modified Jaumann derivative as in the evolution equation (15) can be expected to eliminate the spurious oscillations and provide a satisfactory analysis. Thus the computer codes now in use can be corrected simply by changing the time derivative adopted.

Such a time derivative occurs not only in the evolution equation (15) but also in the plastic flow law where it operates on the stress deviator $\mathbf{s}$ and, for kinematic hardening, takes the form

$$\mathbf{D}^p = \frac{3}{2h\sigma_0^2}\,(\mathbf{s}-\alpha)[(\mathbf{s}-\alpha):\overset{*}{\mathbf{s}}] \tag{18}$$

where h is a strain hardening modulus (see [2] for the infinitesimal displacement version). Summation of the elastic and plastic strain rates to give total strain rate yields

$$\mathbf{D} = \mathbf{D}^e + \mathbf{D}^p. \tag{19}$$

Since for elastic-plastic analysis (19) replaces (8), $\mathbf{D}^p$ is not prescribed by the kinematics so that $(s-\alpha)$ cannot be determined by (9) and (5) but instead must be determined by simultaneous integration of the evolution equation (7) or (15) and the flow law (18).

A modified version of the MARC program was used for such an elastic-plastic analysis and the results fell within 1 percent of the rigid-plastic solutions shown in Figs. 2 and 3. Since the elastic-plastic model does not represent an incompressible material, the stress (not just the deviator) was evaluated. Because the velocity boundary conditions involve no volume change and the flow law (18) prescribes incompressible plastic deformation, the elastic deformation should also be incompressible and hence the stress deviatoric. With σ_{33} zero, σ_{11} and σ_{22} were found to be opposite in sign and equal in magnitude to within 0.1 percent. The close agreement of the finite-element solution may seem surprising in view of the severe element distortion at shear strains $\gamma = 10$. However, it must be borne in mind that the velocity variation is linear which can be modeled exactly by the finite elements even when distorted.

In an earlier report [7] on this topic a Jaumann-type derivative of stress based on the spin of the eigenvector triad of α was used in the flow law. Since only the part of the spin of α associated with material rotation needs to be eliminated from the stress-rate loading term, the Jaumann derivative $\overset{*}{\mathbf{s}}$ should have been adopted. Rotation of the anisotropic yield surface about the stress origin can be generated by plastic flow and this component must be associated with nonzero stress rate. This change in the analysis is very significant since only one rate definition now appears in the elastic-plastic theory which greatly simplifies numerical implementation.

7 General Theory

Consideration so far has been focused on simple shearing because of the unexpected oscillating shear stress results presented in [1]. However, the concepts involved can be generalized and applied to more complex problems. One can expect problems similar to those encountered in simple shearing to arise often in view of the frequent onset of shear localization or banding associated with plastic deformation which will involve a similar deformation-rotation coupling.

A complete investigation of the micromechanics and the structures of possible macroscopic constitutive relations will no doubt be needed to fully understand this phenomenon and to generate a fully tested theory. However, the approach suggested in Section 4 does appear to embody the main essence of the phenomenon and can be generalized to three-dimensional problems.

For simple shear, the deformation (2) occurs in the (x_1, x_2) shearing plane so that the material elements carrying the back stress α must rotate about the axis x_3 normal to the plane. Thus only a direction in the plane is needed to determine the associated spin. In three dimensions a component of spin around such a direction may also be needed. Since the main back-stress influence is embedded in the plane defined by the eigenvectors of α associated with the maximum and minimum eigenvalues, it is suggested that the spin $\mathbf{W}^*$ should be determined by the angular velocity of the material-element line instantaneously coincident with the eigenvector of α corresponding to the eigenvalue with maximum absolute value, with a spin component around this vector determined by rotation of the plane containing the material elements instantaneously coincident with both eigenvectors.

The general theory of constitutive relations of the type considered here was developed by Onat and Fardshisheh [8] who showed that for objectivity of a relation between σ, $\mathbf{D}$, and $\mathbf{W}$ involving a tensor state variable α in addition to scalar state variables (which for simplicity will not be specifically indicated in the following representation) it must take the form

$$\dot{\sigma} = \mathbf{g}(\sigma,\alpha,\mathbf{D}) + \mathbf{W}\sigma - \sigma\mathbf{W} \tag{20}$$

$$\dot{\alpha} = \mathbf{h}(\sigma,\alpha,\mathbf{D}) + \mathbf{W}\alpha - \alpha\mathbf{W} \tag{21}$$

where the functions $\mathbf{g}$ and $\mathbf{h}$ are isotropic tensor functions. It is common to combine the spin terms with the material-rate terms to obtain

$$\mathring{\sigma} = \dot{\sigma} - \mathbf{W}\sigma + \sigma\mathbf{W} = \mathbf{g}(\sigma,\alpha,\mathbf{D}) \tag{22}$$

$$\mathring{\alpha} = \dot{\alpha} - \mathbf{W}\alpha + \alpha\mathbf{W} = \mathbf{h}(\sigma,\alpha,\mathbf{D}) \tag{23}$$

The conventional Jaumann derivative thus appears on the left-hand side of each equation. Since large strains are of interest, rigid-plastic theory will be considered to simplify the discussion and thus $\mathbf{D} = \mathbf{D}^p$.

Discussion will be focused on the evolution equation (15) with the understanding that similar consideration apply to the flow law (18). It was pointed out in Section 4 that equation (15) is objective and so it must be expressible in the form (21). This can be independently established by expressing $\mathbf{W}^*$ in terms of $\mathbf{W}$ and $\mathbf{D}$.

Consider an arbitrary unit vector $\mathbf{n}$ and a linear segment of material elements $\mathbf{n}$ ds. The relative velocity between the ends of $\mathbf{n}$ ds is

$$(\partial v_i/\partial x_j)dx_j = \mathbf{L}\mathbf{n}\ ds \tag{24}$$

The component normal to $\mathbf{n}$ determines the spin $\mathbf{W}^*$of that segment to within an arbitrary spin about the segment. Making use of $\mathbf{L} = \mathbf{D} + \mathbf{W}$ and cancelling ds throughout gives

$$(\mathbf{D}+\mathbf{W})\mathbf{n} - [\mathbf{n}^T(\mathbf{D}+\mathbf{W})\mathbf{n}]\mathbf{n} = \mathbf{W}^*\mathbf{n} \tag{25}$$

The $\mathbf{W}$ term in the brackets reduces to zero because $\mathbf{W}$ is antisymmetric and introduction of $\mathbf{n}^T\mathbf{n} = 1$ and factoring gives

$$(\mathbf{W} + \mathbf{D}\mathbf{n}\mathbf{n}^T - \mathbf{n}\mathbf{n}^T\mathbf{D})\mathbf{n} = \mathbf{W}^*\mathbf{n}$$

so that a solution of (25) is the antisymmetric matrix

$$\mathbf{W}^* = \mathbf{W} + \mathbf{D}\mathbf{n}\mathbf{n}^T - \mathbf{n}\mathbf{n}^T\mathbf{D} \tag{26}$$

and (14) has the form (21). $\mathbf{W}^*$ can readily be shown to involve no spin around $\mathbf{n}$ introduced by the terms involving $\mathbf{D}$.

For simple shearing, $\mathbf{W}^*$ is determined by the spin of a line of material elements instantaneously coincident with an eigenvector of α and (26) gives this rotation about the n_{33} axis. For general deformation it was suggested in the foregoing that $\mathbf{W}^*$ be defined by the spin of material elements lying along one eigenvector direction, the spin around it being determined by the rotation of the plane determined by material elements along another eigenvector. Since the spins of both material lines are of the form (26) it is clear that the resulting spin will have the form $\mathbf{W}$ plus a function of $\mathbf{D}$ and hence will lead to a relation of the form (21).

For simple shearing, equation (14) was integrated in the rigid-plastic case and (14) and (18) in the elastic-plastic case using $\mathbf{W}^*$ from (4) and this permitted accurate numerical integration because the total rotation of α was less than $\pi/4$. Combining all the terms involving $\mathbf{D}$ together as in (20) and (21) separates out self-cancelling, oscillating terms that must then combine to yield a monotonic function. This may lead to increasing the inaccuracy in carrying out numerical integration. However in more complicated problems where a simple relation such as (4) does not exist for $\mathbf{W}^*$, it may be important to separate out the $\mathbf{W}$ and $\mathbf{D}$ variables. Certainly for formulating the structure of the physical theory the *resultant* rotational effect of the back stress already generated, which is dependent on $\mathbf{W}^*$, is a significant and pregnant concept.

As pointed out in Section 4, generalizations of the simple kinematic hardening law attempt to improve the operator $\mathbf{L}$ in (13) but do not address the effect of finite rotation of the α generated by previous plastic flow in contributing to $\dot{\alpha}$. It would thus be a forlorn hope that the more complicated models would remove the oscillating stress anomaly associated with use of $\mathbf{W}$ in place of $\mathbf{W}^*$ in the evolution equation for $\dot{\alpha}$ corresponding to (14). However, reference [1] deduces that the Mróz multisurface model and one involving an additional tensor variable do just that. Study of the laws and methods of evaluation used in [1] reveals that this conclusion arises from shortcomings of the laws selected or the method of evaluation.

The general evolution law used in [1] is

$$\mathring{\alpha} = \mathbf{p}\ (\mathbf{m}:\mathbf{D}^p) \tag{27}$$

where $\mathbf{m} \propto (\mathbf{s} - \alpha)$, and $\mathbf{p}$ is a tensor that takes on different forms for the three laws studied. In the case of simple shearing, (27) reduces to

$$\dot{\alpha}_{11} = (p_{11}/\sqrt{3} + \alpha_{12})k \tag{28}$$

$$\dot{\alpha}_{22} = (p_{22}/\sqrt{3} - \alpha_{12})k \tag{29}$$

$$\dot{\alpha}_{12} = [p_{12}/\sqrt{3} + (\alpha_{22} - \alpha_{11})/2]k \tag{30}$$

The spin terms that generate the rotation of α and hence the oscillating stress are the α_{12} terms in (28) and (29). In simple shear the Bauschinger effect will certainly be most significant for reversed loading in shear, hence α_{12} will be a dominant component. Thus, in conformity with the physical theory developed in Section 4, one would expect oscillatory stress for all the laws since $\mathbf{p}$ expresses the infinitesimal strain model and is not influenced by the rotation.

Study of the individual cases indicates why the anomaly was limited to the kinematic hardening model. The Mróz multisurface model, for example, was solved for the limit of an infinite number of closely adjacent surfaces for which the shift rate of each surface in stress space was proportional to α instead of a linear combination of α and $(\mathbf{s} - \alpha)$ away from that limit. Thus the shift rate direction was independent of stress or $\mathbf{D}^p$, a most unlikely circumstance. Moreover, the α generated as each surface was activated was not accumulated, so that finally the isotropic hardening solution was reproduced – hardly compatible with the anisotropic hardening envisaged. These results therefore do not invalidate the physical concepts on which the theory developed in Section 4 was built nor the error introduced by use of the conventional Jaumann derivative in (15) and (18).

8 Discussion and Conclusions

The modified Jaumann derivative (*), equation (15), has some similarity to the Jaumann-type derivative (ˆ) introduced by Dienes [10] which involves spin associated with the rotation determined by the polar decomposition theorem for the total deformation from the undisturbed configuration. The latter is thus appropriate in formulating the constitutive equation of a material for which the stress depends on the total deformation, for example elasticity when it is expressed in differentiated hypoelastic form. The claim that (ˆ) is also appropriate for plasticity is incorrect however since plasticity obeys an incremental or flow-type functional law, closer to a fluid than a solid type, in which the specific configuration of the initial undeformed state does not appear in the incremental or flow type constitutive relation at later times. Deformation-type plasticity theory, in which the stress is determined by the total plastic strain, lends itself to simplification through use of the polar decomposition theorem but, except in the case of proportional loading, it is known to be inappropriate to represent plasticity, particularly at large strains.

Study of the physical situation described in Section 4 shows that the influence of the anisotropy generated by previous plastic flow on the growth of the back stress α arises from a spin associated with directions embedded in the body in which the residual back stress is also embedded. This spin also determines the appropriate Jaumann-type derivative of stress in the flow law that must eliminate the contribution to the material derivative of stress which is not associated with the current plastic flowing. The physical model presented considers the influence of the dominant principal component of α but an analogous spin and functional law will arise in the more complete analysis, based on the polycrystalline structure, of the generation and influence of the deformation induced residual back stress.

For the polar decomposition of the deformation gradient $\mathbf{F} = \mathbf{RU} = \mathbf{VR}$, the spin of directions embedded in the body depends not only on $\dot{\mathbf{R}}\mathbf{R}^{-1}$ but also on $\mathbf{U}$ or $\mathbf{V}$ and their derivatives. For example, in a plane problem of a constant stretch λ in a time-dependent direction $\theta(t)$, $\mathbf{F}=\mathbf{U}=\mathbf{V}$, $\mathbf{R}=\mathbf{I}$, the spin $\dot{\mathbf{R}}\mathbf{R}^{-1}$ is zero, the principal directions of deformation rotate with angular velocity $\dot{\theta}$, and the lines of material elements coincident with the stretch direction rotate with angular velocity $\dot{\theta}(1-1/\lambda)$. Thus $(\hat{\ })$ based on the spin $\dot{\mathbf{R}}\mathbf{R}^{-1}$ could clearly not express the needed rotational influence of the back stress in this case and hence in general. In the case of principal directions fixed in the body, $\mathbf{U}$ can be diagonalized in the form, $\mathbf{U}=\mathbf{P}\Lambda(t)\mathbf{P}^{-1}$, where the matrix of eigenvectors $\mathbf{P}$ is constant, so that the velocity gradient $\mathbf{L}$ becomes

$$\begin{aligned}\mathbf{L}=\mathbf{D}+\mathbf{W}=\dot{\mathbf{F}}\mathbf{F}^{-1} &= \dot{\mathbf{R}}\mathbf{R}^{-1}+\mathbf{R}\dot{\mathbf{U}}\mathbf{U}^{-1}\mathbf{R}^{-1}\\ &= \dot{\mathbf{R}}\mathbf{R}^{-1}+\mathbf{R}\mathbf{P}\dot{\Lambda}\Lambda^{-1}\mathbf{P}^{-1}\mathbf{R}^{-1}. \quad (31)\end{aligned}$$

Since $\mathbf{P}$ and $\mathbf{R}$ are othogonal and the diagonal matrix product is commutative the last term in (31) is symmetric and hence $\dot{\mathbf{R}}\mathbf{R}^{-1} = \mathbf{W}$ which also equals $\mathbf{W}^*$. Only in such a special situation will the modified Jaumann derivative $(\hat{\ })$ be appropriate for finite-deformation plasticity analysis.

Both the Jaumann-type derivatives (*) and $(\hat{\ })$ as well as the conventional Jaumann derivative fall in the category ($A3$) discussed in the Appendix. Whereas $\mathbf{W}$ in the conventional Jaumann derivative expresses the average angular velocity of all directions around a point and so is an appropriate spin term in the constitutive equation for an isotropic body, for an anisotropic material certain directions will have a special influence and the range of objective derivatives ($A3$) permits this generality to be incorporated. The particular selection will depend on the physical mechanisms involved as already discussed. In the case of plasticity with isotropic hardening, the stress rate term devolves from the derivative of a stress invariant which is independent of rotation, so that the same contribution will result whichever Jaumann-type derivative is selected.

Quite apart from physical appropriateness, it is fortunate that in plasticity analysis it is not necessary to use variables involving the virgin configuration of the material prior to any plastic flow, since many bodies plastically formed in engineering practice have previously been subjected to plastic flow when they were manufactured, for example, forming rolled sheet or extruded rods. The approach presented here for kinematic hardening exhibits the property necessary for application, that measurement of the yield surface (assumed in this case to be consistent with combined isotropic-kinematic hardening) supplies the information needed to formulate the constitutive relation for the analysis of subsequent deformation. The shift tensor α and the isotropic component of the tensile yield stress σ_0 comprise all that is needed concerning the previous history of plastic deformation.

We have suggested a generally applicable formulation of kinematic hardening theory and have chosen a simple hypothesis for the macroscopic influence of the micromechanisms that generate the hardening. Clearly a thorough study of this aspect of the theory is called for. This may require an analysis of the micromechanics of polycrystalline material involving investigation of the interaction between deforming crystallites, combined with a more general study of the formulation and generalization of macroscopic constitutive relations.

Finite-element computer codes which incorporate kinematic hardening and are considered valid for finite strain are in active current use. In view of the research findings presented here they can involve huge errors. There is thus an urgent need to clarify this question and to generate and demonstrate a reliable means of stress and deformation evaluation in this field of considerable technological importance. To date most forming analyses have been based on isotropic hardening theory, but it is known that the Bauschinger effect, which is exhibited by many structural metals, can have an important influence on such technologically important phenomena as the generation of residual stresses due to forming. This will increase the demand for reliable analysis to incorporate anisotropic hardening into computer codes and hence to complete the research task introduced in this paper.

Acknowledgment

The results presented in this paper were obtained in the course of research sponsored by the U.S. Army Research Office under Contract No. DAAG 29-82-K-0016 with Rensselaer Polytechnic Institute and with support from MARC Analysis Research Corporation. The authors gratefully acknowledge these contributions.

We wish to thank Dr. J. C. Nagtegaal of MARC Analysis Research Corporation and Professors R. M. McMeeking and R. T. Shield of the University of Illinois for helpful comments while this work was being formulated. We would also like to acknowledge the usefulness of our reviewers comments, which led to a substantial revision of our exposition.

References

1 Nagtegaal, J. C., and de Jong, J. E., "Some Aspects of Nonisotropic Work Hardening in Finite Strain Plasticity," *Plasticity of Metals at Finite Strain: Theory, Experiment and Computation*, Lee, E. H., and Mallett, R. L., eds., Div. Appl. Mech., Stanford U. and Dept. Mech. Eng., R.P.I., 1982, pp. 65–102.

2 Mróz, Z., Shrivastava, H. P., and Dubey, R. N., "A Nonlinear Hardening Model and its Application to Cyclic Loading," *Acta Mech.*, Vol. 25, 1976, pp. 51–61.

3 Rice, J. R., "A Note on the 'Small Strain' Formulation for Elastic-Plastic Problems," Tech. Rep. N00014-67-A-000318, Div. of Eng., Brown Univ., Providence, R. I., 1970.

4 Jonas, J. J., *Plasticity of Metals at Finite Strain: Theory, Experiment and Computation*, Lee, E. H., and Mallett, R. L., eds., Div. Appl. Mech., Stanford and Dept. Mech. Eng., R.P.I., 1982, pp. 727–734.

5 Johnson, G. R., Hoegfeldt, J. M., Lindholm, U. S., and Nagy, A., "Response of Various Metals to Large Torsional Strains Over a Large Range of Strain Rates," ASME *Journal of Engineering Materials and Technology*, Vol. 105, 1983, pp. 42–47.

6 Hill, R., *The Mathematical Theory of Platicity*, Oxford University Press, 1950.

7 Lee, E. H., Mallett, R. L., and Wertheimer, T. B., "Stress Analysis for Kinematic Hardening in Finite-Deformation Platicity," SUDAM 81-11, Sanford University, 1981.

8 Onat, E. T., and Fardshisheh, F., *Proc. Symp. on Foundations of Plasticity*, Warsaw, Noordhoff, 1973, pp. 89–115.

9 Malvern, L. E., *Introduction to the Mechanics of a Continuous Medium*, Prentice-Hall, Englewood Cliffs, N.J., 1969.

10 Dienes, J. K., "On the Analysis of Rotation and Stress Rate in Deforming Bodies, *Acta Mech.*, Vol. 32, 1979, pp. 217–232.

APPENDIX

Objectivity

Since the modification of the conventional Jaumann derivative is proposed in this paper, it is perhaps worthwhile to write down explicitly the justification for the objectivity of the analysis. This involves investigating the superposition on the deformed body of a time-dependent rigid-body rotation expressed by the proper orthogonal matrix $\mathbf{Q}(t)$ so that the material point coordinates are transformed as $\mathbf{x} \rightarrow \mathbf{Q}\,\mathbf{x}$ and (see for example [9])

$$\mathbf{D} \rightarrow \mathbf{Q}\,\mathbf{D}\,\mathbf{Q}^T, \quad \mathbf{W} \rightarrow \dot{\mathbf{Q}}\,\mathbf{Q}^{-1} + \mathbf{Q}\,\mathbf{W}\,\mathbf{Q}^T \tag{A1}$$

The latter transformation expresses the geometrical interpretation of adding the spin $\dot{\mathbf{Q}}\,\mathbf{Q}^{-1}$ associated with $\mathbf{Q}(t)$ to the original spin $\mathbf{W}$ transformed by the superposed rotation at that time, $\mathbf{Q}(t)$. Such a transformation clearly applies to the spin of any constituent of the motion not associated with a specific coordinate choice such as a line of material points or the eigenvector triad of $\boldsymbol{\alpha}$ or $\boldsymbol{\sigma}$.

For a spin $\boldsymbol{\Omega}$ satisfying the transformation

$$\boldsymbol{\Omega} \rightarrow \dot{\mathbf{Q}}\,\mathbf{Q}^{-1} + \mathbf{Q}\,\boldsymbol{\Omega}\,\mathbf{Q}^T \tag{A2}$$

the associated Jaumann-type derivative of $\boldsymbol{\alpha}$ is

$$\overset{\Omega}{\boldsymbol{\alpha}} = \dot{\boldsymbol{\alpha}} - \boldsymbol{\Omega}\boldsymbol{\alpha} + \boldsymbol{\alpha}\boldsymbol{\Omega} \tag{A3}$$

where $\boldsymbol{\alpha} \rightarrow \mathbf{Q}\,\boldsymbol{\alpha}\,\mathbf{Q}^T$. The derivative $\overset{\Omega}{\boldsymbol{\alpha}}$ transforms as

$$\begin{aligned}\dot{\boldsymbol{\alpha}} - \boldsymbol{\Omega}\boldsymbol{\alpha} + \boldsymbol{\alpha}\boldsymbol{\Omega} \rightarrow\; & \dot{\mathbf{Q}}\boldsymbol{\alpha}\mathbf{Q}^T + \mathbf{Q}\dot{\boldsymbol{\alpha}}\mathbf{Q}^T + \mathbf{Q}\boldsymbol{\alpha}\dot{\mathbf{Q}}^T \\ & - (\dot{\mathbf{Q}}\mathbf{Q}^T + \mathbf{Q}\boldsymbol{\Omega}\mathbf{Q}^T)\mathbf{Q}\boldsymbol{\alpha}\mathbf{Q}^T + \mathbf{Q}\boldsymbol{\alpha}\mathbf{Q}^T(\dot{\mathbf{Q}}\mathbf{Q}^T + \mathbf{Q}\boldsymbol{\Omega}\mathbf{Q}^T).\end{aligned} \tag{A4}$$

Since $\dot{\mathbf{Q}}\,\mathbf{Q}^T$ is antisymmetric, two pairs of terms on the right-hand side of ($A4$) cancel and the transformed operator becomes

$$\mathbf{Q}(\dot{\boldsymbol{\alpha}} - \boldsymbol{\Omega}\boldsymbol{\alpha} + \boldsymbol{\alpha}\boldsymbol{\Omega})\mathbf{Q}^T \tag{A5}$$

This result permits a wide choice of Jaumann-type derivatives all of which are objective.

Corotational Rates for Kinematic Hardening at Large Plastic Deformations

Y. F. Dafalias
Associate Professor of Engineering Science,
Department of Civil Engineering,
University of California at Davis,
Davis, Calif. 95616
Mem. ASME

To illustate the effect of the choice of corotational rates at large plastic deformations, expressions for the stresses developing in large simple shear are obtained in closed analytical form under the assumptions of a rigid-plastic material response and a Mises type isotropically and kinematically hardening constitutive model for two different corotational rates applied to the stress and the back-stress tensors. The observed difference in the simple shear response and the relative merits of the foregoing and other corotational rates are discussed, and a novel approach is proposed based on Mandel' work and the representation theorem for isotropic second-order antisymmetric tensor valued functions.

Introduction

In a recent paper Nagtegaal and de Jong [1] have numerically analyzed the case of simple shear for large plastic deformations using a Mises type kinematic hardening constitutive model. Utilizing the Jaumann (material corotational) rate for the stress and the back stress, they showed by numerical examples that a kinematic hardening rule of the Prager-Ziegler type [2] yields an oscillating stress for monotonically increasing shear strain. The authors attributed this result to the inability of the Prager-Ziegler kinematic hardening rule to realistically model the Bauschinger effect. In a subsequent paper, however, Lee, Mallet, and Wertheimer [3] attributed the stress oscillation to the use of the Jaumann rate rather than the inadequacy of the Prager-Ziegler kinematic hardening. They also proposed a different corotational rate which does not yield the stress oscillation even for a simple linear Prager-Ziegler kinematic hardening.

The analysis in the preceding works [1, 3] was performed by numerical methods and as such some of the features of the associated phenomena cannot be fully revealed. The main objective of this paper is to solve the problem of simple shear analytically for two different corotational rates: the Jaumann rate associated with the material spin $\mathbf{W}$, and a second rate given by a Jaumann type derivative associated with the spin $\dot{\mathbf{R}}\mathbf{R}^T$ where $\mathbf{R}$ is the orthogonal part of the polar decomposition of the deformation gradient (a dot denotes the material time derivative and a T the transpose). The exact analytical solution of the differential equations governing the evolution of the stresses is obtained in closed form for each rate, under the assumption of a rigid-plastic material response and a Mises type nonlinear isotropic/linear kinematic hardening model. Numerical examples illustrate the nature of these solutions. Subsequently, the preceding corotational rates, as well as the one proposed by Lee et al. [3], are briefly discussed, and an alternative approach is proposed based on Mandel's works [4, 5].

The Constitutive Model

The Jaumann type derivative, associated with a second-order antisymmetric tensor $\boldsymbol{\Omega}$ (usually identified as a "spin" tensor), of a second-order tensor $\mathbf{q}$ is symbolized by a superposed °, and defined by

$$\overset{\circ}{\mathbf{q}} = \dot{\mathbf{q}} + \mathbf{q}\boldsymbol{\Omega} - \boldsymbol{\Omega}\mathbf{q} \tag{1}$$

When $\boldsymbol{\Omega} = \mathbf{W}$ (material spin), equation (1) yields the usual Jaumann rate. The definiton of $\boldsymbol{\Omega}$ must be such as to satisfy the objectivity requirement for $\overset{\circ}{\mathbf{q}}$ i.e., under a superposed time-dependent rigid body rotation $\mathbf{Q}$ the $\overset{\circ}{\mathbf{q}}$ must become $\mathbf{Q}\overset{\circ}{\mathbf{q}}\mathbf{Q}^T$.

Representing now by $\mathbf{s}$ the deviator of the Cauchy stress $\boldsymbol{\sigma}$, k the "size" of the yield surface, and $\boldsymbol{\alpha}$ a deviatoric shift stress tensor (or back stress) modeling the kinematic hardening, a Mises type yield criterion is given by

$$f = \frac{3}{2}(\mathbf{s}-\boldsymbol{\alpha}):(\mathbf{s}-\boldsymbol{\alpha}) - k^2 = 0 \tag{2}$$

where the : symbolizes contraction over two indices, equivalent to the usual trace operation for second-order tensors. Henceforth, all stress quantities (including moduli) will be considered being normalized with respect to the initial value k_0 of k, which according to equation (2) represents the initial yield stress for a uniaxial tension-compression experiment if $\boldsymbol{\alpha} = \mathbf{0}$. A nonlinear isotropic hardening will be described by $dk/d\bar{\epsilon}^p = c(k_s - k)$ with $\dot{\bar{\epsilon}}^p = [(2/3)\,\mathbf{D}^p : \mathbf{D}^p]^{1/2}$ where $\mathbf{D}^p$ is the plastic rate of deformation tensor, k_s is a material constant representing a saturation value for k, and c another material constant controlling the pace of saturation. With $\mathbf{n} = (3/2)^{1/2}(\mathbf{s} - \boldsymbol{\alpha})/k$ being the unit normal to $f=0$ ($\mathbf{n} : \mathbf{n}$

Contributed by the Applied Mechanics Division for publication in the JOURNAL OF APPLIED MECHANICS.

Discussion on this paper should be addressed to the Editorial Department, ASME, United Engineering Center, 345 East 47th Street, New York, N.Y. 10017, and will be accepted until two months after final publication of the paper itself in the JOURNAL OF APPLIED MECHANICS. Manuscript received by ASME Applied Mechanics Division, May, 1982; final revision, January, 1983.

= 1), and assuming the normality rule for $\mathbf{D}^p$ and a Prager-Ziegler type kinematic hardening (not necessarily linear), the evolution equations for a state on $f=0$ are given by:

$$\text{Loading index:} \quad L=\frac{3}{2}\frac{1}{h}\overset{\circ}{\boldsymbol{\sigma}}:\mathbf{n} \tag{3}$$

$$\text{Rate Equations:} \quad \mathbf{D}^p=\langle L\rangle\mathbf{n}, \quad \overset{\circ}{\boldsymbol{\alpha}}=\frac{2}{3}h_\alpha\mathbf{D}^p \tag{4}$$

$$\text{Consistency Condition:} \quad \dot{f}=0 \Rightarrow \quad h=h_\alpha+c(k_s-k) \tag{5}$$

where h and h_α are the plastic moduli in uniaxial tension-compression associated with D^p_{11} and $(3/2)\dot{\alpha}_{11}$, respectively, and the Macauley brackets $\langle\ \rangle$ indicate the operation $\langle A\rangle = A$ if $A > 0$ and $\langle A\rangle = 0$ if $A \le 0$. Recalling the normalization with respect to k_0, the previously assumed expression for $dk/d\bar{\epsilon}^p$ can be integrated to yield

$$k=1+(k_s-1)\,[1-\exp(-c\,\bar{\epsilon}^p)] \tag{6}$$

Purely nonlinear isotropic hardening is obtained by setting $h_\alpha=0$, and purely kinematic by $c = 0$. The kinematic hardening can be either linear for h_α constant or nonlinear for h_α variable.

In view of the dependence of $f=0$ on direct and mixed isotropic invariants of $\mathbf{s}$ and $\boldsymbol{\alpha}$ and the use of properly defined corotational rates for $\boldsymbol{\sigma}$ and $\boldsymbol{\alpha}$ according to equation (1), the preceding constitutive relations are objective. The point of interest is to study the effect of the different corotational rates (definition of $\boldsymbol{\Omega}$ in equation (1)) on the material response. This will be studied in relation to the case of large simple shear.

Derivation of the Stress Differential Equations for Simple Shear

The motion in simple shear is given analytically by

$$x_1=X_1+\gamma(t)X_2, \quad x_2=X_2, \quad x_3=X_3 \tag{7}$$

where x_i and X_i, $i = 1, 2, 3$, are the cartesian coordinates of the current (at time t) and initial position of a material point, respectively, and γ will be simply called the shear strain. In the subsequent analysis a rigid-plastic response is assumed, thus all deformation measures are plastic and the superscript p will be dropped from $\mathbf{D}^p$. It is a rather lengthy (for equation $(9)_2$) but straightforward computation to obtain on the basis of equation (7) the expressions:

$$D_{12}=D_{21}=\frac{1}{2}\dot{\gamma}, \quad D_{ij}=0 \quad \text{for all other} \quad i,j \tag{8}$$

$$\mathbf{W}=\frac{1}{2}\dot{\gamma}\begin{bmatrix}0 & 1\\ -1 & 0\end{bmatrix}, \quad \dot{\mathbf{R}}\mathbf{R}^T=\frac{2\dot{\gamma}}{\gamma^2+4}\begin{bmatrix}0 & 1\\ -1 & 0\end{bmatrix} \tag{9}$$

where the kinematic tensors of equation (9) are presented in a 2×2 truncated matrix form with all other components that have an index equal to 3 being identically zero. In obtaining the foregoing, the key relations $\tan\theta = \lambda = (1/2)[\gamma + (\gamma^2 + 4)^{1/2}]$ and $\dot{\theta} = \dot{\gamma}/(\gamma^2 + 4)$ were used, with λ the maximum eigenvalue of $\mathbf{U}$ in the polar decomposition of the deformation gradient $\mathbf{F} = \mathbf{RU}$, and θ the angle of the corresponding eigenvector with the axis x_1. For a unified presentation either one of the antisymmetric tensors in equation (9) will be symbolized by $\boldsymbol{\Omega}$, with $\Omega_{12} = -\Omega_{21} = \omega$ and all other components zero. The preceding $\boldsymbol{\Omega}$ defines objective corotational rates.

The key differential equation is the one governing the evolution of $\boldsymbol{\alpha}$ given according to equation (1) by

$$\dot{\boldsymbol{\alpha}}=\overset{\circ}{\boldsymbol{\alpha}}-\boldsymbol{\alpha}\boldsymbol{\Omega}+\boldsymbol{\Omega}\boldsymbol{\alpha} \tag{10}$$

where $\overset{\circ}{\boldsymbol{\alpha}}$ is obtained from equation (4). Denoting by a prime the derivative with respect to γ, assuming that the initial values of α_{13} and α_{23} are zero but allowing for nonzero initial values of α_{11}, α_{22}, α_{33}, and α_{12} symbolized henceforth by a superposed bar, use of equations (2), (4), (8), and the expanded component form of equation (10) yields:

$$s_{11}=\alpha_{11}, \quad s_{22}=\alpha_{22}, \quad s_{12}=\frac{k}{\sqrt{3}}+\alpha_{12} \tag{11a}$$

$$s_{33}=\alpha_{33}=-(\bar{\alpha}_{11}+\bar{\alpha}_{22}), \quad s_{13}=\alpha_{13}=0, \quad s_{23}=\alpha_{23}=0 \tag{11b}$$

where k is given by equation (6) with $\bar{\epsilon}^p = \gamma/\sqrt{3}$, and

$$\alpha'_{11}=-\alpha'_{22}=2z(\gamma)\,\alpha_{12} \tag{12a}$$

$$\alpha'_{12}=\frac{1}{3}h_\alpha+z(\gamma)\,(\alpha_{22}-\alpha_{11}) \tag{12b}$$

where $z(\gamma) = \omega/\dot{\gamma}$. Use of $s_{ii} = \alpha_{ii} = 0$ and equation $(12a)_1$ was made in deriving equation $(11b)_1$. Integration of the system of equations (12) yields the value of $\boldsymbol{\alpha}$ as a function of γ, and subsequently of $\mathbf{s}$ from equations (11). Nonlinear kinematic hardening is included for a variable h_α. However, to easily obtain an analytical solution of the preceding system in closed form, linear kinematic hardening will be further *assumed with h_α = constant. With this assumption,* successive differentiation of equations (12) and back substitution yields the following two uncoupled second-order differential equations:

$$\alpha''_{11}-\frac{z'}{z}\alpha'_{11}+4z^2\alpha_{11}=2z\left[\frac{1}{3}h_\alpha+(\bar{\alpha}_{11}+\bar{\alpha}_{22})z\right] \tag{13}$$

$$\alpha''_{12}-\frac{z'}{z}\alpha'_{12}+4z^2\alpha_{12}=-\frac{1}{3}h_\alpha\frac{z'}{z} \tag{14}$$

with initial conditions at $\gamma = 0$: $\alpha_{11} = \bar{\alpha}_{11}$, $\alpha'_{11} = 2\,z(0)\bar{\alpha}_{12}$ for equation (13), and $\alpha_{12} = \bar{\alpha}_{12}$, $\alpha'_{12} = (h_\alpha/3) + z(0)\,(\bar{\alpha}_{22} - \bar{\alpha}_{11})$ for equation (14), and always $\alpha_{22} = (\bar{\alpha}_{11} + \bar{\alpha}_{22}) - \alpha_{11}$.

Solution of the Differential Equations and Examples

a. Solution for Corotational Rates Related to W (Jaumann). In this case according to equation $(9)_1$ $z(\gamma) = \omega/\dot{\gamma} = 1/2$, and equations (13) and (14) become

$$\alpha''_{11}+\alpha_{11}=\frac{1}{3}h_\alpha+\frac{1}{2}(\bar{\alpha}_{11}+\bar{\alpha}_{22}) \tag{15}$$

$$\alpha''_{12}+\alpha_{12}=0 \tag{16}$$

subjected to the initial conditions at $\gamma = 0$: $\alpha_{11} = \bar{\alpha}_{11}$, $\alpha'_{11} = \bar{\alpha}_{12}$, $\alpha_{12} = \bar{\alpha}_{12}$, and $\alpha'_{12} = (h_\alpha/3) + (\bar{\alpha}_{22} - \bar{\alpha}_{11})/2$. Equations (15) and (16) are linear of second order with constant coefficients and their solution is straightforward yielding in combination with equation $(11a)$ for the stresses:

$$s_{11}=\frac{1}{3}h_\alpha(1-\cos\gamma)+\frac{1}{2}(\bar{\alpha}_{11}-\bar{\alpha}_{22})\cos\gamma+\bar{\alpha}_{12}\sin\gamma + \frac{1}{2}(\bar{\alpha}_{11}+\bar{\alpha}_{22}) \tag{17}$$

$$s_{12}=\frac{k}{\sqrt{3}}+\frac{1}{3}h_\alpha\sin\gamma-\frac{1}{2}(\bar{\alpha}_{11}-\bar{\alpha}_{22})\sin\gamma+\bar{\alpha}_{12}\cos\gamma \tag{18}$$

The oscillating nature of the stress components is evident. Moreover, elimination of γ from equations (17) and (18) and use of equation $(11a)$ yields a circular path in the $\alpha_{11} - \alpha_{12}$ space. With all $\bar{\alpha}_{ij} = 0$, equations (17) and (18) are the closed-form representation of the corresponding plots obtained numerically in [1, 3]. In this case s_{11} remains non-negative, thus, the negative values of s_{11} shown in [3] can be attributed to round off numerical errors.

b. Solution for Corotational Rates Related to $\dot{\mathbf{R}}\mathbf{R}^T$. It follows from equation $(9)_2$ that in this case $z(\gamma) = \omega/\dot{\gamma} = 2/(\gamma^2 + 4)$ *and equations (13) and (14) become*

$$\alpha_{11}'' + \frac{2\gamma}{\gamma^2+4}\alpha_{11}' + \frac{16}{(\gamma^2+4)^2}\alpha_{11} = \left[\frac{1}{3}h_\alpha + \frac{2}{\gamma^2+4}(\bar{\alpha}_{11}+\bar{\alpha}_{22})\right]\frac{4}{\gamma^2+4} \tag{19}$$

$$\alpha_{12}'' + \frac{2\gamma}{\gamma^2+4}\alpha_{12}' + \frac{16}{(\gamma^2+4)^2}\alpha_{12} = \frac{1}{3}h_\alpha \frac{2\gamma}{\gamma^2+4} \tag{20}$$

subjected to the same initial conditions as equations (15) and (16), since at $\gamma = 0$ the $z(0) = 1/2$ as for the case with **W**. Introducing the change of variable $\phi = \tan^{-1}(\gamma/2)$ the preceding equations become $(d^2y/d\phi^2) + 4y = G$ with $G = (4/3)h_\alpha(1 + \tan^2\phi) + 2(\bar{\alpha}_{11} + \bar{\alpha}_{22})$ for $y = \alpha_{11}$ (equation (19)) and $G = (4/3)h_\alpha \tan\phi(1 + \tan^2\phi)$ for $y = \alpha_{12}$ (equation (20)). The general solution of the corresponding homogeneous equation has the form $c_1\cos 2\phi + c_2 \sin 2\phi$ and a particular solution for each one of equations (19) and (20) can be obtained by the method of variable coefficents. Subsequently, being careful to observe that $(d/d\gamma) = [2(1 + \tan^2\phi)]^{-1}(d/d\phi)$, the corresponding constants c_1, c_2 for each equation can be specified by the initial conditions and, finally, using equation (11*a*) the following expressions are obtained for the stress components in terms of ϕ or γ:

$$\begin{aligned} s_{11} &= \frac{1}{3}h_\alpha[4\cos 2\phi\, ln(\cos\phi) - 2\sin 2\phi(\tan\phi - 2\phi)] \\ &+ \frac{1}{2}(\bar{\alpha}_{11}-\bar{\alpha}_{22})\cos 2\phi + \bar{\alpha}_{12}\sin 2\phi + \frac{1}{2}(\bar{\alpha}_{11}+\bar{\alpha}_{22}) \\ &= \frac{1}{3}h_\alpha\frac{1}{\gamma^2+4}\left[4\gamma\left(4\tan^{-1}\left(\frac{\gamma}{2}\right)-\gamma\right)\right. \\ &\left.-4(\gamma^2-4)ln\left(\frac{2}{(\gamma^2+4)^{1/2}}\right)\right] \\ &-\frac{1}{2}(\bar{\alpha}_{11}-\bar{\alpha}_{22})\frac{\gamma^2-4}{\gamma^2+4} + \bar{\alpha}_{12}\frac{4\gamma}{\gamma^2+4} + \frac{1}{2}(\bar{\alpha}_{11}+\bar{\alpha}_{22}) \end{aligned} \tag{21}$$

$$\begin{aligned} s_{12} &= \frac{k}{\sqrt{3}} + \frac{1}{3}h_\alpha[2\sin^2\phi\tan\phi + 4\phi\cos 2\phi - (1+4ln(\cos\phi))\sin 2\phi] \\ &-\frac{1}{2}(\bar{\alpha}_{11}-\bar{\alpha}_{22})\sin 2\phi + \bar{\alpha}_{12}\cos 2\phi \\ &= \frac{k}{\sqrt{3}} + \frac{1}{3}h_\alpha\frac{1}{\gamma^2+4}\left[\gamma^3 - 4(\gamma^2-4)\tan^{-1}\left(\frac{\gamma}{2}\right)\right. \\ &\left.-4\gamma\left(1+4ln\left(\frac{2}{(\gamma^2+4)^{1/2}}\right)\right)\right] \\ &-\frac{1}{2}(\bar{\alpha}_{11}-\bar{\alpha}_{22})\frac{4\gamma}{\gamma^2+4} - \bar{\alpha}_{12}\frac{\gamma^2-4}{\gamma^2+4} \end{aligned} \tag{22}$$

c. Examples. To illustrate the nature of the preceding solutions, some examples will be presented graphically in the $s_{11} - \gamma$ and $s_{12} - \gamma$ spaces. The stress-strain curves corresponding to equations (17) and (18) will be identified by (*a*), while the ones corresponding to equations (21) and (22) by (*b*).

For purely kinematic hardening and zero initial value of α, we set $c = 0$ in equation (6) (thus $k = 1$), $\bar{\alpha}_{ij} = 0$ and select the rather large value $h_\alpha = 1$ to emphasize the effect of kinematic hardening. The corresponding response is shown in the two plots of Fig. 1. For comparison, the straight line (*c*) in the $s_{12} - \gamma$ plot shows the response for linear purely isotropic hardening having a slope equal to h_α of the kinematic. The s_{11} remains zero for isotropic hardening. The initial and limiting values of the stress and the slopes as γ varies from 0 to ∞ can be easily calculated from the closed-form expressions.

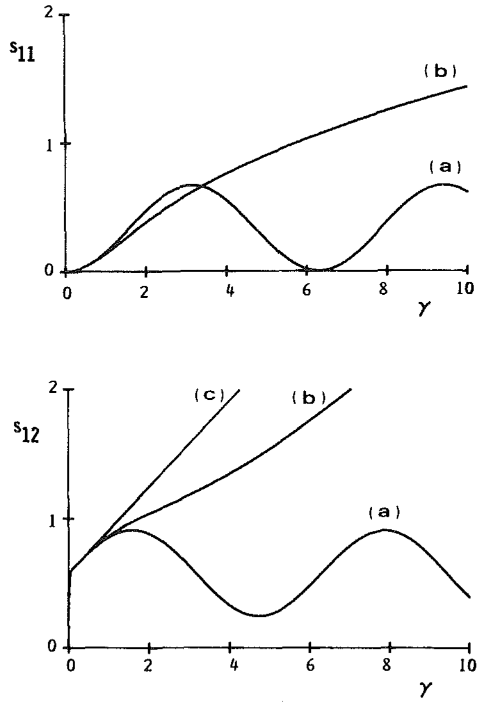

Fig. 1 Simple shear response for kinematic (curves (*a*) and (*b*)) and isotropic (curves (*c*)) hardening. The γ axis is the curve (*c*) for the $s_{11} - \gamma$ plot. Curves (*a*) are associated with W and (*b*) with $\dot{R}R^T$.

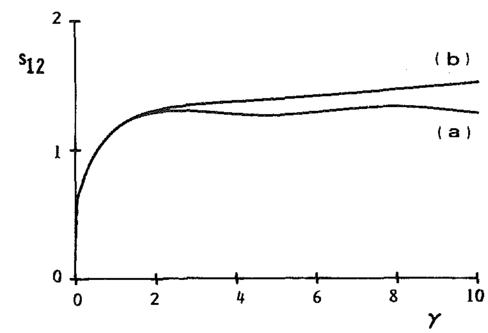

Fig. 2 Simple shear response for combined isotropic/kinematic hardening. Curve (*a*) for W and (*b*) for $\dot{R}R^T$.

A more realistic material description can be achieved by a combination of isotropic and kinematic hardening with a smaller value of h_α. For example, for commercially pure aluminum such description can be obtained with $h_\alpha = 0.1$ and $k_s = 2.25$, $c = 2.57$ in equation (6), recalling that for simple shear $\bar{\epsilon}^p = \gamma/\sqrt{3}$. With all $\bar{\alpha}_{ij} = 0$, the corresponding $s_{12} - \gamma$ plot is shown in Fig. 2, the s_{11} having exactly one tenth of its values shown in Fig. 1. The stress oscillation for curves (*a*) is now less pronounced due to the smaller value of h_α. Finally, the response for the same material constants but with $\bar{\alpha}_{12} = \pm 1/2\sqrt{3}$ and $\bar{\alpha}_{11} = \bar{\alpha}_{22} = 0$ is shown in Figs. 3 and 4, respectively. The observed effect of such initial values of $\bar{\alpha}_{12}$ is remarkable and negative slopes are obtained even for the curves (*b*).

Discussion and Conclusion

The obtained closed-form analytical solution, equations (17) and (18), reveals the exact nature of the oscillating stress response in the analysis of large simple shear with kinematic hardening observed numerically in [1, 3] for the Jaumann rate. The corresponding solution for a rate obtained by a

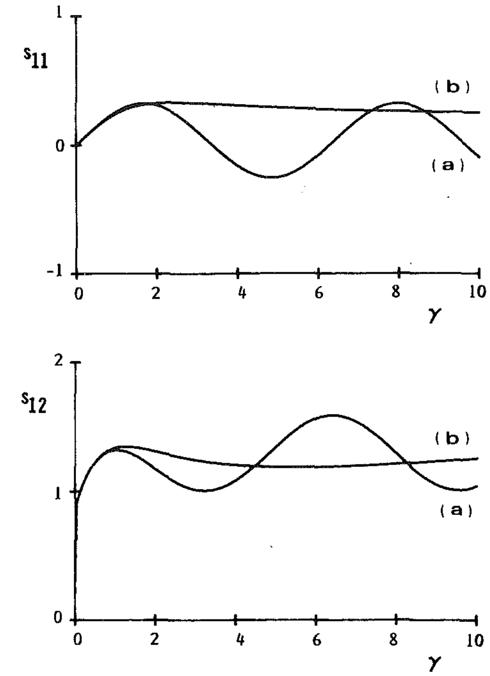

Fig. 3 Simple shear response for combined isotropic/kinematic hardening and a positive initial value of α_{12}. Curves (*a*) for W and (*b*) for $\dot{\mathbf{R}}\mathbf{R}^T$.

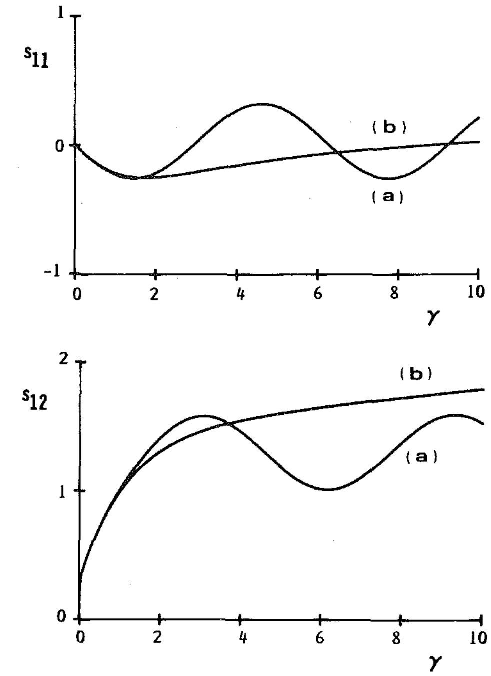

Fig. 4 Simple shear response for combined isotropic/kinematic hardening and a negative initial value of α_{12}. Curves (*a*) for W and (*b*) for $\dot{\mathbf{R}}\mathbf{R}^T$.

Jaumann type derivative associated with $\dot{\mathbf{R}}\mathbf{R}^T$, equations (21) and (22), yields a nonoscillating response for $\bar{\alpha}_{ij} = 0$. Observe from equation $(9)_2$ that the latter rate depends on the previous deformation through γ. This is expected due to the definition of $\mathbf{R}$ and brings again the subject of whether or not a dependence on an initial configuration is proper in plasticity with large deformations by means of both rotation and plastic strain. In general there is no reason why such a dependence should be excluded. Restricting attention to rigid-plastic response (or very small elastic deformations) in order to simplify the discussion, a plausible question is if one can at least in principle experimentally determine $\mathbf{R}$ and the total plastic strain by means of their effect on the current state of an already deformed material sample. With the assumption of a yield surface of the type of equation (2) one can in principle determine experimentally $\boldsymbol{\alpha}$ and k but not an already exisitng $\mathbf{R}$ and total plastic strain and, therefore, $\dot{\mathbf{R}}\mathbf{R}^T$ for the next incremental step. This piece of information must be given separately or assumed. For that reason in the case of initial anisotropy by means of an initial value of α_{12} (examples of Figs. 3 and 4), possibly obtained by previous deformation not necessarily associated with simple shear, we began the analysis with $\mathbf{R} = \mathbf{I}$ (identity) at $\gamma = 0$. Let us observe here that the use of corotational rate for the stress accociated with $\dot{\mathbf{R}}\mathbf{R}^T$ was proposed by Green and Naghdi [6] in a spatial formulation of their theory in which the yield surface expression depends on a plastic strain measure and $\mathbf{R}$ by means of $\mathbf{R}^T\boldsymbol{\sigma}\mathbf{R}$.

Nevertheless, equation (2) is a sufficiently simple and realistic constitutive assumption to deserve further consideration without the disadvantages mentioned in the foregoing. This prompted Lee et al. [3] to propose a corotational rate for $\boldsymbol{\alpha}$ given by equation (1) where $\boldsymbol{\Omega}$ was defined as the spin of a material line element which is parallel to the eigenvector of $\boldsymbol{\alpha}$ with the absolutely largest eigenvalue. Thus, such rate is defined at each step by the present state of $\boldsymbol{\alpha}$ and it was shown in [3] that no oscillation is obtained in the case of simple shear. One point that needs further study is that under a continuous variation of the velocity gradient the preceding spin can change discontinuously if one of the three eigenvalues of $\boldsymbol{\alpha}$ changes sign, because this will cause a discontinuous change of the eigenvector with the absolutely largest eigenvalue (recall that $\boldsymbol{\alpha}$ is a deviatoric tensor).

In view of the foregoing, it is worthwhile to look briefly at the work of Mandel [4, 5]. The reader is referred to these references for details, and here it will briefly be mentioned that the notion of the multiplicative decomposition $\mathbf{F} = \mathbf{EP}$ of the deformation gradient associated with the concept of an intermediate relaxed configuration as proposed by Lee and Liu [7], was supplemented by Mandel with the concept of director vectors fixing the orientation of the material. The corotational rate can then be defined by equation (1) with $\boldsymbol{\Omega}$ identified as the spin ω_D^1 of these vectors attached to the intermediate relaxed configuration κ_1 obtained from the current one by pure elastic deformation (no rotation), and with respect to which all state variables are referred. Restricting attention to small elastic deformations and intiallly isotropic materials such as the one described by equation (2), the explicit dependence on the rotated position of the director vectors disappears from the constitutive relations and $\omega_D^1 = \mathbf{W} - (\overset{\circ}{\mathbf{P}}\mathbf{P}^{-1})_a$, the subscript a indicating the antisymmetric part and with $\overset{\circ}{\mathbf{P}} = \dot{\mathbf{P}} - \omega_D^1\mathbf{P}$ since $\mathbf{P}$ is attached to κ_1 by its first index only. The important point now is that Mandel's theory requires constitutive relations not only for $\mathbf{D}^p$ (can be defined as the symmetric part of $\overset{\circ}{\mathbf{P}}\mathbf{P}^{-1}$), but also for $(\overset{\circ}{\mathbf{P}}\mathbf{P}^{-1})_a$ when loading occurs ($L>0$) in order to obtain ω_D^1.

At this point we would like to propose the following for the formulation of such constitutive relations in the case of kinematic hardening. Since $(\overset{\circ}{\mathbf{P}}\mathbf{P}^{-1})_a$ in addition to its dependence on L is an isotropic second-order antisymmetric tensor-valued function of the arguments $\mathbf{s}$, $\boldsymbol{\alpha}$, and k (recall assumption of initial isotropy), one can use Wang's representation theorems [8] to obtain general expressions for it. The simplest expression would be obtained using only the first generator $\boldsymbol{\alpha}\mathbf{s} - \mathbf{s}\boldsymbol{\alpha}$ given in [8] when loading occurs, i.e.,

$$(\overset{\circ}{\mathbf{P}}\mathbf{P}^{-1})_a = <L> \eta(\boldsymbol{\alpha}\mathbf{s} - \mathbf{s}\boldsymbol{\alpha}) = \eta k\sqrt{\frac{2}{3}}(\boldsymbol{\alpha}\mathbf{D}^p - \mathbf{D}^p\boldsymbol{\alpha}) \quad (23)$$

where η is a scalar function of the isotropic invariants of $\mathbf{s}$, $\boldsymbol{\alpha}$, and k, and the third member of equation (23) was obtained by adding and substracting $<L>\eta\alpha^2$ to the second member and using equation $(4)_1$. When $\boldsymbol{\alpha}$ and $\mathbf{s}$ (or $\boldsymbol{\alpha}$ and $\mathbf{D}^p$) commute, which includes as special case the isotropic one with $\boldsymbol{\alpha} = \mathbf{0}$, one has $(\dot{\mathbf{P}}\mathbf{P}^{-1})_a = \mathbf{0}$ and $\omega_D^1 = \mathbf{W}$, i.e., the usual Jaumann rate is obtained. This approach requires the specification of the material function η (in the simplest case a constant) based on proper experimental data. An initial investigation has shown that oscillations may or may not be induced in the case of simple shear depending on the values of η.

In conlusion it can be said that the study of proper corotational rates for kinematic hardening is a particular case of the corresponding general problem associated with large deformation anisotropic plasticity. It is possible that a macroscopic approach similar to the one used to obtain equation (23), can provide an answer to this area of research.

Note Added to the Proofs

A simple shear analysis within the context of hypoelasticity was given by C. Truesdell [9] for a convected stress rate which can be rewritten in terms of a Jaumann corotational rate (brought to my attention by Prof. Nemat-Nasser), and by J. K. Dienes [10] for a stress corotational rate associated with $\dot{\mathbf{R}}\mathbf{R}^T$. Both of these works refer to hypoelasticity which does not consider the basic concept of plastic internal state variables (like the back stress $\boldsymbol{\alpha}$), and this appears to be the reason they have escaped my attention and that of the reviewers of the paper.

References

1 Nagtegaal, J. C., and de Jong, J. E., "Some Aspects of Non-Isotropic Workhardening in Finite Strain Plasticity," Proceedings of the Workshop on *Plasticity of Metals at Finite Strain: Theory, Experiment and Computation*, pp. 65–102, Stanford University, 1981, Lee, E. H., and Mallett, R. L., eds., published by the Division of Applied Mechanics, Stanford University, Stanford, Calif., and Department of Mech. Eng., Aeronautical Eng. and Mechanics, R.P.I., Troy, N.Y., 1982.

2 Ziegler, H., "A Modification of Prager's Hardening Rule," *Quart. Appl. Math.*, Vol. 17, 1959, pp. 55–65.

3 Lee, E. H., Mallett, R. L., and Wertheimer, T. B., "Stress Analysis for Kinematic Hardening of Finite-Deformation Plasticity," Stanford University, SUDAM Report No. 81-11, 1981, Scientific Report to the Office of Naval Research, Department of the Navy.

4 Mandel, J., "Equations Constitutives et Directeurs dans les Milieux Plastiques et Viscoplastiques," *Int. J. Solids Structures*, Vol. 9, 1973, pp. 725–740.

5 Mandel, J., "Rélations de Comportement des Milieux Elastiques-plastiques et Elastiques - Viscoplatiques. Notion de Repêre Directeur," *Foundations of Plasticity*, Sawczuk, A., ed., Noordhoff, Leyden, 1973, pp. 387–400.

6 Green, A. E., and Naghdi, P. M., "A General Theory of an Elastic-Plastic Continuum," *Arch. Rati. Mech. Anal.*, Vol. 18, 1965, pp. 251–281.

7 Lee, E. H., and Liu, D. T., "Finite-Strain Elastic-Plastic Theory With Application to Plane-Wave Analysis," *J. App. Phys.*. Vol. 38, 1967, pp. 19–27.

8 Wang, C. C., "A New Representation Theorem for Isotropic Functions: An Answer to Professor G. F. Smith's Criticism of my Papers on Representations for Isotropic Functions," *Arch. Rati. Mech. Anal.*, Vol. 36, 1970, pp. 198–223.

9 Truesdell, C., "Hypo-Elastic Shear," *J. Appl. Phys.*, Vol. 27, 1956, pp. 441–447.

10 Dienes, J. K., "On the Analysis of Rotation and Stress Rate in Deforming Bodies," Acta Mech., Vol. 32, 1979, pp. 217–232.

G. Camenschi

N. Cristescu

N. Şandru

Faculty of Mathematics,
University of Bucharest,
Bucharest, Romania

Developments in High-Speed Viscoplastic Flow Through Conical Converging Dies

The problem of high-speed wire drawing is solved based on a global Coulomb friction condition on the die surface. The drawing force is determined as a function of the die angle, friction coefficient, reduction in area, and the Bingham number.

Introduction

In the mechanics of metal-forming processes – particularly in wire drawing – it is often required to determine the load on the machine tool that deforms the material into a new shape, the optimal conditions for the process – namely, the optimal cone angle – and the velocity field, strain rates, and stresses.

Since no exact solutions are available for such problems, in [1-4] an approximate method was proposed for solving the strip or wire drawing problems in viscoplastic deformation. Two fundamental nondimensional numbers emerge from the analysis of the governing equations. One is related to the working speed – the Bingham number – and the second is related to the acceleration – the Reynolds number. The method used in the aforementioned papers is perturbation with respect to one or both of these numbers. The friction that prevails between the rigid tool and the sliding viscoplastic continuum was considered in a special local form, namely $t_{r\theta}=m\sqrt{\Pi_{t'}}$, where $\Pi_{t'}$, is the second invariant of the deviatoric part of the stress tensor and $m\epsilon[0,1]$ is the friction factor.

This friction condition was first considered in [5] as an extension of the friction law used in classical plasticity.

The description of the friction resistance between die and material in plastic forming of metals has been much studied [6], yet very little that is known would facilitate formulation of the exact functional relationship between friction and the other variables such as: normal stress, sliding speed, geometry of the contact surface, lubrication, etc.

Since the friction is one of the most important factors in the study of the drawing process, in the present paper we analyze the high-speed wire drawing problem considering a global Coulomb friction condition on the die surface. A comparison between this solution and that obtained in [2], for some combinations of the process parameters, is made.

Contributed by the Applied Mechanics Division for publication in the JOURNAL OF APPLIED MECHANICS.

Discussion on this paper should be addressed to the Editorial Department, ASME, United Engineering Center, 345 East 47th Street, New York, N.Y. 10017, and will be accepted until two months after final publication of the paper itself in the JOURNAL OF APPLIED MECHANICS. Manuscript received by ASME Applied Mechanics Division, September, 1981; final revision, December, 1982.

Formulation

As in [1-4], let us assume that the mechanical behavior of the material can be described by a Bingham rigid-viscoplastic model.

Let R_1 be the original radius of the wire, which is reduced by drawing through a conical converging die, of the semiangle α, to R_2. The region occupied by the material is divided into three zones (Fig. 1). The material in zones *I* and *II* has a rigid body motion in the negative $0z$ direction, while zone *III* bounded by the die wall and by two surfaces S_1 and S_2 (which are to be determined) is the domain where the viscoplastic deformation takes place.

Assuming a stationary incompressible axisymmetric motion, in the absence of body forces, the governing equations, in spherical coordinates (r,θ,φ) are:

The balance equations:

$$\frac{\partial t_{rr}}{\partial r}+\frac{1}{r}\frac{\partial t_{r\theta}}{\partial \theta}+\frac{1}{r}(2t_{rr}-t_{\theta\theta}-t_{\varphi\varphi}+t_{r\theta}ctg\ \theta)$$
$$=\rho\left(v_r\frac{\partial v_r}{\partial r}+\frac{v_\theta}{r}\frac{\partial v_r}{\partial \theta}-\frac{v_\theta{}^2}{r}\right),\ \frac{\partial t_{r\theta}}{\partial r}+\frac{1}{r}\frac{\partial t_{\theta\theta}}{\partial \theta}+\frac{1}{r}[3t_{r\theta}$$
$$+(t_{\theta\theta}-t_{\varphi\varphi})\text{ctg }\theta]=\rho\left(v_r\frac{\partial v_\theta}{\partial r}+\frac{v_\theta}{r}\frac{\partial v_\theta}{\partial \theta}+\frac{v_r v_\theta}{r}\right),\qquad (1)$$
$$\frac{\partial v_r}{\partial r}+\frac{1}{r}\frac{\partial v_\theta}{\partial \theta}+\frac{2v_r}{r}+\frac{v_\theta\text{ctg }\theta}{r}=0,$$

The constitutive equations:

$$t_{rr}=-p+\left(2\eta+\frac{k}{\sqrt{\Pi_d}}\right)d_{rr},\quad t_{\theta\theta}=-p+\left(2\eta+\frac{k}{\sqrt{\Pi_d}}\right)d_{\theta\theta},$$
$$t_{\varphi\varphi}=-p+\left(2\eta+\frac{k}{\sqrt{\Pi_d}}\right)d_{\varphi\varphi},\quad t_{r\theta}=\left(2\eta+\frac{k}{\sqrt{\Pi_d}}\right)d_{r\theta},\qquad (2)$$
$$t_{\theta\varphi}=t_{r\varphi}=0,\quad \Pi_{t'}>k^2,$$

where $\mathbf{d}$ is the strain rate tensor, given by

$$d_{rr}=\frac{\partial v_r}{\partial r},\quad d_{\theta\theta}=\frac{1}{r}\frac{\partial v_\theta}{\partial \theta}+\frac{v_r}{r},$$

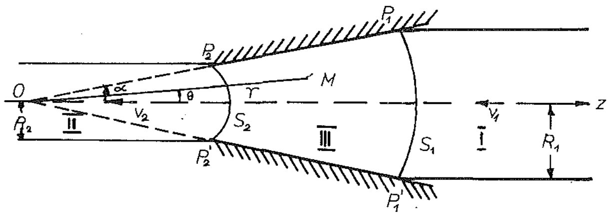

Fig. 1 The geometry of the wire drawing

$$d_{\varphi\varphi}=\frac{v_r}{r}+\frac{v_\theta \operatorname{ctg}\theta}{r},\quad d_{r\theta}=\frac{1}{2}\left(\frac{1}{r}\frac{\partial v_r}{\partial\theta}+\frac{\partial v_\theta}{\partial r}-\frac{v_\theta}{r}\right),\tag{3}$$

$$d_{\theta\varphi}=d_{r\varphi}=0$$

$$\Pi_{\mathbf{d}}=\frac{1}{2}(d_{rr}^2+d_{\theta\theta}^2+d_{\varphi\varphi}^2+2d_{r\theta}^2)$$

is the second invariant of the strain rate tensor, $\mathbf{t}'$ is the deviatoric part of the stress tensor, and v_r, v_θ are the components of the velocity vector.

The preceding equations are valid in the region $0\le\theta<\alpha$, $r_2(\theta)<r<r_1(\theta)$, where $r=r_1(\theta)$ and $r=r_2(\theta)$ are the equations of the surfaces S_1 and S_2, respectively.

If dimensionless variables, denoted by the index "0," are introduced as

$$r=r^0R_2,\quad v_r=v_r^0v_2,\quad v_\theta=v_\theta^0v_2,\quad p=p^0\frac{\eta v_2}{R_2}\tag{4}$$

in the equations (1)-(3), two nondimensional quantities are involved, i.e.,

$$\mathrm{Bg}=\frac{kR_2}{\eta v_2}=\text{the Bingham number, and}$$

$$\mathrm{Re}=\frac{\rho v_2R_2}{\eta}=\text{the Reynolds number.}$$

In what follows we assume that $\mathrm{Bg}<1$ and $\mathrm{Re}<<1$, and accordingly we neglect the inertial terms.

The main problem consists in integrating the equation system (1)-(3) with suitable boundary conditions.

As we have already mentioned, the global Coulomb friction law will be used as a model to describe the friction that takes place between the die and the sliding viscoplastic continuum.

Solution

Introducing the stream function $\psi=\psi(r,\theta)=R_2^2v_2\psi^0(r^0,\theta)$, the equation $(1)_3$ lead to

$$v_r=-\frac{1}{r^2\sin\theta}\frac{\partial\psi}{\partial\theta},\quad v_\theta=\frac{1}{r\sin\theta}\frac{\partial\psi}{\partial r}.\tag{5}$$

We expand the functions $\psi^0(r^0,\theta)$ and $p^0(r^0,\theta)$ in power series of the form

$$\psi^0(r^0,\theta)=\sum_{n\ge0}(\mathrm{Bg})^n\psi_n^0(r^0,\theta),$$

$$p^0(r^0,\theta)=\sum_{n\ge0}(\mathrm{Bg})^np_n^0(r^0,\theta).\tag{6}$$

Substituting (6), via (3) and (2), in the equilibrium equations (1), and equating terms of the same order in Bg, for the first two approximations, one gets

$$\psi_0^0(\theta)=\int_0^\theta u(t)\sin t\,dt,$$

$$\psi_1^0(r^0,\theta)=r^{03}\varphi(\theta)=r^{03}\int_0^\theta v(t)\sin t\,dt,\tag{7}$$

where

$$u(\theta)=a+b\cos 2\theta,$$

$$v(\theta)=\frac{A}{6}+B\left(\frac{1}{3}+\cos 2\theta\right)+K_1(\theta)\left(\frac{1}{3}+\cos 2\theta\right)+K_2(\theta)\left[\left(\frac{1}{3}+\cos 2\theta\right)ln\left(\operatorname{tg}\frac{\theta}{2}\right)-(1-3\cos\theta)(1+\cos\theta)\right]\tag{8}$$

and

$$K_1(\theta)=-\frac{9}{8}\int_0^\theta\mathfrak{F}(t)\sin t\left[\left(\frac{1}{3}+\cos 2t\right)ln\left(\operatorname{tg}\frac{t}{2}\right)-(1-3\cos t)(1+\cos t)\right]dt,$$

$$K_2(\theta)=\frac{9}{8}\int_0^\theta\mathfrak{F}(t)\sin t\left(\frac{1}{3}+\cos 2t\right)dt,$$

$$\mathfrak{F}(\theta)=\frac{12u-u'\operatorname{ctg}\theta}{\sqrt{3u^2+\frac{u'^2}{4}}}-\frac{d}{d\theta}\left(\frac{u'}{\sqrt{3u^2+\frac{u'^2}{4}}}\right).$$

We also have

$$p_0^0(r^0,\theta)=-\frac{2b}{r^{03}}\left(\frac{1}{3}+\cos 2\theta\right)+c,$$
$$p_1^0(r^0,\theta)=-A\,ln\,r^0+h(\theta)+C,\tag{9}$$

where

$$h'(\theta)=v'(\theta)+\frac{6\varphi(\theta)}{\sin\theta}-\frac{d}{d\theta}\left(\frac{u}{\sqrt{3u^2+\frac{u'^2}{4}}}\right)-\frac{3u'}{2\sqrt{3u^2+\frac{u'^2}{4}}}.$$

Here a, b, c, and A, B, and C are constants.

Using the previous expressions we obtain

$$v_r(r,\theta)=-\frac{R_2^2v_2}{r^2}u(\theta)-\frac{k}{\eta}r\,v(\theta)+\mathrm{O}(\mathrm{Bg}^2),$$

$$v_\theta(r,\theta)=3\frac{k}{\eta}r\frac{\varphi(\theta)}{\sin\theta}+\mathrm{O}(\mathrm{Bg}^2)\tag{10}$$

and

$$t_{rr}=\frac{2\eta R_2^2v_2b}{r^3}\left(\frac{1}{3}+3\cos 2\theta\right)+\frac{4\eta R_2^2v_2a}{r^3}-\frac{\eta v_2}{R_2}c+k\left[-h(\theta)+A\ln\frac{r}{R_2}-2v(\theta)+\frac{2u(\theta)}{\sqrt{3u^2+\frac{u'^2}{4}}}-C\right]+\mathrm{O}(\mathrm{Bg}^2),$$

$$t_{\theta\theta}=\frac{2\eta R_2^2v_2}{r^3}\left(\frac{b}{3}-a\right)-\frac{\eta v_2}{R_2}c+k\left[-h(\theta)+A\,ln\frac{r}{R_2}+4v(\theta)-C-6\operatorname{ctg}\theta\frac{\varphi(\theta)}{\sin\theta}-\frac{u}{\sqrt{3u^2+\frac{u'^2}{4}}}\right]+\mathrm{O}(\mathrm{Bg}^2),\tag{11}$$

$$t_{\varphi\varphi}=\frac{2\eta R_2^2v_2}{r^3}\left(\frac{b}{3}-a\right)-\frac{\eta v_2}{R_2}c+k\left[-h(\theta)\right.$$

$$+A\ ln\frac{r}{R_2}-2v(\theta)-C+6\text{ctg}\ \theta\frac{\varphi(\theta)}{\sin\theta}-\frac{u}{\sqrt{3u^2+\frac{u'^2}{4}}}\Bigg]$$

$$+O(Bg^2),$$

$$t_{r\theta}=\frac{2\eta R_2^2v_2b}{r^3}\sin 2\theta-k\Bigg[v'(\theta)+\frac{u'(\theta)}{2\sqrt{3u^2+\frac{u'^2}{4}}}\Bigg]$$

$$+O(Bg^2).$$

Across the surfaces S_1 and S_2 the dynamical conditions of compatibility

$$[v_n]=0,$$

$$[t_{kl}n_k]-\rho v_n[v_l]=0 \tag{12}$$

must be satisfied. Here v_n is the normal component of the velocity on the singular surface. From the relation $(12)_1$ we determine the equations $r=r_i(\theta)$, $i=1,\ 2,\ 0\le\theta\le\propto$, of the surfaces S_1 and S_2 in the form

$$\frac{v_i}{2}r_i^2\sin^2\theta-R_2^2v_2\Big[(b-a)\cos\theta-\frac{2b}{3}\cos^3\theta+a-\frac{b}{3}\Big]$$

$$-\frac{k}{\eta}r_i^3\varphi(\theta)=0,\quad i=1,2 \tag{13}$$

From the relation $(12)_2$ we determine the stress resultants $(X^I,\ Y^I,\ Z^I)$ and $(X^{II},\ Y^{II},\ Z^{II})$ which act on the surfaces S_1 and S_2 toward the rigid zones I and II. Computing the corresponding integrals one gets

$$X^I=Y^I=X^{II}=Y^{II}=0,$$

$$\frac{Z^I}{\pi R_1^2}=\frac{4\eta R_2^2v_2}{R_1^3}\sin^3\propto\Big[a+b\Big(2\cos^2\propto-\frac{1}{3}\Big)\Big]-\frac{\eta v_2}{R_2}c$$

$$+k\Bigg[-h(\propto)+A\Big(ln\frac{R_1}{R_2\sin\propto}-\frac{1}{2}\Big)+\frac{u'(\propto)\text{ctg}\propto}{2\sqrt{3u^2+\frac{u'^2}{4}}}$$

$$-\frac{u(\propto)}{\sqrt{3u^2+\frac{u'^2}{4}}}+4v(\propto)+v'(\propto)\text{ctg}\propto-C\Bigg], \tag{14}$$

$$\frac{Z^{II}}{\pi R_2^2}=-\frac{4\eta v_2}{R_2}\sin^3\propto\Big[a+b\Big(2\cos^2\propto-\frac{1}{3}\Big)\Big]+\frac{\eta v_2}{R_2}c$$

$$+k\Bigg[h(\propto)-A\Big(ln\frac{1}{\sin\propto}-\frac{1}{2}\Big)-\frac{u'(\propto)\text{ctg}\propto}{2\sqrt{3u^2+\frac{u'^2}{4}}}+\frac{u(\propto)}{\sqrt{3u^2+\frac{u'^2}{4}}}$$

$$-4v(\propto)-u'(\propto)\text{ctg}\ \propto+C\Bigg].$$

The tangential and normal stress resultants acting on the die surface $\theta=\propto$, $r_2(\propto)\le r\le r_1(\propto)$, along a line $\varphi=$const. are given by

$$T=\int_{r_2(\propto)}^{r_1(\propto)}t_{r\theta}\Big|_{\theta=\propto}r\sin\propto dr=-R_1^2\sin\propto$$

$$\Bigg[-2\eta v_2\sin 2\propto\ \sin\propto bR_2\frac{R_1-R_2}{R_1^3}+k\frac{1}{2\sin^2\alpha}$$

$$\Big(1-\frac{R_2^2}{R_1^2}\Big)\Big(v'(\propto)+\frac{u'(\propto)}{2\sqrt{3u^2+\frac{u'^2}{4}}}\Big)\Bigg],$$

$$N=\int_{r_2(\propto)}^{r_1(\propto)}t_{\theta\theta}\Big|_{\theta=\propto}r\sin\propto dr=\frac{R_1^2}{2\sin\propto}\Bigg\{4\Big(\frac{b}{3} \tag{15}$$

$$-a\Big)\eta v_2\sin^3\propto\frac{R_2(R_1-R_2)}{R_1{}^3}-c\frac{\eta v_2}{R_2}\Big(1-\frac{R_2^2}{R_1^2}\Big)$$

$$+k\Bigg[-h(\propto)\Big(1-\frac{R_2^2}{R_1^2}\Big)+A\Big(ln\frac{R_1}{R_2\sin\propto}-\frac{R_2^2}{R_1^2}ln\frac{1}{\sin\propto}$$

$$-\frac{1}{2}\Big(1-\frac{R_2^2}{R_1^2}\Big)\Big)-C\Big(1-\frac{R_2^2}{R_1^2}\Big)+\Big(4v(\propto)-\frac{6\cos\propto}{\sin^2\propto}\varphi(\propto)$$

$$-\frac{u(\propto)}{\sqrt{3u^2+\frac{u'^2}{4}}}\Big)\Big(1-\frac{R_2^2}{R_1^2}\Big)\Bigg]\Bigg\}.$$

The Kinematic and Boundary Conditions

To determine the parameters a, b, c, and A, B, and C we shall use the following conditions:

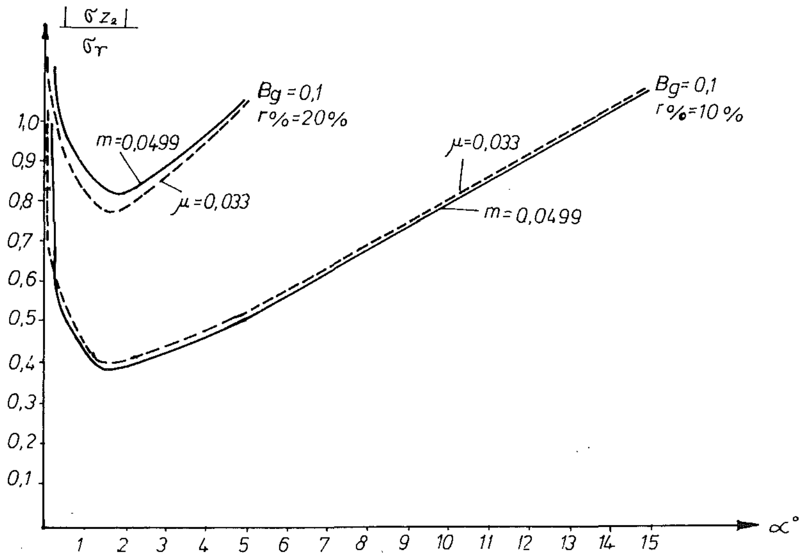

Fig. 2 The relative drawing stress versus die angle

(a) the v_θ component of the velocity is zero on the die surface;

(b) the singular surface S_1 passes through the points P_1 and P_1';

(c) the friction condition on the die surface is prescribed;

(d) the back force Z^I is given.

The condition (a) yields

$$\frac{A}{6}(1-\cos\alpha)+\frac{2}{3}B\cos\alpha\sin^2\alpha + \int_0^\alpha \sin\theta\Big\{K_1(\theta)\left(\frac{1}{3}+\cos2\theta\right)+K_2(\theta)\Big[\left(\frac{1}{3}+\cos2\theta\right)ln\left(\text{tg}\frac{\theta}{2}\right)-(1-3\cos\theta)(1+\cos\theta)\Big]\Big\}d\theta=0. \tag{16}$$

The condition (b) gives

$$\frac{1}{2}+(a-b)\cos\alpha+\frac{2}{3}b\cos^3\alpha-a+\frac{b}{3}=0. \tag{17}$$

The friction condition on the die surface taken in the form

$$T=-\mu N, 0\le\mu \tag{18}$$

gives the following two relations

$$2b\eta v_2\sin 2\alpha\sin^2\alpha\frac{R_2(R_1-R_2)}{R_1{}^3} = -\frac{\mu}{2\sin\alpha}\Big[4\left(\frac{b}{3}-a\right)\eta v_2\sin^3\alpha\frac{R_2(R_1-R_2)}{R_1{}^3} - c\frac{\eta v_2}{R_2}\left(1-\frac{R_2^2}{R_1^2}\right)\Big], \tag{19}$$

$$\left(1-\frac{R_2^2}{R_1^2}\right)\Big[v'(\alpha)+\frac{u'(\alpha)}{2\sqrt{3u^2+\frac{u'^2}{4}}}\Big] = \mu\Big\{-h(\alpha)\left(1-\frac{R_2^2}{R_1^2}\right)+A\Big[ln\frac{R_1}{R_2\sin\alpha}-\frac{R_2^2}{R_1^2}ln\frac{1}{\sin\alpha} - \frac{1}{2}\left(1-\frac{R_2^2}{R_1^2}\right)\Big]-C\left(1-\frac{R_2^2}{R_1^2}\right)+\Big[4v(\alpha)-\frac{6\cos\alpha}{\sin^2\alpha}\varphi(\alpha) - \frac{u(\alpha)}{\sqrt{3u^2+\frac{u'^2}{4}}}\Big]\left(1-\frac{R_2^2}{R_1^2}\right)\Big\}.$$

Assuming $Z^I=0$, the condition (d) gives

$$c\frac{\eta v_2}{R_2}=\frac{4\eta v_2 R_2^2}{R_1^2}\sin^3\alpha\Big[a-\frac{b}{3}+2b\cos^2\alpha\Big],$$

$$C=-h(\alpha)+A\left(ln\frac{R_1}{R_2\sin\alpha}-\frac{1}{2}\right) + \frac{1}{2}\text{ctg}\,\alpha\frac{u'(\alpha)}{\sqrt{3u^2+\frac{u'^2}{4}}}-\frac{u(\alpha)}{\sqrt{3u^2+\frac{u'^2}{4}}} + 4v(\alpha)+v'(\alpha)\text{ctg}\,\alpha. \tag{20}$$

Solving the system of equations (16)–(20) and using (14), after a long and tedious computation, we get the following formula for the magnitude of the relative drawing stress

$$\frac{|\sigma_{z2}|}{\sigma_Y}=\frac{2}{\sqrt{3}\text{Bg}}\Big[\left(1-\frac{R_2^2}{R_1^2}\right)F(\alpha,\mu,r\%) + \text{Bg}\,ln\left(\frac{R_1}{R_2}\right)^3 G(\alpha,\mu,r\%)\Big], \tag{21}$$

where

$$F(\alpha,\mu,r\%) = \frac{12\sin\frac{\alpha}{2}\cos^3\frac{\alpha}{2}(\sin\alpha+\mu\cos\alpha)}{3\sin\alpha+\mu\Big[1+\cos\alpha+\frac{R_2}{R_1}\left(1+\frac{R_2}{R_1}\right)(1-2\cos\alpha)\Big]},$$

$$G(\alpha,\mu,r\%) = \frac{\frac{1}{\sqrt{3}\sin\alpha}(1+\mu\text{ctg}\,\alpha)}{(1+\mu\text{ctg}\,\alpha)\text{tg}\,\frac{\alpha}{2}-\mu\frac{R_2^2}{R_1^2-R_2^2}ln\frac{R_1}{R_2}} \left\{I_1-\frac{2I_2\mu\Big[1+\frac{R_2}{R_1}\left(1+\frac{R_2}{R_1}\right)\Big]}{\sin2\alpha+\frac{2\mu}{3}\Big[2+\frac{R_2}{R_1}\left(1+\frac{R_2}{R_1}\right)(2-3\cos^2\alpha)\Big]}\right\} \tag{22}$$

and

$$I_1=\int_0^\alpha\frac{\sin\theta\,d\theta}{\sqrt{1-\sin^2\theta(\lambda_1-\lambda_2\sin^2\theta)}},$$

$$I_2=\int_0^\alpha\frac{\sin^3\theta\,d\theta}{\sqrt{1-\sin^2\theta(\lambda_1-\lambda_2\sin^2\theta)}},$$

$$\lambda_1=\frac{4\mu\Big[1+\frac{R_2}{R_1}\left(1+\frac{R_2}{R_1}\right)\Big]}{\Big\{\sin2\alpha+\frac{2\mu}{3}\Big[2+\frac{R_2}{R_1}\left(1+\frac{R_2}{R_1}\right)(2-3\cos^2\alpha)\Big]\Big\}^2} \Big\{\sin2\alpha+\mu\Big[1-\frac{R_2}{R_1}\left(1+\frac{R_2}{R_1}\right)\cos2\alpha\Big]\Big\}, \tag{23}$$

$$\lambda_2=\frac{8}{3}\left\{\frac{\mu\Big[1+\frac{R_2}{R_1}\left(1+\frac{R_2}{R_1}\right)\Big]}{\sin2\alpha+\frac{2\mu}{3}\Big[2+\frac{R_2}{R_1}\left(1+\frac{R_2}{R_2}\right)(2-3\cos^2\alpha)\Big]}\right\}^2$$

σ_Y being the tensile yield stress.

Conclusions

The relative drawing stress is a function of the die angle α, the friction coefficient μ, the reduction in area r percent $=100(1-R_2^2/R_1^2)$, and the Bingham number.

The formula (21) allows the analysis of the drawing process, i.e., the estimation of the influence of the drawing parameters on the drawing stress. This formula is similar to that deduced in [2] where the local friction condition $t_{r\theta} = m\sqrt{\Pi_{t'}}$ was used. It should be mentioned that in the foregoing formula the reduction r(percent) is much more involved, appearing too in the arguments of the functions F and G.

In Fig. 2, the relative drawing stresses are plotted comparing those given by formula (21)–the interrupted line–with those in [2]–the full line–for some combinations of the process parameters. Accordingly, if for the reduction $r(\text{percent}) = 10$ percent both these curves practically coincide ($\mu = 0.033$ and $m = 0.049$). for the reduction $r(\text{percent}) = 20$ percent one can see that the stress calculated by the formula (21) gives smaller values. These curves exhibit minima which correspond to the optimal drawing angle of the die.

Finally, we mention that both formulas for the drawing stress are identical in the absence of friciton ($\mu = 0$, $m = 0$).

References

1 Şandru, N., and Camenschi, G., "Viscoplastic Flow Through Inclined Planes With Application to the Strip Drawing," *Lett. Appl. Eng. Sci.*, Vol. 17, 1979, pp. 773–784.

2 Camenschi, G., Cristescu, N., and Sandru, N., "High Speed Wire Drawing," *Archives of Mechanics*, Vol. 31, No. 5, 1979, pp. 741–755.

3 Camenschi, G., and Şandru, N., "Inertia Influence in Strip Drawing Problem," *Rev. Roum. Sci. Tech., Ser. Méc. Appl.*, Vol. 25, No. 2, 1980, pp. 207–216.

4 Camenschi, G., and Sandru, N., "Dynamic Aspects in Wire Drawing Problem," *Lett. Appl. Eng. Sci.*, Vol. 18, 1980, pp. 999–1007.

5 Cristescu, N., "Plastic Flow Through Conical Convergin Dies, Using a Viscoplastic Constitutive Equation," *Int. J. Mech. Sci.*, Vol. 17, 1975, pp. 425–433.

6 Lebanov, A. N., et al., *Contact Friction in Metal Forming Processes* (in Russian), Moscow, 1976.

7 Avitzur, B., *Metal Forming: Processes and Analysis*, McGraw-Hill, New York, 1968.

Statistical Cumulative Damage Theory for Fatigue Life Prediction[1]

Z. Hashin[2]
Nathan Cummings Professor of Mechanics of Solids, Department of Solid Mechanics, Materials and Structures, Tel-Aviv University, Tel-Aviv, Israel
Fellow ASME

A statistical cumulative damage theory is developed with the purpose of prediction of mean, standard deviation and probability density of fatigue lifetime of randomly variable specimens subjected to the same deterministic cyclic loading program. The theory requires availability of a deterministic cumulative damage theory for ideal nonvariable specimens, called clones. Detailed analysis is given for two-stage cyclic loading based on a previously developed deterministic cumulative damage theory and log-normal distribution of $S-N$ curve lifetimes. Results indicate that the usual interpretation of deterministic cumulative damage theory in terms of means of lifetimes is not valid for significant scatter. Preliminary experimental results for two-stage loading are compared with analytical predictions.

Introduction

The problem of the prediction of fatigue lifetime for a specified cyclic loading program is known in the literature as the Cumulative Damage (CD) problem. The loading program may be described by a function $S(n)$ where S is amplitude of stress or strain and n is the number of elapsed cycles. It is required to determine the number of cycles to failure n_f. To minimize complexity it is assumed that the minimum-to-maximum amplitude ratio R and the frequency remain constant during cycling. The first condition is automatically fulfilled in the important case of reversed cycling, $R = -1$.

Experience shows that when specimens of the "same" material are subjected to identical loading programs the resulting lifetimes are quite different and exhibit considerable scatter and thus n_f must be regarded as a random variable. Therefore the goal of CD theory should be defined as determination of the probability density function (PDF) of n_f or, at least, the evaluation of its mean and variance. While there exists a very large body of literature on the cumulative damage problem only a relatively small part is concerned with analytical treatment of scatter. A recent rational approach to the problem in terms of Markoff process statistics has been given by Bogdanoff [1-3]. Reference [1] also contains an excellent discussion of previous work on statistical treatments of the problem.

In the event that $S(n)$ is a deterministic loading program the scatter in n_f is primarily due to internal material variability of the specimens which produces different developments of the fatigue failure process. Another important practical problem is the case when the loading program is of random nature, e.g., spectrum loading. In this case the scatter in n_f is produced both by variability of load and material. This question will not be addressed here. It is felt that treatment of the case of deterministic cyclic loading program is a prerequisite for treatment of random load.

A fundamental question is the nature of the information required for determination of lifetime. The point of view taken here is that this information consists of the statistics of test data for simple cyclic loadings, hopefully, but not necessarily, constant amplitude cycling as expressed by the usual $S-N$ test data for the material specimens investigated. Such a point of view may be termed phenomenological since it is not explicitly concerned with the development of microfailures or with the growth of internal macrocracks. The basic idea underlying the analytical treatment is that a deterministic cumulative damage theory must first be developed for ideal nonvariable specimens and then be randomized to take into account material variability. This is done in the present work in terms of the CD theory developed previously by Hashin and Rotem [4].

General Approach

The basis for statistical treatments of mechanics problems is generally a mathematical formulation for a deterministic realization of the problem. In the case of a random input problem, such as vibrations of a structure under random load, the deterministic realization is the deflection function for deterministic load from which the deflection statistics may be obtained in terms of load statistics. A much more difficult kind of statistical problem is the case of random properties, for example: an elastic body with randomly space variable properties under deterministic loads. In this case the deterministic realization is one nonhomogeneous sample elastic body and the statistical problem is formulated in terms of differential equations with random coefficients. The statistical CD problem is of the latter kind since the scatter in

[1] Support by Naval Air Systems Command and Office of Naval Research Under Contract N00014-78-C-0544 with the University of Pennsylvania is gratefully acknowledged.

[2] Also, Adjunct Professor, College of Engineering and Applied Science, University of Pennsylvania, Philadelphia, Pa. 19104.

Contributed by the Applied Mechanics Division for publication in the JOURNAL OF APPLIED MECHANICS.

Discussion on this paper should be addressed to the Editorial Department, ASME, United Engineering Center, 345 East 47th Street, New York, N.Y. 10017, and will be accepted until two months after final publication of the paper itself in the JOURNAL OF APPLIED MECHANICS. Manuscript received by ASME Applied Mechanics Division, April, 1982; final revision, March, 1983.

lifetimes is due to material variability of the different specimens that are failed in a test program, resulting in a different development and duration of the complex microstructural damage accumulations that terminate in ultimate failure.

To define a deterministic realization we imagine that we can reproduce a fatigue specimen in all minute microdetails in any number of replicas. Such hypothetical specimens will be called *clones* and clones of one kind will be called a *clone species*. (The concept has been introduced in [5] in the context of fatigue failure under three-dimensional cyclic stress.) If members of a clone species are subjected to identical cyclic loading programs they will have exactly the same fatigue lifetime. Therefore a clone species obeys some completely deterministic CD law, which cannot however, be experimentally investigated since clones are not available.

The remaining alternative is theoretical derivation of the CD law of a clone species. Suppose that this has been achieved in some fashion and that the prediction of lifetime for loading program $S(n)$ is n_f which will be a function of certain global material parameters of the clones, which are brought in by the deductive process leading to the CD law. In a real fatigue test, different specimens are subjected to same $S(n)$. Each of these may be regarded as the representative of a clone species. Then the lifetime of the ith specimen is n_{fi} which is a function of the material parameters of the ith specimen and thus the statistics of n_{fi} is determined in terms of the statistics of the specimen parameters, which must be known. Then the test of the success of the theoretical CD law is whether the statistics of n_f derived on its basis, is confirmed by the statistics of test data for n_f.

The most basic fatigue testing information is obtained by constant amplitude testing. Obviously any clone species will have a deterministic $S-N$ curve expressed as

$$S=\phi(a_i, b_i, \ldots, N) \tag{1}$$

with inverse

$$N=\psi(a_i, b_i, \ldots, S) \tag{2}$$

where S is constant maximum amplitude of stress or strain, N is the number of cycles to failure, and a_i, b_i, . . . are parameters of the ith clone species. Since S can be controlled in a fatigue test it is convenient to consider (2) for constant S as basic experimental information. Each specimen in the constant S test is again regarded as the representative of a clone species and thus (2) has a different value for each specimen. This defines the random variable $N(S)$ which assumes values N_i as defined by (2).

As an example for a CD problem we consider the case when $S(n)$ is a multistage cyclic loading, constant S_1 for n_1 cycles, S_2 for n_2 cycles, etc. and let failure occur at amplitude S_k. Then

$$n_f=n_1+n_2+\ldots n_{kf} \tag{3}$$

where n_{kf} is the unknown. The prediction of a deterministic CD theory will generally involve the lifetimes $N_1(S_1)$, $N_2(S_2)$, . . . as given by the $S-N$ curve and perhaps other parameters such as fatigue limit stress S_e. Thus for the ith clone species

$$n_{ki}=\psi(n_1, n_2, \ldots, n_{k-1}; N_{1i}, N_{2i}, \ldots, N_{ki}; S_{ei}, \ldots) \tag{4}$$

where from (2) $N_{ji} = \psi(a_i, b_i, \ldots, S_j)$. If ψ is known, the PDF and moments of (5) can be determined in terms of the joint PDF of the random variables N_j, S_e, etc., entering into (5), by standard methods of probability theory; see e.g., [6]. (The assumption that all specimens (clone species) fail at stress level S_k is not essential and has only been introduced for reasons of simplicity.)

The minimal information to perform any analysis is the PDF of N_j. A popular assumption is that $\eta = \log N$ at any stress level is normally distributed; see e.g., [7]. In this event N is said to obey a log-normal distribution. Many test data have demonstrated that this assumption is quite accurate, see e.g., [7, 8]. An example is shown in the Appendix.

The analysis will be enormously simplified if it can also be assumed that η_j and η_l at two different stress levels S_j and S_l are statistically independent, because in that event, the joint PDF of η_j and η_l reduces to the product of their individual PDF. This cannot of course be expected to be valid when S_j and S_l are very close but this is not a case of practical interest. An analysis of an extensive set of test data given in the Appendix shows that independence is fulfilled with remarkable accuracy. All of the analysis to be given can be carried out without this assumption.

Deterministic Cumulative Damage Theory

A considerable body of literature on the subject exists. For a review, see e.g., [7, 9, 4]. In general the approach has been empirical or semiempirical and many of the treatments have been confined to special cyclic loading programs. The most well known and most often used result is still the primitive Palmgren-Miner rule although it is quite clear that it is not acceptable in any general sense since it is insensitive to sequence of loading effects and its agreement with test data is at best erratic.

It has usually been assumed that a deterministic CD result is expected to predict mean lifetime. For example the Palmgren-Miner rule for two-stage loading would be interpreted in this context as

$$\frac{n_1}{\langle N_1 \rangle} + \frac{\langle n_2 \rangle}{\langle N_2 \rangle} = 1 \tag{5}$$

where the brackets denote means. It will be shown on the basis of present treatment that such an interpretation is questionable.

In the present work a CD theory developed by Hashin and Rotem [4] will be employed and some of its basic ingredients will now be summarized:

1. The information necessary to predict lifetime are the damage curves in the $S-N$ plane. A damage curve represents the residual lifetimes n_2 in a two-stage cyclic loading program where S_1 and n_1 are fixed and S_2 is variable. It is the locus of all n_2 plotted horizontally to the left from the $S-N$ curve.

2. If the $S-N$ curve has a fatigue limit, all damage curves converge into it. This implies that dependence of fatigue limit stress on loading history is neglected.

3. If the $S-N$ curve is linear in S-log$N$ or log$S$-log$N$ plane then the damage curves are also assumed linear in these planes (since the $S-N$ curve is a member of the damage curve family), Fig. 1

4. The state of "damage" is characterized by remaining residual life. Different cyclic loading programs, terminated before failure, with same residual life for subsequent constant amplitude cycling are defined as equivalent. An equivalent loading postulate has been formulated that states: cyclic loading programs that are equivalent for one subsequent stress level are equivalent for all subsequent stress levels.

The equivalent loading postulate leads to uniqueness of damage curves and to a unique procedure for lifetime analysis in terms of damage curves for any cyclic loading program. Such assumptions are reminiscent of that made by Bogdanoff [1] that at any stage of a cyclic loading program further damage accumulation depends on the current state of "damage" and not on its history of accumulation.

Some pertinent results derived in [4] will now be recalled. It

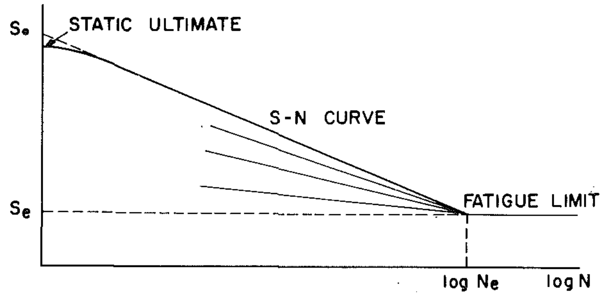

Fig. 1 Semilog linear damage curves through fatigue limit

is assumed that the $S-N$ curve is linear in $S-\log N$ or $\log S-\log N$; see Fig. 1. Thus

$$S = S_0(1+\Gamma \log N) \quad (a) \text{ semilog}$$
$$S = N^{\Gamma} \quad (b) \text{ log-log} \tag{6}$$

and that there is a fatigue limit (S_e; N_e). Then it follows that for two-stage loading: S_1 for n_1 cycles, S_2 for n_2 cycles-to-failure, n_2 is given by

$$\left(\frac{n_1}{N_1}\right)^{\beta} + \frac{n_2}{N_2} = 1 \tag{7}$$

where

$$\beta = \begin{cases} \dfrac{S_2 - S_e}{S_1 - S_e} & \text{semilog} \\ \\ \dfrac{\log(S_2/S_e)}{\log(S_1/S_e)} & \text{log-log} \end{cases} \tag{8}$$

The result (7) is in reasonable agreement with experimental data in the sense of "mean fit" [4, 10]. For three stage loading: S_1 for n_1 cycles, S_2 for n_2 cycles, S_3 for n_3 cycles – to failure

$$[(n_1/N_2)^{\beta_{21}} + n_2/N_2]^{\beta_{32}} + n_3/N_3 = 1 \tag{9}$$

where β_{21} is the same as (8) and β_{32} is similarly defined with stresses S_3 and S_2. The result (9) is easily generalized to any multistage loading program, in particular block loading. Details are given in [4]. In the case when the loading program $S(n)$ is defined by a continuous function of n, the number of elapsed cycles, the determination of lifetime requires the solution of a nonlinear differential equation with initial conditions, [4].

It may be noted that the Palmgren-Miner rule is a special case of the general theory in the sense that it can be derived on the basis of a certain damage curve family, reference [11].

Statistical Analysis of Two-Stage Loading

As a simple example for the general approach to statistical CD theory outlined in the foregoing, the case of two-stage loading will be analyzed. It is assumed that the deterministic CD theory of [4] is valid for a clone species with a deterministic $S-N$ curve of type (6) which has a distinct fatigue limit and linear damage curves through fatigue limit. Denoting

$$\eta_1 = \log N_1(S_1) \quad \eta_2 = \log N_2(S_2) \tag{10}$$

it follows from (7) that

$$n_{2fi} = n_{2i} = 10^{\eta_{2i}}[1 - n_1^{\beta} 10^{-\beta\eta_{1i}}] \tag{11}$$

It is recalled that according to (8) the fatigue limit S_e enters into β and in general this is a random variable, thus different for each clone species. However the scatter of S_e is confined to a relatively small range. For example: the fatigue limit range for steel is quoted in the literature as 32-34 ksi (220.7-234.5 MPa) and it turns out that lifetimes predicted by the analysis to be outlined are only weakly affected by such a variation of S_e. Consequently the scatter of S_e is neglected and thus (11) becomes a function of the two random variables η_1 and η_2.

As has been discussed before and with support of the analysis given in the Appendix, it is assumed that η_1 and η_2 are each normally distributed and are statistically independent. Therefore their PDF are given by

$$p(\eta_1) = \frac{1}{\sigma_1\sqrt{2\pi}} e^{-(\eta_1 - <\eta_1>)^2/2\sigma_1^2}$$
$$p(\eta_2) = \frac{1}{\sigma_2\sqrt{2\pi}} e^{-(\eta_2 - <\eta_2>)^2/2\sigma_2^2} \tag{12}$$

$$p(\eta_1, \eta_2) = p(\eta_1)p(\eta_2) \tag{13}$$

where $<\eta>$ and σ are the mean and standard deviation of η, respectively. Equations (11)–(13) are sufficient information to evaluate the statistical moments and the PDF of n_2. If independence is not valid, equation (13) could be expressed by a bivariate normal distribution.

For purpose of evaluation of moments it must be noted that if $n_1 \geq N_{1i}$ the specimen fails in the first loading stage and therefore $n_{2i} = 0$. This implies the restriction

$$\eta_{1i} \geq \log n_1 = \lambda \tag{14}$$

which is equivalent to the requirement $n_{2i} \geq 0$. Therefore the mean of (11) is given by

$$<n_2> = \int_0^{\infty}\int_{\lambda}^{\infty} 10^{\eta_2}(1 - n_1^{\beta}10^{-\beta\eta_1})p(\eta_1, \eta_2)d\eta_1 d\eta_2 \tag{15}$$

with similar expressions for the other moments. It is easily shown in terms of an integral tabulated in [12, (p. 303, integral 7.4.32)] that

$$\int_{\lambda}^{\infty} 10^{\gamma\eta} p(\eta)\, d\eta = g(\gamma)\, h(\gamma, \lambda) \quad (a)$$

$$g(\gamma) = \frac{1}{2} 10^{\gamma(<\eta> + \gamma ln10\sigma^2/2)} \quad (b)$$

$$h(\gamma, \lambda) = 1 + \operatorname{erf}\left[\left(\frac{<\eta> - \lambda}{\sigma_\eta} + \gamma ln10\sigma_\eta\right)/\sqrt{2}\right] \quad (c) \tag{16}$$

$$\operatorname{erf} z = \frac{2}{\sqrt{\pi}}\int_0^z e^{-t^2} dt \quad (d)$$

It follows from (12)–(13) and (16) that

$$<n_2> = g_2(1)h_2(1,0)[g_1(0)h_1(0,\lambda) - n_1^{\beta} g_1(-\beta)\, h_1(-\beta, \lambda) \tag{17}$$

where a subscript 1 or 2 on a function implies evaluation with $<\eta_1>$, σ_1 or $<\eta_2>$, σ_2, respectively.

It should be noted that the lower limit zero for the η_2 integration in (15) is not exactly correct since integration should start from $N_2 = 0$, thus from $\eta_2 \to -\infty$, while $\eta_2 = 0$ corresponds to $N_2 = 1$. From a practical point of view it is of course evident that one fatigue cycle more or less makes no difference. From a mathematical point of view it should be noted that lower limit of integration $-\infty$ would replace $h_2(1, 0)$ by $h_2(1, \infty) = 2$. Noting that the error function is practically equal to 1 for arguments exceeding 2 it is clear from examination of (16c) that to all practical purposes

$$h_2(\gamma, 0) \cong 2 = h_2(\gamma, \infty) \tag{18}$$

The variance of n_2 is given by

Table 1 Mean and standard deviation of n_2. Semilog S-N curve. Low-high cycling. $S_1 = 0.35 S_0$ $S_2 = 0.45 S_0$ $S_e = 0.25 S_0$ $\beta = 2.0$.

$<\eta_1>$	σ_1	$<\eta_2>$	σ_2	n_1	$<n_2>$	σ_{n_2}	$\tilde{n}_2$	$<N_1>$	σ_{N_1}	$<N_2>$	σ_{N_2}
5.20	0.01	4.40	0.008	40000	23521	440	23520	158531	3651	25123	463
	0.05		0.04		23575	2210	23640	159543	18429	25226	2328
	0.10		0.08		23739	4506	24005	162747	37976	25549	4746
	0.20		0.16		24278	9752	25498	176219	85650	26883	10250
	0.30		0.24		25054	16654	28106	201195	157332	29263	17488
	0.01		0.008	80000	18715	456	18725	158531	3651	25123	463
	0.05		0.04		18625	2312	18883	159543	18429	25226	2328
	0.10		0.08		18316	4911	19375	162747	37976	25549	4746
	0.20		0.16		17563	10392	21342	176219	85650	26883	10250
	0.30		0.24		17816	15923	24636	201195	157332	29263	17488
	0.01		0.008	120000	10705	693	10728	158531	3651	25123	463
	0.05		0.04		10392	3553	10955	159543	18429	25226	2328
	0.10		0.08		10066	6330	11659	162747	37976	25549	4746
	0.20		0.16		10699	10130	14417	176219	85650	26883	10250
	0.30		0.24		12071	14450	18853	201195	157332	29263	17488
	0.01		0.008	150000	2598	1030	2631	158531	3651	25123	463
	0.05		0.04		3374	3439	2927	159543	18429	25226	2328
	0.10		0.08		4695	5456	3845	162747	37976	25549	4746
	0.20		0.16		6939	8938	7405	176219	85650	26883	10250
5.20	0.30	4.40	0.24		8993	13038	12998	201195	157332	29263	17488

Table 2 Mean and standard deviation of n_2. Semilog S-N curve. High-low cycling. $S_1 = 0.45 S_0$ $S_2 = 0.35 S_0$ $S_e = 0.25 S_0$ $\beta = 0.50$.

$<\eta_1>$	σ_1	$<\eta_2>$	σ_2	n_1	$<n_2>$	σ_{n_2}	$\tilde{n}_2$	$<N_1>$	σ_{N_1}	$<N_2>$	σ_{N_2}
4.40	0.008	5.20	0.01	5000	87798	2124	87808	25123	463	158531	3651
	0.04		0.05		88286	10720	88513	25226	2328	159543	18429
	0.08		0.10		89828	22071	90751	25549	4746	162747	37976
	0.16		0.20		96252	49613	100222	26883	10250	176219	85650
	0.24		0.30		107968	90709	118030	29263	17488	201195	157332
	0.008		0.01	10000	58500	1632	58513	25123	463	158531	3651
	0.04		0.05		58771	8242	59092	25226	2328	159543	18429
	0.08		0.10		59624	17003	60929	25549	4746	162747	37976
	0.16		0.20		63198	38427	68742	26883	10250	176219	85650
	0.24		0.30		70536	69932	83581	29263	17488	201195	157332
	0.008		0.01	15000	36019	1401	36034	25123	463	158531	3651
	0.04		0.05		36123	7084	36516	25226	2328	159543	18429
	0.08		0.10		36459	14651	38045	25549	4746	162747	37976
	0.16		0.20		38999	31757	44588	26883	10250	176219	85650
	0.24		0.30		45678	56194	57148	29263	17488	201195	157332
	0.008		0.01	20000	17066	1361	17084	25123	463	158531	3651
	0.04		0.05		17046	6851	17484	25226	2328	159543	18429
	0.08		0.10		17719	12924	18754	25549	4746	162747	37976
	0.16		0.20		22141	25436	24224	26883	10250	176219	85650
4.40	0.24	5.20	0.30		29432	45245	34864	29263	17488	201195	157332

$$\sigma_{n_2}^2 = <n_2^2> - <n_2>^2$$

$$<n_2^2> = \int_0^\infty \int_\lambda^\infty 10^{2\eta_2}(1 - n_1^\beta 10^{-\beta\eta_1})^2 p(\eta_1)p(\eta_2)d\eta_1 d\eta_2 \tag{19}$$

It follows from (15)–(16) that

$$<n_2^2> = g_2(2)h_2(2, 0)[g_1(0)h_1(0, \lambda) - 2n_1^\beta g_1(-\beta)h_1(-\beta, \lambda) + n_1^{2\beta} g_1(-2\beta)h_1(-2\beta, \lambda) \tag{20}$$

It is also of interest to compute the mean and standard deviation of the $S-N$ curve lifetime N in terms of mean and standard deviation of $\eta = \log N$. These results easily follow from (16) with $\gamma = 1, 2$, respectively. Therefore

$$<N> = \int_0^\infty 10^\eta p(\eta)d\eta = g(1)h(1, 0) = 10^{<\eta> + ln10\sigma_\eta^2/2}$$

$$\sigma_N^2 = \int_0^\infty 10^{2\eta} p(\eta)d\eta - <N>^2 = g(2)h(2, 0) - <N>^2 = 10^{2<\eta> + ln10\sigma_\eta^2}(10^{ln10\sigma_\eta^2} - 1) \tag{21}$$

To illustrate the significance of the results obtained numerical calculations have been performed for a material characterized by the $S-N$ curve for hard drawn steel wire in tension-tension fatigue as obtained in [8]. The $S-N$ curve is of semilog type and is given by

$$S = S_0(1 - 0.125 <\eta>)$$

$$S_0 = 1467 \text{ MPa}$$

$$S_e = 0.25\, S_0 \qquad <\eta_e> = 6.0$$

where S_0 is defined by intersection of the $S-N$ curve with the S axis. Calculations of $<n_2>$ and $\sigma_{n_2}^2$ have been performed for the stress levels

$$\text{Low-High} \begin{cases} S_1 = 0.35\, S_0 \\ S_2 = 0.45\, S_0 \end{cases} \qquad \text{High-Low} \begin{cases} S_1 = 0.45\, S_0 \\ S_2 = 0.35\, S_0 \end{cases}$$

for various values of n_1, σ_1, and σ_2. It has been assumed, for computation convenience only that $\sigma_2 = \sigma_1 <\eta_2>/<\eta_1>$ which for the stress levels chosen here implies $\sigma_2 = 0.8\, \sigma_1$. The results are summarized in Tables 1 and 2. To understand the significance of the standard deviations of $S-N$ lifetime it should be recalled that for a normally distributed random variable with mean $<x>$ and standard deviation σ, 95.5

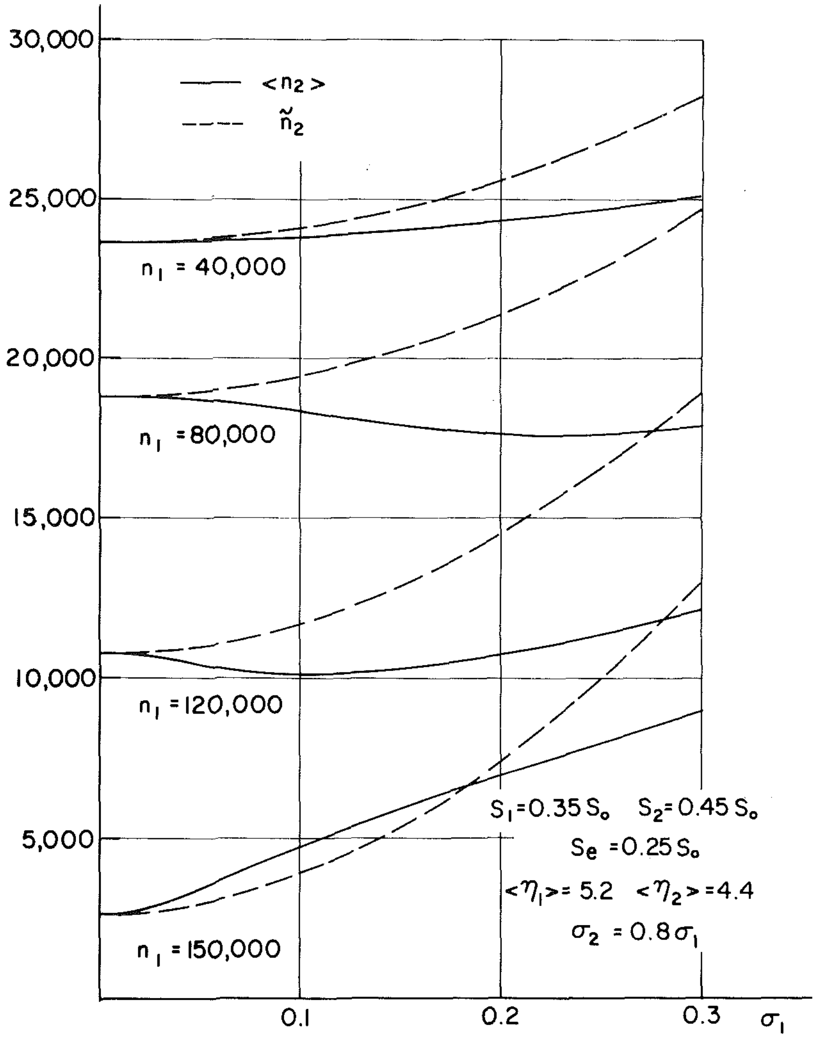

Fig. 2 Mean of n_2 versus standard deviation of log N_1: low-high loading

percent of the values of x fall within the range $[<x>-2\sigma, <x>+2\sigma]$.

The tables also show a quantity $\tilde{n}_2$ which is defined as

$$\tilde{n}_2 = <N_2>[1-(n_1/<N_1>)^{\beta}] \tag{22}$$

This is equivalent to (7) with replacement of N_1 and N_2 by their means. Consequently (22) expresses the usual interpretation of a deterministic cumulative damage theory in terms of means. It is seen that $<n_2>$ and $\tilde{n}_2$ increasingly diverge with increase of scatter of $S-N$ curve lifetimes. A comparative plot of the two quantities as a function of σ_1, is shown in Figs. 2-3. This implies that interpretation of a deterministic cumulative damage theory in terms of means of test data is not acceptable when the scatter is significant. Thus the Palmgren-Miner rule as expressed by (5) has the additional serious deficiency that it takes no account of the magnitude of the scatter of $S-N$ lifetimes.

Another interesting and important phenomenon is the strong increase of the standard deviation σ_{n_2} relative to the mean $<n_2>$. This is also shown in Fig. 4. It is seen that σ_{n_2} can reach values larger than $<n_2>$ itself at the time when the maximum ratio of N lifetime standard deviation to its mean is 0.78 ($\sigma_{N_1}/<N_1>$ for $\sigma_1 = 0.30$). The reason for this seems to be that the scatter of n_2 is dependent on the scatters of N_1 and N_2 which are defined by their standard deviations. Indeed, the results clearly show that the larger n_1, thus the larger the damage incurred at stress level S_1, the larger is the scatter of n_2. As n_1 increases $<n_2>$ decreases. At the same time σ_{n_2} is increasingly governed by σ_{N_1} which is a large number which can easily become much larger than the decreasing $<n_2>$.

Finally, the probability of failure under specified two-stage loading will be evaluated. The Cumulative Distribution Function (CDF), $F(z)$, is defined as the probability that failure occurs under two-stage loading S_1 for n_1 cycles, S_2 for z cycles. This probability may be decomposed as follows

$$F(z) = Pr(0<n_f \le n_1) + Pr(n_1 < n_f \le n_1 + z) \tag{23}$$

where n_f is the lifetime. The first part is the probability of failure during the first stage and is simply given by

$$Pr(0<n_f<n_1) = \frac{1}{\sigma_1\sqrt{2\pi}}\int_{-\infty}^{\lambda} e^{-(\eta_1-<\eta_1>)^2/2\sigma_1^2}\,d\eta_1$$

$$= \frac{1}{2}\left[1+\mathrm{erf}\left(\frac{\lambda-<\eta_1>}{\sigma_1\sqrt{2}}\right)\right] \tag{24}$$

By standard procedure, [6], the second part is given by

$$Pr(n_1<n_f\le n_1+z) = Pr(0<n_{2f}\le z)$$

$$= \int_D\int p(\eta_1,\eta_2)\,d\eta_1 d\eta_2 \tag{25}$$

where D is the region in the η_1, η_2 plane defined by

$$0<n_2(\eta_1,\eta_2)\le z \tag{26}$$

Introducing the functional form of n_2 from (7) into (26) and using (13), (25) assumes the form

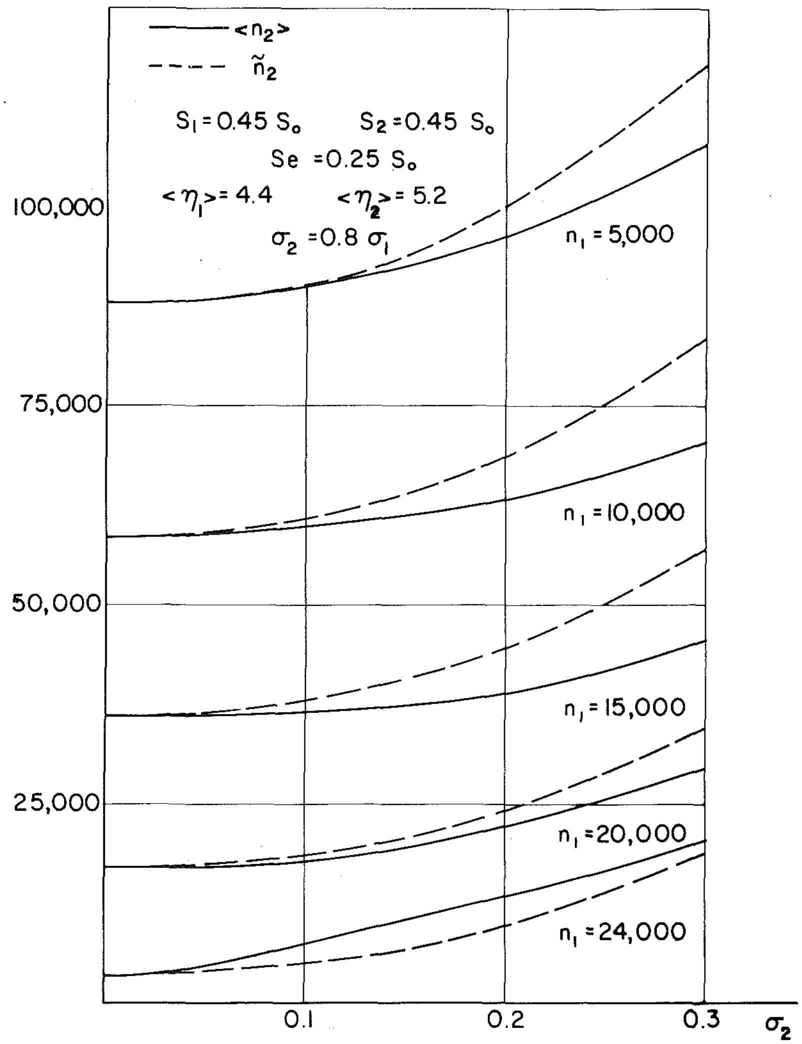

Fig. 3 Mean of n_2 versus standard deviation of log N_1: high-low loading

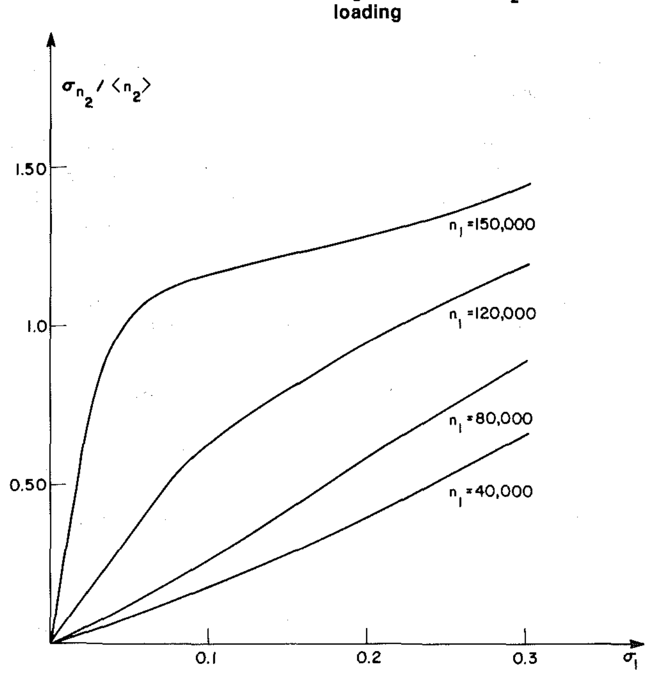

Fig. 4 Standard deviation of n_2 divided by $<n_2>$ versus standard deviation of log N_1: low-high loading

$$Pr(0<n_{2f}<z)=\int_{\lambda}^{\infty}p(\eta_1)\int_{-\infty}^{\rho(z,\eta_1)}p(\eta_2)d\eta_2 d\eta_1 \qquad (27)$$

where

$$\rho(z,\eta_1)=\log\frac{z}{1-n_1^{\beta}10^{-\beta\eta_1}} \qquad (28)$$

and λ is defined by (14). Introducing (12) into (27), carrying out the η_2 integration, and substituting this result and (24) into (23) yields the CDF in the form

$$F(z)=\frac{1}{2}\left[1+\mathrm{erf}\left(\frac{\lambda-<\eta_1>}{\sigma_1\sqrt{2}}\right)\right]+\frac{1}{\sigma_1\sqrt{2}}\int_{\lambda}^{\infty}\left[\mathrm{erf}\left(\frac{<\eta_2>}{\sigma_2\sqrt{2}}\right)\right.$$

$$\left.+\,\mathrm{erf}\left(\frac{\rho(z,\eta_1)-<\eta_2>}{\sigma_2\sqrt{2}}\right)\right]e^{-(\eta_1-<\eta_1>)^2/2\sigma_1^2}d\eta_1 \qquad (29)$$

The integral (29) must be evaluated numerically. Plots of $F(z)$ for various n_1 for the case $<\eta_1> = 5.2$, $<\eta_2> = 4.4$, $\sigma_1 = 0.20$, and $\sigma_2 = 0.16$ are shown in Fig. 5. The values of $F(0)$ are defined by (24). It is seen that with increasing n_1 the probability of failure in the first stage increases and so does the probability of failure in the second stage for specified $n_2 = z$. Figure 6 shows $F(z)$ for specified $n_1 = 80{,}000$ and different σ_1, σ_2. This plot demonstrates the increase in the scatter of n_{2f} with increasing σ_1 and σ_2.

More Complicated Loading Programs

The method of statistical analysis presented can in principle be applied to any loading program but the implementation is complex. Consider for example the case of multistage

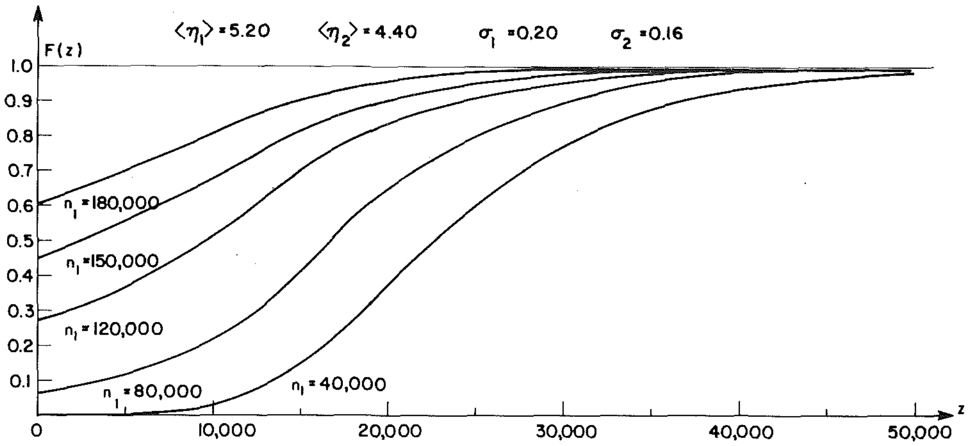

Fig. 5 Probability distribution functions of n_2 for various n_1

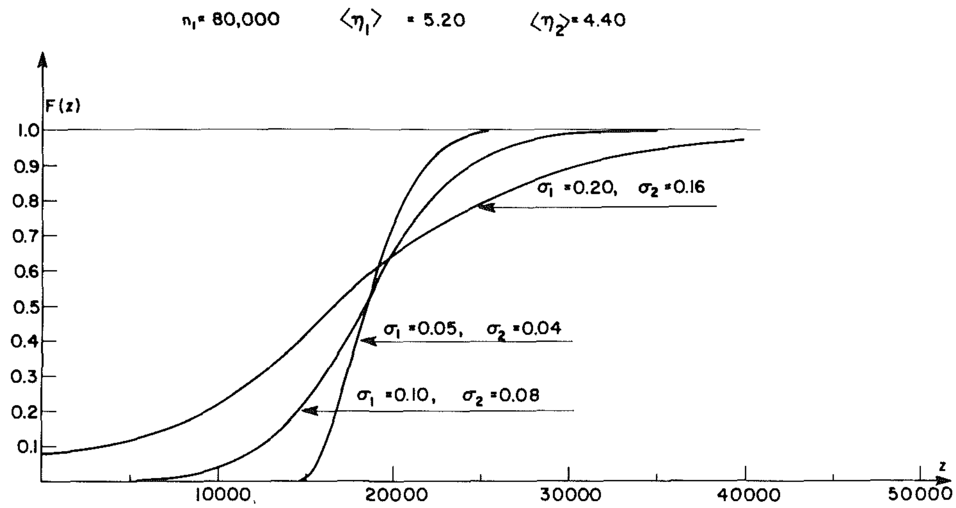

Fig. 6 Probability distribution functions of n_2 for various σ_1, σ_2

loading: S_1 for n_1 cycles, S_2 for n_2 cycles, etc. According to the theory developed in [4] failure in the last stage is given by the following scheme

$$n_{2f} = N_2[1-(n_1/N_1)^{\beta_{21}}] \qquad \text{two stage}$$

$$n_{3f} = N_3[1-[(n_1/N_1)^{\beta_{21}} + n_2/N_2]^{\beta_{32}}\} \qquad \text{three stage} \qquad (30)$$

$$n_{4f} = N_4[1-\{[(n_1/N_1)^{\beta_{21}} + n_2/N_2]^{\beta_{32}} + n_3/N_3\}^{\beta_{43}}] \qquad \text{four stage}$$

.

.

.

where any of the β_{ij} is defined by (8) with stress S_i in the denominator and stress S_j in the numerator.

To evaluate the mean of n_{3f}, for example, each N_i is written 10^{η_i} obtaining $n_3(\eta_1, \eta_2, \eta_3)$. Then the mean is given by

$$> n_3 > = \int_{\log n_1}^{\infty}\int_{\log n_2}^{\infty}\int_0^{\infty} n_3(\eta_1, \eta_2, \eta_3)p(\eta_1)p(\eta_2)p(\eta_3)d\eta_1 d\eta_2 d\eta_3 \quad (31)$$

where the lower limits of integration, $\log n_1$ for η_1 and $\log n_2$ for η_2 express the fact that when failure occurs in the first or second stage, n_{3f} vanishes. The PDF $p(\eta)$ may be of the normal type (12) or any other kind. Similar results may be written down for the variance and for means and variances of n_{kf} for any k stage loading. It appears that all integrations, except the one for η_k, must be performed numerically. If the scatter of η_i is not large the PDF of η_i will be of localized nature which may open up the possibility of simplified approximations for the integrals but this topic is outside the scope of present work.

An important kind of loading program is so-called block loading in which a specified loading program (block) is repeated periodically. In the simplest case the block is two stage, S_1 for n_1 cycles; S_2 for n_2 cycles. A procedure for deterministic lifetime evaluation for block loading has been given in [4]. This will here be recast in the following equivalent and simpler form: The recurrence relations

$$\begin{aligned}
\mu_1 &= n_1/N_1 \\
\mu_2 &= \mu_1^{\beta} + n_2/N_2 \\
\mu_3 &= \mu_2^{1/\beta} + n_1/N_1 \\
&\cdot \\
&\cdot \qquad\qquad\qquad\qquad (32) \\
&\cdot \\
\mu_k &= \mu_{k-1}^{\beta} + n_2/N_2 \quad k \text{ even} \\
\mu_{k+1} &= \mu_k^{1/\beta} + n_1/N_1 \\
&\cdot
\end{aligned}$$

where β is defined by (8), define fatigue failure when

Table 3 Comparison of predicted with experimental data – two-stage loading

Loading Sequence	$L-H$	$L-H$	$H-L$	$H-L$
S_1(MPa)	268	268	298	298
S_2(MPa)	298	298	268	268
n_1	20,000	35,000	5000	9000
$<n_2>$ experimental	10,400	7280	30,140	17,240
$<n_2>$ predicted	12,390	9540	34,330	17,860
$<n_2> P-M$	11,330	8360	52,000	31,770
σ_{n_2} experimental	7660	3520	9530	8920
σ_{n_2} predicted	1000	2400	8830	10,960

$S-N$ data	S	$<N>$	σ_N
	298	15,280	5870
	268	77,300	23,360
	221	Fatigue Limit	

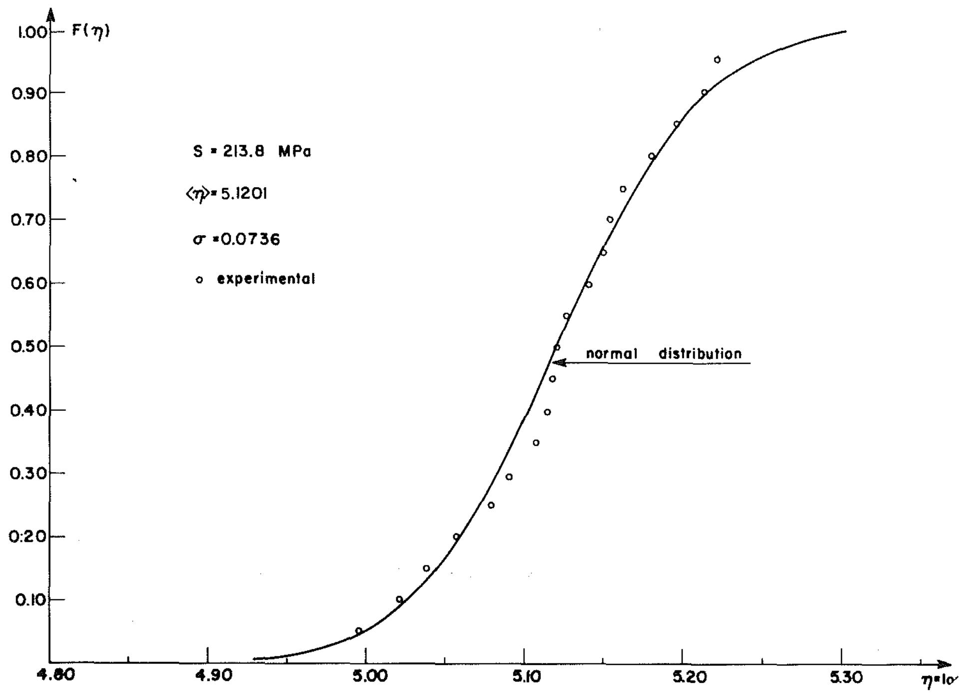

Fig. 7 Log-normal distribution of aluminum 6061-T6 *S-N* lifetimes

$$\mu_k \geq 1 \tag{33}$$

The condition (33) determines the number of stages n_1 and n_2 to failure, thus the lifetime L. The problem of evaluating the statistics of this lifetime when N_1 and N_2 are random variables is not simple. One possibility is numerical evaluation of many lifetimes L_{ij} for sample lifetimes N_{1i} and N_{2j} which are either members of statistical sets (e.g. log-normal with specified mean and standard deviation), or are the actual test data. Then the mean, variance and CDF of L can be found numerically.

Since a deterministic procedure is available for any multistage loading, [4], such an approach can also be utilized for a random loading program consisting of random amplitudes S_i for random numbers of cycles n_i.

Comparison With Test Data: Two-Stage Loading

A preliminary two-stage testing program has been carried out by Dr. T. Gottesman at the mechanical testing laboratory of the University of Pennsylvania, using steel specimens and a MTS machine. Ten specimens were failed for each point of the S – N curve and for each loading sequence. In each case the cycling was fully reversed. The mean $S-N$ curve was approximately of semilog type and therefore predictions were based on semilog damage curves.

Table 3 shows a comparison of predicted with experimental results. Agreement is somewhat encouraging. Also shown are $<n_2>$ as determined by the $P-M$ rule (5). More comparisons with experimental data are obviously needed.

Conclusion

The statistical cumulative damage theory which has been developed here requires two basic kinds of information: (*a*) a deterministic cumulative damage theory for ideal specimens without scatter, and (*b*) the statistical distribution of $S-N$ curve lifetimes for fixed stress levels (analytically, or a sufficient number of test data). In the present work a rational deterministic cumulative damage theory based on damage curves and an equivalent loading postulate has been employed, [4]. The damage curve family employed in this work converges into the fatigue limit but the analysis may of course be performed for other types of damage curve families. The present cumulative damage theory avoids quantification of damage and substitutes for its residual life, which is a measurable quantity. Essentially, the future of a specimen that has undergone cyclic loading depends on the residual life at that time and on the manner of continuation of the cyclic loading program.

The statistics of the present approach is very simple because it essentially consists of interpretation of a deterministic lifetime as a function of random variables, i.e., the statistically variable parameters of the fatigue process that are primarily the $S-N$ lifetimes. It has here been assumed that these lifetimes are log-normally distributed. This is a popular representation but the procedure can be carried out for any statistical distribution of lifetimes and also for any deterministic cumulative damage theory.

The test of the cumulative damage theory chosen is of course experimental verification in the sense that analytically predicted means and standard deviations and CDF of lifetimes under a cyclic loading program must be compared with such quantities evaluated on the basis of test data. Such a comparison has here been given for preliminary test data showing fair agreement.

Acknowledgment

It is a pleasure to acknowledge discussion and collaboration with Dr. T. Gottesman.

References

1 Bogdanoff, J. L., "A New Cumulative Damage Model, Part 1," ASME Journal of Applied Mechanics, Vol. 45, 1978, pp. 246–250.

2 Bogdanoff, J. L., and Krieger, W., "A New Cumulative Damage Model, Part 2," ASME Journal of Applied Mechanics, Vol. 45, 1978, pp. 251–257.

3 Bogdanoff, J. L., "A New Cumulative Damage Model, Part 3," ASME Journal of Applied Mechanics, Vol. 45, 1978, pp. 733–739.

4 Hashin, Z., and Rotem, A., "A Cumulative Damage Theory of Fatigue Failure," *Materials Science and Engineering*, Vol. 34, 1978, pp. 147–160.

5 Hashin, Z., "Fatigue Failure Criteria for Unidirectional Fiber Composites," ASME Journal of Applied Mechanics, Vol. 48, 1981, pp.

6 Papoulis, A., *Probability, Random Variables and Stochastic Processes*, McGraw-Hill, New York, 1965.

7 Frost, N. E., Marsh, K. J., and Pook, L. P., *Metal Fatigue*, Clarendon Press, Oxford, 1974.

8 Liu, H. W., and Corten, H. T., "Fatigue Damage Under Varying Stress Amplitudes," NASA TN D-647, 1960.

9 Leve, H. L., "Cumulative Damage Theories," in *Metal Fatigue: Theory and Design*, Madayag, A. F., ed., Wiley, New York, 1960.

10 Hashin, Z., and Laird, C., "Cumulative Damage Under Two Level Cycling: Some Theoretical Predictions and Test Data," *Fatigue of Engineering Materials and Structures*, Vol. 2, 1980, pp. 345–350.

11 Hashin, Z., "A Reinterpretation of the Palmgren-Miner Rule for Fatigue Life Prediction," ASME Journal of Applied Mechanics, Vol. 47, 1980, pp. 324–328.

12 Abramowitz, M., and Stegun, I. A., *Handbook of Mathematical Functions*, National Bureau of Standards, 1964.

13 Saunders, S. C., "On the Probabilistic Determination of Scatter Factors Using Miner's Rule in Fatigue Life Studies" in *Probabilistic Aspects of Fatigue*, American Society for Testing and Materials, STP 511, 1972, pp. 185–203.

APPENDIX

Log-Normal Distribution and Statistical Independence of Lifetimes

An extensive set of fatigue test data for 6061-T6 aluminum coupons is quoted in [13]. To check the validity of the log-normal distribution the mean and standard deviation of $\eta = \log N$ have been computed for the test data for $S = 213.8$ MPa. The associated normal CDF is shown in Fig. 7. The points shown indicate percentiles that are above 5, 10, 15 percent, etc., of the data. It is seen that the data conform quite well to the log-normal distribution. A similar examination of steel wire test data [8] also shows very good agreement with log-normality.

To test independence the averages of products of log-lifetimes at different stress levels have been compared with the products of the averages. This is shown in Table 4 and it is seen that the values literally coincide, thus are uncorrelated and therefore also independent.

Table 4 Examination of noncorrelation of log-lifetimes

i	S(MPa)	$\langle\eta\rangle$	ij	$\langle\eta_i \eta_j\rangle$	$\langle\eta_i\rangle\langle\eta_j\rangle$
1	144.8	6.1278	23	34.280	34.271
2	179.3	5.5927	31	31.385	31.375
3	213.8	5.1201	12	28.640	28.635

U. W. Cho
Assistant Professor
of Mechanical and Aerospace Engineering,
University of Missouri-Columbia,
Columbia, Mo. 65211
Assoc. Mem. ASME

W. N. Findley
Professor of Engineering,
Brown University,
Providence, R.I. 02912
Fellow ASME

Creep and Plastic Strains Under Side Steps of Tension and Torsion for 304 Stainless Steel at 593°C

Results of nonproportional stress changes on creep and plastic strains resulting from abrupt changes in proportion of tension and torsion are reported. Both step-up and step-down changes are included. Constitutive equations based on data for single step creep and recovery tests previously reported are used to describe the test results. A viscous-viscoelastic model with aging effects and modifications for step-down tests predicted the creep behavior reasonably well. The prediction of time-independent plastic strains is also described.

Introduction

Creep of metals at high temperature under changing stress states has received little experimental observation, especially for nonproportional load changes. References to prior experimental work in this area through 1978 are given in [1]. More recent experimental work is found in [2–6].

The present paper includes experimental work on a reference heat (no. 9T2796) of 304 stainless steel procured by Oak Ridge National Laboratory. This reference heat of steel is being studied extensively in several laboratories. The microstructure of the reference heat of 304 stainless steel over a wide range of temperature and stress was reported in [7–9] and information on aging was reported in [5].

Creep and creep recovery data at 593°C (1100°F) of the same reference heat were reported and analyzed in recent papers by the authors [4–6]. The analysis employed a viscous-viscoelastic model (V-V theory) in which strain was resolved into four components; elastic ϵ^E, time-independent plastic ϵ^P, time-dependent-recoverable viscoelastic ϵ^{VE}, and time-dependent-nonrecoverable viscous strain ϵ^V. In [4] creep and recovery data for combined tension and torsion at stresses above a transition stress were reported and found to be strongly nonlinear and synergistic. In [5] creep for stresses below the transition stress was found to be essentially linear and aging was found to have a considerable effect and was incorporated in the analysis.

From the constitutive equations, including aging, developed in [4, 5] the results of creep tests under step-up and step-down stress changes were predicted with good accuracy in [6] based on results of constant load creep and creep recovery tests reported in [4, 5].

In the present paper results of nonproportional stress changes consisting of side steps of tension and torsion are presented in which abrupt changes are made in the proportion of tension and torsion. The constitutive equations developed in [4–6] are employed to predict from constant stress tests in [4, 5] the creep and plastic behavior under these complex stress changes.

A subsequent paper will describe creep and plastic strains under stress reversal in torsion with and without simultaneous tension for the same material and test conditions as in the present paper.

Material, Experimental Apparatus, and Procedure

Type 304 stainless steel, reference heat no. 9T2796 supplied by Oak Ridge National Laboratory, was reannealed and machined into thin-walled tubes. The material and specimen are the same as described in references [4–6].

The combined tension and torsion machine using dead weight loading was described in [10]. Specimens were soaked at the testing temperature of 593°C (1100°F) for 20 h prior to loading, which was accomplished in less than 10 sec. Additional details are given in references [4–6, 10].

Experimental Results

Creep-time curves are shown in Figs. 1–5 for combined tension σ and torsion τ and Fig. 5 includes step changes in pure torsion stress. An insert on each figure shows the overall test program and the resulting total strain. Figures 1–4 show results of two combined tension and torsion experiments C41 and C49 in which a proportional loading was applied for 100 h in period 1 followed by recovery at zero stress in period 2. The results in periods 1 and 2 were employed in [4, 5] in determining the constants for the nonlinear and linear portions, respectively, of the stress functions. Since periods 1 and 2 were fully described in [4, 5], results in those periods are not

Contributed by the Applied Mechanics Division for presentation at the Winter Annual Meeting, Boston, Mass., November 13–18, 1983 of the AMERICAN SOCIETY OF MECHANICAL ENGINEERS.

Discussion on this paper should be addressed to the Editorial Department, ASME, United Engineering Center, 345 East 47th Street, New York, N. Y. 10017, and will be accepted until two months after final publication of the paper itself in the JOURNAL OF APPLIED MECHANICS. Manuscript received by ASME Applied Mechanics Division, January, 1982; final revision, January 1983. Paper No. 83-WA/APM-1.

Copies will be available until July, 1984.

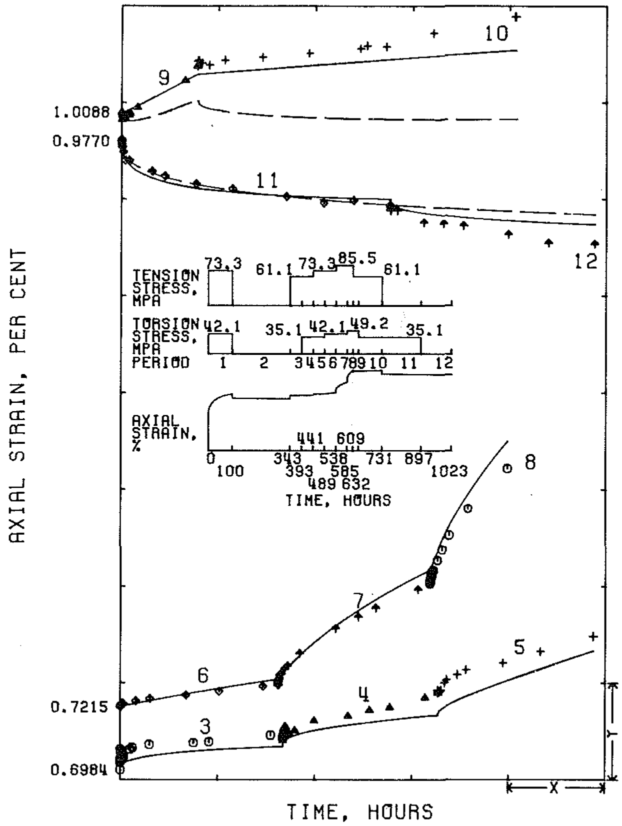

Fig. 1 Test no. C41. Axial strain (CA41) for combined tension and torsion creep of 304 stainless steel at 593°C under side step-up and side step-down stress changes following complete unloading. Numbers 3-12 indicate periods on insert. Scales are X = 30h, Y = 0.01 percent for periods 3-5, 9, 10; X = 30h, Y = 0.08 percent for periods 6-8; and X = 60h, Y = 0.01 percent for periods 11, 12.

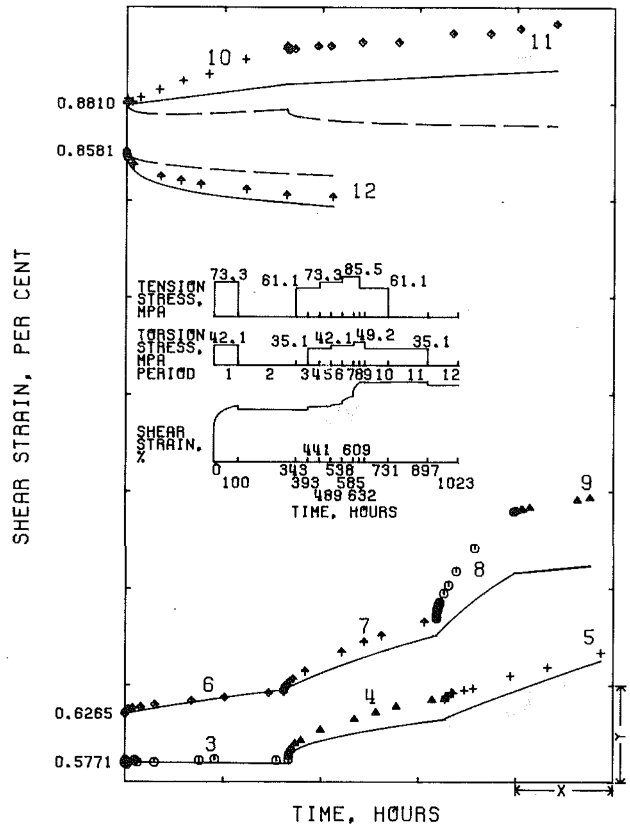

Fig. 2 Test no. C41. Shear strain (CT41) for combined tension and torsion creep of 304 stainless steel at 593°C under side step-up and side step-down stress changes following complete unloading. Numbers 3-12 indicate periods on insert. Scales are X = 30h, Y = 0.01 percent for periods 3-5; X = 30h, Y = 0.08 percent for periods 6-9; and X = 60h, Y = 0.01 percent for periods 10-12.

shown in this paper. Following periods 1 and 2 there were sequences of side steps up then down in which one stress component was held constant while the other was increased or decreased. The effect on the creep corresponding to one unchanging stress component of an increase or decrease in the other component was described in detail in a subsequent section in which the predictions of theory are compared with the test data.

Figure 6 shows the loading history during each test together with the strain trajectories for a selected group of periods for which the current stresses all have the same ratio of tension to torsion but have different prior stress histories. The direction of the strain trajectory (or direction of the strain rate vector) for the first loading of C 41-1 is very nearly that of the normal to the Mises ellipse at the stress point (except for a jog in the curve) (see Figs. 1 and 2 of [4] for creep curves for period 1). For conditions having prior nonproportional stress histories, plastic strain during current loading and a considerable current creep strain rate (C41-8 and C49-5) the strain trajectories nearly coincide with the Mises normal. For conditions having prior nonproportional stress histories, no current plastic strain, and low creep rates (C41-4 and C41-6) the direction of the strain trajectory starts more toward the direction of the most recent change in stress then changes direction toward the Mises normal. C52-3 also follows this pattern but has high creep rate and current plastic strain on loading, but the prior history involved unloading.

Constitutive Equations for Combined Tension and Torsion

The total strain at constant stress was resolved into the following components: elastic strain ϵ_{ij}^E, time-independent plastic strain ϵ_{ij}^P, time-dependent recoverable (viscoelastic) strain ϵ_{ij}^{VE}, and time-dependent nonrecoverable (viscous) strains ϵ_{ij}^V. The time dependence was found to be describable as a power of time t^n. Thus

$$\epsilon_{ij} = \epsilon_{ij}^E + \epsilon_{ij}^P + \epsilon_{ij}^{+VE} t^n + \epsilon_{ij}^{+V} t^n, \tag{1}$$

where ϵ_{ij}^E, ϵ_{ij}^P, ϵ_{ij}^{+VE}, and ϵ_{ij}^{+V} are functions of stress. The stress dependence of ϵ_{ij}^P, ϵ_{ij}^{+VE}, and ϵ_{ij}^{+V} was described, for constant stresses above a transition level, in accordance with a third-order multiple integral representation [11]. In [4] it was shown that there was an apparent limit stress for ϵ_{ij}^{+VE} and ϵ_{ij}^{+V} as well as a yield limit for ϵ_{ij}^P. Incorporating a limit stress, the stress dependence of these terms for combined axial and shear (torsion) stresses had the following forms for the axial ϵ_{11} and shear ϵ_{12} strain components,

$$\epsilon_{11} = F(\sigma,\tau) = F_1(\sigma-\sigma') + F_2(\sigma-\sigma')^2 + F_3(\sigma-\sigma')^3 + F_4(\sigma-\sigma')(\tau-\tau')^2 + F_5(\tau-\tau')^2, \tag{2}$$

$$\epsilon_{12} = G(\sigma,\tau) = G_1(\tau-\tau') + G_2(\tau-\tau')^3 + G_3(\sigma-\sigma')(\tau-\tau') + G_4(\sigma-\sigma')^2(\tau-\tau'), \tag{3}$$

where ϵ_{ij}, F, G, σ', and τ' assume superscripts P, VE, or V according to whether plastic P, viscoelastic VE, or viscous V strains are being described, and where σ' and τ' are the components of the plastic or creep limits. $F(\sigma,\tau) = G(\sigma,\tau) = 0$ for $-\sigma' < \sigma < \sigma'$, $-\tau' < \tau < \tau'$. As shown in [4] these limits were describable by a Mises relation and were calculated from the limits for pure tension σ^* and/or pure torsion τ^*. The values of F, G, σ^*, and τ^* are given in Table 1 of reference [4] for each of the three strain components ϵ_{ij}^P, ϵ_{ij}^{VE}, and ϵ_{ij}^V.

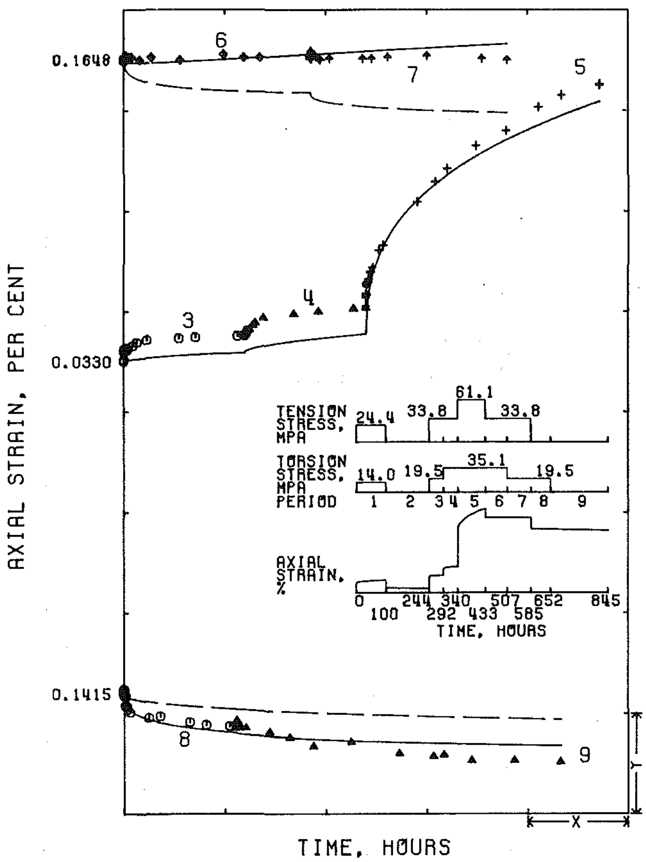

Fig. 3 Test no. C49. Axial strain (CA49) for combined tension and torsion creep of 304 stainless steel at 593°C under side step-up and side step-down stress changes following complete unloading. Numbers 3-9 indicate periods on insert. Scales are $X = 40h$, $Y = 0.02$ percent for periods 3-5; $X = 40h$, $Y = 0.007$ percent for periods 6, 7; and $X = 60h$, $Y = 0.007$ percent for periods 8, 9.

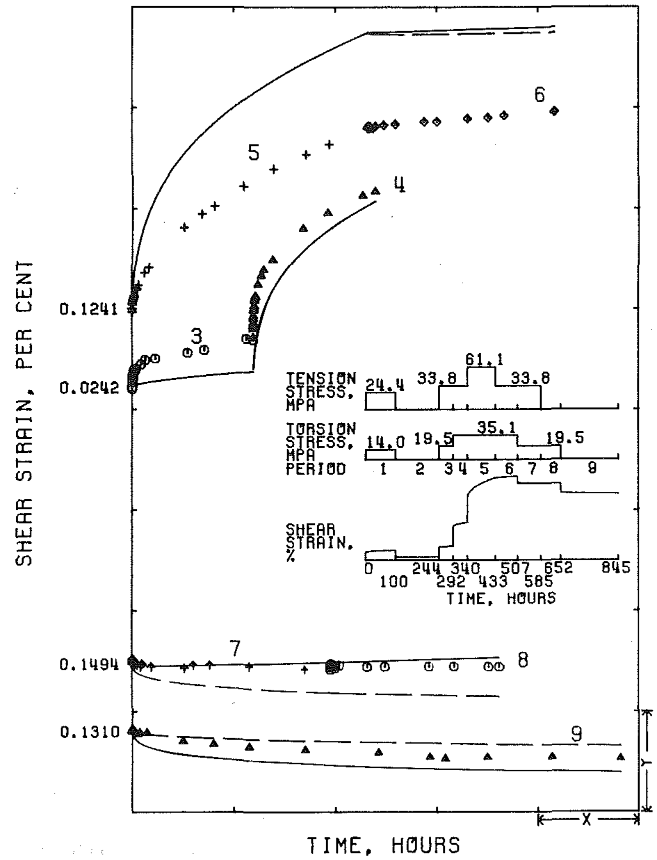

Fig. 4 Test no. C49. Shear strain (CT49) for combined tension and torsion creep of 304 stainless steel at 593°C under side step-up and side step-down stress changes following complete unloading. Numbers 3-9 indicate periods on insert. Scales are $X = 40h$, $Y = 0.007$ percent for periods 3, 4, 7-9; and $X = 40h$, $Y = 0.02$ percent for periods 5,6.

Below a transition stress it was shown in [5] that the behavior was essentially linear and nonsynergistic. Thus the strain components in this stress range were given by

$$\epsilon_{11} = F(\sigma,\tau) = F_0\sigma, \quad \sigma < \sigma^T, \tag{4}$$

$$\epsilon_{12} = G(\sigma,\tau) = G_0\tau, \quad \tau < \tau^T, \tag{5}$$

where, σ^T and τ^T are the transition stresses and where the values of F_0, G_0, σ^T, and τ^T for ϵ_{ij}^{+VE} and ϵ_{ij}^{+V} were determined as shown in the text of reference [5].

Constitutive Equations for Variable Stress

Plastic Strain. The time-independent strain at each stress change in Figs. 1-5 consisted of the sum of the elastic ϵ_{ij}^E and plastic ϵ_{ij}^P strains. Plastic strain occurred on initial loading to stresses above the yield limit in accordance with equations (2) or (3) with superscripts of P. On subsequent loading, plastic strain was considered to occur only when stressed higher than the previous maximum. The new plastic strain increment was computed by equations (2) or (3) minus the plastic strain accumulated prior to the current loading. No interaction between the plastic and time-dependent strains was considered in the present analysis. Aging was found to have a considerable effect of reducing plastic strain [5]. Aging was included in equations (2) and (3) by multiplying each term by g^P (t_s) as given in [6].

Viscoelastic and Viscous Strain. Employing the modified superposition principle (MSP) [11] the viscoelastic strain ϵ_{ij}^{VE} for a continuously varying stress is given by

Table 1 Total time-independent strain data

Test (Fig. No.)	Period	Change in Stress: Tension, σ MPa	Tension, σ ksi	Torsion, τ MPa	Torsion, τ ksi	Axial strain, percent	Shear strain, percent
	1	73.3	10.628	42.1	6.111	0.4333	0.3576
	2	-73.3	-10.628	-42.1	-6.111	-0.0494	-0.0393
CA41	3	61.1	8.857	0.0	0.0	0.0401	0.0001
(Fig. 1)	4	0.0	0.0	35.1	5.093	0.0002	0.0311
	5	12.2	1.771	0.0	0.0	0.0076	-0.0001
and	6	0.0	0.0	7.0	1.018	0.0014	0.0071
	7	12.2	1.771	0.0	0.0	0.0483	0.0275
CT41	8	0.0	0.0	7.1	1.019	0.0575	0.0593
(Fig. 2)	9	-24.4	-3.542	0.0	0.0	-0.0157	0.0004
	10	0.0	0.0	-14.1	-2.037	0.0	-0.0111
	11	-61.1	-8.857	0.0	0.0	-0.0414	0.0028
	12	0.0	0.0	-35.1	-5.093	0.0004	-0.0337
	1	24.4	3.543	14.0	2.037	0.0196	0.0144
CA49	2	-24.4	-3.543	-14.0	-2.037	-0.0164	-0.0129
(Fig. 3)	3	33.8	4.909	19.5	2.823	0.0232	0.0180
	4	0.0	0.0	15.6	2.270	0.0139	0.0355
and	5	27.3	3.948	0.0	0.0	0.0820	0.0506
	6	-27.3	-3.948	0.0	0.0	-0.0191	0.0
CT49	7	0.0	0.0	-15.6	-2.270	-0.0001	-0.0139
(Fig. 4)	8	-33.8	-4.909	0.0	0.0	-0.0230	0.0
	9	0.0	0.0	-19.5	-2.823	0.0001	-0.0180
	1	0.0	0.0	49.8	7.217	0.0	0.1628
C52	2	0.0	0.0	-14.7	-2.124	0.0	-0.0127
(Fig. 5)	3	61.1	8.857	0.0	0.0	0.1219	0.0202
	4	0.0	0.0	-35.1	-5.093	0.0027	-0.0328

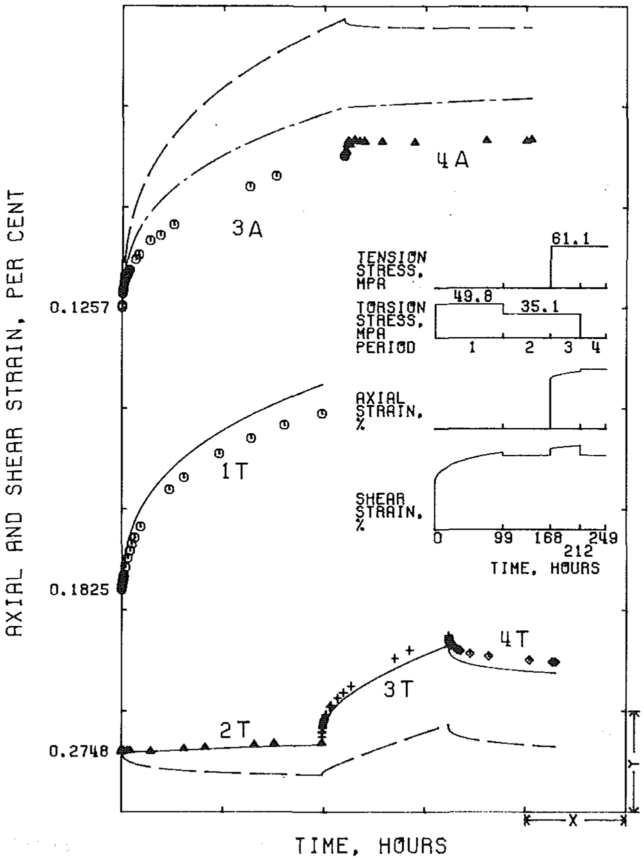

Fig. 5 Test no. C52. Axial (CA52) and shear (CT52) strain for combined *tension and torsion creep of 304 stainless steel at 593°C under side* step-up and side step-down stress changes following a step-down stress change in pure torsion. Numbers 1-4 indicate periods on insert. Scales are X = 20h, Y = 0.015 percent for periods 3A, 4A, axial strain; X = 35h, Y = 0.06 percent for period 1T; and X = 35h, Y = 0.015 percent for periods 2T-4T, shear strain.

$$\epsilon^{VE} = \int_0^t \frac{\partial f[\sigma(\xi), t-\xi]}{\partial\, \sigma(\xi)}\, \dot{\sigma}(\xi)\, d\xi. \tag{6}$$

The nonrecoverable viscous strain ϵ_{ij}^{V} was described by a strain-hardening (SH) relation having the following form for axial strain,

$$\epsilon_{11}^{V} = \left[\int_0^t \{F^V[\sigma(\xi), \tau(\xi)]\}^{1/n} d\xi \right]^n . \tag{7}$$

For the third step of a three-step sequence with stress changes at t_1 and t_2, equations (6) and (7) yield the following [11] after introducing the aging functions as found in [5].

$$\begin{aligned} \epsilon_{11}^{VE}(t) = {} & g^{VE}(20)\, F^{VE}(\sigma_1, \tau_1)[t^n - (t-t_1)^n] \\ & + g^{VE}(20+t_1)\, F^{VE}(\sigma_2,\tau_2)[(t-t_1)^n - (t-t_2)^n] \\ & + g^{VE}(20+t_2)\, F^{VE}(\sigma_3,\tau_3)(t-t_2)^n, \quad t_2 < t, \end{aligned} \tag{8}$$

where $g^{VE}(t_s) = 1.5197\ t_s^{\ -0.1397}$, and $g^{VE}(t_s) = 1$ at $t_s = 20$ h.

$$\begin{aligned} \epsilon_{11}^{V}(t) = {} & g^V(20+t_2)[\{[\epsilon_{11}^V(t_2)]^{1/n} + [F^V(\sigma_3,\tau_3)]^{1/n}(t-t_2)\}^n \\ & - \epsilon_{11}^V(t_2)] + \epsilon_{11}^V(t_2), \end{aligned} \tag{9}$$

where

$$\begin{aligned} \epsilon_{11}^V(t_2) = {} & g^V(20+t_1)[\{[\epsilon_{11}^V(t_1)]^{1/n} \\ & + [F^V(\sigma_2,\tau_2)]^{1/n}(t_2-t_1)\}^n - \epsilon_{11}^V(t_1)] + \epsilon_{11}^V(t_1) \\ \epsilon_{11}^V(t_1) = {} & g^V(20)\{[F^V(\sigma_1,\tau_1)]^{1/n} t_1\}^n, \\ g^V(t_s) = {} & 1.8293\ t_s^{\ -0.2016} \text{ and } g^V(t_s) = 1 \text{ at } t_s = 20 \text{ h}. \end{aligned}$$

Similarly, ϵ_{12}^V was obtained by replacing $F(\sigma,\tau)$ by $G(\sigma,\tau)$ in equations (8) and (9).

Comparison of Predictions and Test Data

The time-independent strain $(\epsilon_{ij}^E + \epsilon_{ij}^P)$ and the time-dependent strain $(\epsilon_{ij}^{VE} + \epsilon_{ij}^V)$ were treated separately in com-

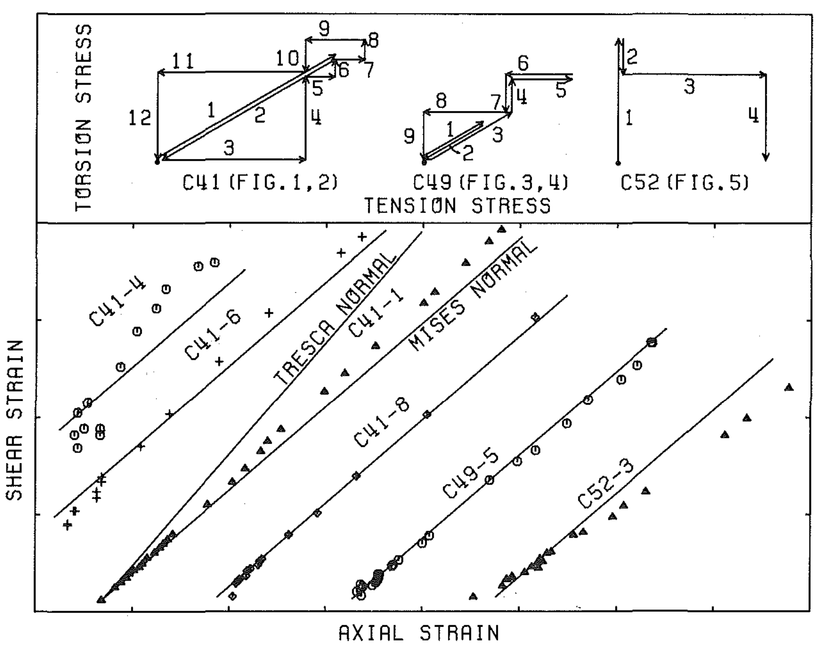

Fig. 6 Stress path diagram (the dot indicates the zero stress state and the numbers indicate loading periods) and strain trajectories (ϵ_{12} versus ϵ_{11})

Table 2 Plastic strain

Test, Strain Component (Fig. No.)	Period	Change in Stress: Tension, σ MPa	Tension, σ ksi	Torsion, τ MPa	Torsion, τ ksi	Aging Time, t_s, h	Aging Factor*, $g^P(t_s)$	Plastic Strain: Data, %	Prediction without Aging, %	Prediction with Aging, %: Pure Term	Mixed Term	Total
CA41, ϵ_{11}	1	73.3	10.628	42.1	6.111	20	1.000	0.3847	0.4075	0.1933	0.2141	0.4075
(Fig. 1)	7	12.2	1.771	0.0	0.0	558	0.680	0.0401	0.2888	0.1167	0.0799	0.1965
	8	0.0	0.0	7.1	1.019	605	0.674	0.0575	0.3014	0.0529	0.1501	0.2030
CT41, ϵ_{12}	1	73.3	10.628	42.1	6.111	20	1.000	0.3186	0.3207	0.1818	0.1389	0.3207
(Fig. 2)	7	12.2	1.771	0.0	0.0	558	0.680	0.0275	0.1465	0.0235	0.0761	0.0997
	8	0.0	0.0	7.1	1.019	605	0.674	0.0530	0.2302	0.0819	0.0731	0.1550
CA49, ϵ_{11}	4	0.0	0.0	15.6	2.270	312	0.728	0.0139	0.0350	0.0223	0.0032	0.0255
(Fig. 3)	5	27.3	3.948	0.0	0.0	360	0.716	0.0636	0.1040	0.0397	0.0346	0.0744
CT49, ϵ_{12}	4	0.0	0.0	15.6	2.270	312	0.728	0.0214	0.0405	0.0283	0.0011	0.0295
(Fig. 4)	5	27.3	3.948	0.0	0.0	360	0.716	0.0506	0.0802	0.0339	0.0234	0.0573
CA52, ϵ_{11}	3A	61.1	8.857	0.0	0.0	188	0.771	0.0807	0.1390	0.0665	0.0407	0.1072
CT52, ϵ_{12}	1T	0.0	0.0	49.8	7.217	20	1.000	0.1180	0.1480	0.1480	0.0	0.1480
(Fig. 5)	3T	61.1	8.857	0.0	0.0	188	0.771	0.0202	0.0343	0.0	0.0264	0.0264

* $g^P(t_s) = 1.4147\, t_s^{-0.1158}$

paring predictions with experimental data. The predictions of time-independent strain were obtained by adding the current elastic strain ϵ_{ij}^E to the plastic strain ϵ_{ij}^P calculated as described previously using constants shown in references [4, 5]. The predicted time-dependent strains were obtained as the sum of equations similar to equation (8) plus equations similar to equation (9) using constants given in Table 1 of reference [4]. All constants were obtained from constant stress creep and recovery data only, as reported in [4, 5].

The predicted results of the *V-V* theory as in the foregoing, together with actual test data are shown in Figs. 1–5. Theory is shown by dash lines. If the theory curves are the same as the improved theory curves described later, only solid lines are shown. For comparison of the predictions with the test data, the time-dependent creep strain data were extracted from the measured total strain as described in [6]. This approach made the first data point following each load change coincide with the theory at the time of the first reading. It is noted that for some continuous sequences of periods such as periods 6–8, Fig. 1, the time-dependent strains only are connected for each period, and the comparison between theory and data are based on each individual periods – rather than the accumulated effect.

Also the data for the time-independent strain at each stress change was obtained as the amount of strain change from the last data point of the previous period (just before load change) to the zero time data of the creep strain of the current period (just after load change) corrected as described in [6]. The resulting time-independent strain data are shown in the seventh and eighth column of Table 1 for axial and shear strains, respectively. The data for plastic strain shown in column 9, Table 2, was obtained by the total time-independent strain minus the elastic strain. The predictions of time-independent plastic strain by equations (2) and (3) without and with aging are given in Table 2. The numbers given as ordinates in Figs. 1–5 indicate the total strain of the first data point shown.

Modifications of (*V-V*) Theory

From the comparisons of the theory with test data, shown in Figs. 1–5, substantial disagreements between theory and data were found for the cases of side step-down stress changes as in periods 9 and 10, Fig. 1, and periods 6 and 7, Fig. 3, where the creep data increased at a reduced rate, but the predicted strain decreased.

As in [6] for partial unloadings in pure tension or pure torsion, the following similar revisions were made to improve the predictions for side step-down stress changes.

Equation (8) represents an open form in so far as stress changes are concerned. For example $\{F^{VE}(\sigma_1,\tau_1) - F^{VE}(\sigma_2,\tau_2)\}(t-t_1)^n$ is an open form. The open form was found satisfactory [6] for increasing steps of stress components. However, as shown in [6] a closed form was required for decreasing steps in stress. For example, $F^{VE}(\sigma_1-\sigma_2,\tau_1-\tau_2)(t-t_1)^n$ is the closed form employed.

The revised superposition principle (RSP) employing the closed form on decreasing steps of stress involving partial unloading yields the following for three steps of unloading equivalent to equation (8),

$$\begin{aligned}\epsilon_{11}^{VE}(t) &= g^{VE}(20)\,F^{VE}(\sigma_1,\tau_1)t^n \\ &- g^{VE}(20)\,F^{VE}(\sigma_1-\sigma_2,\tau_1-\tau_2)(t-t_1)^n \\ &- g^{VE}(20+t_1)\,F^{VE}(\sigma_1-\sigma_3,\tau_1-\tau_3)(t-t_2)^n \\ &- g^{VE}(20+t_2)\,F^{VE}(\sigma_2-\sigma_4,\tau_2-\tau_4)(t-t_3)^n. \qquad (10)\end{aligned}$$

In equation (10) for a series of partial unloadings $F^{VE}(\sigma_1-\sigma_3,\tau_1-\tau_3)$ was used instead of $F^{VE}(\sigma_2-\sigma_3,\tau_2-\tau_3)$ for the second step-down, etc. That is, the creep recovery for all but the first step down of a series of step downs in stress was calculated on the basis of stress changes from one step before the previous to the current stress, as described in [6].

Also further considerations were made on the computation of $F^{VE}(\sigma,\tau)$ for step-down stress changes by separating the pure stress terms and the mixed stress terms in equations (2) and (3). For example, when σ decreased while τ remained constant, $F^{VE}(\sigma,\tau)$ was calculated only by the pure stress terms $(\sigma,\sigma^2,\sigma^3)$ neglecting the mixed stress terms $(\sigma\tau^2,\tau^2)$; and $G^{VE}(\sigma,\tau)$ was calculated only by the mixed stress terms $(\sigma\tau,\sigma^2\tau)$ neglecting the pure stress terms (τ,τ^3).

The preceding calculations are an approximate compensation for the difference in behavior between side step-down stress changes versus step-down stress changes when both σ and τ decreased at the same time.

The new predicted time-dependent strains (RSP) were obtained as the sum of equations similar to equation (9) plus equations similar to equation (8) when the stress increased or equation (10) (separating pure and mixed stress terms) when the stress decreased. The (RSP) curves are shown as solid lines in Figs. 1–4 and periods $1T$–$4T$, Fig. 5.

As shown in Figs. 1–5, the revised superposition principle (RSP), equation (10), improved the overall predictions considerably compared to the (MSP), equation (8), for side step-down stress changes under combined tension and torsion. All characteristics of the experimental time-dependent data are displayed by the theory and the predicted values are reasonably close in most instances.

On complete removal of one stress component while the other remained constant, the creep component corresponding to the stress that did not change showed no change in period 8, Fig. 4, but showed a lower rate in period 11, Fig. 2, and period $4A$, Fig. 5. The predictions of the theory using (RSP) are close to the data. These results in Fig. 2 and 5 differ from the behavior of 2618 aluminum [3] in which several observations showed no change in creep rate of the strain component whose stress component was not removed.

When one stress component was reduced (not removed) while the other component remained constant the creep rate of the component corresponding to the constant stress component was reduced. The creep rate predicted by the theory using (RSP) was close to but less than that of the observed test data in periods 10, Fig. 1, and 9, Fig. 2. This behavior also differs from that observed under similar circumstances for 2618 aluminum [3], where no change was found in the creep rate of the component of creep corresponding to the stress component that was not reduced.

Effect of Prior Yielding

In periods 3 and 4, Figs. 1 and 2, tension was applied for a period then torsion was added with no change in tension. In these instances there was no plastic strain during these loadings (because higher stresses had been sustained previously). In period 4, Fig. 2, the theory predicts a somewhat lower creep rate than observed. In the similar instances, period $3A$, Fig. 5, tension was added with no change in torsion. In this loading there was a substantial plastic strain as shown in Table 2. The (V-V) theory shown by a dashed line in period $3A$, Fig. 5, predicts much greater creep than observed. This is apparently due to plastic flow during the prior torsion loading (period $1T$, Fig. 5). In period 4, Fig. 4, there was no prior plastic flow and the predicted creep rate was about the same as the observed.

As a partial correction for the effect of the prior plastic flow under a different state of stress, the theory for period $3A$, Fig. 5, was recalculated as shown by a dot-dash line by considering only the pure tension terms σ, σ^2, σ^3. Clearly this change is insufficient to account for the work hardening caused by prior plastic flow under a different stress state. Further work on the effect of prior plastic flow on subsequent creep is needed.

Plastic Strains

The side-step change of stress in period 4, Figs. 3 and 4 (Test C49), may be considered to be equivalent to an initial proportional loading as far as plastic strain is concerned since the prior loadings were all below the yield limit. The predicted plastic strains for periods 4 and 5 of test C49, Table 2, were close to the experimental data as was also true of period 1, test C41. However, the latter would be expected as the data of period 1, Test C41, were employed in [4] to determine the constants used in the prediction.

Nonproportional loading, as in abrupt changes of combined tension and torsion, which cause additional yielding under a different stress state, may involve changes in the size and shape of yield surface [12, 13] and accordingly changes in plastic flow conditions. This may account for the poor agreement between the predictions of plastic strains and the test data for periods 7 and 8 of Test C41, Table 2. Another contributing factor may have been the rather large plastic strain in period 1, Test 41. Another observation may be drawn from these data. The plastic strain corresponding to the pure stress terms may be separated from that for the mixed stress terms in equations (2) and (3) as shown in Table 2. Comparing the test data for periods 7 and 8 of Test C41, Table 2, with the calculated plastic strain components for pure stress and mixed stress terms as shown in Table 2 yields the following correlations. For an increase in σ with constant τ (periods 6 to 7) the data for ϵ_{11}^P was close to the prediction for the mixed stress terms. But for an increase of τ with constant σ (periods 7, 8) ϵ_{11}^P was close to the prediction by the pure stress term. Similarly for an increase of τ with constant σ (periods 7, 8) the data for ϵ_{12}^P was close to the prediction by the mixed stress terms. But for an increase in σ with constant τ (periods 6, 7) ϵ_{12}^P was close to the prediction by the pure stress terms. No similar correlation was found for period 5 of Test C49, Table 2, where the total plastic strain was small compared to that in Test C41.

Conclusions

Analysis of creep data of 304 stainless steel at 593°C (1100°F) under combined tension and torsion for varying stress history including side step-up and side step-down stress changes showed that a viscous-viscoelastic model with certain modifications and aging effects predicted most of the features of the observed creep behavior reasonably well.

For recoverable time-dependent (viscoelastic) strain side step-up stress changes were described by an open form for stress differences whereas side step-down stress changes were described by a closed form for stress differences.

For nonrecoverable time-dependent (viscous) strain the prior plastic flow under one stress component preceding application of the other stress component caused a considerable reduction of the subsequent creep due to the other stress application.

Time-independent plastic strains were described reasonably well by a flow rule of form similar to that employed for nonrecoverable time-dependent strains. But the plastic flow on side step-up stress changes needs further study including determination of changes in yield surface.

Acknowledgments

This work was supported by the National Science Foundation under Grant No. ENG76-02519. The early experimental work on this project was supported and all material tested was supplied by the Oak Ridge National Laboratory. The authors are grateful to R. M. Reed for assistance in experiments and Mrs. P. C. Capece for typing the manuscript.

References

1 Findley, W. N., Cho, U. W., and Ding, J. L., "Creep of Metals and Plastics Under Combined Stresses, A Review," ASME *Journal of Engineering Materials and Technology*, Vol. 101, 1979, pp. 365–368.

2 Lai, J. S., and Findley, W. N., "Creep of 2618 Aluminum Under Step Stress Changes Predicted by a Viscous-Viscoelastic Model," ASME Journal of Applied Mechanics, Vol. 47, 1980, pp. 21–26.

3 Findley, W. N., and Lai, J. S., "Creep of 2618 Aluminum Under Side-Steps of Tension and Torsion and Stress Reversal Predicted by a Viscous-

Viscoelastic Model," ASME JOURNAL OF APPLIED MECHANICS, Vol. 48, 1981, pp. 47–54.

4 Cho, U. W., and Findley, W. N., "Creep and Creep Recovery of 304 Stainless Steel Under Combined Stress With a Representation by a Viscous-Viscoelastic Model," ASME JOURNAL OF APPLIED MECHANICS, Vol. 47, 1980, pp. 755–790.

5 Cho, U. W., and Findley, W. N., "Creep and Creep Recovery of 304 Stainless Steel at Low Stresses With Effects of Aging on Creep and Plastic Strains," ASME JOURNAL OF APPLIED MECHANICS, Vol. 48, 1981, pp. 785–790.

6 Cho, U. W., and Findley, W. N., "Creep and Plastic Strains of 304 Stainless Steel at 593°C Under Step Stress Changes, Considering Aging," ASME JOURNAL OF APPLIED MECHANICS, Vol. 49, 1982, pp. 297–304.

7 Bhargava, R., Moteff, J., and Swindeman, R. W., "Correlation of the Microstructure With the Creep and Tensile Properties of AISI 304 Stainless Steel," ASME *Symposium on Structural Materials for Service at Elevated Temperatures in Nuclear Power Generation*, Doc. MPC-1, 1975, pp. 31–54.

8 Swindeman, R. W., Bhargava, R., Sikka, V. K., and Moteff, J., "Substructures Developed During Creep and Cyclic Tests of Type 304 Stainless Steel" (Heat 9T2796), Oak Ridge National Laboratory, ORNL-5293, Sept. 1977.

9 Swindeman, R. W., "Correlation of Rupture Life, Creep Rate, and Microstructure for Type 304 Stainless Steel," Oak Ridge National Laboratory, ORNL-5523, June 1979.

10 Findley, W. N., and Gjelsvik, A., "A Biaxial Testing Machine for Plasticity, Creep, or Relaxation Under Variable Principal-Stress Ratios," *Proceedings, ASTM*, Vol. 62, 1962, pp. 1103–1118.

11 Findley, W. N., Lai, J. S., and Onaran, K., *Nonlinear Creep and Relaxation of Viscoelastic Materials, With an Introduction to Linear Viscoelasticity*, North Holland, Amsterdam, 1976.

12 Michno, M. J., Jr., and Findley, W. N., "Experiments to Determine Small Offset Yield Surfaces for 304L Stainless Steel Under Combined Tension and Torsion," *Acta Mechanica*, Vol. 18, 1973, pp. 163–179.

13 Michno, M. J., Jr., and Findley, W. N., "An Historical Perspective of Yield Surface Investigations for Metals," *International Journal of Nonlinear Mechanics*, Vol. 11, 1976, pp. 59–82.

U. W. Cho
Assistant Professor of Mechanical and Aerospace Engineering, University of Missouri-Columbia, Columbia, Mo. 65211
Assoc. Mem. ASME

W. N. Findley
Professor of Engineering, Brown University, Providence, R.I. 02912
Fellow ASME

Creep and Plastic Strains Under Stress Reversal in Torsion With and Without Simultaneous Tension for 304 Stainless Steel at 593°C

Results of creep experiments under stress reversals in torsion with and without constant tension are reported. Constitutive equations based on data for single step creep and creep recovery tests previously reported are used to describe the test results. A viscous-viscoelastic model with aging effects and modifications for step-down stress changes and stress reversals predicted the creep behavior reasonably well. The prediction of time-independent plastic strains is also described.

Introduction

Results of creep experiments under combined tension and torsion on 304 stainless steel at 593°C (1100°F) have been reported by the authors. Creep and creep recovery data at moderate stresses [1] and low stresses [2] together with aging experiments [2] provided information on the creep characteristics of the material. A nonlinear viscous-viscoelastic model [1, 2] was employed in describing the creep characteristics. This information was then used together with a strain-hardening concept for nonrecoverable time-dependent strain and viscoelastic behavior for recoverable time-dependent strain to predict creep and plastic strains under step changes in stress with aging [3]. In another paper [4], creep and plastic strains were predicted for combined tension and torsion creep involving nonproportional step changes in stress including increasing or decreasing one stress component while the other component remained constant. These predictions were compared with actual test data.

In the present paper results of creep tests consisting of reversals of torsion stress with and without simultaneous tension are reported. Partial reversal and overreversal of stresses were also included. These results are compared with predictions based on results of the constant stress creep and creep recovery tests just described.

In all of this work, the experiments were performed on specimens from the same lot of steel: the "reference heat 9T2796." A study of the microstructure of the same reference heat of 304 stainless steel over a wide range of temperature and stress was reported in [5–7]. Earlier work on creep of 2618 aluminum under stress reversals in torsion was reported in [8].

Material, Experimental Apparatus, and Procedure

Type 304 stainless steel, reference heat no. 9T2796 supplied by Oak Ridge National Laboratory, was reannealed and machined into thin-walled tubes. A description of the material and specimens is given in references [1–3]. The material used is the same as in references [1–4].

The combined tension and torsion machine using dead weight loading was described in [9]. The specimen was soaked at the testing temperature of 593°C (1100°F) for 20 h prior to loading, which was accomplished in less than 10 sec. Additional details are given in references [1–3, 9].

Experimental Results

Three creep experiments, which include stress reversals in torsion, are shown in Figs. 1–3. The loading programs and resulting total strain-time data are shown as inserts in Figs. 1–3.

Data and theory for periods 1–4 of Fig. 1 were reported in [4]. When torsion was reversed in period 5 with no change in tension new plastic strain occurred in tension (and torsion) followed by new primary creep whose time-dependent strain was nearly the same as that in period 3, Figs. 1(*a*), (*b*). During tensile recovery in periods 6 and 7 of Fig. 1(*a*), a new primary-type accelerated strain recovery in "tension" resulted when the reversed torsion was increased in period 7. On removal of tension in period 6 of Fig. 1(*b*) there was a small reduction in shear creep rate (negative).

The tensile strain under constant tension in Fig. 2(*a*) showed new plastic strain and considerable new primary creep when torsion was added in period 2. Under constant tension but reversing torsion in periods 3–5 the tensile strain showed new plastic strain and small new primary creep at each reversal of torsion. On removing tension while maintaining

Contributed by the Applied Mechanics Division for presentation at the Winter Annual Meeting, Boston, Mass., November 13–18, 1983 of The American Society of Mechanical Engineers.

Discussion on this paper should be addressed to the Editorial Department, ASME, United Engineering Center, 345 East 47th Street, New York, N.Y. 10017, and will be accepted until two months after final publication of the paper itself in the Journal of Applied Mechanics. Manuscript received by ASME Applied Mechanics Division, August, 1982; final revision, January, 1983. Paper No. 83-WA/APM-2.

Copies will be available until July, 1984.

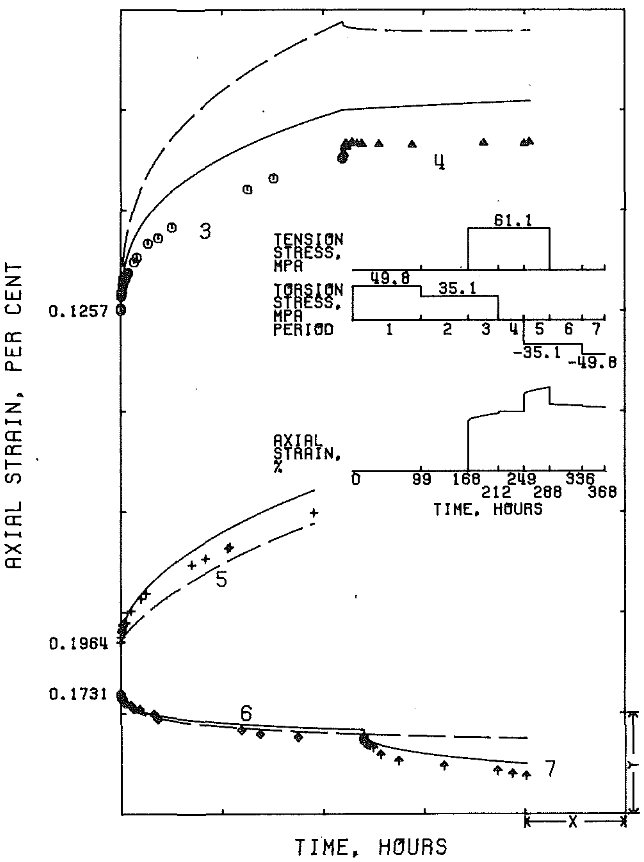

Fig. 1(*a*) **Test no. 52. Axial strain for combined tension and torsion creep of 304 stainless steel at 593°C under step-up and step-down stress changes including stress reversal in torsion with constant tension. Numbers 3-7 indicate periods on insert. Scales are $X = 20$ h, $Y = 0.015$ percent for periods 3-5, and $X = 20$ h, $Y = 0.01$ percent for periods 6 and 7.**

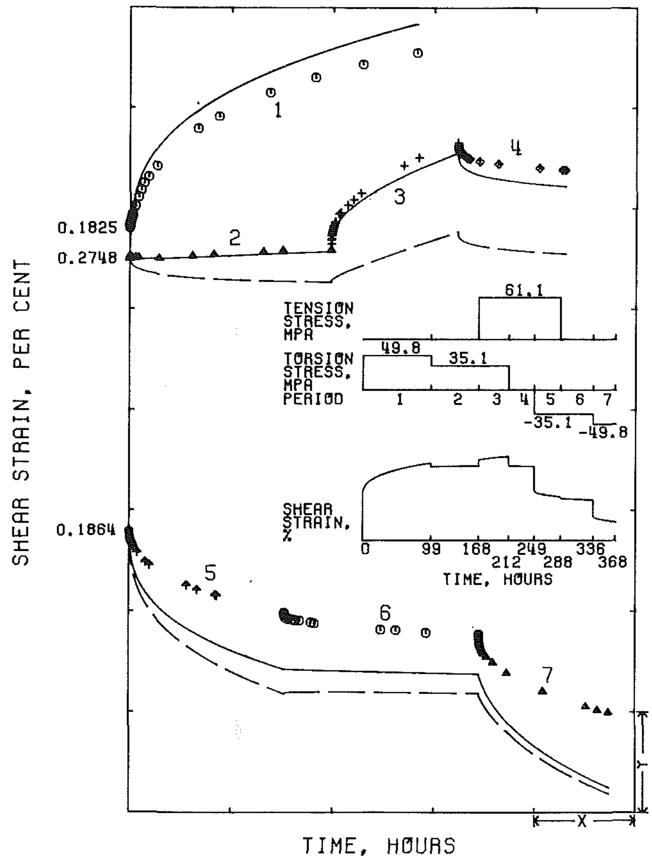

Fig. 1(*b*) **Test no. 52. Shear strain for combined tension and torsion creep of 304 stainless steel at 593°C under step-up and step-down stress changes including stress reversal in torsion with constant tension. Numbers 1-7 indicate periods on insert. Scales are $X = 35$ h, $Y = 0.06$ percent for period 1; $X = 35$ h, $Y = 0.015$ percent for periods 2-4; and $X = 25$ h, $Y = 0.03$ percent for periods 5-7.**

Fig. 1

torsion constant in period 6, tensile recovery occurred at a rate that was slightly increased when torsion was removed in period 7.

In Fig. 2(*b*), plastic strain in torsion occurred on adding torsion to the constant tension and on each reversal of torsion. The complete reversal of torsion in periods 2 and 3 resulted in nearly identical time-dependent creep strain in each period (but of opposite sign). Similarly, the time-dependent creep in periods 4 and 5 were nearly identical, but showed less creep than periods 2 and 3. In other words, positive creep in period 4 was affected by the prior positive stressing in period 2 and similarly, period 5 was affected by period 3 stressing. But apparently prior positive creep, period 2, did not affect negative creep in period 3, and similarly for periods 4 and 5.

The pure torsion stressing in Fig. 3 again showed nearly identical time-dependent creep between the first stressing in period 1 and the first complete reversal in period 2. It was also observed that the creep in period 6 at the same stress as in periods 1 and 2 but following period 5 at a higher stress was only slightly less than that observed in periods 1 and 2. Plastic strain occurred at each stress reversal in Fig. 3.

Analysis

The total strain at constant stress was resolved into the following components: elastic strain ϵ_{ij}^E, time-independent plastic strain ϵ_{ij}^P, time-dependent recoverable (viscoelastic) strain ϵ_{ij}^{VE}, and time-dependent nonrecoverable (viscous) strain ϵ_{ij}^V with independent positive and negative parts. The time dependence was found to be well represented for this material by a power function of time with a constant exponent n [1]. Thus,

$$\epsilon_{ij} = \epsilon_{ij}^E + \epsilon_{ij}^P + \epsilon_{ij}^{+VE} t^n + \epsilon_{ij}^{+V} t^n, \tag{1}$$

where ϵ_{ij}^E, ϵ_{ij}^P, ϵ_{ij}^{+VE}, and ϵ_{ij}^{+V} are functions of stress. As shown in [1, 2] the stress dependence of ϵ_{ij}^{+VE} and ϵ_{ij}^{+V} was described, for constant stresses above a transition level, in accordance with a third-order, nonlinear, multiple integral representation [10], and below the transition stress, it was described by a linear relation. The constants of the relations were obtained from a series of constant-stress creep and creep recovery experiments under combined tension and torsion. This information was used in predicting the creep behavior under variable stress in [3, 4] by a method summarized in the following.

Plastic Strain ϵ_{ij}^P. Plastic strain occurred on initial loading to stresses above the yield limit, see [1, 3]. On subsequent loading, plastic strain was considered to occur only when stressed higher than the previous maximum. The new plastic strain increment was computed by equations (2) and (3) of reference [4] minus the plastic strain accumulated prior to the current loading. No interaction between the plastic and time-dependent strains was considered in the present analysis. Aging considerably reduced the plastic strain. Aging was included as shown in equation (16) of reference [3].

Viscoelastic Strain ϵ_{ij}^{VE}. Employing the modified superposition principle (MSP) [10], the strain for a series of steps in stress is described as follows for axial strain ϵ_{11}^{VE} for three steps of stress, for example,

$$\epsilon_{11}^{VE}(t) = g^{VE}(20)\, F^{VE}(\sigma_1,\tau_1)\, [t^n - (t-t_1)^n] + g^{VE}(20+t_1)\, F^{VE}(\sigma_2,\tau_2)\, [(t-t_1)^n - (t-t_2)^n] + g^{VE}(20+t_2)\, F^{VE}(\sigma_3,\tau_3)\, (t-t_2)^n,\ t_2 < t, \quad (2)$$

where t is the time measured from first load application, and where the following aging function was introduced, $g^{VE}(t_s) = 1.5197\, t_s^{-0.1397}$, equation (12) of [3], where $g^{VE}(t_s) = 1$ at $t = 20$ h.

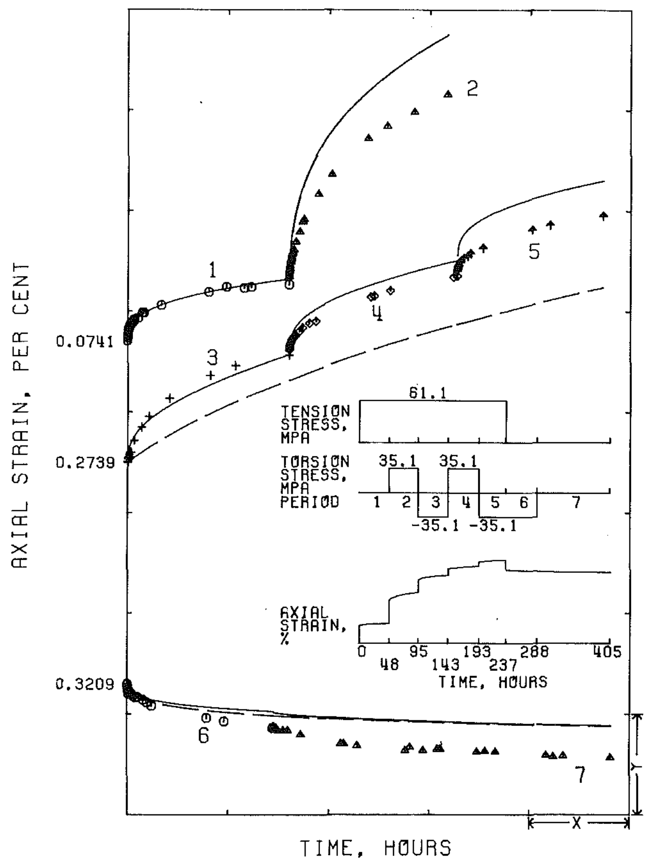

Fig. 2(*a*) Test no. 53. Axial strain for combined tension and torsion creep of 304 stainless steel at 593°C under stress reversals in torsion with constant tension. Numbers 1-7 indicate periods on insert. Scales are $X = 30$ h, $Y = 0.02$ percent for periods 1-5, and $X = 35$ h, $Y = 0.015$ percent for periods 6 and 7.

Viscous Strain ϵ_{ij}^V. The nonrecoverable (viscous) strain was described by a strain-hardening (SH) relation for a series of m steps in stress after introducing the aging function $g^V(t_s) = 1.8293\ t_s^{-0.2016}$ from equation (13) of [3]. For example, for the third step of a three-step sequence with stress changes at t_1 and t_2 the nonrecoverable strain was,

$$\epsilon_{11}^V(t) = g^V(20+t_2)\left[\left\{[\epsilon_{11}^V(t_2)]^{1/n} + [F^V(\sigma_3,\tau_3)]^{1/n}(t-t_2)\right\}^n - \epsilon_{11}^V(t_2)\right] + \epsilon_{11}^V(t_2), \quad (3)$$

where

$$\epsilon_{11}^V(t_2) = g^V(20+t_1)\left[\left\{[\epsilon_{11}^V(t_1)]^{1/n} + [F^V(\sigma_2,\tau_2)]^{1/n}(t_2-t_1)\right\}^n - \epsilon_{11}^V(t_1)\right] + \epsilon_{11}^V(t_1),$$

$$\epsilon_{11}^V(t_1) = g^V(20)\left\{[F^V(\sigma_1,\tau_1)]^{1/n} t_1\right\}^n.$$

In equations (1)-(3) the stress functions F and G include both the linear and nonlinear regions as described in [4].

Modification of ϵ_{ij}^V for Stress Reversal. On stress reversals, as in period 5, Fig. 1, periods 3-5, Fig. 2, and periods 2-6 of Fig. 3, the nonrecoverable (viscous) shear strain ϵ_{12}^V was considered as if the reversed stress were applied to a new specimen at each stress reversal, i.e., all the prior strain hardening was erased so that it had no effect on the subsequent shear creep strain. Summing this primary-type creep for ϵ_{12}^V as in the foregoing and ϵ_{12}^{VE} by equation (2), and accounting for aging, yielded the predictions for time-dependent strain on stress reversals shown by dashed lines in the figures. Where the curves are the same as theory curves described later, only solid lines are shown. The results showed some substantial disagreements between data and theory for all cases except periods 2 and 3 of Fig. 3. Some revisions were made to improve the predictions as follows.

Revision (RSP) of (MSP) for Side Step-Down. Equation (2) represents an open form in so far as stress changes are concerned. For example $[F^{VE}(\sigma_1, \tau_1) - F^{VE}(\sigma_2, \tau_2)](t-t_1)^n$ is an open form. The open form was found satisfactory [3, 4] for increasing steps of stress. However, as shown in [3, 4] a

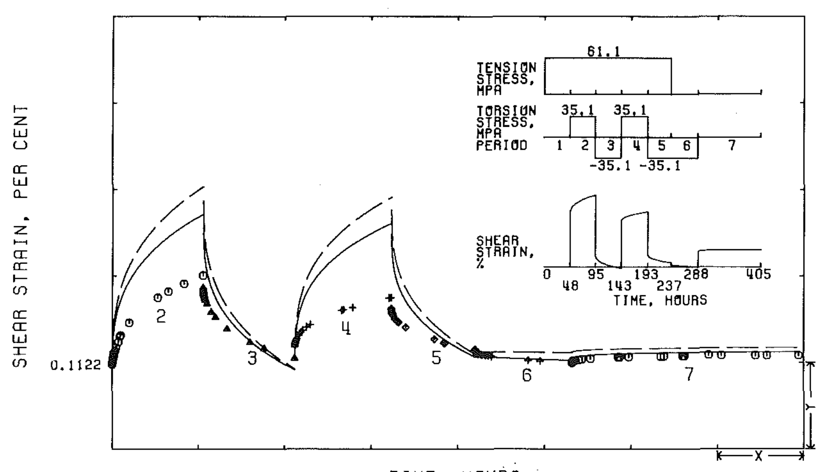

Fig. 2(*b*) Test no. 53. Shear strain for combined tension and torsion creep of 304 stainless steel at 593°C under stress reversals in torsion with constant tension. Numbers 2-7 indicate periods on insert. Scales are $X = 45$ h, $Y = 0.033$ percent for periods 2-7.

Fig. 2

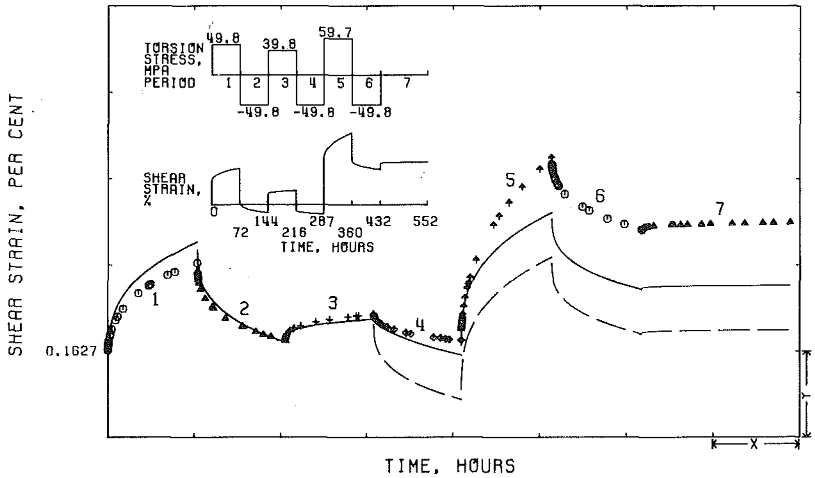

Fig. 3 Test no. 50. Shear strain for pure torsion creep of 304 stainless steel at 593°C under stress reversals. Numbers 1-7 indicate periods on insert. Scales are X = 70 h, Y = 0.087 percent for periods 1-7.

closed form was required for decreasing steps in stress. For example, $F^{VE}(\sigma_1-\sigma_2,\ \tau_1-\tau_2)\ (t-t_1)^n$ is the closed form employed.

The revised superposition principle (RSP) employing the closed form on decreasing steps of partial unloading yields the following for three steps of unloading equivalent to equation (2),

$$\begin{aligned}\epsilon_{11}(t) = & g^{VE}(20)\, F^{VE}(\sigma_1,\tau_1)t^n \\ & - g^{VE}(20)\, F^{VE}(\sigma_1-\sigma_2,\tau_1-\tau_2)(t-t_1)^n \\ & - g^{VE}(20+t_1)\, F^{VE}(\sigma_1-\sigma_3,\tau_1-\tau_3)(t-t_2)^n \\ & - g^{VE}(20+t_2)\, F^{VE}(\sigma_2-\sigma_4,\tau_2-\tau_4)(t-t_3)^n. \qquad (4)\end{aligned}$$

In equation (4) for a series of partial unloadings, $F^{VE}(\sigma_1-\sigma_3,\tau_1-\tau_3)$ was used instead of $F^{VE}(\sigma_2-\sigma_3,\tau_2-\tau_3)$ for the second step-down, etc. That is, the creep recovery for all but the first step-down of a series of step downs in stress was calculated on the basis of stress changes from one step before the previous to the current stress, as described in [3, 4]. Also the computations of $F^{VE}(\sigma,\tau)$ and $G^{VE}(\sigma,\tau)$ were made by separating the pure stress terms and the mixed stress terms in equations (2) and (3) of reference [4] as explained in [4]. The new predicted time-dependent creep strains (RSP) were obtained as the sum of equations similar to equation (3) plus equations similar to equation (2) when the stress increased, or equation (4) (separating pure and mixed stress terms) when the stress decreased. The (RSP) curves are shown as solid lines in periods 2, 4, and 6, Fig. 1, and periods 6 and 7, Fig. 2. These showed generally better predictions than the (MSP) for side step-down stress changes under combined tension and torsion as also found in [3] for step-down stresses.

Comparison With Time-Dependent Strain

Stress Reversal in Pure Torsion. On stress reversal in pure torsion, as in periods 2-6 of Fig. 3, the good agreement between data and theory for periods 2 (complete reversal), 3, and 6 (partial reversals) supported the assumption that there was no effect of prior strain hardening on ϵ^V at each subsequent stress reversal. But the data of period 4 was much smaller than the prediction (dashed line) and period 5 showed a much larger strain rate than predicted. Those observations yielded the following assumptions: (*a*) the same or larger magnitude of reversed stress than the previous stress erased all prior strain hardening in the opposite direction. For example, the reverse loading of period 2 erased the strain hardening during period 1 and the reverse loading of step 5 erased all the strain hardening during periods 2 and 4; (*b*) a partial stress reversal did not erase the prior strain hardening, i.e., the reverse loading of step 3 did not erase the strain hardening during period 2; and (*c*) the viscous creep strain ϵ_{12}^V after each stress reversal is not affected by any of the prior strain hardening in the opposite sense.

According to the new assumptions (*b*) and (*c*), the calculation of ϵ_{12}^V for period 4 included the strain hardening during period 2 by using equation (3), because the strain hardening during period 2 was not erased by the partial stress reversal of step 3. This modification shown as a solid line yielded a much better prediction. This supports assumption (*b*). The solid lines for periods 5–7 are the same shape as the dashed lines shifted by the difference between curves at the end of period 4. The much larger strain data than predicted for period 5 was not explained by the preceding assumptions, which described all the other periods quite well. Some other factors must contribute to the creep in period 5 such as a change of the creep surface or yield surface resulting from stress reversals.

Stress Reversal of Torsion With Constant Tension. The predictions by the original theory for the time-dependent strain are shown as dashed lines in period 5 of Fig. 1 and periods 3–5 of Fig. 2. As shown in Figs. 1 and 2, the actual shear creep rate was much smaller than predicted for these periods. The dashed lines were computed on the assumption that there was no effect of prior strain hardening on ϵ_{12}^V following each stress reversal of torsion in the presence of constant tension.

The first torsion loading, period 2 of Fig. 2(*b*), also showed the same order of disagreement between the theory and data as the subsequent stress reversals, periods 3–5. This observation suggested that there was a defect in the theory for prediction of period 2 where torsion was applied following period 1 of axial creep under the intitial pure tension loading. That case could not be treated the same as simultaneous tension and torsion loading because of prior strain hardening accumulated during plastic and creep strains in the axial direction by the initial pure tension loading. The shear creep strain on torsion loading in the presence of constant tension appeared to have been affected by prior tension creep and plastic strain, which is known to occur for plastic strain on nonproportionate loading [11].

The effect of strain hardening under creep in pure tension on subsequent creep under combined tension and torsion was approximated in periods 2–5 of Fig. 2(*b*) and period 5 of Fig. 1(*b*) by calculating ϵ_{12}^V from only the pure stress terms and considering no contribution from the mixed stress terms.

Similarly, for period 3 of Fig. 1(a), ϵ_{11}^{V} was calculated from only the pure stress terms as described in [4]. The predictions of this modified theory are shown as solid lines in the aforementioned periods of Figs. 1 and 2. The actual creep rate was still smaller than the predictions. Thus it appears that the preceding modifications are not sufficient to account for the effect of strain hardening during the prior plastic and creep strain under pure tension or pure torsion on the creep under the subsequent combined stress state as found also in [4].

In periods 3–5, Fig. 2(b), the same magnitude of torsion stress as the first loading was reversed at each stress reversal. In the preceding section, it was considered that stress reversal in each period erased the strain hardening during the previous period. But the data of periods 4 and 5 are smaller than that of periods 2 and 3 and the change is greater than expected from the theory considering aging. This observation suggests that the effect of strain hardening in the axial direction on the shear strain is not the same for every shear stress reversal in the presence of constant tension. This is because more strain hardening would be accumulated in the axial direction by constant tension, even if the prior strain hardening in the shear strain direction was erased by complete reversal of torsion. It may be noted that the assumption of no effect of prior strain hardening at each complete stress reversal found in pure torsion probably would be applicable to the case of simultaneous stress reversals of combined tension and torsion, but not sequential tension and torsion, as in the foregoing.

If complete reversal to the same magnitude of shear stress erased the prior strain hardening only in the shear strain direction as discussed in the foregoing, the axial viscous creep strain, ϵ_{11}^{V}, under constant tension with stress reversals of torsion, as in periods 3–5, Fig. 2(a), should be calculated by including the effect of stress reversal. As shown in Fig. 2(a), the data of periods 3–5 showed new primary-type axial creep strain at each stress reversal of torsion, which supports the preceding observation. Therefore the effect of stress reversal of torsion on the axial viscous creep strain under combined tension and torsion was approximated in the theory in periods 3–5 of Fig. 2 by calculating new ϵ_{11}^{V} at each stress reversal with no prior strain hardening. This new ϵ_{11}^{V} was calculated only for the mixed stress terms $\sigma\tau^2$, τ^2. The strain from the pure stress terms σ, σ^2, and σ^3 was calculated as continuous creep at constant σ. This resulted in quite satisfactory predictions, shown as solid lines in Fig. 2(a). The same type modification was applied to period 5 of Fig. 1(a), which also resulted in a good prediction, shown as a solid line.

Comparison With Plastic Strain

Experiments on plasticity show that loading above the initial yield limit changes the whole yield surface in shape and size even by loading in only one direction [12].

The data for the time-independent strain at each of the stress changes were determined as described in [4] and are shown in Table 1. The predictions of plastic strain for stress reversals were calculated as in reference [4] with and without considering aging except with an assumption that there was no effect of prior yielding, i.e., as if the stress were applied to a new specimen at each stress reversal (see Table 1).

Stress Reversal in Pure Torsion. The larger plastic strain observed in step 2 than predicted and larger than that of period 1 suggests that the yield limit for negative torsion decreased as a result of prior yielding under positive torsion. If period 2 (negative loading) did not change the yield surface for positive torsion, no plastic strain would have occurred on period 3, because the stress level of 3 was less than that of 1. But relatively large plastic strain did occur on step 3, which indicated that the yield surface for positive torsion had been lowered as a result of yielding under negative torsion in period 2. In the same manner, the data of plastic strain on periods 4–6 is consistent with a movement of the yield surface in response to each prior yielding.

Considering the yield limit to be affected by prior yielding, the following inferences were obtained from the data at each stress reversal: (a) stress reversal to the same stress or higher stress magnitude than the previous stress (periods 1 → 2, periods 3 → 4, and periods 4 → 5 in Fig. 3) erased the prior yielding in the opposite direction (periods 1, 3, 4, respectively). Then the plastic strain on the subsequent stress reversal (periods 3, 5, and 6, respectively), may be ap-

Table 1 Total time-independent strain and plastic strain

Test (Fig. No.) Strain Component	Period	Change in Stress, Tension, σ or Torsion, τ	MPa	ksi	Total Time-independent Strain, %	Aging Time t_s, h	Aging Factor $g^P(t_s)$	Plastic Strain: Data, %	Plastic Strain: Prediction Without Aging, %	Plastic Strain: Prediction With Aging, %
52	3	σ	61.1	8.857	0.1219	188	0.771	0.0807	0.1390	0.1072
(Fig. 1A)	5	τ	-35.1	-5.093	0.0422	269	0.740	0.0422	0.1390	0.1029
ϵ_{11}	6	σ	-61.1	-8.857	-0.0424	*	*	*	*	*
52	1	τ	49.8	7.217	0.1628	20	1.000	0.1180	0.1480	0.1480
(Fig. 1B)	2	τ	-14.7	-2.124	-0.0127	*	*	*	*	*
ϵ_{12}	3	σ	61.1	8.857	0.0202	188	0.771	0.0202	0.0343	0.0264
	4	τ	-35.1	-5.093	-0.0328	*	*	*	*	*
	5	τ	-35.1	-5.093	-0.0853	269	0.740	-0.0537	-0.1207	-0.0893
	7	τ	-14.7	-2.124	-0.0612	356	0.717	-0.0480	-0.0273	-0.0196
53	1	σ	61.1	8.857	0.0731	20	1.000	0.0319	0.0212	0.0212
(Fig. 2A)	2	τ	35.1	5.093	0.0977	68	0.868	0.0977	0.1178	0.1023
ϵ_{11}	3	τ	-70.2	-10.186	0.0522	115	0.816	0.0522	0.1390	0.1135
	4	τ	70.2	10.186	0.0257	163	0.784	0.0257	0.1390	0.1090
	5	τ	-70.2	-10.186	0.0151	213	0.760	0.0151	0.1390	0.1057
	6	σ	-61.1	-8.857	-0.0424	*	*	*	*	*
53	2	τ	35.1	5.093	0.0913	68	0.868	0.0597	0.1207	0.1047
(Fig. 2B)	3	τ	-70.2	-10.186	-0.1165	115	0.816	-0.0533	-0.1207	-0.0985
ϵ_{12}	4	τ	70.2	10.186	0.0912	163	0.784	0.0280	0.1207	0.0946
	5	τ	-70.2	-10.186	-0.0829	213	0.760	-0.0197	-0.1207	-0.0917
	7	τ	35.1	5.093	0.0316	*	*	*	*	*
50	1	τ	49.8	7.217	0.1437	20	1.000	0.0989	0.1480	0.1480
(Fig. 3)	2	τ	-99.6	-14.434	-0.2304	92	0.838	-0.1408	-0.1480	-0.1240
ϵ_{12}	3	τ	89.6	12.990	0.1285	164	0.784	0.0479	0.0427	0.0335
	4	τ	-89.6	-12.990	-0.1318	236	0.751	-0.0512	-0.1480	-0.1112
	5	τ	109.5	15.877	0.3784	307	0.729	0.2799	0.3614	0.2634
	6	τ	-109.5	-15.877	-0.1830	380	0.711	-0.0845	-0.1480	-0.1053
	7	τ	49.8	7.217	0.0452	*	*	*	*	*

proximated by the predictions with no effect of prior yielding, only aging. (*b*) Stress reversal to a smaller magnitude of stress than the previous stress (periods 2 → 3 in Fig. 3) did not completely erase the prior yielding in the opposite direction (the yielding by period 2). Then the plastic strain on the subsequent stress reversal period 4 was affected by prior yielding (the yielding by period 2 remained).

Stress Reversal of Torsion With Constant Tension. The data of plastic strain for complete stress reversals simultaneously with a constant tension as in periods 3-5 of Fig. 2 showed a gradual decrease of plastic strain at every stress reversal for both ϵ_{11}^P and ϵ_{12}^P. These results suggest that if the stress reversals were continued in the same pattern of stress state changes, there finally would be no more plastic strain. That is, the changing yield surface would converge to a fixed yield surface.

Nonproportional Loading. Consider a change of stress state from pure torsion to combined tension and torsion on the same Mises' effective stress level $\sigma = 86.2$ MPa (12.5 ksi) as in periods 1-3 of Fig. 1 (see Table 1). Period 2 may be neglected because it caused no plastic strain. If isotropic hardening of a Mises' type occurred, period 3 would yield no plastic strain, because period 3 lies on the isotropic subsequent yield surface caused by period 1. But the data of plastic strain for both ϵ_{11}^P and ϵ_{12}^P on period 3 showed new additional plastic strain, where $\Delta\epsilon_{11}^P$ was four times larger than $\Delta\epsilon_{12}^P$. This result suggests that loading in period 1 increased the yield surface mainly in the direction of pure torsion.

The first loading of torsion in the presence of constant tension as in periods 1 → 2 of Fig. 2 may have the opposite effect to the foregoing, because the initial tension loading in period 1 may change the yield surface mainly in the direction of pure tension. But the data of ϵ_{11}^P in period 2 was rather close to the prediction with aging as shown in Table 1.

Some of the features of plastic (time-independent nonrecoverable) strain were similar to those for viscous creep (time-dependent nonrecoverable) strain. Considering that interaction is possible between plastic strain and viscous creep strain, a more precise interpretation of experimental data might be possible with information from creep experiments with more exact control of loading conditions.

Conclusions

Analysis of creep data of 304 stainless steel at 593°C (1100°F) under combined tension and torsion for varying stress history including stress reversals in torsion with or without constant tension showed that a viscous-viscoelastic model with certain modifications and aging effects predicted most of the features of the observed creep behavior reasonably well.

Both time-dependent nonrecoverable (viscous) strain and time-independent nonrecoverable (plastic) strain are considerably affected by prior strain hardening at the same or different stress states, and also are similar in some of the features under stress reversals, where the same or larger magnitude of reversed stress erased the effect of prior strain hardening on creep or plastic strain in the opposite sense (partial reversal did not). Separate treatment of pure and mixed stress terms was required to describe nonrecoverable creep under stress reversal of torsion with constant tension. Further improvement of theory may be possible by including other metallurgical concepts, such as hardening and softening. Further experiments under multiaxial stresses are needed to study the effects of prior yielding and interactions among the strain components.

Acknowledgments

This work was supported by the National Science Foundation under Grant No. ENG76-02519. The early experimental work on this project was supported and all material tested was supplied by the Oak Ridge National Laboratory. The authors are grateful to R. M. Reed for assistance in experiments and Mrs. P. C. Capece for typing the manuscript.

References

1 Cho, U. W., and Findley, W. N., "Creep and Creep Recovery of 304 Stainless Steel Under Combined Stress With a Representation by a Viscous-Viscoplastic Model," ASME Journal of Applied Mechanics, Vol. 47, 1980, pp. 755-761.

2 Cho, U. W., and Findley, W. N., "Creep and Creep Recovery of 304 Stainless Steel at Low Stresses With Effects of Aging on Creep and Plastic Strains," ASME Journal of Applied Mechanics, Vol. 48, 1981, pp. 785-790.

3 Cho, U. W., and Findley, W. N., "Creep and Plastic Strains of 304 Stainless Steel at 593°C Under Step Stress Changes, Considering Aging," ASME Journal of Applied Mechanics, Vol. 49, 1982, pp. 297-304.

4 Cho, U. W., and Findley, W. N., "Creep and Plastic Strains Under Side Steps of Tension and Torsion for 304 Stainless Steel at 593°C," ASME Journal of Applied Mechanics, Vol. 50, 1983, pp. 580-586.

5 Bhargava, R., Moteff, J., and Swindeman, R. W., "Correlation of the Microstructure With the Creep and Tensile Properties of AISI 304 Stainless Steel," ASME *Symposium on Structural Materials for Service at Elevated Temperatures in Nuclear Power Generation*, Doc. MPC-1, 1975, pp. 31-54.

6 Swindeman, R. W., Bhargava, R., Sikka, V. K., and Moteff, J., "Substructures Developed During Creep and Cyclic Tests of Type 304 Stainless Steel (Heat 9T2796)," Oak Ridge National Laboratory, ORNL-5293, Sept. 1977.

7 Swindeman, R. W., "Correlation of Rupture Life, Creep Rate, and Microstructure for Type 304 Stainless Steel," Oak Ridge National Laboratory, ORNL-5523, June 1979.

8 Findley, W. N., and Lai, J. S., "Creep of 2618 Aluminum Under Side Steps of Tension and Torsion and Stress Reversal Predicted by a Viscous-Viscoelastic Model," ASME Journal of Applied Mechanics, Vol. 48, 1981, pp. 47-54.

9 Findley, W. N., and Gjelsvik, A., "A Biaxial Testing Machine for Plasticity, Creep, or Relaxation Under Variable Principal-Stress Ratios," *Proceedings*, ASTM, Vol. 62, 1962, pp. 1103-1118.

10 Findley, W. N., Lai, J. S., and Onaran, K., *Nonlinear Creep and Relaxation of Viscoelastic Materials, With an Introduction to Linear Viscoelasticity*, North Holland, Amsterdam, 1976.

11 Michno, M. J. Jr., and Findley, W. N., "Experiments to Determine Small Offset Yield Surfaces for 304L Stainless Steel Under Combined Tension and Torsion," *Acta Mechanica*, Vol. 18, 1973, pp. 163-179.

12 Michno, M. J. Jr., and Findley, W. N., "Subsequent Yield Surfaces for Annealed Mild Steel Under Dead-Weight Loading: Aging, Normality, Convexity, Corners, Bauschinger, and Cross Effects," ASME *Journal of Engineering Materials and Technology*, Vol. 96, 1974, pp. 56-64.

Ductile Fracture of Rapidly Expanding Rings

J. N. Johnson
Staff Member,
Los Alamos National Laboratory,
Los Alamos, N.Mex. 87545

Heterogeneous plastic deformation (necking) of thin ductile rings given an initial outward impulse is described in terms of the ordinary differential equations of thermoplasticity and the partial differential equations of mass and momentum conservation in one spatial dimension (circumference) and time. Flaws in cross-sectional area and porosity are introduced and the resulting plastic deformation is calculated numerically for a prescribed initial radial velocity. Plastic deformation is initially homogeneous but soon concentrates in the weakest region, which then thins rapidly and fractures. Effects of flaw wavelength, work-hardening rate, thermal softening, and rate-dependent plastic flow on the flaw growth rate are studied.

Introduction

When an initially uniform ring of ductile material is given an outward radial velocity sufficient to cause large-scale plastic flow leading to tensile fracture, simple analysis based on cylindrical symmetry would predict fracture taking place everywhere simultaneously. However, practical experience and experimental measurement show that expanding rings fail by the process of inhomogeneous plastic flow and localized necking. The specific points at which necking begins depend on the imperfections that destroy the ideal circumferential uniformity which exists only in concept.

The ideas of inhomogeneous plastic flow are well known and have been considered in the stability analysis of the quasi-static tensile test beginning with Considère [1], and more recently Swift [2], Hill [3], and others [4–10]. When specific flaws were considered, they were generally due to cross-sectional area variation, although Needleman and Triantafyllidis [11] have considered the role of voids as the imperfection leading to necking, plastic instability, and fracture. One-dimensional models of dynamic fracture and fragmentation of expanding cylinders were considered by Mott [12], Wesenberg and Sagartz [13], and Grady [14].

The relationship between ductile fracture of expanding rings and spallation was studied by Johnson [15] with the conclusion that, although both are controlled by the nucleation, growth, and coalescence of voids, the tensile stress states were of a sufficiently different nature to preclude any simple relationship between the two phenomena.

Work by Fyfe and Rajendran [16] and Rajendran and Fyfe [17] on expanding rings and cylinders considers the dynamic effects of inertia on deformational stability and localized necking. The effects of metallurgical imperfections (porosity) are also considered.

In the aforementioned work, excluding fragmentation, much of the detail of the necking process is not considered; the emphasis is on conditions leading to the *onset* of instability. The advantage of leaving out some of these details (such as the temporal evolution of a particular flaw into a region of unstable plastic flow) is that analytical expressions can be obtained that provide insight to the general physical processes involved.

Taylor, Harlow, and Amsden [18] treated the problem of necking in stretching plates and shells as a one-dimensional hydrodynamic problem in which the shell thickness is one of the dependent variables and each material point is given an initial velocity u proportional to its distance from some arbitrary origin: $u = \dot{\epsilon}x$, where $\dot{\epsilon}$ is a constant strain rate. This simulates the behavior of an expanding cylinder (radius r) in which an outward radial velocity v produces a strain rate $\dot{\epsilon} = v/r$. Their analysis results in a set of coupled partial differential equations which can be solved numerically by finite-difference methods. By these means the growth or decay of various large-scale thickness variations were studied with the inclusion of mechanical effects such as work-hardening and rate-dependent plastic flow. In the work of Taylor et al., effects of porosity as a property influencing necking and fracture was not included.

The present work is closely related to that of Taylor et al., with the following additions to the theoretical analysis: (1) the full equations of ring geometry are used, with the radial and circumferential velocity as separate dependent variables; (2) effects of material porosity are included in addition to cross-sectional area variations; (3) a more general thermoplastic constitutive description is used, and temperature is calculated; and (4) the effects of work-hardening, thermal softening, and rate-dependent plastic flow on imperfection growth are considered.

The state of stress in the necked region is assumed to be uniform. This approximation is reasonable only as long as the radius of curvature of the neck is large compared to the minimum thickness. When this condition is not satisfied, a multiaxial stress state exists which raises the stress necessary

Contributed by the Applied Mechanics Division and presented at the 1983 ASME Applied Mechanics, Bioengineering, and Fluids Engineering Conference, Houston, Texas, June 20–22, 1983 of THE AMERICAN SOCIETY OF MECHANICAL ENGINEERS.

Discussion on this paper should be addressed to the Editorial Department, ASME, United Engineering Center, 345 East 47th Street, New York, N.Y. 10017, and will be accepted until two months after final publication of the paper itself in the JOURNAL OF APPLIED MECHANICS. Manuscript received by ASME Applied Mechanics Division, August, 1982; final revision, December, 1982. Paper No. 83-APM-33.

Copies will be available until February, 1984.

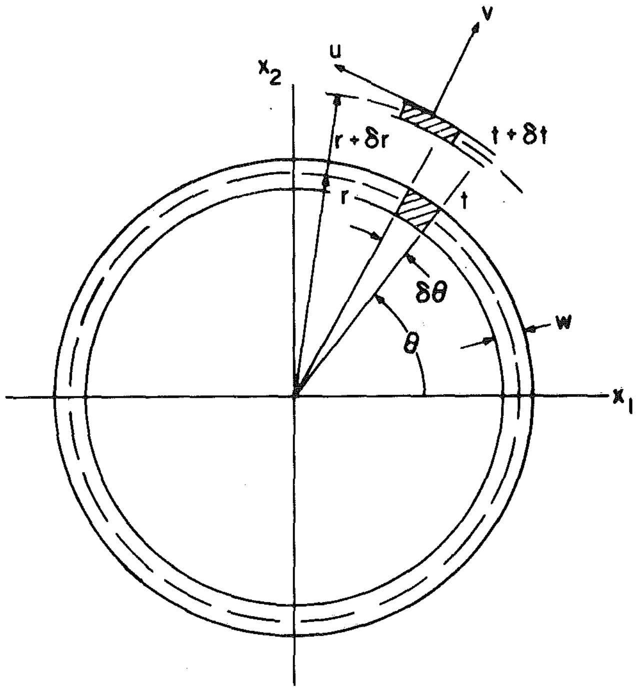

Fig. 1 Geometry of the expanding ring. The height of the cylinder is h and the cross-sectional area is $A = wh$.

to cause plastic flow [19]. Consideration of the effects of a multiaxial stress state on void growth in the necked region is avoided in the present work by using a purely empirical relationship between void volume and axial plastic strain. Fracture occurs when the void volume reaches a maximum allowable value (a few percent of the initial solid volume) determined by experimental measurement.

Instabilities related to heterogeneous plastic flow phenomena such as shear banding are not considered.

Differential Equations of Motion

We consider a thin ring of average initial radius r_0, as shown in Fig. 1. Eulerian (spatial) coordinates describing the motion are r and θ, with θ being included to allow for circumferential variation in initial density, wall thickness, etc. A Lagrangian (material) circumferential distance coordinate a is defined according to

$$a = r_0\theta. \tag{1}$$

and t is time. The radius of the midplane of the ring is assumed to be independent of a, and the outward radial velocity is $v = dr/dt$. Other quantities defining the ring (all functions of a and t) are as follows: u, circumferential velocity; w, wall thickness; h, height of cylinder (not shown); $A = wh$, cross-sectional area; ρ, density; $m = \rho A$, mass per unit circumferential length; σ, circumferential stress (positive in compression); $F = \sigma A$, circumferential force; and $s = \sigma/\rho$.

Mass Conservation. Consider the mass element (shaded region) shown in Fig. 1. At time t it is located at radius r between θ and $\theta + \delta\theta$. At time $t + \delta t$ it is displayed radially and circumferentially: the latter displacement is due to circumferential imperfections. The change in mass δM between fixed θ and $\theta + \delta\theta$ over the time increment δt is

$$\delta M = (\rho A)_{t+\delta t}(r+\delta r)\,\delta\theta - (\rho A)_t r\delta\theta, \tag{2}$$

which must equal the difference between mass flow in (at θ) and mass flow out (at $\theta + \delta\theta$):

$$\delta M = (\rho A u)_\theta \delta t - (\rho A u)_{\theta+\delta\theta}\delta t. \tag{3}$$

From equations (2) and (3), we then have, in the limit as δt, δr, and $\delta\theta$ go to zero, with $v = \lim(\delta r/\delta t)$,

$$\left[\frac{\partial(\rho A)}{\partial t}\right]_\theta + \frac{\rho A v}{r} + \left(\frac{1}{r}\right)\left[\frac{\partial(\rho A u)}{\partial\theta}\right]_t = 0 \tag{4}$$

Mass conservation also requires that at any particular time

$$\rho A r d\theta = \rho_0 A_0 da \tag{5}$$

in the definition of the Lagrangian coordinate a. Thus,

$$\left(\frac{1}{r}\right)\left(\frac{\partial}{\partial\theta}\right)_t = \left(\frac{\rho A}{\rho_0 A_0}\right)\left(\frac{\partial}{\partial a}\right)_t = \frac{m}{m_0}\left(\frac{\partial}{\partial a}\right)_t, \tag{6}$$

where $m = \rho A$ is the mass per unit circumferential length. Equation (4) then becomes, with the identification $(\partial/\partial t)_a = (\partial/\partial t)_\theta + (u/r)\,(\partial/\partial\theta)_t$:

$$\left(\frac{\partial m}{\partial t}\right)_a + \frac{mv}{r} + \left(\frac{m^2}{m_0}\right)\left(\frac{\partial u}{\partial a}\right)_t = 0. \tag{7}$$

Momentum Conservation. The vector position of the mass element (shaded) in Fig. 1 is given by

$$\mathbf{x} = r(\cos\theta, \sin\theta), \tag{8}$$

from which we find the acceleration to be

$$\ddot{\mathbf{x}} = (\ddot r - r\dot\theta^2)(\cos\theta,\sin\theta) + (2\dot r\dot\theta + r\ddot\theta)(-\sin\theta,\cos\theta). \tag{9}$$

A dot above a variable indicates time differentiation at fixed material element. The force transmitted circumferentially across a Lagrangian material boundary is $F = \sigma A$ and the net force acting on the material element between θ and $\theta + \delta\theta$ is

$$\Phi = \left(F\cos\theta + \sin\theta\,\frac{\partial F}{\partial\theta},\quad F\sin\theta - \cos\theta\,\frac{\partial F}{\partial\theta}\right)\delta\theta. \tag{10}$$

Direct application of Newton's second law then gives

$$mr\delta\theta\ddot{\mathbf{x}} = \Phi. \tag{11}$$

In terms of the radial and circumferential velocity components, v and u,

$$u = r\dot\theta, \tag{12}$$

$$v = \dot r, \tag{13}$$

equation (11) becomes, in Lagrangian coordinates,

$$\left(\frac{\partial v}{\partial t}\right)_a = \frac{(s+u^2)}{r}, \tag{14}$$

$$m_0\left[\left(\frac{\partial u}{\partial t}\right)_a + \frac{uv}{r}\right] = -\left[\frac{\partial(ms)}{\partial a}\right]_t, \tag{15}$$

where $s \equiv \sigma/\rho$.

In equation (14) the radial acceleration depends on the local stress and circumferential particle velocity, which are functions of a and t. But we have already assumed that the midplane of the ring maintains cylindrical symmetry. Equation (14) is therefore replaced by

$$\dot v = \frac{\langle s+u^2\rangle}{r}, \tag{16}$$

where $\langle\,\rangle$ defines a spatial average around the circumference.

Material Constitutive Description

Following Wallace [20], we write the equations of thermoplastic flow in the absence of rotation as follows:

$$\dot\sigma_{ij} = c_{ijkl}\dot\epsilon^e_{kl} + \delta_{ij}\Gamma\sigma_{kl}\dot\epsilon^p_{kl}, \tag{17}$$

$$\dot T = T\Gamma\dot\epsilon^e_v + \sigma_{ij}\frac{\dot\epsilon^p_{ij}}{(\rho_0 c_\epsilon)}, \tag{18}$$

where σ_{ij} is the stress tensor, T is the temperature, c_{ijkl} is the fourth-order adiabatic elastic moduli tensor, $\dot\epsilon^e_{kl}$ and $\dot\epsilon^p_{kl}$ are the elastic and plastic strain-rate tensors, Γ is the Grüneisen coefficient, and c_ϵ is the specific heat at constant strain configuration. The total strain rate is the sum of the elastic and plastic contributions:

$$\dot\epsilon_{ij} = \dot\epsilon^e_{ij} + \dot\epsilon^p_{ij}. \tag{19}$$

The total volumetric strain rate $\dot\epsilon_v$ is given by $\dot\epsilon_{kk}$.

Total Strain Rate. For a thin ring, the total circumferential strain rate, denoted $\dot\epsilon$, is due to two effects: (1) outward radial motion, and (2) variation in u around the circumference. Consider a material element whose initial length is $r\delta\theta$ at time t. At time $t + \delta t$, its new length is

$$(r+v\delta t)\,\delta\theta + \left(u+\delta a\,\frac{\partial u}{\partial a}\right)\delta t - u\delta t,$$

and therefore the circumferential strain rate (positive in compression) is given by

$$\dot\epsilon = -\frac{v}{r} - \frac{1}{r}\,\frac{\partial a}{\partial\theta}\,\frac{\partial u}{\partial a}, \tag{20}$$

which becomes, with the aid of equation (5),

$$\dot\epsilon = -\frac{v}{r} - \frac{m}{m_0}\,\frac{\partial u}{\partial a}. \tag{21}$$

Plastic Strain Rate. The plastic strain-rate tensor in the θ, r, z coordinate system (where the r and z directions are equivalent, because both are stress relieved if w and h are small) is written as

$$\dot\epsilon^p = \begin{bmatrix} -\dot\psi & 0 & 0 \\ 0 & \frac{1}{2}\left(\dot\psi - \frac{\dot\alpha}{\alpha}\right) & 0 \\ 0 & 0 & \frac{1}{2}\left(\dot\psi - \frac{\dot\alpha}{\alpha}\right) \end{bmatrix}, \tag{22}$$

where ψ is the circumferential plastic strain and α is the distention (the ratio of the specific volume to the crystalline voidless volume). The plastic volumetric strain rate due to void growth is given by

$$Tr[\dot\epsilon^p] = -\frac{\dot\alpha}{\alpha}. \tag{23}$$

The plastic strain-rate components $\dot\psi$ and $\dot\alpha$ are positive for extension and not independent: for A533B stainless steel, Shockey et al. [21] find that

$$ln\left(\frac{\alpha}{\alpha}\right)_0 - ln\alpha_f\left(\frac{\psi}{\psi_f}\right)^n = 0, \tag{24}$$

where $ln\ \alpha_f = 0.03$, $\psi_f = 1.0$ (plastic strain at fracture), and $n = 1.74$. In general, we write the relationship between α and ψ in differential form as

$$g_\alpha\,\dot\alpha + g_\psi\,\dot\psi = 0. \tag{25}$$

The porosity ϕ is related to α according to

$$\phi = \frac{\alpha - 1}{\alpha}. \tag{26}$$

Yield Condition. For rate-independent plastic flow due to application of uniaxial stress σ, we write the yield condition in differential form

$$f_\sigma\dot\sigma + f_\alpha\dot\alpha + f_\psi\dot\psi + f_T\dot T = 0. \tag{27}$$

It is realized that α and ψ are not independent, but it is convenient to include both explicitly in the yield condition. For example, in the absence of work hardening and thermal softening, the function f in equation (27) might take the form

$$f = |\sigma| - \frac{Y_0}{\alpha} = 0, \tag{28}$$

for elastic-perfectly-plastic flow of solid material surrounding the voids (if present). The solid yield strength is Y_0. For materials that exhibit work hardening and thermal softening, equation (28) might be modified as follows:

$$f = |\sigma| - \left(\frac{1}{\alpha}\right)\left[Y_0 + Y_w\psi - Y_T(T - T_0)\right], \tag{29}$$

where Y_w and Y_T are positive constants. Equation (29) applies only in the specific case that ψ is nondecreasing (i.e., plastic flow is not reversed).

For rate-dependent plastic flow, plastic strain rate is specified as a function of the other variables:

$$\dot\psi = e(\sigma,\alpha,\psi,T). \tag{30}$$

The particular form of the function e used here is

$$e(\sigma,\alpha,\psi,T) = \frac{f}{\eta}, \tag{31}$$

where $f > 0$ is the function given by equation (28) and η is a constant with units of viscosity.

One-Dimensional Ring Geometry. With the foregoing definitions, the general equations of thermoplastic flow reduce to

$$\dot\sigma = \mathrm{E}(\dot\epsilon + \dot\psi) - (1 - 2\nu)\,\Gamma\sigma\dot\psi, \tag{32}$$

$$\dot T = T\Gamma\left(\dot\epsilon_v + \frac{\dot\alpha}{\alpha}\right) - \frac{\sigma\dot\psi}{\rho_0 c_\epsilon}, \tag{33}$$

$$\dot\epsilon_v + \frac{\dot\alpha}{\alpha} = (1 - 2\nu)\left[\dot\epsilon + \left(1 + \frac{\Gamma\sigma}{G}\right)\dot\psi\right], \tag{34}$$

where E and G are the isotropic adiabatic Young's and shear moduli, respectively, and ν is Poisson's ratio:

$$\nu = \frac{\mathrm{E} - 2G}{2G} \tag{35}$$

The moduli E and G are functions of the porosity as determined by Mackenzie [22] with modifications suggested by Johnson [15].

For simplicity, it is further assumed that density changes are due only to changes in porosity:

$$\rho = \frac{\rho_s}{\alpha}, \tag{36}$$

where ρ_s is the constant crystalline density. For the magnitude of the tensile stresses considered in the remainder of this work, this is a very reasonable approximation.

Thermal conduction has been neglected in the preceding theoretical development. This is acceptable as long as the characteristic time for significant heat conduction remains large compared to the times of localized plastic flow and necking. An initial sinusoidal variation in temperature of wavelength λ will tend to smooth out in times on the order of

$$\tau = \left(\frac{\lambda}{2\pi}\right)^2 \frac{\rho_0 c_\epsilon}{\kappa}, \tag{37}$$

where κ is the thermal conductivity. If N_λ is the integral number of wavelengths in the circumference $2\pi r$, equation (37) becomes

$$\tau = \left(\frac{r}{N_\lambda}\right)^2 \frac{\rho_0 c_\epsilon}{\kappa}. \tag{38}$$

Thus, for $\kappa = 0.2$ cal cm^{-1}s^{-1}K^{-1}, $r = 2.5$ cm, $N_\lambda = 32$, and other material constants listed in Table 1, for A533B steel, $\tau \cong 2500\ \mu$s. The time is long for all calculations presented here and we are, therefore, justified in omitting

Table 1 Material properties: A533B pressure vessel steel. c_0 and s are constants in straight-line fit of shock velocity U_s as a function of particle velocity U_p: $U_s = c_0 + sU_p$ (see reference [15]).

Initial density	ρ_0	7.89 g/cm^3
Bulk sound velocity	c_0	0.458 cm/μs
Bulk modulus	$K=\rho_0 c_0{}^2$	1.655 Mbar
U_s,U_p slope	s	1.5
Grüneisen constant	Γ	2.0
Specific heat	C_ϵ	0.1 cal/g•K
Shear modulus	G	0.790 Mbar
Poisson ratio	$(3K-2G)/2(3K+G)$	0.294
Young's modulus	$E=2G(1+\nu)$	2.045 Mbar
Bar velocity	$c_b=\sqrt{E/\rho_0}$	0.509 cm/μs
Yield strength	Y_0	0.0055 Mbar

Table 2 Summary of equations

Equation number	Function	Variables
(7)	Mass conservation	m,u,v
(15)	Momentum conservation (circumferential)	m,u,v,s
(16)	Momentum conservation (radial)	u,v,s
(21)	Strain rate definition	m,u,v,ϵ
(25)	Plastic strain distention relationship	α,ψ
27 (or(30))	Yield condition	σ,α,ψ,T
(31)	Strain rate	σ,ϵ,ψ
(32)	Temperature rate	$\sigma,\epsilon_v,\alpha,\psi,T$
(33)	Volume strain rate	$\sigma,\epsilon_v,\alpha,\psi,\epsilon$

thermal conduction. It is implicitly assumed that ductile flow and failure occurs homogeneously on a reasonably small scale. We do not consider instabilities related to effects such as adiabatic shear banding, for example.

Numerical Calculation

The foregoing theoretical analysis provides nine independent equations in nine unknowns whose solution describes the response of a nonuniform ring to an outward impulse. The variable unknowns are m, u, v (or r), σ (or $s = \alpha\sigma/\rho_s$), ϵ, ψ, ϵ_v, α (or $\rho = \rho_s/\alpha$), and T. The equations are summarized in Table 2.

This collection of ordinary and partial differential equations (of one spatial dimension a) are of the form that can be solved by simple finite-difference methods. The first four (partial) differential equations are written in centered finite-difference form as described in the Appendix. The solution is started by specifying an initial outward radial velocity $v = v_0$ and $u(a, 0) = 0$. The initial imperfection is specified in terms of $m_0(a)$ arising from variation in either cross-sectional area A or in porosity $\phi = (\alpha - 1)/\alpha$.

In all calculations presented in this paper, we consider only one material and a single geometry. The material is A533B pressure vessel steel with material properties listed in Table 1. The initial radius is 2.5 cm and the average cross-sectional area normal to the ring circumference is 0.1 cm^2.

Cross-Sectional Area Imperfection. Calculations are performed for 0.5 percent cosine variation in initial cross-sectional area with $N_\lambda = 8$, 16, and 32. The initial outward velocity is $v_0 = 0.020$ cm/μs. The ideally plastic yield condition is given by equation (29) with $Y_w = 0$ and $Y_T = 0$. Figure 2 shows the nondimensional radial velocity v/v_0 is a function of time for the three cases. The horizontal lines for $N_\lambda = 16$ and 32 indicate that fracture has occurred.

The necking process leading to fracture for $N_\lambda = 16$ is shown in Fig. 3. The nondimensional dependent variables are $m/\bar{m}_0$ (where $\bar{m}_0$ is the *average* initial mass/length), $T/1000$ K (with $T_0 = 300$ K), $-\phi/\phi_f$ (where ϕ_f is the porosity at fracture, $(\alpha_f - 1)/\alpha_f = 0.02996$), and $\alpha\sigma/Y_0$. These quantities

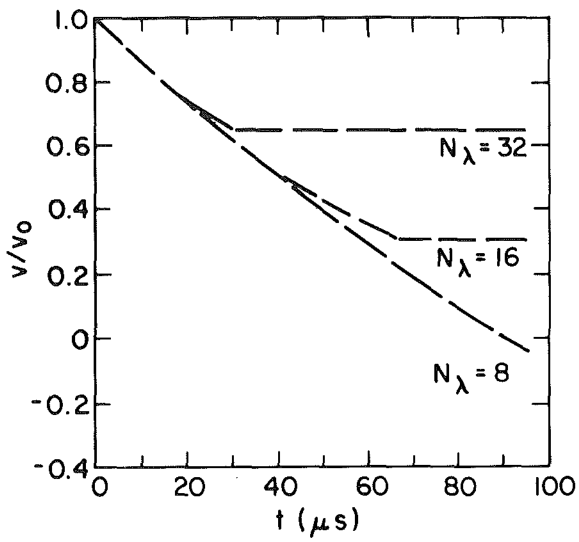

Fig. 2 Radial velocity of expanding ring with 0.5 percent initial cross-sectional area (cosine) variation

are denoted by M, T, ϕ, and σ, respectively, in Fig. 3 and similar figures that follow. In every case, porosity is a few percent or less and, therefore, variation in M is due predominantly to variation in cross-sectional area.

At $t = 10$ μs (Fig. 3) the variables m, T, ϕ, and σ are relatively uniform—the departure from the initial 0.5 percent cross-sectional area variation is not great. Plastic flow is taking place uniformly, with $\alpha\sigma/Y_0 = -1$ everywhere. At $t = 30$ μs the imperfection has grown substantially, and plastic flow has become localized between $0.25 \leqq (a/\lambda_0) \leqq 0.75$. Outside this region the stress state has moved back within the failure surface; i.e., $(\alpha\sigma/Y_0) > -1$. As time proceeds, the plastic flow region becomes more and more localized, the temperature goes up, m decreases dramatically at $a/\lambda_0 = 0.5$, and fracture occurs at $t = 66$ μs (not shown) when the plastic strain ψ reaches $\psi_f = 1.0$.

The time to fracture is a monotonically decreasing function of N_λ for constant imperfection amplitude. This does not mean that in practice ring fracture is controlled by flaws of infinitesimal size (i.e., $N_\lambda \rightarrow \infty$). Fracture is controlled by the average imperfection amplitude for a given value of N_λ, and statistical calculation of fracture requires this type of information.

Initial Porosity Imperfection. Similar calculations are performed with uniform area cross section, but with 0.5 percent cosine variation in initial porosity. Figure 4 shows the nondimensional radial velocity v/v_0 as a function of time for the three cases; $N_\lambda = 8$, 16, and 32. They are similar to those shown in Fig. 2, but not identical. Figure 5 shows the evolution of the necking region for $N_\lambda = 16$. This too is very similar to the result for cross-sectional area variation (Fig. 3), with the exception of the porosity. At $t = 10$ μs the initial porosity imperfection is apparent in Fig. 5. At $t = 30$ μs plastic flow becomes localized, and at $t = 55$ μs the necked region is fully developed. Fracture occurs at $t = 62$ μs (not shown).

As in the case of cross-sectional-area imperfections, the time to fracture is a monotonically decreasing function of N_λ for constant imperfection amplitude. Again, additional information is required on the relationship between average imperfection amplitude and N_λ to perform fracture calculations for a specific experimental situation.

Stabilizing Influences. For rate-independent elastic-perfectly-plastic flow, in the absence of work hardening, small initial imperfections in porosity and cross-sectional area

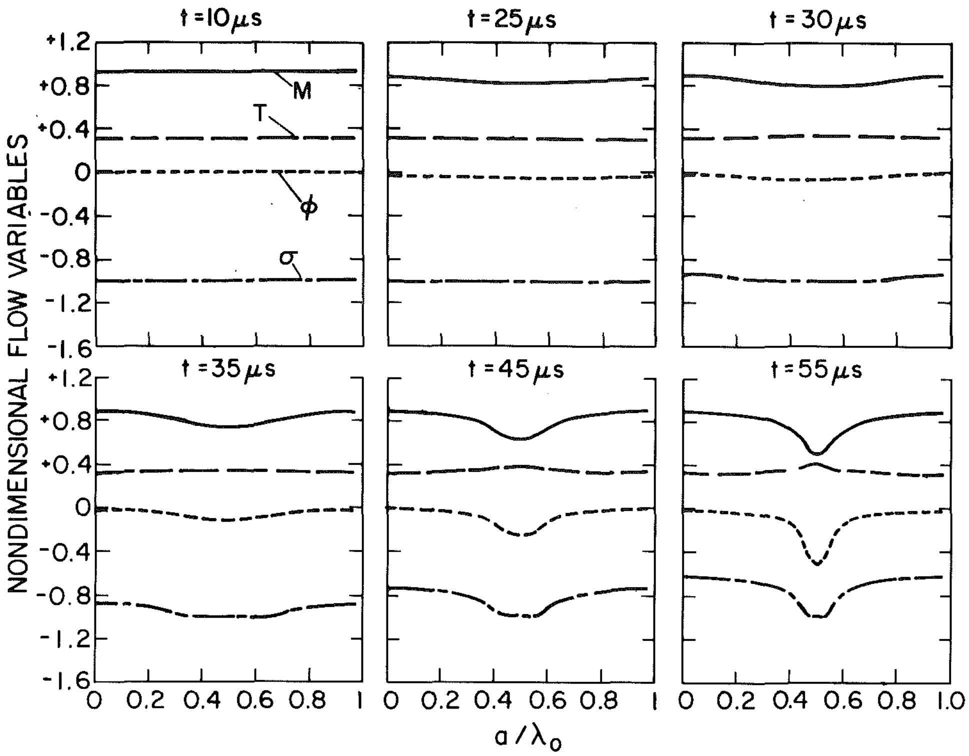

Fig. 3 Spatial dependence of flow variables for one wavelength of 0.5 percent initial cross-sectional area (cosine) variation: N_λ = 16

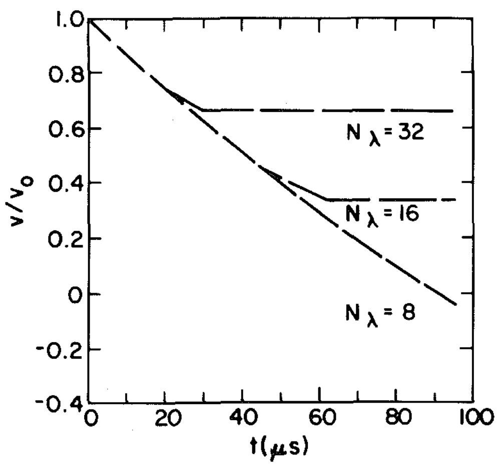

Fig. 4 Radial velocity of expanding ring with 0.5 percent initial porosity (cosine) variation

grow unstably. Calculations were also performed for the case of work-hardening material with Y_w = 0.002, 0.004, 0.005, and 0.01 Mbar in equation (29) and the results are shown in Fig. 6. The ring geometry (r_0 = 2.5 cm), initial outward velocity (v_0 = 0.020 cm/μs), and porosity imperfection (0.5 percent with N_λ = 16) are the same as for calculations shown in Fig. 5. A value of Y_w on the order of 0.01 Mbar provides sufficient work hardening to maintain homogeneous plastic deformation.

The effect of thermal softening counteracts work hardening. This can be seen quantitatively from combination of equations (25), (27), and (32)-(34):

$$\left[f_\sigma + f_T \frac{T\Gamma(1-2\nu)}{\mathrm{E}}\right]\dot{\sigma}$$

$$+\left[f_\psi - \frac{f_\alpha g_\psi}{g_\alpha} - f_T\sigma\left\{\frac{1}{\rho c_\epsilon} - \frac{3T\Gamma^2(1-2\nu)}{\mathrm{E}}\right\}\right]\dot{\psi}=0 \qquad (39)$$

for tensile flow.

If f and g are given by equations (24) and (29), equation (39) becomes, in the limit as $\psi \to 0$, $\sigma \to -Y_0$, $T \to T_0$, and $\alpha \to 1$,

$$\dot{\sigma} = -\frac{Y_w[1-\{Y_T Y_0/(Y_w \rho c_\epsilon)\}\{1-3\rho c_\epsilon \Gamma^2 T_0(1-2\nu)/\mathrm{E}\}]\dot{\psi}}{1-Y_T T_0 \Gamma(1-2\nu)/\mathrm{E}}. \qquad (40)$$

Nominal values for Y_w and Y_T are [23, 24]

$$Y_w \sim Y_0 = 5.5\times 10^{-3}\ \text{Mbar},$$

$$Y_T \sim 10^{-3} Y_0 = 5.5\times 10^{-6}\ \text{Mbar}^{-1}.$$

Thus, the magnitudes of the various nondimensional terms in equation (40) are

$$\frac{Y_T T_0 \Gamma(1-2\nu)}{\mathrm{E}} = 0.007$$

$$\frac{3\rho c_\epsilon \Gamma^2 T_0(1-2\nu)}{\mathrm{E}} = 0.024$$

$$\frac{Y_T Y_0}{Y_w \rho c_\epsilon} = 0.167$$

showing that work-hardening considerations dominate the flow, but not sufficiently to be able to completely ignore the compensating effect of thermal softening. A useful approximation to equation (40) is

$$\dot{\sigma} \cong -Y_w\left(1-\frac{Y_T Y_0}{Y_w \rho c_\epsilon}\right)\dot{\psi} \qquad (41)$$

and one must check in each specific case whether or not the second term in the brackets is negligible. Thermal softening becomes important when $Y_T \sim Y_w \rho c_\epsilon / Y_0$.

Rate-dependent plastic flow also tends to slow the growth of imperfections as shown in Fig. 7 for the plastic strain rate given by equation (31) with η = 10 kp and 100 kp. The geometry and imperfections are the same as for calculations shown in Figs. 5 and 6. For η = 10 kp the response is very nearly the same as for the rate-independent behavior—Fig. 5

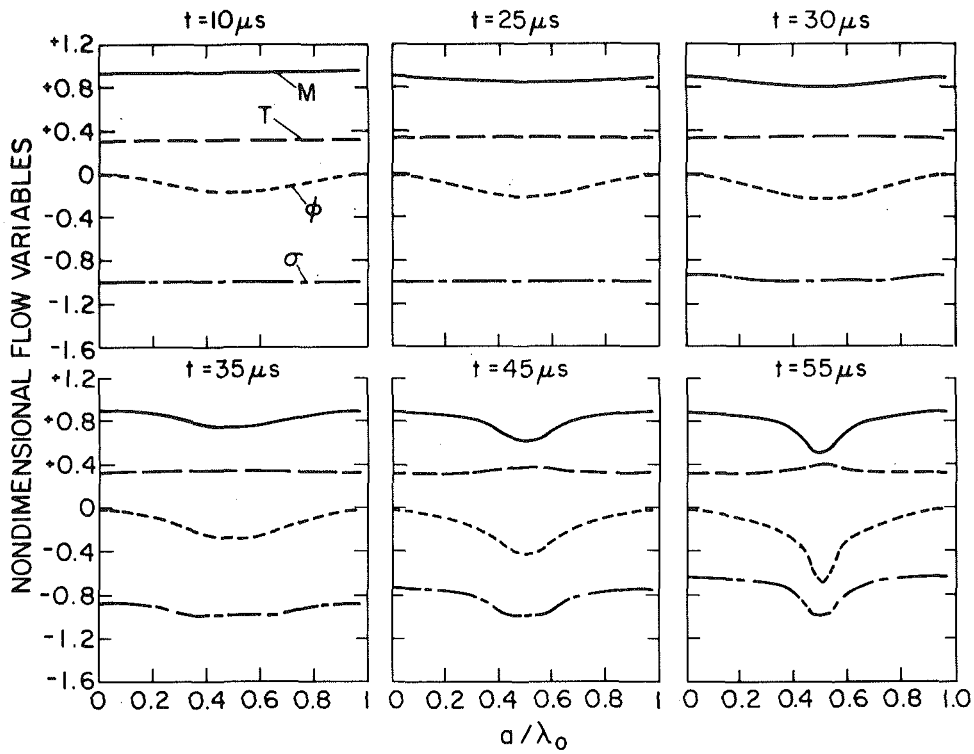

Fig. 5 Spatial dependence of flow variables for one wavelength of 0.5 percent initial porosity (cosine) variation (N_λ = 16)

(t = 55 μs). The stabilizing effect becomes evident for η = 100 kp.

Summary

The ordinary and partial differential equations governing inhomogeneous plastic flow and dynamic ductile fracture of expanding rings are presented. The flaws that are investigated here are variations in cross-sectional area and initial porosity. The system of equations is solved numerically for a single material (A533B steel), a single geometry (r_0 = 2.5 cm and A_0 = 0.10 cm^2) and initial impulse (with v_0 = 0.020 cm/μs), and a single imperfection amplitude (0.5 percent in cross-sectional area and initial porosity). Whether the flaw is in the cross-sectional area A or in the porosity ϕ makes only a small difference in the time at which fracture occurs, although A and ϕ enter into the theory in quite different ways. Additional calculations were made with the same initial porosity distribution, but with several different values of the work-hardening coefficient Y_w and the rate-dependent plastic flow parameter η. These calculations show the time evolution of the flawed region up to the point of complete separation, which occurs at the empirically determined void fraction of 0.03 percent and axial plastic strain of 1.0 [21].

As expected, flaw growth is inhibited by work hardening and rate-dependent effects. For the case of A533B steel, effects of thermal softening are overcome by work hardening, but not by such a magnitude as to suggest that local heating can always be ignored. The calculated temperature increase at fracture was typically 140 K. There may be other materials for which the localized temperature increase substantially speeds the necking process. This effect is generally ignored in stability analyses of the necking and fracture.

Measurement of radial velocity as a function of time has already been used in determining material constitutive behavior at intermediate strain rates [25, 26]. Similar experiments on expanding rings with premachined flaws may be useful in the determination of tensile fracture properties, when performed in conjunction with the analysis presented here. This removes the dependence on statistical variability for starting the necking process. Recovery and microscopic examination of samples taken up to and through complete fracture provide necessary information on the relationship between porosity and plastic strain.

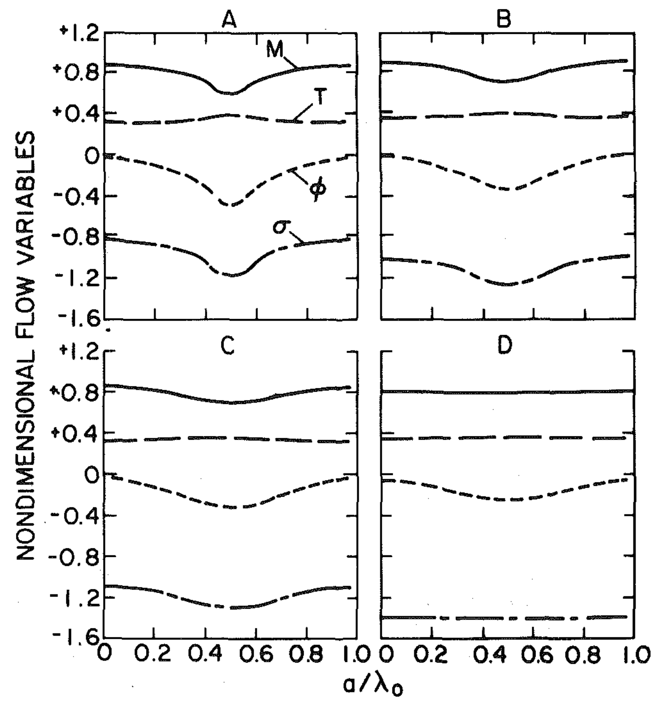

Fig. 6 Spatial dependence of flow variables for one wavelength of 0.5 percent initial porosity (cosine) variation (N_λ = 16) at t = 55 μs for various values of the hardening coefficient Y_w: (A) 0.002, (B) 0.004, (C) 0.005, and (D) 0.01 Mbar

There are a number of advantages in using the expanding ring to study fracture. The tensile stress state is highly

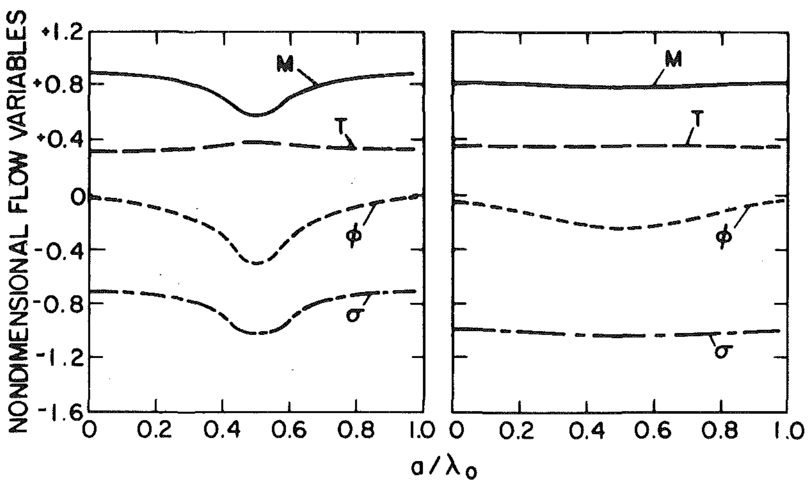

Fig. 7 Spatial dependence of flow variables for one wavelength of 0.5 percent initial porosity (cosine) variations (N_λ = 16) at t = 55 μs for two values of rate-dependent plasticity coefficient η: (left) 10 kp and (right) 100 kp

nonisotropic in contrast to spallation experiments [15] and fracture takes place following considerable plastic straining. Rates of loading are controllable and measurable [25, 26]. Constitutive properties can be obtained simultaneously. Because of the ease of recovery and the possibility of prescribing the initial flaw magnitude and location by premachining, experiments with expanding rings can provide a new means of studying dynamic fracture.

Acknowledgment

The author wishes to thank Thomas A. Duffey, Paul S. Follansbee, and Charles A. Forest, Los Alamos National Laboratory, for numerous helpful discussions in the course of this work.

References

1 Considère, A., "L'Emploi du Fer et de L'Acier dans les Constructions," *Ann. des Ponts and Chaussée*, Vol. 9, No. 6, 1885, p. 574.

2 Swift, H. W., "Plastic Instability Under Plane Stress," *Journal of the Mechanics and Physics of Solids*, Vol. 1, 1952, p. 1.

3 Hill, R., "On Discontinuous Plastic States, With Special Reference to Localized Necking in Thin Sheets," *Journal of the Mechanics and Physics of Solids*, Vol. 1, 1952, p. 19.

4 Hart, E. E., "Theory of the Tensile Test," *Acta Metallurgica*, Vol. 15, 1967, p. 351.

5 Campbell, J. D., "Plastic Instability in Rate-Dependent Materials," *Journal of the Mechanics and Physics of Solids*, Vol. 15, 1967, p. 359.

6 Marciniak, Z., and Kuczyński, K., "Limit Strains in the Processes of Stretch-Forming Sheet Metal," *International Journal of the Mechanical Sciences*, Vol. 9, 1967, p. 609.

7 Ghosh, A. K., "Strain Localization in the Diffuse Neck in Sheet Metal," *Metallurgical Transactions*, Vol. 5, 1974, p. 1607.

8 Ghosh, A. K., "Tensile Instability and Necking in Materials With Strain Hardening and Strain-Rate Hardening,"*Acta Metallurgica*, Vol. 25, 1977, p. 1413.

9 Jonas, J. J., Holt, R. A., and Coleman, C. E., "Plastic Stability in Tension and Compression," *Acta Metallurgica*, Vol. 24, 1976, p. 911.

10 Hutchinson, J. W., and Neale, K. W., "Influence of Strain-Rate Sensitivity on Necking Under Uniaxial Tension," *Acta Metallurgica*, Vol. 25, 1977, p. 839.

11 Needleman, A., and Triantafyllidis, N., "Void Growth and Local Necking in Biaxially Stretched Sheets," *Journal of Engineering Materials and Technology*, Vol. 100, 1978, p. 164.

12 Mott, N. F., "Fragmentation of Shell Cases," *Proceedings of the Royal Society*, London, Vol. 300, Series *A*, 1947, p. 300.

13 Wesenberg, D. L., and Sagartz, M. J., "Dynamic Fracture of 6061-T6 Aluminum Cylinders," ASME Journal of Applied Mechanics, Vol. 44, 1977, p. 643.

14 Grady, D. E., "Fragmentation of Solids Under Impulsive Stress Loading," *Journal of Geophysical Research*, Vol. 86, 1981, p. 1047.

15 Johnson, J. N., "Dynamic Fracture and Spallation in Ductile Solids," *Journal of Applied Physics*, Vol. 52, 1981, p. 2812.

16 Fyfe, I. M., and Rajendran, A. M., "Dynamic Pre-Strain and Inertia Effects on the Fracture of Metals," *Journal of the Mechanics and Physics of Solids*, Vol. 28, 1980, p. 17.

17 Rajendran, A. M., and Fyfe, I. M., "Inertial Effects on the Failure of Thin Rings," ASME Journal of Applied Mechanics, Vol. 49, 1982, p. 31.

18 Taylor, J. W., Harlow, F. H., and Amsden, A. A., "Dynamic Plastic Instabilities in Stretching Plates and Shells," ASME Journal of Applied Mechanics, Vol. 45, 1978, p. 105.

19 Dieter, G. E., Jr., *Mechanical Metallurgy*, McGraw-Hill, New York, 1961, p. 250.

20 Wallace, D. C., "Irreversible Thermodynamics of Flow in Solids," *Physical Review*, Vol. 22*B*, 1980, p. 1477.

21 Shockey, D. A., Seaman, L., Dao, K. C., and Curran, D. R., "Kinetics of Void Growth in Fracturing A533B Tensile Bars," ASME *Journal of Pressure Vessel Technology*, Vol. 102, 1980, p. 14.

22 Mackenzie, J. H., "The Elastic Constants of a Solid Containing Spherical Holes," *Proceedings of the Royal Society*, London, Vol. 63, Series *B*, 1950, p. 2.

23 Shockey, D. A., Dao, K. C., Seaman, L., Burback, R., and Curran, D. R., "*Computational Modeling of Microstructural Fracture Processes in A533B* Pressure Vessel Steel," Electric Power Research Institute Report NP-1398, Palo Alto, Calif., May, 1980.

24 Hucek, H. J., ed., "Structural Alloys Handbook," Vol. 1, Battelle Columbus Laboratories, Columbus, Ohio, 1981.

25 Warnes, R. H., Duffey, T. A., Karpp, R. R., and Carden, A. E., "An Improved Technique for Determining Dynamic Material Properties Using the Expanding Ring," in *Shock-Waves and High-Strain-Rate Phenomena in Metals*, Meyers, M. A., and Murr, L. E., eds., Plenum, New York, 1981, p. 23.

26 Carden, A. E., Williams, P. E., and Karpp, R. R., "Comparison of the Flow Curves of 6061 Aluminum Alloy at High and Low Strain Rates," in *Shock Waves and High-Strain-Rate Phenomena in Metals*, Meyers, M. A., and Murr, L. E., eds., Plenum, New York, 1981, p. 37.

27 Margenau, H., and Murphy, G. M., *The Mathematics of Physics and Chemistry*, D. Van Nostrand, Princeton, N.J., 1956, p. 490.

APPENDIX

Numerical Solution Scheme

The centered finite-difference scheme can be described by reference to Fig. A-1. The a, t plane is divided into a series of rectangular grids of uniform spacing $\Delta a/2$ in the spatial direction and $\Delta t/2$ in the time direction. Because v (and r) are independent of a, their values depend only on t: v is calculated along integer multiples of Δt and r is calculated along half-integer multiples of Δt. Circumferential velocities u are calculated at positions marked by x; strain rates $\dot{\epsilon}$ are calculated at positions marked by the squares; s (or σ), m, and all other material variables are calculated at nodal points marked by the circles. It is assumed that the variables are known at times t and $t + \Delta t/2$, and we are interested in finding new quantities at times $t + \Delta t$ and $t + 3\Delta t/2$.

Equation (16) gives the velocity v at time $t + \Delta t$:

$$v(t+\Delta t) = v(t) + \frac{\langle s+u^2 \rangle \Delta t}{r(t+\Delta t/2)}, \qquad (A\text{-}1)$$

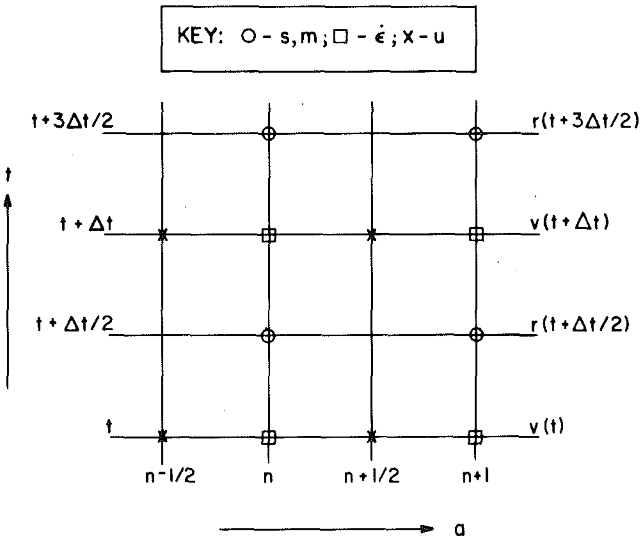

Fig. A-1

where

$$<s+u^2> = \frac{1}{N}\sum_{n=1}^{N}\left[s_n\left(t+\frac{\Delta t}{2}\right)+u^2_{n+1/2}(t)\right], \quad (A\text{-}2)$$

and N is the number of computational cells in the ring circumference or other repetitive unit (such as a single wavelength for sinusoidal variation in cross-sectional area). The u^2 term in equation (A-2) is not centered; that is, we are using a value one-half a time step behind. To properly center this term requires a simultaneous difference solution of equations (15) and (16). In view of the very small contribution of the u^2 term in comparison to s in determining the radial acceleration, we chose the simpler, noncentered form of the equation. The remainder of the difference equations are properly centered. The radial position at $t + 3\Delta t/2$ is given by

$$r\left(t+\frac{3\Delta t}{2}\right)=r\left(t+\frac{\Delta t}{2}\right)+v(t+\Delta t)\cdot\Delta t. \quad (A\text{-}3)$$

Integration of equation (15) begins by writing it as

$$\left(\frac{\partial u}{\partial t}\right)_a+\xi u=\lambda, \quad (A\text{-}4)$$

where the centered quantities,

$$\xi=\frac{v(t)+v(t+\Delta t)}{2r(t+\Delta t/2)}, \quad (A\text{-}5)$$

$$\lambda=-\frac{m_{n+1}(t+\Delta t/2)s_{n+1}(t+\Delta t/2)-m_n(t+\Delta t/2)s_n(t+\Delta t/2)}{\Delta a(m_{0,n}+m_{0,n+1})/2}, \quad (A\text{-}6)$$

are treated as constants over the interval from t to $t + \Delta t$. Thus

$$\frac{u_{n+1/2}(t+\Delta t)-u_{n+1/2}(t)}{\Delta t}+\xi\frac{u_{n+1/2}(t+\Delta t)+u_{n+1/2}(t)}{2}=\lambda. \quad (A\text{-}7)$$

or

$$u_{n+1/2}(t+\Delta t)=\frac{u_{n+1/2}(t)(1-\xi\Delta t/2)+\lambda\Delta t}{1+\xi\Delta t/2}, \quad (A\text{-}8)$$

The mass conservation relationship, equation (7), is written as

$$\left(\frac{\partial m}{\partial t}\right)_a=m(\gamma+\beta m), \quad (A\text{-}9)$$

where the centered quantities,

$$\gamma=-\frac{2r(t+\Delta t/2)}{v(t)+v(t+\Delta t)}, \quad (A\text{-}10)$$

$$\beta=-\frac{u_{n+1/2}(t+\Delta t)-u_{n-1/2}(t+\Delta t)}{\Delta a\, m_{0,n}}, \quad (A\text{-}11)$$

are treated as constants over the interval from $t + \Delta t/2$ to $t + 3\Delta t/2$. Thus, equation (A-9) can be integrated to give

$$m_n\left(t+\frac{3\Delta t}{2}\right)=\frac{\gamma}{\zeta-\beta}, \quad (A\text{-}12)$$

where

$$\zeta=\frac{\gamma+\beta m_n(t+\Delta t/2)}{m_n(t+\Delta t/2)}\exp(-\gamma\Delta t). \quad (A\text{-}13)$$

The total strain rate is given by equation (21), which is written in finite-difference form as

$$\dot{\epsilon}_n(t+\Delta t)=\frac{-2v(t+\Delta t)}{r(t+\Delta t/2)+r(t+3\Delta t/2)}-\frac{m_n(t+\Delta t/2)+m_n(t+3\Delta t/2)}{2m_{0,n}}\cdot\frac{u_{n+1/2}(t+\Delta t)-u_{n-1/2}(t+\Delta t)}{\Delta a}. \quad (A\text{-}14)$$

Once the average total strain rate over the interval from $t + \Delta t/2$ to $t + 3\Delta t/2$ is known, the last five coupled ordinary differential equations in Table 1 can be integrated numerically by standard methods to give σ, ϵ_v, α, ψ, and T from $t + \Delta t/2$ to $t + 3\Delta t/2$ at constant a. For all calculations in this work a one-step Runge-Kutta method is used [27].

To limit the formation of compressive shock waves and numerical instabilities, an artificial viscous stress q_n is added to s_n in equations (A-2) and (A-6):

$$q_n=-\left\{(L_1\Delta a)^2\left|\left(\frac{\partial u}{\partial a}\right)_n\right|+(L_2\Delta a)c_b\right\}\left(\frac{\partial u}{\partial a}\right)_n, \quad (A\text{-}15)$$

where L_1 and L_2 are nondimensional constants, c_b is the elastic bar velocity, and

$$\left(\frac{\partial u}{\partial a}\right)_n=\frac{u_{n+1/2}(t)-u_{n+1/2}(t)}{\Delta a}. \quad (A\text{-}16)$$

The constants L_1 and L_2 are small enough to have negligible effect on the physical processes involved: typically, $L_1 \sim 2$ and $L_2 \sim 0.1$.

Cyclic boundary conditions are imposed. For example, if the repetitive unit contains M spatial cells:

$$s_{n+M}=s_n, \quad (A\text{-}17)$$

with similar restrictions on m and n. The repetitive unit is obtained by dividing the circumference by an integer N_λ. This integer is the number of wavelengths of the initial imperfection that can be fit exactly into the initial circumference.

L. N. McCartney
Division of Materials Applications,
National Physical Laboratory,
Teddington, Middlesex, U.K.

R. L. Smith
Department of Mathematics,
Imperial College of Science and Technology,
London SW7 2BZ, U.K.

Statistical Theory of the Strength of Fiber Bundles

Following a review of statistical models of the failure of single fibers and bundles of these fibers, algebraic recurrence formulas are derived that generate expressions for the failure probabilities of bundles of classical fibers. One of these recurrence relations is suitable for the accurate numerical calculation of failure probabilities of bundles consisting of up to 500 single fibers. It is shown how account can be taken of the effect of defect-free fibers having finite strength. Numerical results are compared to three asymptotic analytic approximations, two of which have been proposed in the statistical literature and are now applied to fiber problems for the first time.

1 Introduction

This paper is concerned with the statistical distributions of the strength of single fibers and the strength of bundles of fibers. The principal objective of the paper is to summarize and review some recent developments of the classical model of Daniels [1].

The fibers are assumed to be made of an elastic material such that the defects they contain do not grow in size during loading. The uniaxial stress in a fiber thus depends only on the extension when inertia effects are negligible and is independent of the rate of loading. When considering bundles of such fibers, the loading mechanism is assumed to share the applied load equally among the surviving fibers of the bundle. Interactions between the fibers, which arise when the fibers are twisted to form a rope or embedded in a matrix to form a composite, are neglected.

The main features of Daniels' model are presented in the next section. The remainder of the paper is concerned with the accurate numerical determination of the probability of failure of a large bundle of fibers. An improved recursive formula for the exact calculation of this probability is given, and numerical results are compared with three asymptotic approximations which have been proposed in the literature.

2 Review of Statistical Models for Fibers and Bundles of Fibers

The principal idea underlying statistical models for individual fibers is the "weakest-link" concept. This was apparently introduced by Chaplin [2, 3] (see review in Harter [4]) and further developed by Peirce [5] and Weibull [6]. The connection with the statistical theory of extreme values was exploited by Epstein [7, 8], Gumbel [9], and Coleman [10].

Contributed by the Applied Mechanics Division for publication in the JOURNAL OF APPLIED MECHANICS.

Discussion on this paper should be addressed to the Editorial Department, ASME, United Engineering Center, 345 East 47th Street, New York, N.Y. 10017, and will be accepted until two months after final publication of the paper itself in the JOURNAL OF APPLIED MECHANICS. Manuscript received by ASME Applied Mechanics Division, November, 1981; final revision, December, 1982.

Different aspects of the theory as applied to brittle materials have been investigated by McClintock and Argon [11], Argon [12], and Hunt and McCartney [13].

Suppose the fibers are of length a, and the probability of failure of a fiber of unit length under the stress increase from 0 to σ is $F(\sigma)$. The weakest-link failure hypothesis asserts that the probability of failure of a fiber of length a, under the stress increase from 0 to σ, is given by the relation

$$P_F(\sigma) = 1 - \{1 - F(\sigma)\}^a. \tag{1}$$

This is equivalent on differentiation to equation (1) of Peirce [5]. Weibull [6, equation (4)] derived the same formula in the form

$$P_F(\sigma) = 1 - \exp\{-a\, n(\sigma)\} \quad \text{where} \quad n(\sigma) = -\ln\{1 - F(\sigma)\} \tag{2}$$

and interpreted the function $n(\sigma)$ as "that number of weak places per unit volume which causes rupture at a stress equal to, or less than, the amount σ."

Weibull proposed the functional form

$$n(\sigma) = (\sigma/\sigma_0)^m, \tag{3}$$

where σ_0 and m are positive constants, as a convenient form for mathematical analysis. This leads to the distribution function

$$P_F(\sigma) = 1 - \exp\{-a(\sigma/\sigma_0)^m\} \tag{4}$$

in which the length a appears explicitly as a parameter.

More generally, if it is assumed that $F(\sigma)$ obeys the asymptotic relation

$$F(\sigma) \sim (\sigma/\sigma_0)^m \quad \text{as} \quad \sigma \to 0 \tag{5}$$

then the statistical theory of extreme values maybe used to show that (4) is again valid as an asymptotic relation for large a. This approach was taken by Coleman [10], for example. Thus it appears that equation (4), known as the Weibull distribution, is well suited to the statistical analysis of strength of fibers. The Weibull distribution is further supported by theoretical arguments based on extreme value theory [7–10]. In view of equation (1), as $a \to \infty$ we would expect the distribution function P_F, under suitable renormalization, to be approximated by one of the three limiting distributions for the minimum of a random sample. Of these three distributions, the Weibull distribution is the only one concentrated on the positive half-line and is therefore the most suitable for material strength. In practice the Weibull distribution is extensively applied with the scale parameter σ_0 and the shape parameter m estimated from stress-rupture data.

For the study of bundles of fibers it will be assumed that the function $P_F(\sigma)$ is known for each $\sigma>0$. It *need not* satisfy (4), although in view of the wide applicability of this distribution, equation (4) will be assumed in all numerical calculations.

The first detailed treatment of the statistical distribution of the strength of a bundle of fibers was given by Daniels [1]. The main features of Daniels' model are that fiber failure is independent of the rate of loading, and hence is determined by the function $P_F(\sigma)$, and that the load on the bundle, in a typical situation where some fibers have failed and the remainder are supporting the applied load, is distributed *equally* over the surviving elements. In recent years a number of extensions of this basic model have been analyzed. Coleman [14-16] introduced a class of models for fatigue failure which has been used by Phoenix [17-19]. Another direction of research has been the relaxation of the "equal load-sharing" assumption to allow for such features as random slack in the fibers (Phoenix and Taylor [20]) or interfiber frictional forces (Smith and Phoenix [21]). In particular, much attention has been given to the development of models for composite materials when the fibers are embedded in matrix, e.g., Harlow and Phoenix [22, 23], Smith [24]. The present paper, however, is concerned with the original model of Daniels [1], in which recent improvements to both the exact and asymptotic formulas given by Daniels' appear to be of considerable interest.

The model under discussion comprises a bundle of elastic fibers arranged in parallel and subjected to some uniaxial stress applied along the direction in which the fibers are aligned. The probability of failure of a single fiber under stress increase from 0 to σ is assumed known for each $\sigma>0$, and in all numerical calculations it is assumed to satisfy (4). The load on the fibers is shared equally over all surviving fibers. Thus, if there are N fibers in the bundle, the applied load on the bundle is L, and there are r failed fibers, then the stress in each of the surviving fibers of the bundle is given by

$$\sigma_r^{(N)} = \frac{L}{(N-r)A}, \quad r=0,1,\ldots,N-1, \tag{6}$$

where A is the cross-sectional area of a fiber.

For this model, extensive results for both *exact* and *approximate* determinations of the probability of failure are known. The next two sections present results for the exact probability of failure.

3 Probability of Failure of a Bundle of Classical Fibers

A bundle of N fibers is formed by random sampling from the population of single fibers. The bundle is subjected to a load L and it is assumed that the surviving fibers share the load equally. The stress in each surviving fiber when r fibers have failed is given by (6). It is clear that

$$\sigma_0^{(N)} < \sigma_1^{(N)} < \ldots . < \sigma_{N-2}^{(N)} < \sigma_{N-1}^{(N)}.$$

For a single fiber $P_F(\sigma)$ is the probability that it fails during the stress increase $0\rightarrow\sigma$ and $P_S(\sigma)\equiv 1-P_F(\sigma)$ is the corresponding probability of survival. It follows that

$$P_S(\sigma_0^{(N)}) > P_S(\sigma_1^{(N)}) > \ldots . > P_S(\sigma_{N-1}^{(N)}).$$

The failure of a bundle of N fibers can occur only if the fiber strengths $s_1, s_2, \ldots, s_N$, arranged in ascending order, satisfy the inequalities

$$0\le s_1\le\sigma_0^{(N)},\ s_1\le s_2\le\sigma_1^{(N)}, \ldots s_{N-1}\le s_N\le\sigma_{N-1}^{(N)}. \tag{7}$$

Following Daniels [1] the probability of this event is given by

$$P^{(N)}(L) = N!\int_0^{\sigma_0^{(N)}} P_F'(s_1)ds_1 \int_{s_1}^{\sigma_1^{(N)}} P_F'(s_2)ds_2 \ldots$$

$$\int_{s_{N-1}}^{\sigma_{N-1}^{(N)}} P_F'(s_N)ds_N.$$

By means of the substitution $t_r=P_F(s_r)$ for $1\le r\le N$, and using $P_F(\sigma)\equiv 1-P_S(\sigma)$, it follows that

$$P^{(N)}(L)$$

$$= N!\int_0^{1-x_0^{(N)}} dt_1 \int_{t_1}^{1-x_1^{(N)}} dt_2 \ldots \int_{t_{N-1}}^{1-x_{N-1}^{(N)}} dt_N, N\ge 1, \tag{8}$$

where

$$x_r^{(N)} = P_S(\sigma_r^{(N)}),\ r=0,1\ldots N-1.$$

The expression (8) is not however convenient for the direct calculation of the bundle failure probability $P^{(N)}(L)$ using a computer. Two recurrence formulas will now be derived, the

Nomenclature

a = length of bundle
σ = stress
$F(\sigma)$ = cumulative failure probability for fiber of unit length
$P_F(\sigma)$ = cumulative failure probability for fiber of length a
σ_0 = Weibull scale parameter
m = Weibull shape parameter
N = number of fibers in a bundle
A = cross-sectional area of one fiber
$P_s(\sigma)$ = survival probability $(1-P_F(\sigma))$
$\sigma_r^{(N)}$ = stress in each surviving fiber when r out of N have failed
σ_c = ultimate tensile strength
L = total applied load
$G(L)$ = probability that a single fiber fails under load L
M,S,L_0,B,γ,β = constants derived from G
λ,ϕ = absolute constants (0.996, −0.317, respectively)
T_N = maximum load in a bundle of N fibers
$\Phi(x)$ = cumulative distribution function for standard normal deviates
$1=L/NA$ = nominal stress (per fiber) applied to the bundle
$1_0=M/A$ = limiting failure stress (per fiber of the original bundle) as $N\rightarrow\infty$

second a generalization of the first, which facilitates this calculation.

It may be seen that the expression for $P^{(N)}(L)$ depends only on N and the survival probabilities $x_0^{(N)}, x_1^{(N)}, \ldots, x_{N-1}^{(N)}$, and not otherwise on L or the function P_S. Accordingly, let us define, for any $N \geq 1$ and any $x_0 > x_1 > \ldots > x_{N-1} > 0$, the function

$$\phi_N(x_0, x_1, \ldots, x_{N-1}) = N! \int_0^{1-x_0} dt_1 \int_{t_1}^{1-x_1} dt_2 \ldots \int_{t_{N-1}}^{1-x_{N-1}} dt_N, \quad N \geq 1. \tag{9}$$

This is probability of failure of a bundle of N fibers given that x_r, for $0 \leq r \leq N-1$, is the probability that any specified fiber survives a stress increase from zero to the stress that would arise from the failure of exactly r fibers of the bundle. The probability of failure of the bundle may be expressed in terms of ϕ_N as follows

$$\left.\begin{aligned} P^{(N)}(L) &= \phi_N(x_0^{(N)}, \quad x_1^{(N)}, \ldots, x_{N-1}^{(N)}) \\ \text{where} \quad x_r^{(N)} &= P_S(\sigma_r^{(N)}), \quad r = 0, 1, \ldots, N-1. \end{aligned}\right\} \tag{10}$$

The next step is to obtain an expression for the probability of exactly r failures in a bundle of size N when successive fiber failures are controlled by the parameters $x_0, x_1, \ldots, x_{N-1}$. The probability that r *specified* fibers all fail and the rest survive is

$$\phi_r(x_0, x_1, \ldots x_{r-1}) x_r^{N-r};$$

the first factor being the probability that the r fibers fail and the second being the probability of survival of the remaining $N-r$ fibers under the influence of the increased stress. Now the number of ways in which a subset of r fibers can be chosen from a bundle of N is

$$\binom{N}{r} \equiv \frac{N!}{r!(N-r)!} \equiv \binom{N}{N-r}.$$

Consequently the probability of exactly r failures in a bundle of size N is

$$\binom{N}{r} \phi_r(x_0, x_1, \ldots, x_{r-1}) x_r^{N-r}, \quad r = 0, 1, \ldots, N,$$

where $\phi_0 = 1$. Now when a bundle is loaded it is certain that either no fibers fail, or just one fiber fails, or . . . . , or all N fibers fail. Thus the functions ϕ_r, $r = 0, 1, \ldots, N$ must satisfy the relation

$$\sum_{r=0}^{N} \binom{N}{r} \phi_r(x_0, x_1, \ldots, x_{r-1}) x_r^{N-r} = 1, \tag{11}$$

which can be recast in the form

$$\phi_N(x_0, x_1, \ldots, x_{N-1}) = 1 - \sum_{r=0}^{N-1} \binom{N}{r} \phi_r(x_0, x_1, \ldots, x_{r-1}) x_r^{N-r}. \tag{12}$$

The relation (12) is valid for all $N \geq 1$ and it can thus be used to compute the functions ϕ_N, $N \geq 1$, recursively. On setting $x_r = P_S(\sigma_r^{(N)})$, $r = 0, 1, \ldots N-1$, so that the equal load-sharing rule applies, it follows that the failure probability $P^{(N)}(L)$ of a bundle of N fibers subjected to a load L may be computed from the formula

$$P^{(N)}(L) = 1 - \sum_{r=0}^{N-1} \binom{N}{r} \Phi_r^{(N)} \{P_S(\sigma_r^{(N)})\}^{N-r}, \tag{13}$$

where the quantities $\Phi_r^{(N)}$, $r = 0, 1 \ldots N-1$ are defined recursively by $\Phi_0^{(N)} = 1$,

$$\Phi_m^{(N)} = 1 - \sum_{r=0}^{m-1} \binom{m}{r} \Phi_r^{(N)} \{P_S(\sigma_r^{(N)})\}^{m-r}, \quad m = 1, 2, \ldots N-1. \tag{14}$$

Furthermore the probability that just r fibers in the bundle fail when the load L is applied is given by

$$P_r^{(N)}(L) = \binom{N}{r} \Phi_r^{(N)} \{P_S(\sigma_r^{(N)})\}^{N-r}, \quad r = 0, 1. . N-1. \tag{15}$$

Although equations (13) and (14) could be used to calculate $P^{(N)}(L)$ for any N and L, experience has shown that considerable numerical errors arise during the course of their application. A second recursive formula will now be derived which is much more satisfactory for numerical computations.

It follows from (11) that

$$\sum_{r=0}^{m} \binom{m}{r} \phi_r(x_0, x_1, \ldots x_{r-1}) x_r^{m-r} = 1, \quad m \geq 0,$$

and thus

$$\sum_{m=0}^{N} \binom{N}{m} z^{N-m} \left\{ \sum_{r=0}^{m} \binom{m}{r} \phi_r(x_0, x_1, \ldots x_{r-1}) x_r^{m-r} \right\} = (1+z)^N$$

for all values of z. By making use of the identity

$$\binom{N}{m}\binom{m}{r} \equiv \binom{N}{r}\binom{N-r}{m-r},$$

and interchanging the orders of the m and r summations, it can be shown that

$$\sum_{r=0}^{N} \binom{N}{r} \phi_r(x_0, x_1, \ldots x_{r-1}) \left\{ \sum_{m=r}^{N} \binom{N-r}{m-r} z^{N-m} x_r^{m-r} \right\} = (1+z)^N,$$

i.e.,

$$\sum_{r=0}^{N} \binom{N}{r} \phi_r(x_0, x_1, \ldots, x_{r-1})(z + x_r)^{N-r} = (1+z)^N,$$

which leads to the recurrence relation

$$\phi_N(x_0, x_1, \ldots x_{N-1}) = (1+z)^N - \sum_{r=0}^{N-1} \binom{N}{r} \phi_r(x_0, x_1, \ldots x_{r-1})(z + x_r)^{N-r}$$

$$N \geq 1, \quad \text{where} \quad \phi_0 = 1. \tag{16}$$

This is a generalization of the recurrence relation (12). The parameter z may be chosen for computational convenience, and moreover it may be different for each stage of the recursive procedure. It has been shown (McCartney, [25]) that the choice $z = -x_{N-1}$, when ϕ_N is being calculated, reduces significantly the numerical error of computation when the number of fibers is large. On substituting $x_r = P_S(\sigma_r^{(N)})$, $r = 0, 1, \ldots N-1$ as before, it follows from (16) that the failure probability $P^{(N)}(L)$ of a bundle of N fibers subjected to a load L may also be calculated using the formula

$$P^{(N)}(L) = \{1 - P_S(\sigma_{N-1}^{(N)})\}^N - \sum_{r=0}^{N-1} \binom{N}{r} \Phi_r^{(N)} \{P_S(\sigma_r^{(N)}) - P_S(\sigma_{N-1}^{(N)})\}^{N-r} \tag{17}$$

where the quantities $\Phi_r^{(N)}$, $r = 0, 1, \ldots, N-1$ are now defined by $\Phi_0^{(N)} = 1$,

$$\Phi_m^{(N)} = \{1 - P_S(\sigma_{m-1}^{(N)})\}^m - \sum_{r=0}^{m-1} \binom{m}{r} \Phi_r^{(N)} \{P_S(\sigma_r^{(N)}) - P_S(\sigma_{m-1}^{(N)})\}^{m-r}$$

$$m = 1, 2, \ldots N-1. \tag{18}$$

The probability that just r fibers in the bundle fail when the load L is applied is again given by (15). The recurrence relation (18) has been used when calculating the numerical results presented in this paper.

4 Accounting for the Effect of the Finite Strength of Defect-Free Fibers

In the analysis presented so far, no explicit allowance has been made for the fact that there is an ultimate tensile strength that is never exceeded. This could be incorporated into the analysis by modifying equation (4) so that $P_F(\sigma) = 1$ whenever $\sigma \geq \sigma_c$, where σ_c is the ultimate tensile strength of the material. A method of allowing for the effect of this will now be presented, which has the advantage that the basic recursive equations remain unchanged and it is only at the final step that the allowance for σ_c is made.

When considering the effect of the finite strength σ_c of defect-free fibers the following applied load ranges must be considered

$$n\sigma_c \leq L < (n+1)\sigma_c, \quad n=1,2,\ldots,N-1, \; N\sigma_c \leq L.$$

If the load L applied to a bundle of N fibers lies in the range $n\sigma_c \leq L < (n+1)\sigma_c$ then the bundle fails if $r \geq N-n$ fibers break because of the presence of defects. The probability of this occurring is the failure probability of the bundle when a load L is applied and this is given by

$$P^{(N)}(L) = \begin{cases} \sum_{r=N-n}^{N} P_r^{(N)}(L), n\sigma_c \leq L < (n+1)\sigma_c, & n=0,1..N-1, \\ 1, \quad N\sigma_c \leq L, \end{cases} \tag{19}$$

where $P_r^{(N)}(L)$ defined by (15) is the probability that just r fibers fail in a bundle of N fibers when the load is applied.

The expression (19) has the advantage that the failure probabilities for the bundle can be computed for a variety of values of σ_c without having to recalculate the value of $P_r^{(N)}(L)$, $r = 1..N$. An alternative approach is simply to redefine the function $P_S(\sigma)$ as follows

$$P_S(\sigma) = \begin{cases} \{1-F(\sigma)\}^a, & \sigma < \sigma_c \\ 0, & \sigma \geq \sigma_c \end{cases}$$

and to proceed as before.

5 Asymptotic Approximations to the Probability of Failure

In Section 3 a recursive formula was given for the calculation of $P^{(N)}(L)$, the probability that a bundle of N fibers fails under the application of a load L. This was extended in Section 4 to allow for the case of finite σ_c, where σ_c is the largest stress that may be supported by a defect-free fiber. In this section three approximations to $P^{(N)}(L)$ will be described. The approximations are all based on the normal distribution, but differ in their means and variances.

Let $G(L)$ denote the probability that a single fiber fails under a load L. For a fiber of cross-sectional area A, the function G is related to the function P_F of (1) by

$$G(L) = P_F(L/A). \tag{20}$$

The approximations depend on constants M, S, L_0, and B, all of which are derived from the function G, and also on two universal constants λ and ϕ, whose numerical values are known. The constant L_0 is defined as the value of L for which the function $L(1-G(L))$ attains its maximum; it is assumed that L_0 is thus uniquely defined. The maximum value is denoted M, i.e.,

$$M = L_0(1-G(L_0)). \tag{21}$$

It is assumed that dG/dL and d^2G/dL^2 exist and are continuous at $L = L_0$ and that

$$\frac{d}{dL}\{L(1-G(L))\}\Big|_{L=L_0} = 0, \tag{22}$$

$$\frac{d^2}{dL^2}\{L(1-G(L))\}\Big|_{L=L_0} < 0. \tag{23}$$

Then S and B are defined by

$$S^2 = L_0^2 G(L_0)(1-G(L_0)), \tag{24}$$

$$B^3 = \left\{\frac{dG}{dL}(L_0)\right\}^2 L_0^4 \Big/ \left\{2\frac{dG}{dL}(L_0) + L_0\frac{d^2G}{dL^2}(L_0)\right\}. \tag{25}$$

Note that (23) guarantees that the denominator of (25) is nonzero.

Let T_N denote the maximum load that can be supported by a bundle of N fibers. It was shown by Peirce [5] that $T_N/N \simeq M$ as $N \to \infty$. The approximations described here are successive refinements of this crude approximation. The first approximation is due to Daniels [1] who showed that the distribution of T_N is approximately normal with mean NM and standard deviation $N^{1/2}S$. Thus

$$P_0^{(N)} = P\{T_N \leq L\} \simeq \Phi\left(\frac{L-NM}{N^{1/2}S}\right) \tag{26}$$

where Φ is the normal distribution function

$$\Phi(x) = (2\pi)^{-1/2}\int_{-\infty}^{x} \exp(-t^2/2)dt.$$

This approximation is valid asymptotically as $N \to \infty$, but the rate of convergence is slow, so that some form of improvement is needed for practical applications.

The realization that the probability of bundle failure could be reformulated as the probability of a random walk crossing a certain curved boundary led to an improved version, described by Daniels [26, 27] in the context of a related problem in epidemic theory and further investigated by Barbour [28] and Smith [29]. This consists of replacing the asymptotic mean NM by $NM + N^{1/3}\lambda B$ where λ is an absolute constant whose value is approximately 0.996. For the definition of λ see any of the cited papers. The new approximation (which will be referred to as the first improvement) is then

$$P_1^{(N)} \simeq \Phi\left(\frac{L-NM-0.996N^{1/3}B}{N^{1/2}S}\right). \tag{27}$$

A second improvement, described by Barbour [30], involves a correction to the asymptotic variance as well. The mean is again taken to be $NM + N^{1/3}\lambda B$ but the variance is now given by $NS^2 + N^{2/3}\phi B^2$ where ϕ is another absolute constant whose numerical value is -0.317. Thus the second improvement yields the approximation

$$P_2^{(N)} \simeq \Phi\left(\frac{L-NM-0.996N^{1/3}B}{(NS^2-0.317N^{2/3}B^2)^{1/2}}\right). \tag{28}$$

It is useful to rewrite the approximations (26), (27), and (28) in the following simpler forms:

$$\left.\begin{aligned} P_0^{(N)} &\simeq \Phi\left(\sqrt{N}\frac{x-1}{\gamma}\right), && \text{(Daniels)} \\ P_1^{(N)} &\simeq \Phi\left(\sqrt{N}\frac{x-1-0.996\beta N^{-2/3}}{\gamma}\right), && \text{(1st improvement)} \\ P_2^{(N)} &\simeq \Phi\left(\sqrt{N}\frac{x-1-0.996N^{-2/3}}{\sqrt{(\gamma^2-0.317\beta^2N^{-1/3})}}\right), && \text{(2nd improvement)} \end{aligned}\right\} \tag{29}$$

where

$$x=\frac{L}{NM},\quad \gamma=\frac{S}{M},\quad \beta=\frac{B}{M}. \tag{30}$$

The parameter x is the ratio of the load per fiber (L/N) applied to the bundle and the maximum load per fiber M that can be supported by an infinite bundle of fibers. It is convenient to introduce the parameters l and l_c defined by

$$l=\frac{L}{NA},\quad l_c=\frac{M}{A},\quad \text{so that}\quad x\equiv\frac{l}{l_c}. \tag{31}$$

The parameter l is the nominal stress applied to the bundle and l_c is the strength of an infinite bundle of fibers.

Now suppose that the strength distribution for single fibers follows the Weibull law

$$P_F(\sigma)=1-\exp\{-(\sigma/\sigma_0)^m\}. \tag{32}$$

The parameters l_c, γ, and β are then given by

$$l_c=\sigma_0 m^{-1/m}e^{-1/m},\quad \gamma=\{e^{1/m}-1\}^{1/2},\quad \beta=m^{-1/3}e^{2/(3m)}. \tag{33}$$

The question of finite σ_c has not been discussed so far in this section. If the inequality

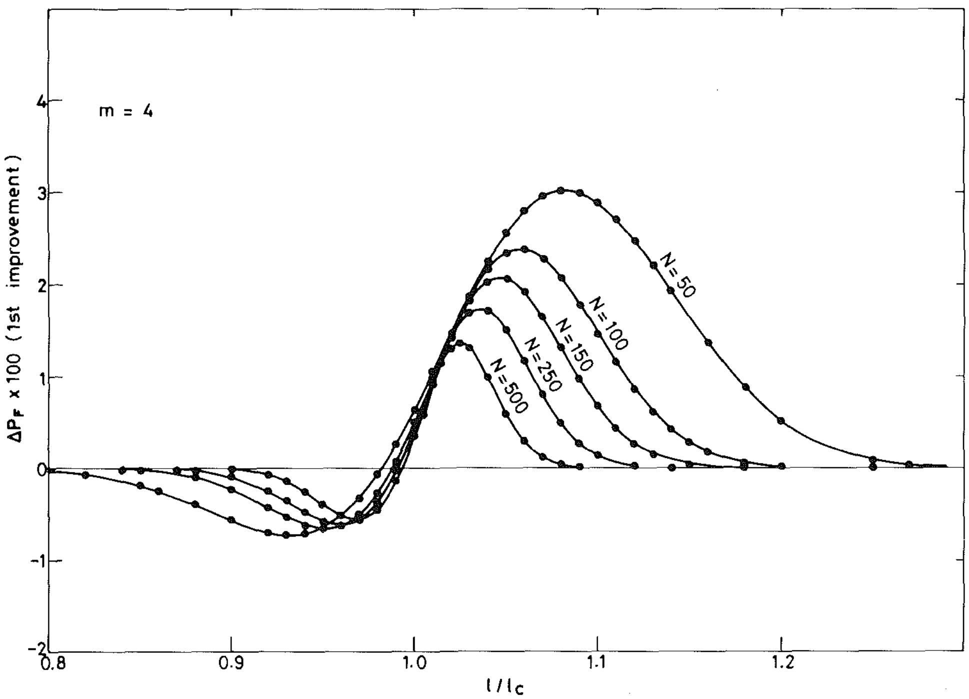

Fig. 1 The dependence of ΔP_F on l/l_c when $m=4$ for the first improvement to Daniels' formula

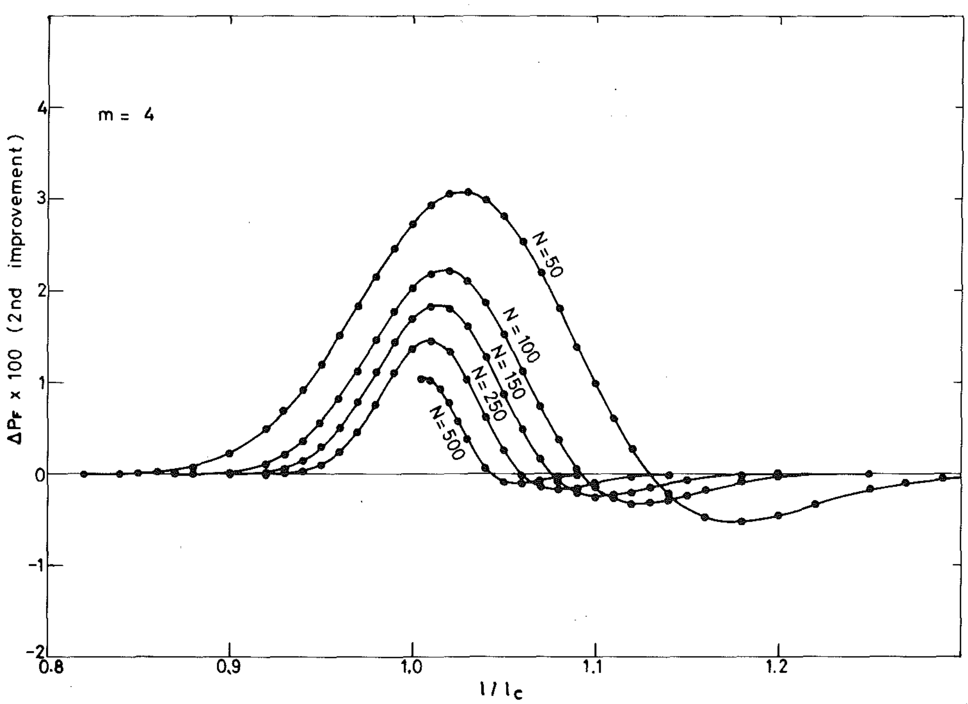

Fig. 2 The dependence of ΔP_F on l/l_c when $m=4$ for the second improvement to Daniels' formula

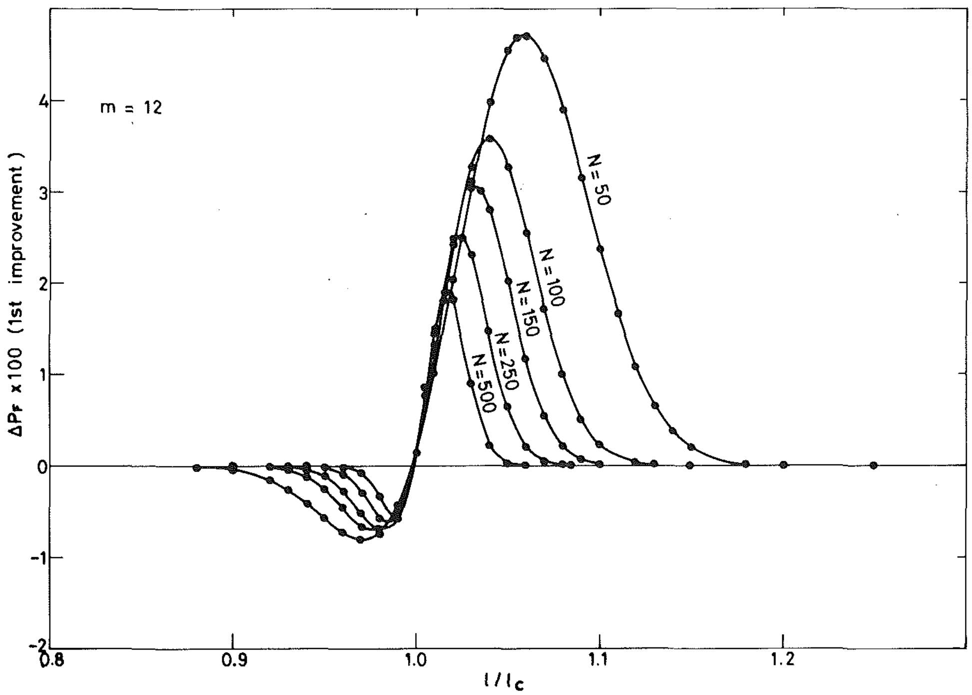

Fig. 3 The dependence of ΔP_F on $1/1_c$ when $m = 12$ for the first improvement to Daniels' formula

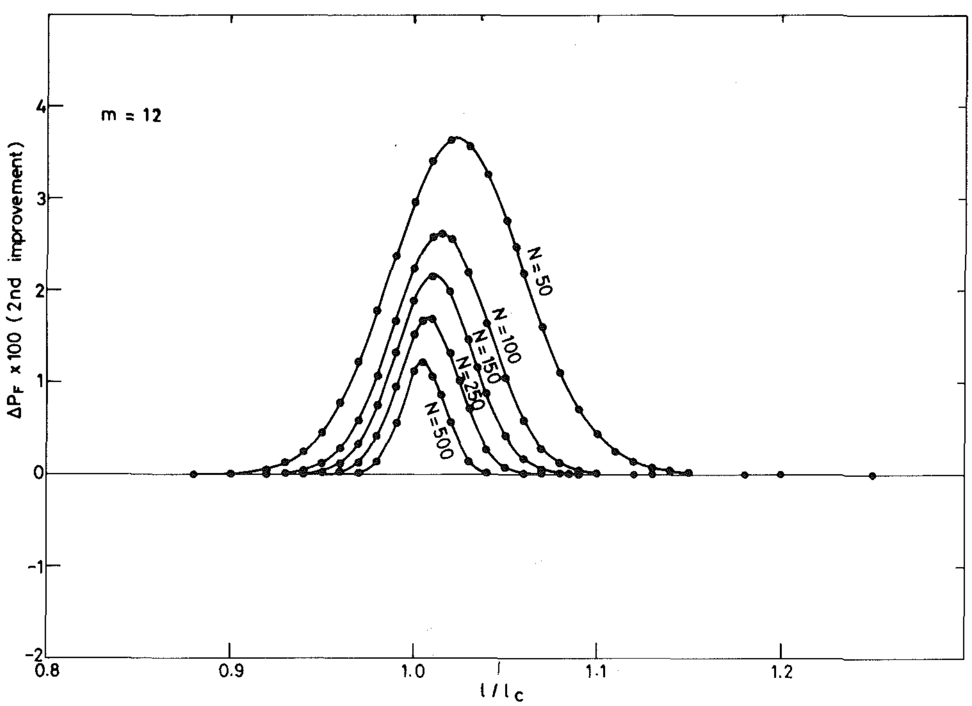

Fig. 4 The dependence of ΔP_F on $1/1_c$ when $m = 12$ for the second improvement to Daniels' formula

$$\sigma_c > L_0/A \tag{34}$$

holds, then the foregoing approximations continue to apply without any change. The reason for this is that the approximations depend only on the local behavior of $P_F(\sigma)$ near $\sigma = L_0/A$, and this is not changed if (34) holds. If (34) were false then the approximations would not be valid because of the nonexistence of derivatives of $G(L) = P_F(L/A)$ at $L = A\sigma_c$, but in this case the fibers ultimately fail at stress σ_c itself. In practice (34) is usually satisfied.

6 Numerical Results

Numerical computations of the failure probabilities of bundles of fibers have been performed on an ICL 2972 computer. Numerical estimates of the exact failure probabilities have been obtained, for bundles of $N = 50$, 100, 150, 250, and 500 fibers, using the relations (17) and (18) for the special case when the survival probability of a single fiber has the Weibull form

$$P_S(\sigma) = \exp(-(\sigma/\sigma_0)^m). \tag{35}$$

The quantities $\sigma_r^{(N)}$, $r = 0, 1, . .N-1$ appearing in the relations (17) and (18) are expressed in terms of the parameter $1/1_c$ as follows

$$\frac{\sigma_r^{(N)}}{\sigma_0} = \frac{N}{N-r} m^{-1/m} e^{-1/m} \frac{1}{1_c}, \qquad (36)$$

where use has been made of the expression (33) for the strength 1_c of an infinite bundle of fibers. Numerical calculations have been performed for the values $m = 4, 8, 12$ for a variety of values of the parameter $1/1_c$ lying in the range $0.8 \leq 1/1_c \leq 1.3$. The asymptotic approximations $P_1^{(N)}$ and $P_2^{(N)}$ defined by the relations (29), (31), and (33) have also been calculated for the same values of the parameters m and $x = 1/1_c$ so that failure probability differences ΔP_F defined by

$$\Delta P_F = P^{(N)}(L) - P_I^{(N)}(L), \quad I = 1,2, \qquad (37)$$

could be computed. The universal constant λ was set equal to 1 for these computations. Very little change was observed using the more precise value $\lambda = 0.996$.

Figures 1 and 2 illustrate the accuracy of the first and second improvements, respectively, when the Weibull exponent $m = 4$, for bundles of $N = 50, 100, 150, 250$, and 500 fibers. The curves for $N = 500$ are incomplete because of numerical errors. The criterion for accepting numerical solutions of the relations (17) and (18) is that

$$\sum_{r=0}^{N} P_r^{(N)}(L) = 1,$$

where $P_r^{(N)}$ is the probability, defined by (15), that just r fibers, in a bundle of N fibers, fail when the load L is applied. It is interesting to note that the first improvement shown in Fig. 1 is most accurate when $1/1_c \simeq 1$ whereas the second improvement shown in Fig. 2 is most inaccurate in this region. Also worthy of note is the slow convergence of the accurate probabilities to the asymptotic solutions as N increases to 500.

Corresponding estimates of the failure probability differences when the Weibull exponent $m = 12$ are shown in Figs. 3 and 4. Again the first improvement is most accurate when $1/1_c \simeq 1$ whereas the second improvement is most inaccurate in this region. Again the convergence is slow as N increases to 500. It is interesting to observe from Fig. 4 that the second improvement consistently underestimates the failure probability. As to be expected, a comparison of Figs. 1 and 3 and Figs. 2 and 4 reveals that the scatter in the strength of the bundles is reduced when m is increased from 4 to 12. The maximum errors of the asymptotic formulas are however increased.

Other aspects of the approximations are illustrated in Figs. 5-7. In Fig. 5, the exact failure probability is plotted against load on normal probability paper, for $m = 4$ and $N = 50$, 250. It may be seen that the resulting curve is, in each case, almost exactly a straight line, which suggests very strongly that a normal approximation is appropriate. In Fig. 6 the corresponding probability density functions dP/dL are plotted, for $m = 4$ and $N = 250$, derived from the exact

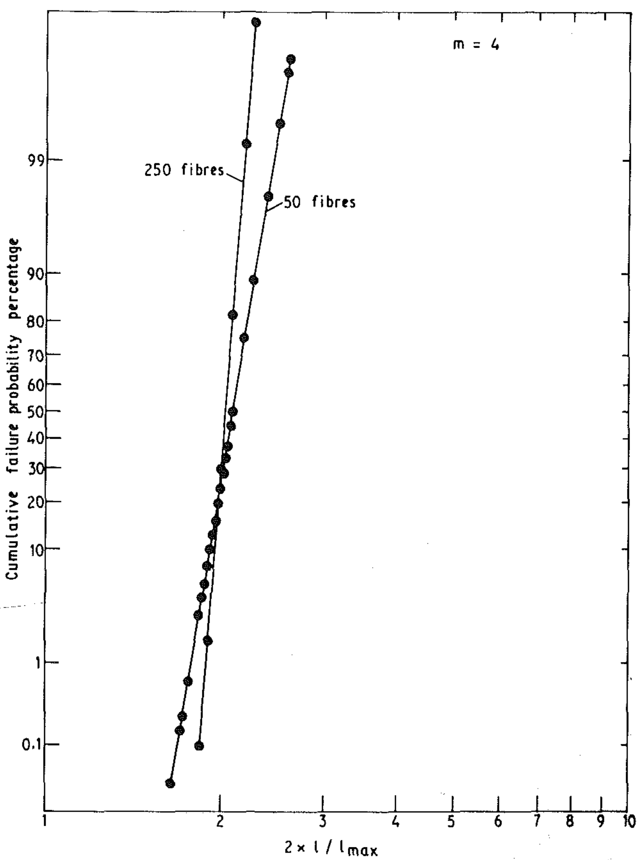

Fig. 5 The dependence of $P^{(N)}(L)$ on L plotted on normal probability paper, $N = 50$ and 250, $m = 4$.

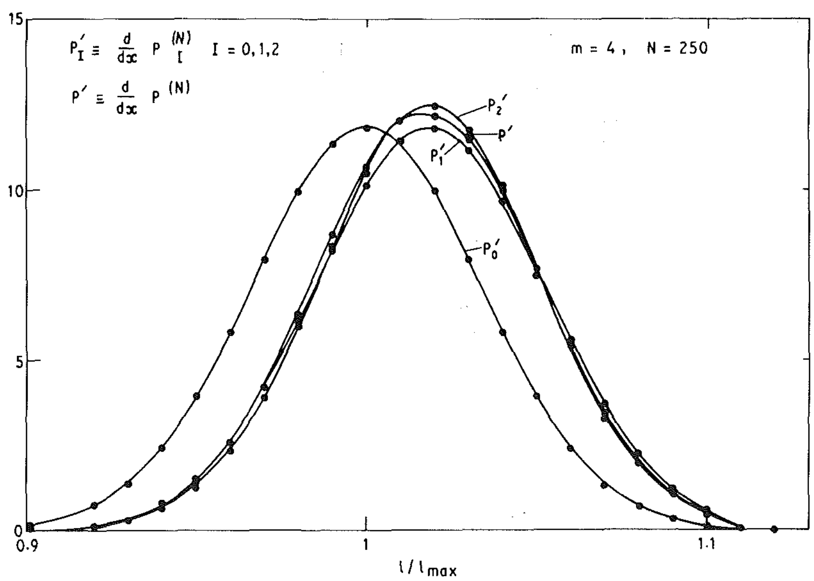

Fig. 6 The four density curves (i.e., P', P_0', P_1', P_2') for $m = 4$, $N = 250$ (closed symbols denote $1/1_c$ values for which the cumulative distribution was known)

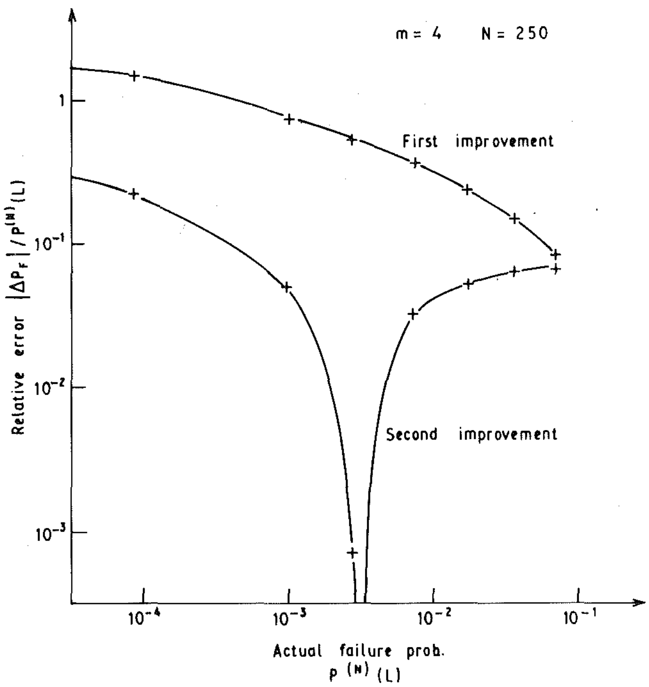

Fig. 7 Plot of $|\Delta P_F| / P^{(N)}(L)$ for $I = 1,2$ ($m = 4$, $N = 250$) when $\lambda = 1$

probabilty of failure and each of the three approximations. This figure shows very clearly that most of the error in P_0 arises from the approximating distribution being shifted to the left compared with the true distribution, and this is corrected by using P_1 in place of P_0. The second improvement, giving rise to P_2, is a distribution with slightly smaller variance than P_1, but Fig. 6 does not by itself provide clear evidence for preferring P_2 to P_1.

The final figure, Fig. 7, illustrates the calculation of relative error in the lower tail. This problem is of particular interest with regard to series-parallel structures (Smith and Phoenix [21]) but is of more general interest because, in most engineering applications, one is really concerned with designing systems with very low failure probability. When, as here, some approximation is used for calculating the failure probability, it is important that the relative error be small when the true probability of failure is small. In Fig. 7 the relative error

$$|\Delta P_F| / P^{(N)}(L) = |P^{(N)}(L) - P_I^{(N)}(L)| / P^{(N)}(L)$$

is plotted for $m = 4$, $N = 250$, and each of the two improvements ($I = 1, 2$). The corresponding curve using P_0 was not plotted, but it is clear from Fig. 6 that P_0 is a noncompetitor in this range ($0.9 \leq 1/1_c \leq 0.99$). Figure 7 is not very easy to interpret because the error in the second improvement changes sign at approximately 3×10^{-3}, but it may be seen that, within the range of values plotted, the relative error in the second improvement is consistently less than that in the first. Similar behavior was observed for other values of m and N. Thus it appears that the second improvement is distinctly better than the first improvement from this point of view.

In conclusion, either of the two improvements is substantially better than the original asymptotic approximation of Daniels [1]. The choice between the two improvements is not nearly so clear-cut, but the evidence available suggests that the second improvement performs significantly better in the lower tail of the distribution.

Acknowledgment

The authors wish to thank Mrs. Pamela Cooper for computing the various curves presented in this paper.

References

1 Daniels, H. E., "The Statistical Theory of the Strength of Bundles of Threads I," *Proc. Roy. Soc.*, London, Series *A*, Vol. 183, 1945, pp. 405–435.

2 Chaplin, W. S., "The Relation Between the Tensile Strengths of Long and Short Bars," Van Nostrand's *Engineering Magazine*, Vol. 23, 1880, pp. 441–444.

3 Chaplin, W. S., "On the Relative Tensile Strengths of Long and Short Bars," *Proceedings of the Engineers Club*, Philadelphia, Vol. 3, 1882, pp. 15–28.

4 Harter, L., "A Chronological Annotated Bibliography on Order Statistics," Vol. 1, 1950, published by the USAF.

5 Peirce, F. T., "Tensile Strength for Cotton Yarns. V.—'The Weakest Link'—Theorems on the Strength of Long and of Composite Specimens," *J. Text. Inst. (Trans.)* Vol. 17, 1926, pp. 355–368.

6 Weibull, W., "A Statistical Theory of the Strength of Materials," *Proc. Ing. Vetenskapsakad.*, No. 151, 1939.

7 Epstein, B., "Statistical Aspects of Fracture Problems," *J. Appl. Phys.*, Vol. 19, 1948, pp. 140–147.

8 Epstein, B., "Applications of the Theory of Extreme Values in Fracture Problems," *J. Am. Stat. Assoc.*, Vol. 43, 1948, pp. 403–412.

9 Gumbel, E. J., "Statistical Theory of Extreme Values and Some Practical Applications," *Nat. Bur. Standards. Appl. Maths. Series*, 33, 1954.

10 Coleman, B. D., "On the Strength of Classical Fibres and Fibre Bundles," *J. Mech. Phys. Solids*, Vol. 7, 1958, pp. 60–70.

11 McClintock, F. A., and Argon, A. S., "Mechanical Behaviour of Materials," Addison-Wesley, Reading, Mass. 1966.

12 Argon, A. S., "Statistical Aspects of Fracture," In: *Composite Materials* Vol. V, Broutman, L. J., ed., Academic Press, New York, 1974, pp. 184–190.

13 Hunt, R. A., and McCartney, L. N., "A New Approach to Weibull's Statistical Theory of Brittle Fracture," *Int. J. Fract.*, Vol. 15, 1979, pp. 365–375.

14 Coleman, B. D., "Time Dependence of Mechanical Breakdown in Bundles of Fibers. I. Constant Total Load," *J. Appl. Phys.*, Vol. 28, 1957, pp. 1058–1064.

15 Coleman, B. D., "Time Dependence of Mechanical Breakdown in Bundles of Fibers. III. The Power Law Breakdown Rule," *Trans. Soc. Rheol.*, Vol. 2, 1958, pp. 195–218.

16 Coleman, B. D., "Statistics and Time Dependence of Mechanical Breakdown in Fibers," *J. Appl. Phys.*, Vol. 29, 1958, pp. 968–983.

17 Phoenix, S. L., "Stochastic Strength and Fatigue of Fiber Bundles," *Int. J. Fracture*, Vol. 14, 1978, pp. 327–344.

18 Phoenix, S. L., "The Asymptotic Time to Failure of a Mechanical System of Parallel Members," *SIAM. J. Appl. Math.*, Vol. 34, 1978, pp. 227–246.

19 Phoenix, S. L., "The Asymptotic Distribution for the Time to Failure of a Fiber Bundle," *Adv. Appl. Prob.*, Vol. 11, 1979, pp. 153–187.

20 Phoenix, S. L., and Taylor, H. M., "The Asymptotic Strength Distribution of a General Fiber Bundle," *Adv. Appl. Prob.*, Vol. 5, 1973, pp. 200–216.

21 Smith, R. L., and Phoenix, S. L., "Asymptotic Distributions for the Failure of Fibrous Materials Under Series-Parallel Structure and Equal Load-Sharing," ASME JOURNAL OF APPLIED MECHANICS, Vol. 48, 1981, pp. 75–82.

22 Harlow, D. G., and Phoenix, S. L., "Probability Distributions for the Strength of Composite Materials. I. Two Level Bounds," *Int. J. Fract.*, Vol. 17, 1981, pp. 347–372.

23 Harlow, D. G., and Phoenix, S. L., "Probability Distributions for the Strength of Composite Materials. II: a Convergent Sequence of Tight Bounds." *Int. J. Fract.*, Vol. 17, 1981, pp. 601–630.

24 Smith, R. L., "A Probability Model for Fibrous Composites With Local Load Sharing," *Proc. Roy. Soc.*, London, Series A, Vol. 372, 1980, pp. 539–553.

25 McCartney, L. N., "Statistics for the Strength of Fibre Bundles" presented at Conference on *Micromechanisms of Fracture* at Cambridge, Mar. 1980. (published in *Metal Science*, Vol. 15, 1981, pp. 471–474.)

26 Daniels, H. E., "An Approximation Technique for a Curved Boundary Problem," *Adv. Appl. Prob*, Vol. 6, 1974, pp. 194–196.

27 Daniels, H. E., "The Maximum Size of a Closed Epidemic," *Adv. Appl. Prob.*, Vol. 6, 1974, pp. 607–621.

28 Barbour, A. D., "A Note on the Maximum Size of a Closed Epidemic," *J. Roy. Stat. Soc.*, Series B, Vol. 37, 1975, pp. 459–460.

29 Smith, R. L., "The Asymptotic Distribution of the Strength of a Series-Parallel System With Equal Load-Sharing," *Ann. Prob.*, Vol. 10, 1982, pp. 137–171.

30 Barbour, A. D., "Brownian Motion and a Sharply Curved Boundary," *Adv. Appl. Prob.*, Vol. 13, 1981, pp. 736–750.

The Crack Problem for a Nonhomogeneous Plane[1]

F. Delale
Department of Mechanical Engineering and Mechanics, Drexel University, Philadelphia, Pa. 19104

F. Erdogan
Department of Mechanical Engineering and Mechanics, Lehigh University, Bethlehem, Pa. 18015
Mem. ASME

In this paper the plane elasticity problem for a nonhomogeneous medium containing a crack is considered. It is assumed that the Poisson's ratio of the medium is constant and the Young's modulus E *varies exponentially with the coordinate parallel to the crack. First the half plane problem is formulated and the solution is given for arbitrary tractions along the boundary. Then the integral equation for the crack problem is derived. It is shown that the integral equation having the derivative of the crack surface displacement as the density function has a simple Cauchy-type kernel. Hence, its solution and the stresses around the crack tips have the conventional square-root singularity. The solution is given for various loading conditions. The results show that the effect of the Poisson's ratio and consequently that of the thickness constraint on the stress intensity factors are rather negligible. On the other hand, the results are highly affected by the parameter β describing the material nonhomogeneity in* $E(x) = E_0 exp(\beta x)$.

1 Introduction

In practical applications the material nonhomogeneity becomes an important factor to be considered particularly in two classes of problems. The first is a group of problems in geophysics in which, because of the size of the medium, the spatial variation of the material constants cannot be assumed to be negligible. The foundation and contact problems in soil mechanics and the wave propagation problems in the earth's crust may be mentioned as some of the examples. The second group of problems relates to the fracture of essentially nonhomogeneous solids. "Hydraulic fracturing" of the medium which consists of sandstone and shale, the fracture of structural materials with periodically varying material properties (as in certain laminated structures), and the fracture of variety of fuse-bonded materials used in electronics industry are some typical examples. The distinguishing feature of these materials is that the material constants are continuous and generally differentiable functions of the space coordinates, whereas in the standard particulate, layered, and fiber-reinforced composites the material constants are discontinuous functions. The consequence of the discontinuous behavior of the material in crack problems is that the nature of singularity of the stresses at the crack tip that is on the interface and at the point of intersection of a crack and the interface is quite different from the singularity exhibited by a crack tip that is fully imbedded in a homogeneous medium. Even though no systematic study of the problem appears to have been made, it is reasonable to expect that in nonhomogeneous materials with continuous and continuously differentiable elastic constants the nature of the stress singularity at a crack tip would be identical to that of a homogeneous solid. The existing solutions of crack and punch problems in certain specific nonhomogeneous materials seem to support this view.

In most of the existing solutions to problems relating to nonhomogeneous solids it is assumed that the material is isotropic, the Poisson's ratio is constant, and the Young's (or the shear) modulus is either an exponential or a power function of a space variable [1]. In the wedge problem described in [2] the class of functions $E(r, \theta)$ for the Young's modulus leading to a feasible solution has been investigated. Some sample studies of the Boussinesq and contact problems for a nonhomogeneous half space may be found in [3-8]. The corresponding "torsion" problem for a half space is described in [9, 10]. The equivalent crack problems in a nonhomogeneous medium under torsion and under antiplane shear loading are discussed in [11] and [12], respectively. In the studies described in [3, 8], the shear modulus is assumed to be $\mu_0 \exp(\gamma y)$ and in [12] $\mu_0 \exp(\alpha x + \beta y)$, where $y=0$ is either the boundary of the half plane or the plane of the crack. In [4-7] and [9-11] it is assumed that $\mu = \mu_0 |y|^m$, $(0<m<1)$. This latter assumption clearly has the undesirable physical feature in that at $y=0$ the shear modulus becomes zero. It is particularly difficult to attach any physical meaning to the solution of a crack problem carried out under this assumption. This difficulty has been removed in the crack problem considered in [13] where it was assumed that the shear modulus is given by $\mu = \mu_0/(1+c|y|)$, where c is a constant. It

[1] This work was supported by NASA-Langley under the Grant NGR 39-007-011 and by NSF under the Grant CME 78-09737.

Contributed by the Applied Mechanics Division and presented at the 1983 ASME Applied Mechanics, Bioengineering, and Fluids Engineering Conference, Houston, Texas, June 20-22, 1983 of THE AMERICAN SOCIETY OF MECHANICAL ENGINEERS.

Discussion on this paper should be addressed to the Editorial Department, ASME, United Engineering Center, 345 East 47th Steet, New York, N.Y. 10017 and will be accepted until two months after final publication of the paper itself in the JOURNAL OF APPLIED MECHANICS. Manuscript received by ASME Applied Mechanics Division, July, 1982; final revision, January, 1983. Paper No. 83-APM-35.

Copies will be available until February, 1984.

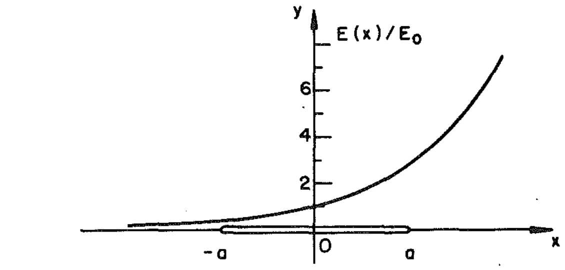

Fig. 1 The crack geometry in the nonhomogeneous medium and the variation of the Young's modulus $E = E_0 e^{\beta x}$

should again be noted that the solutions given in [3–13] are based on the assumption that the Poisson's ratio is constant.

In the studies mentioned in the foregoing (with the exception of [12] which deals with the relatively simple problem of antiplane shear) it is assumed that in the direction(s) parallel to the boundary of the half plane or the plane of the crack the shear modulus does not vary. In the case of fracture of such a nonhomogeneous medium since, generally, the plane of the crack is not a plane of symmetry, the inplane shear component of the stress intensity factor would not be zero and hence the propagating crack would eventually align itself parallel to the direction in which the modulus varies. In the problem considered in this paper it is then assumed that the crack is located on the $y=0$ plane, the Young's modulus is an exponential function of x, and the Poisson's ratio is constant (Fig. 1).

2 Formulation of the Crack Problem

Consider the plane elasticity problem for a nonhomogeneous solid in which the Poisson's ratio ν is constant and the Young's modulus E is a function of x and y. Let $F(x,y)$ be the Airy stress function. The stresses are given by

$$\sigma_{xx} = \frac{\partial^2 F}{\partial y^2}\,, \quad \sigma_{yy} = \frac{\partial^2 F}{\partial x^2}\,, \quad \sigma_{xy} = -\frac{\partial^2 F}{\partial x \partial y}\,. \tag{1}$$

Substituting from (1) through the Hooke's Law into the compatibility equation, for the plane problem we obtain

$$\begin{aligned} \mathrm{E}^2 \nabla^4 F \;-\; & 2\mathrm{E}\left(\frac{\partial \mathrm{E}}{\partial x}\frac{\partial}{\partial x} + \frac{\partial \mathrm{E}}{\partial y}\frac{\partial}{\partial y}\right)\nabla^2 F \\ & + 2(1+\nu)\left(2\frac{\partial E}{\partial x}\frac{\partial \mathrm{E}}{\partial y} - \mathrm{E}\frac{\partial^2 \mathrm{E}}{\partial x \partial y}\right)\frac{\partial^2 F}{\partial x \partial y} \\ & + \left[2\left(\frac{\partial \mathrm{E}}{\partial x}\right)^2 - 2\nu\left(\frac{\partial \mathrm{E}}{\partial y}\right)^2 \right. \\ & \left. - \mathrm{E}\frac{\partial^2 \mathrm{E}}{\partial x^2} + \nu \mathrm{E}\frac{\partial^2 \mathrm{E}}{\partial y^2}\right]\frac{\partial^2 F}{\partial x^2} \\ & + \left[2\left(\frac{\partial \mathrm{E}}{\partial y}\right)^2 - 2\nu\left(\frac{\partial \mathrm{E}}{\partial x}\right)^2 \right. \\ & \left. - \mathrm{E}\frac{\partial^2 \mathrm{E}}{\partial y^2} + \nu \mathrm{E}\frac{\partial x^2}{\partial^2 \mathrm{E}}\right]\frac{\partial^2 F}{\partial y^2} = 0. \end{aligned} \tag{2}$$

Equation (2) is for the generalized plane stress. The differential equation for plane strain is obtained by replacing E and ν by $\mathrm{E}/(1-\nu^2)$ and $\nu/(1-\nu)$, respectively. From (2) it may easily be verified that if we let

$$\mathrm{E} = \mathrm{E}_0 \,\exp\, (\beta x + \gamma y), \quad \nu = \text{constant} \tag{3}$$

the differential equation becomes one of constant coefficients which may be written as

$$\begin{aligned} \nabla^4 F - 2\left(\beta\frac{\partial}{\partial x} + \gamma\frac{\partial}{\partial y}\right)\nabla^2 F + (\beta^2 - \nu\gamma^2)\frac{\partial^2 F}{\partial x^2} \\ + 2(1+\nu)\beta\gamma\frac{\partial^2 F}{\partial x \partial y} + (\gamma^2 - \nu\beta^2)\frac{\partial^2 F}{\partial y^2} = 0. \end{aligned} \tag{4}$$

In problems involving the study of localized phenomena such as perturbation in stress state due to the presence of a crack or a punch, a material representation such as (3) would not be very unrealistic. In most cases a reasonable approximation to the actual distribution of $\mathrm{E}(x,y)$ can be obtained by adjusting the constants E_0, β, and γ. Referring to Fig. 1, in this problem we will further assume that E is independent of y. Thus, $y=0$ is a plane of symmetry provided we also consider only those external loads that are symmetric with respect to $y=0$. It is therefore sufficient to consider one half of the medium $(-\infty < x < \infty, y > 0)$ only. By letting $\gamma = 0$ in (4) the differential equation of the problem becomes

$$\nabla^4 F - 2\beta\left(\frac{\partial^3 F}{\partial x^3} + \frac{\partial^3 F}{\partial x \partial y^2}\right) + \beta^2\frac{\partial^2 F}{\partial x^2} - \nu\beta^2\frac{\partial^2 F}{\partial y^2} = 0. \tag{5}$$

Note that (5) reduces to the standard biharmonic equation for $\beta = 0$.

Assuming the solution of (5) in the form

$$F(x,y) = \frac{1}{2\pi}\int_{-\infty}^{\infty} f(y,\alpha)e^{-ix\alpha}d\alpha, \quad (-\infty < x < \infty, y > 0), \tag{6}$$

we obtain

$$\frac{d^4 f}{dy^4} + (2i\beta\alpha - 2\alpha^2 - \beta^2\nu)\frac{d^2 f}{dy^2} + (\alpha^4 - 2i\beta\alpha^3 - \beta^2\alpha^2)f = 0. \tag{7}$$

If we now look for a solution to (7) of the form $f = \exp(my)$ we find

$$m^4 + (2i\beta\alpha - 2\alpha^2 - \beta^2\nu)m^2 + (\alpha^4 - 2i\beta\alpha^3 - \beta^2\alpha^2) = 0. \tag{8}$$

The solution to (8) is found to be

$$\begin{aligned} m_1 \;&=\; -m_3 = [(-\gamma_1 + \gamma_2)/2]^{1/2}, \;\; m_2 = \\ & \quad -m_4 = [(-\gamma_1 - \gamma_2)/2]^{1/2}, \\ \gamma_1 \;&=\; 2i\beta\alpha - 2\alpha^2 - \beta^2\nu, \quad \gamma_2 = (\beta^4\nu^2 - 4i\beta^3\nu\alpha + 4\beta^2\nu\alpha^2)^{1/2}. \end{aligned} \tag{9}$$

In (9) roots m_j are ordered in such a way that $Re(m_1) > 0$, $Re(m_2) > 0$. It is assumed that the problem in the absence of the crack has been solved under the actual loading conditions, and that the crack length $2a$ is "small" compared to other (planar) dimensions of the solid. Through a superposition the singular part of the solution may then be reduced to that of an infinite nonhomogeneous plane with the self-equilibrating crack surface tractions as the only external loads. Thus, in the problem of interest the stresses and displacements vanish for $(x^2 + y^2) \to \infty$, and the solution to (7) may be expressed as

$$f(y,\alpha) = A_1(\alpha)e^{-m_1 y} + A_2(\alpha)e^{-m_2 y}, \quad (0 < y < \infty). \tag{10}$$

From (1), (6), and (9) it then follows that

$$\sigma_{xx}(x,y) \;=\; \frac{1}{2\pi}\int_{-\infty}^{\infty}\sum_1^2 A_j m_j^{\,2} e^{-m_j y}e^{-ix\alpha}d\alpha, \tag{11}$$

$$\sigma_{yy}(x,y) \;=\; -\frac{1}{2\pi}\int_{-\infty}^{\infty}\alpha^2\sum_1^2 A_j e^{-m_j y}e^{-ix\alpha}d\alpha, \tag{12}$$

$$\sigma_{xy}(x,y) \;=\; -\frac{i}{2\pi}\int_{-\infty}^{\infty}\alpha\sum_1^2 A_j m_j e^{-m_j y}e^{-ix\alpha}d\alpha. \tag{13}$$

This completes the formulation of the problem for the half plane $y > 0$ in which the functions A_1 and A_2 are determined from the two boundary conditions at $y=0$, $-\infty < x < \infty$. For example, let the half plane be subjected to tractions

$$\sigma_{yy}(x,0) = \sigma(x), \quad \sigma_{xy}(x,0) = \tau(x), \quad (-\infty < x < \infty) \tag{14}$$

on the boundary $y=0$ and be kept in equilibrium by a resultant force applied to the medium at infinity which is collinear with a force defined by the following x and y-components:

$$P_x=\int_{-\infty}^{\infty}\tau(x)dx, \quad P_y=\int_{-\infty}^{\infty}\sigma(x)\,dx. \tag{15}$$

From (12) and (13) A_1 and A_2 may then be obtained as follows:

$$A_1(\alpha) = \frac{1}{m_1-m_2}\left(\frac{Q_1}{\alpha^2}+i\frac{Q_2}{\alpha}\right), \tag{16}$$

$$A_2(\alpha) = -\left(1+\frac{1}{m_1-m_2}\right)\frac{Q_1}{\alpha^2}-\frac{i}{m_1-m_2}\frac{Q_2}{\alpha}, \tag{17}$$

where

$$Q_1(\alpha) = \int_{-\infty}^{\infty}\sigma(x)e^{ix\alpha}dx,\ Q_2(x)=\int_{-\infty}^{\infty}\tau(x)e^{ix\alpha}dx. \tag{18}$$

3 The Integral Equation

We assume that the original cracked solid is loaded symmetrically in such a way that

$$\sigma_{xy}(x,0)=0, \quad -\infty<x<\infty. \tag{19}$$

In the perturbation problem, in addition to (19), we then have the following mixed boundary condition

$$\sigma_{yy}(x,+0)=p(x), \quad (-a<x<a), \tag{20}$$

$$v(x,0)=0, \quad a<|x|<\infty, \tag{21}$$

where $p(x)$ is a known function and v is the y-component of the displacement. From (13) and (19) it follows that

$$m_1A_1+m_2A_2=0. \tag{22}$$

To obtain the second equation to determine A_1 and A_2 we introduce a new unknown function $g(x)$ by

$$g(x)=\frac{\partial}{\partial x}v(x,+0), \tag{23}$$

From (21) and (23) it is seen that $g(x)=0$ for $|x|>a$ and

$$\int_{-a}^{a}g(x)\,dx=0. \tag{24}$$

By using the Hooke's law from (11) and (12) it can be shown that

$$\frac{\partial}{\partial x}v(x,y)=-\frac{1}{2\pi}\frac{1}{\mathrm{E}(x)}\int_{-\infty}^{\infty}(\beta+i\alpha)\left[\frac{A_1}{m_1}(\alpha^2+\nu m_1{}^2)e^{-m_1y}+\frac{A_2}{m_2}(\alpha^2+\nu m_2{}^2)e^{-m_2y}\right]e^{-ix\alpha}d\alpha, \quad (y>0). \tag{25}$$

Equations (23) and (25) would then give

$$-\frac{\beta+i\alpha}{\mathrm{E}_0}\left[\frac{A_1}{m_1}(\alpha^2+\nu m_1{}^2)+\frac{A_2}{m_2}(\alpha^2+\nu m_2{}^2)\right]=\int_{-a}^{a}g(t)e^{(\beta+i\alpha)t}dt. \tag{26}$$

From (22) and (26) the functions A_1 and A_2 are now determined as follows:

$$A_1(\alpha)=\frac{\mathrm{E}_0m_1m_2{}^2}{\alpha^2(m_1{}^2-m_2{}^2)(\beta+i\alpha)}\int_{-a}^{a}g(t)e^{(\beta+i\alpha)t}dt=-\frac{m_2}{m_1}A_2. \tag{27}$$

By substituting from (27) and (12) into (20) we obtain the following integral equation to determine $g(x)$:

$$\lim_{y\to+0}\frac{1}{2\pi}\int_{-a}^{a}g(t)e^{\beta t}dt\int_{-\infty}^{\infty}\frac{\mathrm{E}_0m_1m_2}{(\beta+i\alpha)(m_1{}^2-m_2{}^2)}(m_1e^{-m_2y}-m_2e^{-m_1y})e^{i(t-x)\alpha}\,d\alpha=p(x), \quad |x|<a. \tag{28}$$

To investigate and to separate a possible singular part of the kernel in (28) the asymptotic behavior of the inner integral must be examined. From (9) we observe that for $|\alpha|\to\infty$ $m_1\to|\alpha|$ and $m_2\to|\alpha|$. Now, by expressing the inner integral in (28) as

$$h(x,y,t)=\int_{-\infty}^{\infty}K(y,\alpha)e^{i(t-x)\alpha}\,d\alpha \tag{29}$$

and by noting that any singular part h may have must be due to the behavior of K at $|\alpha|\to\infty$, we may write h as follows:

$$h(x,y,t)=\int_{-\infty}^{\infty}[K(y,\alpha)-K_\infty(y,\alpha)]e^{i(t-x)\alpha}\,d\alpha+\int_{-\infty}^{\infty}K_\infty(y,\alpha)e^{i(t-x)\alpha}\,d\alpha. \tag{30}$$

where K_∞ is the asymptotic value of $K(y,\alpha)$ for large values of $|\alpha|$. The first integral in (30) is uniformly convergent and, therefore, when substituted into (28) the limit can be put under the integral sign. It may easily be shown that

$$K_\infty(y,\alpha)=\frac{\mathrm{E}_0}{2i}\frac{\alpha}{|\alpha|}e^{-|\alpha|y}, \tag{31}$$

and the second integral in (28) may be expressed as

$$\int_{-\infty}^{\infty}\frac{\mathrm{E}_0}{2i}\frac{\alpha}{|\alpha|}e^{-|\alpha|y}[\cos(t-x)\alpha+i\sin(t-x)\alpha]d\alpha=\frac{\mathrm{E}_0(t-x)}{(t-x)^2+y^2}. \tag{32}$$

Also, by defining

$$M(\alpha)=\frac{m_1m_2}{(\beta+i\alpha)(m_1+m_2)}e^{i(t-x)\alpha}, \tag{33}$$

and by substituting $y=0$ in the first integral, equation (30) may now be written as follows:

$$h(x,y,t)=\mathrm{E}_0\int_0^{\infty}[M(\alpha)+M(-\alpha)-\sin(t-x)\alpha]d\alpha+\frac{\mathrm{E}_0(t-x)}{(t-x)^2+y^2}. \tag{34}$$

Finally, if we substitute from (34) into (28) and go to limit we obtain

$$\frac{1}{\pi}\int_{-a}^{a}\left[\frac{e^{\beta t}}{t-x}+k(x,t)\right]g(t)\,dt=\frac{1+\kappa}{4\mu_0}p(x), \quad (-a<x<a), \tag{35}$$

where the Fredholm kernel is defined by

$$k(x,t)=e^{\beta t}\int_0^{\infty}[M(\alpha)+M(-\alpha)-\sin(t-x)\alpha]d\alpha, \tag{36}$$

and $\mathrm{E}_0/2$ is replaced by $4\mu_0/(1+\kappa)$ in order to cover both generalized plane stress and plane strain problems. Here μ_0 is the shear modulus at $x=0$, i.e., $\mu_0=\mathrm{E}_0/2(1+\nu)$, $\kappa=3-4\nu$ for plane strain, and $\kappa=(3-\nu)/(1+\nu)$ for the generalized plane stress. Note that for $\beta=0$, $K=K_\infty$, $k(x,t)=0$, and (35) reduces to the known integral equation of the simple (Mode I) crack problem for a homogeneous plane.

For numerical solution the interval $(-a,a)$ is normalized by defining

$$s=t/a,\ r=x/a,\ \phi(s)=g(t),\ n(r,s)=k(x,t),\ q(r)=p(x),\ -1<(r,s)<1,\ -a<(x,t)<a. \tag{37}$$

In terms of the normalized quantities the integral equation (35) and the single-valuedness condition (24) may be expressed as

$$\frac{1}{\pi}\int_{-1}^{1}\left[\frac{e^{\beta as}}{s-r}+n(r,s)\right]\phi(s)ds$$

$$=\frac{1+\kappa}{4\mu_0}q(r), \quad (-1<r<1), \tag{38}$$

$$\int_{-1}^{1}\phi(s)\,ds=0. \tag{39}$$

4 Stress Intensity Factors

The index of the singular integral equation (38) is $+1$. Therefore its solution is of the following form:

$$e^{a\beta s}\phi(s)=\frac{G(s)}{\sqrt{1-s^2}}, \quad -1<s<1, \tag{40}$$

where $G(s)$ is a bounded function. The unknown function G may be determined from (38) and (39) to any desired degree of accuracy by using a Gaussian integration technique to solve the singular integral equation (see, for example, [14]). By observing that the left-hand side of (35) gives $\sigma_{yy}(x,0)$ for $|x|>a$ as well as for $|x|<a$, through a simple asymptotic analysis, the Mode I stress intensity factors at the crack tips defined by

$$k_1(a)=\lim_{x\to a}\sqrt{2(x-a)}\sigma_{yy}(x,0), \tag{41}$$

$$k_1(-a)=\lim_{x\to -a}\sqrt{2(-x-a)}\sigma_{yy}(x,0), \tag{42}$$

may be expressed in terms of $G(s)$ as follows[2]:

$$k_1(a)=-\frac{4}{1+\kappa}\mu_0 G(1)\sqrt{a}, \tag{43}$$

[2] Note that $\mu_0\exp(\beta a)=\mu(a)$ and the expressions (43) and (44) are identical to those found for the homogeneous materials.

$$k_1(-a)=\frac{4}{1+\kappa}\mu_0 G(-1)\sqrt{a}. \tag{44}$$

From (23) and (37) it is seen that after obtaining $G(s)$ the crack surface displacement may be calculated as

$$\frac{v(x)}{a}=\int_{-1}^{x/a}\frac{G(s)}{\sqrt{1-s^2}}e^{-a\beta s}ds. \tag{45}$$

It should again be emphasized that the structure of the integral equation (35) is essentially the same as that of a homogeneous medium, namely its kernel has a simple Cauchy singularity. Therefore, its solution and consequently the stress

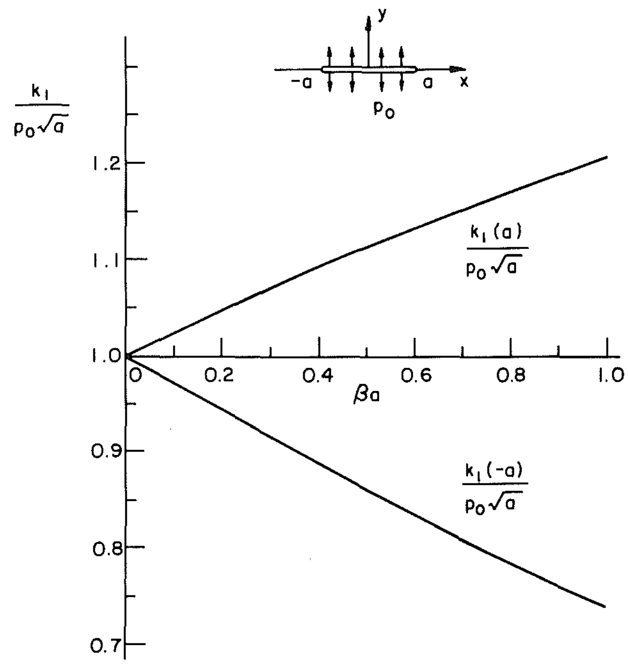

Fig. 2 Stress intensity factors in a nonhomogeneous medium having a uniformly pressurized crack ($E(x)=E_0e^{\beta x}$, $\nu=0.3$, plane stress *conditions*)

Table 1 The normalized stress intensity factors for various loading conditions for the case of generalized plane stress ($\nu=0.3$)

βa	$\frac{k_1(a)}{\epsilon_0E_0\sqrt{a}}$	$\frac{k_1(-a)}{\epsilon_0E_0\sqrt{a}}$	$\frac{k_1(a)}{\epsilon_1E_0\sqrt{a}}$	$\frac{k_1(-a)}{\epsilon_1E_0\sqrt{a}}$	$\frac{k_1(a)}{p_0\sqrt{a}}$	$\frac{k_1(-a)}{p_0\sqrt{a}}$	$\frac{k_1(a)}{p_1\sqrt{a}}$	$\frac{k_1(-a)}{p_1\sqrt{a}}$	$\frac{k_1(a)}{p_2\sqrt{a}}$	$\frac{k_1(-a)}{p_2\sqrt{a}}$	$\frac{k_1(a)}{p_3\sqrt{a}}$	$\frac{k_1(-a)}{p_3\sqrt{a}}$
→0	1.0	1.0	0.5	-0.5	1.0	1.0	0.5	-0.5	0.5	0.5	0.375	-0.375
0.01	1.008	0.992	0.505	-0.495	1.003	0.997	0.500	-0.500	0.501	0.499	0.375	-0.375
0.10	1.078	0.925	0.552	-0.453	1.025	0.973	0.500	-0.500	0.506	0.493	0.375	-0.375
0.25	1.202	0.820	0.640	-0.389	1.060	0.930	0.498	-0.499	0.515	0.483	0.374	-0.375
0.50	1.435	0.665	0.814	-0.302	1.113	0.861	0.495	-0.495	0.528	0.466	0.372	-0.373
0.75	1.713	0.535	1.031	-0.234	1.162	0.797	0.489	-0.489	0.540	0.450	0.369	-0.370
1.00	2.048	0.429	1.301	-0.181	1.209	0.740	0.483	-0.480	0.552	0.435	0.366	-0.366

Table 2 The normalized stress intensity factors for various loading conditions for the case of plane strain ($\nu=0.3$)

βa	$\frac{(1-\nu^2)k_1(a)}{\epsilon_0E_0\sqrt{a}}$	$\frac{(1-\nu^2)k_1(-a)}{\epsilon_0E_0\sqrt{a}}$	$\frac{(1-\nu^2)k_1(a)}{\epsilon_1E_0\sqrt{a}}$	$\frac{(1-\nu^2)k_1(-a)}{\epsilon_1E_0\sqrt{a}}$	$\frac{k_1(a)}{p_0\sqrt{a}}$	$\frac{k_1(-a)}{p_0\sqrt{a}}$	$\frac{k_1(a)}{p_1\sqrt{a}}$	$\frac{k_1(-a)}{p_1\sqrt{a}}$	$\frac{k_1(a)}{p_2\sqrt{a}}$	$\frac{k_1(-a)}{p_2\sqrt{a}}$	$\frac{k_1(a)}{p_3\sqrt{a}}$	$\frac{k_1(-a)}{p_3\sqrt{a}}$
→0	1.0	1.0	0.5	-0.5	1.0	1.0	0.5	-0.5	0.5	0.5	0.375	-0.375
0.01	1.008	0.992	0.505	-0.495	1.003	0.997	0.500	-0.500	0.501	0.499	0.375	-0.375
0.10	1.078	0.925	0.552	-0.453	1.026	0.973	0.500	-0.500	0.506	0.493	0.375	-0.375
0.25	1.203	0.821	0.640	-0.389	1.061	0.931	0.498	-0.499	0.515	0.483	0.374	-0.375
0.50	1.439	0.667	0.814	-0.302	1.117	0.863	0.494	-0.495	0.529	0.466	0.372	-0.373
0.75	1.721	0.539	1.032	-0.234	1.170	0.801	0.489	-0.489	0.542	0.451	0.369	-0.370
1.00	2.063	0.433	1.304	-0.181	1.222	0.745	0.483	-0.481	0.555	0.436	0.366	-0.366

Table 3 The effect of Poisson's ratio on the stress intensity factors ($\beta a = 0.5$) ($E_0^* = E_0$ for plane stress, $E_0^* = E_0/1-\nu^2$ for plane strain)

	ν	$\frac{k_1(a)}{\epsilon_0 E_0^* \sqrt{a}}$	$\frac{k_1(-a)}{\epsilon_0 E_0^* \sqrt{a}}$	$\frac{k_1(a)}{\epsilon_1 E_0^* \sqrt{a}}$	$\frac{k_1(-a)}{\epsilon_1 E_0^* \sqrt{a}}$	$\frac{k_1(a)}{p_0 \sqrt{a}}$	$\frac{k_1(-a)}{p_0 \sqrt{a}}$	$\frac{k_1(a)}{p_1 \sqrt{a}}$	$\frac{k_1(-a)}{p_1 \sqrt{a}}$	$\frac{k_1(a)}{p_2 \sqrt{a}}$	$\frac{k_1(-a)}{p_2 \sqrt{a}}$	$\frac{k_1(a)}{p_3 \sqrt{a}}$	$\frac{k_1(-a)}{p_3 \sqrt{a}}$
Plane Stress	0.01	1.425	0.660	0.813	-0.302	1.104	0.856	0.494	-0.494	0.525	0.464	0.372	-0.372
	0.15	1.430	0.662	0.813	-0.302	1.108	0.858	0.494	-0.495	0.526	0.465	0.372	-0.373
	0.30	1.435	0.665	0.814	-0.302	1.113	0.861	0.495	-0.493	0.528	0.466	0.372	-0.373
	0.50	1.441	0.668	0.815	-0.302	1.119	0.865	0.495	-0.496	0.529	0.467	0.372	-0.373
Plane Strain	0.01	1.425	0.660	0.813	-0.302	1.104	0.856	0.494	-0.494	0.525	0.464	0.372	-0.372
	0.15	1.431	0.663	0.813	-0.302	1.109	0.589	0.494	-0.495	0.527	0.465	0.372	-0.373
	0.30	1.439	0.667	0.814	-0.302	1.117	0.863	0.494	-0.495	0.529	0.466	0.372	-0.373
	0.50	1.457	0.677	0.817	-0.302	1.134	0.874	0.495	-0.497	0.533	0.469	0.372	-0.374

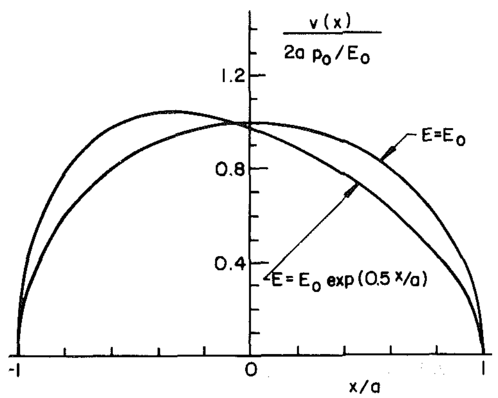

Fig. 3 Crack surface displacement $v(x)$ in a nonhomogeneous and a homogeneous medium under uniform pressure p_0 applied to the crack surfaces. ($E(x) = E_0 \exp(0.5x/a)$ for the nonhomogeneous medium, $E(x) = E_0$ for the homogeneous medium, $\nu = 0.5$, $\beta a = 0.5$, plane stress conditions.)

state around the crack tip would have the conventional square-root singularity (see (40)–(42)).

5 Results and Discussion

The crack problem is solved for two types of loading. In the first it is assumed that the plane is loaded by prescribing the displacements in such a way that in the uncracked medium we have

$$\epsilon_{yy}(x,0) = \epsilon_0 + \epsilon_1(x/a), \quad \epsilon_{xy}(x,0) = 0, \quad \sigma_{xx}(x,0) = 0. \tag{46}$$

From (46) the crack surface tractions in the perturbation problem may be expressed as follows:

$$\sigma_{yy}(x,0) = p(x) = -\epsilon_0 E_0 e^{\beta x} - \epsilon_1 E_0 \left(\frac{x}{a}\right) e^{\beta x}, \quad \sigma_{xy}(x,0) = 0, \quad |x| < a. \tag{47}$$

In the second type of loading crack surface traction $p(x)$ will simpy be assumed to be a polynominal of the form

$$p(x) = -p_0 - p_1\left(\frac{x}{a}\right) - p_2\left(\frac{x}{a}\right)^2 - p_3\left(\frac{x}{a}\right)^3. \tag{48}$$

In the normalized integral equation (38) the material parameter β enters into the kernel through $a\beta$ only. Thus the calculated stress intensity factors are given with $a\beta$ as the variable. The results are given in Tables 1 and 2. Note that in the nonhomogeneous material problem since the kernel is also dependent on the Poisson's ratio ν, the solution must be obtained for a given value of ν, and for the cases of plane stress and plane strain separately. Tables 1 and 2 give the normalized stress intensity factors at the crack tips a and $-a$ for plane stress and plane strain cases, respectively, by assuming that $\nu = 0.3$. The results are obtained by taking only one of the six input parameters ϵ_0, ϵ_1, p_0, p_1, p_2, and p_3 nonzero at a time. Since the problem is linear the results can be superimposed in any suitable manner. Note that for $\beta a \to 0$, that is, for a given a and $\beta \to 0$ or a given β and $a \to 0$, as expected, the stress intensity factor ratios reduce to those of a homogeneous medium, which, for an arbitrary traction $p(x)$, are given by

$$k_1(a) = \frac{1}{\pi\sqrt{a}} \int_{-a}^{a} p(x) \left(\frac{a+x}{a-x}\right)^{1/2} dx, \tag{49}$$

$$k_1(-a) = \frac{1}{\pi\sqrt{a}} \int_{-a}^{a} p(x) \left(\frac{a-x}{a+x}\right)^{1/2} dx. \tag{50}$$

For $\beta a = 0.5$ the effect of Poisson's ratio on the stress intensity factors in plane stress and plane strain cases is shown in Table 3. The results show that this effect is rather insignificant. Consequently, as seen from Tables 1–3 the difference between plane stress and plane strain results is also insignificant.

Since the effect of the Poisson's ratio and the thickness constraint on the stress intensity factors is negligibly small, from the results given in Tables 1 and 2 it is possible to develop simple empirical formulas for the stress intensity factors. For example, from Fig. 2, reproducing the results for a uniformly pressurized crack (columns 6 and 7, Table 1) it may be seen that the stress intensity factors vary approximately linearly with the variable βa. Hence, in this case, the following approximate formulas may be used to evaluate the stress intensity factors:

$$k_1(a) \simeq p_0\sqrt{a}(1 + 0.22\beta a), \tag{51}$$

$$k_1(-a) \simeq p_0\sqrt{a}(1 - 0.26\beta a). \tag{52}$$

A sample result showing the crack surface displacement $v(x)$ for a uniformly pressurized crack as calculated from (45) is given in Fig. 3. The figure also shows $v(x)$ for a homogeneous material. As expected, in the nonhomogeneous medium in the stiffer portion of the material, the crack surface displacement is smaller that that of the homogeneous medium, and the reverse trend may be observed in the less stiff portion of the material.

In this as well as in the previous studies the assumption of constant Poisson's ratio has been made for analytical reasons. Even though not very conclusive, the results given in this paper show that neglecting the possible special variation of the Poisson's ratio is not a very restrictive assumption.

References

1 Olszak, W., ed., *Nonhomogeneity in Elasticity and Plasticity*, Proc. IUTAM Symposium, Warsaw, Pergamon Press, 1958.

2 Lekhnitskii, S. G., "Radial Distribution of Stresses in a Wedge and in a

Half-Plane With Variable Modulus of Elasticity," *PMM*, Vol. 26, 1962, pp. 146–151.

3 Rostovtsev, N. A., "On the Theory of Elasticity of a Nonhomogenous Medium," *PMM*, Vol. 28, 1964, pp. 601–611.

4 Kassir, M. K., "Boussinesq Problems for a Nonhomogeneous Solid," *Proc. ASCE, Journal of Engineering Mechanics Division*, Vol. 98, 1972, pp. 457–470.

5 Belik, G. I., and Protsenko, V. S., "The Contact Problem of a Half-Plane for Which the Modulus of Elasticity of the Material is Expressed by a Power Function of the Depth," *Prikladnaya Mekhanika*, Vol. 3, No. 6, 1967, pp. 137–140.

6 Kassir, M. K., and Chuaprasert, M. F., "A Rigid Punch in Contact With Nonhomogenous Elastic Solid," ASME JOURNAL OF APPLIED MECHANICS, Vol. 42, 1974, pp. 1019–1024.

7 Popov, G. I., "Axisymmetric Contact Problem for an Elastic Inhomogenous Half Space in the Presence of Cohesion," *PMM*, Vol. 37, 1973, pp. 1052–1059.

8 Bakirtas, "The Problem of a Rigid Punch on a Nonhomogeneous Elastic Half Space," *Int. J. Eng. Sci.*, Vol. 18, 1980, pp. 597–610.

9 Protsenko, V. S., "Torsion of an Elastic Half Space With the Modulus of Elasticity Varying According to a Power Law," *Prikladnaya Mekhanika*, Vol. 3, No. 11, 1967, pp. 127–130.

10 Kassir, M. K., "The Reissner-Sagoci Problem for a Nonhomogeneous Solid," *Int. J. Eng. Sci.*, Vol. 8, 1970, pp. 875–885.

11 Kassir, M. K., "Note on the Twisting Deformaton of a Nonhomogenous Shaft Containing a Circular Crack," *Int. J. Fracture Mechanics*, Vol. 8, 1972, pp. 325–334.

12 Dhaliwal, R. S., and Singh, B. M., "On the Theory of Elasticity of a Non-homogeneous Medium," *Journal of Elasticity*, Vol. 8, 1978, pp. 211–219.

13 Gerasoulis, A., and Srivastav, R. P., "A Griffith Crack Problem for a Nonhomogenous Medium," *Int. J. Eng. Sci.*, Vol. 18, 1980, pp. 239–247.

14 Erdogan, F., "Mixed Boundary Value Problems in Mechanics," *Mechanics Today*, Nemat-Nasser, S., ed., Vol. 4, Pergamon Press, Oxford, 1978, pp. 1–86.

G. R. Miller

L. M. Keer
Mem. ASME

Department of Civil Engineering,
Northwestern University,
Evanston, Ill. 60201

Interaction Between a Rigid Indenter and a Near-Surface Void or Inclusion

A solution is presented to the two-dimensional problem of a rigid indenter sliding with friction on a half plane containing a near-surface imperfection in the form of a circular void or rigid inclusion. The complex variable formulation of Muskhelishivili is used to reduce the problem to a Fredholm integral equation of the second kind. This integral equation is solved numerically thus enabling the numerical calculation of the stress field. The behavior of the stress field is depicted in plots of the contact stress distribution and the subsurface maximum shear stress field. Results are presented showing location and size effects in the case of an inclusion, and finally, comparisons are made between the disturbances due to inclusions and voids.

Introduction

Impurities in the form of near-surface inclusions are known to have detrimental effects on the life of bearing surfaces. The actual failure mechanisms produced by these impurities, however, are not quantitatively well understood. An inclusion in an actual test roller specimen is shown in Fig. 1. The crack emanating from the top of the inclusion indicates one possible failure mechanism by which an early pitting failure may be associated with the presence of an inclusion. The stress field associated with such impurities can provide a mechanism that serves as a catalyst for crack propagation.

This paper considers the interaction of a near-surface circular inclusion with a rough indenter sliding on the bearing surface. The actual loading found in combined rolling and sliding contacts may be approximated by such a model (Fig. 2). The resulting stress calculations should provide a firm base on which further study of inclusion-related failure mechanisms can be built.

Inclusion problems for semi-infinite regions have received limited attention in the literature, although some solutions do exist (see e.g., [1-3]). In general, these solutions assume a known distribution of inelastic strain within the inclusion, and then seek the resulting stress distribution in the matrix. Problems with complex external loadings and interaction effects appear to be too cumbersome for these methods.

Problems involving subsurface voids have received somewhat more attention than inclusion problems. In particular, Barjansky solved the problem of a Boussinesq field disturbed by a circular hole using bipolar coordinates [4]. His work was later corrected by Evan-Iwanowsky [5]. Although Barjansky mentions in his conclusions that he was working on extending his method to the case of a rigid inclusion in place of the hole, such a solution was apparently never published.

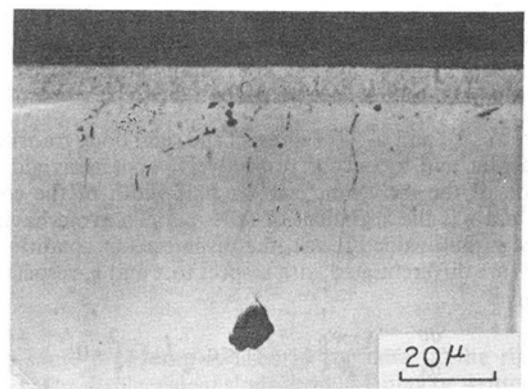

Fig. 1 Photographic cross section showing subsurface inclusion in a test roller

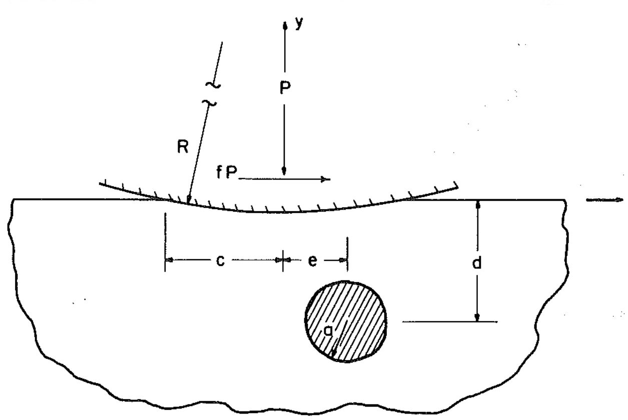

Fig. 2 Problem configuration with inclusion

Contributed by the Applied Mechanics Division for presentation at the Winter Annual Meeting, Boston, Mass., November 13-18, 1983, of THE AMERICAN SOCIETY OF MECHANICAL ENGINEERS.

Discussion on this paper should be addressed to the Editorial Department, ASME, United Engineering Center, 345 East 47th Street, New York, N.Y. 10017, and will be accepted until two months after final publication of the paper itself in the JOURNAL OF APPLIED MECHANICS. Manuscript received by ASME Applied Mechanics Division, December, 1982. Paper No. 83-WA/APM-6.

Copies will be available until July, 1984.

To apply this method to interaction effects would be very cumbersome.

The solution presented in this paper considers the two extreme cases of both a rigid inclusion and a hole or void. Interaction effects are taken into account by assuming that a perfectly rigid, rough sliding indenter of parabolic shape acts on the surface. The analysis is two-dimensional; the inclusion and the indenter are assumed to be parallel cylinders. Attention is focused on the variation of the contact stress distribution and the near-inclusion stress field as functions of defect size and location. The effect of varying the coefficient of friction is also considered, and results are presented in curves calculated numerically.

Formulation

The complex potentials of Muskhelishvili are used along with standard results for the half plane and circular region (see [6]). The stresses and displacements may be written in terms of the analytic functions ϕ and ψ as

$$\sigma_{xx}+\sigma_{yy}=2[\phi'(z)+\overline{\phi'(z)}] \tag{1}$$

$$\sigma_{yy}-\sigma_{xx}-2i\,\tau_{xy}=2[z\overline{\phi''(z)}+\overline{\psi'(z)}] \tag{2}$$

$$2\mu(u+iv)=\kappa\,\phi(z)-z\,\overline{\phi'(z)}-\overline{\psi(z)} \tag{3}$$

where $z = x + iy$, μ is the shear modulus, $\kappa = 3 - 4\nu$ for plane strain, and $\kappa = (3 - \nu)/(1 + \nu)$ for plane stress, with Poisson's ratio ν.

The boundary conditions corresponding to a rigid, subsurface, circular inclusion of radius a centered at the point z_1 and bonded to an elastic half space loaded by a rigid indenter with radius of curvature R and coefficient of friction f (see Fig. 2) may be written as follows:

$$\left.\begin{aligned} &v=\left(\frac{x-x_0}{2R}\right)^2+\delta_0; && |x|<c && (4)\\ &\sigma_{yy}-i\,\tau_{xy}=0; && |x|>c && (5)\\ &f\,\sigma_{yy}+\tau_{xy}=0; && |x|<\infty && (6)\end{aligned}\right\}\ I_m\{z\}=0$$

$$u+iv=u_0+iv_0-a\,\epsilon_0\,e^{i\eta};\quad |z-z_1|=a \tag{7}$$

Here x_0, δ_0, and u_0, v_0 represent the rigid body translations of indenter and inclusion, respectively, ϵ_0 is the rigid body rotation of the inclusion, c is the half-width of the contact strip; and η is the argument of $(z - z_1)$. To avoid having to deal with multivalued terms, the displacement conditions (4) and (7) are differentiated with respect to x and η, respectively. This gives

$$\frac{\partial v}{\partial x}=\frac{x-x_0}{R};\quad |x|<c,\quad I_m\{z\}=0 \tag{8}$$

$$\frac{\partial}{\partial\eta}(u+iv)=-i\,a\,\epsilon_0\,e^{i\eta};\quad |z-z_1|=a \tag{9}$$

The conditions of zero net traction and net moment acting on the inclusion will be accommodated by a proper choice of constants arising in the initial stage of the analysis.

The boundary conditions corresponding to the void problem are the same as those given in the foregoing with the exception of equation (7), which is replaced by

$$\sigma_{\rho\rho}+i\,\tau_{\rho\eta}=0;\quad |z-z_1|=a \tag{10}$$

where $z - z_1 = \rho e^{i\eta}$.

Method of Solution

The solution is constructed in three stages. First, the general solution to the displacement or the stress boundary value problem for a hole in an unloaded half plane is obtained. Second, the solution to the problem of a rigid rough indenter sliding on a half space is determined. Finally, the potentials corresponding to the interaction of these solutions are calculated using contour integration. The superposition of the resulting solutions then satisfies all the required boundary conditions except for condition (7) or (10). Employing the final boundary conditions leads to a Fredholm integral equation of the second kind that can be solved numerically, thus giving the desired solution.

1 Solution for a Hole in a Half Plane. Consider first the general solution to the displacement or stress boundary value problem for a hole of radius a, Γ, centered at the origin in an infinite plane. Using results in [6] and [7] pertaining to circular regions, the solution may be expressed as

$$\Phi_0(z)=\begin{cases}\Theta(z); & |z|>a\\ \gamma\,\Theta(z); & |z|<a\end{cases} \tag{11}$$

$$\Psi_0(z)=\frac{a^2}{z^2}\left\{\Theta(z)+\gamma\,\bar{\Theta}\left(\frac{a^2}{z}\right)-z\,\Theta'(z)\right\}+\frac{id}{z^2};\quad |z|>a \tag{12}$$

where

$$\Theta(z)=\int_\Gamma\frac{p(t)\,dt}{t-z}+A+\frac{B}{z}+\frac{C}{z^2} \tag{12}$$

For the displacement problem $\gamma = \kappa$ and

$$p(t)\equiv\frac{\mu}{\kappa\pi i}\frac{\partial}{\partial t}(u_x+iv_y) \tag{13}$$

while for the stress problem $\gamma = 1$ and

$$p(t)=-\frac{1}{2\pi i}(\sigma_{\rho\rho}+i\,\tau_{\rho\eta}) \tag{14}$$

with $t = ae^{i\eta}$.

For the case of no loading or rotation at infinity, and requiring zero net load and net moment to be acting on the hole, the complex constants A, B, C, and real constant d may be determined from considerations of the proper behavior of $\Phi_0(z)$ and $\Psi_0(z)$ for $|z| \to \infty$. In the case of the rigid inclusion this gives (see e.g., [7]) $A = B = C = 0$, and

$$d=-\kappa\,Re\left\{i\int_\Gamma\overline{p(t)}\ t\,\overline{dt}\right\} \tag{15}$$

For the void, all four constants are zero.

To obtain the solution for the case of Γ being centered away from the origin at a point z_1, the following transformation is sufficient (see [6]):

$$\begin{aligned}\Phi_1(z)&=\Phi_0(z-z_1)\\ \Psi_1(z)&=\Psi_0(z-z_1)-\bar{z}_1\,\Phi_0'(z-z_1)\end{aligned} \tag{16}$$

It is now necessary to clear the line $I_m\{z\} = 0$ of tractions arising from Φ_1 and Ψ_1 so as to determine a half-plane solution. This is accomplished most conveniently by employing analytic continuation as discussed in [8] and [9]. Introducing the additional potential $\Phi_2(z)$ such that

$$\Phi_2(z)=\begin{cases}-\bar{\Phi}_1(z)-z\,\bar{\Phi}_1'(z)-\bar{\Psi}(z); & I_m\{z\}<0\\ \Phi_1(z); & I_m\{z\}>0\end{cases} \tag{17}$$

It can be that the tractions, given by

$$\begin{aligned}\sigma_{yy}-i\,\tau_{xy}=&\ \Phi_1(z)+\overline{\Phi_1(z)}+z\,\overline{\Phi_1'(z)}+\overline{\Psi_1(z)}\\ &+\Phi_2(z)-\Phi_2(\bar{z})+(z-\bar{z})\,\overline{\Phi_2'(z)}\end{aligned} \tag{18}$$

do indeed vanish for $I_m\{z\} \to 0^-$. Thus, the following two potentials give the general solution to the displacement or stress boundary value problem for a hole in an unloaded half plane, $I_m\{z\} < 0$:

$$\Phi_3(z)=\Phi_1(z)-\bar{\Phi}_1(z)-z\,\bar{\Phi}'(z)-\bar{\Psi}_1(z)$$
$$\Psi_3(z)=\Psi_1(z)+\bar{\Psi}_1(z)+z\,\bar{\Psi}_1'(z)$$
$$+2z\,\Phi_1'(z)+z^2\,\bar{\Phi}_1''(z)+z\,\bar{\Phi}'(z) \qquad (19)$$

2 A Sliding Rough Indenter. Again using methods and results found in [6], the problem corresponding to the boundary conditions (4)-(6) may be reduced to the following Hilbert problem (here the superscripts "+" and "−" refer to the upper and lower half planes, respectively):

$$\Phi^+ + m\,\Phi^- = g(x) \qquad (20)$$

where

$$m \equiv \frac{(\kappa+1)+if\,(\kappa-1)}{(\kappa+1)-if\,(\kappa-1)}=e^{2i\alpha}$$
$$g(x)\equiv \frac{4i\mu(1+if)}{(\kappa+1)-if\,(\kappa-1)}\,v'(x) \qquad (21)$$

The solution to (20) is

$$\Phi(z)=\frac{X(z)}{2\pi i}\int_{-c}^{c}\frac{g(t)\,dt}{X^+(t)\,(t-z)}+X(z)\,P_n(z) \qquad (22)$$

where

$$X(z)=(z+c)^{1/2-\alpha/\pi}(z-c)^{1/2+\alpha/\pi}$$

Since $X(z) = 0(z)$ for $|z| \to \infty$, the arbitrary polynomial, $P_n(z)$, must be taken to be zero, and the following condition must be satisfied by $g(t)$:

$$\int_{-c}^{c}\frac{g(t)\,dt}{X^+(t)}=0 \qquad (23)$$

This condition leads to the determination of x_0 in equation (4). In the absence of a disturbance in the half plane the solution thus becomes

$$\Phi_4(z)=\frac{2i\mu(1+if)}{R(\kappa+1)}\left[z-2c\,\frac{\alpha}{\pi}-X(z)\right] \qquad (24)$$

3 Interaction Effects. To account for the interaction between the inclusion or void and the indenter, the vertical displacement effects on $I_m\{z\} = 0$ due to Φ_3 and Ψ_3 are calculated and substituted into (23) and (22) with a change of sign. Thus the net displacement slope due to Φ_3, Ψ_3 and the interaction terms will be zero beneath the indenter, resulting in the proper matching of boundary condition (8).

The vertical displacement slope arising from Φ_3 and Ψ_3 is obtained by substituting (19) into the derivative with respect to z of (3), and may be written (recalling the definition of γ and d):

$$2\mu v'=(\kappa+1)Im\Big\{-\int_\Gamma\frac{p(t)\,dt}{x-(t+z_1)}+\frac{a^2}{(x-\bar{z}_1)^2}\int_\Gamma\frac{\overline{p(t)}\;\overline{dt}}{x-(\bar{t}+\bar{z}_1)}$$
$$-\int_\Gamma\frac{[z_1-(\bar{z}_1+\bar{t})]\,\overline{p(t)}\;\overline{dt}}{[x-(\bar{t}+\bar{z}_1)]^2}-\frac{\gamma}{(x-\bar{z}_1)}\int_\Gamma\frac{\bar{t}\,p(t)\,dt}{x-(\bar{t}+\bar{z}_1)}$$
$$+\frac{a^2}{x-\bar{z}_1}\int_\Gamma\frac{\overline{p(t)}\;\overline{dt}}{[x-(\bar{t}+z_1)]^2}+\frac{id}{(x-\bar{z}_1)^2}\Big\} \qquad (25)$$

Putting (25) into (22) and (23), switching the order of integration, and carrying out the resulting inner integrations using contour methods, leads to the following expression for the interaction potential:

$$\Phi_5(z)=\frac{(1+if)}{2}\Big\{\int_\Gamma p(t)[F(z;\;z_0)+a^2\,L(z;\;z_0,z_1,t)$$
$$+(\bar{z}_1-z_0)\,G(z;\;z_0)+\gamma\,\bar{t}\,H(z;\;z_0,z_1,t)$$
$$+a^2\,M(z;\;z_0,z_1,t)]\,dt$$
$$-\int\overline{p(t)}[F(z;\;\bar{z}_0)+a^2\,L(z;\;\bar{z}_0,\bar{z}_1,\bar{t})$$
$$+(z_1-\bar{z}_0)\,G(z;\;\bar{z}_0)$$
$$+\gamma\,t\,H(z;\;\bar{z}_0,\bar{z}_1,\bar{t})+a^2\,M(z;\;\bar{z}_0,\bar{z}_1,\bar{t})]\,\overline{dt}$$
$$-id[G(z;\;\bar{z}_1)+G(z;\;z_1)]\Big\}\;\frac{-2i\mu(1+if)}{R(\kappa+1)}\,\hat{x}_0 \qquad (26)$$

where $\hat{x}_0$ represents the change in x_0 due to the inclusion or void and is given by

$$\hat{x}_0=\frac{R(\kappa+1)}{4i\mu}\,\frac{R}{2\mu}\Big\{\int_\Gamma p(t)\,[F_\infty(z_0)+a^2\,L_\infty(z_0,z_1,t)$$
$$+(\bar{z}_1-z_0)\,G_\infty(z_0)+\gamma\,\bar{t}\,H_\infty(z_0,z_1\,t)$$
$$+a^2\,M_\infty(z_0,z_1,t)]\,dt$$
$$-\int_\Gamma\overline{p(t)}\,[F_\infty(\bar{z}_0)+a^2\,L_\infty(\bar{z}_0,\bar{z}_1,\bar{t})$$
$$+(z_1-\bar{z}_0)\,G_\infty(\bar{z}_0)$$
$$+\gamma\,t\,H_\infty(\bar{z}_0,\bar{z}_1,\bar{t})+a^2\,M_\infty(\bar{z}_0,\bar{z}_1,\bar{t})]\,\overline{dt}$$
$$+id\,[G_\infty(\bar{z}_1)+G(z_1)]\Big\} \qquad (27)$$

The functions F, F_∞, G, G_∞, H, H_∞, L, L_∞, M, and M_∞ are given in the Appendix, and $z_0 \equiv z_1 + t$.

4 Integral Equation. It is now necessary to satisfy the boundary conditions on the perimeter of the void or inclusion given by (10) and (9), respectively. Consider first the case of a void. The normal and shear stresses on the circle may be written

$$\sigma_{\rho\rho}+i\,\tau_{\rho\eta}=\Phi(z)+\overline{\Phi(z)}-e^{-2i\eta}[z\,\overline{\Phi'(z)}+\overline{\Psi(z)}] \qquad (28)$$

Substituting the various potentials into (28) and (10) and recalling the way in which Φ_1 was determined leads directly to a Fredholm integral equation of the second kind for the unknown function $p(s)$:

$$-(\sigma_{\rho\rho}+i\,\tau_{\rho\eta})_{\Phi_4}=2\pi\,i\,p(s)+\int_\Gamma K_V(s,s,t;\;\;p(t))\;dt \quad (29)$$

Here $s = ae^{i\eta_0}$, and the term on the left-hand side of the equation represents the stresses due to the contact alone, embodied in $\Phi_4(z)$. The kernel $K_V(s,t,p(t))$ is given by

$$K_V(s,t;\;\;p(t))=\Phi_2(z)+(1+e^{-2i\eta_0})\overline{\Phi_2(z)}$$
$$+e^{-2i\eta_0}\,\Phi_2(\bar{z})-(z-\bar{z})\,e^{-2i\eta_0}\,\overline{\Phi_2'(z)}$$
$$+\Phi_5(z)+(1+e^{-2i\eta_0})\overline{\Phi_5(z)}+e^{-2i\eta_0}\Phi_5(\bar{z})$$
$$-(z-\bar{z})\,e^{-2i\eta_0}\,\overline{\Phi_5'(z)} \qquad (30)$$

where $z = s + z_1$.

The same procedure is used in the case of the rigid inclusion. The displacement slope around Γ may be written:

$$2\mu\frac{\partial}{\partial\eta}\,(u+iv)=i(z-z_1)[\kappa\,\Phi(z)-\overline{\Phi(z)}$$
$$+z\,e^{-2i\eta}\,\overline{\Phi'(z)}+e^{-2i\eta}\,\overline{\Psi(z)}] \qquad (31)$$

Substituting into (31) and (9) in analogous fashion leads to a similar integral equation to that obtained in the foregoing. The inhomogeneous term in equation (9) representing the rigid body rotation of the inclusion is related directly to the constant d. Using (15), ϵ_0 may be written as

$$\epsilon_0=\frac{\kappa}{4\mu a^2}\,Re\{i\int_\Gamma\overline{p(t)}\;\;t\,\overline{dt}\} \qquad (32)$$

The integral equation is given by

$$-2\mu\frac{\partial}{\partial\eta}\,(u+iv)_{\Phi_4}=2\;\pi\;i\;\kappa\;sp(s)$$
$$+\int_\Gamma K_R(s,t;\;\;p(t))\;dt \qquad (33)$$

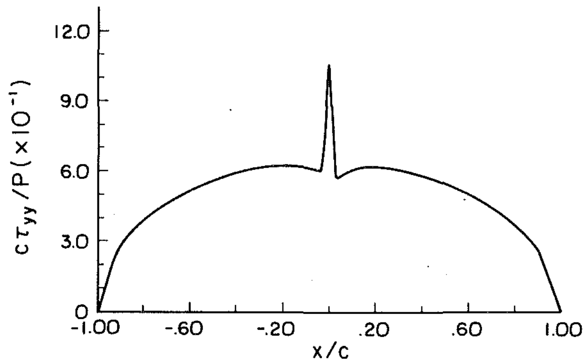

Fig. 3 Contact stress beneath the indenter; $c/a = 50.0$; $d/c = 0.03$; $e/c = 0.0$; $f = 0.1$

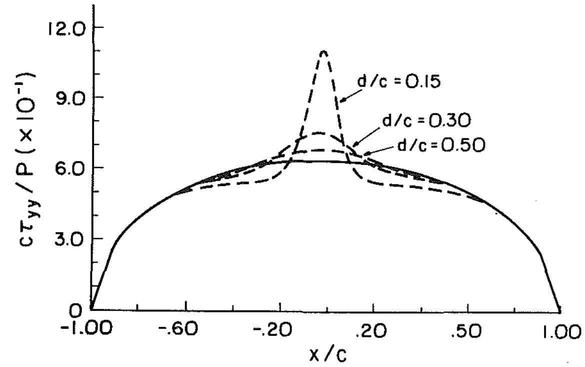

Fig. 4 Contact stresses beneath the indenter for $c/a = 10.0$; $e/c = 0.0$; $f = 0.1$

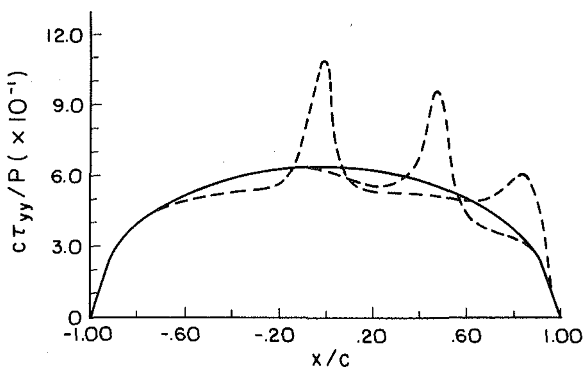

Fig. 5 Contact stresses beneath the indenter for $c/a = 10.0$; $d/c = 0.15$; $f = 0.1$. The solid line represents the Hertzian distribution; the dotted lines illustrate the effect of the inclusion at the three locations: $e/c = 0.0, 0.5, 0.9$.

with

$$K_R(s,\ t;\ \ p(t)) = is\left[\kappa\,\Phi_2(z) - (1+e^{-2i\eta_0})\overline{\Phi_2(z)} - e^{-2i\eta_0}\,\Phi_2(\bar z) + (z-\bar z)\ e^{-2i\eta_0}\overline{\Phi_2'(z)} + \kappa\,\Phi_5(z) - (1+e^{-2i\eta_0})\overline{\Phi_5(z)} - e^{-2i\eta_0}\Phi_5(\bar z) + (z-\bar z)e^{-2i\eta_0}\overline{\Phi_5'(z)}\right] \tag{34}$$

Numerical Results and Conclusions

Dimensionless forms of equations (30) and (33) were solved numerically using a collocation scheme employing Simpson's rule for the integrations. The resulting numerical solutions were then used to calculate the stress state at any desired location. Calculations were performed for various combinations of inclusion and void size, location, and surface coefficient of friction. The results of these calculations are summarized in Figs. 3–9.

Figures 3–6 show the behavior of the contact stresses. It can be seen that the presence of a subsurface void or inclusion can

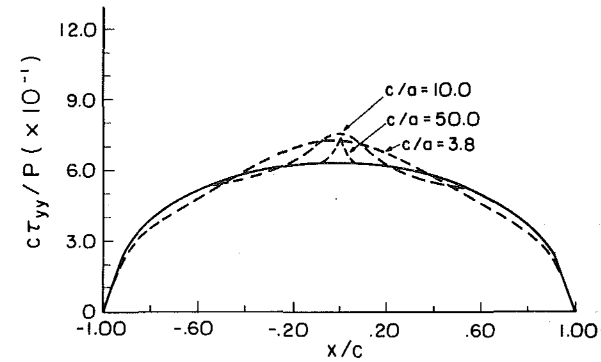

Fig. 6 Contact stress distribution showing effect of inclusion size; $d/a = 3.0$ (nondimensionalization); $e/c = 0.0$; $f = 0.1$

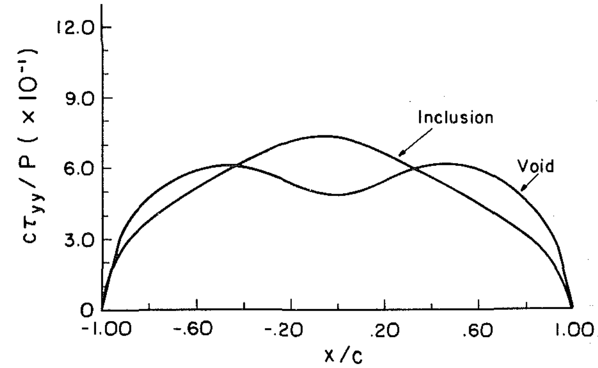

Fig. 7 Comparison of contact stress distribution for a void and an inclusion; $c/a = 3.8$; $d/c = 0.79$; $e/c = 0.0$; $f = 0.1$

cause a significant alteration in the contact stress distribution. For small inclusions ($c/a >> 1$) the effect is similar to that of an asperity (see Fig. 3). The surface disturbance diminishes rapidly as the depth of the inclusion beneath the surface increases, as is shown clearly in Fig. 4. In Fig. 6 the *distributions corresponding to a void and an inclusion with* identical geometries are compared. Variations due to horizontal movement of an inclusion are shown in Fig. 5, and inclusion size effects are illustrated in Fig. 7 (note that d/a is held constant, not d/c).

Subsurface stress behavior is depicted in Figs. (8) and (9), which are contour plots of maximum shear stress for the case of a void and inclusion, respectively. The geometry corresponds to that of Fig. 6 and was chosen to allow comparison with some photoelastic experimental results obtained by Yamamoto and coworkers [10], who have recently studied voids. Figure 8 shows good agreement with the work of Yamamoto both qualitatively and quantitatively. Due to expense, rigorous and exhaustive comparisons were not performed.

In the absence of any defect, the maximum shear stress ($c\,\tau_{max}/p$) would be about 0.25. For the case of the void shown, this value is increased to 0.73, while for the case of the inclusion it becomes 0.43. The void gives a larger increase, but the maximum occurs near the sides of the void boundary. For the inclusion, however, the maximum occurs near the top and bottom of the inclusion, thus placing this effect nearer the surface. For large inclusions this could be significant.

It can be concluded that the observed detrimental effects of subsurface defects on bearing surfaces are directly related to the stress field variations caused by these defects. This is not surprising, but now that the nature of these stress field variations can be quantified it should be possible to accurately model the actual mechanisms of defect-induced failures.

Acknowledgment

The authors are grateful for support from the National

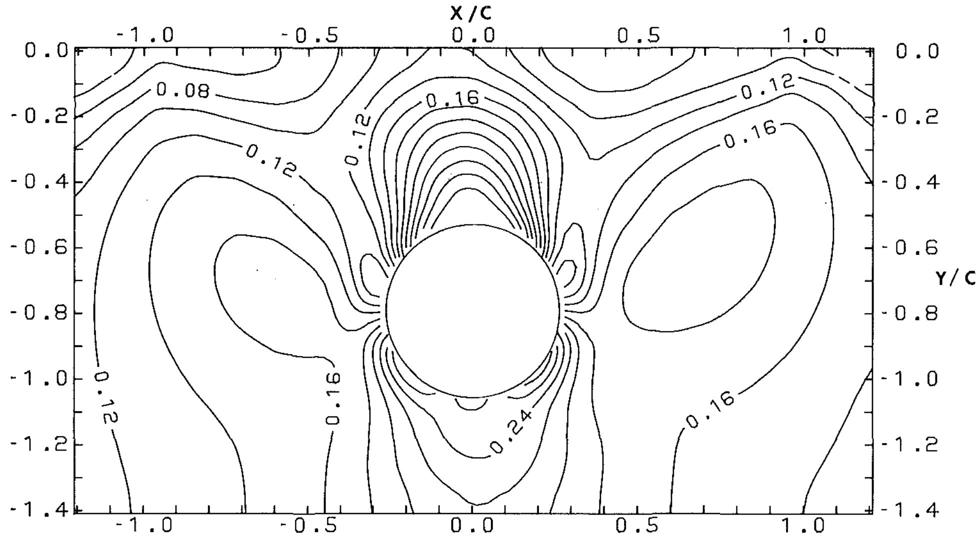

Fig. 8 Contour plot of $c\tau_{max}/P$ for an inclusion with $c/a = 3.8$; $d/c = 0.789$; $e/c = 0.0$; $f = 0.1$

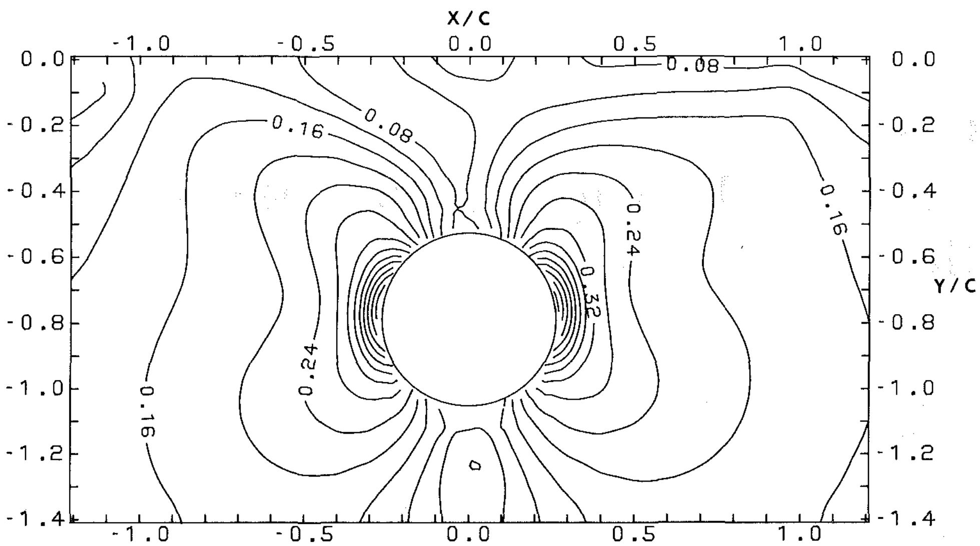

Fig. 9 Contour plot of $c\tau_{max}/P$ for a void of $c/a = 3.8$; $d/c = 0.789$; $e/c = 0.0$; $f = 0.1$

Science Foundation, Grant MEA-7923261. The authors express thanks for many stimulating conversations with coinvestigators: Professors H. S. Cheng and T. Mura, Northwestern University; T. M. Clarke and V. K. Sharma, International Harvester; and D. H. Breen, Packer Engineering. International Harvester provided Fig. 1.

References

1 Guell, D. L., and Dundurs, J., "Further Results on Center of Dilatation and Residual Stresses in Joined Elastic Half-Spaces," *Development in Theoretical and Applied Mechanics*, Vol. 3, Pergamon Press, Oxford, 1967, pp. 105–115.

2 Chiu, Y. P., "On the Stress Field and Surface Deformation in a Half Space With a Cuboidal Zone in Which Initial Strains are Uniform," ASME Journal of Applied Mechanics, Vol. 45, 1978, pp. 302–306.

3 Seo, K., and Mura, T., "The Elastic Field in a Half Space Due to Ellipsoidal Inclusions With Uniform Dilitational Eigenstrains," ASME Journal of Applied Mechanics, Vol. 46, 1979, pp. 568–572.

4 Barjansky, A., "Distortion of the Boussinesq Field Due to Circular Hole," *Quarterly of Applied Mathematics*, Vol. 2, 1944, pp. 16–30.

5 Evan-Iwanowski, R. M., "Distortion of Boussinesq Field Due to Circular Hole," *Quarterly of Applied Mathematics*, Vol. 19, 1961, pp. 359–365.

6 Muskhelishvili, N. I., *Some Basic Problems in the Theory of Elasticity*, 4th ed., Noordhoff, Leyden, The Netherlands, 1954.

7 Milne-Thompson, L. M., *Plane Elastic Systems*, Springer-Verlag, Berlin, 1968.

8 England, A. H., *Complex Variable Methods in Elasticity*, Wiley-Interscience, London, 1971.

9 Green, A. E., and Zerna, W., *Theoretical Elasticity*, Clarendon Press, Oxford, 1960.

10 Yamamoto, T., Eguchi, E., and Murayama, K., "Stress Concentration in the Vicinity of a Hole Defect Under Conditions of Hertzian Contact," NASA Technical Memorandum 82649, 1981.

APPENDIX

$$F(z;\quad z_0)=\frac{1}{z-z_0}\left[1-\frac{X(z)}{X(z_0)}\right]$$

$$F_\infty(z_0)=-\frac{1}{X(z_0)}$$

$$G(z;\quad z_0)=\frac{1}{z-z_0}\left[\frac{1}{z-z_0}-\frac{X(z)}{X(z_0)\,(z-z_0)}+\frac{X(z)X'(z_0)}{X^2(z_0)}\right]$$

$$G_\infty(z_0)=\frac{X'(z_0)}{X^2(z_0)}$$

$$H(z;\quad z_0, z_1, t) = \frac{1}{z-z_1}\left[\frac{1}{z-z_0} + \frac{X(z)}{X(z_1)t}\right] - \frac{X(z)}{X(z_0)(z-z_0)t}$$

$$H_\infty(z_0, z_1, t) = \frac{1}{X(z_1)t} - \frac{1}{X(z_0)t}$$

$$L(z;\quad z_0, z_1, t) = \frac{1}{(z-z_1)^2(z-z_0)} - \frac{X(z)}{X(z_0)(z-z_0)t^2}$$

$$-\frac{X(z)}{X(z_1)t}\left[\frac{X'(z_1)}{X(z_1)} - \frac{1}{z-z_1} - \frac{1}{t}\right]$$

$$L_\infty(z_0, z_1, t) = -\frac{1}{t^2X(z_0)} - \frac{X'(z_1)}{tX^2(z_1)} - \frac{1}{t^2X(z_1)}$$

$$M(z;\quad z_0, z_1, t) = \frac{1}{(z-z_1)(z-z_0)^2} - \frac{X(z)}{X(z_1)(z-z_1)t^2} +$$

$$\frac{X(z)}{(z-z_0)t}\left[\frac{X'(z_0)}{X^2(z_0)} - \frac{1}{X(z_0)(z-z_0)} + \frac{1}{X({}_0)t}\right]$$

$$M_\infty(z_0, z_1, t) = -\frac{1}{X(z_1)t^2} + \frac{X'(z_0)}{X^2(z_0)t} + \frac{1}{t^2X(z_0)}$$

H. Boduroglu[2]

F. Erdogan
Mem. ASME

Department of Mechanical Engineering and Mechanics,
Lehigh University,
Bethlehem, Pa. 18015

Internal and Edge Cracks in a Plate of Finite Width Under Bending[1]

In this paper the title problem is studied by using Reissner's transverse shear theory. The main purpose of the paper is to investigate the effect of stress-free boundaries on the stress intensity factors in plates under bending. Among the results found particularly interesting are those relating to the limiting cases of the crack geometries. The numerical results are given for a single internal crack, two collinear cracks, and two edge cracks. Also studied is the effect of Poisson's ratio on the stress intensity factors.

1 Introduction

In many relatively thin-walled plate and shell structures through cracks may develop as a result of cyclic loading. To analyze this fatigue crack propagation process the stress intensity factor calculated from the elastic analysis of the structure appears to be the most widely used correlation parameter representing the severity of part-flaw geometry and the intensity of applied loads. In plates containing through cracks and subjected to membrane loading only, usually the solution obtained by ignoring local three-dimensional effects and by assuming the validity of conditions of the generalized plane stress seems to be quite adequate. Partly because of the practical importance of the problem of plates under membrane loading and partly because of the relative simplicity of the related elasticity problems, the two-dimensional crack problems have been studied very extensively. Even though in many applications the bending components of the external loads are also present, as in, for example, transversely loaded plates and structures undergoing flow-induced vibrations, the solution of the plate bending problem seems to have been carried out only for an infinite plate [1-5]. These studies have demonstrated the importance of transverse shear effects on the stress intensity factors and have shown that the bending results are sufficiently different from the plane stress results. It is, therefore, worthwhile to investigate the influence of finite in-plane dimensions, particularly that of stress-free edges on the stress intensity factors in plates undergoing bending.

The problem considered in this paper is a relatively long rectangular plate containing collinear cracks perpendicular to its long sides. Of particular interest is the investigation of the edge cracks and crack-free boundary interaction. As in [1-4] external loads are assumed to be symmetric with respect to the plane of the crack and a transverse shear theory [6, 7] is used to formulate the problem.

2 The Formulation of Bending Problem

Consider a relatively long flat plate of finite width which contains symmetrically located collinear cracks perpendicular to its sides (Fig. 1). It is assumed that $x_2 = 0$ is a plane of symmetry with respect to loading and geometry and the problem in the absence of cracks has been solved under the given applied loads. Thus, through a proper superposition the crack problem may be reduced to a stress perturbation problem in which the self-equilibrating crack surface tractions are the only external loads. Also, it is assumed that the plate is acted on by a sufficiently large tensile membrane load so that

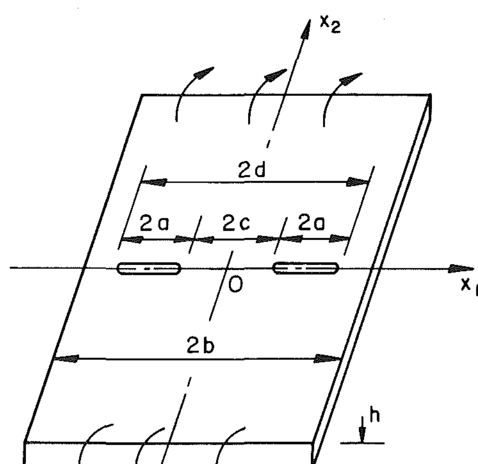

Fig. 1 The geometry of the plate

[1]This work was supported by NSF under the Grant ENG 78-09737 and by NASA-Langley under the Grant NGR 39-007-011.

[2]Permanent address: Department of Civil Engineering, Istanbul Technical University, Istanbul, Turkey.

Contributed by the Applied Mechanics Division for publication in the JOURNAL OF APPLIED MECHANICS.

Discussion on this paper should be addressed to the Editorial Department, ASME, United Engineering Center, 345 East 47th Street, New York, N.Y. 10017, and will be accepted until two months after final publication of the paper itself in the JOURNAL OF APPLIED MECHANICS. Manuscript received by ASME Applied Mechanics Division, December, 1982.

there is no crack surface interference (on the compression side) in the bending problem. Thus, the results given in this paper should be considered together with the solution given in [8] where the corresponding generalized plane stress problem was studied for the same crack geometry as Fig. 1.

By using the Reissner's transverse shear theory, the basic equations for elastic plates under bending may be expressed as follows (see, for example, [9] for the shell equations of which the following system is a special case)

$$\nabla^4 w = 0, \tag{1}$$

$$\frac{1-\nu}{2}\kappa\,\nabla^2\Omega - \Omega = 0, \tag{2}$$

$$\kappa\,\nabla^2\psi - \psi - w = 0, \tag{3}$$

$$\beta_x = \frac{\partial\psi}{\partial x} + \frac{1-\nu}{2}\kappa\frac{\partial\Omega}{\partial y},$$

$$\beta_y = \frac{\partial\psi}{\partial y} - \frac{1-\nu}{2}\kappa\frac{\partial\Omega}{\partial x}, \tag{4}$$

$$M_{xx} = \frac{a^*}{h\lambda^4}\left[\frac{\partial^2\psi}{\partial x^2} + \nu\frac{\partial^2\psi}{\partial y^2} + \frac{\kappa}{2}(1-\nu)^2\frac{\partial^2\Omega}{\partial x\partial y}\right], \tag{5}$$

$$M_{yy} = \frac{a^*}{h\lambda^4}\left[\frac{\partial^2\psi}{\partial y^2} + \nu\frac{\partial^2\psi}{\partial x^2} - \frac{\kappa}{2}(1-\nu)^2\frac{\partial^2\Omega}{\partial x\partial y}\right], \tag{6}$$

$$M_{xy} = \frac{a^*(1-\nu)}{2h\lambda^4}\left[2\frac{\partial^2\psi}{\partial x\partial y} + \frac{\kappa}{2}(1-\nu)\left(\frac{\partial^2\Omega}{\partial y^2} - \frac{\partial^2\Omega}{\partial x^2}\right)\right], \tag{7}$$

$$V_x = \frac{\partial w}{\partial x} + \frac{\kappa}{2}(1-\nu)\frac{\partial\Omega}{\partial y} + \frac{\partial\psi}{\partial x}, \tag{8}$$

$$V_y = \frac{\partial w}{\partial y} - \frac{\kappa}{2}(1-\nu)\frac{\partial\Omega}{\partial x} + \frac{\partial\psi}{\partial y}. \tag{9}$$

The dimensionless quantities which appear in (1)–(9) are defined in Appendix A. The dimensions are given in Fig. 1. In the usual notation M_{ij} and V_i, $(i,j=1,2)$ are the bending and the transverse shear resultants β_1 and β_2 are the components of the rotation vector, u_1, u_2, and u_3 are the components of the displacement vector, and a^* is a length parameter representing the crack size ($a^*=a$ for $c>0$, $d\le b$, $a^*=d$ for $c=0$, $d<b$, Fig. 1).

As in the corresponding plane stress problem [8], here it is assumed that $x_1=0$ is a plane symmetry. Thus, in the perturbation problem under consideration the solution of the differential equations (1)–(3) may be expressed as

$$w(x,y) = \frac{2}{\pi}\int_0^\infty (A_1 + yA_2)e^{-\alpha y}\cos\alpha x\, d\alpha + \frac{2}{\pi}\int_0^\infty (C_1\cosh\beta x + C_2 x\sinh\beta x)\cos\beta y\, d\beta, \tag{10}$$

$$\Omega(x,y) = \frac{2}{\pi}\int_0^\infty B_1 e^{-r_1 y}\sin\alpha x\, d\alpha + \frac{2}{\pi}\int_0^\infty B_2\sinh r_2 x\sin\beta y\, d\beta, \tag{11}$$

$$\psi(x,y) = \frac{2}{\pi}\int_0^\infty [-A_1 + (2\kappa\alpha - y)A_2]e^{-\alpha y}\cos\alpha x\, d\alpha + \frac{2}{\pi}\int_0^\infty [-(C_1 + 2\kappa\beta C_2)\cosh\beta x - C_2 x\sinh\beta x]\cos\beta y\, d\beta, \tag{12}$$

where

$$r_1 = \left[\alpha^2 + \frac{2}{\kappa(1-\nu)}\right]^{1/2}, \quad r_2 = \left[\beta^2 + \frac{2}{\kappa(1-\nu)}\right]^{1/2}, \tag{13}$$

and the unknowns A_1, A_2 and B_1 are functions of α, and C_1, C_2, and B_2 are functions of β.

By substituting from (10)–(12) into (4)–(9) the components of rotation, the moment resultants, and transverse shear resultants are found to be

$$\beta_x(x,y) = \frac{2}{\pi}\int_0^\infty \left(-[-A_1 + (2\kappa\alpha - y)A_2]\alpha e^{-\alpha y} + \frac{r_1}{\gamma^2}B_1 e^{-r_1 y}\right)\sin\alpha x\, d\alpha + \frac{2}{\pi}\int_0^\infty \left[-(C_1 + 2\kappa\beta C_2)\beta\sinh\beta x - C_2 x\beta\cosh\beta x - C_2\sinh\beta x - \frac{\beta}{\gamma^2}B_2\sinh r_2 x\right]\cos\beta y\, d\beta, \tag{14}$$

$$\beta_y(x,y) = \frac{2}{\pi}\int_0^\infty \left[-(-A_1 + (2\kappa\alpha - y)A_2)\alpha e^{-\alpha y} - \frac{\alpha}{\gamma^2}B_1 e^{-r_1 y}\right]\cos\alpha x\, d\alpha + \frac{2}{\pi}\int_0^\infty \left[[(C_1 + 2\kappa\beta C_2)\cosh\beta x + C_2 x\sinh\beta x]\beta - \frac{r_2}{\gamma^2}B_2\cosh r_2 x\right]\sin\beta y\, d\beta, \tag{15}$$

$$M_{xx}(x,y) = \frac{a^*}{h\lambda^4}\,\frac{2}{\pi}\left\{\int_0^\infty \left([(1-\nu)\alpha^2 A_1 - (\alpha^2(1-\nu)(2\kappa\alpha - y) - 2\nu\alpha)A_2]e^{-\alpha y} - \frac{1-\nu}{\gamma^2}\alpha r_1 B_1 e^{-r_1 y}\right)\cos\alpha x\, d\alpha + \int_0^\infty\left(\frac{1-\nu}{\gamma^2}\beta r_2 B_2\cosh r_2 x - (1-\nu)\beta^2 C_1\cosh\beta x - [(1-\nu)x\beta^2\sinh\beta x + 2\beta(1+(1-\nu)\kappa\beta^2)\cosh\beta x]C_2\right)\cos\beta y\, d\beta\right\}, \tag{16}$$

$$M_{yy}(x,y) = \frac{a^*}{h\lambda^4}\,\frac{2}{\pi}\left\{\int_0^\infty \left([-(1-\nu)\alpha^2 A_1 + (\alpha^2(1-\nu)(2\kappa\alpha - y) + 2\alpha)A_2]e^{-\alpha y} + \frac{(1-\nu)}{\gamma^2}\alpha r_1 B_1 e^{-r_1 y}\right)\cos\alpha x\, d\alpha + \int_0^\infty\left(-\frac{(1-\nu)}{\gamma^2}\beta r_2 B_2\cosh r_2 x + \beta^2(1-\nu)C_1\cosh\beta x + \left[\left(\frac{4\beta^3}{\gamma^2} - 2\nu\beta\right)\cosh\beta x + (1-\nu)\beta^2 x\sinh\beta x\right]C_2\right)\cos\beta y\, d\beta\right\}, \tag{17}$$

$$M_{xy}(x,y) = \frac{a^*}{h\lambda^4}\,\frac{2}{\pi}\left\{\int_0^\infty \left([2\alpha^2 A_1 + (2\alpha^2 y - 2\alpha - 4\kappa\alpha^3)A_2]e^{-\alpha y} - \frac{1}{\gamma^2}(r_1{}^2 + \alpha^2)B_1 e^{-r_1 y}\right)\sin\alpha x\, d\alpha\right.$$

$$+\int_0^\infty\left[\frac{1}{\gamma^2}(\beta^2+r_2{}^2)B_2\sinh r_2x\right.$$

$$+2\beta^2C_1\sinh\beta x+(2\beta^2x\cosh\beta x$$

$$\left.+(2\beta+4\kappa\beta^3)\sinh\beta x)C_2\right]\sin\beta y\,d\beta\Big\},\tag{18}$$

$$V_x(x,y)=-\frac{2}{\pi}\int_0^\infty\left[2\kappa\alpha^2A_2e^{-\alpha y}+\frac{r_1}{\gamma^2}B_1e^{-r_1y}\right]\sin\alpha x\,d\alpha$$

$$+\frac{2}{\pi}\int_0^\infty\left[\frac{\beta}{\gamma^2}B_2\sinh r_2x\right.$$

$$\left.-2\kappa\beta^2C_2\sinh\beta x\right]\cos\beta y\,d\beta,\tag{19}$$

$$V_y(x,y)=-\frac{2}{\pi}\int_0^\infty\left[2\kappa\alpha^2A_2e^{-\alpha y}+\frac{\alpha}{\gamma^2}B_1e^{-r_1y}\right]\cos\alpha x\,d\alpha$$

$$+\frac{2}{\pi}\int_0^\infty\left[-\frac{r_2}{\gamma^2}B_2\cosh r_2x+C_1\cosh\beta x\right.$$

$$\left.+(2\kappa\beta^2\cosh\beta x+\beta\sinh\beta x)C_2\right]\sin\beta y\,d\beta,\tag{20}$$

where

$$\gamma^2=\frac{2}{\kappa(1-\nu)}=\frac{10(a^*)^2}{h^2}.\tag{21}$$

Because of the assumed symmetry, it is sufficient to consider the problem for $0\le x_1<b$, $0\le x_2<\infty$ only. Thus, referring to Fig. 1, the boundary and symmetry conditions of the problem may be expressed as follows:

$$M_{xx}(b',y)=0,\ M_{xy}(b',y)=0,\ V_x(b',y)=0,\ 0\le y<\infty,\tag{22}$$

$$M_{xy}(0,y)=0,\ V_x(0,y)=0,\ \beta_x(0,y)=0,\ 0\le y<\infty,\tag{23}$$

$$M_{xy}(x,0)=0,\ V_y(x,0)=0,\ 0\le x<b',\tag{24}$$

$$M_{yy}(x,0)=m(x),\ c'<x<d',\tag{25}$$

$$\beta_y(x,0)=0,\ 0\le x<c',\ d'<x<b',\tag{26}$$

where the normalized length parameters are defined by

$$b'=b/a^*,\ c'=c/a^*,\ d'=d/a^*.\tag{27}$$

From the expressions (14), (18), and (19) it may be seen that the (symmetry) conditions (23) are identically satisfied. By using the five homogeneous conditions (22) and (24), five of the unknowns A_i,B_i,C_i, $(i=1,2)$ may be eliminated. The sixth unknown may then be determined from the mixed boundary conditions (25) and (26). By substituting from (18) and (20) into the homogeneous conditions (24) we find

$$A_1=\frac{1+\nu}{4\alpha^2}B_1,\quad A_2=-\frac{1-\nu}{4\alpha}B_1.\tag{28}$$

If we now define

$$\frac{\partial}{\partial x}\beta_y(x,+0)=f(x),\quad 0\le x\le b',\tag{29}$$

from (15), (26), and (28) it can be shown that (Fig. 1)

$$B_1(\alpha)=-2\int_{c'}^{d'}f(t)\sin\alpha t\,dt,\tag{30}$$

and

$$A_1(\alpha)=-\frac{1+\nu}{2\alpha^2}\int_{c'}^{d'}f(t)\sin\alpha t\,dt,$$

$$A_2(\alpha)=\frac{1-\nu}{2\alpha}\int_{c'}^{d'}f(t)\sin\alpha t\,dt.\tag{31}$$

By using the expressions (16), (18), and (19) the boundary conditions (22) may be reduced to

$$B_2\frac{\beta}{\gamma^2}\sinh r_2b'-C_2\,2\beta^2\kappa\sinh\beta b'$$

$$=\frac{2}{\pi}\int_0^\infty\frac{\beta^2}{(r_1{}^2+\beta^2)(\alpha^2+\beta^2)}B_1\sin b'\alpha\,d\alpha,\tag{32}$$

$$B_2\frac{\beta^2+r_2{}^2}{\gamma^2}\sinh r_2b'-2C_1\beta^2\sinh\beta b'-2C_2\beta[\beta b'\cosh\beta b'$$

$$+(1+2\beta^2\kappa)\sinh\beta b']=\frac{2}{\pi}\int_0^\infty\left[\frac{2\alpha^2\beta}{\kappa\gamma^2(\alpha^2+\beta^2)^2}\right.$$

$$\left.-\frac{\beta\gamma^2+2\alpha^2\beta}{(\alpha^2+\beta^2)(r_1{}^2+\beta^2)}\right]B_1\sin b'\alpha\,d\alpha,\tag{33}$$

$$B_2\frac{1-\nu}{\gamma^2}\beta r_2\cosh r_2b'-C_1(1-\nu)\beta^2\cosh\beta b'$$

$$-C_2[(1-\nu)\beta^2b'\sinh\beta b'+2\beta(1+(1-\nu)\beta^2\kappa)\cosh\beta b']$$

$$=-\frac{(1-\nu)^2}{2\pi}\int_0^\infty\left[-\frac{2\alpha\beta^2\gamma^2\kappa}{(\alpha^2+\beta^2)(r_1{}^2+\beta^2)}\right.$$

$$\left.-\frac{\alpha(\alpha^2-\beta^2)}{(\alpha^2+\beta^2)^2}\right]B_1\cos b'\alpha\,d\alpha.\tag{34}$$

Equations (30)–(34) indicate that all of the unknowns in the problem can be expressed in terms of the new unknown function $f(t)$. It is also seen that all of the boundary conditions (22)–(26) except (25) are satisfied. The equation to determine $f(t)$ may, therefore, be obtained by substituting from (30)–(34) and (17) into (25). From the formulation of the problem one may observe that the unknown functions A_1, A_2, and B_1 refer to the "infinite" plate and should give the kernel found in [4]. Indeed, after some simple manipulations it may be shown that

$$\frac{a^*(1-\nu^2)}{2\pi h\lambda^4}\int_{c'}^{d'}f(t)\left\{\frac{3+\nu}{1+\nu}\left(\frac{1}{t-x}+\frac{1}{t+x}\right)\right.$$

$$-\frac{4\kappa(1-\nu)}{1+\nu}\left[\frac{1}{(t-x)^3}+\frac{1}{(t+x)^3}\right]$$

$$\left.+\frac{4}{1+\nu}\left[\frac{1}{t-x}K_2(\gamma|t-x|)+\frac{1}{t+x}K_2(\gamma|t+x|)\right]\right\}dt$$

$$+\lim_{y\to+0}\int_0^\infty\left[\frac{4\beta^2}{1+\nu}C_1\cosh\beta x\right.$$

$$+\frac{8}{1+\nu}\left(\kappa\beta^3\cosh\beta x+\frac{\beta^2}{2}x\sinh\beta x\right.$$

$$\left.-\frac{\nu}{1-\nu}\beta\cosh\beta x\right)C_2$$

$$\left.-\frac{2\kappa(1-\nu)}{1-\nu}r_2\beta\,B_2\cosh r_2x\right]\cos\beta y\,d\beta=m(x),c'<x<d',\tag{35}$$

where K_2 is the modified Bessel function of the second kind. By solving (32)–(34) for C_1, C_2, and B_2 and by substituting into (35) we find

$$\frac{a^*(1-\nu^2)}{2\pi h\lambda^4}\int_{c'}^{d'}\left\{\left(\frac{3+\nu}{1+\nu}\left(\frac{1}{t-x}+\frac{1}{t+x}\right)\right.\right.$$

$$-\frac{4\kappa(1-\nu)}{1+\nu}\left(\frac{1}{(t-x)^3}+\frac{1}{(t+x)^3}\right)$$

$$+\frac{4}{1+\nu}\left[\frac{1}{t-x}K_2(\gamma|t-x|)+\frac{1}{t+x}K_2(\gamma|t+x|)\right]\Big)+k(x,t)$$

$$-k(x,-t)\Big\}f(t)dt=m(x),\quad c'<x<d', \tag{36}$$

where the Fredholm kernel $k(x,t)$ is given by

$$k(x,t)=\int_0^\infty\Big\{\Big[-\frac{3+\nu}{1+\nu}-\frac{1-\nu}{1+\nu}\beta(b'-t)\Big]$$

$$\frac{1+e^{-2\beta x}}{1-e^{-2\beta b'}}e^{-(2b'-t-x)\beta}$$

$$-\frac{2\kappa(1-\nu)}{1+\nu}\frac{1+e^{-2r_2x}}{1-e^{-2r_2b'}}(\beta^2e^{-(b'-t)r_2}$$

$$-\beta r_2e^{-(b'-t)\beta})e^{-(b'-x)r_2}$$

$$+\Big[\Big(\frac{2\beta}{1-\nu}-\frac{2b'\beta^2}{1+\nu}\frac{1+e^{2b'\beta}}{1-e^{-2b'\beta}}\Big)(1+e^{-2\beta x})$$

$$+\frac{4}{1+\nu}\Big\{\kappa\beta^3(1+e^{-2\beta x})$$

$$+\frac{\beta^2}{2}x(1-e^{-2\beta x})-\frac{\nu}{1-\nu}\beta(1+e^{-2\beta x})\Big\}\Big]\frac{1}{D}[D_1e^{-(2b'-t-x)\beta}$$

$$+D_2e^{-(b'-x)\beta}e^{-(b'-t)r_2}]$$

$$-\frac{4\kappa}{1+\nu}\beta^2r_2(1+e^{-2r_2x})\frac{1}{D}[D_1e^{-(b'-t)\beta}$$

$$+D_2e^{-(b'-t)r_2}]\frac{1-e^{-2b'\beta}}{1-e^{-2b'r_2}}e^{-(b'-x)r_2}\Big\}d\beta, \tag{37}$$

$$D_1=\frac{2\beta}{\gamma^2}r_2(1-e^{-2b'\beta})\frac{1+e^{-2b'r_2}}{1-e^{-2b'r_2}}-2(1+e^{-2b'\beta})$$

$$+\frac{1+e^{-2b'\beta}}{\kappa\gamma^2}[1-(b'-t)\beta]$$

$$-(1-\nu)\Big[\frac{\beta}{2}(b'-t)-\kappa\beta^2\Big](1-e^{-2b'\beta}), \tag{38}$$

$$D_2=-\frac{2\beta^2}{\gamma^2}\frac{1+e^{-2b'r_2}}{1-e^{-2b'r_2}}(1-e^{-2b'\beta})$$

$$-\kappa\beta^2(1-\nu)(1-e^{-2b'\beta}), \tag{39}$$

$$D=4b'\beta^2e^{-2b'\beta}-\Big(\frac{3+\nu}{1-\nu}\beta+2\kappa\beta^3\Big)(1-e^{-4b'\beta})$$

$$+2\beta^2\kappa r_2\frac{1+e^{-2b'r_2}}{1-e^{-2b'r_2}}(1-e^{-2b'\beta})^2. \tag{40}$$

If the cracks are internal cracks as shown in Fig. 1, then from (26) and (29) it follows that

$$\int_{c'}^{d'}f(t)\,dt=0. \tag{41}$$

Thus, the integral equation (36) must be solved under the additional condition (41).

From the following asymptotic behavior of $K_2(z)$ for small values of z

$$K_2(z)=\frac{2}{z^2}-\frac{1}{2}+0(z^2\log z), \tag{42}$$

it may be shown that the kernel of the integral equation (36) has only a Cauchy-type singularity. Hence, the solution is of the form

$$f(t)=\frac{F(t)}{(t-c')^{1/2}(d'-t)^{1/2}},\quad c'<t<d', \tag{43}$$

and the bounded function $F(t)$ may be obtained by using the numerical method described, for example, in [10].

If the plate contains a single symmetrically located crack, i.e., for $c=0$, $d<b$ (see Fig. 1 and 3), by using the symmetry of the problem and by observing that $f(t)=-f(-t)$, (36), (41), and (43) may be expressed as

$$\frac{d(1-\nu^2)}{2\pi h\lambda^4}\int_{-d'}^{d'}\Big\{\Big[\frac{3+\nu}{1+\nu}\frac{1}{t-x}-\frac{4\kappa(1-\nu)}{1+\nu}\frac{1}{(t-x)^3}$$

$$+\frac{4}{1+\nu}\frac{1}{t-x}K_2(\gamma|t-x|)\Big]$$

$$+k(x,t)\Big\}f(t)\,dt=m(x),\quad -d'<x<d', \tag{44}$$

$$\int_{-d'}^{d'}f(t)\,dt=0, \tag{45}$$

$$f(t)=\frac{F(t)}{\sqrt{d^2-t^2}},\quad -d<t<d, \tag{46}$$

where $a^*=d$ is used for the normalizing length parameter (Appendix A).

3 The Stress Intensity Factors

In the symmetric plate problem under consideration the bending component of the Mode I stress intensity factor at the crack tips is defined by (Fig. 1)

$$k_{1c}(x_3)=\lim_{x_1\to c}[2(c-x_1)]^{1/2}\sigma_{22}(x_1,0,x_3), \tag{47}$$

$$k_{1d}(x_3)=\lim_{x_1\to d}[2(x_1-d)]^{1/2}\sigma_{22}(x_1,0,x_3). \tag{48}$$

Let σ_b be a stress amplitude calculated on the plate surface and used for normalizing the stress intensity factors. For example, in a plate subjected to uniform bending $M_{22}=M_0$ away from the crack region

$$\sigma_b=6M_0/h^2. \tag{49}$$

The stress intensity factors are then normalized with respect to $\sigma_b\sqrt{a^*}$. If the stress intensity factors on the plate surface are defined by

$$k(c)=k_{1c}(h/2),\ \ k(d)=k_{1d}(h/2), \tag{50}$$

it is sufficient to calculate $k(c)$ and $k(d)$ in terms of which we have

$$k_{1c}(x_3)=\frac{x_3}{h/2}k(c),\ \ k_{1d}(x_3)=\frac{x_3}{h/2}k(d). \tag{51}$$

We now note that (36) gives the normalized bending resultant $m(x)$ on $y=0$ outside as well as inside the crack. Thus, a relatively straightforward asymptotic analysis would show that [11]

$$k_{1c}(x_3)=\frac{x_3}{h/2}\frac{hE}{4}\lim_{x_1\to c}\sqrt{2(x_1-c)}\frac{\partial\beta_2}{\partial x_1}, \tag{52}$$

$$k_{1d}(x_3)=-\frac{x_3}{h/2}\frac{hE}{4}\lim_{x_1\to d}\sqrt{2(d-x_1)}\frac{\partial\beta_2}{\partial x_1}. \tag{53}$$

From (43) and (51)–(53) it then follows that

$$k(c)=\frac{hE}{4a^*\sigma_b}F(c'),\ \ k(d)=-\frac{hE}{4a^*\sigma_b}F(d'). \tag{54}$$

In plane elasticity problems for cracks it is known that in the close neighborhood of a crack tip $x_1=d$, $x_2=0$ we have

$$\sigma_{22}(x_1,0)=\frac{k_1}{\sqrt{2(x_1-d)}}+0(1), \tag{55}$$

$$k_1=-\frac{2\mu}{1+\kappa_0}\lim_{x_1\to d}\sqrt{2(d-x_1)}\frac{\partial}{\partial x_1}[u_2(x_1,+0)-u_2(x_1,-0)], \tag{56}$$

where k_1 is the Mode I stress intensity factor, μ is the shear modulus, $\kappa_0=4-3\nu$ for plane strain, and $\kappa_0=(3-\nu)/(1+\nu)$ for the generalized plane stress. In the symmetric bending problem under consideration crack surface displacement is given by

$$u_2(x_1,+0,x_3)=x_3\beta_2(x_1,+0). \tag{57}$$

From (48), (53), and (55)-(57) it may be observed that the results found from the solution of the plane elasticity and the bending problems given by (53) and (55) are identical provided κ_0 is selected as $(3-\nu)/(1+\nu)$ (i.e., if the value for plane stress rather than for plane strain is used for κ_0). Also, as shown in [9] and [11] the transverse shear theory used in the present analysis gives an angular distribution for the asymptotic stress state around the crack tip which is identical to that found for the plane elasticity problem.

4 The Edge Cracks

An important special case of the problem described in Fig. 1 is the edge cracks for which $d=b$ and $c>0$. In this case as x and t approach the end point $d'=b'$ simultaneously, the kernel $k(x,t)$ given by (37) becomes unbounded and consequently influences the singular nature of the solution. Since the integrand in (37) is bounded in any finite interval in $0\le\beta<\infty$, the unbounded terms in $k(x,t)$ will be due to the asymptotic behavior of the integrand. Thus, by separating the asymptotic part of the integrand, equation (37) may be expressed as

$$k(x,t)=\int_0^\infty[K(x,t,\beta)-K_\infty(x,t,\beta)]d\beta+\int_0^\infty K_\infty(x,t,\beta)d\beta. \tag{58}$$

The first integral in (58) is bounded and the second may be evaluated in closed form. After a somewhat lengthy analysis similar to that described in [8] we obtain

$$\int_0^\infty K_\infty(x,t,\beta)d\beta=k_s(x,t)=\frac{1}{2b'-x-t}-\frac{6(b'-x)}{(2b'-x-t)^2}+\frac{4(b'-x)^2}{(2b'-x-t)^2}. \tag{59}$$

One may note that $k_s(x,t)$ given by (59) is identical to that found for the plane edge crack problem given in [8] and, together with the Cauchy kernel $1/(t-x)$, constitutes a generalized Cauchy kernel.

Referring to the definition of $f(t)$ given by (29) and the boundary condition (26), it is seen that the condition (41) is not valid for the edge crack and, as pointed out in [8], is not needed for the solution of the integral equation (36). In this case the generalized Cauchy kernel $k_g(x,t)=1/(t-x)+k_s(x,t)$ has the property that $k_g(x,b')=0$, $k_g(b',t)=0$, and $f(t)$ is nonsingular at $t=b'$. Thus, the numerical solution of the problem is obtained by letting

$$f(t)=\frac{F(t)}{\sqrt{t-c'}},\quad c'<t<b'. \tag{60}$$

5 Results and Discussion

The problem is solved for three crack geometries shown in Fig. 1, 3, and 4 for a uniform bending moment $M_{22}=M_0$ (per unit plate width) away from the crack region. The results for a symmetrically located internal crack of length $2d$ are given in Tables 1-3 (see the insert in Fig. 3). Since the problem has three length parameters, namely h, b, and d, the results depend on two dimensionless length constants. Table 1 shows the normalized stress intensity factor as a function of b/d for fixed values of b/h. One may note that, as expected for $(b/d)\to1$ the stress intensity factor becomes unbounded. Also, for fixed plate dimensions b and h in the other limiting case of $d\to0$ the stress intensity ratio is seen to approach unity, which is the result given by the plane elasticity solution for an infinite medium with a through crack. These trends are clearly observed in Fig. 2 where the asymptotes are indicated by $b/h=$constant lines. The behavior of the solution for the limiting case of $(d/h)\to0$ may also be shown analytically. Referring to (44), in this case the problem is one of an infinite

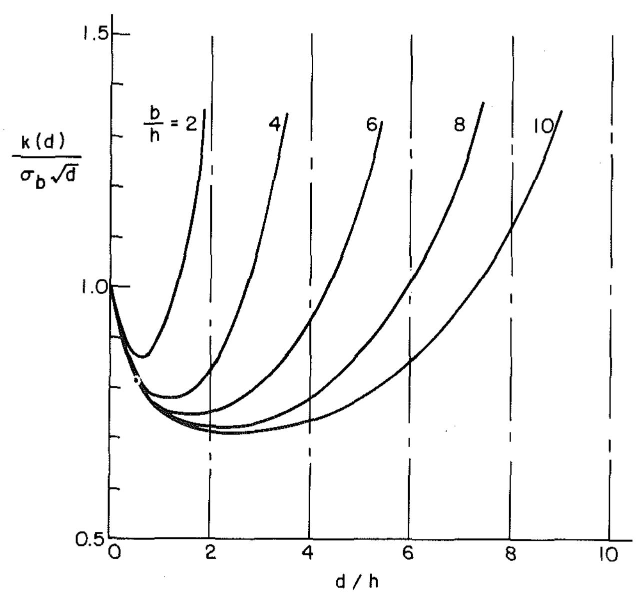

Fig. 2 The stress intensity factor in a plate of finite width containing a symmetrically located single internal through crack which is subjected to uniform bending moment $M_{22}=M_0$ away from the crack region (see insert in Fig. 3); $\nu=0.3$, $\sigma_b=6M_0/h^2$

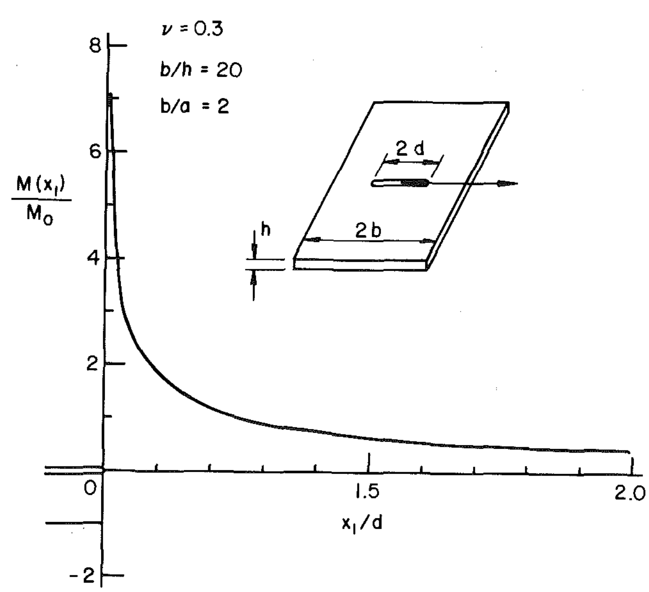

Fig. 3 Distribution of the bending moment $M_{22}(x_1,0)=M(x_1)$ in the plane of the crack for a plate containing a single symmetric crack and subjected to $M_{22}(x_1,0)=-M_0$ on the crack surface $-d<x_1<d$

Table 1 Stress intensity factor in a plate of finite width containing a symmetrically located single crack and subjected to uniform bending (M_0) away from the crack region, $\nu = 0.3$, $\sigma_b = 6M_0/h^2$ (Fig. 1, c = 0)

b = 2h		b = 4h		b = 6h		b = 8h		b = 10h	
b/d	$k(d)/\sigma_b\sqrt{d}$	b/d	$k(d)/\sigma_b\sqrt{d}$	b/d	$k(d)/\sigma_b\sqrt{d}$	b/d	$k(d)/\sigma_b\sqrt{d}$	b/d	$k(d)/\sigma_b\sqrt{d}$
$\to\infty$	$\to 1.0$	$\to\infty$	$\to 1.0$	$\to\infty$	$\to 1.0$	$\to\infty$	$\to 1.0$	$\to\infty$	$\to 1.0$
40	0.9887	40	0.9680	60	0.9676	80	0.9676	100	0.9675
20	0.9697	20	0.9231	30	0.9218	40	0.9213	50	0.9210
10	0.9296	10	0.8530	15	0.8491	20	0.8476	25	0.8469
5	0.8747	6.666	0.8125	10	0.8045	13.333	0.8019	12.5	0.7716
2.5	0.8694	5	0.7910	7.5	0.7780	10	0.7737	10	0.7526
2	0.9094	4	0.7812	6.0	0.7620	8	0.7556	7.5	0.7332
1.5	1.0664	2	0.8320	3.0	0.7502	4	0.7267	5	0.7166
1.04	3.7426	1.04	3.4252	1.5	0.9282	2	0.7817	2.5	0.7347
$\to 1.0$	$\to\infty$	1.02	5.1526	1.04	3.2040	1.04	3.0449	2	0.7702
		1.01	7.4209	1.01	7.1933	1.01	6.9928	1.04	2.9256
		$\to 1.0$	$\to\infty$	$\to 1.0$	$\to\infty$	$\to 1.0$	$\to\infty$	1.01	6.8141
								$\to 1.0$	$\to\infty$

Table 2 The effect of Poisson's ratio on the stress intensity factor in a plate of finite width containing a single crack and subjected to uniform bending ($\sigma_b = 6M_0/h^2$, $b/h = 10$, Fig. 1 c = 0)

b/d	$k(d)/\sigma_b\sqrt{d}$			
	$\nu = 0$	$\nu = 0.2$	$\nu = 0.3$	$\nu = 0.5$
$\to\infty$	$\to 1.0$	$\to 1.0$	$\to 1.0$	$\to 1.0$
100	0.9583	0.9650	0.9675	0.9717
50	0.9002	0.9151	0.9210	0.9307
25	0.8119	0.8368	0.8469	0.8638
12.5	0.7278	0.7587	0.7716	0.7938
10	0.7074	0.7392	0.7526	0.7758
7.5	0.6868	0.7194	0.7332	0.7573
5	0.6689	0.7023	0.7166	0.7416
2.5	0.6850	0.7197	0.7347	0.7612
2	0.7192	0.7547	0.7707	0.7975
1.04	2.8152	2.8916	2.9258	2.9881
1.01	6.6721	6.7715	6.8141	6.8886
$\to 1.0$	$\to\infty$	$\to\infty$	$\to\infty$	$\to\infty$

Table 3 Stress intensity factor versus width-to-crack length ratio in a plate containing a single crack and subjected to uniform bending ($\nu = 0.3$, $d/h = 1$, $\sigma_b = 6M_0/h^2$, Fig. 1, c = 0)

b/d	$\to 1$	2	4	8	10	20	$\to\infty$
$k(d)/\sigma_b\sqrt{d}$	$\to\infty$	0.9094	0.7812	0.7556	0.7526	0.7488	0.7475

plate for which the Fredholm kernel $k(x,t)$ is zero. Noting that for $d\to 0$ $\gamma\to 0$, by using (42) it may easily be shown that in limit the kernel of the integral equation (44) would reduce to $1/(t-x)$. Also, by observing that the crack opening displacement on the plate surface is $u_2 = \beta_y h/2$, $m(x) = M_{22}/(h^2E) = M_0/(h^2E) = \sigma_b/(6E)$, and $\lambda^4 = 12(1-\nu^2)d^2/h^2$, if we replace $f(x)$ by

$$f(x) = \partial\beta_y/\partial x = (2d/h)\partial v/\partial x, \quad v = u_2(x_1, +0, h/2), \tag{61}$$

equation (44) becomes

$$\frac{E}{2}\,\frac{1}{\pi}\int_{-d'}^{d'} \frac{1}{t-x}\,\frac{\partial v}{\partial t}\,dt = -\sigma_b, \quad -d' < x < d' \tag{62}$$

which is the integral equation for an infinite plane under uniform stress σ_b and for which the stress intensity factor is $k(d) = \sigma_b\sqrt{d}$.

In the bending problem the kernel of the integral equation is a function of the Poisson's ratio ν. Therefore, unlike the plane elasticity problems the stress intensity factors in bending are dependent on ν. Most of the results given in this paper have been calculated for $\nu = 0.3$. However, to show the influence of ν on the stress intensity factors, for a central crack and for two edge cracks the results are also given for $\nu = 0$, 0.2, and 0.5. Table 2 shows the results for the internal crack. It is seen that the stress intensity factor slightly increases with increasing Poisson's ratio.

Table 3 shows the effect of b/d ratio on $k(d)$ for $d/h = 1$. Again, as $b\to d$ $k(d)$ becomes unbounded, and as $b\to\infty$ $k(d)$ is seen to approach the infinite plate result given in [4].

To give some idea about the distribution of the stresses in the plate, the bending moment $M_{22}(x_1,0) = M(x)$ is given in Fig. 3. The result is obtained from (44) which shows that the moment is $-M_0$ for $0 \le x_1 < d$, and has a singularity at $x_1 = d + 0$. The figure indicates that M_{22} is a monotonically decreasing function of x_1.

Some results for collinear cracks shown in Fig. 1 are given in Table 4. One set of results shows the stress intensity factors for fixed cracks and plate dimensions and for varying crack location. The other set of results shows the effect of crack length for a fixed crack location (as determined by its mid-

Table 4 Stress intensity factors in a plate containing two symmetrically located collinear cracks and subjected to uniform bending (Fig. 1, $\nu=0.3$, $a=(d-c)/2$, $b/h=10$, $\sigma_b=6M_0/h^2$)

$b/h = 10$			$c+d = b$		
$\frac{2a}{c+d}$	$k(c)/\sigma_b\sqrt{a}$	$k(d)/\sigma_b\sqrt{a}$	b/a	$k(c)/\sigma_b\sqrt{a}$	$k(d)/\sigma_b\sqrt{a}$
→1/9	→1.0170		→∞	→ 1.0	→ 1.0
0.14	0.7758	0.7835	10	0.76846	0.76847
0.15	0.7720	0.7765	8	0.76058	0.76060
0.2	0.7685	0.7685	7.5	0.75969	0.75971
0.3	0.7764	0.7720	6	0.76299	0.76292
0.4	0.7923	0.7803	5	0.77550	0.77552
0.5	0.8167	0.7916	4	0.81218	0.81212
0.6	0.8519	0.8058	3	0.9442	0.9432
0.7	0.9014	0.8232	2.5	1.2083	1.2041
0.8	0.9751	0.8447	2.08	3.1343	3.2639
0.9	1.1172	0.8734	→ 2	→ ∞	→ ∞
0.95	1.3018	0.8944			
0.96	1.3743	0.9000			
0.97	1.4791	0.9066			
0.98	1.6516	0.9148			
0.99	2.0268	0.9265			
→1.0	→ ∞	→1.0134			

Table 5 Stress intensity factors in a plate of finite width containing symmetric edge cracks and subjected to uniform bending or membrane loading away from the crack region, $\sigma_b=6M_0/h^2$, $\sigma_m=N_0/h$, $\nu=0.3$ (see insert in Fig. 3)

c/b	Bending: $k(c)/\sigma_b\sqrt{a}$			Tension
	b=10h	b=6h	b=2h	$k(c)/\sigma_m\sqrt{a}$
→ 0	→ ∞	→ ∞	→ ∞	→ ∞
0.01	8.7889			
0.05	3.4726			
0.1	2.2893	2.4567	2.7957	2.9467
0.2	1.5754	1.6656	1.9359	2.1769
0.3	1.3082	1.3690	1.5802	1.8744
0.4	1.1693	1.2171	1.3922	1.7136
0.5	1.0878	1.1130	1.2849	1.6328
0.6	1.0396	1.0800	1.2266	1.6080
0.7	1.0157	1.0583	1.2069	1.5970
0.8	1.0170	1.0665	1.2320	1.5915
0.9	1.0694	1.1369	1.3501	1.5883
0.95	1.1666	1.2645	1.4798	
0.98	1.3466	1.4383	1.5452	
0.99	1.4589			
→1.0	→1.5869	→1.5869	→1.5869	→1.5869

point). As $c\rightarrow 0$ or $2a/(c+d)\rightarrow 1$ it is seen that $k(c)$ becomes unbounded which is expected. The somewhat unusual result in this case is the steep rise of $k(d)$ to the single central crack value as $c\rightarrow 0$. As pointed out in [4], a smooth continuation of $k(d)$ as $c\rightarrow 0$ would correspond to the "pinched" crack solution, the steep rise in $k(d)$ being the result of the relaxation of the crack surface rotation β_2 at $x_1=0$ from zero the the single crack value. Even though it does not seem to be possible to analyze this phenomenon in the bending problem, it can be done for the collinear cracks in plane elasticity. For example, from the expression given for $k(d)$ [12]

$$\frac{k(d)}{\sigma_0\sqrt{d}}=\frac{1}{k}\left[1-\frac{E(k)}{K(k)}\right],k=\sqrt{1-c^2/d^2} \qquad (63)$$

in an infinite plane containing two collinear cracks along $x_2=0$, $c<|x_1|<d$ and subjected to uniform tension σ_0 away from the crack region, if we consider $k(d)$ a function of c, it may be shown that for fixed d

$$\frac{k(d)}{\sigma\sqrt{d}}\rightarrow 1 \quad \text{and} \quad \frac{d}{dc}k(d)\rightarrow -\infty \quad \text{for} \quad c\rightarrow 0, \qquad (64)$$

meaning that for $c\rightarrow 0$ the approach of $k(d)$ to the single crack value is very steep. In (63) K and E are the complete elliptic integrals of first and second kind, respectively.

The results for the edge cracks are shown in Tables 5 and 6 and in Fig. 4. Table 5 and Fig. 4 also show the results obtained

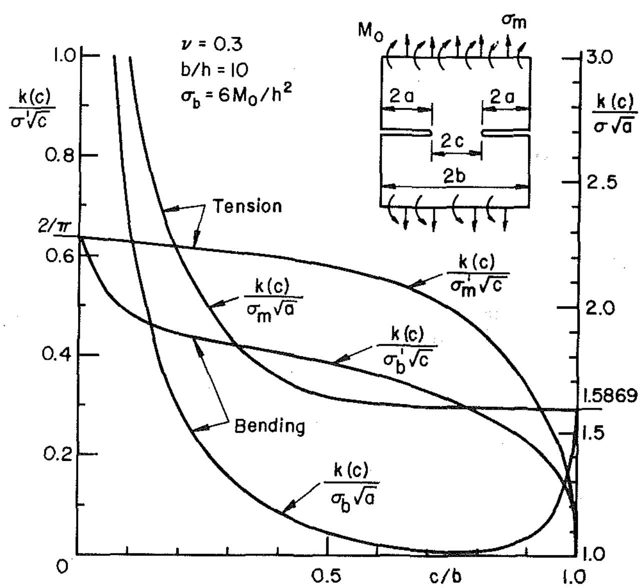

Fig. 4 Stress intensity factor in a plate containing two symmetric edge cracks which is subjected to uniform bending moment M_0 or uniform tensile stress σ_m away from the crack region; $\nu=0.3$, $b/h=10$, $\sigma_b=6M_0/h^2$, $\sigma_b{}'=\sigma_b b/c$, $\sigma_m{}'=\sigma_m b/c$ where $\sigma_b{}'$ and $\sigma_m{}'$ are the average net section stresses

Table 6 Effect of Poisson's ratio on the stress intensity factors in a plate containing symmetric edge cracks which is subjected to uniform bending away from the crack region, $b/h = 10$, $\sigma_b = 6M_0/h^2$ (Fig. 1, $d = b$, $2a = b - c$)

c/b	$k(c)/\sigma_b\sqrt{a}$			
	$\nu = 0$	$\nu = 0.2$	$\nu = 0.3$	$\nu = 0.5$
$\to 0$	$\to \infty$	$\to \infty$	$\to \infty$	$\to \infty$
0.05	3.3451	3.4352	3.4726	3.5360
0.1	2.1681	2.2533	2.2893	2.3514
0.2	1.4744	1.5452	1.5754	1.6281
0.3	1.2197	1.2816	1.3082	1.3548
0.4	1.0889	1.1450	1.1693	1.2118
0.5	1.0132	1.0653	1.0878	1.1274
0.6	0.9695	1.0184	1.0396	1.0769
0.7	0.9495	0.9956	1.0157	1.0510
0.8	0.9548	0.9981	1.0170	1.0502
0.9	1.0127	1.0522	1.0694	1.1000
0.95	1.1159	1.1151	1.1666	1.1943
0.98	1.3003	1.3293	1.3466	1.3631
$\to 1$	$\to 1.5869$	$\to 1.5869$	$\to 1.5869$	$\to 1.5869$

from the plane elasticity problem for the identical crack geometry. The effect of the Poisson's ratio on the stress intensity factor in the plate under bending is shown in Table 6.

The results given in the tables are self-explanatory. It should, however, be emphasized that (*a*) the stress intensity factor for the plate under bending increases with decreasing b/h ratio; (*b*) bending values are always smaller than those of the plane elasticity; (*c*) as $c \to b$ (or as the crack length $2a$ approaches zero) bending as well as the plane elasticity results approach that of a semi-infinite plane containing an edge crack (i.e., $k(c) \to 1.5869\sigma\sqrt{a}$, $\sigma = \sigma_b$ or $\sigma = \sigma_m$) (see [8]); and (*d*) if the results are normalized with respect to $\sigma'\sqrt{c}$ (rather than $\sigma\sqrt{a}$), it is seen that as $c \to 0$ in both cases $k(c)/\sigma'\sqrt{c}$ approach $2/\pi$ which is the value obtained from the closed-form elasticity solution of an infinite plane containing two semi-infinite edge cracks and subjected to tension equivalent to an average net section stress σ_m', where $\sigma_m' = \sigma_m b/c$, $\sigma_b' = \sigma_b b/c$ (see Fig. 4).

One reviewer raised a question with regard to the relevance of an interesting recent study [13] to the results given in this paper. The conclusion in [13] was that in cracked plates under bending the "thickness effect on the energy release rate integral is minor," meaning that the energy release rate may be estimated with sufficient accuracy by using the classical theory. It is rather difficult to comment on the question. However, the following remarks may perhaps be worthwhile.

(*a*) Equation (120) in [13] appears to give an *estimate* not a *bound* for the difference between the strain energy release rates calculated from classical and Reissner plate theories. Thus the difference estimated as $(I^R - I^C)/I^C \sim (4/\sqrt{10})(h/a)\, ln(h/a)$ may simply be the leading term of an expression which, for practical thickness-to-half-crack length (h/a) ratios, may have numerical values that are significantly different than the estimate (where I^R and I^C are the Sanders integrals giving the energy release rate obtained from the Reissner and the classical theory, respectively).

(*b*) For a thickness-to-crack length ratio of $h/2a = 1/10$ the estimated difference $\Delta I/I$ is approximately 12 percent and becomes greater for larger (and somewhat more realistic) $h/2a$ ratios. For some applications such approximations may not be acceptable.

(*c*) Since the problem is linear, in both theories the path independent integral should give an energy release rate that is identical to the crack closure energy obtained from the corresponding asymptotic stresses and displacements at the crack tips. For example, in plates under general membrane and bending loads the crack closure energy may be expressed as [14]

$$\mathcal{G} = \frac{\pi h}{E}\left[k_m{}^2 + k_s{}^2 + \frac{k_b{}^2}{3} + \frac{k_t{}^2}{3} + \frac{4(1+\nu)}{15}k_v{}^2\right] \tag{65}$$

where k_m, k_s, k_b, k_t, and k_v, respectively, the "membrane," in-plane "shear," "bending," "twisting" and "transverse shear" components are related to the modes *I*, *II* and *III* stress intensity factors by

$$k_1(x_3) = k_m + \frac{x_3}{h/2}k_b, \tag{66}$$

$$k_2(x_3) = k_s + \frac{x_3}{h/2}k_t, \tag{67}$$

$$k_3(x_3) = \left[1 - \left(\frac{x_3}{h/2}\right)^2\right]k_v. \tag{68}$$

Even though the difference between the stress intensity factors (k_b) given by the classical and Reissner theories in a plate under symmetric bending may be considered relatively minor, the difference for the skew-symmetric case (in which Modes *II* and *III* are coupled) is both conceptual and quantitative and is far from being minor.

One should again emphasize that the actual problem is one of three-dimensional elasticity. The foregoing comparison refer to two of the simplest approximations in which the problem is rendered two dimensional through certain thickness averaging of stresses. In crack problems, since the most important information is in the asymptotic solution around the crack tips, it would be preferable that the approximate theory used satisfy certain minimum requirements, namely the asymptotic results given by the plate (or the shell) theory (i.e., the singularity and the angular distribution of stresses) should be compatible with the corresponding in-plane and antiplane elasticity solutions, and the theory should contain all local relevant length parameters (h/a in plates, and h/a and R_{ij}/a in shells). Reissner's transverse shear theory appears to be the simplest plate theory satisfying these requirements. Furthermore, as indicated in this section, in all limiting cases investigated in this paper the results reduce *quantitatively* to known elasticity solutions. Considering the approximate nature of the theory, this point is rather important and is one more indication that the results may be accepted with certain degree of confidence.

References

1 Knowles, J. K., and Wang, N. M., "On the Bending of Elastic Plate Containing a Crack," *J. of Mathematics and Physics*, Vol. 39, 1960, pp. 223–236.

2 Wang, N. M., "Effect of Plate Thickness on the Bending of an Elastic Plate Containing a Crack," *J. of Mathematics and Physics*, Vol. 47, 1968, pp. 371–390.

3 Hartranft, R. J., and Sih, G. C., "Effect of Plate Thickness on the Bending Stress Distribution Around Through Cracks," *J. of Mathematics and Physics*, Vol. 47, 1968, pp. 276–291.

4 Civelek, M. B., and Erdogan, F., "Elastic-Plastic Problem for a Plate With a Part-Through Crack Under Extension and Bending," *Int. J. of Fracture*, Vol. 20, 1982, pp. 33–36.

5 Delale, F., and Erdogan, F., "The Effect of Transverse Shear in a Cracked Plate Under Skewsymmetric Loading," ASME Journal of Applied Mechanics, Vol. 46, 1979, pp. 618–624.

6 Reissner, E., "On Bending of Elastic Plates," *Quart. Appl. Math.*, Vol. 5, 1947, pp. 55–68.

7 Reissner, E., "The Effect of Transverse Shear Deformation on the Bending of Elastic Plates," ASME Journal of Applied Mechanics, Vol. 12, 1945, pp. A69–77.

8 Gupta, G. D., and Erdogan, F., "The Problem of Edge Cracks in an Infinite Strip," ASME Journal of Applied Mechanics, Vol. 41, 1974, pp. 1001–1006.

9 Krenk, S., "Influence of Transverse Shear on an Axial Crack in a Cylindrical Shell," *Int. J. of Fracture*, Vol. 14, 1978, pp. 123–143.
10 Erdogan, F., "Mixed Boundary Value Problems in Mechanics," *Mechanics Today*, Nemat-Nasser, S., ed., Vol. 4, Pergamon Press, 1978, pp. 1–86.
11 Delale, F., and Erdogan, F., "Transverse Shear Effect in a Circumferentially Cracked Cylindrical Shell," *Quart. Appl. Math.*, Vol. 37, 1979, pp. 239–258.
12 Erdogan, F., "On the Stress Distribution in Plates With Collinear Cuts Under Arbitrary Loads," Proc. *Fourth U.S. Nat. Congr. Theor. and Appl. Mech.*, Vol. 1, ASME, 1962, pp. 547–555.
13 Simmonds, J. G., and Duva, J., "Thickness Effects are Minor in the Energy Release Rate Integral for Bent Plates Containing Elliptic Holes or Cracks," ASME Journal of Applied Mechanics, Vol. 48, 1981, pp. 320–326.
14 Yahsi, O. S., and Erdogan, F., "A Cylindrical Shell With An Arbitrarily Oriented Crack," *Int. J. Solids, Structures*, to appear, 1984.

APPENDIX *A*

The normalized quantities for the plate bending problem.

$$x = x_1/a^*, y = x_2/a^*, z = x_3/a^*;$$

$$u = u_1/a^*, v = u_2/a^*, w = u_3/a^*;$$

$$\beta_x = \beta_1, \beta_y = \beta_2;$$

$$M_{xx} = \frac{M_{11}}{h^2E}, M_{yy} = \frac{M_{22}}{h^2E}, M_{xy} = \frac{M_{12}}{h^2E};$$

$$\sigma_{xx} = \frac{\sigma_{11}}{E}, \sigma_{yy} = \frac{\sigma_{22}}{E}, \sigma_{xy} = \frac{\sigma_{12}}{E};$$

$$V_x = \frac{V_1}{hB}, V_y = \frac{V_2}{hB};$$

$$B = \frac{5E}{12(1+\nu)}, \kappa = \frac{E}{B\lambda^4}, \lambda^4 = \frac{12(1-\nu^2)a^{*2}}{h^2}.$$

In the problem described by Fig. 1, $a^* = a$ for $0 < c < d < b$ and $a^* = d$ for $c = 0, d < b$.

M. K. Kassir
Professor,
Department of Civil Engineering,
City College of City
University of New York,
New York, N.Y. 10031
Mem. ASME

K. K. Bandyopadhyay
Senior Engineer,
Gibbs and Hill, Inc.,
New York, N.Y. 10001

Impact Response of a Cracked Orthotropic Medium

A solution is given for the problem of an infinite orthotropic solid containing a central crack deformed by the action of suddenly applied stresses to its surfaces. Laplace and Fourier transforms are employed to reduce the transient problem to the solution of standard integral equations in the Laplace transform plane. A numerical Laplace inversion technique is used to compute the values of the dynamic stress-intensity factors, $k_1(t)$ and $k_2(t)$, for several orthotropic materials, and the results are compared to the corresponding elastostatic values to reveal the influence of material orthotropy on the magnitude and duration of the overshoot in the dynamic stress-intensity factor.

Introduction

When a structural component is subjected to impact or shock loading, transient stress waves are generated, and the propagation of these waves can cause high stress elevation especially in local regions surrounding mechanical defects or cracks. In particular, near the vicinity of a crack tip, the magnitude of the dynamic stress-intensity factor is considerably larger than the corresponding statical one and in many instances may trigger crack extension and eventual failure of the component [1–5]. Thus, a knowledge of the overshoot in the dynamic stress-intensity factor and the time interval in which it occurs is essential to determine the response and fracture behavior of a structural element deformed by a sudden state of loading.

The purpose of this study is to determine the elastodynamic response of an orthotropic solid containing a crack under the action of impact loading. An infinite orthotropic medium in plane stress (or plane strain) is assumed to contain a central crack subjected to a sudden state of loading. The plane of the crack is assumed to coincide with one of the planes of elastic symmetry of the material. Both normal and in-plane shear loading are considered, and the aim is to determine the distribution of stress and displacement throughout the solid. In particular, attention is focused on finding the degree of influence of material orthotropy on the amplification of the dynamic stress-intensity factor and the elapsed time required to attain the peak value.

Laplace and Fourier integral transforms are employed to reduce the two-dimensional wave propagation problem to the solution of a standard pair of dual integral equations in the Laplace transform plane. The solution of the dual equations is reduced to the determination of an auxiliary function governed by a Fredholm integral equation of the second kind. Numerical methods are then employed to solve the Fredholm equation and to obtain the time dependency of the solution by way of a Laplace inversion technique [6, 7]. The dynamic stress-intensity factors for normal and in-plane shear loading, $k_1(t)$ and $k_2(t)$, are computed for several orthotropic materials and the normalized values are listed in tables and displayed graphically. For the orthotropic materials considered, the overshoot in the value of $k_1(t)$ as compared to the analogous statical value is about 16–20 percent and takes place in a time interval of $C_s t/a = 2.2$–2.6, while for mode 2, the amplification in the stress-intensity factor is about 4–15 percent and takes place in a time interval of $C_s t/a = 2.0$–2.5. Here, $a =$ half the crack length and C_s^2 stands for μ_{12}/ρ with μ_{12} being the shear modulus of the material and ρ the mass density. In the isotropic solid C_s represents the velocity of the shear wave. The technique employed, which is similar to one recently used in reference [8] to solve the problem of a moving Grifith crack in an orthotropic medium, can be extended to treat internal and edge crack problems in orthotropic strips.

Basic Equations

Consider the plane problem of an infinite orthotropic medium containing a central crack of length ($2a$) and subjected to a sudden state of loading. Let E_i, μ_{ij}, and $\nu_{ij}(i, j = 1, 2, 3)$ denote the engineering elastic constants of the material where the indices 1, 2, 3 correspond to the directions (x, y, z) of a system of cartesian coordinates chosen to coincide with the axes of material orthotropy. In this system of coordinates the crack is defined by the relations $y = \mp 0$, $|x| \leq a$, $|z| \leq \infty$. Since the problem under discussion is restricted to wave propagation in the plane, it is readily shown by setting the displacement component along the z-direction and all derivatives with respect to z to be zero that the displacement equations of motion reduce to [9]

$$c_{11}\frac{\partial^2 u}{\partial x^2} + \frac{\partial^2 u}{\partial y^2} + (1+c_{12})\frac{\partial^2 v}{\partial x \partial y} = \frac{1}{C_s^2}\frac{\partial^2 u}{\partial t^2}, \qquad (1)$$

Contributed by the Applied Mechanics Division for publication in the JOURNAL OF APPLIED MECHANICS.

Discussion on this paper should be addressed to the Editorial Department, ASME, United Engineering Center, 345 East 47th Street, New York, N.Y. 10017, and will be accepted until two months after final publication of the paper itself in the JOURNAL OF APPLIED MECHANICS. Manuscript received by ASME Applied Mechanics Division, October, 1982; final revision, February, 1983.

$$c_{22}\frac{\partial^2 v}{\partial y^2}+\frac{\partial^2 v}{\partial x^2}+(1+c_{12})\frac{\partial^2 u}{\partial x\partial y} = \frac{1}{C_s^2}\frac{\partial^2 v}{\partial t^2}, \quad (2)$$

in which u, v are the x, y-components of the displacement vector, and $c_{ij}\,(i, j = 1, 2)$ are nondimensional parameters related to the elastic constants by the relations[1]:

$$\left.\begin{aligned} c_{11} &= E_1/\mu_{12}[1-(E_2/E_1)\nu_{12}^2] \\ c_{22} &= (E_2/E_1)c_{11} \\ c_{12} &= \nu_{12}c_{22}=\nu_{21}c_{11} \end{aligned}\right\}, \quad (3)$$

for generalized plane stress, and by

$$\left.\begin{aligned} c_{11} &= (E_1/\mu_{12}\Delta)(1-\nu_{23}\nu_{32}) \\ c_{22} &= (E_2/\mu_{12}\Delta)(1-\nu_{13}\nu_{31}) \\ c_{12} &= (E_1/\mu_{12}\Delta)(\nu_{21}+\frac{E_2}{E_1}\nu_{13}\nu_{32}) \\ &= (E_2/\mu_{12}\Delta)(\nu_{12}+\frac{E_1}{E_2}\nu_{23}\nu_{31}) \\ \Delta &= 1-\nu_{12}\nu_{21}-\nu_{23}\nu_{32}-\nu_{31}\nu_{13}-\nu_{12}\nu_{23}\nu_{31}-\nu_{13}\nu_{21}\nu_{32} \end{aligned}\right\}, \quad (4)$$

for plane strain. The stresses are related to the displacements by the equations:

$$\left.\begin{aligned} \sigma_x/\mu_{12} &= c_{11}\frac{\partial u}{\partial x}+c_{12}\frac{\partial v}{\partial y} \\ \sigma_y/\mu_{12} &= c_{12}\frac{\partial u}{\partial x}+c_{22}\frac{\partial v}{\partial y} \\ \tau_{xy}/\mu_{12} &= \frac{\partial u}{\partial y}+\frac{\partial v}{\partial x} \end{aligned}\right\}, \quad (5)$$

In equations (1) and (2), the time variable may be removed by application of the Laplace transform relations

$$f^*(p) = \int_0^\infty f(t)\,e^{-pt}\,dt$$

$$f(t) = \frac{1}{2\pi i}\int_{Br} f^*(p)e^{pt}\,dp, \quad (6)$$

where Br denotes the Bromwich path of integration which is line to the right-hand side and parallel to the imaginary axis in the p-plane. Applying relations (6) to equations (1) and (2) and assuming zero initial conditions for the displacements and velocities, the transformed field equations become

$$c_{11}\frac{\partial^2 u^*}{\partial x^2}+\frac{\partial^2 u^*}{\partial y^2}+(1+c_{12})\frac{\partial^2 v^*}{\partial x\partial y}-\frac{p^2u^*}{C_s^2}=0, \quad (7)$$

$$c_{22}\frac{\partial^2 v^*}{\partial y^2}+\frac{\partial^2 v^*}{\partial x^2}+(1+c_{12})\frac{\partial^2 u^*}{\partial x\partial y}-\frac{p^2v^*}{C_s^2}=0, \quad (8)$$

where the transformed displacement components, u^* and v^* are now functions of the variables x, y, and p.

Normal Impact

When the solid is subjected to a suddenly applied state of normal loading, the problem of applying stresses to the surfaces of the crack – obtained by utilizing the usual principle of superposition – yields the following symmetry and boundary conditions in the $y = 0$ plane:

$$\tau_{xy}(x,0,t) = 0, \quad |x|<\infty, \quad (9)$$

$$\sigma_y(x,0,t) = -\sigma_0(x)\,H(t), \quad 0\le|x|\le a, \quad (10a)$$

$$v(x,0,t) = 0, \quad |x|>a \quad (10b)$$

in which the crack surface traction, $\sigma_0(x)$, is a known function of x and $H(t)$ is the Heaviside step function. In addition to equation (9) and (10), all components of displacement and stress must vanish at remote distances from the crack region. In the Laplace transform plane these conditions become:

$$\tau^*_{xy}(x,0;p) = 0, \quad \text{all} \quad x, \quad (11)$$

$$\sigma^*_y(x,0;P) = -\sigma_0(x)/p, \quad |x|\le a, \quad (12a)$$

$$v^*(x,0;p) = 0, \quad |x|>a \quad (12b)$$

To obtain an integral solution of the differential equations (7) and (8) subject to conditions (11) and (12), let

$$u^*(x,y;p) = \int_0^\infty A(s,y;p)\sin(sx)\,ds, \quad (13a)$$

$$v^*(x,y;p) = \int_0^\infty B(s,y;p)\cos(sx)\,ds, \quad (13b)$$

where A and B are arbitrary functions. Substituting from equations (13) into equations (7) and (8), the functions A and B are found to satisfy the simultaneous equations:

$$(c_{11}s^2+p^2/C_s^2)A-\frac{d^2A}{dy^2}+(1+c_{12})\,s\,\frac{dB}{dy}=0, \quad (14a)$$

$$(s^2+p^2/C_s^2)B-c_{22}\frac{d^2B}{dy^2}-(1+c_{12})\,s\,\frac{dA}{dy}=0, \quad (14b)$$

A proper solution to equations (14) which vanishes for large y is

$$\begin{aligned} A(s,y;p) &= A_1(s,p)\,e^{-\gamma_1 y}+A_2(s,p)e^{-\gamma_2 y} \\ B(s,y;p) &= \frac{\alpha_1}{s}A_1(s,p)\,e^{-\gamma_1 y}+\frac{\alpha_2}{s}A_2(s,p)e^{-\gamma_2 y}, \end{aligned} \quad (15)$$

Here, A_1 and A_2 are arbitrary functions, $\alpha_j(s,p)$ stand for the abbreviation

$$\alpha_j(s,p) = \frac{c_{11}s^2+p^2/C_s^2-\gamma_1^2}{(1+c_{12})\gamma_j}, \quad j=1,2, \quad (16)$$

and γ_1^2 and γ_2^2 are the two roots of the quadratic

$$c_{22}\gamma^4+[(c_{12}^2+2c_{12}-c_{11}c_{22})s^2-(1+c_{22})p^2/C_s^2]\gamma^2 + (c_{11}s^2+p^2/C_s^2)(s^2+p^2/C_s^2)=0. \quad (17)$$

The nature of the roots depends on the values of the elastic constants c_{ij} as well as on the wave speed C_s and the variables s and p. In many situations the roots γ_1 and γ_2 are real and positive and the expressions for the displacements in the Laplace plane become:

$$u^* = \int_0^\infty (A_1e^{-\gamma_1 y}+A_2e^{-\gamma_2 y})\sin(sx)\,ds, \quad (18a)$$

$$v^* = \int_0^\infty (\alpha_1A_1e^{-\gamma_1 y}+\alpha_2A_2e^{-\gamma_2 y})\frac{\cos(sx)}{s}ds, \quad (18b)$$

and the corresponding expression for τ^*_{xy} is given as

$$\tau^*_{xy}=-\mu_{12}\int_0^\infty[(\alpha_1+\gamma_1)A_1e^{-\gamma_1 y}+(\alpha_2+\gamma_2)A_2e^{-\gamma_2 y}]\sin(sx)\,ds, \quad (19)$$

Applying condition (11) to equation (19) renders

[1]The same notation of reference [8] has been adopted here except that the elastic constants c_{ij} $(i,j = 1, 2)$ of reference [8] are nondimensionlized with respect to μ_{12} for the sake of algebraic convenience.

$$A_2(s,p) = -\beta A_1(s,p), \quad \beta = \frac{\gamma_1+\gamma_1}{\alpha_2+\gamma_2} \tag{20}$$

It follows that the expressions for the transformed components of displacement assume the form

$$u^*(x,y;p) = \int_0^\infty (e^{-\gamma_1 y} - \beta e^{-\gamma_2 y}) A_1(s,p) \sin(sx)\, ds, \tag{21a}$$

$$v^*(x,y;p) = \int_0^\infty (\alpha_1 e^{-\gamma_1 y} - \beta\alpha_2 e^{-\gamma_2 y}) \frac{A_1(s,p)}{s} \cos(sx)\, ds, \tag{21b}$$

and the associated stresses are

$$\sigma_x^* = \mu_{12}\int_0^\infty [(c_{11}s^2 - \alpha_1\gamma_1 c_{12})e^{-\gamma_1 y} - (c_{11}s^2 - \alpha_2\gamma_2 c_{12})e^{-\gamma_2 y}]\cdot \frac{A_1(s,p)}{s}\cos(sx)\, ds, \tag{22a}$$

$$\sigma_y^* = \mu_{12}\int_0^\infty [(c_{12}s^2 - \alpha_1\gamma_1 c_{22})e^{-\gamma_1 y} - (c_{12}s^2 - \alpha_2\gamma_2 c_{22})e^{-\gamma_2 y}]\cdot \frac{A_1(s,p)}{s}\cos(sx)\, ds, \tag{22b}$$

$$\tau_{xy}^* = -\mu_{12}\int_0^\infty (\alpha_1+\gamma_1)(e^{-\gamma_1 y} - e^{-\gamma_2 y}) A_1(s,p)\sin(sx)\, ds, \tag{22c}$$

Introducing the abbreviations

$$D(s,p) = \frac{1}{s}(\alpha_1 - \beta\alpha_2) A_1(s,p) \tag{23a}$$

$$F(s,p) = \frac{1}{(\alpha_1-\beta\alpha_2)s\xi}[c_{12}s^2 - \alpha_1\gamma_1 c_{22} - \beta(c_{12}s^2 - \alpha_2\gamma_2 c_{22})], \tag{23b}$$

$$\xi = \frac{1}{c_{11}(1+c_{12})(N_1+N_2)}\{(c_{12}^2 + c_{12} - c_{11}c_{22})(c_{12}N_1N_2 - c_{11}) - c_{22}[c_{12}N_1^2N_2^2 - c_{11}(N_1^2 + N_1N_2 + N_2^2)]\}, \tag{23c}$$

$$N_{12}^2 = \frac{1}{2c_{22}}\{c_{11}c_{22} - c_{12}^2 - 2c_{12} \pm [(c_{11}c_{22} - c_{12}^2 - 2c_{12})^2 - 4c_{11}c_{22}]^{1/2}\}, \tag{23d}$$

and in view of boundary conditions (12), equations (21b) and (22b) yield the following pair of dual integral equations for the determination of the function $D(s,p)$

$$\int_0^\infty sF(s,p)\, D(s,p)\, \cos(sx)\, ds = -\frac{\sigma_0(x)}{\mu_{12}\xi p}, \quad 0 \le x \le a, \tag{24a}$$

$$\int_0^\infty D(s,p)\, \cos(sx)\, ds = 0, \quad x > a, \tag{24b}$$

In equations (23b) and (24), the constant ξ has been chosen such that for large values of the argument s, the expansion of the function $F(s,p)$ is given as

$$F(s,p) = 1 + 0(1/s)$$

Equations (24) form a pair of dual integral equations with a known weight function and its solution can be effected by writing

$$D(s,p) = \int_0^a \phi(t,p)\, J_0(st)\, dt, \tag{25}$$

where J_0 is the zero-order Bessel function of the first kind and the auxiliary function, $\phi(t,p)$, is governed by the Fredholm equation [10]

$$\phi(t,p) + \int_0^a \phi(\theta,p) K(\theta,t;p)\, d\theta = -\frac{2t}{\pi\mu_{12}p\xi}\int_0^t \frac{\sigma_0(x)\,dx}{(t^2-x^2)^{1/2}}, \tag{26}$$

in which the kernel, $K(\theta,t;p)$, is given by

$$K(\theta,t) = t\int_0^\infty s[F(s,p) - 1] J_0(st)\, J_0(s\theta)\, ds, \tag{27}$$

When the medium is stretched by a suddenly applied constant stress, i.e., $\sigma_0(x) = \sigma_0$, equation (26) reduces to

$$\phi(t,p) + \int_0^a \phi(\theta,p) K(\theta,t;p)\, d\theta = -\frac{\sigma_0 t}{\mu_{12}p\xi}, \tag{28}$$

To the extent that the function $\phi(t,p)$ has been obtained, the problem of determining the displacements and stresses in the transformed plane is reduced to quadrature. In particular, for purposes of computing the stress-intensity factor at the crack tip, expression (25) is integrated by parts and the result is inserted in conjunction with equation (23a) into relation (22b) to render

$$\sigma_y^* = \xi\mu_{12}\left\{\phi(a)\int_0^\infty F(s,p)\cos(sx)\, J_1(as)\, ds - \int_0^a F(s,p)\cos(sx)\, ds\int_0^\alpha tJ_1(st)\frac{d}{dt}[t^{-1}\phi(t)]\, dt\right\}, \tag{29}$$

Near the crack tip, the singular part of the expression in equation (29) can be extracted by noting that the integrals are

Table 1 Engineering elastic constants

Material	E_1	E_2	μ_{12}	ν_{12}
Boron-epoxy Type I	32.5×10^6 psi 224.06×10^9 N/m^2	1.84×10^6 psi 12.69×10^9 N/m^2	0.642×10^6 psi 4.43×10^9 N/m^2	0.256
Boron-epoxy Type II	8×10^6 psi 55.16×10^9 N/m^2	24.75×10^6 psi 170.65×10^9 N/m^2	0.7×10^6 psi 4.83×10^9 N/m^2	0.036
Glass-fiber (50 percent)	5.55×10^6 psi 38.27×10^9 N/m^2	1.33×10^6 psi 9.17×10^9 N/m^2	0.54×10^6 psi 3.72×10^9 N/m^2	0.28
Graphite-fiber (50 percent)	25.2×10^6 psi 173.75×10^9 N/m^2	1.0×10^6 psi 6.89×10^9 N/m^2	0.55×10^6 psi 3.79×10^9 N/m^2	0.28
Steel-mylar	26.28×10^6 psi 181.21×10^9 N/m^2	4.1×10^6 psi 28.3×10^9 N/m^2	0.9×10^6 psi 6.2×10^9 N/m^2	0.44
Beryllium	42.52×10^6 psi 293.19×10^9 N/m^2	49.29×10^6 psi 339.84×10^9 N/m^2	16.3×10^6 psi 112.4×10^9 N/m^2	0.24

finite throughout their range except the first integral, which become singular at the upper limit. In view of these observations and because of the behavior of $F(s,p)$ for large s noted earlier, equation (29) may be expanded for $r = x-a$, $r<<a$, to yield

$$\sigma_y^* = \frac{k_1^*(p)}{(2r)^{1/2}} + \ldots\ldots, \tag{30}$$

with the stress-intensity factor in the p-plane given by the relation

$$k_1^* = -\xi\mu_{12}\frac{\phi(a)}{(a)^{1/2}}, \tag{31}$$

With a view toward obtaining a numerical solution to equation (28), it is found convenient to adopt the following nondimensional parameters in equations (27)–(31)

$$t = ar, \quad \theta = a\rho, \quad \lambda = as \tag{32}$$

Moreover, upon setting

$$\phi(t) = \phi(ar) = -\frac{\sigma_0 a r^{1/2}\Phi(r)}{\mu_2 \xi p}, \tag{32}$$

it is readily shown that equation (28) simplifies to

$$\Phi(r,p) + \int_0^1 \Phi(\rho,p) L(a\rho,\, ar)\, d\rho = r^{1/2}, \tag{33}$$

where the kernel, $L(a\rho, ar)$, is now given by the symmetrical form

$$L(a\rho,\, ar) = (r\rho)^{1/2}\int_0^\infty \lambda[F(\lambda/a,p) - 1]J_0(\lambda r)J_0(\lambda\rho)\, d\lambda, \tag{34}$$

The factor k_1^* is determined as

$$k_1^*(p) = \sigma_0 (a)^{1/2}\frac{\Phi(1,p)}{p}, \tag{35}$$

The next step in the analysis is to determine the time dependence of the solution. For this purpose, expression (35) is inverted to yield the dynamic stress-intensity factor

$$k_1(t) = \frac{\sigma_0(a)^{1/2}}{2\pi i}\int_{Br}\frac{\Phi(1,p)}{p}e^{pt}\, dp, \tag{36}$$

Equation (33) is solved numerically for several orthotropic materials (listed in Table 1) and the values of $\Phi(1,p)$ are inserted in equation (36). The Laplace inversion in the time domain is then carried out numerically by the method described in reference [7] to obtain the stress-intensity factor.

In-Plane Shear Loading

In this case the crack surfaces are deformed by sudden application of in-plane shearing stresses such that the symmetry and boundary conditions read as

$$\sigma_y(x,0,t) = 0, \quad \text{all} \quad x, \tag{37}$$

$$\tau_{xy}(x,0,t) = -\tau_0(x)\, H(t), \quad 0 \le x \le a, \tag{38a}$$

$$u(x,0,t) = 0, \quad x > a, \tag{38b}$$

The same regularity requirements and initial conditions as in the preceding case are used. It follows that in the Laplace transform plane, equations (37) and (38) become

$$\sigma_y^*(x,0;p) = 0, \quad \text{all} \quad x, \tag{39}$$

$$\tau_{xy}^*(x,0;p) = -\frac{\tau_0(x)}{p}, \quad 0 \le x \le a, \tag{40a}$$

$$u^*(x,0;p) = 0, \quad x > a, \tag{40b}$$

To utilize the results of the preceding section, the following relations are assumed for the displacement components in the transformed plane

$$u^*(x,y;p) = \int_0^\infty A(s,y;p)\cos(sx)\, ds, \tag{41a}$$

$$v^*(x,y;p) = -\int_0^\infty B(s,y;p)\sin(sx)\, ds, \tag{41b}$$

As a consequence, it is found that equations (7) and (8) are satisfied and the functions A and B are governed by equations (14)–(17). It follows that the expressions for the displacement components become:

$$u^* = \int_0^\infty (A_1 e^{-\gamma_1 y} + A_2 e^{-\gamma_2 y})\cos(sx)\, ds, \tag{42a}$$

$$v^* = -\int_0^\infty (\alpha_1 A_1 e^{-\gamma_1 y} + \alpha_2 A_2 e^{-\gamma_2 y})\sin(sx), \tag{42b}$$

where α_j, $j = 1,2$, are defined in equation (16). The stress component σ_y^* is readily expressed by the relation

$$\sigma_y^* = -\mu_{12}\int_0^\infty [(c_{12}s^2 - c_{22}\alpha_1\gamma_1)A_1 e^{-\gamma_1 y} + (c_{12}s^2 - c_{22}\alpha_2\gamma_2)A_2 e^{-\gamma_2 y}]\frac{\sin(sx)}{s}\, ds, \tag{43}$$

Now, boundary conditions (39) immediately give rise to

$$A_2(s,p) = -\beta A_1(s,p), \tag{44a}$$

with

$$\beta = \frac{c_{12}s^2 - c_{22}\alpha_1\gamma_1}{c_{12}s^2 - c_{22}\alpha_2\gamma_2}, \tag{44b}$$

Making use of equations (42) and (44) in conjunction with the stress displacement relations, the stresses in the Laplace plane are found as

$$\sigma_x^* = -\mu_{12}\int_0^\infty [(c_{11}s^2 - c_{12}\alpha_1\gamma_1)e^{-\gamma_1 y} - (c_{11}s^2 - c_{12}\alpha_2\gamma_2)e^{-\gamma_2 y}]\cdot\frac{A_1(s,p)}{s}\sin(sx)\, ds, \tag{45a}$$

$$\sigma_y^* = -\mu_{12}\int_0^\infty (c_{12}s^2 - c_{22}\alpha_1\gamma_1)(e^{-\gamma_1 y} - e^{-\gamma_2 y})\frac{A_1(s,p)}{s}\sin(sx)\, ds, \tag{45b}$$

$$\tau_{xy}^* = \mu_{12}\int_0^\infty [-(\alpha_1 + \gamma_1)e^{-\gamma_1 y} + \beta(\alpha_2 + \gamma_2)e^{-\gamma_2 y}]A_1(s,p)\cos(sx)\, ds, \tag{45c}$$

The following abbreviations are found to be convenient

$$E(s,p) = (1-\beta)A_1(s,p), \tag{46a}$$

$$G(s,p) = \frac{-(\alpha_1+\gamma_1) + \beta(\alpha_2+\gamma_2)}{s(1-\beta)\eta}, \tag{46b}$$

$$\eta = (1+c_{12})^{-1}[c_{11}(c_{11} - N_1^2) - c_{22}(c_{11} - N_2^2)]^{-1}\left[\frac{1}{N_2}(c_{11} + c_{12}N_2^2)\cdot(c_{12}^2 + c_{12} - c_{11}^2 + c_{11}N_1^2) - \frac{1}{N_1}(c_{11} + c_{12}N_1^2)(c_{12}^2 + c_{12} - c_{11}c_{22} + c_{22}N_2^2)\right], \tag{46c}$$

where the constants N_1 and N_2 are defined in equations (23d). Applying boundary conditions (40) to equations (42) and (45) yields the following pair of dual integral equations for the finding of $E(s,p)$

$$\int_0^\infty s\, G(s,p)\; E(s,p)\; \cos(sx)\; ds = -\frac{\tau_0(x)}{\eta p \mu_{12}}, \quad 0 \leq x \leq a, \quad (47a)$$

$$\int_0^\infty E(s,p)\; \cos(sx)\; ds = 0, x > a, \qquad (47b)$$

In equations (46), the constant η has been chosen so that for large values of the argument (s) the function $G(s,p)$ defined in equation (46b) approaches unity. The set of equations (47) and the present formulation is seen to be identical to that of the previous case. Hence for the case of constant shearing stresses (τ_0) applied suddenly to the crack surfaces, the stress τ^*_{xy} may be expanded near the crack tip

$$\tau^*_{xy} = \frac{k^*_2(p)}{(2r)^{1/2}} + \ldots\ldots, \qquad (48)$$

in which the mode II stress-intensity factor is given by

$$k^*_2(p) = \tau_0(a)^{1/2} \frac{\Psi(1,p)}{p}, \qquad (49)$$

and the auxiliary function, $\Psi(1,p)$, is governed by the integral equation

$$\Psi(r,p) + \int_0^1 \Psi(\rho,p) M(a\rho,\; ar)\; d = r^{1/2}, \qquad (50)$$

with

$$M(a\rho,ar) = (r\rho)^{1/2} \int_0^\infty \lambda[G(\lambda/a,p) - 1] J_0(r\lambda) J_0(\lambda\rho)\; d\lambda, \qquad (51)$$

In the real domain, $k_2(t)$ is obtained through the integral

$$\frac{k_2(t)}{\tau_0(a)^{1/2}} = \frac{1}{2\pi i} \int_{Br} \frac{\Psi(1,p)}{p} e^{pt}\; dp, \qquad (52)$$

Numerical values of $k_1(t)$ and $k_2(t)$ for several orthotropic materials are presented in the next section.

Numerical Results and Discussion

Beryllium and several composite materials were selected for

Table 2 Stress-intensity factor $k_1(t)/\sigma_0(a)^{1/2}$ for normal impact loading

	$k_1(t)/\sigma_0(a)^{1/2}$					
$C_s t/a$	Boron-epoxy type I	Boron-epoxy type II	Glass-fiber (50 percent)	Graphite-fiber (50 percent)	Steel-mylar	Beryllium
0.1	0.2815	0.2921	0.2476	0.2727	0.2797	0.2178
0.5	0.6581	0.6653	0.6315	0.6518	0.6571	0.5989
1.0	0.9494	0.9534	0.9315	0.9457	0.9491	0.9020
1.5	1.1056	1.1071	1.0955	1.1039	1.1056	1.0728
2.0	1.1751	1.1749	1.1717	1.1749	1.1754	1.1575
2.5	1.1913	1.1898	1.1933	1.1922	1.1916	1.1876
3.0	1.1765	1.1742	1.1829	1.1784	1.1769	1.1849
3.5	1.1457	1.1429	1.1553	1.1482	1.1461	1.1639
4.0	1.1085	1.1054	1.1202	1.1113	1.1089	1.1341
4.5	1.0707	1.0676	1.0838	1.0737	1.0710	1.1016
5.0	1.0359	1.0328	1.0496	1.0389	1.0362	1.0700
5.5	1.0059	1.0029	1.0196	1.0087	1.0061	1.0415
6.0	0.9813	0.9786	0.9946	0.9840	0.9815	1.0171
6.5	0.9624	0.9599	0.9749	0.9649	0.9625	0.9971
7.0	0.9488	0.9466	0.9603	0.9510	0.9489	0.9814
7.5	0.9399	0.9880	0.9501	0.9418	0.9310	0.9698
8.0	0.9351	0.9336	0.9440	0.9368	0.9352	0.9617

Table 3 Stress-intensity factor $k_2(t)/\tau_0(a)^{1/2}$ for in-plane shear loading

	$k_1(t)/\sigma_0(a)^{1/2}$					
$C_s t/a$	Boron-epoxy type I	Boron-epoxy type II	Glass-fiber (50 percent)	Graphite-fiber (50 percent)	Steel-mylar	Beryllium
0.1	0.9209	0.8127	0.7396	0.9057	0.8913	0.4356
0.5	0.9674	0.9315	0.8934	0.9601	0.9572	0.7460
1.0	1.0017	1.0170	1.0066	1.0003	1.0052	0.9810
1.5	1.0182	1.0562	1.0613	1.0201	1.0279	1.1019
2.0	1.0238	1.0670	1.0798	1.0271	1.0349	1.1507
2.5	1.0229	1.0614	1.0770	1.0265	1.0329	1.1560
3.0	1.0186	1.0474	1.0627	1.0219	1.0261	1.1369
3.5	1.0128	1.0300	1.0435	1.0155	1.0173	1.1059
4.0	1.0067	1.0124	1.0233	1.0086	1.0082	1.0710
4.5	1.0010	0.9965	1.0045	1.0022	0.9989	1.0371
5.0	0.9962	0.9831	0.9884	0.9967	0.9928	1.0068
5.5	0.9923	0.9726	0.9755	0.9923	0.9872	0.9816
6.0	0.9895	0.9651	0.9659	0.9890	0.9832	0.9618
6.5	0.9876	0.9603	0.9595	0.9868	0.9806	0.9474
7.0	0.9866	0.9580	0.9560	0.9855	0.9792	0.9379
7.5	0.9864	0.9577	0.9549	0.9851	0.9790	0.9328
8.0	0.9867	0.9593	0.9559	0.9854	0.9796	0.9314

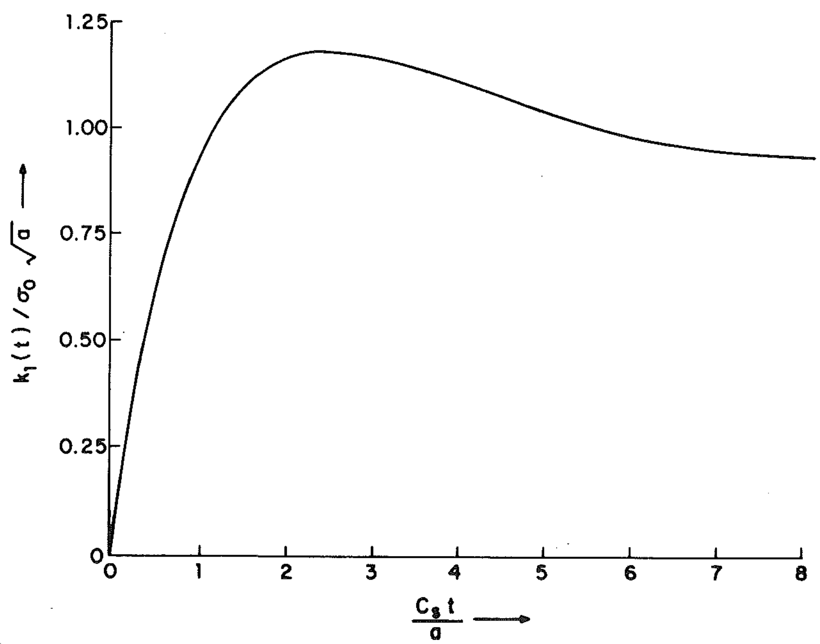

Fig. 1 Dynamic stress-intensity factor versus time for normal impact loading (boron-epoxy composite, type I)

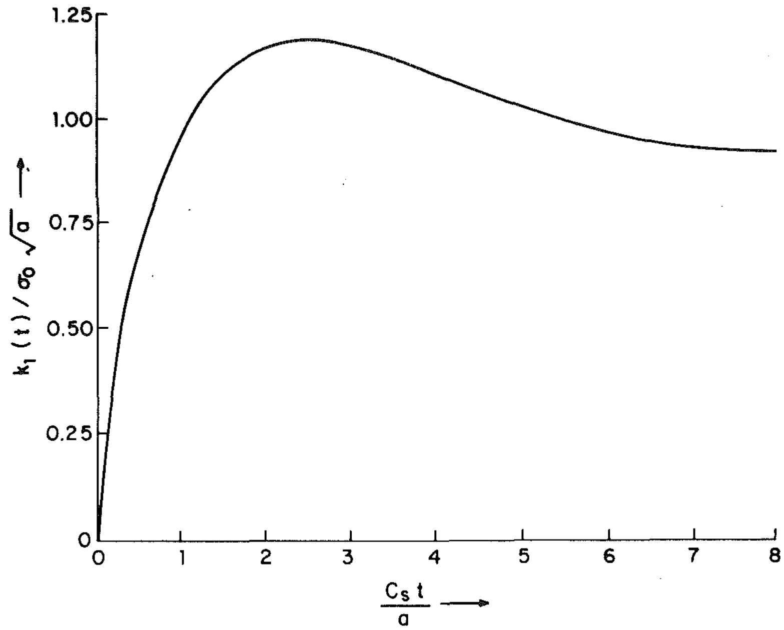

Fig. 2 Dynamic stress-intensity factor versus time for normal impact loading (boron-epoxy composite, type *II*)

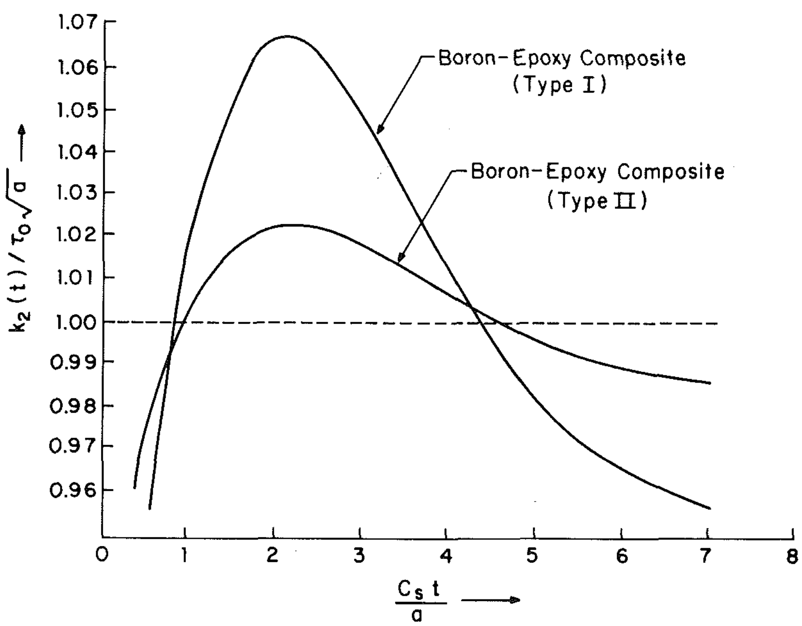

Fig. 3 Dynamic stress-intensity factor versus time for in-plane shear loading

numerical computation and application of the solution presented. The elastic constants are listed in Table 1. Except for the beryllium, which is nearly isotropic, all other materials are distinctly orthotropic. For the materials considered, the roots of the quadratic equation (17), are real and positive and the preceding formulation applies directly. However, in case the roots are negative or complex conjugates, as undoubtedly will occur for some other materials, the formulation must be modified to insure real displacements and stresses that vanish at the remote distances from the crack region.

The Fredholm equations (33) and (50) were solved numerically by the method described in [6] to yield the values of the functions $\Phi(1,p)$ and $\Psi(1,p)$ at several discrete points. These values were then inserted into equations (36) and (52) to determine the corresponding stress-intensity factors. This was accomplished numerically by the method of [7] using a five-term series expansion in Legendre polynomials orthogonal in the interval $(-1,1)$. In all cases examined the numerical computation converged smoothly and no unusual difficulties were encountered. Tables 2 and 3 show the values of the normalized dynamic stress-intensity factors, $k_1(t)/\sigma_0(a)^{1/2}$ and $k_2(t)/\tau_0(a)^{1/2}$ for few initial values of the normalized time variable $C_s t/a$. The results for the boron-epoxy composites are also displayed graphically in Figs. 1–3. A close examination of the results reveal that, for each material, the dynamic stress-intensity factor rises very quickly with time, reaching a peak and then decreases in magnitude and tends to the static solution for sufficiently long time. This behavior can be attributed to the scattered Rayleigh wave at the crack tip.

For the boron-epoxy composite (type *I*) with the following material characteristics [11]

$$E_1/E_2 = 17.65, \quad \mu_{12}/E_2 = 0.35, \quad \nu_{12} = 0.256$$

$$\text{Shear modulus } \mu_{12} = 4.43 \times 10^9 \text{ Pa}$$

$$\text{Density } \rho = 0.244 \times 10^{-2} \text{ Kg/cm}^3$$

$$C_s = (\mu_{12}/\rho)^{1/2} = 0.135 \text{ cm}/\mu\text{sec}$$

the overshoot in the value of $k_1(t)$ is about 19 percent and occurs at a time of $C_s t/a = 2.5$. Thus, for a crack of half length $a = 2.54$ cm (1 in.), the elapsed time needed for $k_1(t)$ to reach its maximum amplitude is estimated to be approximately 4.75×10^{-5} of a second. The elapsed time should satisfy the condition $C_s t >> \delta$, where δ is a small quantity ($\delta << a$) so that the asymptotic solution will be valid near the crack tip. On the other hand, in the boron-epoxy composite of type *II* [12], even though the material characteristics are different ($E_1/E_2 = 0.32$, $\mu_{12}/E_2 = 0.028$, $\nu_{12} = 0.036$), the variation of $k_1(t)$ with time is similar to the previous case (see Figs. 1 and 2). Similar conclusions can be made concerning the remaining materials. For purposes of comparison with the isotropic medium, reference [2] reports an overshoot of about 23 percent attained after a time of 2.4×10^{-5} of a second in a material made of steel with Poisson's ratio $\nu = 0.29$. While, in refernece [13], where elastodynamic stress-intensity factors were computed for diffraction of a longitudinal wave by a crack of finite length in an isotropic solid, the peak value of $k_1(t)$ was found to be 30 percent greater than the analogous static factor. Moreover, it was noted that this result is valid from the instant the incident wave arrives at the crack tip until a diffracted longitudinal wave reaches the opposite crack tip, is rediffracted, and then reaches the original tip; and, most likely, there are no higher maximum values in $k_1(t)$ for longer times. Greater peaks in the values of $k_1(t)$ were given in [4,5] where finite element and finite difference methods were employed to evaluate the dynamic stress-intensity factors for a crack in an isotropic sheet of finite width subjected to incident step-stress waves.

The mode *II* stress-intensity factors are given in Table 3. For beryllium, the rise in the stress-intensity factor is about 16 percent and occurs at an elapsed time of $C_s t/a = 2.5$. This result is in excellent agreement with the analogous results given for the isotropic material [2, 13]. For the remaining materials considered, the peak in $k_2(t)$ is very small (it varies between 3–8 percent) and occurs at smaller time $C_s t/a$ than the corresponding time for the normal loading. More specifically, in the boron-epoxy composite designated by type *I*, the value of $k_2(t)$ is about 2.5 percent greater than the static factor and occurs at an elapsed time of 3.77×10^{-5} of a second. While in the type *II* boron-epoxy composite with $E_1 < E_2$, the peak in $k_2(t)$ is about 7 percent and occurs at $C_s t/a = 2$. Thus, it seems that there is a higher rise in the value of $k_2(t)$ when the material possesses stronger modulus in the direction normal to the crack plane. The variation of $k_2(t)$ with time is exhibited in Fig. (3) for both boron-epoxy composites. Generally speaking, the dynamic overshoot in orthotropic materials is smaller for the shearing mode and occurs at shorter time than the case for the normal loading.

References

1 Achenbach, J. D., *Wave Propagation in Elastic Solids*, North Holland, Amsterdam, The Netherlands, 1973.

2 Chen, E. P., and Sih, G. C., *Elastodynamic Crack Problems, Mechanics of Fracture*, Vol. 4, Noordhoff, Leyden, The Netherlands, 1977.

3 Freund, L. B., "The Analysis of Elastodynamic Crack Tip Stress Fields," in *Mechanics Today*, Vol. 3, Nemat-Nasser, S., ed., Pergamon Press, New York, 1975, Chapter 2.

4 Anderson, J. M., Aberson, J. A., and King, W. W., "Finite Element Analysis of Cracked Structures Subjected to Shock Loads," *Computational Fracture Mechanics*, Rybicki, E. F., ed., ASME, New York, 1975.

5 Chen, Y. M., "Numerical Computation of Dynamic Stress-Intensity Factors by a Lagrangian Finite-Difference Method (The Hemp Code)," *Engineering Fracture Mechanics*, Vol. 7, 1975, pp. 653–660.

6 Krylov, V. I., and Kantorovich, L. V., *Approximate Methods of Higher Analysis*, Interscience, New York, 1957.

7 Miller, M. K. and Guy, W. T., "Numerical Inversion of the Laplace Transform by Use of Jacobi Polynomials," *SIAM Journal of Numerical Analysis*, Vol. 3, 1966, pp. 624–635.

8 Kassir, M. K., and Tse, S., "Moving Griffith Crack in an Orthotropic Material," *International Journal of Engineering Science*, Vol. 21, pp. 315–325.

9 Lekhnitskii, S. G., *Theory of Elasticity of an Anisotropic Elastic Body*, Holden-Day, San Francisco, 1963.

10 Sneddon, I. N., *Mixed Boundary Value Problems in Potential Theory*, North-Holland, Amsterdam, The Netherlands, 1966.

11 Vinson, J. R., and Chow, T. W., *Composite Materials and Their Use in Structures*, Wiley, New York, 1975.

12 Delale, F., and Erdogan, F., "The Problem of Internal and Edge Cracks in an Orthotropic Strip," ASME Journal of Applied Mechanics, Vol. 44, 1977, pp. 237–242.

13 Thau, S. A., and Lu, T. H., "Transient Stress-Intensity Factors for a Finite Crack in an Elastic Solid Caused by a Dilatational Wave," *International Journal of Solids and Structures*, Vol. 7, 1971, pp. 731–750.

A. Mioduchowski
Mem. ASME

M. G. Faulkner

A. Pielorz[1]

W. Nadolski[1]

Department of Mechanical Engineering,
The University of Alberta,
Edmonton, Alberta,
Canada

Longitudinal Collision of Rod-Rigid Element Systems

One-dimensional wave propagation theory is used to investigate the forces, velocities, and displacements in a series of elastic rods connected to rigid elements. The method is applied to the case of two subsystems that collide. The technique allows the calculations to be done during a short-lived event such as a collision.

1 Introduction

In many mechanical systems collision-like processes occur between elements coming into contact. A detailed description of these processes and their effects is virtually impossible. It is possible however, to obtain a good understanding of the physical phenomena through the investigation of simplified physical models which can be described by known mathematical apparatus.

In this paper a method of investigation is proposed for those mechanical systems that can be modeled by series of rods and rigid elements. The method, based on the theory of propagation of one-dimensional waves [1], is developed and discussed for simultaneous longitudinal collisions of three known initial velocities $\tilde{v}_1$, $\tilde{v}_2$, and $\tilde{v}_3$. It is assumed that the colliding rods have flat ends perpendicular to the direction of motion and their cross sections undergo only longitudinal displacemnts, i.e., radial effects are neglected. For modeling purposes, curved surfaces of colliding elements may be replaced by flat surfaces and even at the small distance from the point of contact, calculated values differ only negligibly from those obtained for curved surfaces [2]. Additionally, since the time of collision is very small, damping in the system under consideration is neglected [3].

While the model itself is extremely interesting, its practical applications range from investigation of colliding machine elements through mining and forging machinery to colliding railway cars and river barges. While the theory is presented for three subsystems – and can be easily extended to more – calculations are presented for a system consisting of two subsystems moving with velocities $\tilde{v}_1$ and $\tilde{v}_2$, respectively. Numerical results for velocities and deformations at various points of the system are presented in graphical form.

2 Basic Equations and Development of the Numerical Technique

While the development of the governing equations can be done for n subsystems of multistage rods, it will be considered in the following for only three separate ones. Each of the subsystems (see Fig. 1) is modeled as being composed of rigid elements with masses M_i to which elastic rods of length l are attached to both sides. Each of the rods have length l, mass density ρ, elastic modulus E, and cross-sectional area A. The three subsystems have α_1, α_2, and α_3 rods, respectively. Since each mass has rods on both sides α_1, α_2, and α_3 must be even numbers and the subsystems contain $\alpha_1/2$, $\alpha_2/2$, and $\alpha_3/2$ masses, respectively. Each of the masses is numbered with an odd number so that subsystems 1 contains masses M_1, $M_3 \ldots M_{\alpha_1-1}$, etc. The rods are numbered consecutively so that subsystem 1 contains rods from 1 to α_1, subsystems 2 has rods $\alpha_1 + 1$ to $\alpha_1 + \alpha_2$, and subsystem 3 has rods $\alpha_1 + \alpha_2 + 1$ to $\alpha_1 + \alpha_2 + \alpha_3$.

Before collision each of the subsystems is in rectilinear motion with speeds $\tilde{v}_1$, $\tilde{v}_2$, and $\tilde{v}_3$ respectively. At time $t = 0$ the subsystems undergo simultaneous longitudinal collision at the points of contact between rods α_1 and $\alpha_1 + 1$ as well as between $\alpha_1 + \alpha_2$ and $\alpha_1 + \alpha_2 + 1$.

The governing equations are written in terms of the position coordinate $\tilde{x}$, time τ, the displacement $\tilde{u}_i(\tilde{x},\tau)$ of a cross section of the ith rod, and c the speed of a longitudinal wave in the rods. For ease of calculation nondimensional variables are introduced. These include

$$x = \frac{\tilde{x}}{l} \quad t = \frac{c\tau}{l} \quad v_j = \frac{\tilde{v}_j}{\tilde{v}_1} \quad (j = 1,2,3)$$

$$u_i = \frac{c\tilde{u}_i}{\tilde{v}_1 l} \quad i = 1,2, \ldots \alpha_1 + \alpha_2 + \alpha_3 \tag{2.1}$$

[1] On leave from the Institute of Fundamental Technological Research, Polish Academy of Sciences, Warsaw, Poland.

Contributed by the Applied Mechanics Division for presentation at the Winter Annual Meeting, Boston, Mass., November 13–18, 1983 of THE AMERICAN SOCIETY OF MECHANICAL ENGINEERS.

Discussion on this paper should be addressed to the Editorial Department, ASME, United Engineering Center, 345 East 47th Street, New York, N.Y. 10017, and will be accepted until two months after final publication of the paper itself in the JOURNAL OF APPLIED MECHANICS. Manuscript received by ASME Applied Mechanics Division, November, 1982; final revision, January, 1983. Paper No. 83-WA/APM-3.

Copies will be available until July 1984.

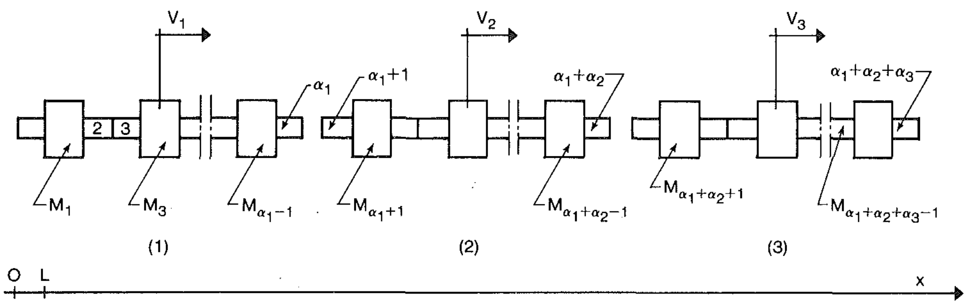

Fig. 1

The governing differential equations are then the wave equation for each individual rod. In terms of the nondimensional variables these become

$$\frac{\partial^2 u_i(x,t)}{\partial t^2} - \frac{\partial^2 u_i(x,t)}{\partial x^2} = 0 \qquad i=1,2,\ldots\ \alpha_1+\alpha_2+\alpha_3 \tag{2.2}$$

The boundary conditions include zero force at the ends

$$\frac{\partial u_1}{\partial x} = 0 \quad x=0$$
$$\frac{\partial u_n}{\partial x} = 0 \quad x=n \quad n=\alpha_1+\alpha_2+\alpha_3 \tag{2.3}$$

The forces between rods must equal

$$\frac{\partial u_i}{\partial x} = \frac{\partial u_{i+1}}{\partial x} \qquad x=i=2,4,\ldots n-2 \tag{2.4}$$

The displacements must be continuous therefore

$$u_i = u_{i+1} \qquad x=i=1,2,\ldots,n-1 \tag{2.5}$$

As well there must be a force balance for each of the masses so that

$$\frac{1}{K_i}\frac{\partial^2 u_i}{\partial t^2} + \left(\frac{\partial u_i}{\partial x} - \frac{\partial u_{i+1}}{\partial x}\right) = 0 \qquad x=i=1,3,\ldots,n-1 \tag{2.6}$$

and

$$K_i = \frac{A\rho l}{M_i}.$$

In addition the initial conditions are as follows:

$$u_i(x,0)=0 \quad i=1,2.\ldots,n$$
$$\frac{\partial u_i}{\partial t}(x,t)\Big|_{t=0} = v_j \tag{2.7}$$

where

$j = 1 \quad i=1,2,\ldots,\alpha_1$

$j = 2 \quad i=\alpha_1+1,\ldots,\alpha_1+\alpha_2$

$j = 3 \quad i=\alpha_1+\alpha_2+1,\ldots,\alpha_1+\alpha_2+\alpha_3$

As the governing differential equations (2.2) and the boundary conditions are linear a solution of the following form is assumed

$$u_i(x,t) = f_i(t-t_{i0}-x+x_{i0}) + g_i(t-t_{i0}+x-x_{i0}) + F_i(t-T_{i0}-x+X_{i0}) + G_i(t-T_{i0}+x-X_{i0}) + v_i t \tag{2.8}$$

where

$$t_{i0} = \begin{cases} \alpha_1 - i & i=1,2,\ldots,\alpha_1 \\ i-\alpha_1-1 & i=\alpha_1+1,\ldots,\alpha_1+\alpha_2+\alpha_3 \end{cases}$$

$$x_{i0} = \begin{cases} i & i=1,2,\ldots,\alpha_1 \\ i-1 & i=\alpha_1+1,\ldots,\alpha_1+\alpha_2+\alpha_3 \end{cases}$$

$$T_{i0} = \begin{cases} \alpha_1+\alpha_2-i & i=1,2,\ldots,\alpha_1+\alpha_2 \\ i-\alpha_1-\alpha_2-1 & i=\alpha_1+\alpha_2+1,\ldots,\alpha_1+\alpha_2+\alpha_3 \end{cases}$$

$$X_{i0} = \begin{cases} i & i=1,2,\ldots,\alpha_1+\alpha_2 \\ i-1 & i=\alpha_1+\alpha_2+1,\ldots,\alpha_1+\alpha_2+\alpha_3 \end{cases}$$

The assumed solution (2.8) consists of two sets of waves f_i, g_i and F_i, G_i as well as a displacement due to the initial velocity of the subsystem. The terms f_i, g_i represent waves formed in the ith rod as a result of the collision between subsystem 1 and 2 while F_i, G_i represent waves from the collision between subsystem 2 and 3. The terms f_i and F_i represent waves traveling in the positive direction while g_i and G_i travel in the negative direction.

The constants in equations (2.8) are chosen to denote instants in time t and end of rods such that the disturbance caused by the appropriate collision will have reached the particular location. It is also assumed that for negative arguments (i.e., before arrival of the first perturbation) the functions f_i, g_i, F_i, and G_i are identically zero, and all of them are of class C°. The form the these functions is determined by boundary conditions of the considered problem. By substituting the assumed form (2.8) into the boundary conditions (2.3)–(2.6) we get system of equations for these functions. For example, equation (2.3) gives:

$$-f_1'(t-\alpha_1+2) + g_1'(t-\alpha_1) - F_1'(t-\alpha_1-\alpha_2+2) + G_1'(t-\alpha_1-\alpha_2) = 0$$
$$-f_n'(t-\alpha_2-\alpha_3) + g_n'(t-\alpha_2-\alpha_3+2) - F_n'(t-\alpha_3) + G_n'(t-\alpha_3+2) = 0,$$

equations (2.4), for $i = 2,4,\ldots,\alpha_1$, give:

$$-f_i'(t-\alpha_1+i) + g_i'(t-\alpha_1+i) - F_i'(t-\alpha_1-\alpha_2+i) + G_i'(t-\alpha_1-\alpha_2+i) = -f_{i+1}'(t-\alpha_1+i+2) + g_{i+1}'(t-\alpha_1+i) - F_{i+1}'(t-\alpha_1-\alpha_2+i+2) + G_{i+1}'(t-\alpha_1-\alpha_2+i)$$
$$i=2,4,\ldots,\alpha_1-2$$

$$-f_{\alpha_1}'(t) + g_{\alpha_1}'(t) - F_{\alpha_1}'(t-\alpha_2) + G_{\alpha_1}'(t-\alpha_2) = -f_{\alpha_1+1}'(t) + g_{\alpha_1+1}'(t) - F_{\alpha_1+1}'(t-\alpha_1+2) + G_{\alpha_1+1}'(t-\alpha_2)$$
$$(i=\alpha_1),$$

while equations (2.6). for $i = 1,3,\ldots,\alpha_1-1$, are rewritten as

$$f_i''(t-\alpha_1+i) + g_i''(t-\alpha_1+i) + F_i''(t-\alpha_1-\alpha_2+i) + G_i''(t-\alpha_1-\alpha_2+i) + K_i[-f_i'(t-\alpha_1+i) + g_i'(t-\alpha_1+i) - F_i'(t-\alpha_1-\alpha_2+i) + G_i'(t-\alpha_1-\alpha_2+i) + f_{i+1}'(t-\alpha_1+i+2) - g_{i+1}'(t-\alpha_1+i) + F_{i+1}'(t-\alpha_1-\alpha_2+i+2) - G_{i+1}'(t-\alpha_1-\alpha_2+i)] = 0$$
$$i=1,3,\ldots,\alpha_1-1.$$

All other equations are derived in a similar manner. Since in all these relations (2.3), (2.4), and (2.6), derivatives of appropriate functions appear rather than then functions themselves it is convenient to differentiate equations (2.5) with respect to time as well.

In all those equations for the functions f_i, g_i, F_i, and G_i there exist simple relationships between arguments of the functions appearing in the same equation; however, these relationships may vary from equation to equation.

Since the discussed problem is of linear type one can investigate functions f_i and g_i, and F_i and G_i separately. It means physically that the effect of each collision can be treated separately. For the final result, however, one has to superpose both collision effects. It is expressed mathematically by the relation (2.8) for displacements.

Upon denoting the largest argument in each equality by z (separately for f_i and g_i, and for F_i and G_i) we have arguments of the remaining functions shifted by 2 or 0. This leads to the following final system of equations for the unknown functions $f_i(z)$ and $g_i(z)$.

$$
\begin{aligned}
f_1'(z) &= g_1'(z-2)\\
f_i'(z) &= f_{i-1}'(z-2), \quad i=3,5,\ldots,\alpha_1-1\\
f_i'(z) &= f_{i-1}'(z-2)+g_{i-1}'(z-2)-g_i'(z-2)\\
&\qquad i=2,4,\ldots,\alpha_1\\
g_i'(z) &= f_i'(z-2); \quad i=\alpha_1+\alpha_2+\alpha_3 \qquad (2.9)\\
g_i'(z) &= g_{i+1}'(z-2),\\
&\qquad i=\alpha_1+2,\alpha_1+4,\ldots,\alpha_1+\alpha_2+\alpha_3-2\\
g_i'(z) &= f_{i+1}'(z-2)+g_{i+1}'(z-2)-f_1'(z-2)\\
&\qquad i=\alpha_1+1,\\
&\qquad \alpha_1+3,\ldots,\alpha_1+\alpha_2+\alpha_3-1\\
g_{\alpha_1}'(z) &= g_{\alpha_1+1}'(z)+\frac{1}{2}(v_2-v_1)\\
f_{\alpha_1+1}'(z) &= f_{\alpha_1}'(z)-\frac{1}{2}(v_2-v_1)\\
g_i'(z) &= g_{i+1}'(z) \quad i=\alpha_1-2, \quad \alpha_1-4,\ldots,2\\
g_i''(z) &+ 2K_ig_i'(z)=-f_i''(z)+2K_ig_{i+1}'(z)\\
&\qquad i=\alpha_1-1,\ldots,3,1\\
f_i''(z) &+ 2K_{i-1}f_i'(z)=-g_i''(z)+2K_{i+1}f_{i-1}'(z)\\
i&=\alpha_1+2, \quad \alpha_1+4,\ldots,\alpha_1+\alpha_2+\alpha_3\\
f_i'(z) &= f_{i-1}'(z), i=\alpha_1+3,\\
&\qquad \alpha_1+5,\ldots,\alpha_1+\alpha_2+\alpha_3-1
\end{aligned}
$$

and to the following final system of equations for the unknown functions $F_i(z)$ and $G_i(z)$

$$
\begin{aligned}
F_1'(z) &= G_1'(z-2)\\
F_i'(z) &= F_{i-1}'(z-2) \quad i=3,5,\ldots,\alpha_1+\alpha_2-1\\
F_i'(z) &= F_{i-1}'(z-2)+G_{i-1}'(z-2)-G_i'(z-2)\\
&\qquad i=2,4,\ldots,\alpha_1+\alpha_2\\
G_i'(z) &= G_{i+1}'(z-2) \quad i=\alpha_1+\alpha_2+2,\\
&\qquad \alpha_1+\alpha_2+4,\ldots,\alpha_1+\alpha_2+\alpha_3-2\\
G_i'(z) &= F_{i+1}'(z-2)+G_{i+1}'(z-2)-F_i'(z-2)\\
&\qquad i=\alpha_1+\alpha_2+1,\\
&\qquad \alpha_1+\alpha_2+3,\ldots,\alpha+\alpha_2+\alpha_3-1\\
G_i'(z) &= F_i'(z-2), i=\alpha_1+\alpha_2+\alpha_3 \qquad (2.10)\\
F_i'(z) &= F_{i+1}'(z)-\frac{1}{2}(v_3-v_2) \quad \text{for} \quad i=\alpha_1+\alpha_2\\
F_i'(z) &= G_{i+1}'(z)+\frac{1}{2}(v_3-v_2), \quad i=\alpha_1+\alpha_2\\
F_i'(z) &= F_{i-1}'(z), i=\alpha_1+\alpha_2+3,\\
&\qquad \alpha_1+\alpha_2+5,\ldots,\alpha_1+\alpha_2+\alpha_3-1\\
F_i''(z) &+ 2K_{i-1}F_i'(z)=-G_i''(z)+2K_{i-1}F_{i-1}'(z)\\
&\qquad i=\alpha_1+\alpha_2+2, \alpha_1+\alpha_2+4,\ldots,\alpha_1+\alpha_2+\alpha_3\\
G_i'(z) &= G_{i+1}'(z), \quad i=2,4,\ldots,\alpha_1+\alpha_2-2\\
G_i''(z) &+ 2K_iG_i'(z)=-F_i''(z)+2K_iG_{i+1}'(z)\\
&\qquad i=1,3,\ldots,\alpha_1+\alpha_2-1
\end{aligned}
$$

These two systems of equations (2.9) and (2.10) are systems of linear, ordinary differential equations of first and second order. These sets are solved in the given sequence in the successive intervals of argument z, beginning with even numbers. Since the functions f_i, g_i and F_i, G_i are equal zero for negative arguments, therefore when solving equations (2.9) and (2.10) in the given sequence the right-hand sides of these equations are always known.

3 Example

As an example consider two subsystems, one with two masses and four rods while the other has one mass of two

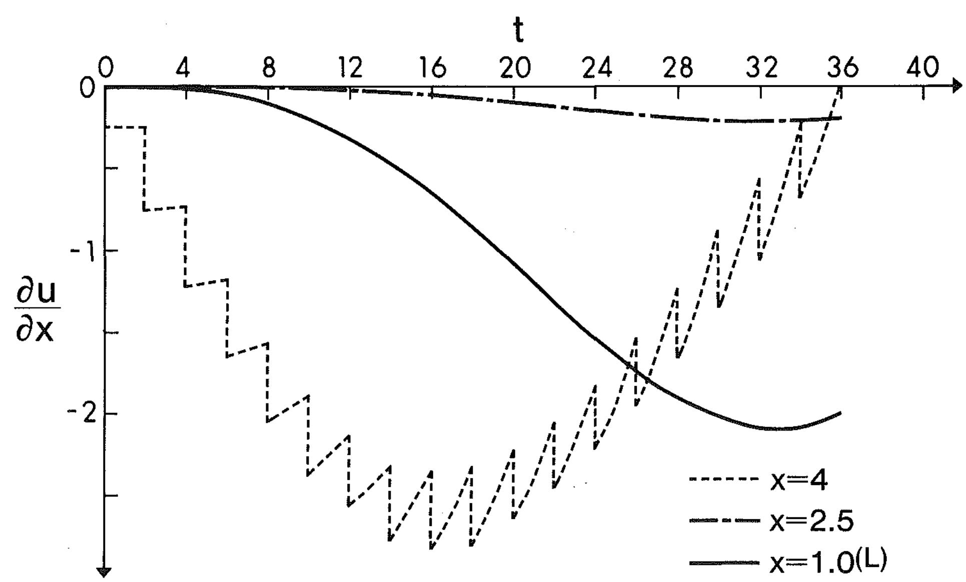

Fig. 2

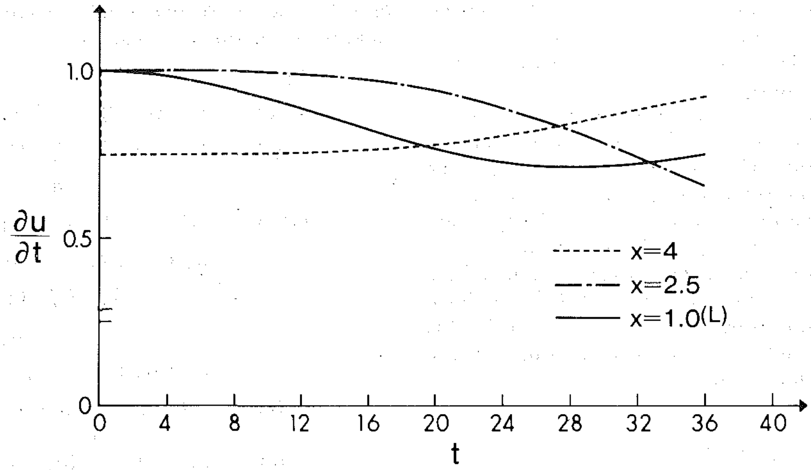

Fig. 3

rods. Consequently $\alpha_1 = 4$, $\alpha_2 = 2$, and $\alpha_3 = 0$, as shown in Fig. 1, and from the system of equations (2.9) we get:

$$
\begin{aligned}
f_1'(z) &= g_1'(z-2) \\
f_3'(z) &= f_2'(z-2) \\
f_i'(z) &= f_{i-1}'(z-2)+g_{i-1}'(z-2)-g_i'(z-2) \quad i=2,4 \\
g_6'(z) &= f_6'(z-2) \\
g_5'(z) &= f_6'(z-2)+g_6'(z-2)-f_5'(z-2) \\
g_4'(z) &= g_5'(z)+\frac{1}{2}(v_2-v_1) \\
f_5'(z) &= f_4'(z)-\frac{1}{2}(v_2-v_1) \\
g_3''(z) &+ 2K_3g_3'(z)=-f_3''(z)+2K_3g_4'(z) \\
g_2'(z) &= g_3'(z) \\
g_1''(z) &+ 2K_1g_1'(z)=-f_1''(z)+2K_1g_2'(z) \\
f_6''(z) &+ 2K_5f_6'(z)=-g_6''(z)+2K_5f_5'(z)
\end{aligned}
$$

This set of equations is to be solved in the given sequence in the successive intervals of the argument $z \geq 0$, beginning with even numbers, since arguments of functions in right-hand sides of some equations are shifted by 2. Equations (3.1) together with (2.8) can be used to calculate velocities, strains, and displacements for any cross section x of any rod at any instant t during collision.

The set of equations (3.1) was solved using method of finite differences with $\Delta z = 0.025$ and for the parameters of the system:

$$
\begin{aligned}
&K_1=K_2=K_3=0.01, \\
&V_1=1.0 \quad \text{and} \quad V_2=0.5 \qquad (3.2)
\end{aligned}
$$

Numerical results for strains in the cross sections $x = 1.0^{(L)}$, $x = 2.5$, and $x = 4$ are shown in Fig. 2. It can be seen that the strain for cross section $x = 4$ (the point of collision) changes in a jumplike manner, with jump occurring every $\Delta t = 2$. At $t = 36$ this strain reaches zero and at this point we have to terminate our calculations. This instant physically represents the end of contact between the two subsystems and the beginning of separate motions. Further it follows from Fig. 2 that the strains at $x = 1.0^{(L)}$ and $x = 2.5$ are continuous with the first one being much smaller than the second.

Numerical results for velocities in the cross sections $x = 1.0$, $x = 2.5$, and $x = 4.0$ are shown in Fig. 3. It can be seen that the velocity for the cross section $x = 4$ undergoes a jumplike change at $t = 0$, in order that the two subsystems could move together with the same velocity. This common velocity is changing continuously during the duration of collision.

If for some practical application we have, for example, $l = 0.5$ m and $c = 5000$ m/s, then nondimensional unit of time $t = 1$ corresponds to 10^{-4} sec. Then the total duration of collision is approximately 3.6×10^{-3} sec and all jumplike changes of strain for $x = 4.0$ occur at intervals of time $\Delta t = 2 \times 10^{-4}$ sec.

4 Concluding Remarks

In the paper a simple method is proposed for investigation of colliding systems that consist of series of elastic rods connected with rigid elements. Dimensions of elastic and rigid parts should be such that the theory of one-dimensional waves is applicable. Effectiveness of the method is illustrated in the case of two, and three colliding subsystems. Displacements, velocities, and stresses can then be easily calculated for any cross section in any subsystem at any interval of time during a shortlived event such as a collision.

References

1 Baldock, G. R., and Bridgeman, T., *Mathematical Theory of Wave Motion*, Ellis Harwood Ltd., Chichester, 1981.
2 Sears, J. E., "On the Longitudinal Impact of Metal Rods With Rounded Ends," *Trans. Comb., Phil. Soc.*, Vol. 21, 1908, pp. 49–170.
3 Goldsmith, W., *Impact*, Edward Arnold Ltd., London 1960.

A. B. Mason, Jr.
Chevron Oil Field Research Company,
P.O. Box 446,
La Habra, Calif. 90631
Assoc. Mem. ASME

W. D. Iwan
Division of Engineering and
Applied Science,
California Institute of Technology,
Pasadena, Calif. 91125
Mem. ASME

An Approach to the First Passage Problem in Random Vibration

The first passage problem for the response of a linear oscillator excited by a random excitation is considered. An approximate analytical technique is presented for calculation of the distribution of the time to first excursion across a symmetric double barrier. The approach may be applied to the case of nonstationary response to modulated Gaussian noise with nonwhite spectral density. Results for the limiting decay rate parameter are presented and are compared with those of other analytical methods and simulation results. The first passage probability is calculated for a system subjected to a suddenly applied white noise and the results also compared with those of other methods and computer simulations. The results of the proposed method show generally good agreement with simulation results.

Introduction

The determination of the probability that the value of some response variable remains below a given threshold throughout a specified time interval is an important problem for many engineering applications. A system of particular interest in structural dynamics and vibration is the linear oscillator subject to a stationary Gaussian white noise. The equation of motion may be written as

$$\ddot{x}+2\zeta\omega_0\dot{x}+\omega_0^2x=w(t) \tag{1}$$

where ζ is the fraction of critical damping, and ω_0 is the undamped natural frequency. The spectral density of $w(t)$ will be assumed to be S_0.

Let $W(T)$ be the probability that the magnitude of x remains less than some barrier level b throughout the interval $[0,T]$, where b is a positive constant. Then, $W(t)$ will in general be dependent on the initial conditions imposed on equation (1). However, it has been observed by Crandall and others that the effects of the initial conditions tend to die out as T becomes large compared with the natural period of the oscillator [1]. Specifically, it has been observed that $W(T)$ eventually approaches a decaying exponential of the form

$$W(T)\sim e^{-\alpha T} \tag{2}$$

independent of the initial conditions [2]. The parameter α is referred to as the limiting decay rate of the first crossing density.

Although the first passage problem for the linear oscillator may be precisely formulated [1], no closed-form solution for this problem has yet been presented. In the absence of an exact analytical solution, numerous approximate solutions have been proposed. Of these, the most accurate schemes generally involve the generation of an approximate solution for the conditional transition probability density governing first passage. An obvious approach of this sort would be to attempt a numerical solution of the Smoluchowsky integral equation [3] or its associated Fokker-Planck-Kolmogorov equation. An interesting variation of this approach is based on a discretized version of the Smoluchowsky equation. This so-called "diffusion of probability" method has been employed by Crandall, et al. [2], to obtain approximate values for the limiting decay rate α for a number of damping values and a range of barrier levels. For a sufficiently fine discretization, this procedure generates values of α that agree quite well with those obtained by both analog and digital simulation as indicated in Fig. 1.

The best approximation for α currently available appears to have been obtained by Mark [4]. For sufficiently small damping, the sample functions of $x(t)$ have an approximately sinusoidal appearance. Hence, the magnitudes of the peaks of these quasi-sinusoidal sample functions may be treated as a one-dimensional, continuous-state, discrete time Markov process. Mark makes the approximation that the peaks are separated by intervals of exactly $\Delta t=\pi/\omega_0$; an assumption that will become increasingly valid as the damping decreases. A conditional transition probability density function $\hat{p}(\hat{a}_0\,|\,\hat{a}_1;\Delta t)$ for the magnitude of a peak $\hat{a}_1$, given the value of the preceding peak $\hat{a}_0$, is then derived. This leads to an integral equation, similar to the Smoluchowsky equation, which must be solved numerically. This method also agrees well with simulation results for small damping as indicated in Fig. 1.

Most of the accurate approximate analytical solutions presently available still require substantial numerical computation. However, strictly numerical schemes, such as Monte Carlo simulation and diffusion of probability, require much greater computational effort. A number of simple approximate solutions for the limiting decay rate also exist. These require much less effort to implement but do not exhibit acceptable accuracy. The simplest approximation involves the

Contributed by the Applied Mechanics Division for publication in the JOURNAL OF APPLIED MECHANICS.

Discussion on this paper should be addressed to the Editorial Department, ASME, United Engineering Center, 345 East 47th Street, New York, N.Y. 10017, and will be accepted until two months after final publication of the paper itself in the JOURNAL OF APPLIED MECHANICS. Manuscript received by ASME Applied Mechanics Division, October, 1980; final revision, December, 1981.

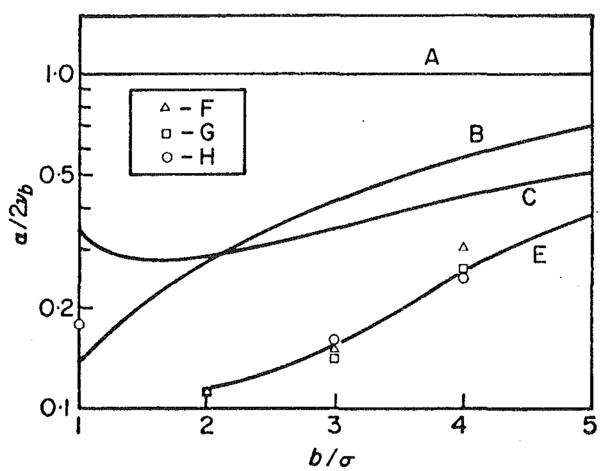

A - Assumption of Independent D-Crossings.
B - Assumption of Independent E-Crossings.
C - Vanmarcke's Modified Two-State Markov Process.
E - Mark's Continuous State-Discrete Time Markov Process.
F - Digital Simulation.
G - Analog Simulation.
H - Numerical Diffusion of Probability.

Fig. 1 Comparison of analytical estimates for limiting decay rate with results of simulations, $\zeta = 0.01$. From reference [1].

assumption that the barrier crossings are statistically independent events. This will be approximately true when the value of b is large compared with the root-mean-square value of the response σ so that the average interval between successive up-crossings of b becomes very long. Making this assumption, the times at which such up-crossings occur constitutes a Poisson process, and the intervals between up-crossings will be exponentially distributed. Solving for the average rate of up-crossing of the level $x = b$, denoted by ν_b gives [5]

$$\nu_b = \frac{\omega_0}{2\pi} \exp\left(-\frac{b^2}{2\sigma^2}\right). \tag{3}$$

The rate of down-crossings of $-b$ will be the same as ν_b. Thus, the average of the number of crossings out of the safe region per unit time is just $2\nu_b$. This gives the Poisson process average rate as

$$\alpha = 2\nu_b. \tag{4}$$

For barrier levels of practical interest, the Poisson approximation is usually overly conservative as indicated in Fig. 1. For very high barrier levels, however, the approximation becomes quite good, and in fact, equation (4) becomes asymptotic to the actual limiting decay rate as $b \to \infty$. The Poisson average crossing rate $2\nu_b$ provides a convenient normalizing factor for other estimates of the limiting decay rate as employed in Fig. 1.

Corotis, Vanmarcke, and Cornell [6] have proposed a scheme to obtain more accurate approximations for α. The stationary envelope response $\hat{\alpha}$ is treated as a two state, continuous time, Markov process in which state 0 corresponds to $\hat{\alpha} < b$. The intervals T_0 and T_1 spent in states 0 and 1, respectively, are assumed to be independent random variables with exponential distributions. Using physical arguments to estimate the fraction of envelope-crossings that are immediately followed by a barrier-crossing yields

$$\alpha = 2\nu_b \left[\frac{1 - \exp\left(-\dfrac{n_b}{2\nu_b}\right)}{1 - \exp\left(-\dfrac{b^2}{2\sigma^2}\right)} \right] \tag{5}$$

where n_b is the average frequency of envelope up-crossings. As indicated in Fig. 1, the results of this method (C) are clearly more accurate than those of the Poisson process approximation (A), and the correct qualitative behavior of α with variation in barrier level is predicted. Vanmarcke [7] has improved on this estimate by accounting for the pattern of clustering of barrier crossings. However, it appears possible to achieve a still further improvement with little additional computational effort as outlined in the following section.

Formulation

It is widely agreed that the basic reason the Poisson process approximation for α breaks down for low barrier levels is that the crossings out of the safe region are, in fact, not statistically independent events. Since the envelope varies slowly, when a peak occurs above the threshold level, the probability is higher than usual that the next peak will also be above the threshold. Thus, barrier crossings tend to occur together in clumps [8]. For decreasing damping ratio or barrier level, the tendency toward clumping will increase. Therefore, if allowance were made for the clumping tendency, one might expect a more accurate estimate for α to result.

Let the clump size N_c be defined as the number of successive peaks that occur outside the safe region with no intervening peak inside this region. Since it is assumed that the response is quasi-harmonic, successive barrier crossings in a clump will be separated by an interval of approximately $1/2\nu_0$, where ν_0 is the natural period of the oscillator. Let T_1 be the clump duration and T_0 be the interval between the end of one clump and the beginning of the next clump. Then, assuming ergodicity, it may be shown that the expected number of up-crossings of the $+b$ level per unit time may be expressed as

$$2\nu_b = \frac{E[N_c]}{E[T_0 + T_1]}. \tag{6}$$

Assuming that T_0 is exponentially distributed leads to [9]

$$\alpha = \frac{\nu_b/\nu_0}{E[T_1]} \left(1 - \frac{\nu_b}{\nu_0}\right)^{-1}. \tag{7}$$

Hence, the problem has been reduced to the determination of $E[T_1]$.

Let the probability that T_1 is greater than t be denoted by $P_{T_1}(t)$. To determine the detailed structure of this probability would be very difficult. However, it is possible to surmise the qualitative behavior of $P_{T_1}(t)$ from physical considerations. Consider the conditional probability $\hat{P}(n+1|n)$ that a clump, which already contains n crossings, will continue for at least one more crossing. Then,

$$\hat{P}(n+1|n) \equiv Pr\left[T_1 > \frac{n+1}{2\nu_0} \,\middle|\, T_1 > \frac{n}{2\nu_0}\right] = \frac{P_{T_1}\left(\dfrac{n+1}{2\nu_0}\right)}{P_{T_1}\left(\dfrac{n}{2\nu_0}\right)}. \tag{8}$$

It may be shown that $\hat{P}(n+1|n)$ increases rapidly with n for n small. However, as n becomes large, one would expect $\hat{P}(n+1|n)$ to lose its dependence on n. Thus $\hat{P}(n+1|n)$ should approach a constant value as $n \to \infty$. Let this limiting value be denoted by P^*. Then,

$$P^* \equiv \lim_{n\to\infty} \hat{P}(n+1|n) = \lim_{n\to\infty} \frac{P_{T_1}\left(\dfrac{n+1}{2\nu_0}\right)}{P_{T_1}\left(\dfrac{n}{2\nu_0}\right)}. \tag{9}$$

The precise form of the probability density function $p_{T_1}(t)$ associated with $P_{T_1}(t)$ is now known. However, it is clear that a negative exponential relationship would provide the desired asymptotic behavior as $n \to \infty$ $(t \to \infty)$. The dependence of P on n for n small may be accounted for by introducing a time-dependent coefficient for the exponential distribution. Based on numerical studies [9] it has been found that P_{T_1} may be adequately approximated by

$$P_{T_1}(t) = \frac{1}{C} t^{\gamma} e^{-\beta t} \tag{10}$$

where C is a normalizing constant and γ and β are parameters. For narrow-band stationary response, a value of $\gamma = 1$ provides the best agreement with simulation data. When the response process is broad band, γ must be reduced to reflect the greater independence of barrier level crossings. The parameter β is determined by an examination of the stationary density of peaks occurring in a clump.

Stationary Response

Integrating equation (10) and substituting into equation (9) gives

$$P^* = \exp\left(\frac{-\beta}{2\nu_0}\right) \tag{11}$$

where γ has been set to one for the stationary response case.

$$E[T_1] = \frac{2}{\beta}. \tag{12}$$

Substituting from equations (11) and (12) into equation (7) then yields

$$\alpha = -\nu_b \left[1 - \exp\left(-\frac{b^2}{2\sigma^2}\right)\right]^{-1} ln(P^*). \tag{13}$$

P^* will be estimated by considering the response of the system for one-half cycle of oscillation after a peak greater than b has occurred.

Let $q(x_0 | x_1 \;; t) dx_1$ be the probability that a solution trajectory of (1) which starts at x_0 reaches the differential element of measure dx_1 centered at x_1 a time t later. This quantity is readily expressable as a function of the spectral density of the excitation and the natural frequency and damping at the system [10]. Suppose that the oscillator is at a peak during a clump in which k barrier crossings have already occurred and let $p_k(r)$ be the conditional probability density of such peaks, given that $r \geq b$. Due to the narrow-bandedness of the response, it will be assumed that any two successive peaks will be separated by an interval of π/ω_d, and that x changes sign during this interval. With this assumption, $p_{k+1}(r)$ may be expressed as

$$\begin{aligned} p_{k+1}(r) &= \lambda_k \int_b^\infty p_k(x) q(-x | r; \pi/\omega_d) dx; \qquad r \geq b \\ &= 0; \quad r < b. \end{aligned} \tag{14}$$

The factor λ_k is determined from the condition that the integrated probability density must be equal to one. Hence,

$$\frac{1}{\lambda_k} = \int_b^\infty \int_b^\infty p_k(x) q(-x | r; \pi/\omega_d) dx\, dr. \tag{15}$$

The quantity on the right of equation (15) will be recognized as the probability that the clump will continue for at least one more barrier crossing given that k crossings have already occurred. Hence, from equation (8) as $k \to \infty$, $1/\lambda_k \to P^*$, and $p_k(r)$ approaches a stationary density $p_\infty(r)$. This gives

$$P^* = \int_b^\infty \int_b^\infty p_\infty(x) q(-x | r; \pi/\omega_d) dx\, dr. \tag{16}$$

As formulated, $1/P^*$ is the eigenvalue of an integral equation for $p_\infty(x)$. Since this integral equation does not appear to be amenable to an exact analytical solution, an approximate solution will be sought. This approximate solution will be generated by assuming the form of the eigenfunction $p_\infty(x)$ and then calculating the resulting eigenvalue. This is recognized as the first step of a Picard iteration procedure. Successive iterations could be carried out to refine the estimate of the eigenvalue but this will not be undertaken in the present analysis.

The probability density of the stationary response of the system will be a Gaussian distribution. Although $p_\infty(x)$ will not be Gaussian distributed, it is reasonable to assume that it will have a similar shape especially for x substantially larger than b. Therefore, it is herein assumed that $p_\infty(x)$ may be approximated by the clipped Gaussian distribution

$$\begin{aligned} p_\infty(x) &= \frac{\sqrt{2}}{\sigma\sqrt{\pi}\,\mathrm{erfc}\left(\frac{b}{\sqrt{2}\sigma}\right)} \exp\left(-\frac{x^2}{2\sigma^2}\right); \qquad x \geq b \\ &= 0 \qquad\qquad ; \quad x < b. \end{aligned} \tag{17}$$

Substituting from equations (17) into equation (16) and using the known expression for $q(-x/r; \pi/\omega_d)$ yields

$$P^* = \int_b^\infty \frac{\exp\left(-\frac{r^2}{2\sigma^2}\right)}{\sigma\sqrt{2\pi}\,\mathrm{erfc}\left(\frac{b}{\sqrt{2}\sigma}\right)} \mathrm{erfc}\left[\frac{b - rc}{\sqrt{2}\sigma(1-c^2)^{1/2}}\right] dr \tag{18}$$

where

$$c = \exp\left(-\frac{\pi\zeta\omega_0}{\omega_d}\right) \tag{19}$$

The integral of equation (18) may be approximated analytically by assuming a trilinear representation for the complementary error function that matches the function exactly as its two asymptotes and at the point where the argument is equal to zero. This gives

$$P^* = \frac{1}{\mathrm{erfc}\left(\frac{b}{\sqrt{2}\sigma}\right)} \left\{ \frac{1}{2}\left[1 - \frac{\sqrt{2}b/\sigma}{\sqrt{\pi(1-c^2)}}\right] [\mathrm{erf}(y_1) - \mathrm{erf}(y_2)] + \frac{c}{\pi\sqrt{1-c^2}} (e^{-y_2^2} - e^{-y_1^2}) + \mathrm{erfc}(y_1) \right\} \tag{20}$$

where

$$y_1 = \frac{1}{c}\left[\frac{b}{\sqrt{2}\sigma} + \frac{1}{2}\sqrt{\pi(1-c^2)}\right]$$

$$y_2 = \max\left[\frac{b}{\sqrt{2}\sigma}, \frac{1}{c}\left(\frac{b}{\sqrt{2}\sigma} - \frac{1}{2}\sqrt{\pi(1-c^2)}\right)\right]. \tag{21}$$

In Figs. 2 and 3, the variations of $\alpha/2\nu_b$ with barrier level b/σ is displayed for two values of damping. for comparison, simulation results and the corresponding values from the Poisson approximation and Vanmarcke's improved two-state Markov process approximation [7] are also presented. The latter method was chosen for comparison because it involves computational effort comparable to that of the present approach. Although Mark's method [4] corresponds with simulation results more consistently than any of the approximations shown in Fig. 1, it has not been used for comparison since it involves considerably more computational effort than the methods compared.

It will be observed that the results of the present analysis are, for the most part, somewhat less conservative than the Vanmarcke estimate—especially for low damping and barrier

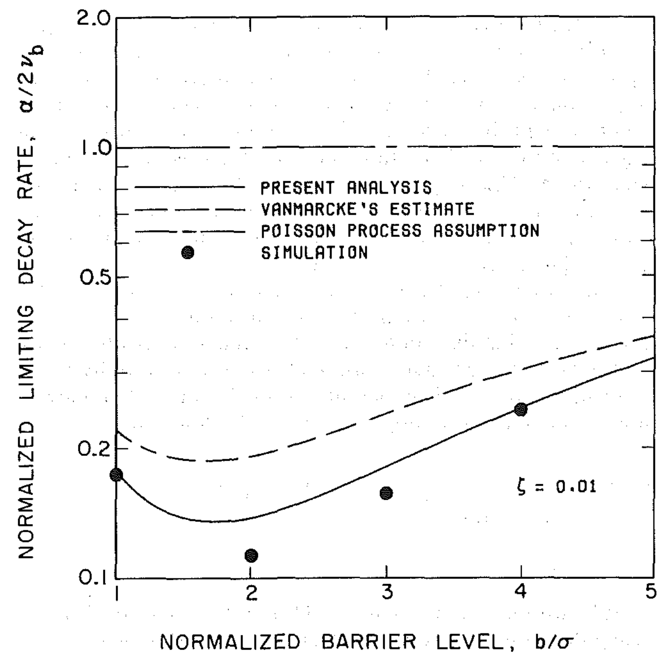

Fig. 2 Limiting decay rate versus barrier level, ζ = 0.01. Simulation results from reference [2].

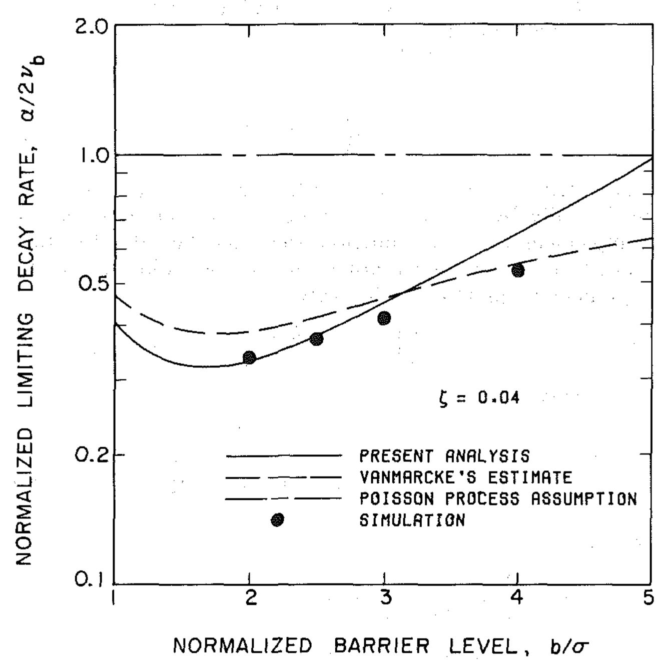

Fig. 3 Limiting decay rate versus barrier level, ζ = 0.04. Simulation results from reference [2].

levels. The present results appear to correspond well with simulation results for the damping levels shown.

Extension to Nonstationary Response

Using the results for stationary response, the nonstationary response problem may be treated approximately by applying the approach proposed by Corotis, et al. [6]. Let the differential equation of motion of the system be

$$\ddot{x}+2\zeta\omega_0\dot{x}+\omega_0{}^2x=\theta(t)\,w(t) \qquad x(0)=0, \quad \dot{x}(0)=0 \tag{22}$$

where $w(t)$ is a white noise process with spectral density S_0, and $\theta(t)$ is a modulating function. The Fourier transform of the autocorrelation of the excitation will then be $\theta^2(t)S_0$ which may be thought of as a time-dependent intensity or "spectral density."

In the analysis of the stationary response, it was assumed that the response was narrow-banded. This assumption will obviously be violated if the level of excitation changes rapidly relative to the response time constant $1/(\zeta\omega_0)$ of the system. One of the critical places where the narrow-bandedness assumption enters into the analysis is in the specification of the parameter γ in equation (10). When the level of excitation is such that it will sustain a stationary response variance σ_s which is substantially greater than the actual response variance σ, the response process will, in the short term, tend to be more nearly broad-banded in nature and the probability density p_{T_1} should reflect this trend by yielding higher probabilities for smaller values of t. One way that this can be accounted for is to allow the parameter γ to be a function that depends somehow on the degree of nonstationarity of the response. For excitation processes with monotonically increasing evelopes $\theta(t)$, it has been found by simulation studies that satisfactory results are obtained by using a probability density of the form

$$p_{T_1}(t)=\frac{1}{C}\,t^{\frac{\sigma^4(k)}{\sigma_s^4(t)}}\,e^{-\beta t} \tag{23}$$

where $\sigma(t)$ is the instantaneous variance of the response and $\sigma_s(t)$ is the stationary response variance associated with the instantaneous value of the excitation. Other assumptions could be made concerning the nature of γ. However, the form selected possesses the desired qualitative features to account for some of the effects of nonnarrow-bandedness and generates acceptable response results.

After modifying the form of $p_{T_1}(t)$, it is assumed that the probability density of the response may be approximated by a stationary density over one period of the system. It is further assumed that the first barrier crossing during a period of the system will occur with approximately the same frequency as if the response were truly stationary. Making these assumptions an expression for the instantaneous first crossing rate $\alpha(t)$ may be derived in a fashion entirely analogous to the derivation of the limiting decay rate given by equation (13). For the nonstationary case, this expression takes the form

$$\alpha(t)=\frac{-2\nu_b(t)\,ln[P^*(t)]}{[1+\sigma^4(t)/\sigma_s^4(t)][1-\nu_b(t)/\nu_0]} \tag{24}$$

As in the stationary case, ν_b is given by

$$\nu_b(t)=\int_0^\infty \dot{x}p(b,\dot{x},t)\,d\dot{x}. \tag{25}$$

Using the quasi-stationary assumption to specify $p(x,\dot{x},t)$ and integrating gives

$$\nu_b(t)=\frac{\sqrt{\mathrm{Det}(Q)}}{\pi q_{11}}\left[\exp\left(-\frac{1}{2}\phi_{11}b^2\right)\right.$$
$$\left.-b\phi_{12}\sqrt{\frac{\pi}{2\phi_{22}}}\exp\left(-\frac{1}{2}\frac{b^2}{q_{11}}\right)\mathrm{erfc}\left(\frac{b\phi_{12}}{\sqrt{2\phi_{22}}}\right)\right] \tag{26}$$

where

$$\Phi(t)=[\phi_{ij}(t)]=Q^{-1}(t) \tag{27}$$

and Q is the covariance matrix of the joint probability density of x and $\dot{x}$ at time t.

The procedure to obtain $P^*(t)$ is similar to that followed to determine the corresponding quantity P^* for the stationary case. However, the excitation intensity is now $\theta^2(t)S_0$. With $\nu_b(t)$ and $P^*(t)$ thus specified, equation (21) may be used to obtain approximate first passage probability for nonstationary response.

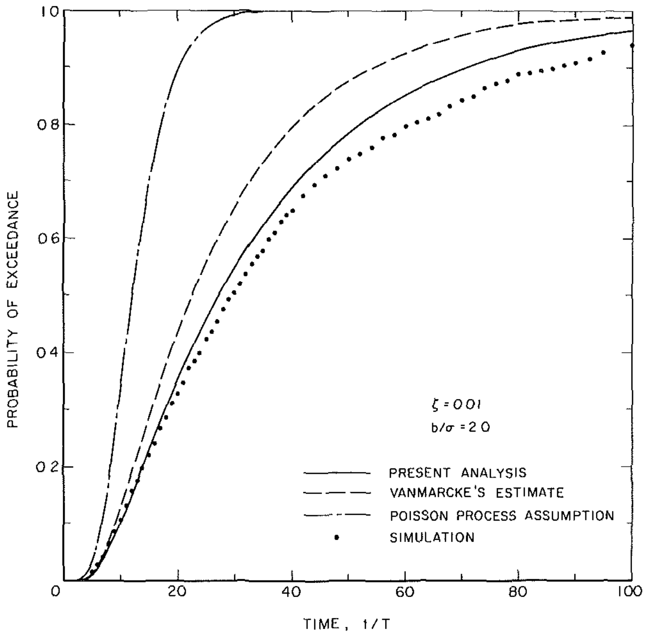

Fig. 4 Probability of exceedance versus time, ζ = 0.01, b/σ = 2.0

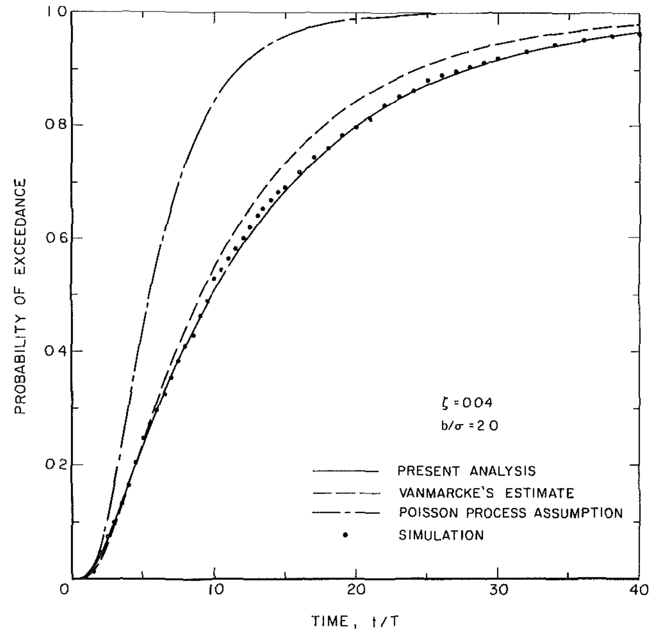

Fig. 6 Probability of exceedance versus time, ζ = 0.04, b/σ = 2.0

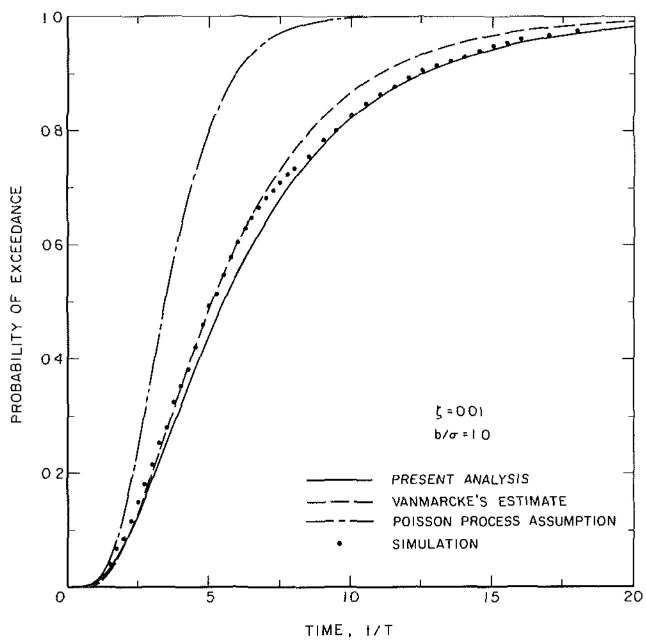

Fig. 5 Probability of exceedance versus time, ζ = 0.01, b/σ = 1.0

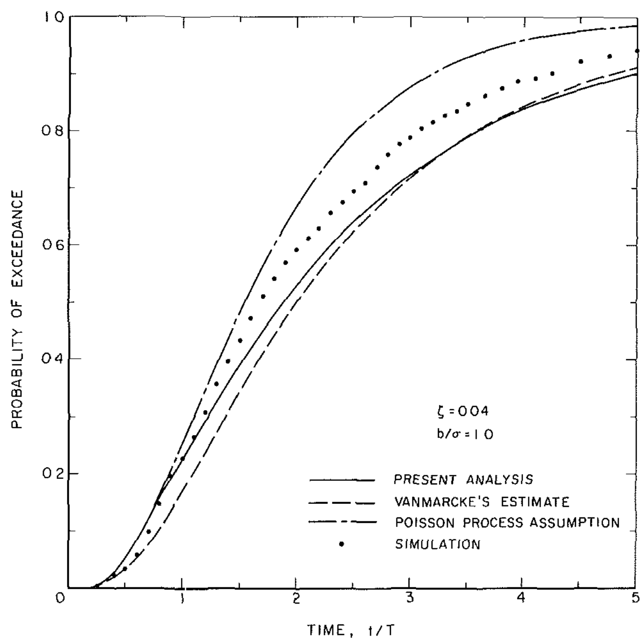

Fig. 7 Probability of exceedance versus time, ζ = 0.04, b/σ = 1.0

From the definition of the first passage probabilty $W(t)$ and the fact that $W(0) = 1$, it is seen that

$$W(t) = \exp\left[-\int_0^t \alpha(s)\,ds\right]. \tag{28}$$

Hence, the first passage probability density $p_c(t)$ will be

$$p_c(t) = \alpha(t)\exp\left[-\int_0^t \alpha(s)\,ds\right]. \tag{29}$$

Numerical Example

To obtain an indication of the accuracy of the approximate nonstationary solution, consider the special case of an oscillator subjected to a suddenly applied white noise. That is,

$$\theta(t) = 1; \quad \forall\, t \geq 0 \tag{30}$$

Figures 4–7 show the first passage probability as a function of t/T where T is the undamped natural oscillator period. The integration in equation (28) is performed numerically for this study. Also displayed are the approximations resulting from the Poisson process assumption and Vanmarcke's method. For comparison, simulation results obtained from ensembles of 1000 times histories are also shown.

As a general observation, it will be seen that the present analysis gives a reasonably good estimate of the probability of exceedance over the range of parameters considered. As might be anticipated, the poorest results are obtained when the probability is a rapidly varying function of t/T. In this case, the effects of broad-bandedness and nonstationarity are strong and the assumptions of the analysis are stretched to their limits. If the modification of $p_{T_1}(t)$ for broad-bandedness according to equation (23) is not made, the transient results for cases of low barrier level are particularly poor even though the limiting decay rates are quite reasonable. It is quite possible that alternative assumptions on the form of $p_{T_1}(t)$ might yield results that are even more accurate than those presented herein.

Except for the case $\zeta = 0.04$, $b/\sigma = 1.0$ the results of the present analysis represent a substantial improvement over the Poisson process assumption. In the early stages of the response when the process is broad-banded, the Poisson process assumption is fairly accurate. However, as the process becomes more nearly narrow-banded, this approach considerably overestimates the probability of exceedance as anticipated. Only when the probability of exceedance is a very strong function of t/T as in the case of $\zeta = 0.04$, $b/\sigma = 1.0$ does the Poisson process provide a somewhat reasonable estimate of the response. In this latter case, both the present approach and Vanmarcke's approach underestimate the probability of exceedance over most of the range of t/T.

In most cases, the accuracy of the present approach is comparable to that of the Vanmarcke estimate. The only case where the two approaches give substantially different results is for $\zeta = 0.01$, $b/\sigma = 2.0$ where the present approach gives an improved estimate.

Finally, it may be noted that the accuracy of the present approach appears to be quite uniform as a function of ζ, b/σ and t/T. The range of parameters considered is not exhaustive but the results presented are felt to be representative of general trends that may be expected for other parameters values.

Acknowledgments

The authors acknowledge the assistance of Shawn A. Hall in carrying out the computations to obtain the nonstationary simulation results presented herein. This investigation was supported in part by a grant from the National Science Foundation. Any opinions, findings, and conclusions are those of the authors and do not necessarily reflect the views of the National Science Foundation.

References

1 Crandall, S. H., "First Crossing Probabilities of the Linear Oscillator," *J. Sound Vib.*, Vol. 12, 1970, pp. 285–299.

2 Crandall, S. H., Chadiramani, K. L., and Cook, R. G., "Some First Passage Problems in Random Vibration," ASME Journal of Applied Mechanics, Vol. 33, 1966, pp. 532–538.

3 Wang, M. C., and Uhlenbeck, G. E., "On the Theory of Brownian Motion II," in: *Selected Papers on Noise and Stochastic Processes*, Wax, N., ed., Dover, New York, 1954.

4 Mark, W. D., "On False Alarm Probabilities of Filtered Noise," *Proc. IEEE*, Vol. 54, 1966, p. 316.

5 Rice, S. O., "Mathematical Analysis of Random Noise," in: *Selected Papers on Noise and Stochastic Processes*, Wax, N., ed., Dover, New York, 1954.

6 Corotis, R. B., Vanmarcke, E. H., and Cornell, C. A., "Power Spectra and First Passage of Nonstationary Processes," *J. Engr. Mech. Div.*, Vol. 98, No. EM2, Trans ASCE, 1972, pp. 401–414.

7 Vanmarcke, E. H., "On the Distribution of the First Passage Time for Normal Stationary Random Processes," ASME Journal of Applied Mechanics, Vol. 42, 1975, pp. 215–220.

8 Stratonovich, R. L., *Topics in the Theory of Random Noise*, Volume II, Gordon & Breach, New York, 1967, pp. 7–20.

9 Mason, A. B., Jr., "Some Observations on the Random Response of Linear and Nonlinear Dynamical Ssytems," Ph.D. Thesis, California Institute of Technology, Pasadena, Calif., 1979.

10 Caughey, T. K., and Stumpf, H. J., "Transient Response of a Dynamic System Under Random Excitation," ASME Journal of Applied Mechanics, Vol. 28, 1961, pp. 563–566.

T. R. Kane
Professor of Applied Mechanics,
Stanford University,
Stanford, Calif. 94305
Fellow ASME

A. K. Banerjee
Research Specialist,
Lockheed Missiles and Space Company,
Sunnyvale, Calif.

A Conservation Theorem for Simple Nonholonomic Systems

When the Hamiltonian of a **holonomic** *system is free of explicit time dependence it remains constant throughout all motions of the system. In this paper, it is shown how, given a homogeneous simple* **nonholonomic** *system S, one can form a function E that remains constant throughout all motions of S, providing the forces acting on S fulfill certain requirements. An illustrative example is examined in detail.*

1 Introduction

It is a well known and most useful fact that the Hamiltonian H of a holonomic system S possessing n degrees of freedom in a Newtonian reference frame N furnishes an integral of the equations of motion of S when the time t does not appear explicitly in H. It is the purpose of this paper to establish the validity of an analogous proposition applicable to homogeneous simple nonholonomic systems.

To set the stage for the general discussion that follows, equations of motion for a specific nonholonomic system are written and a first integral of these equations is set forth in Section 2. Next, a conservation theorem is stated and proved in Section 3. An explicit procedure for constructing a first integral based on this theorem is then set forth in Section 4. Finally, in Section 5, the procedure of Section 4 is applied to the system considered in Section 2.

2 Example

Figure 1 shows a system S formed by two particles, A and B, and a rigid rod, C, which connects A and B and has a length L. Particle A has a mass α, B a mass β, and C a mass that is negligible in comparison with α and β. S is free to move in a vertical plane containing the axes x_1 and x_2, and a force having components of magnitudes $|P|$ and $|Q|$ is applied to A, while a force of magnitude $|R|$ acts on B, the various forces being directed as shown in Fig. 1. (S may be regarded as an idealized representation of a rocket.)

Letting k be a constant, $\mathbf{p}$ the position vector from 0 to A, and $\mathbf{n}_1'$ and $\mathbf{n}_2'$ unit vectors directed as shown in Fig. 1, suppose that P and Q are specified as

$$P=k, \quad Q=-\frac{k}{L}\mathbf{p}\cdot\mathbf{n}_2' \tag{1}$$

while R takes on whatever values are necessary to keep the velocity vector of B parallel to $\mathbf{n}_1'$ at all times. Then, if q_1, q_2, and q_3 measure two distances and an angle as indicated in Fig. 1, Q can be expressed as

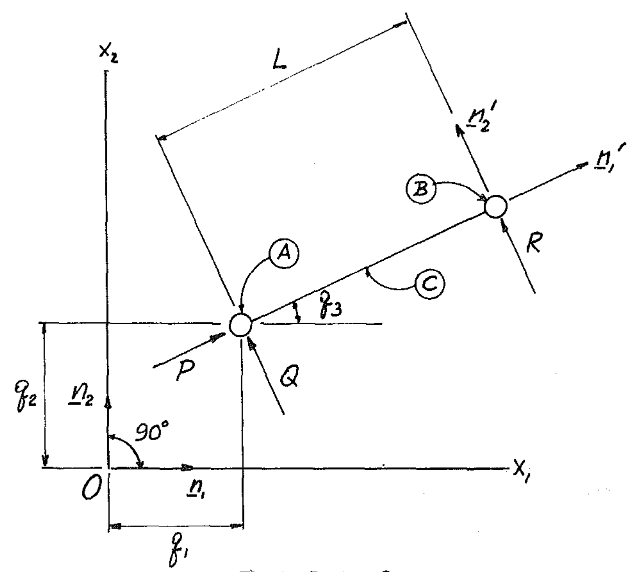

Fig. 1 System S

$$Q=\frac{k}{L}(q_1s_3-q_2c_3) \tag{2}$$

where s_3 and c_3 stand for sin q_3 and cos q_3, respectively, and the requirement that the velocity of B must be kept parallel to $\mathbf{n}_1'$ leads to the differential constraint equation

$$\dot{q}_3=(s_3\dot{q}_1-c_3\dot{q}_2)/L \tag{3}$$

where dots denote time differentiation. Two additional differential equations governing q_1, q_2, and q_3, formulated with the aid of Newton's Second Law, can be written

$$\ddot{q}_1c_3+(\ddot{q}_2+g)s_3-\beta L\dot{q}_3^2/(\alpha+\beta)=P/(\alpha+\beta) \tag{4}$$

and

$$\ddot{q}_1s_3-(\ddot{q}_2+g)c_3=-Q/\alpha \tag{5}$$

where g is the local gravitational acceleration; and, while not needed in the sequel, a third differential equation, based on the angular momentum principle, can be used in conjunction with equation (3) to show that

Contributed by the Applied Mechanics Division for publication in the Journal of Applied Mechanics.

Discussion on this paper should be addressed to the Editorial Department, ASME, United Engineering Center, 345 East 47th Street, New York, N.Y. 10017, and will be accepted until two months after final publication of the paper itself in the Journal of Applied Mechanics. Manuscript received by ASME Applied Mechanics Division, February, 1983.

$$R = \beta[\dot{q}_3(c_3\dot{q}_1 + s_3\dot{q}_2) + gc_3] \quad (6)$$

which is of interest because it is an explicit statement of the feedback control law associated with equation (3). [If A and B are supported by a horizontal plane on which A can slide freely, whereas B is prevented from moving perpendicularly to C because a sharp-edged knife blade is embedded in B (but B can move freely in the direction of C), then equation (3) applies and, with g set equal to zero, equation (6) describes the force exerted on B by the supporting plane.]

If E is defined as

$$E \triangleq [(\alpha+\beta)(\dot{q}_1^2 + \dot{q}_2^2) - \beta(L\dot{q}_3)^2]/2 - k(q_1c_3 + q_2s_3) + g[(\alpha+\beta)q_2 + \beta Ls_3] \quad (7)$$

then the equation

$$E = E_0, \quad \text{a constant} \quad (8)$$

is a first integral of equations (3), (4), and (5); that is, q_1, q_2, q_3 satisfy equation (8) whenever they satisfy equations (3), (4), and (5) [with k in place of P in equation (4) and $k(q_1s_3 - q_2c_3)/L$ in place of Q in equation (5)]. To verify this, start by differentiating equation (7) with respect to t, which yields

$$\dot{E} = (\alpha+\beta)(\dot{q}_1\ddot{q}_1 + \dot{q}_2\ddot{q}_2) - \beta L^2\dot{q}_3\ddot{q}_3 - k[\dot{q}_1c_3 + \dot{q}_2s_3 - \dot{q}_3(q_1s_3 - q_2c_3)] + g[(\alpha+\beta)\dot{q}_2 + \beta L\dot{q}_3c_3] \quad (9)$$

Next, solve equations (4) and (5) for $\ddot{q}_1$ and $\ddot{q}_2$, obtaining

$$\ddot{q}_1 = -\frac{Q}{\alpha}s_3 + \frac{P + \beta L\dot{q}_3^2}{\alpha+\beta}c_3 \quad (10)$$

and

$$\ddot{q}_2 = \frac{Q}{\alpha}c_3 + \frac{P + \beta L\dot{q}_3^2}{\alpha+\beta}s_3 - g \quad (11)$$

and differentiate equation (3) with respect to t, thus showing that

$$\ddot{q}_3 = [\dot{q}_3(c_3\dot{q}_1 + s_3\dot{q}_2) - (\ddot{q}_2c_3 - \ddot{q}_1s_3)]/L \quad (12)$$

or, in view of equation (5), that

$$L\ddot{q}_3 = \dot{q}_3(c_3\dot{q}_1 + s_3\dot{q}_2) + gc_3 - Q/\alpha \quad (13)$$

Substitution from equations (10), (11), and (13) into equation (9) in order to eliminate all second derivatives then yields

$$\dot{E} = P(c_3\dot{q}_1 + s_3\dot{q}_2) + (Q/\alpha)[(\alpha+\beta)(c_3\dot{q}_2 - s_3\dot{q}_1) + \beta L\dot{q}_3] - k[\dot{q}_1c_3 + \dot{q}_2s_3 - \dot{q}_3(q_1s_3 - q_2c_3)] \quad (14)$$

which, upon elimination of $\dot{q}_3$ with the aid of equation (3), is seen to imply

$$\dot{E} = [Pc_3 - Qs_3 - kc_3 + \frac{k}{L}s_3(q_1s_3 - q_2c_3)]\dot{q}_1 + [Ps_3 + Qc_3 - ks_3 - \frac{k}{L}c_3(q_1s_3 - q_2c_3)]\dot{q}_2 \quad (15)$$

Finally, use of equations (1) and (2) to eliminate P and Q from the last equation leads to the conclusion that the coefficients of $\dot{q}_1$ and $\dot{q}_2$ are identically equal to zero, which means that $\dot{E} = 0$ and that, therefore, equation (8) is, indeed, an integral of equations (3)–(5). However, this does not answer the following rather natural question: Where did E originate? Or, to put it another way, how is E as defined in equation (7) related to the gravitational forces and the forces P, Q, and R acting on S?

It is easy to see [by taking equation (3) into account] that $[(\alpha+\beta)(\dot{q}_1^2 + \dot{q}_2^2) - \beta(L\dot{q}_3)^2]/2$ is the kinetic energy of S. Similarly, after $g[(\alpha+\beta)q_2 + \beta Ls_3]$ has been rewritten as $(\alpha+\beta)gh$, where h is the distance from the mass center of S to line x_1, this term of equation (7) is seen to have a form familiar in connection with energy considerations. But to explain the origin of the middle term in equation (7) we must first undertake a general discussion of the relationship between forces, generalized speeds, and a certain function V of the generalized coordinates used to characterize the configuration of a system.

3 Theorem

Consider a set S of ν particles $P_1, \ldots, P_\nu$ whose permissible configurations in a Newtonian reference frame N can be characterized by n generalized coordinates $q_1, \ldots, q_n$ and which is subject to motion constraints such that the m equations

$$\dot{q}_s = \sum_{r=1}^{p}(Z_{sr}\dot{q}_r) \quad (s = p+1, \ldots, n) \quad (16)$$

are satisfied throughout every motion of S in N. Here p, defined as $p \triangleq n - m$, denotes the number of degrees of freedom of S in N; Z_{sr} $(r = 1, \ldots, p;\ s = p+1, \ldots, n)$ are explicit functions of $q_1, \ldots, q_n$, and, possibly, the time t. Under these circumstances, S is called a *homogeneous simple nonholonomic system*.

Let $F_1, \ldots, F_p$ denote the nonholonomic generalized active forces [1] associated with $\dot{q}_1, \ldots, \dot{q}_p$, respectively; let V be any function of $q_1, \ldots, q_n$ that satisfies the equations

$$\frac{\partial V}{\partial q_r} + \sum_{s=p+1}^{n}\frac{\partial V}{\partial q_s}Z_{sr} = -F_r \quad (r = 1, \ldots, p) \quad (17)$$

Finally, define E as

$$E \triangleq \sum_{r=1}^{n}\left(\frac{\partial K}{\partial \dot{q}_r}\dot{q}_r\right) - K + V \quad (18)$$

where K, the kinetic energy of S in N, is presumed to be expressible as a function of $q_1, \ldots, q_n$ and $\dot{q}_1, \ldots, \dot{q}_n$, but not explicitly of t. Then E remains constant throughout every motion of S in N that satisfies equations (16) and the dynamical equations (see [1]; p. 177)

$$F_r + F_r^* = 0 \quad (r = 1, \ldots, p) \quad (19)$$

where $F_1^*, \ldots, F_p^*$ are the nonholonomic generalized inertia forces (see [1], p. 89) associated with $\dot{q}_1, \ldots, \dot{q}_p$, respectively.

The *proof* of this theorem hinges on a proposition established by Passerello and Huston [2], namely that $F_r^*(r = 1, \ldots, p)$ can be expressed as

$$F_r^* = \frac{\partial K}{\partial q_r} - \frac{d}{dt}\frac{\partial K}{\partial \dot{q}_r} + \sum_{s=p+1}^{n}\left(\frac{\partial K}{\partial q_s} - \frac{d}{dt}\frac{\partial K}{\partial \dot{q}_s}\right)Z_{sr} \quad (r = 1, \ldots, p) \quad (20)$$

For substitution of F_r from equations (17) and F_r^* from equations (20) into equations (19) yields

$$\frac{d}{dt}\frac{\partial K}{\partial \dot{q}_r} - \frac{\partial K}{\partial q_r} + \frac{\partial V}{\partial q_r} + \sum_{s=p+1}^{n}\left(\frac{d}{dt}\frac{\partial K}{\partial \dot{q}_s} - \frac{\partial K}{\partial q_s} + \frac{\partial V}{\partial q_s}\right)Z_{sr} = 0 \quad (r = 1, \ldots, p) \quad (21)$$

and, as will be shown presently, the first time-derivative of E as defined in equation (18) is given by

$$\dot{E} = \sum_{r=1}^{p}\left[\frac{d}{dt}\frac{\partial K}{\partial \dot{q}_r} - \frac{\partial K}{\partial q_r} + \frac{\partial V}{\partial q_r} + \sum_{s=p+1}^{n}\left(\frac{d}{dt}\frac{\partial K}{\partial \dot{q}_s} - \frac{\partial K}{\partial q_s} + \frac{\partial V}{\partial q_s}\right)Z_{sr}\right]\dot{q}_r \quad (22)$$

so that, substituting from equations (21) into equation (22), one finds that $\dot{E}=0$, which means that E is a constant.

To establish the validity of equation (22), it is helpful, first, to rewrite equation (18) with the aid of equations (16) as

$$E=\sum_{r=1}^{p}\left(\frac{\partial K}{\partial \dot{q}_r}\dot{q}_r\right)+\sum_{s=p+1}^{n}\left[\frac{\partial K}{\partial \dot{q}_s}\sum_{r=1}^{p}(Z_{sr}\dot{q}_r)\right]-K+V \tag{23}$$

Differentiation of this equation with respect to t gives

$$\begin{aligned}\dot{E}=&\sum_{r=1}^{p}\left[\left(\frac{d}{dt}\frac{\partial K}{\partial \dot{q}_r}\right)\dot{q}_r+\frac{\partial K}{\partial \dot{q}_r}\ddot{q}_r\right]\\&+\sum_{s=p+1}^{n}\left[\left(\frac{d}{dt}\frac{\partial K}{\partial \dot{q}_s}\right)\sum_{r=1}^{p}(Z_{sr}\dot{q}_r)\right.\\&\left.+\frac{\partial K}{\partial \dot{q}_s}\sum_{r=1}^{p}(\dot{Z}_{sr}\dot{q}_r+Z_{sr}\ddot{q}_r)\right]-\dot{K}+\dot{V}\end{aligned} \tag{24}$$

Now,

$$\begin{aligned}\dot{K}=&\sum_{r=1}^{n}\left(\frac{\partial K}{\partial q_r}\dot{q}_r+\frac{\partial K}{\partial \dot{q}_r}\ddot{q}_r\right)=\sum_{r=1}^{p}\left(\frac{\partial K}{\partial q_r}\dot{q}_r+\frac{\partial K}{\partial \dot{q}_r}\ddot{q}_r\right)\\&+\sum_{s=p+1}^{n}\left(\frac{\partial K}{\partial q_s}\dot{q}_s+\frac{\partial K}{\partial \dot{q}_s}\ddot{q}_s\right)\end{aligned} \tag{25}$$

so that, making use of equations (16), one can write

$$\begin{aligned}\dot{K}=&\sum_{r=1}^{p}\left(\frac{\partial K}{\partial q_r}\dot{q}_r+\frac{\partial K}{\partial \dot{q}_r}\ddot{q}_r\right)+\sum_{s=p+1}^{n}\left[\frac{\partial K}{\partial q_s}\sum_{r=1}^{p}(Z_{sr}\dot{q}_r)\right.\\&\left.+\frac{\partial K}{\partial \dot{q}_s}\sum_{r=1}^{p}(\dot{Z}_{sr}\dot{q}_r+Z_{sr}\ddot{q}_r)\right]\end{aligned} \tag{26}$$

Similarly, $\dot{V}$ can be expressed as

$$\dot{V}=\sum_{r=1}^{p}\left(\frac{\partial V}{\partial q_r}\dot{q}_r\right)+\sum_{s=p+1}^{n}\left[\frac{\partial V}{\partial q_s}\sum_{r=1}^{p}(Z_{sr}\dot{q}_r)\right] \tag{27}$$

Substitution from equations (26) and (27) into equation (24), and subsequent interchanging of the order in which double summations are performed, leads to equation (22), and thus concludes the proof.

It is worth pointing out that the theorem under consideration may be regarded as a generalization of a familiar one applicable to holonomic systems. If S is not subject to constraints represented by equations (16), one can set Z_{sr} $(r=1,\ldots,p;\,s=p+1,\ldots,n)$ equal to zero in equations (17); V then reduces to the potential energy of S in N, and E as defined in equation (18) becomes the Hamiltonian of S in N.

Finally, it is at times helpful to recall the fact that, if K is a homogeneous quadratic function of $\dot{q}_1,\ldots,\dot{q}_n$, then equation (18) can be replaced with

$$E=K+V \tag{28}$$

(This is true both when S is a homogeneous simple nonholonomic system and when S is holonomic.)

4 Procedure

Having established in the preceding section that one can write an integral of the constraint equations, equations (16), and the dynamical equations, equations (19), namely, $E=E_0$, where E is given by equation (18), provided one can find a function V of $q_1,\ldots,q_n$ that satisfies equations (17), we shall now show how to either find V or prove its nonexistence. To these ends, one may take the seven steps that follow.

Step 1. Introduce m quantities f_{s-p} $(s=p+1,\ldots,n)$ as

$$f_{s-p}\triangleq\frac{\partial V}{\partial q_s}\quad(s=p+1,\ldots,n) \tag{29}$$

and regard f_{s-p} as a function of $q_1,\ldots,q_n$ except when for some value of r in equations (17), say $r=i$, F_i is a function of only q_i and, in addition,

$$\frac{\partial V}{\partial q_i}=-F_i \tag{30}$$

In that event, let f_{s-p} $(s=p+1,\ldots,n)$ be free of q_i. [Unless this is done, equations (29) and (30) lead to conflicting expressions for the second partial derivatives of V with respect to q_s and q_i.]

Step 2. Use equations (29) to eliminate $\partial V/\partial q_s$ $(s=p+1,\ldots,n)$ from equations (17) to obtain

$$\frac{\partial V}{\partial q_s}=-\sum_{r=p+1}^{n}Z_{rs}f_{r-p}-F_s\quad(s=1,\ldots,p) \tag{31}$$

Step 3. Write $n(n-1)/2$ linear algebraic equations in the mn quantities $\partial f_i/\partial q_j$ $(i=1,\ldots,m;\ j=1,\ldots,n)$ by substituting from equations (29) and (31) into

$$\frac{\partial}{\partial q_j}\left(\frac{\partial V}{\partial q_i}\right)=\frac{\partial}{\partial q_i}\left(\frac{\partial V}{\partial q_j}\right)\quad(i,j=1,\ldots,n;i\neq j) \tag{32}$$

Step 4. Identify an $n(n-1)/2$ by mn matrix $[W]$ and an $n(n-1)/2$ by 1 matrix $\{Y\}$ such that the set of equations written in Step 3 is equivalent to the matrix equation $[W]\{X\}=\{Y\}$, where $\{X\}$ is an mn by 1 matrix having $\partial f_i/\partial q_j$ $(i=1,\ldots,m;\ j=1,\ldots,n)$ as elements.

Step 5. Determine the rank ρ of $[W]$; select arbitrarily any ρ rows of $[W]$, hereafter called the independent rows of $[W]$, and express each of the remaining rows, hereafter called the dependent rows, as a weighted, linear combination of the ρ independent rows; and determine the weighting factors by equating corresponding elements of the matrices in the resulting equations.

Step 6. Express each element of $\{Y\}$ corresponding to a dependent row of $[W]$ as a weighted, linear combination of the ρ elements of $\{Y\}$ corresponding to the independent rows of $[W]$, using the weighting factors found in Step 5, and solve the resulting equations for f_i $(i=1,\ldots,m)$. If this cannot be done uniquely, or if one or more of $f_1,\ldots f_m$ turns out to be a function of a generalized coordinate of which it should be free (see Step 1), then V does not exist.

Step 7. Substitute the functions $f_1,\ldots,f_m$ into equations (29) and (31), thus obtaining $\partial V/\partial q_r$ $(r=1,\ldots,n)$ as explicit functions of $q_1,\ldots,q_n$, and determine V by performing the quadratures indicated in the equation

$$\begin{aligned}V=&\int_0^{q_1}\frac{\partial V}{\partial q_1}(\zeta,0,\ldots,0)d\zeta\\&+\int_0^{q_2}\frac{\partial V}{\partial q_2}(q_1,\zeta,0,\ldots,0)d\zeta\\&+\ldots+\int_0^{q_n}\frac{\partial V}{\partial q_n}(q_1,\ldots,q_{n-1},\zeta)d\zeta\end{aligned} \tag{33}$$

Steps 5 and 6 cannot be taken as indicated when ρ as found in Step 5 is equal to $n(n-1)/2$. In that event, V exists only if $m=(n-1)/2$. [A well-known case in point is that of the rolling disk, for which the set of equations formed in Step 3 is homogeneous in the quantities $\partial f_i/\partial q_j$ $(i=1,\ldots,m;\ j=1,\ldots,n)$; in other words, all of these derivatives are equal to zero. Consequently, $f_1,\ldots f_m$ are constants.] Under these circumstances, one can proceed directly to Step 7.

The rationale underlying the procedure just set forth is the following. Step 1 is taken in recognition of the fact that equations (17) form a set of p equations in the n quantities $\partial V/\partial q_i$ $(i=1, \ldots, n)$, so that m additional relationships are required for the determination of all of these derivatives. In Step 2, the construction of a set of equations uncoupled in the partial derivatives $\partial V/\partial q_r$ $(r=1, \ldots, n)$ is brought to completion. Step 3 consists of imposing requirements that must be satisfied in order that V possess continuous first partial derivatives. Steps 4, 5, and 6 allow one to determine f_i $(i=1, \ldots, m)$ by making use of the fact [3] that the matrix equation $[W]\{X\}=\{Y\}$ can be solved for $\{X\}$ if and only if the rank of $[W]$ is equal to that of the matrix $[[W]|\{Y\}]$. Finally, in Step 7, the procedure employed by Schultz [4] to construct Liapunov functions is employed to find V.

5 Application

At the end of Section 2, the origin of the middle term in equation (7) was left unexplained. We shall now show that this term emerges when one implements the procedure of Section 4.

The system S considered in Section 2 possesses three generalized coordinates and is subject to one motion constraint expressed by an equation having the form of equations (16), namely, equation (3). Hence, $n=3$, $m=1$, and $p=2$. Consequently, one must form Z_{sr} and F_r for $r=1, 2$ and $s=3$ in preparation for applying the procedure of Section 4.

The quantities Z_{31} and Z_{32}, found by comparing equation (3) with equations (16) are given by

$$Z_{31}=s_3/L, \quad Z_{32}=-c_3/L \tag{34}$$

To determine the generalized active forces F_1 and F_2, one needs the nonholonomic partial velocities $\mathbf{v}_r^A$ and $\mathbf{v}_r^B$ $(r=1,2)$ of A and B, which are, by definition, the coefficients of $\dot{q}_r\,(r=1,2)$ in expressions for the velocities, $\mathbf{v}^A$ and $\mathbf{v}^B$, of A and B in N. Now, if $\mathbf{n}_1$, $\mathbf{n}_2$, $\mathbf{n}_1'$, and $\mathbf{n}_2'$ are unit vectors directed as shown in Fig. 1, then

$$\mathbf{v}^A=\dot{q}_1\mathbf{n}_1+\dot{q}_2\mathbf{n}_2 \tag{35}$$

and

$$\mathbf{v}^B=\mathbf{v}^A+L\dot{q}_3\mathbf{n}_2' \tag{36}$$

or, after $\dot{q}_3$ has been eliminated by reference to equation (3),

$$\mathbf{v}^B=(\mathbf{n}_1+s_3\mathbf{n}_2')\dot{q}_1+(\mathbf{n}_2-c_3\mathbf{n}_2')\dot{q}_2 \tag{37}$$

Hence, from equation (35), the nonholonomic partial velocities of A are

$$\mathbf{v}_1^A=\mathbf{n}_1, \quad \mathbf{v}_2^A=\mathbf{n}_2 \tag{38}$$

while, from equation (37), those of B are

$$\mathbf{v}_1^B=\mathbf{n}_1+s_3\mathbf{n}_2', \quad \mathbf{v}_2^B=\mathbf{n}_2-c_3\mathbf{n}_2' \tag{39}$$

In addition to partial velocities, expressions for $\mathbf{F}_A$ and $\mathbf{F}_B$, the external forces acting on A and B, respectively, are required for the formation of the generalized active forces F_1 and F_2. From Fig. 1,

$$\mathbf{F}_A=P\mathbf{n}_1'+Q\mathbf{n}_2'-g\alpha\mathbf{n}_2, \quad \mathbf{F}_B=R\mathbf{n}_2'-g\beta\mathbf{n}_2 \tag{40}$$

Consequently, F_1 and F_2, found by substituting from equations (38)-(40) into

$$F_r=\mathbf{v}_r^A\cdot\mathbf{F}_A+\mathbf{v}_r^B\cdot\mathbf{F}_B \quad (r=1,2) \tag{41}$$

are given by

$$F_1=\mathbf{n}_1\cdot(P\mathbf{n}_1'+Q\mathbf{n}_2'-g\alpha\mathbf{n}_2)+(\mathbf{n}_1+s_3\mathbf{n}_2')\cdot(R\mathbf{n}_2'-g\beta\mathbf{n}_2)=Pc_3-(Q+g\beta c_3)s_3 \tag{42}$$

and

$$F_2=\mathbf{n}_2\cdot(P\mathbf{n}_1'+Q\mathbf{n}_2'-g\alpha\mathbf{n}_2)+(\mathbf{n}_2-c_3\mathbf{n}_2')\cdot(R\mathbf{n}_2'-g\beta\mathbf{n}_2)=(P-g\beta s_3)s_3+Qc_3-g\alpha \tag{43}$$

or, after Q and P have been eliminated with the aid of equations (1) and (2),

$$F_1=k\left[c_3-\frac{s_3}{L}(q_1s_3-q_2c_3)\right]-g\beta s_3c_3 \tag{44}$$

and

$$F_2=k\left[s_3+\frac{c_3}{L}(q_1s_3-q_2c_3)\right]-g(\alpha+\beta s_3^2) \tag{45}$$

Since K, the kinetic energy of S, is a homogeneous quadratic function of $\dot{q}_1$, $\dot{q}_2$, and $\dot{q}_3$, substitution from equations (34), (44), and (45) into equations (17) leads to the conclusion that $K+V$ furnishes an integral of equations (3)-(5) when P and Q are given by equations (1) and (2), provided that V be a function of q_1, q_2, and q_3 that satisfies the two equations

$$\frac{\partial V}{\partial q_1}+\frac{\partial V}{\partial q_3}\frac{s_3}{L}=-k\left[c_3-\frac{s_3}{L}(q_1s_3-q_2c_3)\right]+g\beta s_3c_3 \tag{46}$$

$$\frac{\partial V}{\partial q_2}-\frac{\partial V}{\partial q_3}\frac{c_3}{L}=-k\left[s_3+\frac{c_3}{L}(q_1s_3-q_2c_3)\right]+g(\alpha+\beta s_3^2) \tag{47}$$

All of the information required to implement the procedure of Section 4 is now in hand.

Step 1. In accordance with equations (29), f_1 is introduced as

$$f_1\triangleq\frac{\partial V}{\partial q_3} \tag{48}$$

and is regarded as a function of q_1, q_2, and q_3 because F_1 and F_2 each are functions of all of these variables, as can be seen by reference to equations (44) and (45). Since f_1 is the only function introduced, the subscript 1 is omitted hereafter.

Step 2. When equation (48) is used to eliminate $\partial V/\partial q_3$ from equations (46) and (47), the following equations corresponding to equations (31) result:

$$\frac{\partial V}{\partial q_1}=-f\frac{s_3}{L}-k\left[c_3-\frac{s_3}{L}(q_1s_3-q_2c_3)\right]+g\beta s_3c_3 \tag{49}$$

$$\frac{\partial V}{\partial q_2}=f\frac{c_3}{L}-k\left[s_3+\frac{c_3}{L}(q_1s_3-q_2c_3)\right]+g(\alpha+\beta s_3^2) \tag{50}$$

Step 3. Differentiating equation (49) partially with respect to q_2, equation (50) with respect to q_1, and equating the results gives

$$c_3\frac{\partial f}{\partial q_1}+s_3\frac{\partial f}{\partial q_2}=0 \tag{51}$$

Proceeding similarly in connection with equations (48) and (50) one has

$$\frac{\partial f}{\partial q_2}-\frac{c_3}{L}\frac{\partial f}{\partial q_3}=-k\left[c_3+\frac{q_1}{L}(c_3^2-s_3^2)+\frac{2q_2}{L}s_3c_3\right]+2g\beta s_3c_3-\frac{fs_3}{L} \tag{52}$$

while equations (48) and (49) yield

$$\frac{\partial f}{\partial q_1}+\frac{s_3}{L}\frac{\partial f}{\partial q_3}=k\left[s_3+\frac{2q_1}{L}s_3c_3+\frac{q_2}{L}(s_3^2-c_3^2)\right]-g\beta(s_3^2-c_3^2)-\frac{fc_3}{L} \tag{53}$$

Step 4. Inspection of equations (51)-(53) shows that this set of equations is eqivalent to $[W]\{X\}=\{Y\}$ if $[W]$, $\{X\}$, and $\{Y\}$ are taken to be

$$[W] \triangleq \begin{bmatrix} c_3 & s_3 & 0 \\ 0 & 1 & -c_3/L \\ 1 & 0 & s_3/L \end{bmatrix} \tag{54}$$

$$\{X\} \triangleq \begin{Bmatrix} \partial f/\partial q_1 \\ \partial f/\partial q_2 \\ \partial f/\partial q_3 \end{Bmatrix} \tag{55}$$

and

$$\{Y\} \triangleq \begin{Bmatrix} 0 \\ -k\left[c_3 + \frac{q_1}{L}(c_3^2 - s_3^2) + \frac{2q_2}{L}s_3c_3\right] + 2g\beta s_3c_3 - \frac{fs_3}{L} \\ k\left[s_3 + \frac{2q_1}{L}s_3c_3 + \frac{q_2}{L}(s_3^2 - c_3^2)\right] - g\beta(s_3^2 - c_3^2) - \frac{fc_3}{L} \end{Bmatrix} \tag{56}$$

Step 5. $[W]$ is singular, but possesses a nonvanishing determinant of order two. Hence, $\rho = 2$. Selecting the first two rows of $[W]$ as independent, and hence the third row as dependent, we express the third row as

$$[1 \quad 0 \quad s_3/L] = w_1[c_3 \quad s_3 \quad 0] + w_2[0 \quad 1 \quad -c_3/L] \tag{57}$$

where w_1 and w_2 are weighting factors. Equating first elements on the right-hand and left-hand sides of equation (57), one finds that $w_1 = 1/c_3$, and equating second elements then leads to $w_2 = -s_3/c_3$.

Step 6. Expressing Y_3, the element in the third row of $\{Y\}$ in equation (56), as $w_1Y_1 + w_2Y_2$, where Y_1 and Y_2 are the elements in the first two rows of $\{Y\}$, one has

$$k\left[s_3 + \frac{2q_1}{L}s_3c_3 + \frac{q_2}{L}(s_3^2 - c_3^2)\right] - g\beta(s_3^2 - c_3^2) - \frac{fc_3}{L}$$

$$= \frac{s_3}{c_3}k\left[c_3 + \frac{q_1}{L}(c_3^2 - s_3^2) + \frac{2q_2}{L}s_3c_3\right] - 2g\beta s_3^2 + \frac{f}{L}\frac{s_3^2}{c_3} \tag{58}$$

which reduces to

$$f = k(q_1s_3 - q_2c_3) + g\beta Lc_3 \tag{59}$$

Step 7. Substituting f as given in equation (59) into equations (48)–(50), one obtains

$$\frac{\partial V}{\partial q_1} = -kc_3 \tag{60}$$

$$\frac{\partial V}{\partial q_2} = -ks_3 + g(\alpha+\beta) \tag{61}$$

$$\frac{\partial V}{\partial q_3} = k(q_1s_3 - q_2c_3) + g\beta Lc_3 \tag{62}$$

and, proceeding in accordance with equation (33), one can express V as

$$V = \int_0^{q_1}[-k\cos(0)]d\zeta + \int_0^{q_2}[-k\sin(0) + g(\alpha+\beta)]d\zeta + \int_0^{q_3}[k(q_1\sin\zeta - q_2\cos\zeta) + g\beta L\cos\zeta]d\zeta \tag{63}$$

so that, after performing the indicated quadratures, one finds that

$$V = -k(q_1c_3 + q_2s_3) + g[(\alpha+\beta)q_2 + \beta Ls_3] \tag{64}$$

Clearly, E as defined in equation (7) is simply $K + V$.

It is interesting to note that there exists no counterpart to the integral under consideration if S is rendered holonomic by removal of both the force of magnitude $|R|$ and the requirement that the velocity vector of B be parallel to $\mathbf{n}_1'$ at all times. In that event, S possesses three degrees of freedom, the three associated generalized active forces are given by

$$F_1 = k\left[c_3 - \frac{s_3}{L}(q_1s_3 - q_2c_3)\right] \tag{65}$$

$$F_2 = k\left[s_3 + \frac{c_3}{L}(q_1s_3 - q_2c_3)\right] - g(\alpha+\beta) \tag{66}$$

$$F_3 = -g\beta Lc_3 \tag{67}$$

and S is nonconservative because F_1, F_2, and F_3 do not satisfy the equation $\partial F_r/\partial q_s = \partial F_s/\partial q_r$ for all r and s that differ from each other $(r, s = 1, 2, 3)$.

Lastly, the following point deserves attention: Once it has been established in connection with a particular system that E as given in equation (18) or equation (28) remains constant, one can work with variables other than $\dot{q}_1, \ldots, \dot{q}_n$, such as generalized speeds [5], when writing the integral $E = E_0$. For instance, introduction of generalized speeds u_1 and u_2 as

$$u_1 \triangleq c_3\dot{q}_1 + s_3\dot{q}_2, \quad u_2 \triangleq -s_3\dot{q}_1 + c_3\dot{q}_2 \tag{68}$$

is advantageous in connection with the example at hand because this makes it possible to replace the governing equations, equations (3)–(5), with the simpler relationships

$$\dot{q}_3 = -u_2/L \tag{69}$$

$$\dot{u}_1 = \frac{1}{\alpha+\beta}\left(P - \frac{\alpha}{L}u_2^2\right) - gs_3 \tag{70}$$

$$\dot{u}_2 = \frac{Q}{\alpha} + \frac{1}{L}u_1u_2 - gc_3 \tag{71}$$

Since the kinetic energy of S now can be expressed as

$$K = \frac{1}{2}\left[(\alpha+\beta)u_1^2 + \alpha u_2^2\right] \tag{72}$$

one can appeal to the theorem in Section 3 to write the following integral of equations (68)–(71) when P and Q are given by equations (1) and (2):

$$\frac{1}{2}\left[(\alpha+\beta)u_1^2 + \alpha u_2^2\right] - k(q_1c_3 + q_2s_3) + g[(\alpha+\beta)q_2 + \beta Ls_3] = E_0 \tag{73}$$

This result can serve as a check on a numerical simulation of motions of S when the integration algorithm used for this purpose is based on equations (68)–(71).

References

1 Kane, T. R., *Dynamics*, Holt, Rinehart, and Winston, New York, 1968, p. 78.

2 Passerello, C. E., and Huston, R. L., "Another Look at Nonholonomic Systems," ASME Journal of Applied Mechanics, Vol. 40, 1973, pp. 101–104.

3 Protter, M. H., and Morrey, C. B., Jr., *Modern Mathematical Analysis*, Addison-Wesley, Reading, Mass., 1966, p. 300.

4 Schultz, D. G., "The Generation of Liapunov Functions," *Advances in Control Systems*, Leondes, C. T., ed., Vol. 2, 1965, pp. 1–64.

5 Kane, T. R., Likins, P. W., and Levinson, D. A., *Spacecraft Dynamics*, McGraw-Hill, New York, 1983, p. 78.

J. A. P. Aranha

C. A. Martins

Instituto de Pesquisas Tecnologicas,
Cidade Universita,
São Paulo, Brazil

Nonlinear Analysis of a Dynamical System Being Pulled by Cables

Offshore pipeline must, in certain situation, be pulled by means of cables placed in a barge. An important nonlinear aspect of the wave-induced dynamic motion is the fact that the cable can become loose. This paper analyzes a simplified dynamical model whose steady state is obtained analytically. A feature of this model is that the output steady state frequency changes from ω to ω/2 as the input (wave) frequency ω increases. An order of magnitude analysis shows that this nonlinear effect is of importance for the usual offshore pipeline.

Introduction

During the operation of laying a pipeline on the ocean floor, it is sometimes necessary to abandon it at the bottom and, afterward, to pull it back to the laying barge. This operation is usually done by means of davits, placed on the barge, and connected to the pipeline by means of cables. In the absence of surface waves, the problem is static and highly nonlinear.

Several methods were developed aiming to determine the static equilibrium configuration and the static stresses; see, for instance [1–3]. Once an equilibrium position has been reached we can "turn on" the waves and evaluate the dynamic stresses. The dynamical displacement is of the order of magnitude of the wave amplitude and much smaller than the static one. This makes possible to linearize the dynamical motion by considering it as a small perturbation around a known equilibrium configuration. In spite of this, two sources of nonlinearities remain. The first is the viscous drag that can generally be linearized. The second is related to the fact that the cable can become loose, introducing stresses that can be dangerous to the pipe and cable. The objective of this paper is to study this second form of nonlinearity. Due to the inherent complexibility of the problem some simplifications are needed and in what follows, we introduce the most obvious simplifications that still contains the main features of the dynamical pipeline problem.

Simplified Model

Consider the static equilibrium position of the pipeline, indicated in Fig. 1, where A is the amplitude of the incoming wave and ω its frequency. τ_e is the static tension in the cable and we assume that the davit's vertical displacement D is given by $D(t) = A_0 \sin\omega t$ where $A_0 = H(\omega)$. A and $H(\omega)$ is the barge's transfer function. Taking in account the effect of buoyancy and the added mass (kinetic energy of the fluid that oscillates with the pipeline) we can compute the dynamical mass m. Knowing the natural frequency ω_0, we can determine $K = m \cdot \omega_0$. In this way the dynamics of the pipeline is very much similar to the dynamics of the linear spring-mass system shown in Fig. 1. The effect of the viscous drag has been neglected in the simplified model. A preliminary analysis, assuming the cable as being a rigid bar, has indicated that in a typical situation more than 10 waves are necessary to reach a steady state, showing that the effect of the damping is small at the time scale of the incident wave.

The behavior of the system depends basically on two nondimensional parameters.

$$\Omega = \frac{\omega}{\omega_0}$$

$$\beta = \frac{\tau_e}{K \cdot A_0} \tag{1}$$

Clearly the higher Ω is and the smaller β is, the easier the cable will become loose. In the next section we analyze the simplified model when β is fixed and Ω is increased continuously. We will use, however, an assumption to the checked latter on: the typical value of β for an offshore pipeline is much larger than one ($\beta >> 1$).

Steady State Analysis of the Model

Let ω^{-1}, A_0, and $k\,A_0$ be the time, length, and force scales, respectively. In what follows, $D(t) = \sin t$ stands for the nondimensional davit's displacement and $\tau(t) = \beta + p(t)$ is the nondimensional force in the cable. The equation to be

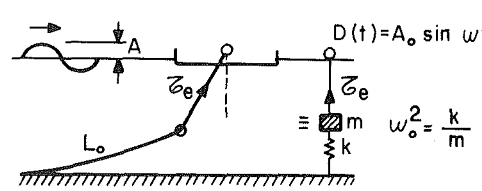

Fig. 1 Offshore pipeline and simplified model

Contributed by the Applied Mechanics Division for publication in the JOURNAL OF APPLIED MECHANICS.

Discussion on this paper should be addressed to the Editorial Department, ASME United Engineering Center, 345 East 47th Street, New York, N.Y. 10017, and will be accepted until two months after final publication of the paper itself in the JOURNAL OF APPLIED MECHANICS. Manuscript received by ASME Applied Mechanics Division, August, 1982; final revision, November, 1982.

solved is then: $\Omega^2\ddot{y}+y=p(t)$. There are two different sort of solutions for this equation. First the cable is fastened and the mass follows the davit. Second, the cable is loose and $\tau(t)=0$. The fastened solution is given by

$$y_f(t)=D(t)=\sin t$$
$$\tau_f(t)=\beta-(\Omega^2-1)\sin t \qquad (2)$$

A necessary condition for the cable to become loose is that $\tau_f(t)=0$. For $\beta>1$ this is possible if and only if $\Omega>\Omega_1=(1+\beta)^{1/2}$. Assuming $\beta>>1$ we can take this condition as $\Omega>\Omega_1\cong\beta^{1/2}$. It is convenient then to define

$$\Omega=\alpha\bullet\beta^{1/2} \qquad (3)$$

For $\alpha\leq 1$, the cable will always be fastened.

We next study only the case $\alpha>1$, and latter on we show that this condition is also sufficient for the cable to become loose. Let us assume that the motion has started at time $t=0$. The cable is initially fastened and since $\alpha>1$ it will become loose at the time $t_0<\pi/2$ where:

$$\sin t_0(\alpha)=\frac{\beta}{\Omega^2-1}\cong\frac{1}{\alpha^2} \qquad (4)$$

We must now determine the loose solution $y_l(t)$. In this case $\tau(t)=0$ and $p(t)=-\beta$.

It follows then that $\Omega^2\ddot{y}_l+y_l=-\beta$. For future reference let us assume that the cable becomes loose at $t=\hat{t}$ and so $y(\hat{t})=\sin t, \dot{y}_l(\hat{t})=\cos\hat{t}$. Using $\Delta t=t-\hat{t}$, the cable will remain loose if $e(\Delta t)=D(t)-y_l(t)<0$ for $\Delta t>0$. Since $\beta>>1$ we take $\Delta t/(\alpha\beta^{1/2})<<1$ in the expression for $e(\Delta t)$. If $\hat{\gamma}=(\sin t_0/\sin\hat{t})=(\alpha^2\sin\hat{t})^{-1}$ then the loose solution can be written as:

$$y_l(t;\hat{t})=-\beta+(\beta+\sin\hat{t})\cos[(t-\hat{t})/\alpha\beta^{1/2}]$$
$$+\beta^{1/2}\bullet\alpha\bullet\cos\hat{t}\bullet\sin[(t-\hat{t})/\alpha\beta^{1/2}]$$
$$e(\Delta t;\hat{t})=\sin\hat{t}\left[\cos\Delta t+\frac{1}{2}\hat{\gamma}(\Delta t)^2-1\right]-\cos\hat{t}[\Delta t-\sin\Delta t] \qquad (5)$$

For $\hat{t}=t_0$ and $\alpha>1$, but otherwise arbitrary, $e(\Delta t)<0$ at least for Δt small enough. The condition $\alpha>1$ is then sufficient for the cable to become loose. It will become fastened again for a particular $\Delta t_0=\Delta t_0(\alpha)$ at which $e(\Delta t_0;t_0)=0$. From (4) and (5) we obtain that $\Delta t_0(\alpha)$ must be a root of the equation:

$$\frac{\cos\Delta t_0+0.5(\Delta t_0)^2-1}{\Delta t_0-\sin\Delta t_0}=\operatorname{cotg}t_0=(\alpha^4-1)^{1/2} \qquad (6)$$

It can be shown that equation (6) has a solution and this solution is unique (see [5]). The uniqueness does not imply that y_l crosses $D(t)$ just once. They will cross each other an infinitude of times, but at such Δt where the approximation $\Delta t/(\alpha\beta^{1/2})<<1$ is not valid anymore. Let us now study some properties of the root $\Delta t_0(\alpha)$ of equation (6). Referring to Fig. (2), we define the functions $C(\alpha)=\pi-2t_0(\alpha)$; $G(\alpha)=\Delta t_0(\alpha)-C(\alpha)$; $S(\alpha)=0.5[\Delta t_0(\alpha)+G(\alpha)]$ as indicated.

It can be shown (see [5]) that $\Delta t_0(\alpha)$, $C(\alpha)$, $G(\alpha)$, and $S(\alpha)$ are all positive and monotonically increasing with α. Since $G(\alpha)>0$, $\Delta t_0(\alpha)>C(\alpha)$; that is, $-y_l(t)$ will cross $y_f(t)$ outside the first "compression zone," for arbitrary $\alpha>1$. The fact that $S(\alpha)$ increases with α has important consequences. Point (B) in Fig. 2 moves to the right as α increases. There exist then values $\alpha_2<\alpha_5<\alpha_6$ for which $B=B_2$, $B=B_5$, and $B=B_6$, respectively, as indicated in Fig. 2. For $\alpha=\alpha_2$, $\Delta t_0=t(B_2)-t_0=2\pi$, and, using equation (6), $\alpha_2=(1+\pi^2)^{1/4}\cong 1.82$. For $\alpha=\alpha_6$, $\Delta t_0=t(B_6)-t_0=4\pi$ and so $\alpha_6=(1+4\pi^2)^{1/4}\cong 2.52$. For $\alpha=\alpha_5$, $\Delta t_0=t(B_5)-t_0=3\pi-2t_0(\alpha_5)$. Placing this value into equation (6) and

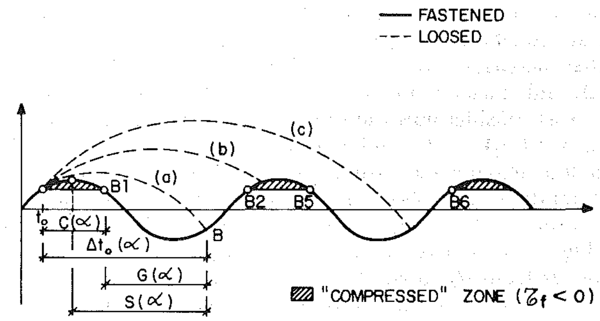

Fig. 2 Graphic representation of equation (6)

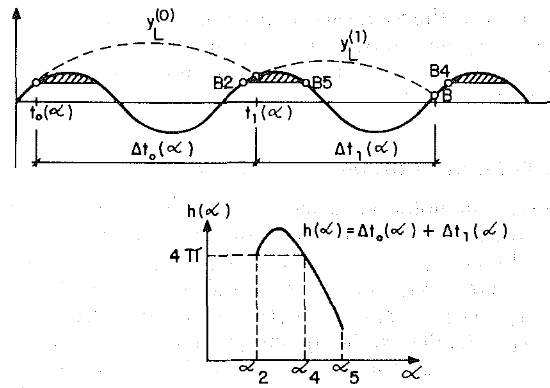

Fig. 3 Typical solution for $\alpha_4<\alpha<\alpha_5$

using equation (4) we obtain a transcendental equation in α_5, which can be solved numerically. The result is $\alpha_5\cong 2.15$.

Since $S(\alpha)$ is monotonically increasing then the equality $y_l(t)=y_f(t)$ holds at a $t=t(B)$ where (a) B is between B_1 and B_2 if $1=\alpha_1<\alpha<\alpha_2$; ($b$) B is between B_2 and B_5 if $\alpha_2<\alpha<\alpha_5$; (c) B is between B_5 and B_6 if $\alpha_5<\alpha<\alpha_6$. Let us now analyze a solution of class (a) ($1=\alpha_1<\alpha<\alpha_2$). The cable becomes loose at $t_0=t_0(\alpha)$ and fastened again at $t(B)=t_0+\Delta t_0$, where $\Delta t_0(\alpha)$ is a solution to equation (6). Afterward the mass follows the davit until the time $t=t_0+2\pi$ is reached, when the cable becomes loose again. Solutions of class (a) are then periodic, nonharmonic, with period 2π (frequency ω). Notice that in B the mass velocity changes abruptly from $\dot{y}_l(t_B)$ to $\dot{D}(t_B)=\dot{y}_f(t_B)=\cos t_B$. This introduces an impact load on the cable given by $p(t)=\Omega^2.[\dot{D}(t_B)-\dot{y}_l(t_B)]\,\delta(t-t_B)$, where δ is the Dirac function. A similar sort of analysis shows that solutions of class (c) are periodic, with period 4π (frequency $\omega/2$). Solutions of class (b) are more difficult to be analyzed. In fact $y_l(t)$ crosses $D(t)$ in a point B, within the "compression zone." The mass adjust its velocity, making it compatible with the davit's velocity, but since $\tau_f<0$ the cable becomes loose again. Figure (3) displays the typical situation.

Solutions $y_l^{(0)}(t)$ and $y_l^{(1)}(t)$ are given by equation (5), with $\hat{t}=t_0(\alpha)$ and $\hat{t}=t_1(\alpha)=t_0+\Delta t_0$, respectively. Equality $y_l^{(1)}(t)=y_f(t)$ holds for $t=t_2=t(B)=t_1+\Delta t_1$ ($e(\Delta t_1;t_1)=0$) where Δt_1 satisfies the following equation:

$$\hat{\gamma}=(\alpha^2\bullet\sin\hat{t})^{-1}$$
$$\frac{\cos\Delta\hat{t}+0.5\bullet\hat{\gamma}\bullet(\Delta\hat{t})^2-1}{\Delta\hat{t}-\sin\Delta\hat{t}}=\operatorname{cotg}\hat{t} \qquad (7)$$

with $\hat{t}=t_1$ and $\Delta\hat{t}=\Delta t_1$. It can be shown that, for $\alpha_2<\alpha<\alpha_5$, equation (7) has a unique solution (see [5]). Notice that as $\alpha\rightarrow\alpha_2$, $t_1\rightarrow t_0+2\pi$, $\gamma\rightarrow 1$ and $\Delta t_1\rightarrow 2\pi$. On the other hand, as $\alpha\rightarrow\alpha_5$, $t_1\rightarrow t_0+2\pi\,C(\alpha)$, $\gamma\rightarrow 1$ and $\Delta t_1\rightarrow 0$ since cotg $t_1\approx -$cotg $t_0<0$. We observe here the following: Δt, the time elapsed before $y_l(t)$ cuts again $D(t)=y_f(t)$, increases with the initial velocity $\cos \hat{t}$; see equation (5). For $y_l^{(0)}(t)$ the initial velocity is $\cos t_0(\alpha)$, and since $t_0(\alpha)$ decreases with α, $\Delta t_0(\alpha)$ increases with α. For $y_l^{(1)}(t)$ the initial velocity is $\cos t_1(\alpha)$, and since $t_1(\alpha)$ increases with α, $\Delta t_1(\alpha)$ decreases with α. Let us consider now the function $h(\alpha) = \Delta t_0(\alpha) + \Delta t_1(\alpha)$. Clearly $h(\alpha_2) = 4\pi$ and $h(\alpha_5) = 2\pi + C(\alpha_5) < 4\pi$. The function $\Delta t_0(\alpha)$ is increasing with α and $\Delta t_1(\alpha)$ is decreasing. It is not difficult to show that $h(\alpha)$ has the structure shown in Fig. 3 for $\alpha_2 < \alpha < \alpha_5$. For $\alpha = \alpha_4$, $h(\alpha) = 4\pi$ and $B \cong B_4$; see Fig. 3. As α increases, $(\alpha > \alpha_4)$ $h(\alpha)$ decreases, and point B moves from B_4 to B_5. For $\alpha = \alpha_5$, $\Delta t_1 = 0$ and $B \equiv B_5$. For $\alpha_4 \le \alpha < \alpha_5$ the solutions have typically the structure indicated in Fig. 3. They are all periodic, with period 4π (frequency $\omega/2$). The threshold value α_4 can be determined numerically. It is given by $\alpha_4 \cong (4{,}65 + \pi^2)^{1/4} \cong 1.95$. Notice that for $\alpha \le \alpha_2$ the solutions are periodic, with period 2π. For $\alpha_4 \le \alpha \le \alpha_6$ the solutions are periodic, with period 4π. The region $\alpha_2 < \alpha < \alpha_4$ is where the transition takes places, and will be analyzed next.

Quasi-Periodic Solution $\alpha_2 < \alpha < \alpha_4$

To make the notation easier we will call, from now on, t_n the actual value of t_n subtracted from $2n\pi$. In this way $t_1 = t_0 + \Delta t_0 - 2\pi$; $t_2 = t_1 + \Delta t_1 - 2\pi = t_0 + \Delta t_0 + \Delta t_1 - 4\pi$, etc. Notice that $t_2 = t(B) - 4\pi$, where $t(B)$ is indicated in Fig. 3. For $\alpha_2 < \alpha < \alpha_4$, $h(\alpha) = \Delta t_0(\alpha) + \Delta t_1(\alpha) > 4\pi$, and $\Delta t_1(\alpha) < 2\pi$. So $t_0 < t_2 < t_1$; that is, the equality $y_l^{(1)}(t) = y_f^{(t)}$ holds at $t(B) = t_2 + 4\pi$, where $t(B)$ is within the "compression zone." The situation here is analogous to the transition from $y_l^{(0)}(t)$ to $y_l^{(1)}(t)$ as shown in Fig. 3. The new solution $y_l^{(2)}(t)$, starting at $t(B) = t_2 + 4\pi$, is given by equation (5), where we must use t_2 in place of $\hat{t}$.

The equality $y_l^{(2)}(t) = y_f(t)$ holds now at a time $t = t_3 + 6\pi$, where $t_3 = t_2 + \Delta t_2 - 2\pi$, and Δt_2 is a solution to equation (7) with $\hat{t} = t_2$ and $\Delta\hat{t} = \Delta t_2$. As we are going to see, t_3 is also within the "compression zone" and, as a matter of fact, $t_0 < t_3 < t_1$. We can then define a new function $y_l^{(3)}(t)$ and a new time $t_4 = t_3 + \Delta t_3 - 2\pi$, where Δt_3 is again a solution to equation (7) with $\hat{t} = t_3$. In this way, we construct an infinite sequence of values $\{t_k\}$, and we will show next that $t_0 < t_k < t_1$, any $k > 2$ (remember that $t_0 < t_2 < t_1$ if $\alpha_2 < \alpha < \alpha_4$). Since $t_{k+1} = t_k + \Delta t_k - 2\pi$, where Δt_k is the solution to equation (7) with $\hat{t} = t_k$, it is worthwhile to consider the function

$$g(\hat{t}) = \hat{t} + \Delta\hat{t}(\hat{t}) - 2\pi \tag{8}$$

where $\Delta\hat{t}$ is the solution to equation (7). Notice that $t_{k+1} = g(t_k)$. It can be shown (see [5]) that if $\alpha_2 < \alpha < \alpha_4$ and $t_0 < \hat{t} < t_1$, then $\Delta\hat{t}(\hat{t})$, the solution to equation (7), is such that $d\Delta\hat{t}/d\hat{t} < -1$. Two important facts are a direct consequence of this inequality. First, since $\Delta\hat{t}(t_0) = \Delta t_0 > 2\pi$ and $\Delta\hat{t}(t_1) = \Delta t_1 < 2\pi$, there exists one and only one $\bar{t}$, $t_0 < \bar{t} < t_1$, such that $\Delta\hat{t}(\bar{t}) = 2\pi$. The uniqueness is a consequence of the fact that $\Delta\hat{t}(\hat{t})$ is monotonically decreasing. Placing $\Delta\hat{t}(\bar{t}) = 2\pi$ into equation (7) we obtain that

$$\cos \bar{t} = \frac{\pi}{\alpha^2} \tag{9}$$

Notice that $\bar{t}$ is well defined for all $\alpha \ge \alpha_2 = (1 + \pi^2)^{1/4}$ and also that $g(\bar{t}) = \bar{t}$. The derivative of $\Delta\hat{t}$ with respect to $\hat{t}$ is smaller than -1. So, if $\alpha_2 < \alpha < \alpha_4$ and $t_0 < \hat{t} < t_1$, the function $g(\hat{t})$, as defined by equation (8), is monotonically decreasing with $\hat{t}$. By definition $t_{k+1} = g(t_k)$ and we have already shown that $t_0 < t_2$. Now $\bar{t} < t_1$ and so $\bar{t} = g(\bar{t}) > g(t_1) = t_2$, leading to the inequality $t_0 < t_2 < \bar{t}$. In the same way $t_1 = g(t_0) > t_3 = g(t_2) > \bar{t} = g(\bar{t})$ or $\bar{t} < t_3 < t_1$. Also $t_2 = g(t_1) < t_4 = g(t_3) < \bar{t} = g(\bar{t})$ and so $t_2 < t_4 < \bar{t}$. As a conclusion we obtain: the sequence of values $\{t_k\}$ has an even $\{t_{2k}\}$ and an odd subsequence $\{t_{2k+1}\}$. The even subsequence $\{t_{2k}\}$ is monotonically increasing and is bounded from above by $\bar{t}$ $(t_0 \le t_{2k} < t_{2k+2} < \bar{t})$. The odd subsequence is decreasing and bounded from below by $\bar{t}$ $(\bar{t} < t_{2k+3} < t_{2k+1} \le t_1)$. By necessity, then, $t_{2k} \to \bar{t}_L \le \bar{t}$ and $t_{2k+1} \to \bar{t}_R > \bar{t}$ as $k \to \infty$ and, clearly, $g(\bar{t}_L) = \bar{t}_R$; $g(\bar{t}_R) = \bar{t}_L$.

This mathematical convergence can be physically described in the following way: if $\alpha_2 < \alpha < \alpha_4$, the cable becomes loose at $t = t_0$ and from there on it remains so, exception made to the discrete set of values $\{t_k\}$, when the cable becomes instantaneously fastened and the mass velocity is adjusted. In this range of frequencies the solutions are not periodic, although they approach a periodic one as $t \to \infty$. For this reason we call them "quasi-periodic." The limiting solution, here called by "steady state," has either a period 2π (when $\bar{t}_L = \bar{t} = \bar{t}_R$) or else a period 4π $(\bar{t}_L < \bar{t} < \bar{t}_R)$. The important question is to determine under what condition the limiting state is one or the other. We first write the general expression of this limiting state and the equation that allow us to determine it. With the help of equation (5) this "steady state" can be described by the two functions:

$$y_l(t) = -\beta + (\beta + \sin \bar{t}_L)\cdot\cos\left[\frac{t - \bar{t}_L}{\alpha\beta^{1/2}}\right] + \beta^{1/2}\cdot\alpha\cdot\cos \bar{t}_L\cdot\sin\left[\frac{t - \bar{t}_L}{\alpha\beta^{1/2}}\right]$$

$$y_l(t) = -\beta + (\beta + \sin \bar{t}_R)\cdot\cos\left[\frac{t - \bar{t}_R}{\alpha\beta^{1/2}}\right] + \beta^{1/2}\cdot\alpha\cdot\cos \bar{t}_R\cdot\sin\left[\frac{t - \bar{t}_R}{\alpha\beta^{1/2}}\right] \tag{10}$$

The first of these is defined for $\bar{t}_L \le t \le \bar{t}_R + 2\pi$ and the second for $\bar{t}_R + 2\pi \le t \le \bar{t}_L + 4\pi$. Notice that if $\bar{t}_L = \bar{t} = \bar{t}_R$ the two branches above are the same. To determine the values of $\bar{t}_L$ and $\bar{t}_R$ we define $\bar{t}_L = \bar{t} - \Delta_L$ and $\bar{t}_R = \bar{t} + \Delta_R$, where both Δ_L and Δ_R are positive. Since $g(\bar{t}_L) = \bar{t}_R$ and $g(\bar{t}_R) = \bar{t}_L$, then $\Delta\hat{t}(\bar{t}_L) = 2\pi + \Delta$ and $\Delta\hat{t}(\bar{t}_R) = 2\pi - \Delta$, where $\Delta = \Delta_R + \Delta_L$. Now $\Delta\hat{t}(\bar{t}_L)$ and $\Delta\hat{t}(\bar{t}_R)$ are roots of equation (7) when $\hat{t}$ is equal to $\bar{t}_L$ and $\bar{t}_R$, respectively. It is not difficult to check that Δ_R and Δ_L must satisfy the following set of equations

$$\frac{1}{2\alpha^2}(2\pi + \Delta)^2 - \sin(\bar{t} - \Delta_L)(1 - \cos\Delta) = 2\pi\cdot\cos(\bar{t} - \Delta_L) + (\Delta - \sin\Delta)\cos(\bar{t} - \Delta_L)$$

$$\frac{1}{2\alpha^2}(2\pi + \Delta)^2 - \sin(\bar{t} + \Delta_R)(1 - \cos\Delta) = 2\pi\cdot\cos(\bar{t} + \Delta_R) - (\Delta - \sin\Delta)\cos(\bar{t} + \Delta_R) \tag{11}$$

Notice that $\Delta = \Delta_R = \Delta_L = 0$ is always a root of equation (11). This root is certainly associated with the limiting periodic state of period 2π $(\bar{t}_L = \bar{t} = \bar{t}_R)$. For $\alpha = \alpha_2$, the solution is periodic with period 2π (see point B_2, Fig. 2) and $\bar{t} = t_0$ (see equation (4), (9), and remember that $\alpha_2 = (1 + \pi^2)^{1/4}$). We expect then that for α such that $\alpha_2 < \alpha < \alpha_4$, but close to α_2, the sequence $\{t_k\}$ actually converges to $\bar{t}(\Delta = \Delta_R = \Delta_L = 0)$. On the other hand, for $\alpha = \alpha_4$ the solution is periodic with period 4π (point $B \equiv B_4$ in Fig. 3) and so we expect that $\bar{t}_L \to t_0$ and $\bar{t}_R \to t_1$ as $\alpha \to \alpha_4$ $(\Delta_R \ne \Delta_L \ne 0)$. The root $\Delta = \Delta_R = \Delta_L = 0$ is, however, defined for all $\alpha > \alpha_2$. Since it should not represent the limiting state for α close to α_4, it must become unstable somewhere in the interval $\alpha_2 < \alpha < \alpha_4$. The stability analysis that follows is in fact a necessary condition for $\{t_k\}$ to converge to $\bar{t}$ as $k \to \infty$. Suppose we start the system at some $t_k = \bar{t} + \epsilon$, where $|\epsilon| << 1$. If $\Delta\hat{t}(t_k) = 2\pi + \delta$, then $t_{k+1} = t_k + \Delta\hat{t}(t_k) - 2\pi = \bar{t} + \epsilon + \delta$. Since t_{k+1} must be in the other side of $\bar{t}$, we anticipate that $\delta = -E(\alpha).\ \epsilon$, where $E(\alpha) > 1$.

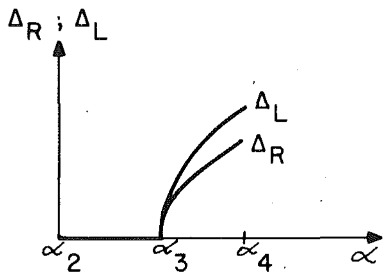

Fig. 4 Stable roots of equation (11)

Observe now that $t_{k+1} - \bar{t} = -[E(\alpha)-1]\epsilon$; $t_{k+2} - \bar{t} = +[E(\alpha)-1]^2\epsilon$ and, generically, $t_{k+n+1} - \bar{t} = (-1)^n \cdot r^n(\alpha) \cdot \epsilon$, where $r(\alpha) = E(\alpha) - 1$. A necessary and sufficient condition for stability is that $r(\alpha) < 1$. Also, the smaller $r(\alpha)$ is, the faster is the convergence. Since $|\epsilon| << 1$ we can write, to leading order, $\gamma_K = (\alpha^2 \cdot \sin t_K)^{-1} \sim \bar{\gamma} - \pi/(\alpha^2 - \pi^2) \cdot \epsilon$; $\operatorname{cotg} t_k = \operatorname{cotg} \bar{t} - [\alpha^4/(\alpha^4 - \pi^2)] \cdot \epsilon$, where $\bar{\gamma} = (\alpha^2 \cdot \sin \bar{t})^{-1} = (\alpha^4 - \pi^2)^{-1/2}$. Placing $\Delta\hat{t}(t_k) = 2\pi + \delta$ into equation (7) we obtain $\delta = -\dot{\bar{\gamma}}^{-1} \cdot \epsilon$. So $E(\alpha) = \bar{\gamma}^{-1}$ and $r(\alpha) = (\alpha^4 - \pi^2)^{1/2} - 1$. For $\alpha > \alpha_2 = (\pi^2 + 1)^{1/4}$, but close to it, $r(\alpha) << 1$ and the convergence is very fast. As α increases so does $r(\alpha)$ and the rate of convergence slows down. The threshold value is given by $\alpha_3 = (4 + \pi^2)^{1/4} \cong 1.93$, where $r(\alpha) = 1$. For $\alpha > \alpha_3$, $r(\alpha) > 1$, and the solution $\Delta = \Delta_R = \Delta_L = 0$ is unstable. In this situation the series $\{t_k\}$ certainly cannot converge to $\bar{t}$ and so $\bar{t}_L < \bar{t} < \bar{t}_R$. A second-order analysis shows that for $\alpha = \alpha_3$ convergence still holds, but the rate of convergence is pretty slow. Remember that the condition $r(\alpha) < 1$ is necessary, although nonsufficient, in order that $\bar{t}_L = \bar{t} = \bar{t}_R$. A similar analysis shows, however, that a necessary condition in order that $\bar{t}_L < \bar{t} < \bar{t}_R$ is that $\alpha > \alpha_3$. Again the convergence is very fast when α is near α_4 and slows down as α approaches α_3 from above. As a conclusion we obtain: for $\alpha_2 \leq \alpha \leq \alpha_3$ the root $\Delta = \Delta_R = \Delta_L = 0$ of equation (11) is stable and the sequence $\{t_k\}$ converges to $\bar{t}$. For $\alpha_3 < \alpha \leq \alpha_4$ the root $\Delta = \Delta_R = \Delta_L = 0$ is unstable. The even and odd subsequences of $\{t_k\}$ converges to $\bar{t}_L$ and $\bar{t}_R$, respectively, where $\bar{t}_L < \bar{t} < \bar{t}_R$. The value $\alpha = \alpha_3$ is the point where the transition from ω to $\omega/2$ takes place.

It remains now to determine the nontrivial solution to equation (11) for $\alpha > \alpha_3$. The situation is analogous to the bifurcation of an equilibrium configuration in an elastic stability analysis. We expect that for $0 < \alpha - \alpha_3 << 1$, Δ_R and Δ_L are very small. Equation (11) can be linearized and we obtain, to leading order, an homogeneous system that admits a nontrivial solution only when $\alpha = \alpha_3$. In analogy with the classical theory of elastic stability, we expect here a square root behavior at the branching point. Assuming that both Δ_R and Δ_L can be expanded in power series of $(\alpha - \alpha_3)^{1/2}$ we obtain, after some algebra, the following asymptotic solution:

$$\begin{aligned}
\Delta_R &\sim 1.65(\alpha-\alpha_3)^{1/2} - 1.71(\alpha-\alpha_3) \\
&\quad - 1.01(\alpha-\alpha_3)^{3/2} + 0[(\alpha-\alpha_3)^2] \\
\Delta_L &\sim 1.65(\alpha-\alpha_3)^{1/2} + 1.71(\alpha-\alpha_3) \\
&\quad - 1.01(\alpha-\alpha_3)^{3/2} + 0[(\alpha-\alpha_3)^2]
\end{aligned} \qquad (12)$$

Since $\alpha_4 - \alpha_3 \cong 0.03$ this asymptotic series should be good enough for all $\alpha_3 < \alpha < \alpha_4$. A check of this is provided by the following fact: for $\alpha = \alpha_4$, $\Delta_R = t_1 - \bar{t} \cong 0.273 rd$ and $\Delta_L = \bar{t} - t_0 \cong 0.3566\ rd$. The asymptotic values of Δ_R and Δ_L are, respectively, 0.2404 rd and 0.3570 rd. Figure 4 displays the stable roots of equation (11).

Summary

The threshold values of α are $\alpha_1 = 1.0$; $\alpha_2 = (1 + \pi^2)^{1/4} \cong 1.82$; $\alpha_3 = (4 + \pi^2)^{1/4} \cong 1.93$; $\alpha_4 \cong 1{,}95$; $\alpha_5 \cong 2.15$; $\alpha_6 = (1 + 4\pi^2)^{1/4} \cong 2.52$. Remember that $\Omega = \alpha \cdot \beta^{1/2}$. For $0 < \alpha \leq \alpha_1$, the cable is always fastened and $y(t) = y_f(t) = \sin t$. For $\alpha_1 < \alpha < \alpha_2$, the steady state is periodic with period 2π (frequency ω). A typical solution is indicated by Fig. 2, where $t_0(\alpha)$ is given by equation (4), and $\Delta t_0(\alpha)$ is the solution to equation (6). For $\alpha_2 < \alpha \leq \alpha_4$ the solution is quasi-periodic. As $t \to \infty$, it approaches a limiting solution given by equation (10), where $\bar{t}_L = \bar{t} - \Delta_L$; $\bar{t}_R = \bar{t} + \Delta_R$ and $\bar{t}$ is given by equation (9). For $\alpha_2 < \alpha \leq \alpha_3$, $\Delta_R = \Delta_L = 0$, and for $\alpha_3 < \alpha \leq \alpha_4$, Δ_R and Δ_L are given by equation (12). In the range $\alpha_2 < \alpha \leq \alpha_3$, the limiting solution has period 2π. For $\alpha_3 < \alpha \leq \alpha_4$, it has period 4π (frequency $\omega/2$). Two features of this "quasi-periodic" solution are worth mentioning. First, in the range $\alpha_2 < \alpha < \alpha_4$ once the cable becomes loose it remains so forever, exception made to a discrete set of values $\{t_k\}$. At these points the cable becomes instantaneously fastened, the mass picks up the davit's velocity, and the cable becomes loose again. A second feature is that the rate of convergence, toward the limiting state decreases as α becomes closer to α_3. For $\alpha_4 \leq \alpha < \alpha_5$ the motion is periodic with period 4π and has the structure shown in Fig. 3. The values of t_0 and Δt_0 are determined as indicated in the foregoing and $t_1 = t_0 + \Delta t_0$. Δt_1 is the root of equation (7) with $\hat{t} = t_1$. As α increases, point B tends toward B_5. For $\alpha_5 \leq \alpha \leq \alpha_6$ the solution is periodic with period 4π, and has the structure shown by curve (*c*), Fig. 2.

For $\alpha \geq \alpha_6 \cong 2.52$ the behavior is very much the same as the one indicated so far. The response must keep changing its basic period from 4π to 6π (frequency from $\omega/2$ to $\omega/3$) and so on. Values of α greater than α_6 are, however, unrealistic for an offshore pipeline. We close this summary with the following observation: most of the results were derived under the assumption that $\beta >> 1$. By numerically computing the exact value of α_2 we can state that for $\beta > 20$ the error due to the approximation is smaller than 0.55 percent. As we are going to see, working values of β are usually larger than 20.

Typical Values for an Offshore Pipeline

Due to the smallness of the wave amplitude A as compared with the suspended length L_0, the pipeline works dynamically as if it were clamped at a point 0 (Fig. 1). If the pipeline were straight, a good approximation for the stiffness would be $k \approx 3EJ/L_0{}^3$. If ρ_T/g and ρ_a/g are the density and buoyancy, per unit of length, of the pipeline then ρ_e/g is the effective density, where $\rho_e = \rho_T - \rho_a$. An important parameter is the so-called specific gravity, defined as the ratio $\rho_T/\rho_a = \rho_e/\rho_a + 1$. The weight of the suspended pipeline in the static configuration is $\rho_e L_0$ and so τ_e, the static tension, is of order $\tau_e \approx 0.5\,(\rho_e L_0)$, see [3]. In this way $\beta = \tau_e/kA_0 \approx L_0/(6\alpha_f{}^2 A_0)$, where $\alpha_f = EJ/\rho_e L_0{}^3$ and $A_0 = A \cdot H(\omega)$ is the davit's vertical displacement. For a water depth around 40 m, the suspended length L_0 is of order 150 m or even more and the nondimensional rigidity, $\alpha_f{}^2$, of order 0.3 or even less, see [3]. The displacement A_0 should not be much greater than 4 m ($A \approx 2$ m; $H(\omega) \approx 2$) and so β is usually larger than 20. The approximation $\beta >> 1$ is then valid for an offshore pipeline. From equation (3), $\alpha^2 = \Omega^2/\beta \approx 2.\ (m\omega^2 A_0)/\rho_e L_0 = 2\,(m\omega^2 AH(\omega))/\rho_e L_0$. The mass m is given by $m \approx 0.5\,(\rho_T/g) \cdot L_0[1 + C_m(\rho_a/\rho_T)]$ where $C_m \cdot (\rho_a/\rho_T)$ is the effect of the added mass. If $T = 2\pi/\omega$ is the wave period then $\alpha^2 \approx [1 + (1 + C_m) \cdot (\rho_a/\rho_e)] \cdot H(\omega) \cdot W^{-1}$, where $W = gT^2/4\pi^2 A$ depends only on the wave. Using the Pierson-Moskowitz spectrum to characterize the sea wave, we can easily check that W is very much constant and roughly equal to 6.3, for wind speeds ranging from 10 to 50 knots, see [4]. A typical value for the added mass coefficient is $C_m = 1$ and the ratio ρ_a/ρ_e, between buoyancy and effective density, is usually of order 5 (specific gravity $\approx$ 1,2). The transfer function $H(\omega)$ is in the range 1 to 2, depending on the position of the davit in the barge. The parameter α is then commonly larger than 1, indicating that in an actual offshore pipeline the cable can become loose. It is to be noticed that this is caused mainly by the effect of the added mass.

We close this section with a further observation: the only pipeline parameter affecting the loosening of the cable is the specific gravity, represented by the term ρ_a/ρ_e in the expression for α^2. This is a curious result since one would expect that the rigidity EJ, the suspended length L_0, and the static tension τ_e would play a relevant part in this nonlinear problem.

Conclusion

A simplified dynamical model imitating an actual offshore pipeline has been analyzed. The importance of this study is two-fold. First, it offers a guideline that helps the analysis of the complex pipeline problem. Second, we can use the analytical solution to understand other complex questions. An example of this would be the behavior of the pipeline in a random sea. With respect to the result itself, it is to be emphasized the peculiar way the system changes its frequency from ω to $\omega/2$, where ω is the input (wave) frequency. The existence of a region where the solution is "quasi-periodic" and the slowing down of the rate of convergence, toward the limiting (periodic) solution, as the input frequency approaches the value where the transition takes place, where not anticipated beforehand.

References

1 Petersen, P. T., "Equilibrium of Off-shore Cable and Pipe-lines During Laying," *Shipbuilding Progress*, Dec. 1975.

2 OPLS User's Manual for Programs OPLS2D, OPLS3D, Mar. 1980, Intercomp Resources Development and Engineering, Inc.

3 Aranha, J. A., Lima, J. de, and Cruz, J. J., "A Method to Solve the Problem of Abandon/Recovery Operation of a Pipeline," Rio Off-shore 81.

4 Newman, J. N., *Marine Hydrodynamics*, MIT Press, 1977.

5 Martins, C. A., "Análise Dinâmica da Operação de Resgate La teral de Oleoduto Submarino," M.Sc. Thesis, Civil Engineering Dept., EPUSP, Brazil, 1983.

H. Hatwal
Research Associate,
Department of Mechanical Engineering,
The University of Calgary,
2500 University Drive, N.W.,
Calgary, Alberta,
Canada, T2N 1N4

A. K. Mallik
Assistant Professor.

A. Ghosh
Professor.

Department of Mechanical Engineering,
Indian Institute of Technology Kanpur
Kanpur-208016, India

Forced Nonlinear Oscillations of an Autoparametric System—Part 1: Periodic Responses

Forced oscillations of a two degree-of-freedom autoparametric system are studied with moderately high excitations. The approximate results obtained by the method of harmonic balance are found to be satisfactory by comparing with those obtained by numerical integration. In the primary parametric instability zone, separate regions of stable and unstable harmonic solutions are obtained. In the regions of unstable harmonic solutions, depending on the forcing amplitude and frequency, the solutions may be amplitude modulated or completely nonperiodic. In the latter case the numerical integrations do not converge.

1 Introduction

A simple, nonlinear, two degree-of-freedom system giving rise to several interesting features is studied in this paper. One coordinate is directly excited by a harmonic force while the other is excited due to internal resonance. The system is termed an autoparametric system because the internal resonance occurs over a range of frequency. Similar systems with harmonic excitation were studied in [1, 2] with limitations on the excitation amplitude so that the responses remain harmonic. For moderately higher excitations the regions and nature of the nonharmonic solutions are studied in this work.

The nonlinearities are introduced due to large oscillations of a pendulum which constitutes a part of the system. To the first-order approximation, the equations of motion have quadratic nonlinearities and these equations have been studied in detail [3, 4]. It was noted in [2] that for the system considered in this work, with moderately high excitations, the first-order approximation does not predict the true stability behavior of the steady state solutions. The necessary higher order approximations are carried out in the present work considering higher order nonlinear terms. For forced oscillations with harmonic inputs, the method of harmonic balance [5], being more straightforward, is used to study the nature and amplitudes of the responses. The steady state solutions are assumed to have only the first harmonic and these assumed solutions are shown to depict the behavior of the system with reasonable accuracy.

The boundaries of parametric instabilities are obtained in the forcing amplitude-frequency plane. In the primary unstable zone, two separate regions of unstable harmonic solutions and one region of stable harmonic solutions are obtained. In the regions of unstable harmonic solutions, numerical integrations are carried out to check the nature of responses. In one of these regions the numerical integrations do not converge and the detailed discussions on this region are taken up in Part 2 of this paper [6].

Contributed by the Applied Mechanics Division for publication in the JOURNAL OF APPLIED MECHANICS.

Discussion on this paper should be addressed to the Editorial Department, ASME, United Engineering Center, 345 East 47th Street, New York, N.Y. 10017, and will be accepted until two months after final publication of the paper itself in the JOURNAL OF APPLIED MECHANICS. Manuscript received by ASME Applied Mechanics Division, March 1982; final revision January, 1983.

2 System Description and Equations of Motion

Figure 1 shows the two degree-of-freedom system in which the primary consists of a linear spring-mass-damper system and the secondary system is a simple damped pendulum

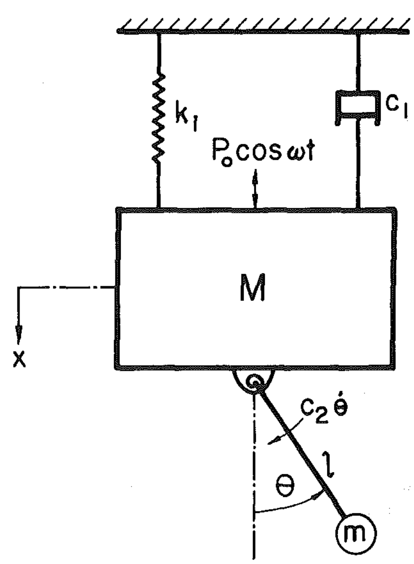

Fig. 1 Two degree-of-freedom autoparametric system

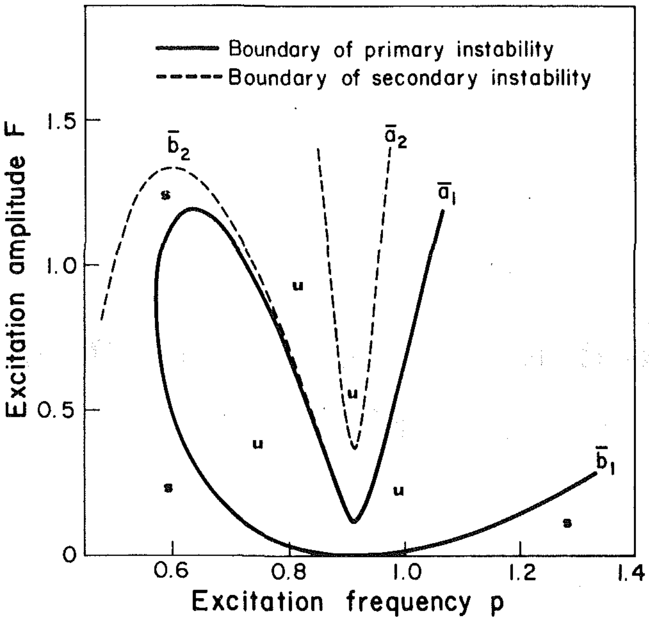

Fig. 2 Parametric instability boundaries in *F-p* plane

hinged to the primary mass M. The primary mass is excited directly by a harmonic force $P_0 \cos \omega t$. The equations of motion are

$$(M+m)\ddot{x} + c_1 \dot{x} + k_1 x - m1(\ddot{\theta}\sin\theta + \dot{\theta}^2\cos\theta) = P_0 \cos \omega t \qquad (1)$$

and

$$m1^2\ddot{\theta} + c_2\dot{\theta} + m1(g-\ddot{x})\sin\theta = 0, \qquad (2)$$

where x represents the displacement of M, θ is the rotation of the pendulum, and the dot implies the derivative with respect to time, t. These equations are written in the nondimensional form as

$$(1+R)p^2\eta'' + 2\zeta_1 p\eta' + \eta - p^2R(\theta''\sin\theta + \theta'^2\cos\theta) = F\cos\tau \qquad (3)$$

and

$$p^2\theta'' + \frac{2\zeta_2 qp}{\sqrt{1+R}}\theta' + \left(\frac{q^2}{1+R} - p^2\eta''\right)\sin\theta = 0, \qquad (4)$$

where

$$\tau = \omega t, \quad \eta = x/1, \quad R = m/M, \quad F = P_0/k_1 1,$$

$$p = \omega/\Omega_1, \Omega_1 = \sqrt{k_1/M}, \quad q = \omega_2/\omega_1,$$

$$\omega_1 = \sqrt{k_1/M+m}, \quad \omega_2 = \sqrt{g/1}, \quad \zeta_1 = \frac{c_1}{2M\Omega_1},$$

$$\zeta_2 = \frac{c_2}{2m1^2\omega_2}$$

and the prime denotes the derivative with respect to the nondimensional time τ.

3 Boundaries of Parametric Instabilities

For studying the boundaries of the regions of unstable zero solutions of θ (when the sytem is oscillating at steady state as a locked mass), $\sin\theta$ is replaced by θ in (4) rendering it to the following form:

$$p^2\theta'' + \frac{2\zeta_2 pq}{\sqrt{1+R}}\theta' + \left(\frac{q^2}{1+R} - p^2\eta_L''\right)\theta = 0 \qquad (5)$$

Here η_L is the locked mass response and is given by

$$\eta_L = A_L\cos(\tau - \phi_0), \qquad (6)$$

where

$$A_L = \frac{F}{\sqrt{[1-p^2(1+R)]^2 + (2\zeta_1 p)^2}}$$

and (7)

$$\phi_0 = \tan^{-1}\left[\frac{2\zeta_1 p}{1-p^2(1+R)}\right]$$

Equation (5) is transformed to the standard form of Mathieu equation [7] as

$$\frac{d^2\psi}{du^2} + (\alpha - 2\beta\cos 2u)\psi = 0, \qquad (8)$$

where

$$2u = \tau - \phi_0 + \pi$$

$$\psi = \theta\exp\left(\frac{2\zeta_2 qu}{p\sqrt{1+R}}\right) \qquad (9)$$

and

$$\alpha = \frac{4q^2(1-\zeta_2^2)}{p^2(1+R)}$$

$$\beta = 2A_L \qquad (10)$$

The boundaries of instabilities for (8) in the $\alpha - \beta$ plane can be determined directly from the standard tables [8]. Since the value of ζ_2 is considered to be small, the boundaries for θ and ψ are almost the same, except for very small F.(It can be shown that with $q = 1/2$, F needs to be greater than $2\zeta_1\zeta_2/\sqrt{1+R}$ to cause instability of $\theta = 0$ in (5).) After obtaining the instability boundaries for (8) the same are plotted for (5) in the $F - p$ plane by using (10). These boundaries are shown in Fig. 2 with $R = 0.2$, $q = 1/2$, $\zeta_1 = 0.02$, and $\zeta_2 = 0.05$, where u and s in Fig. 2 represent the unstable and stable regions, respectively. The primary unstable region is bounded by two periodic solutions of 4π — one of them being odd ($\bar{b}_1$) and the other being even ($\bar{a}_1$). $\bar{a}_1$ and $\bar{b}_1$ meet near $p = [(1-\zeta_2^2)/(1+R)]^{1/2}$, i.e., $\alpha = 1$. Similarly, the secondary unstable region is bounded by two solutions of period 2π — the odd solution represented by $\bar{b}_2$ and the even solution by $\bar{a}_2$. $\bar{a}_1$ and $\bar{b}_2$ have the same asymptote as $\beta \to \infty$. Similarly $\bar{b}_3$ (the odd solution for the third unstable region and not shown in Fig. 2) will have same asymptote as $\bar{a}_2$ for the range of $\bar{a}_2$ shown in the figure. This is because β is quite high and α is near 1 for this range. Thus the region inside $\bar{a}_2$ will include the third and higher regions of instability for which $\theta = 0$ is unstable.

4 Approximate Solutions and Their Stability

Because the excitation is harmonic, the steady state solution of the primary mass is also assumed to be harmonic with the same frequency ω. The solution being sought near the primary unstable region of (5) (i.e., $q^2/p^2(1+R) \approx 1/4$), the steady state motion of the pendulum is taken as harmonic with frequency $\omega/2$. Thus the steady state solutions are assumed to be of the form

$$\eta = A\cos(\tau + \phi_1)$$

and (11)

$$\theta = B\cos\left(\frac{\tau}{2} + \phi_2\right)$$

Substituting (11) into (3) and (4) and equating the coefficients of sine and cosine terms the following four equations, in terms of the four unknowns A, B, ϕ_1, and ϕ_2, are obtained:

$$(v_1^2 + v_2^2)\, v_4 + v_3^2 + 2\, v_3\, [\{1 - p^2(1+R)\}\, v_1 + (2\,\zeta_1\, p)\, v_2] = F^2 \tag{12}$$

$$A^2 = v_1^2 + v_2^2 \tag{13}$$

$$\tan 2\,\phi_2 = \frac{[1 - p^2\,(1+R)]\, v_2 - (2\,\zeta_1\, p)\, v_1}{[1 - p^2\,(1+R)]\, v_1 + (2\,\zeta_1\, p)\, v_2 + v_3} \tag{14}$$

and

$$\tan\,(2\,\phi_2 - \phi_1) = \frac{v_2}{v_1}, \tag{15}$$

where

$$v_1 = \frac{\dfrac{B}{4} - \dfrac{q^2}{p^2\,(1+R)}\, 2\, J_1\,(B)}{J_1\,(B) - J_3\,(B)},$$

$$v_2 = \frac{\zeta_2\, q\, B}{p\sqrt{1+R}\,[J_1\,(B) + J_3\,(B)]},$$

$$v_3 = \frac{p^2\, R\, B}{8}\, [2\,\{J_1\,(B) - J_3\,(B)\} + B\,\{J_0\,(B) + 2\, J_2\,(B) + J_4\,(B)\}],$$

$$v_4 = [1 - p^2\,(1+R)]^2 + (2\,\zeta_1\, p)^2$$

and $J_n\,(B)$ is the Bessel's coefficient of order n arising out of expansions of the terms like $\sin\,\{B\cos\,(\tau/2 + \phi_2)\}$ [9].

For the ith-order approximation, terms up to $B^{(2i-1)}$ are retained in (12)–(15). For first-order approximation the polynomial (12) can be solved in closed form. For any higher order approximation, this equation has to be solved only numerically.

The stability of the assumed solutions is investigated by providing small perturbations to them as

$$\eta = A\cos\,(\tau + \phi_1) + y_1$$

and (16)

$$\theta = B\cos\left(\frac{\tau}{2} + \phi_2\right) + y_2$$

where y_1 and y_2 are small perturbations. Substitution of (16) in (3) and (4) yields

$$(1+R)\, p^2\, y_1'' + 2\,\zeta_1\, p\, y_1' + y_1 - p^2\, R\, [f_1\,(\tau)\, y_2'' + f_2\,(\tau)\, y_2' + f_3\,(\tau)\, y_2] = 0$$

and (17)

$$p^2\, y_2'' + \frac{2\,\zeta_2\, q\, p}{\sqrt{1+R}}\, y_2' + \left[\frac{q^2}{1+R} + f_4\,(\tau)\right] y_2 - p^2 f_1\,(\tau)\, y_1'' = 0,$$

where

$$f_1\,(\tau) = \sin\left[B\cos\left(\frac{\tau}{2} + \phi_2\right)\right]$$

$$f_2\,(\tau) = -\,B\sin\left(\frac{\tau}{2} + \phi_2\right)\cos\left[B\cos\left(\frac{\tau}{2} + \phi_2\right)\right]$$

$$f_3\,(\tau) = -\,\frac{B}{4}\cos\left(\frac{\tau}{2} + \phi_2\right)\cos\left[B\cos\left(\frac{\tau}{2} + \phi_2\right)\right] - \frac{B^2}{4}\sin^2\left(\frac{\tau}{2} + \phi_2\right)\sin\left[B\cos\left(\frac{\tau}{2} + \phi_2\right)\right]$$

and

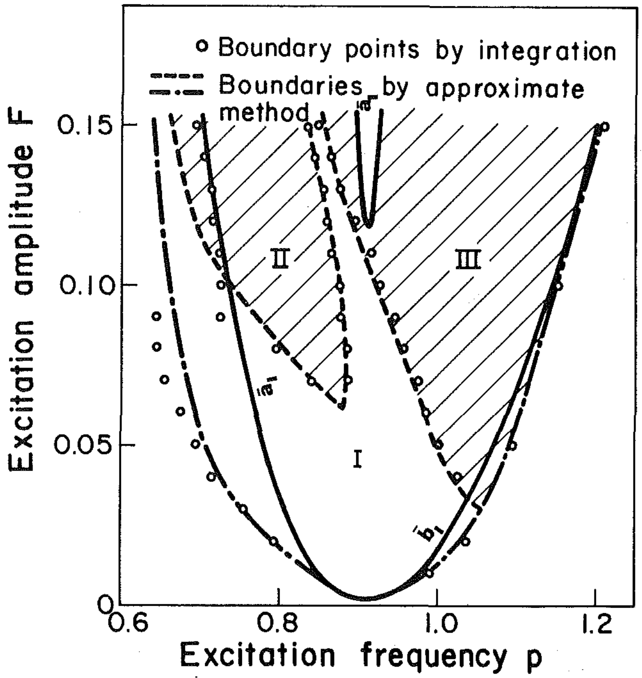

Fig. 3 Boundaries of stable and unstable harmonic solutions

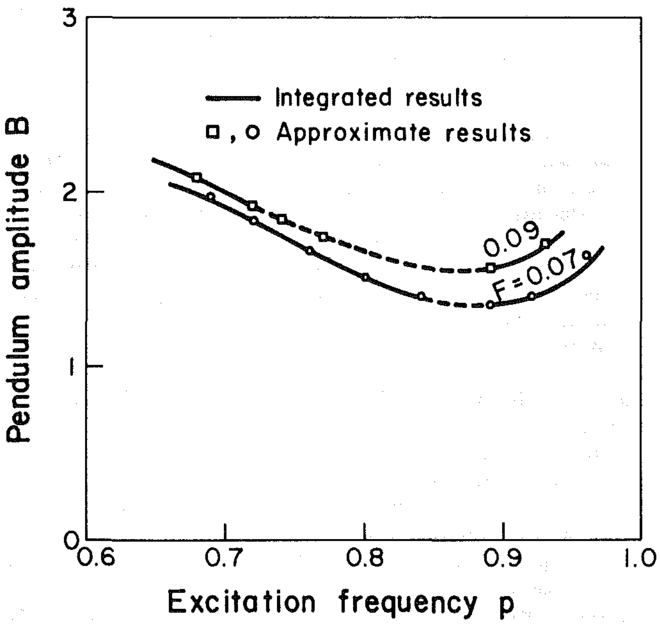

Fig. 4 Amplitude of pendulum obtained by approximate method and integration

$$f_4\,(\tau) = \frac{q_1^2}{1+R} + p^2 A\cos\,(\tau + \phi_1) \times \cos\left[B\cos\left(\frac{2}{\tau} + \phi_2\right)\right]$$

Equations (17) are linear equations with periodic coefficients. Floquet's theory [4] is used to investigate the stability of these equations.

5 Results and Discussions

Numerical results are presented for the following values of the parameters: $R = 0.2$, $q = 1/2$, $\zeta_1 = 0.02$, and $\zeta_2 = 0.05$. The range of excitation frequency is around the natural frequency of the locked mass system, i.e., $p\sqrt{1+R} \approx 1$. The approximate solutions are obtained by considering terms up

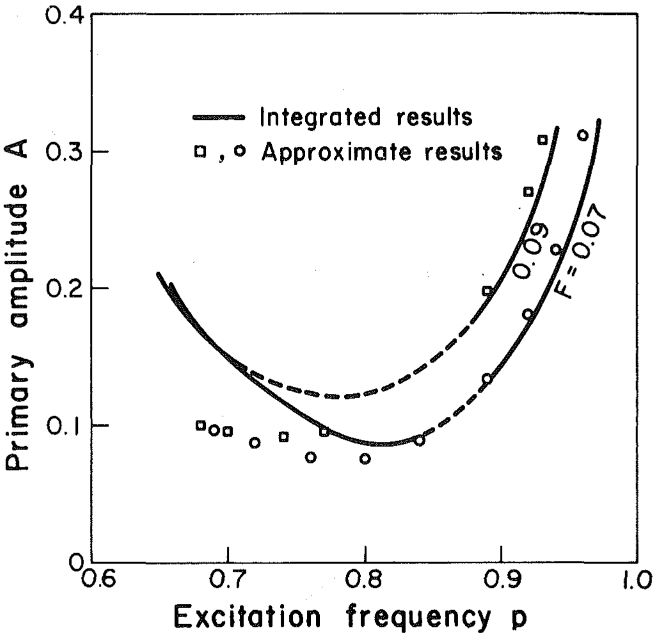

Fig. 5 Amplitude of primary obtained by approximate method and integration

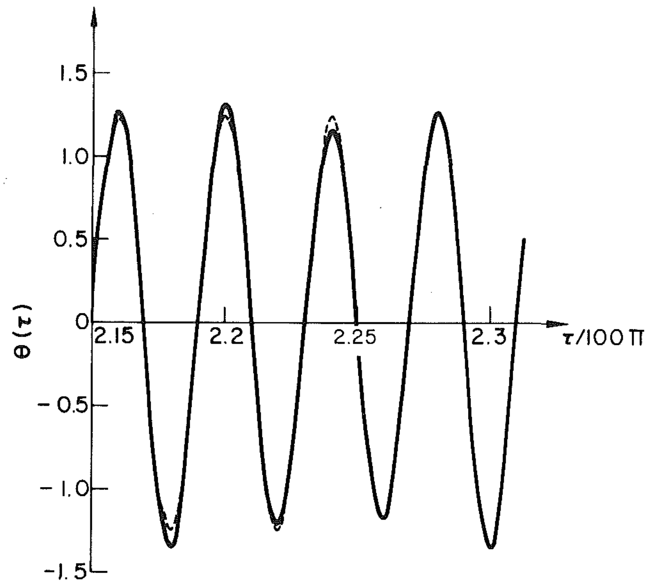

Fig. 6 Response time histories of θ with two different set of initial conditions: $F = 0.06$, $p = 0.88$; ----; $\eta(0) = 0.08$, $\eta'(0) = 0.06$, $\theta(0) = 1.24$, $\theta'(0) = 0.07$; ——: $\eta(0) = -0.03$, $\eta'(0) = 0.05$, $\theta(0) = 1.25$, $\theta'(0) = -0.03$

to B^5 in (12)-(14). Further inclusion of higher order nonlinear terms does not change the results significantly. The integrated results presented are by Gill's modification of the fourth-order Runge-Kutta method.

5.1 Boundaries of Stable and Unstable Harmonic Solutions. Figure 3 shows the enlarged view of boundaries of the primary instability, already given in Fig. 2, for F up to 0.15. Because of dampings ζ_1 and ζ_2 the primary instability boundary starts from a nonzero value of F (≈ 0.0018). The boundary of the primary instability is shown by the firm lines $\bar{a}_1$ and $\bar{b}_1$, inside which $\theta = 0$ is unstable. Region *I* includes combinations of F and p for which the harmonic solutions, given by (11), are stable. For the values of F and p in regions *II* and *III*, all the harmonic solutions, given by (11), are unstable. The number of such unstable harmonic solutions can be more than one.

The areas between the firm line and the chain dotted lines show the overhang regions where the zero solution of θ is a stable solution. The nonzero solution of θ (i.e., the solutions (11)) in the overhang regions may or may not be stable depending on whether or not the representative point (F, p) lies in region *I*. The integrated results show that at $F = 0.09$ region *II* widens sharply toward the left and touches the boundary of the left overhang. For $F > 0.09$, the left overhang almost disappears for integrated results, whereas approximate results yield a small overhang. Thus, except in a narrow region in the left overhang, the results obtained by integration and the approximate method match very well.

5.2 Stable Harmonic Solutions in Region *I*. The amplitudes of θ and η are shown in Figs. 4 and 5, respectively, where both the integrated and the approximate results are illustrated. For the integrated results, when the responses are seen to be periodic (with η and θ having periods of 2π and 4π, respectively), the maximum value in one cycle is taken as the amplitude. For representative points in region *I* (Fig. 3) the integrated responses reach harmonic or near harmonic steady states. These steady state amplitudes are joined by firm lines in Figs. 4 and 5. The dotted lines in these figures do not represent the amplitudes but are only the extrapolations of the respective firm lines. These dotted lines are for combinations of F and p lying in region *II* of Fig. 3 when the integrated responses do not have fundamental period of η and θ as 2π and 4π, respectively. Similarly no amplitudes are shown for F and p in region *III* as the solutions (11) are unstable and integration also does not yield periodic responses. Figure 4 shows that the amplitudes of θ obtained by the approximate method and numerical integration are in very close agreement. At lower values of p, however, these two methods yield somewhat different values for the amplitudes of η. This is due to the presence of higher harmonics in the response of η for lower values of p, as shown by the Fourier analysis of the steady state integrated responses, whereas θ remains almost harmonic. Approximate results can also be refined by considering higher harmonics in (11). But this changes results only quantitatively and that too, not very significantly. It is seen from Figs. 4 and 5 that the amplitudes increase sharply at certain frequencies. In fact, these are the frequencies at which region *III* (Fig. 3) is approached. On the other hand, as region *II* is entered while decreasing p, the amplitudes A and B decrease. Similarly, for phase angles as well, it is seen [10] that the transition to region *II* is smooth, whereas the transition to region *III* occurs with a jump in the values.

With the combinations of F and p lying well inside region *I* the harmonic solutions are strongly stable. As the representative point approaches region *II* or *III*, while checking the stability of (17) the eigenvalues approach unity and the solutions become weakly stable. For example, with $F = 0.06$ and $p = 0.88$ the representative point is in region *I* and very close to region *II*. Figure 6 shows the integrated steady state response time histories of θ with two different, but close, initial conditions. The response represented by dotted line is harmonic with a period of 4π, whereas, the firm lined response has small modulation with a period of 12π. Both of these responses represent stable steady state, each being achievable only from a particular set of initial conditions. The 4π-period response can be approximately obtained by (11) and the amplitude of θ thus obtained is 1.24.

5.3 Integrated Response in Regions *II* and *III*. While checking the stability of (17), for moderate values of F such that (F, p) point lies in region *II*, the eigenvalues are complex and slightly greater than unity. This suggests that the growth of the trivial solution of (17) will be slow and oscillatory. Therefore, with initial conditions calculated from (11) with τ

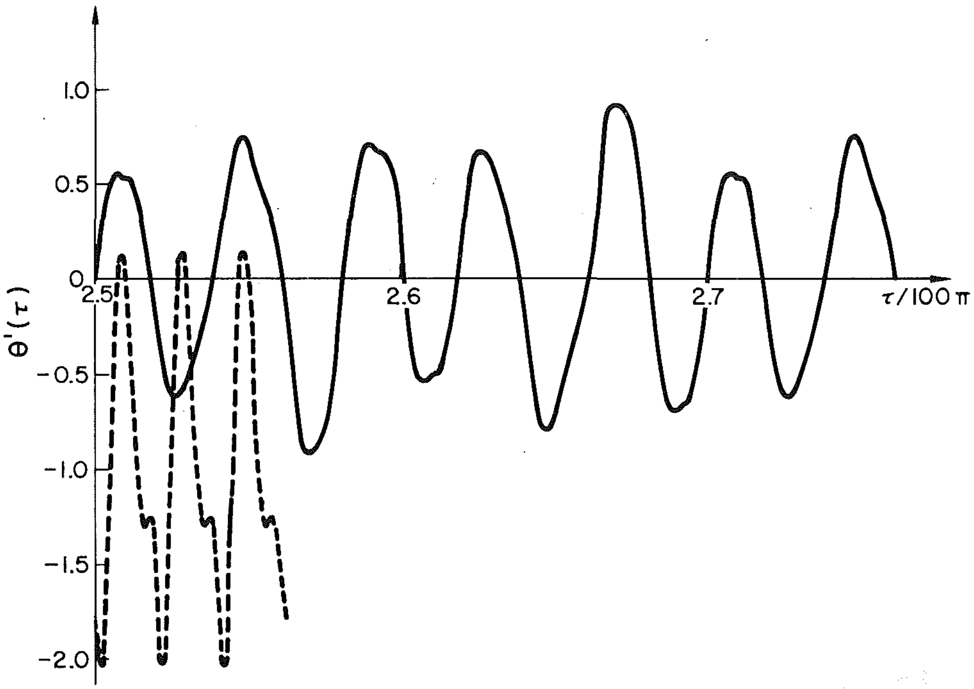

Fig. 7 Response time histories of θ' with two different set of initial conditions: $F = 0.08$, $p = 0.86$; ——: $\eta(0) = 0.13$, $\eta'(0) = 0.06$, $\theta(0) = 1.44$, $\theta'(0) = -0.01$; ----: $\eta(0) = 0.91$, $\eta'(0) = 0.94$, $\theta(0) = 1.32$, $\theta'(0) = -1.30$

$= 0$ the numerical integration is expected to give a steady state that will be close to the harmonic state given by the approximate solution. Further, these steady states are expected to be influenced strongly by the initial conditions. Figure 7 shows the steady state response time histories of θ' with $F = 0.08$ and $p = 0.86$ with two different initial conditions. The firm lined response is obtained with initial conditions from the approximate solution and has a modulation of period 20π. The dotted line has a period of 2π and the mean value of θ' is nonzero. This implies that during the steady state the pendulum keeps on rotating in the same direction, the time taken for each rotation being 2π.

As the excitation amplitude is increased in region *II*, the modulation of the response becomes more irregular as is evident from Figs. 6 and 7. Moreover, there is no fixed pattern of the amplitude modulation. For a particular combination of F and p, depending on initial conditions, it is observed [10] that there may be more than one amplitude modulated steady states and these states are weakly stable. If the initial conditions are sufficiently far away from these periodic trajectories, the integrated responses become irregular and nonperiodic. For sufficiently large F in region *II* the maximum eigenvalue becomes appreciably greater than unity and the integrated responses become nonperiodic with any choice of initial conditions.

For points in region *III*, the maximum eigenvalues are found to be real and much greater than unity. This implies that no stable harmonic or near harmonic steady state exists in the neighborhood of the solutions obtained by the approximate method. In such cases, for any choice of initial conditions, the integrated responses are seen to be nonperiodic. In other words, even after a long time, when the effects of the transients are expected to die down due to the presence of significant damping, the responses do not show any periodicity and are quite irregular. Moreover, by decreasing the step size of integration, the results do not converge uniformly to a common limit for all τ. In such cases it is observed that a change, even in the eighth decimal place, in the initial conditions change the response history completely. Similar nonconvergent results are also obtained by Hamming's modified predictor-corrector method. In comparison, for region *I*, where the harmonic steady states are strongly stable, even a coarse step size of integration with any initial condition carries the solution to the same periodic steady state.

For (F, p) in region *I* but close to region *III*, the harmonic steady states can be obtained by selecting initial conditions properly. But these steady states are weakly stable and a small disturbance to these or a slightly different initial condition (than mentioned in the foregoing) carries the solution to a completely nonperiodic state. Further discussions on the region *III* are taken up in Part 2 of this paper [6].

6 Conclusions

For the forced system with harmonic excitation, the method of harmonic balance correctly predicts the existence or absence of stable harmonic or near harmonic solutions, as also verified by numerical integrations. With increasing values of the excitation amplitude, the steady state response cease to be harmonic in certain frequency ranges. It was shown in [2] that for the system with a spring-controlled pendulum, the deviation from the harmonic solution was associated with a jump in the amplitude values. For the system with a gravity-controlled pendulum, two separate regions of unstable harmonic solutions are obtained. As the frequency decreases, the transition from the region of stable harmonic solutions to one of these regions takes place without any jump and is associated with a decrease in the amplitudes. Moreover, in this region, depending on the initial conditions, one or more amplitude modulated steady states are possible. These modulated states are weakly stable and nonperiodic states may result if sufficiently large disturbances are introduced.

Transition to the second region of unstable harmonic solutions is associated with a sharp increase in the amplitudes and in these regions no periodic solutions exist. In such cases, given a set of initial conditions, the response at a future instant of time can not be determined uniquely. Lastly, with increase in forcing amplitudes the overhangs almost disappear.

References

1 Haxton, R. S., and Barr, A. D. S., "The Autoparametric Vibration Absorber," ASME *Journal of Engineering for Industry*, Vol. 94, 1972, pp. 119–125.

2 Hatwal, H., Mallik, A. K., and Ghosh, A., "Nonlinear Oscillations of a Harmonically Excited Autoparametric System," *Journal of Sound and Vibration*, Vol. 81, No. 2, pp. 153–164.

3 Sethna, P. R., "Vibrations of Dynamical Systems With Quadratic Nonlinearities," ASME JOURNAL OF APPLIED MECHANICS, Vol. 32, 1965, pp. 576–582.

4 Nayfeh, A. H., and Mook, D. T., *Nonlinear Oscillations*, Wiley, New York, 1979.

5 Bolotin, V. V., *The Dynamic Stability of Elastic Systems*, Holden Day, San Francisco, 1964.

6 Hatwal, H., Mallik, A. K., and Ghosh, A., "Forced Nonlinear Oscillations of an Autoparametric System—Part 2: Chaotic Responses," ASME JOURNAL OF APPLIED MECHANICS, Vol. 50, 1983, pp. 663–668.

7 McLachlan, N. W., *Theory and Application of Mathieu Functions*, Dover, New York, 1964.

8 "Tables Relating to Mathieu Functions: Characteristic Values, Coefficients, and Joining Factors," National Bureau of Standards, Applied Mathematics Series 59, Washington, U.S. Government Printing Office, 1967.

9 Whittaker, E. T., and Watson, G. N., *A Course of Modern Analysis*, Cambridge University Press, 1958.

10 Hatwal, H., "Nonlinear Oscillations of Harmonically Excited Autoparametric Systems," Ph.D. Thesis, Indian Institute of Technology, Kanpur, Sept. 1981.

H. Hatwal
Research Associate,
Department of Mechanical Engineering,
The University of Calgary,
2500 University Drive, N.W.,
Calgary, Alberta, Canada T2N IN4

A. K. Mallik
Assistant Professor.

A. Ghosh
Professor.

Department of Mechanical Engineering,
Indian Institute of Technology,
Kanpur Kanpur-20816, India

Forced Nonlinear Oscillations of an Autoparametric System—
Part 2: Chaotic Responses

Chaotic oscillations arising in forced oscillations of a two degree-of-freedom autoparametric system are studied. Statistical analysis of the numerically integrated nonperiodic responses is shown to be a meaningful description of the mean square values and the frequency contents of the responses. Some qualitative experimental results are presented to substantiate the necessity of performing the statistical analysis of the responses even though the system and the input are deterministic.

1 Introduction

An interesting feature of some nonlinear systems is their capability of yielding random-looking (chaotic) responses to a deterministic input even in the presence of damping. Although this phenomenon has been observed in different disciplines, there is no unified approach to the problem. May [1] has reviewed some systems governed by difference equations which give rise to chaotic oscillations. Lorenz [2] stated that for systems with bounded solutions the nonperiodic solutions are ordinarily unstable with respect to small modifications. This in turn signifies that slightly different initial states can evolve into considerable different states. Holmes [3] studied in detail a nonlinear oscillator for which chaotic motions arise. As a mechanical example Moon and Holmes [4] and Moon [5] examined the forced vibrations of a cantilever beam buckled by magnetic forces. The basic unforced system in [3-5] had two stable static equilibrium positions. For the critical forcing amplitude and frequencies the motion is chaotic with the beam tip jumping from one fixed point to the other. The present work shows a possibility of chaotic motions with a two degree-of-freedom system where one of the coordinates is parametrically excited and the unforced system has only one stable static equilibrium position.

The system under consideration and its equations of motion were described in Part 1 of this paper [6].[1] It was shown there that in the forcing amplitude-frequency plane there is a region where the harmonic solutions are unstable and with successive approximations the numerical integrations do not converge uniformly (for all time) to a common limit. Thus, though the large disturbances die out due to dampings and the responses remain bounded, it is not possible to describe these responses uniquely. The approximate methods obviously fail in this chaotic regime. We propose to show in this work that for these chaotic responses a meaningful description (and possibly the only) is possible through statistical analyses and further that the statistics can be inferred from a single integrated response record (even though the integrations do not converge.) Lastly, some qualitative experimental results are presented to substantiate the necessity of performing the statistical analysis of the responses even though the system and the input are deterministic.

All the discussions in this paper are for the combinations of F and p lying in region *III* (Fig. 3 [6]), which is also referred to as the chaotic regime.

2 Integrated Responses in the Chaotic Regime

It was mentioned in [6] that for combinations of F and p in region *III* (Fig. 3 [6]) the integrated responses are nonperiodic and these responses depend on the step size of integration, h, and the initial conditions. With $F=0.05$ and $p=1.0$, Fig. 1 shows typical time histories of θ' for two different step sizes with the same initial conditions. For the case with $h = \pi/40$, η-response record is shown in Fig. 2. Since η coordinate is directly driven by the external harmonic excitation, its response is expected to have more regularity as compared to that for θ and this is evident from Fig. 2 as well.

The results presented in Figs. 1 and 2 as such do not convey any meaning since these results have not converged, as was mentioned in [6]. The numerical integrations are affected by the numerical roundups and the inherent errors in the numerical schemes used. Likewise any actual physical experiment will have unaccountable disturbances. The control on the parameter values during the numerical integration, in fact, is much better than in any physical experiment where the parameters, like frequency etc., do not remain exactly at the predetermined value.

For (F, p) lying well inside region *I* (Fig. 3 [6]) the harmonic solutions are strongly stable, the integrations with any initial conditons yield the same harmonic steady state, and therefore an experiment producing identical results (within the limits of experimental error) can be repeated many times and the

[1] The nomenclature is employed in both parts 1 [6] and 2.

Contributed by the Applied Mechanics Division for publication in the JOURNAL OF APPLIED MECHANICS.

Discussion on this paper should be addressed to the Editorial Department, ASME, United Engineering Center, 345 East 47th Street, New York, N.Y. 10017, and will be accepted until two months after final publication of the paper itself in the JOURNAL OF APPLIED MECHANICS. Manuscript received by Applied Mechanics Division, March, 1982; final revision, January, 1983.

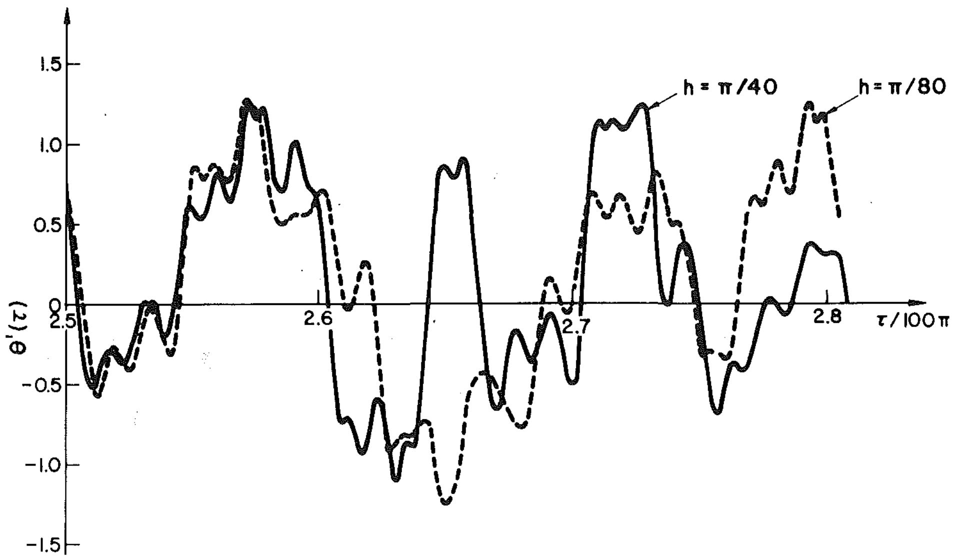

Fig. 1 Response time histories of θ' with different step sizes of integration: $F = 0.05$, $p = 1.0$, $\theta(0) = 0.05$, $\theta'(0) = \eta(0) = \eta'(0) = 0$

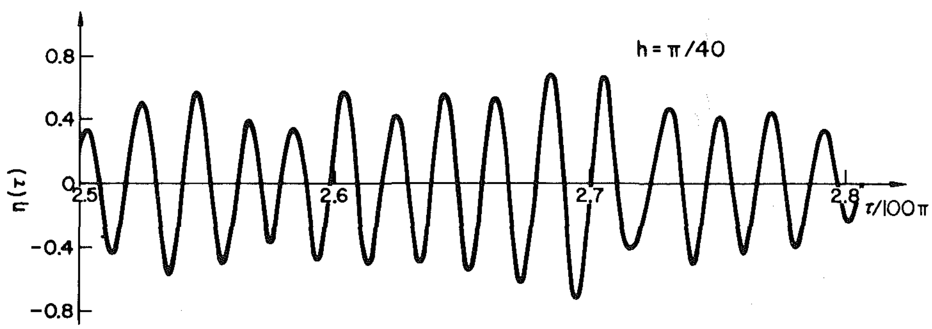

Fig. 2 Response time history of η: $F = 0.05$, $p = 1.0$, $\theta(0) = 0.05$, $\theta'(0) = \eta(0) = \eta'(0) = 0$

responses are deterministic. On the other hand, for the parameter values within or very close to region *III* (Fig. 3[6]), the experimental results cannot be reproduced because of the inherent disturbances that change the responses drastically. These disturbances can only be considered random and the nonperidoic solutions are unstable with respect to these disturbances. So it is impossible to predict the exact value of the response at a future instant of time though the large disturbances die down and the responses remain bounded. Hence the only meaningful description of the integrated response time histories can be attempted by treating these as sample records of a random process.

The following statistical analysis is done for the sample records of θ', instead of θ. This is to avoid confusion as the pendulum is found to make some complete revolutions in either direction without any fixed pattern.

Nomenclature

c_1, c_2 = damping coefficients
F = nondimensional amplitude of the exciting force
$\hat{G}$ = smoothened power spectral density function
h = step size of integration
I = mass moment of intertia of the compound pendulum
k_1 = spring stiffness
l = effective length of the pendulum
M = mass of the primary
m = mass of the pendulum
N = number of data points in the sample record
p = forcing frequency nondimensionalized with respect to the natural frequency of the primary mass
$\bar{p}$ = forcing frequency nondimensionalized with respect to the natural frequency of the locked mass
q = ratio of natural frequencies of the pendulum and the locked mass
R = mass ratio = m/M
$\bar{R}$ = normalized autocorrelation function
r = lag number
s = maximum lag number
t = time
x = displacement of the primary mass
y = displacement of the base of primary mass
Y = amplitude of the base displacement
$\bar{Y}$ = nondimensional amplitude of the base displacement
ζ_1 = damping ratio of the primary mass
$\bar{\zeta}_1$ = damping ratio of the locked mass
ζ_2 = damping ratio of the pendulum
η = nondimensional displacement of the primary mass
θ = angular displacement of the pendulum
θ' = nondimensional angular velocity of the pendulum
τ = nondimensional time = ωt
ω = forcing frequency
$\bar{\omega}$ = $10\,j/s, j = 0, 1, 2, ---, s$ = discrete frequencies at which PSD functions are evaluated

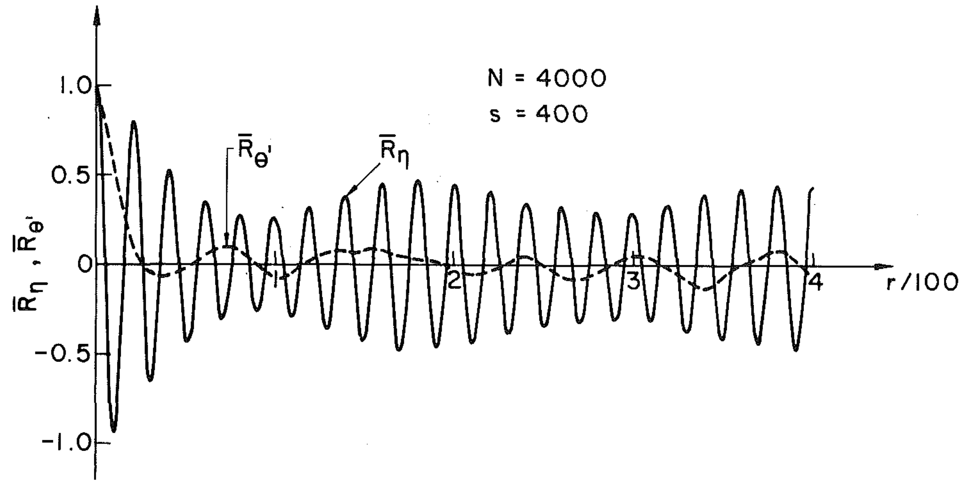

Fig. 3 Autocorrelation function for η and θ': $F = 0.05$, $p = 1.0$, $\theta(0) = 0.05$, $h = \pi/40$

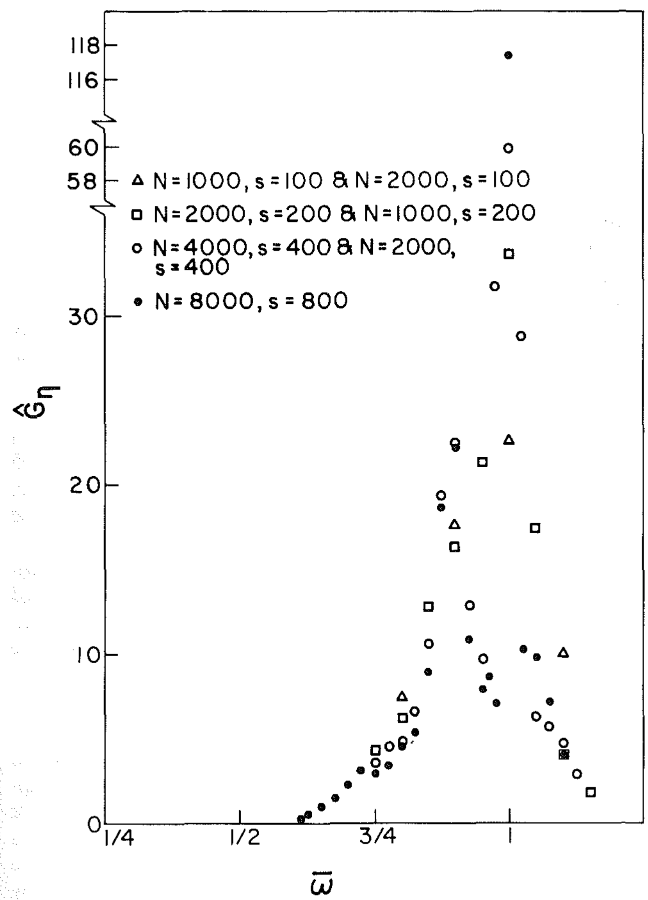

Fig. 4 PSD function for η with different record lengths: $F = 0.05$, $p = 1.0$, $\theta(0) = 0.05$, $h = \pi/40$

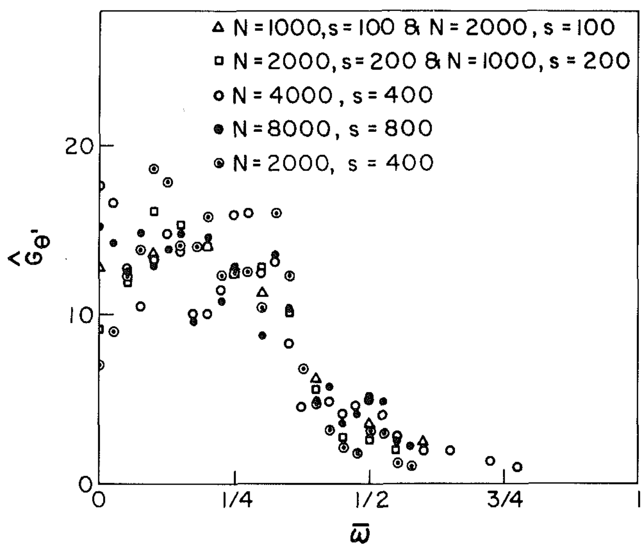

Fig. 5 PSD function for θ' with different record lengths: $F = 0.05$, $p = 1.0$, $\theta(0) = 0.05$, $h = \pi/40$

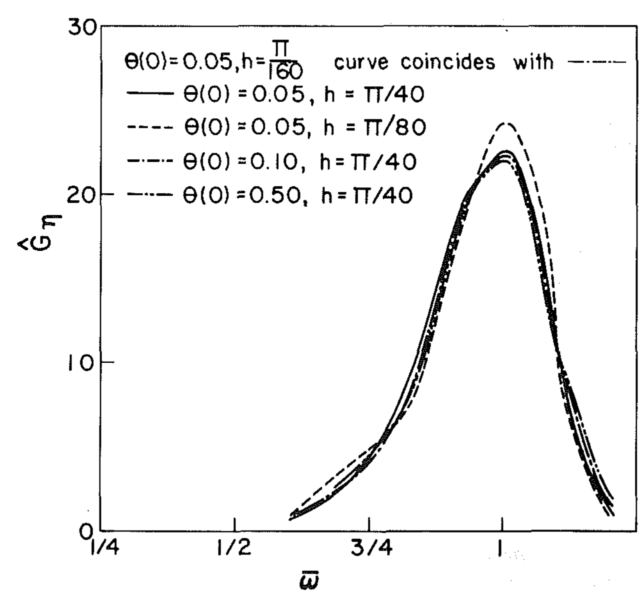

Fig. 6 PSD function for η with different initial conditions and step sizes: $F = 0.05$, $p = 1.0$

3 Statistical Analysis of the Response Time Histories

It was mentioned earlier that the responses depend on the initial conditions and the step size of integration. It is assumed now that with other parameters remaining the same, the integrated response record, for each combination of h and the initial conditions, is a sample record from the same random process. Thus different sample records are obtained by changing h and/or the initial conditions and the statistical quantities are shown to be independent of these parameters.

It is further checked whether these sample records can be treated as the realizations of a weakly ergodic process; in

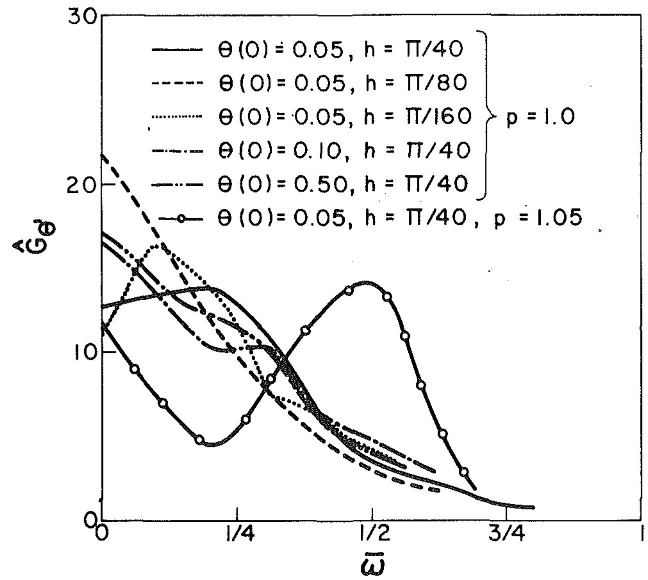

Fig. 7 PSD function for θ' with different initial conditions and step sizes: $F = 0.05$

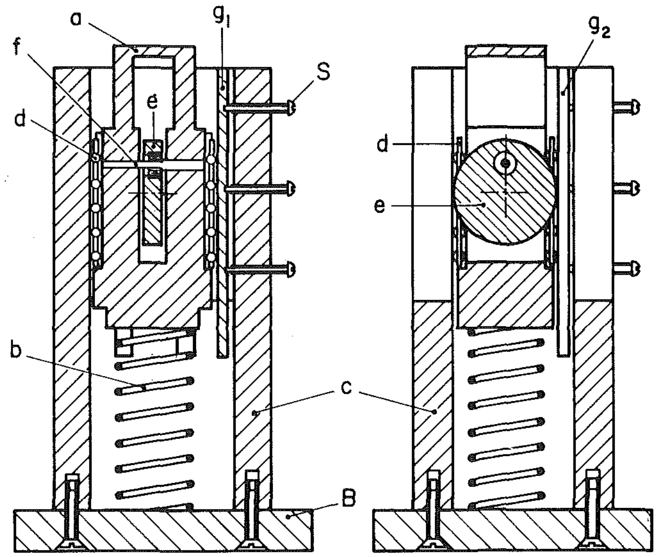

Fig. 9 Sectional views of the experimental model

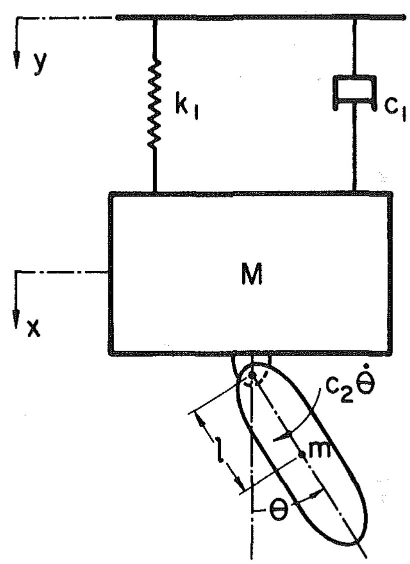

Fig. 8 Mathematical model of the experimental system

other words, if these can be considered to be stationary. By this it is meant that, except for the variations due to normal statistical sampling, the properties computed over short time intervals do not vary significantly from one interval to the next. The stationarity of the random process is tested by considering a single record and computing the mean square values over contiguous short time intervals and performing the "run test" [7]. These run tests are performed for various combinations of parameters and the hypothesis of stationarity is found to be acceptable with 0.05 level of significance [8].

3.1 Results and Discussions. The results are presented for $R = 0.2$, $q = 1/2$, $\zeta_1 = 0.02$, and $\zeta_2 = 0.05$. The parameters varied are F, p, h, and $\theta(0)$. The initial conditions for other coordinates are taken as zero. The data points are taken at interval equal to $\pi/10$.

Figure 3 shows the typical autocorrelograms for η and θ', respectively. Figures 4 and 5 reveal that different values of N and s give the same trend for power spectral density functions (PSD), where $\hat{G}$ represents the smoothened PSD estimate at $s + 1$ discrete frequencies $\bar{\omega}$ [7]. Due to the presence of a periodic component at $\bar{\omega} = 1.0$ the peak of $\hat{G}_\eta$ increases almost proportionately with the increase in the record lengths. Figures 6 and 7 show that with $F = 0.05$, $p = 1.0$ the different combinations of $\theta(0)$ and h (i.e., the independent realizations) yield the same trend of PSD's implying that all the realizations are from the same random process. The variances are also observed to be almost the same for different combinations of h and $\theta(0)$ [8]. Thus, though the integrations do not converge with decreasing step sizes and also the response histories depend on the initial conditions, these differently appearing response histories are sample records from the same ergodic process.

Figure 3 suggests that the sample record of θ' behaves like that of a wide band random process, whereas, the record of η has a strong periodic trend. However, as $\bar{R}\eta$ falls below 0.5 for $r > 20$, the data cannot be considered as deterministic. Figures 4 and 6 show a high content at $\bar{\omega} = 1.0$ (i.e., at the forcing frequency). Figures 5 and 7 indicate low frequency contents for θ'-response. At $p = 1.0$, no periodic component is present in θ'-response and consequently no peak is observed at $\bar{\omega} = 1/2$. At $p = 1.05$, θ'-response has a periodic component at $\bar{\omega} = 1/2$ besides having low frequency contents due to randomness of the motion.

4 Experimental Model

Figures 8 and 9 show the mathematical and experimental models, respectively. In Fig. 9, a is the primary mass supported on the linear spring b. Fixed to the base B is the outside guide block c. The primary mass oscillates freely within this block on strip ball bearings d. On two adjacent faces of the primary mass, the strip bearings are pressed from sides by adjusting plates g_1 and g_2. The screws S are set with an optimum pressure, obtained by trial and error, to ensure free movement of the primary mass. The compound pendulum e is hinged to the shaft f which in turn is fixed to the primary mass. Inertia of the compund pendulum is I and the dampings are idealized as viscous type.

In the nondimensional form the equations of motion for this system are

$$\bar{p}^2\eta'' + 2\bar{\zeta}_1\bar{p}\eta' + \eta = \bar{p}^2 \frac{I_f R}{1+R} (\theta'' \sin\theta + \theta'^2 \cos\theta)$$
$$= \bar{Y}\sqrt{1+(2\,\bar{\zeta}_1\,\bar{p})^2} \cos\bar{\tau} \qquad (1)$$

and

$$\bar{p}^2\theta'' + 2\zeta_2\bar{p}\,q\theta' + (q^2 - \bar{p}^2\eta'')\sin\theta = 0 \qquad (2)$$

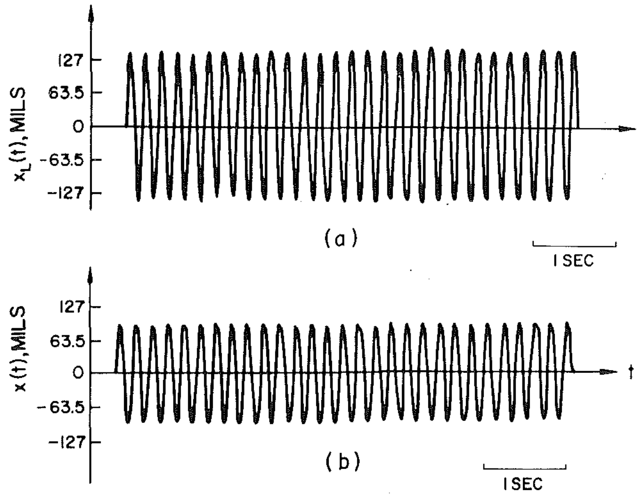

Fig. 10 Response record of the primary at $\bar{p}$ = 0.8: (a) locked mass response x_L (t); (b) primary response x(t) with pendulum oscillating harmonically

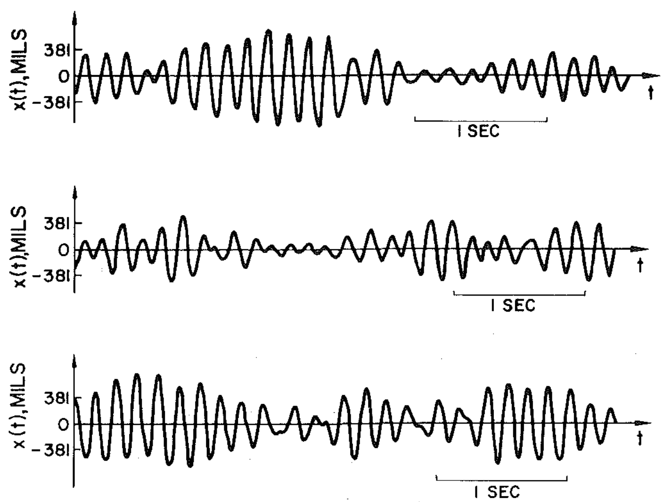

Fig. 11 Primary response x(t) with pendulum oscillating randomly: $\bar{p}$ = 0.97

where

$$\omega_1 = \sqrt{\frac{k_1}{M+m}}, \quad I_f = \frac{m\,1^2}{m\,1^2 + I}, \quad \omega_2 = \sqrt{I_f (g/1)},$$

$$R = m/M, \quad \bar{\zeta}_1 = \frac{c_1}{2\,\omega_1\,(M+m)}, \quad \zeta_2 = \frac{c_2}{2\omega_2\,(m\,1^2 + I)}$$

$$\bar{p} = \frac{\omega}{\omega_1}, \quad q = \frac{\omega_2}{\omega_1}, \quad \eta = I_f\left(\frac{x}{1}\right), \quad \bar{Y} = I_f\left(\frac{Y}{1}\right),$$

$$\bar{\tau} = \omega t + \tan^{-1}(2\,\bar{\zeta}_1\,\bar{p}) \quad \text{and} \quad y = Y\cos\omega t$$

is the base displacement.

For $\bar{\zeta}_1 << 1$ and $\bar{p} \approx 1$ equations (1) and (2) have similar characteristics as those of equations (3) and (4) in reference [6].

The experimental model is mounted on the table of a mechanical vibrator. The table provides a harmonic displacement, independent of the load acting on it. Experiments are conducted to verify the existence of parameters for which, with a certain amplitude of the base excitation, the pendulum, at different frequencies, exhibit the following different motions when disturbed from its static equilibrium postion: The pendulum (*i*) returns to it, (*ii*) reaches a harmonic steady state, or (*iii*) oscillates randomly even after a long time. Measurement of either the displacement or the velocity of the pendulum is quite complicated. Since the quantitative results are not aimed at, the pendulum motion is not measured. Instead the pendulum motion is observed only visually and the response of the primary is recorded. The details of the experimental procedure are reported in reference [8].

4.1 Experimental Results. For the experimental model the values of the parameters are $1 = 1.53$ cm, $I_f = 0.356$, $\bar{\zeta}_1 = 0.044$, $\zeta_2 = 0.005$, $R = 0.305$, $q = 0.375$, and $\bar{p} = 1/6.4\ T$, where T is the time period of the base excitation in seconds.

With $Y = 0.132$ cm ($\bar{Y} = 0.031$) random responses of the primary and the pendulum are observed over a certain frequency range. At low frequencies the static equilibrium position of the pendulum is a stable one and the system oscillates like a locked mass. As the frequency is increased to $\bar{p} = 0.8$, the static equilibrium position of the pendulum becomes unstable. When the pendulum is not disturbed from its equilibrium position, the steady state locked mass response history, x_L (t), is shown in Fig. 10. The nondimensional primary amplitude in this case is 0.083 and 0.084 from experimental and theoretical results, respectively. The pendulum, when disturbed slightly, reaches a harmonic steady state and the primary response, x (t), in this case, is also shown in Fig. 10. The nondimensional primary amplitude obtained from the experiment, is 0.055, whereas, numerical integration yields a stable harmonic steady state as $\eta = 0.076 \cos(\bar{\tau} - 8.6)$, $\theta = 0.45 \cos(\bar{\tau}/2 - 2.5)$.

At $\bar{p} = 0.97$, if the pendulum is disturbed slightly the subsequent pendulum motion does not show any regular pattern even after a long time. It oscillates irregularly for some time and then makes few revolutions. The number and the direction of revolution also do not show any patttern. Consequently the response of the primary ceases to be periodic. The experiment is repeated at the same frequency by stopping the pendulum and then again letting it oscillate. After a lapse of sufficient time, when the transients are expected to die down, the response x (t) is recorded. Three such records at the same frequency ($\bar{p} = 0.97$) are shown in Fig. 11. The records, though having some regularity, are not periodic. This regularity is because the primary is directly driven by the harmonic base excitation. The pendulum motion is observed to be much more irregular and appears to be random in nature. At this excitation frequency the numerical integrations ($\theta(0) = 0.05$, $\eta(0) = \eta'(0) = \theta'(0) = 0$, $h = \pi/40$, $\pi/80$ and $\pi/60$) also do not converge.

For $\bar{p} \geq 1.1$ the static equilibrium position of the pendulum is again a stable one.

5 Conclusions

For the two degree-of-freedom autoparametric system considered, it is shown that for certain combinations of forcing amplitude and frequency the responses become random. Existence of chaotic motion is also verified experimentally. In these cases the numerical integration do not converge; the integrated results can, however, be used to obtain the mean square values and the frequency content of the response. This is achieved by considering the integrated response history as a sample record which is shown to be stationary. The statistical quantities are shown to be independent of the initial conditions and the step size. The statistical quantities, of course, depend on the values of the system parameters like F and p. The primary mass, being excited directly, has a response with a strong periodic component at the forcing frequency. The pendulum response has a wider spectrum and it may or may not have a periodic component at half the forcing frequency.

References

1 May, R. M., "Simple Mathematical Models With Very Complicated Dynamics," *Nature*, Vol. 261, 1976, pp. 459–467.

2 Lorenz, E. N., "Deterministic Nonperiodic Flow," *Journal of the Atmospheric Sciences*, Vol. 20, 1963, pp. 130–141.

3 Holmes, P. J., "A Nonlinear Oscillator With a Strange Attractor," *Philosophical Trans. of Royal Society*, London, Vol. 292, No. 1394, Oct. 1979, pp. 419–448.

4 Moon, F. C., and Holmes, P. J., "A Magnetoelastic Strange Attractor," *Journal of Sound and Vibration*, Vol. 65, No. 2, 1979, pp. 276–296.

5 Moon, F. C., "Experiments on Chaotic Motions of a Forced Nonlinear Oscillator: Strange Attractors," ASME Journal of Applied Mechanics, Vol. 47, 1980, pp. 638–644.

6 Hatwal, H., Mallik, A. K., and Ghosh, A., "Forced Nonlinear Oscillations of an Autoparametric System—Part 1: Periodic Responses," ASME Journal of Applied Mechanics, Vol. 50, 1983, pp. 657–662.

7 Bendat, J. S., and Piersol, A. G., *Random Data: Analysis and Measurement Procedures*, Wiley, New York, 1971.

8 Hatwal, H., "Nonlinear Oscillations of Harmonically Excited Autoparametric Systems," Ph.D. Thesis, Indian Institute of Technology, Kanpur, Sept. 1981.

P. K. C. Wang[1]
Professor.

J. C. Sarina
Graduate Student.

Department of System Science,
University of California,
Los Angeles, Calif. 90024

Control of Reflector Vibrations in Large Spaceborne Antennas by Means of Movable Dampers

A simple approach to the design of feedback controls for damping the vibrations in large spaceborne antennas with flexible dish reflectors is proposed. The feedback controls consist of movable velocity-feedback dampers whose positions are determined by minimizing the rate of change of total vibrational energy at any time. The performance of the proposed feedback controls is studied via computer simulations.

1 Introduction

In the design of deployable spaceborne antennas with large flexible dish-reflectors, it is of importance to damp out the reflector vibrations induced by external disturbances and/or spacecraft motions as quickly as possible so that the antenna performance will not be degraded. It has been proposed that active feedback controls be used to damp out the vibrations [1-3]. Unfortunately, such controls are not readily implementable due to their complexity. Moreover, the simultaneous actuation of controls may induce unbalanced forces and moments on the spacecraft, and serious problems may arise if the control system malfunctions. To damp out the dish vibrations, it is desirable to dissipate the dish's vibrational energy as quickly as possible. Ideally, the dish should be made of light-weight rigid material having large internal structural damping so that, in effect, we have a spatially distributed damper. Lacking such material, it is of interest to design simple reliable control systems for damping the dish vibrations.

In this paper, we propose to use feedback controls consisting of movable dampers whose positions are determined by minimizing the rate of change of total vibrational energy at any time. We begin with the introduction of the basic mathematical model for dish vibrations. Then, various forms of movable dampers are discussed. Their performance is studied using computer-simulated models.

2 Mathematical Model

Consider a circular dish whose vibratory motions about a given static equilibrium configuration (for example, a parabolic cross-sectional profile) is describable by the following wave equation:

$$\rho w_{tt} = \nabla \cdot (T \nabla w) + f \tag{1}$$

defined on the spatial domain $\Omega = \{(r, \theta): 0 \leq \theta \leq 2\pi, 0 < r_{in} < r < r_0\}$ as shown in Fig. 1, where w is the displacement about the static equilibrium; $\rho = \rho(r, \theta)$ is the mass density; $T = T(r, \theta)$ is the tension, and f corresponds to the control or a damping force. The lettered subscripts denote partial differentiation. In polar coordinates, equation (1) has the explicit form:

$$\rho w_{tt} = (Tw_r)_r + Tr^{-1} w_r + r^{-1}(r^{-1} Tw_\theta)_\theta + f. \tag{2}$$

Assuming that the dish is clamped at the inner and outer rims, the boundary conditions are

$$w(t, r_0, \theta) = w(t, r_{in}, \theta) = 0 \quad \text{for all } t \text{ and } 0 \leq \theta \leq 2\pi. \tag{3}$$

In addition to (3), we have the periodicity requirement:

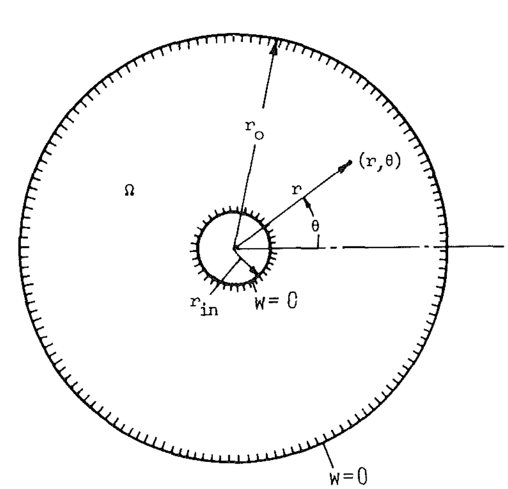

Fig. 1 Spatial domain of the dish reflector

[1]Consultant, Jet Propulsion Laboratory, California Institute of Technology, Pasadena, Calif.

Contributed by the Applied Mechanics Division for publication in the JOURNAL OF APPLIED MECHANICS.

Discussion on this paper should be addressed to the Editorial Department, ASME, United Engineering Center, 345 East 47th Street, New York, N.Y. 10017, and will be accepted until two months after final publication of the paper itself in the JOURNAL OF APPLIED MECHANICS. Manuscript received by ASME Applied Mechanics Division, October, 1982; final revision, March, 1983.

$$w(t,r,0)=w(t,r,2\pi) \quad \text{for } r_{in}<r<r_0. \tag{4}$$

Let $v = w_t$ and $\bar\Omega = \Omega \cup \partial\Omega$, where $\partial\Omega$ is the boundary of Ω. We assume that ρ and T are given real-valued positive continuous functions defined on $\bar\Omega$. Moreover, T is continuously differentiable on $\bar\Omega$. Equations (1) or (2) can be rewritten in the form of an evolution equation:

$$\frac{d}{dt}\begin{bmatrix} w(t,\bullet) \\ v(t,\bullet) \end{bmatrix} = \mathbf{A}\begin{bmatrix} w(t,\bullet) \\ v(t,\bullet) \end{bmatrix} + \begin{bmatrix} 0 \\ f(t,\bullet) \end{bmatrix}, \tag{5}$$

with

$$\mathbf{A} = \begin{bmatrix} 0 & I \\ \rho^{-1}\nabla\bullet(T\nabla) & 0 \end{bmatrix} \tag{6}$$

defined on a suitable state space Σ.

Let $H^m(\Omega)$ denote the real Sobolev space of integral order $m>0$ defined by $H^m(\Omega) = \{u(\bullet): \|u\|_{H^m(\Omega)} < \infty\}$, where $\|u\|_{H^m(\Omega)}$ is the norm induced by the inner product:

$$\langle u,\tilde u\rangle_{H^m(\Omega)} = \sum_{|\alpha|\le m}\int_\Omega D^\alpha u D^\alpha \tilde u \, d\Omega, \tag{7}$$

where $\boldsymbol\alpha = (\alpha_1, \alpha_2)$ is a vector with non-negative integral components; $|\alpha| = \alpha_1 + \alpha_2$ and $D^{|\alpha|}u = \partial^{|\alpha|}u/\partial x_1{}^{\alpha_1} x_2^{\alpha_2}$, $\mathbf{x} = (x_1, x_2) \in \Omega$. The completion of

$$C_0(\bar\Omega) = \bigcap_{k=0}^{\infty} C_0^k(\bar\Omega) \text{ in } H^m(\Omega)$$

is denoted by $H_0^m(\Omega)$, where $C_0^k(\bar\Omega)$ is the set of all real-valued functions vanishing on the boundary $\partial\Omega$ and having continuous partial derivatives up to order k in $\bar\Omega$. Let $\mathcal{H}_1$ and $\mathcal{H}_2$ denote the spaces $H_0^1(\Omega) \oplus H^0(\Omega)$ and $(H^2(\Omega) \cap H_0^1(\Omega)) \oplus H_0^1(\Omega)$, respectively, with their inner products given by

$$\langle (w_1,v_1),(w_2,v_2)\rangle_{\mathcal{H}_1} = \int_\Omega (T\nabla w_1 \bullet \nabla w_2 + \rho v_1 \bullet v_2)d\Omega, \tag{8a}$$

$$\langle (w_1,v_1),(w_2,v_2)\rangle_{\mathcal{H}_2} = \langle w_1,w_2\rangle_{H^2(\Omega)} + \langle v_1,v_2\rangle_{H^1(\Omega)}. \tag{8b}$$

For the undamped system ($f = 0$), we may take the state space $\Sigma = \mathcal{H}_1$ and $D(\mathbf{A})$ (the domain of $\mathbf{A}$) as $\mathcal{H}_2$. In this case, it is well known [4–6] that $\mathbf{A}$ generates a strongly continuous group on Σ, or (5) and (6) define a dynamical system on Σ. Moreover, the inner product (8a) induces an "energy norm" $\|(w,v)\|_{\mathcal{H}_1} = \sqrt{\langle (w,v),(w,v)\rangle_{\mathcal{H}_1}}$ which is well defined along each system trajectory. In what follows, we will consider various simple physically implementable feedback controls of the form $f = B(t)v$ such that the resulting operator

$$\tilde{\mathbf{A}}(t) = \mathbf{A} + \begin{bmatrix} 0 & 0 \\ 0 & B(t) \end{bmatrix}$$

with domain $D(\tilde{\mathbf{A}}(t)) = \mathcal{H}_2$ for all $t \ge 0$ generates a strongly continuous semigroup on $\Sigma = \mathcal{H}_1$. Furthermore, the resulting dynamical system is dissipative in the sense that the energy $\|(w(t), v(t))\|^2_{\mathcal{H}_1}/2$ along each trajectory decays to zero as $t \to \infty$.

3 Feedback Controls

First, consider the total energy of the system at any time given by

$$\mathcal{E}(t) = \|(w,v)\|^2_{\mathcal{H}_1}/2 = \frac{1}{2}\int_\Omega \{\rho|w_t|^2 + T|\nabla w|^2\}d\Omega$$

$$= \frac{1}{2}\int_0^{2\pi}\int_{r_{in}}^{r_0} \{\rho|w_t|^2 + T(|w_r|^2 + |r^{-1}w_\theta|^2)\}r\,dr\,d\theta. \tag{9}$$

Using (2)–(4) and integration by parts, it can be readily verified that the time rate of change of total energy is simply

$$\dot{\mathcal{E}}(t) = \int_0^{2\pi}\int_{r_{in}}^{r_0} f(t,r,\theta)w_t(t,r,\theta)r\,dr\,d\theta. \tag{10}$$

A possible approach to vibration damping is to choose the control or damping force f in a given admissible class such that $d\mathcal{E}(t)/dt$ is minimized [7–8]. Consequently, the vibrational energy $\mathcal{E}(t)$ is reduced as quickly as possible. A simple choice for f is a spatially distributed feedback control in the form of a linear damping force given by

$$f(t,r,\theta) = -g(t,r,\theta)w_t(t,r,\theta), \tag{11}$$

where g is a non-negative damping coefficient. Assuming that g is a piecewise continuous function defined for all $(t, r, \theta) \in Q = [0, \infty] \times \bar\Omega$, and $g(t, r, \theta) > 0$ almost everywhere in Q, it can be verified (following [6] with minor modifications) that the operator

$$\tilde{\mathbf{A}}(t) = \mathbf{A} + \begin{bmatrix} 0 & 0 \\ 0 & -g(t,r,\theta)I \end{bmatrix}$$

with domain $D(\tilde{\mathbf{A}}(t)) = \mathcal{H}_2$ for all $t \ge 0$ generates a strongly continuous semigroup on $\mathcal{H}_1$. Moreover, it is dissipative, since

$$\langle \tilde{\mathbf{A}}(t)\begin{bmatrix} w_1 \\ v_1 \end{bmatrix}, \begin{bmatrix} w_1 \\ v_1 \end{bmatrix}\rangle_{\mathcal{H}_1}$$

$$= \int_\Omega \{T\nabla v_1 \bullet \nabla w_1 + [\nabla\bullet(T\nabla w_1) + \rho B(t)v_1]\bullet v_1\}d\Omega$$

$$= -\int_\Omega v_1 \bullet \nabla\bullet(T\nabla w_1)d\Omega + \int_\Omega [\nabla\bullet(T\nabla w_1)]\bullet v_1 d\Omega$$

$$-\int_\Omega \rho g(t,r,\theta)|v_1|^2 d\Omega = -\int_\Omega \rho g(t,r,\theta)|v_1|^2 d\Omega \le 0. \tag{12}$$

Thus, equation (11) represents an effective damper for (5). Unfortunately, such a control or damper is difficult to realize physically. Therefore, we will consider various restricted forms of (11) that are amenable to physical implementation.

3.1 Patch Damper. In silencing a large drum, we observe that the drummer usually puts some form of dampers (e.g., hands or damping pads) over certain portions of the drum's vibrating surface. Here, the dampers are only effective over certain portions of the drum surface. We may ask: where should the drummer place the dampers to silence the drum as quickly as possible? This suggests the following optimization problem:

Let $\Omega_c(t)$ denote the effective region for the control or damping force at time t. We assume that

$$f(t,r,\theta) = \begin{cases} -gw_t(t,r,\theta) & \text{on } \Omega_c(t) \subset \Omega, \\ 0 & \text{on } \Omega - \Omega_c(t), \end{cases} \tag{13}$$

where g is a specified real positive number, and the area of $\Omega_c(t)$ is fixed. We define $\mathcal{U}_{ad}$, the set of all admissible $\Omega_c(t)$'s, as the set of all subsets of Ω such that measure $\Omega_c(t) = \alpha$ (modulo sets of measure zero), where α is a given positive number. Find a $\Omega_c(t) \in \mathcal{U}_{ad}$ such that

$$\dot{\mathcal{E}}(t) = \int_\Omega f(t,r,\theta)w_t(t,r,\theta)d\Omega$$

$$= -\int_{\Omega_c(t)} g|w_t(t,r,\theta)|^2 d\Omega \tag{14}$$

takes on its minimum value.

This problem has a simple solution. For a given fixed t, consider the level sets Γ_β of the function $p = |w_t(t,r,\theta)|^2$ on Ω as defined by

$$\Gamma_\beta = \{ (r,\theta)\in\Omega: p(r,\theta) < \beta\}, \quad \beta \text{ a real number.} \tag{15}$$

Then an optimal choice for $\Omega_c(t)$ is given by a level set $\Gamma_\beta 0$ such that measure $\Gamma_\beta{}^o = \alpha$ (see [9, 10] for justification of this result). Physically, this result implies that the control or damping force should be applied over a region where the vibration speed (or the kinetic energy, in the case of a dish with uniform density) is the highest, provided that α is sufficiently small. This agrees with the intuitive deduction that the damping force should be applied over the region where the dish vibrates the most. Note that $\Gamma_\beta{}^o$ may be composed of disconnected sets. A more realistic approach is to take $\mathfrak{U}_{ad}$ as the set of all $\Omega_c(t)$'s corresponding to translations of a given nonempty subset $\Omega_{co} \subset \Omega$ such that $\Omega_c(t) \subset \Omega$. The complexity of this problem depends on the geometric shape of Ω_{co}. In what follows, we will consider a simple, but useful specialized case.

3.2 Sweeping Damper. Let $\Omega_{co} = \{ (r, \theta): 0 < r_{in} < r < r_0; 0 \le \theta \le \theta_0 < 2\pi\}$, where θ_0 is a given aperture angle. We define $\Omega_c(\delta(t))$ as a rotation of Ω_{co} given by

$$\Omega_c(\delta(t)) = \{(r,\theta): 0<r_{in}<r<r_0; \delta(t) \le \theta \le \theta_0 + \delta(t)\} \tag{16}$$

corresponding to the effective region for the control or damping force specified by (16). The rotation angle $\delta(t)$ is to be chosen to achieve rapid damping of the dish vibrations. This form of control or damper can be implemented physically by a rotating arm equipped with suitable vibration damping material in close contact with the dish surface as shown in Fig. 2. Thus, we have, in effect, a sweeping passive damper. The simplest form of sweeping damper is one in which the damper arm rotates at a constant speed. In a space environment, it may be desirable to rotate the damper arm only when the vibration amplitude is sufficiently large. We may also optimize the damper arm position by considering the rate of change of the total energy corresponding to this form of damper given by

$$\dot{\mathcal{E}}(t,\delta(t)) = -\int_{\delta(t)}^{\theta_0+\delta(t)} q(t,\theta)d\theta = -\int_0^{\theta_0} q(t,\theta+\delta(t))\,d\theta, \tag{17a}$$

where

$$q(t,\theta) = \int_{r_{in}}^{r_0} g\,|w_t(t,r,\theta)|^2 r\,dr. \tag{17b}$$

Here, we choose $\delta(t)\in\mathbb{R}$ to minimize $\dot{\mathcal{E}}(t, \delta(t))$. Since the function $w_t = w_t(t,r,\theta)$ is periodic in θ with period 2π, we may restrict $\delta(t)$ to the interval $[0, 2\pi]$. Evidently, $\dot{\mathcal{E}} = \dot{\mathcal{E}}(t, \delta(t))$ is continuous with respect to $\delta(t)$ on the compact interval $[0, 2\pi]$. Hence there exists a $\delta(t) = \delta^*(t)\,\mathcal{E}\,[0, 2\pi]$ that minimizes $\dot{\mathcal{E}}(t, \delta(t))$. However, the minimum point $\delta^*(t)$ may not be unique. When $w_t = w_t(t,r,\theta)$ is a continuous periodic function of θ on $\mathbb{R}$ with period 2π, $\dot{\mathcal{E}} = \dot{\mathcal{E}}(t, \delta(t))$ is differentiable with respect to $\delta(t)$. Thus, a necessary condition for $\delta^*(t)$ to be a minimum point is:

$$\frac{\partial\dot{\mathcal{E}}(t,\delta(t))}{\partial[\delta(t)]}\bigg|_{\delta^*(t)} = \int_{r_{in}}^{r_0} g\{\,|w_t(t,r,\delta^*(t))|^2 - |w_t(t,r,\theta_0+\delta^*(t))|^2\}\,r\,dr = 0 \tag{18}$$

or

$$\int_{r_{in}}^{r_0} |w_t(t,r,\delta^*(t))|^2 r\,dr = \int_{r_{in}}^{r_0} |w_t(t,r,\theta_0+\delta^*(t))|^2 r\,dr. \tag{19}$$

This condition implies that at the optimum position of the damper arm, the average values of $|w_t(t, \bullet, \bullet)|^2$ along the two arm edges are equal. When $w_t = w_t(t, r, \theta)$ is a continuously differentiable periodic function of θ on $\mathbb{R}$ with period 2π for fixed t and r, $\dot{\mathcal{E}} = \dot{\mathcal{E}}(t, \delta(t))$ is twice differentiable with respect to $\delta(t)$. Consequently, a sufficient condition for $\delta^*(t)$ to be a local minimum point is that

$$\frac{\partial^2\dot{\mathcal{E}}(t,\delta(t))}{\partial[\delta(t)]^2}\bigg|_{\delta^*(t)} = g\bigg\{\frac{\partial}{\partial\theta}\int_{r_{in}}^{r_0} |w_t(t,r,\theta)|^2 r\,dr\bigg|_{\theta=\delta^*(t)} - \frac{\partial}{\partial\theta}\int_{r_{in}}^{r_0} |w_t,(t,r,\theta)|^2 r\,dr\bigg|_{\theta=\theta_0+\delta^*(t)}\bigg\} > 0, \tag{20}$$

or

$$\frac{\partial}{\partial\theta}\bigg\{\int_{r_{in}}^{r_0} |w_t(t,r,\theta)|^2 r\,dr\bigg\}\bigg|_{\theta=\delta^*(t)} > \frac{\partial}{\partial\theta}\bigg\{\int_{r_{in}}^{r_0} |w_t(t,r,\theta)|^2 r dr\bigg\}\bigg|_{\theta=\theta_0+\delta^*(t)} \tag{20}$$

This condition implies that the rate of change of the average value of $|w_t(t, \bullet, \bullet)|^2$ along the arm edge $\theta = \delta^*(t)$ with respect to θ is greater than that along the arm edge $\theta = \theta_0 + \delta^*(t)$. The determination of the behavior of the minimum point $\delta^*(t)$ with respect to t is a difficult task. We expect that δ^* may be a discontinuous function of t, since the oscillatory nature of $w = w(t, r, \theta)$ with respect to t and θ may cause the optimum position of the damper arm to switch from one portion of the disk to another.

It is useful to derive the modal representation of the equation of motion for the dish with a sweeping damper and with constant ρ and T. Consider the Laplacian operator

$$\gamma^2\nabla^2 w = \gamma^2(w_{rr} + r^{-1}w_r + r^{-2}w_{\theta\theta}) \tag{21}$$

with domain $H_0^2(\Omega)$ where $\gamma^2 = T/\rho > 0$. It is well known [11] that this operator is self-adjoint in $L^2(\Omega)$ and its spectrum is purely discrete, real, and negative. Moreover, its orthonormalized eigenfunctions $\phi_{mn} = \phi_{mn}(r, \theta)$ corresponding to eigenvalue $-\lambda_{mn}$ given by

$$\Theta_m(\theta) = R_{mn}(r)\,\Theta_m(\theta), \quad m,n = 1,2,\ldots, \tag{22a}$$

$$R_{mn}(r) = A_{mn}\{J_m(\lambda_{mn}r/\gamma) - [J_m(\lambda_{mn}r_{in}/\gamma)/Y_m(\lambda_{mn}r_{in}/\gamma)]Y_m(\lambda_{mn}r/\gamma)\}, \tag{22b}$$

$$\Theta_m(\theta) = \pi^{-\frac{1}{2}}\cos(m\theta+\psi_m), \tag{22c}$$

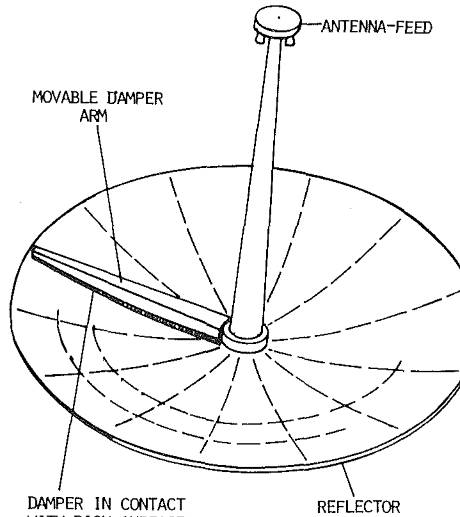

Fig. 2 Sketch of dish reflector with a movable damper (the damper may also be placed on the backside of the reflector for reducing its effect on the antenna characteristics)

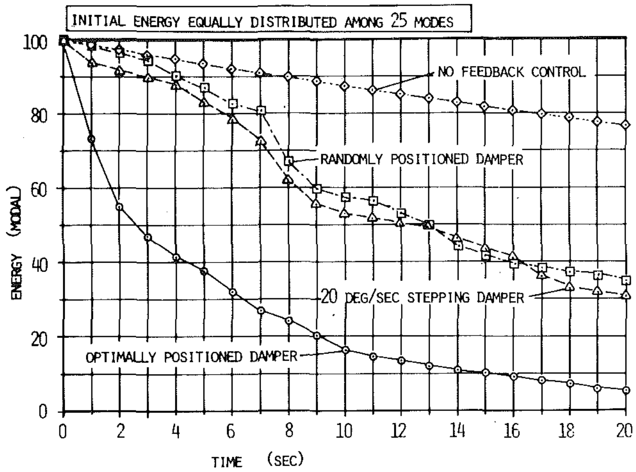

Fig. 3(*a*)

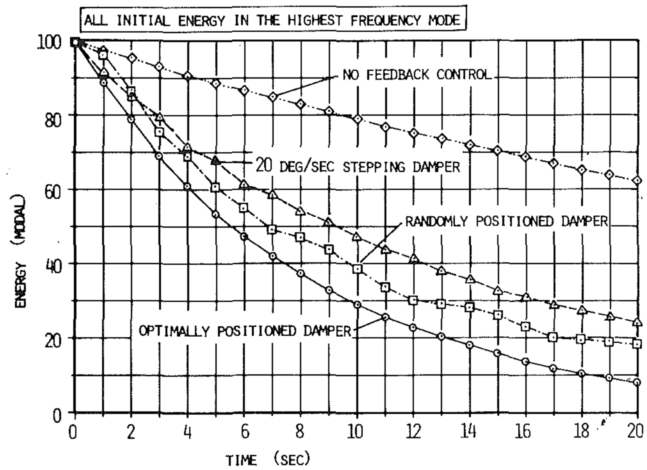

Fig. 3(*b*)

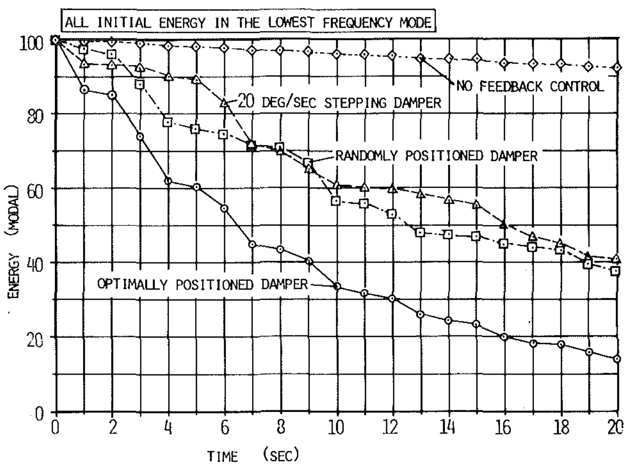

Fig. 3(*c*)

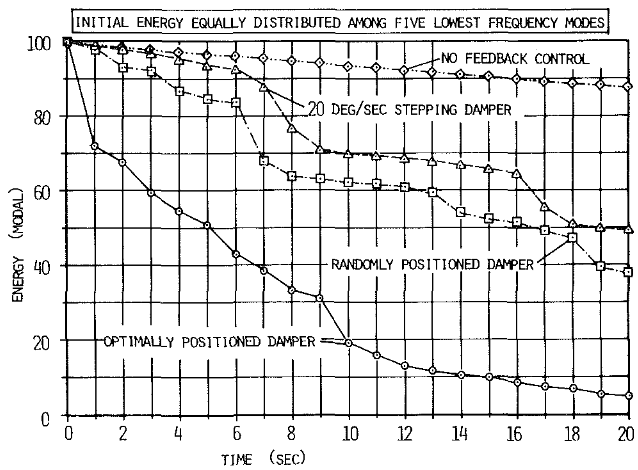

Fig. 3(*d*)

Fig. 3 Energy decay for various initial energy distributions and different forms of movable dampers

Table 1 Eigenvalues λ_{mn}, $m,n=1,\ldots,5$ for $\rho=0.05$ kg/m^2, $T=8.9$ kg/sec^2, $r_{in}=1$ m and $r_0=51$ m

$n \backslash m$					
1	1.003561	1.839108	2.669140	3.498581	4.328277
2	1.343446	2.201984	3.039824	3.870689	4.698590
3	1.669067	2.553370	3.404627	4.243911	5.077489
4	1.985120	2.894538	3.759853	4.608258	5.448244
5	2.294629	3.227786	4.107166	4.965010	5.812149

$$A_{mn} = \sqrt{2}/[r_0 p(r_0) - r_{in} p(r_{in})], \tag{22d}$$

where

$$p(r) = J_{m-1}(\lambda_{mn} r/\gamma) - [J_m(\lambda_{mn} r/\gamma) / Y_m(\lambda_{mn} r/\gamma)] Y_{m-1}(\lambda_{mn} r/\gamma)] \tag{23}$$

form an orthonormal basis for $L^2(\Omega)$, where J_m and Y_m denote the mth order Bessel function of the first and second kind, respectively. The eigenvalue λ_{mn} is the nth root of the equation:

$$J_m(\lambda r_{in}/\gamma) Y_m(\lambda r_0/\gamma) = J_m(\lambda r_0/\gamma) Y_m(\lambda r_{in}/\gamma). \tag{24}$$

Thus, we can express the solutions to system (2)–(4) (with a sweeping damper and constant T and ρ) in the form:

$$w(t,r,\theta) = \sum_{m,n=1}^{\infty} a_{mn}(t) R_{mn}(r) \Theta_m(\theta). \tag{25}$$

It can be readily verified that the coefficients $a_{mn}(t)$ satisfy the following countably infinite dimensional system of ordinary differential equations:

$$\ddot{a}_{mn}(t) + \lambda_{mn}^2 a_{mn}(t)$$

$$= -g\rho^{-1} \sum_{k,l=1}^{\infty} \cdot \left\{ \int_{\Omega_c(t)} \phi_{mn}(r,\theta) \phi_{kl}(r,\theta) d\Omega \right\} \dot{a}_{kl}(t),$$

$$m,n = 1,2,\ldots. \tag{26}$$

For the case of a sweeping damper with $\Omega_c(t) = \Omega_c(\delta(t))$ given by (14), the damping coefficient corresponding to the integral in (26) can be rewritten as

$$\int_{\Omega_c(\delta(t))} \phi_{mn}(r,\theta) \phi_{kl}(r,\theta) d\Omega$$

$$= \int_{r_{in}}^{r_0} R_{mn}(r) R_{kl}(r) r dr \int_{\delta(t)}^{\theta_0 + \delta(t)} \Theta_m(\theta) \Theta_k(\theta) d\theta. \tag{27}$$

For $k = m$, we have

$$\int_{r_{in}}^{r_0} R_{mn}(r)R_{ml}(r)rdr = \begin{cases} 1 & \text{when } n=l, \\ 0 & \text{otherwise,} \end{cases} \tag{28}$$

$$\Delta_m(t) \triangleq \int_{\delta(t)}^{\theta_0+\delta(t)} |\Theta_m(\theta)|^2 d\theta = \frac{1}{2\pi}\{\theta_0 - m^{-1}\sin^2 m\theta_0 \sin[2(m\delta(t)+\psi_m)] + (2m)^{-1}\sin(2m\theta_0)[1-2\sin^2(m\delta(t)+\psi_m)]\}. \tag{29}$$

Thus, equation (26) becomes:

$$\ddot{a}_{mn}(t) + g\rho^{-1}\Delta_m(t)\dot{a}_{mn}(t) + \lambda_{mn}^2 a_{mn}(t) = -g\rho^{-1}\sum_{\substack{k,l=1\\k\neq m}}^{\infty}\left\{\int_{r_{in}}^{r_0} R_{mn}(r)R_{kl}(r)rdr\int_0^{\theta_0}\Theta_m(\theta+\delta(t))\Theta_k(\theta+\delta(t))d\theta\right\}\dot{a}_{kl}(t), m,n=1,2,\ldots. \tag{30}$$

Evidently, as $m\rightarrow\infty$, the diagonal terms of the damping matrix given by $g\rho^{-1}\Delta_m(t)$ tend to $g\theta_0/(2\pi\rho)$ which is independent of $\delta(t)$.

3.3 Computer Simulation Studies. It is of interest to obtain estimates of the energy decay of the dish with sweeping dampers. Unfortunately, such estimates are not readily obtainable from a priori estimates of the solutions. Therefore we resort to computer simulations for gaining some idea on the performance of various forms of sweeping dampers. Here we use truncated versions of (30) with additional small residual damping terms $g_0\rho^{-1}\dot{a}_{mn}(t)$, where $g_0 = 0.001$. The numerical values for the dish parameters used in the simulation are

$$\rho = 0.05\text{kg/m}^2, \quad T = 8.9\text{kg/sec}^2, \quad r_{in} = 1\text{m}, \; r_0 = 51 \text{ m}$$

and $g = 0.1$. For these parameter values, the eigenvalues λ_{mn} for $m,n = 1, \ldots, 5$ are given in Table 1. In the computer simulations, the dish is partitioned into 36 10 deg sectors. The optimal damper position at each time step is determined by locating a sector with the highest kinetic energy. Here $\delta(t)$ is allowed to take on one of the 36 values. Thus, the resulting $\delta^*(t)$ represents an approximation to the optimal $\delta(t)$. Figure 3 shows the energy decay for various initial kinetic energy distributions and different forms of sweeping dampers including a damper stepping at a constant rate of 20 deg/sec, a randomly positioned damper, and the approximate optimally positioned damper as discussed earlier. In the case of a randomly positioned damper, the set of all admissible $\delta(t)$'s (i.e., $\{0, \pi/18, 2\pi/18, \ldots, 35\pi/18\}$) is uniformly distributed. The selection of the damper position at any time is made with the aid of a random number generator. From the numerical results, it is apparent that in all cases, the total modal energy (first 25 modes) decays monotonically with time. As expected, the fastest energy decay is achieved by the approximate optimally positioned damper.

4 Concluding Remarks

The proposed approach for damping the dish-reflector vibrations in large spaceborne antennas leads to simple vibration dampers or control systems that can be implemented physically. Their effectiveness depends primarily on the performance of the damping mechanism attached to the movable arm for energy dissipation. This mechanism may correspond to a passive or an active velocity feedback control. In the actual physical system, the optimal location for the damper arm of a sweeping damper can be determined by measuring the rate of energy dissipation given by (17). This may be accomplished by using an optical velocity sensor array that radially scans over the entire dish at a rapid rate.

In this paper, a simplified mathematical model is used to illustrate the basic ideas. The proposed approach may also be applied to more complex realistic situations where the dish is constructed from elastic ribs covered with thin flexible material. In this case, movable patch dampers may be more suitable. Finally, in the simplified analysis given here, it has been assumed that the damper arm motion is instantaneous. When the damper arm is driven by an electric motor, we may model the damper-arm motor dynamics by

$$J_0 d^2\delta(t)/dt^2 + k_\delta d\delta(t)/dt = k_\tau u(t), \tag{31}$$

where J_0 is the moment of inertia of the damper-arm and motor rotor; k_τ is a positive torque constant; k_δ is a friction coefficient; and u is the input voltage. It is required to find a feedback control u which minimizes $\mathcal{E}(t,\delta(t))$. The inclusion of the foregoing equation into the mathematical model leads to a new interesting problem in optimal control.

Acknowledgment

The work of the first author was performed at the Jet Propulsion Laboratory, California Institute of Technology, under contract to the National Aeronautics and Space Administration. He also wishes to acknowledge many helpful discussions with Dr. G. Rodriguez of the Jet Propulsion Laboratory.

References

1 Strunce, R. R., and Henderson, T. C., "Application of Modern Modal Controller Design to a Large Space Structure," *Proc. of Second AIAA Symp. on Dynamics and Control of Large Flexible Spacecraft*, Meirovitch, L., ed., AIAA Publications, 1979, pp. 661-675.

2 Caglayan, A. K., VanLandingham, H. F., and Sathe, S. G., "A Procedure for Optimal Control of Flexible Surface Vibrations," *ibid*, pp. 129-144.

3 Balas, M., and Canavin, J., "An Active Modal Control System Philosophy for a Class of Large Space Structures," *Proc. of First AIAA Symp. on Dynamics and Control of Large Flexible Spacecraft*, AIAA Publications, 1977.

4 Chen, Goong, "Control and Stabilization for the Wave Equation in a Bounded Domain," *SIAM J. Control and Optimization*, Vol. 17, No. 1, 1979, pp. 66-81.

5 Slemrod, M., "A Note on Complete Controllability and Stabilizability for Linear Control Systems in Hilbert Space," *SIAM J. Control*, Vol. 12, No. 3, 1974, pp. 500-508.

6 Pazy, A., "Semigroup of Linear Operators and Applications to Partial Differential Equations," Lecture Note. No. 10, Dept. of Math., University of Maryland, College Park, 1974.

7 Komkov, V., *Optimal Control Theory for the Damping of Vibrations of Simple Elastic Systems*, Lecture Notes in Math. No. 253, Springer-Verlag, New York, 1972.

8 Sirazetdinov, T. K., "Analytical Design of Regulators in Processes With Distributed Parameters," *Avtomatika i Telemekhanika*, Vol. 26, No. 9, 1965, pp. 1449-1457.

9 Wang, P. K. C., "On a Class of Optimization Problems Involving Domain Variations," *Proc. International Symp. on New Trends in System Analysis*, Lecture Notes in Control and Information Sciences, No. 2, Springer-Verlag, Berlin, 1977, pp. 49-61.

10 Morris, R. J. T., "Optimal Constrained Selection of a Measurable Subset," *J. Math. Anal. Appl.*, Vol. 70, 1979, pp. 546-562.

11 Courant, R., and Hilbert, D., *Methods of Mathematical Physics*, Vol. II Wiley-Interscience, New York, 1962.

Journal of Applied Mechanics

Brief Notes

A Brief Note is a short paper that presents a specific solution of technical interest in mechanics but which does not necessarily contain new general methods or results. A Brief Note should not exceed 1500 words *or equivalent* (a typical one-column figure or table is equivalent to 250 words; a one line equation to 30 words). Brief Notes will be subject to the usual review procedures prior to publication. After approval such Notes will be published as soon as possible. The Notes should be submitted to the Technical Editor of the JOURNAL OF APPLIED MECHANICS. Discussions on the Brief Notes should be addressed to the Editorial Department, ASME, United Engineering Center, 345 East 47th Street, New York, N. Y. 10017, or to the Technical Editor of the JOURNAL OF APPLIED MECHANICS. Discussions on Brief Notes appearing in this issue will be accepted until two months after publication. Readers who need more time to prepare a Discussion should request an extension of the deadline from the Editorial Department.

Analogy Between Dispersion in Porous Media and in MHD

K. K. Mandal[1], **G. Mandal**[2], **and M. Mandal**[2]

Introduction

Recently Chandrasekhara et al. [1] have studied the asymptotic analysis of the convective diffusion of a solute in a Brinkman flow of a viscous liquid through a porous bed between two parallel horizontal plates. Using the Brinkman equation [2] for flow through porous media they have obtained Darcy velocity profile and calculated the dispersion coefficient taking Taylor's model [3] for convective diffusion. But Taylor's model is asymptotically valid for large time only. Moreover, in many situations is it necesary to study all-time dispersion analysis taking the Brinkman model for the flow. Gill and Sankarasubramanian [4] have constructed a dispersion model which is valid for all time by allowing the dispersion coefficient to vary with time. Following [4], Annapurna and Gupta [5] have studied unsteady MHD convective diffusion taking the Hartmann profile as the velocity profile.

In this Note we have studied the unsteady convective diffusion for a flow through a porous bed between two parallel horizontal plates taking Gill and Sankarasubramanian's model and using the velocity profile of Chandrasekhara et al. [1]. Ultimately, we have reduced our convective diffusion equation to a form that is analogue to that obtained in [5]. A physical explanation justifying this analogy may be given as follows: Both for the Hartmann problem and the Brinkman equation, the liquid is taken to be viscous. It is well known that in the Hartmann flow the Lorentz force opposes the fluid to flow across the magnetic lines of force and thus gives rise to a resistance against the flow. Similarly in the case of flow through a porous medium the granular particles forming the matrix of the medium offer an analogous resistance as the viscous fluid passes through the pores between the granular particles. After obtaining the analogy we have exploited the results of [5] to deduce analogous analytic results.

[1] Reader, and Research Scholar, respectively, Department of Mathematics, University of Burdwan, Burdwan, India.

[2] Lecturer, Department of Physics, Bethune College, Calcutta, India.

Manuscript received by ASME, Applied Mechanics Division, May, 1982; final revision, December, 1982.

Mathematical Formulation and Establishment of Analogy

We consider the laminar flow of a viscous fluid through a porous bed between two infinite parallel plates $y = \pm h$ under the action of a uniform pressure gradient P. Chandrasekhara et al. [1] have obtained the velocity u_x along x-axis (parallel to the plates) for such a flow in the form

$$u_x = Q\left[1 - \frac{\cosh(\sigma y/h)}{\cosh\sigma}\right], \tag{1}$$

where

$$Q = P/\sigma^2, \quad \sigma = h/\sqrt{k}, \quad P = -(h^2/\mu)(\partial p/\partial x). \tag{2}$$

and p is the hydrodynamic pressure. The average velocity $\bar{u}$ is given by

$$\bar{u} = \frac{1}{2h}\int_{-h}^{h} u_x\, dy = Q\left[1 - \frac{\tanh\sigma}{\sigma}\right]. \tag{3}$$

If the solute diffuses in the preceding fully developed flow, the concentration $C(t,x,y)$ of the solute satisfies the convective diffusion equation:

$$\frac{\partial C}{\partial t} + u_x \frac{\partial C}{\partial x} = D\left(\frac{\partial^2 C}{\partial x^2} + \frac{\partial^2 C}{\partial y^2}\right), \tag{4}$$

where the molecular diffusivity D is assumed to be independent of C. We introduce the dimensionless variables

$$\theta = \frac{C}{C_0}, \quad X = \frac{Dx}{h^2\bar{u}}, \quad \tau = \frac{Dt}{h^2}, \quad \eta = \frac{y}{h}, \quad X_s = \frac{Dx_s}{h^2\bar{u}}, \tag{5}$$

where C_0 is the concentration of the initial slug input satisfying

$$C(0,x,y) = C_0 \quad \text{for} \quad |x| \le \frac{1}{2}x_s \quad \text{and} \quad C(0,x,y) = 0$$

$$\text{for } |x| > \frac{1}{2}x_s. \tag{6}$$

We now define a new axial coordinate moving with the average velocity $\bar{u}$ of the flow as $x_1 = x - \bar{u}t$ or $\xi = X - \tau$ in the dimensionless form.

Using (1) and (5) in (4) and transforming to the (τ, ξ, η) coordinate system, we get

$$\frac{\partial\theta}{\partial\tau} + \frac{\sigma}{(\sigma\coth\sigma - 1)}\left[\frac{1}{\sigma} - \frac{\cosh\sigma\eta}{\sinh\sigma}\right]\cdot\frac{\partial\theta}{\partial\xi} = \frac{1}{Pe^2}\cdot\frac{\partial^2\theta}{\partial\xi^2} + \frac{\partial^2\theta}{\partial\eta^2}, \tag{7}$$

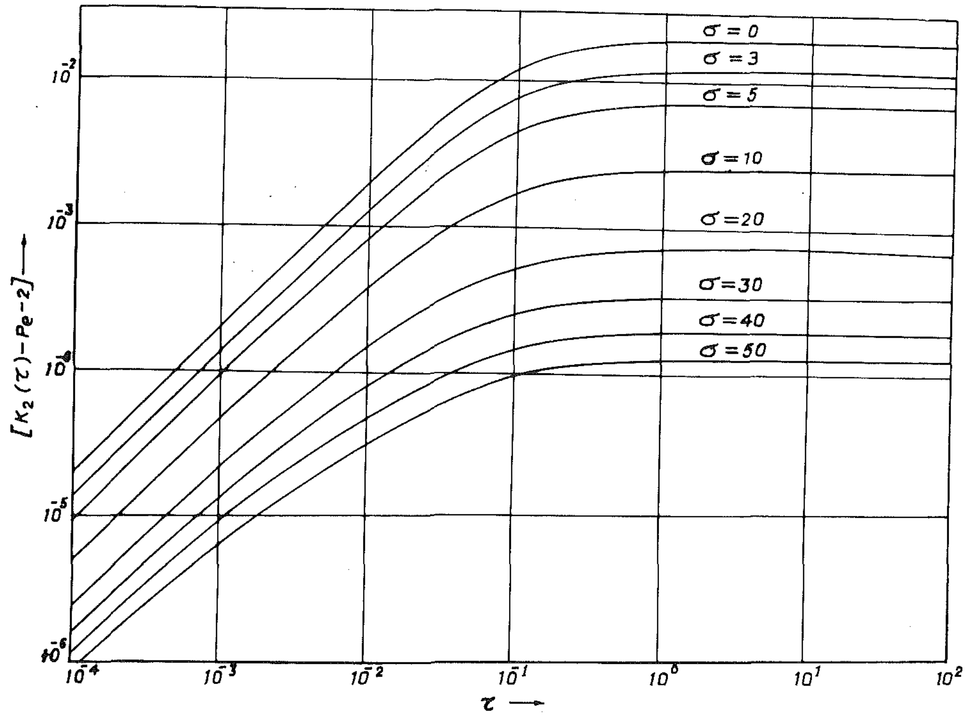

Fig. 1 Plot of $[K_2(\tau) - Pe^{-2}]$ against τ for several values of impermeability parameter, σ

where $Pe(= \bar{u}h/D)$ is the Péclet number. The initial and boundary conditions for (7) are

$$\left.\begin{aligned} &\theta(0,X,\eta)=1 \quad \text{for} \quad |X| \leq \frac{1}{2}X_s, \\ &\theta(0,X,\eta)=0 \quad \text{for} \quad |X| > \frac{1}{2}X_s, \\ &\theta(\tau,\infty,\eta)=0, \\ &\frac{\partial\theta}{\partial\eta}(\tau,X,-1)=\frac{\partial\theta}{\partial\eta}(\tau,X,1)=0 \end{aligned}\right\} \tag{8}$$

where the last two conditions are consistent with no mass transfer at the channel walls.

At this stage we observe that our equation (7) and conditions (8) become identical with the equation (8) and conditions (9), respectively, of [5] only if we replace M in [5] by σ. Thus an analogy between our problem and that discussed in [5] is fully established. Our nondimensional impermeability parameter σ plays the role similar to that of the Hartmann number M in [5].

Following [4] and [5] we expand θ in the form,

$$\theta=\theta_m(\tau,\xi)+\sum_{R=1}^{\infty} f_k(\tau,\eta)\,\frac{\partial^k\theta_m}{\partial\xi k}, \quad \theta_m=\frac{1}{2}\int_{-1}^{+1}\theta\,d\eta, \tag{9}$$

and introduce the generalized dispersion model in the form

$$\frac{\partial\theta_m}{\partial\tau}=\sum_{i=1}^{\infty}K_i(\tau)\,\frac{\partial^i\theta_m}{\partial\xi^i}, \tag{10}$$

to get

$$K_1(\tau)=0, \tag{11}$$

$$K_2(\tau)=\frac{1}{Pe^2}+\frac{1}{(\sigma\coth\sigma-1)^2}\left[\frac{5}{6}+\frac{2}{\sigma^2}-\frac{3\coth\sigma}{2\sigma}-\frac{\coth^2\sigma}{2}\right]$$
$$-\frac{2\sigma^4}{(\sigma\coth\sigma-1)^2}\sum_{n=1}^{\infty}\frac{e^{-n^2\pi^2\tau}}{n^2\pi^2(n^2\pi^2+\sigma^2)^2}. \tag{12}$$

It may be pointed out that higher order dispersion coefficients will decrease in magnitude rapidly and accordingly $K_2(\tau)$ is the most important dispersion coefficient.

Results and Discussion

The authors of [5] concluded from their numerical calculations that for small values of M the values of

$K_2(\tau)-Pe^{-2}$,

$$K_2^*(=\lim_{\tau\to\infty}[K_2(\tau)-Pe^{-2}]), \text{ and } K_3(=\lim_{\tau\to\infty}K_3(\tau))$$

are highly oscillatory and the amplitude of oscillation gradually decays with increase in M. However, they mentioned that the physical reason for such a behavior was somewhat obscure. Also such oscillations are absent in [4]. Moreover, the range of σ [as indicated by Katto and Masuoka [6]) for which the Brinkman equation is valid is wider than the range covered in [5]. Therefore, we have, recalculated the numerical results accurately and widely using double precision variables with the help of Burroughs B 6700 computer. Our calculations show that none of $K_2(\tau)-Pe^{-2}$, K_2^*, and K_3 oscillates for any value of σ which is in conformity with [4]. Consequently we present our numerical results in detail to discuss the effect of impermeability parameter σ on dispersion coefficients $K_2(\tau)-Pe^{-2}$, K_2^*, and K_3. The hydromagnetic analogue of this discussion immediately follows if one replaces σ by M.

Table 1

σ	K_2^*	σ	K_2^*
0	1.9048×10^{-2}	1	1.7854×10^{-2}
0.02	1.9047×10^{-2}	3	1.1845×10^{-2}
0.2	1.8997×10^{-2}	5	7.0743×10^{-3}
0.4	1.8846×10^{-2}	10	2.5103×10^{-3}
0.6	1.8601×10^{-2}	100	3.2500×10^{-5}
0.8	1.8267×10^{-2}	200	8.2292×10^{-6}

The values of K_2^* against σ are shown in Table 1 which shows that with increase in σ, K_2^* monotonically decreases.

Physically, this may be expected from the fact that a decrease in permeability flatens the Darcy velocity profile and thereby decreases dispersion.

Figure 1 shows that for a fixed σ, $[K_2(\tau) - Pe^{-2}]$ first increases with increase in τ and then attains its asymptotic value at a time of order 0.5 for all values of σ. This figure also presents that with increase in σ, $[K_2(\tau) - Pe^{-2}]$ always decreases. The figure further shows that although the attainment of state of steady dispersion remains unaffected by σ, at the initial stage the effect of σ is to reduce the rate of growth of the spreading of the solute.

References

1 Chandrasekhara, B. C., Rudraiah, N., and Nagaraj, S. T., "Velocity and Dispersion in Porous Media," *International Journal of Engineering Science*, Vol. 18, No. 7, 1980, pp. 921–929.

2 Brinkman, H. C., "A Calculation of the Viscous Force Exerted by a Flowing Fluid on a Dense Swarm of Particles," *Applied Scientific Research*, Section *A*, Vol. 1, No. 1, 1947, pp. 27–34.

3 Taylor, G. I., "Dispersion of Soluble Matter in Solvent Flowing Slowly Through a Tube," *Proceeding of the Royal Society*, London, Series *A*, Vol. 219, 1953, pp. 186–203.

4 Gill, W. N., and Sankarasubramanian, R., "Exact Analysis of Unsteady Convective Diffusion," *Proceeding of the Royal Society*, London, Series *A*, Vol. 316, 1970, pp. 341–350.

5 Annapurna, N., and Gupta, A. S., "Exact Analysis of Unsteady MHD Convective Diffusion," *Proceedings of the Royal Society*, London, Series *A*, Vol. 367, 1979, pp. 281–289.

6 Katto, Y., and Masuoka, T., "Criterion for the Onset of Convective Flow in a Fluid in a Porous Medium," *International Journal of Heat and Mass Transfer*, Vol. 10, No. 3, 1967, pp. 297–309.

Tresca's Yield Condition and the Rotating Disk

U. Gamer[1]

The displacement field belonging to the elastic-plastic stress field in a rotating solid disk that can be found with the help of Tresca's yield condition, in textbooks on plasticity, is discontinuous at the elastic-plastic interface. Tresca's yield condition cannot be applied to this problem since its associated flow rule predicts a negative plastic strain caused by a tensile stress.

1 Introduction

The theoretical treatment of elastic-plastic rotating disks was started by F. László in 1925 [1] and since then, interest in this problem has never ceased. Much experimental and theoretical work has been done under various assumptions and the topic has entered many textbooks.

The elastic-plastic stress distribution in a rotating annular disk can be easily calculated with the principle of momentum, Hooke's law, Tresca's yield condition, and the conditions of vanishing radial stress at the free edges of the disk and continuous radial stress at the elastic-plastic interface, respectively [2–4]. Displacement need not be taken into account.

The same approach is usually made for the determination of the elastic-plastic stresses in a rotating solid disk. The condition of vanishing radial stress at the inner free edge of the annulus is replaced with the condition of finite radial stress in the center of the solid disk without consideration of displacement [2–5]. Some authors do not investigate explicitly the elastic-plastic stress distribution but consider only the fully plastic state in order to find the critical angular velocity that causes bursting [6, 7]. C. R. Calladine [7] is interested in deformation and studies the collapse mechanism. He finds: "For a solid disc the mechanism $\dot\epsilon_\theta = \dot u/r$, $\dot\epsilon_z = -\dot u/r$, $\dot\epsilon_r = 0$, gives singularities in the strain increments at the centre, which can be interpreted as a tendency for the disc to 'thin' so much as to produce a small hole very quickly. These singularities are in fact a consequence of the precise angularity of the Tresca yield condition. If a small 'rounding' of the edge could be allowed, the singularity would disappear, because in the immediate vicinity of the centre the stress components σ_r and σ_θ are very close. This somewhat curious state of affairs should not be regarded as reflecting discredit on the Tresca condition; it must always be remembered that our main aim here is to predict bursting speeds."

In the following it is shown that the displacement field in the solid disk derived from the flow rule associated with Tresca's yield condition and the usual stress distribution is discontinuous at the elastic-plastic interface and that it is not possible to receive a meaningful solution with the help of Tresca's yield condition and its associated flow rule at all. The same is true for the spinning solid cylinder in a state of plane strain.

2 Stresses and Displacement in the Elastic and Plastic Region

The distribution of stresses and displacement in a rotating elastic disk are well known. One finds, e.g., in [8]

$$\sigma_{rr} = -\frac{E}{1+\nu}\frac{A}{r^2} + \frac{E}{1-\nu}B - \frac{3+\nu}{8}\rho\omega^2 r^2, \qquad (2.1)$$

$$\sigma_{\theta\theta} = \frac{E}{1+\nu}\frac{A}{r^2} + \frac{E}{1-\nu}B - \frac{1+3\nu}{8}\rho\omega^2 r^2, \qquad (2.2)$$

$$u = \frac{A}{r} + Br - \frac{1-\nu^2}{8E}\rho\omega^2 r^3 \qquad (2.3)$$

where the usual notation has been adopted.

For perfectly plastic material Tresca's yield condition and the principle of momentum give for $\sigma_{\theta\theta} > \sigma_{rr} > \sigma_{zz}$

$$\sigma_{rr} = \sigma_0 - \frac{1}{3}\rho\omega^2 r^2 + \frac{C}{r}, \qquad (2.4)$$

$$\sigma_{\theta\theta} = \sigma_0 \qquad (2.5)$$

with the yield stress σ_0.

Since according to the flow rule there is no radial plastic strain increment, Hooke's law applies for the radial strain

$$\epsilon_{rr} = \frac{1}{E}\left[(1-\nu)\sigma_0 - \frac{1}{3}\rho\omega^2 r^2 + \frac{C}{r}\right]$$

and integration yields

$$u = \frac{1}{E}\left[(1-\nu)\sigma_0 r - \frac{1}{9}\rho\omega^2 r^3 + C\log r + D\right]. \qquad (2.6)$$

The elastic solution shows that onset of plastic flow occurs in the center of the disk. Hence, the plastic zone contains the center, $r = 0$, where σ_{rr} and $\sigma_{\theta\theta}$ have to be equal and finite and u must vanish. Therefore, in the plastic zone of a solid disk $C = D = 0$.

The outer zone behaves elastically according to equations (2.1)–(2.3). The radial stress vanishes at the outer edge, $r = b$, and is continuous at the elastic-plastic interface, $r = z$. There, the displacement has to be continuous, too. Finally, the elastic circumferential stress must reach the yield limit, σ_0, at $r = z$. These conditions read

[1] Professor, Institut für Mechanik, Technische Universität Wien, Karlsplatz 13, A-1040 Wien, Austria.

Manuscript received by ASME Applied Mechanics Division, December, 1982; final revision, February, 1983.

Physically, this may be expected from the fact that a decrease in permeability flatens the Darcy velocity profile and thereby decreases dispersion.

Figure 1 shows that for a fixed σ, $[K_2(\tau) - Pe^{-2}]$ first increases with increase in τ and then attains its asymptotic value at a time of order 0.5 for all values of σ. This figure also presents that with increase in σ, $[K_2(\tau) - Pe^{-2}]$ always decreases. The figure further shows that although the attainment of state of steady dispersion remains unaffected by σ, at the initial stage the effect of σ is to reduce the rate of growth of the spreading of the solute.

References

1 Chandrasekhara, B. C., Rudraiah, N., and Nagaraj, S. T., "Velocity and Dispersion in Porous Media," *International Journal of Engineering Science*, Vol. 18, No. 7, 1980, pp. 921–929.

2 Brinkman, H. C., "A Calculation of the Viscous Force Exerted by a Flowing Fluid on a Dense Swarm of Particles," *Applied Scientific Research*, Section *A*, Vol. 1, No. 1, 1947, pp. 27–34.

3 Taylor, G. I., "Dispersion of Soluble Matter in Solvent Flowing Slowly Through a Tube," *Proceeding of the Royal Society*, London, Series *A*, Vol. 219, 1953, pp. 186–203.

4 Gill, W. N., and Sankarasubramanian, R., "Exact Analysis of Unsteady Convective Diffusion," *Proceeding of the Royal Society*, London, Series *A*, Vol. 316, 1970, pp. 341–350.

5 Annapurna, N., and Gupta, A. S., "Exact Analysis of Unsteady MHD Convective Diffusion," *Proceedings of the Royal Society*, London, Series *A*, Vol. 367, 1979, pp. 281–289.

6 Katto, Y., and Masuoka, T., "Criterion for the Onset of Convective Flow in a Fluid in a Porous Medium," *International Journal of Heat and Mass Transfer*, Vol. 10, No. 3, 1967, pp. 297–309.

Tresca's Yield Condition and the Rotating Disk

U. Gamer[1]

The displacement field belonging to the elastic-plastic stress field in a rotating solid disk that can be found with the help of Tresca's yield condition, in textbooks on plasticity, is discontinuous at the elastic-plastic interface. Tresca's yield condition cannot be applied to this problem since its associated flow rule predicts a negative plastic strain caused by a tensile stress.

1 Introduction

The theoretical treatment of elastic-plastic rotating disks was started by F. László in 1925 [1] and since then, interest in this problem has never ceased. Much experimental and theoretical work has been done under various assumptions and the topic has entered many textbooks.

The elastic-plastic stress distribution in a rotating annular disk can be easily calculated with the principle of momentum, Hooke's law, Tresca's yield condition, and the conditions of vanishing radial stress at the free edges of the disk and continuous radial stress at the elastic-plastic interface, respectively [2–4]. Displacement need not be taken into account.

The same approach is usually made for the determination of the elastic-plastic stresses in a rotating solid disk. The condition of vanishing radial stress at the inner free edge of the annulus is replaced with the condition of finite radial the center of the solid disk without consideration of displacement [2–5]. Some authors do not investigate explicitly the elastic-plastic stress distribution but consider only the fully plastic state in order to find the critical angular velocity that causes bursting [6, 7]. C. R. Calladine [7] is interested in deformation and studies the collapse mechanism. He finds: "For a solid disc the mechanism $\dot{\epsilon}_\theta = \dot{u}/r$, $\dot{\epsilon}_z = -\dot{u}/r$, $\dot{\epsilon}_r = 0$, gives singularities in the strain increments at the centre, which can be interpreted as a tendency for the disc to 'thin' so much as to produce a small hole very quickly. These singularities are in fact a consequence of the precise angularity of the Tresca yield condition. If a small 'rounding' of the edge could be allowed, the singularity would disappear, because in the immediate vicinity of the centre the stress components σ_r and σ_θ are very close. This somewhat curious state of affairs should not be regarded as reflecting discredit on the Tresca condition; it must always be remembered that our main aim here is to predict bursting speeds."

In the following it is shown that the displacement field in the solid disk derived from the flow rule associated with Tresca's yield condition and the usual stress distribution is discontinuous at the elastic-plastic interface and that it is not possible to receive a meaningful solution with the help of Tresca's yield condition and its associated flow rule at all. The same is true for the spinning solid cylinder in a state of plane strain.

2 Stresses and Displacement in the Elastic and Plastic Region

The distribution of stresses and displacement in a rotating elastic disk are well known. One finds, e.g., in [8]

$$\sigma_{rr} = -\frac{E}{1+\nu}\frac{A}{r^2} + \frac{E}{1-\nu}B - \frac{3+\nu}{8}\rho\omega^2 r^2, \tag{2.1}$$

$$\sigma_{\theta\theta} = \frac{E}{1+\nu}\frac{A}{r^2} + \frac{E}{1-\nu}B - \frac{1+3\nu}{8}\rho\omega^2 r^2, \tag{2.2}$$

$$u = \frac{A}{r} + Br - \frac{1-\nu^2}{8E}\rho\omega^2 r^3 \tag{2.3}$$

where the usual notation has been adopted.

For perfectly plastic material Tresca's yield condition and the principle of momentum give for $\sigma_{\theta\theta} > \sigma_{rr} > \sigma_{zz}$

$$\sigma_{rr} = \sigma_0 - \frac{1}{3}\rho\omega^2 r^2 + \frac{C}{r}, \tag{2.4}$$

$$\sigma_{\theta\theta} = \sigma_0 \tag{2.5}$$

with the yield stress σ_0.

Since according to the flow rule there is no radial plastic strain increment, Hooke's law applies for the radial strain

$$\epsilon_{rr} = \frac{1}{E}\left[(1-\nu)\sigma_0 - \frac{1}{3}\rho\omega^2 r^2 + \frac{C}{r}\right]$$

and integration yields

$$u = \frac{1}{E}\left[(1-\nu)\sigma_0 r - \frac{1}{9}\rho\omega^2 r^3 + C\log r + D\right]. \tag{2.6}$$

The elastic solution shows that onset of plastic flow occurs in the center of the disk. Hence, the plastic zone contains the center, $r = 0$, where σ_{rr} and $\sigma_{\theta\theta}$ have to be equal and finite and u must vanish. Therefore, in the plastic zone of a solid disk $C = D = 0$.

The outer zone behaves elastically according to equations (2.1)–(2.3). The radial stress vanishes at the outer edge, $r = b$, and is continuous at the elastic-plastic interface, $r = z$. There, the displacement has to be continuous, too. Finally, the elastic circumferential stress must reach the yield limit, σ_0, at $r = z$. These conditions read

[1] Professor, Institut für Mechanik, Technische Universität Wien, Karlsplatz 13, A-1040 Wien, Austria.

Manuscript received by ASME Applied Mechanics Division, December, 1982; final revision, February, 1983.

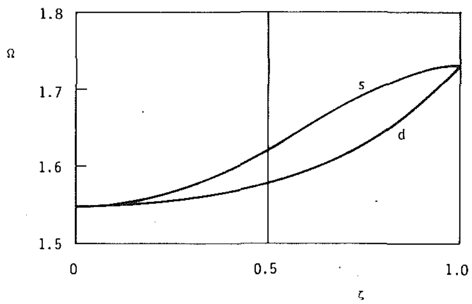

Fig. 1 Angular velocity as a function of elastic-plastic interface radius for continuous stress (s) and continuous displacement (d)

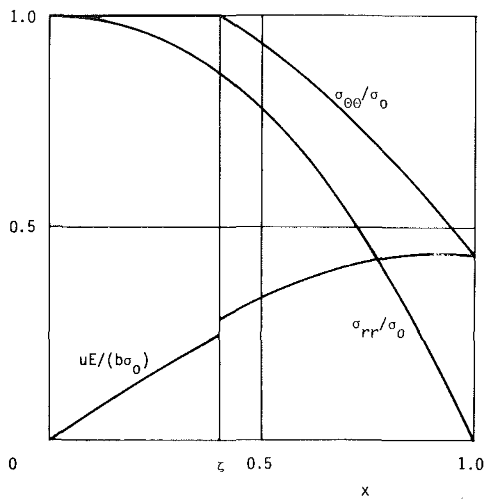

Fig. 2 Stresses and discontinuous displacement as functions of radius for $\Omega^2 = 2.55$

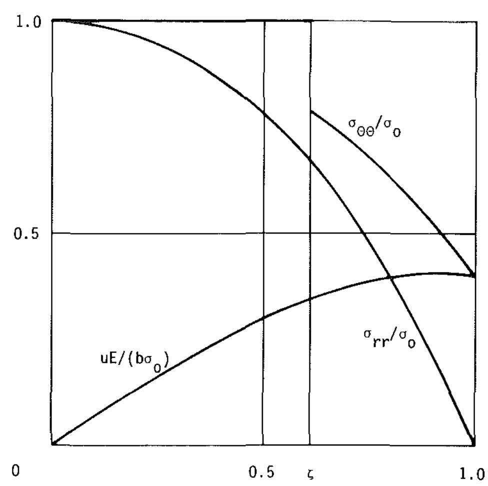

Fig. 3 Radial stress, discontinuous circumferential stress, and displacement as functions of radius for $\Omega^2 = 2.55$

$$-\frac{E}{1+\nu}\frac{A}{b^2}+\frac{E}{1-\nu}B-\frac{3+\nu}{8}\rho\omega^2 b^2=0, \qquad (2.7)$$

$$-\frac{E}{1+\nu}\frac{A}{z^2}+\frac{E}{1-\nu}B-\frac{3+\nu}{8}\rho\omega^2 z^2=\sigma_0-\frac{1}{3}\rho\omega^2 z^2, \quad (2.8)$$

$$\frac{EA}{z^2}+EB-\frac{1-\nu^2}{8}\rho\omega^2 z^2=(1-\nu)\sigma_0-\frac{1}{9}\rho\omega^2 z^2, \qquad (2.9)$$

$$\frac{E}{1+\nu}\frac{A}{z^2}+\frac{E}{1-\nu}B-\frac{1+3\nu}{8}\rho\omega^2 z^2=\sigma_0. \qquad (2.10)$$

Thus, there are four conditions but only three open unknowns A, B and z and there is no solution that satisfies all requirements.

3 Elastic-Plastic Stress Distribution

In the references quoted, displacement and hence the condition of continuity at the elastic-plastic interface is ignored. The conditions (2.7), (2.8), and (2.10) give

$$\Omega^2[(1+3\nu)\zeta^4-2(1+3\nu)\zeta^2+3(3+\nu)]=24, \qquad (3.1)$$

$$\frac{EA}{1+\nu}=\frac{1}{24}(1+3\nu)\rho\omega^2 z^4, \qquad (3.2)$$

$$\frac{EB}{1-\nu}=\sigma_0+\frac{1}{12}(1+3\nu)\rho\omega^2 z^2 \qquad (3.3)$$

where the nondimensional angular velocity $\Omega^2 = \rho\omega^2 b^2/\sigma_0$ and the nondimensional interface radius $\zeta = z/b$ [4].

On the other hand, if the yield condition (2.10) is ignored and substituted by the indispensable condition of continuity of displacement (2.9) there follow the results

$$\Omega^2[-(1+3\nu)\zeta^4-2(1+3\nu)\zeta^2+9(3+\nu)]=72, \qquad (3.4)$$

$$\frac{EA}{1+\nu}=\frac{b^2\zeta^2}{1-\zeta^2}\left\{-\sigma_0+\frac{1}{8}\left[3+\nu-\frac{1}{3}(1+3\nu)\zeta^2\right]\rho\omega^2 b^2\right\}, \qquad (3.5)$$

$$\frac{EB}{1-\nu}=\frac{1}{1-\zeta^2}\left\{-\sigma_0\zeta^2+\frac{1}{8}\left[3+\nu-\frac{1}{3}(1+3\nu)\zeta^4\right]\rho\omega^2 b^2\right\}. \qquad (3.6)$$

4 Numerical Results

For $\nu = 1/3$, Fig. 1 shows the relations between the nondimensional angular velocity $\Omega^2 = \rho\omega^2 b^2/\sigma_0$ and the nondimensional elastic-plastic interface radius $\zeta = z/b$ for continuous circumferential stress (s) and for continuous displacement (d) according to equations (3.1) and (3.4), respectively. The onset of plastic flow, $(\Omega^*)^2 = 8/(3+\nu)$, depends only on the elastic stresses. At the occurrence of unrestricted plastic flow, on the other hand, the elastic region disappears, and the corresponding angular velocity, $(\Omega^{**})^2 = 3$, comes from equation (2.4). So, the two curves coincide for $\zeta = 0$ and $\zeta = 1$.

Figure 2 gives for $\Omega^2 = 2.55$, the nondimensional stresses σ_{ij}/σ_0, and the nondimensional displacement $uE/(b\ \sigma_0)$ in dependence of the nondimensional radius $x = r/b$. At the elastic-plastic interface, $x = \zeta = 0.40$, one recognizes the expected discontinuity of the displacement. Therefore this result is not an admissible solution.

On Fig. 3, also for $\Omega^2 = 2.55$, the second result with discontinuous circumferential stress at $x = \zeta = 0.61$ is shown. This state of stress is certainly admissible but, as a solution to the rotating solid disk problem, it is still unsatisfactory since a small increase of Ω is connected with a jump of $\sigma_{\theta\theta}$: the yield condition is violated. So, neither of the two results solves the problem.

5 Plastic Strain

The plastic circumferential strain is the difference between the total strain that follows from equation (2.6)

$$\epsilon_{\theta\theta}=\frac{1}{E}\left[(1-\nu)\sigma_0-\frac{1}{9}\rho\omega^2 r^2+\frac{C}{r}\log r+\frac{D}{r}\right] \qquad (5.1)$$

and the elastic strain according to Hooke's law

$$\epsilon^{el}_{\theta\theta}=\frac{1}{E}\left[(1-\nu)\sigma_0+\frac{\nu}{3}\rho\omega^2 r^2-\frac{\nu C}{r}\right],$$

$$\epsilon_{\theta\theta}^{pl} = \frac{1}{E}\left[-\frac{1}{9}(1+3\nu)\rho\omega^2 r^2 + \frac{C}{r}(\log r + \nu) + \frac{D}{r}\right]. \qquad (5.2)$$

In the case of the solid disk, C and D have to vanish and therefore, at the center, $r = 0$, where the stress is largest there is no plastic strain at all and outside of it the plastic strain belonging to a tensile stress is negative [9]! The conclusion is that the stress distribution based on Tresca's yield condition cannot be meaningful even in the totally plastic disk where the problem of violated continuity does not arise.

In the related problem of the spinning solid shaft with free ends in the elastic state the relations

$$\sigma_{\theta\theta} > \sigma_{rr} > \sigma_{zz} \quad \text{for} \quad 0 < r \leq b$$

$$\sigma_{\theta\theta} = \sigma_{rr} > \sigma_{zz} \quad \text{for} \quad r = 0$$

hold as in the spinning elastic disk. The yield condition

$$\sigma_{\theta\theta} - \sigma_{zz} = \sigma_0,$$

of which equation (2.5) is a special case, leads to similar results concerning the plastic strain as discussed here for the disk [10].

The assumption

$$\sigma_{\theta\theta} = \sigma_{rr} = \sigma_{zz} + \sigma_0$$

for the whole plastic region is made by some authors [2, 6, 11] but it does not work for compressible material either [12].

References

1 Lászlǒ, F., "Geschleuderte Umdrehungskörper im Gebiet Bleibender Deformation," *ZAMM*, Vol. 5, 1925, pp. 281–293.

2 Nádai, A., *Theory of Flow and Fracture of Solids*, Vol. I, 2nd Ed., McGraw-Hill, New York, 1950.

3 Johnson, W., and Mellor, P. B., *Engineering Plasticity*, Van Nostrand Reinhold, New York, 1973.

4 Kollmann, F. G., "Elastisch-Plastisch Beanspruchte, Rotierende Scheiben," *Konstruktion*, Vol. 32, 1980, pp. 71–77.

5 Szabó, I., *Höhere Technische Mechanik*, 4.Aufl., Springer, Berlin, 1964.

6 Hoffman, O., and Sachs, G., *Introduction to the Theory of Plasticity*, McGraw-Hill, New York, 1953.

7 Calladine, C. R., *Engineering Plasticity*, Pergamon, Oxford, 1969.

8 Timoshenko, S. P., and Goodier, J. N., *Theory of Elasticity*, 3rd Ed., McGraw-Hill, New York, 1970.

9 Gamer, U., "Zur Elastisch-Plastischen Deformation des Rotierenden Kreisrings," *ZAMM*, in print.

10 Gamer, U., "On the Applicability of Tresca's Yield Condition to the Rotating Solid Shaft," *Rev. Roum. Sci. Techn.-Mec. Appl.*, in print.

11 Hodge, P. G. Jr., and Balaban, M., "Elastic-Plastic Analysis of a Rotating Cylinder," *Int. J. Mech. Sci.*, Vol. 4, 1962, pp. 465–476.

12 Gamer, U., "Tresca's Yield Condition and the Rotating Solid Shaft," submitted for publication.

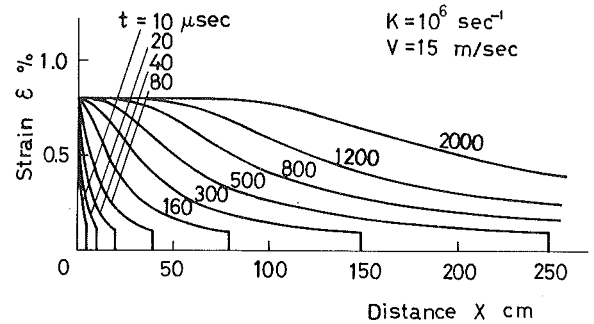

Fig. 1 Strain distribution along a bar at various instants after impact with constant velocity of 15 m/sec

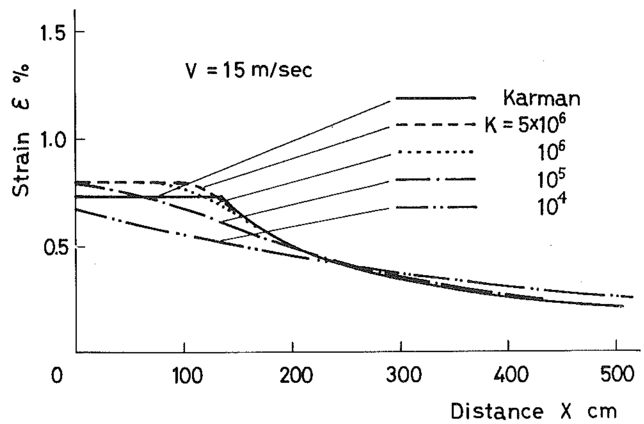

Fig. 2 Strain distribution for various values of K at 2000 μsec after impact

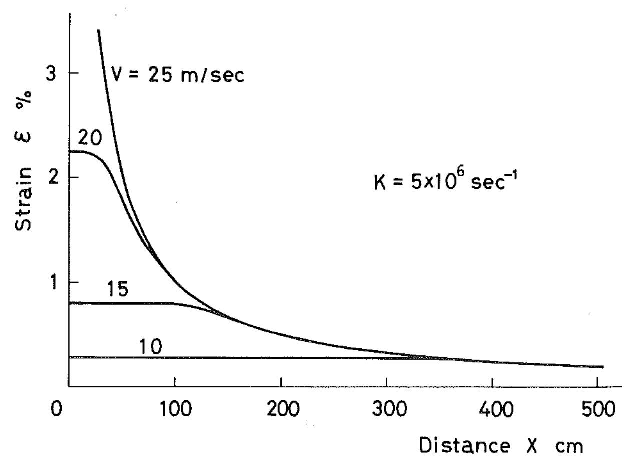

Fig. 3 Strain distribution and appearance of a strain plateau at 2000 μsec after impact for different impact velocities

On the Existence of a Strain Plateau in the Strain-Rate Dependent Theory of Malvern for Plastic Wave Propagation

M. Daimaruya[1] and M. Naitoh[1]

Introduction

The theory of plastic wave propagation in a thin rod subjected to longitudinal impact has been developed by Karman [1] and Taylor [2], under the assumption of an invariant stress-strain relation independent of strain rate. Predictions based on the strain-rate independent theory were generally in agreement with the experimental results by Duwez and Clark [3] and many other investigaters. In particular, the experiments indicated the existence of a plateau of uniform strain adjacent to the impact end of a bar which was predicted by the theory. But there were the following discrepancies. First, the observed force-time variation at the impact end of a bar showed a higher stress than the theory predicted. Second, the wave front might propagate at the elastic wave velocity even in the bar prestressed into a plastic state while the rate-independent theory predicted the plastic wave velocity associated with the tangent modulus of the static stress-strain curve.

Taking into consideration the strain-rate effect of the

[1] Associate Professor and Professor, respectively, Department of Mechanical Engineering, Muroran Institute of Technology, 27-1, Mizumoto-cho, Muroran 050, Japan.

Manuscript received by ASME Applied Mechanics Division, July, 1982; final revision, February, 1983.

$$\epsilon_{\theta\theta}^{pl} = \frac{1}{E}\left[-\frac{1}{9}(1+3\nu)\rho\omega^2 r^2 + \frac{C}{r}(\log r + \nu) + \frac{D}{r}\right]. \quad (5.2)$$

In the case of the solid disk, C and D have to vanish and therefore, at the center, $r = 0$, where the stress is largest there is no plastic strain at all and outside of it the plastic strain belonging to a tensile stress is negative [9]! The conclusion is that the stress distribution based on Tresca's yield condition cannot be meaningful even in the totally plastic disk where the problem of violated continuity does not arise.

In the related problem of the spinning solid shaft with free ends in the elastic state the relations

$$\sigma_{\theta\theta} > \sigma_{rr} > \sigma_{zz} \quad \text{for} \quad 0 < r \leq b$$

$$\sigma_{\theta\theta} = \sigma_{rr} > \sigma_{zz} \quad \text{for} \quad r = 0$$

hold as in the spinning elastic disk. The yield condition

$$\sigma_{\theta\theta} - \sigma_{zz} = \sigma_0,$$

of which equation (2.5) is a special case, leads to similar results concerning the plastic strain as discussed here for the disk [10].

The assumption

$$\sigma_{\theta\theta} = \sigma_{rr} = \sigma_{zz} + \sigma_0$$

for the whole plastic region is made by some authors [2, 6, 11] but it does not work for compressible material either [12].

References

1 László, F., "Geschleuderte Umdrehungskörper im Gebiet Bleibender Deformation," *ZAMM*, Vol. 5, 1925, pp. 281–293.

2 Nádai, A., *Theory of Flow and Fracture of Solids*, Vol. I, 2nd Ed., McGraw-Hill, New York, 1950.

3 Johnson, W., and Mellor, P. B., *Engineering Plasticity*, Van Nostrand Reinhold, New York, 1973.

4 Kollmann, F. G., "Elastisch-Plastisch Beanspruchte, Rotierende Scheiben," *Konstruktion*, Vol. 32, 1980, pp. 71–77.

5 Szabó, I., *Höhere Technische Mechanik*, 4.Aufl., Springer, Berlin, 1964.

6 Hoffman, O., and Sachs, G., *Introduction to the Theory of Plasticity*, McGraw-Hill, New York, 1953.

7 Calladine, C. R., *Engineering Plasticity*, Pergamon, Oxford, 1969.

8 Timoshenko, S. P., and Goodier, J. N., *Theory of Elasticity*, 3rd Ed., McGraw-Hill, New York, 1970.

9 Gamer, U., "Zur Elastisch-Plastischen Deformation des Rotierenden Kreisrings," *ZAMM*, in print.

10 Gamer, U., "On the Applicability of Tresca's Yield Condition to the Rotating Solid Shaft," *Rev. Roum. Sci. Techn.-Mec. Appl.*, in print.

11 Hodge, P. G. Jr., and Balaban, M., "Elastic-Plastic Analysis of a Rotating Cylinder," *Int. J. Mech. Sci.*, Vol. 4, 1962, pp. 465–476.

12 Gamer, U., "Tresca's Yield Condition and the Rotating Solid Shaft," submitted for publication.

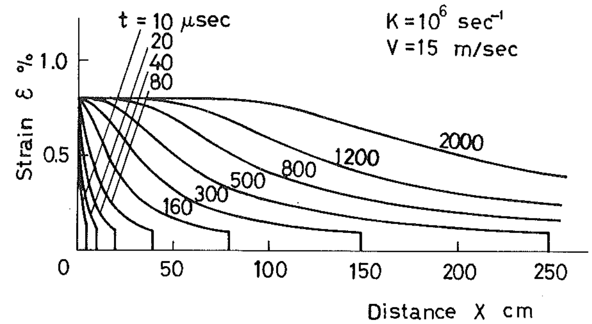

Fig. 1 Strain distribution along a bar at various instants after impact with constant velocity of 15 m/sec

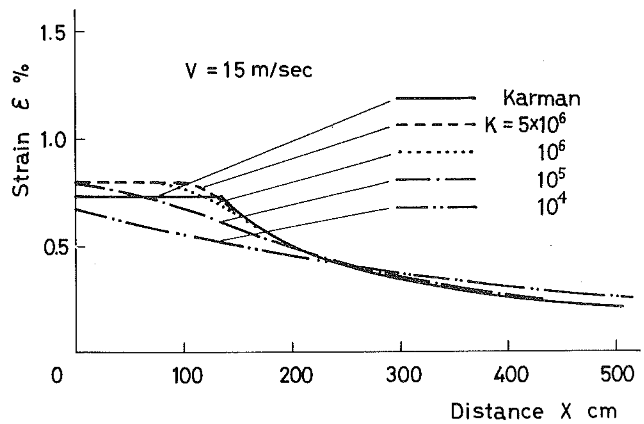

Fig. 2 Strain distribution for various values of K at 2000 μsec after impact

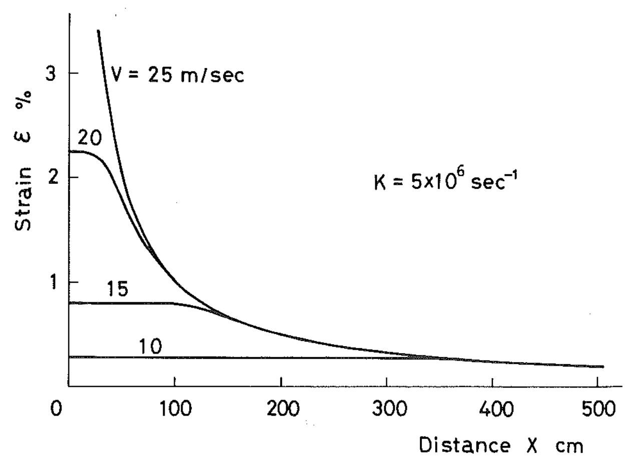

Fig. 3 Strain distribution and appearance of a strain plateau at 2000 μsec after impact for different impact velocities

On the Existence of a Strain Plateau in the Strain-Rate Dependent Theory of Malvern for Plastic Wave Propagation

M. Daimaruya[1] and M. Naitoh[1]

Introduction

The theory of plastic wave propagation in a thin rod subjected to longitudinal impact has been developed by Karman [1] and Taylor [2], under the assumption of an invariant stress-strain relation independent of strain rate. Predictions based on the strain-rate independent theory were generally in agreement with the experimental results by Duwez and Clark [3] and many other investigaters. In particular, the experiments indicated the existence of a plateau of uniform strain adjacent to the impact end of a bar which was predicted by the theory. But there were the following discrepancies. First, the observed force-time variation at the impact end of a bar showed a higher stress than the theory predicted. Second, the wave front might propagate at the elastic wave velocity even in the bar prestressed into a plastic state while the rate-independent theory predicted the plastic wave velocity associated with the tangent modulus of the static stress-strain curve.

Taking into consideration the strain-rate effect of the

[1] Associate Professor and Professor, respectively, Department of Mechanical Engineering, Muroran Institute of Technology, 27-1, Mizumoto-cho, Muroran 050, Japan.

Manuscript received by ASME Applied Mechanics Division, July, 1982; final revision, February, 1983.

material, Malvern [4] could account for these contradictions, but his calculations did not exhibit the strain plateau. This appeared to be the main weakness of Malvern's strain-rate dependent theory [5]. Later, Malvern [6] and Wood and Phillips [7] pointed out that a strain plateau might be obtained with Malvern's theory. It should be remarked, however, that while in Malvern's earlier paper a constant velocity boundary condition was used, in his later paper and reference [7] a constant stress boundary condition was applied. Further, Suliciu, Malvern, and Cristescu [8] demonstrated that Malvern's linear overstress law could not predict a true plateau $\partial\epsilon/\partial x=0$ over any finite distance; an asymptotic plateau could occur. In addition, Cristescu [9] showed the existence of a stress plateau (asymptotic) under a constant velocity boundary condition.

However, the existence of strain plateau has still not explicitly showed within Malvern's theory under the condition of constant velocity impact and his constitutive equation of linear rate-dependence.

In this paper, we show that the existence of the strain plateau (asymptotic) can be predicted by Malvern's strain-rate dependent theory even under the foregoing conditions and its appearance is governed not only by the strain-rate dependence of the material but also the impact velocity at the end of a bar.

Numerical Analysis and Discussion

The strain-rate dependent theory of Malvern for plastic wave propagation along a bar results in the following system of three quasi-linear partial differential equations:

$$\left.\begin{aligned} \frac{\partial\sigma}{\partial x} &= \rho\frac{\partial v}{\partial t} \\ \frac{\partial\epsilon}{\partial t} &= \frac{\partial v}{\partial x} \\ \mathrm{E}_0\frac{\partial\epsilon}{\partial t} &= \frac{\partial\sigma}{\partial t} + g(\sigma,\epsilon) \end{aligned}\right\} \tag{1}$$

where σ and ϵ are the nominal stress and strain, v is the particle velocity, E_0 is Young's modulus, ρ is the density, t is the time, and x is the initial distance from the impact end. Malvern has assumed that the strain rate is proportional to the excess stress over the stress at the same strain in a static test, namely

$$g(\sigma,\epsilon)=K\{\sigma-f(\epsilon)\} \tag{2}$$

where $f(\epsilon)$ is the static stress-strain relation, and K is a multiplicative constant that determines the magnitude of the dependence of the stress-strain curve on the strain-rate. The system of equations (1) and (2) is hyperbolic, which can be solved numerically by the method of characteristics.

For hardened aluminum specimins, Malvern used $f(\epsilon)=6.89(20-0.01/\epsilon)$MPa($(2\times10^4-10/\epsilon)$lb/in.^{2}) together with the constants $\mathrm{E}_0=68.9$ GPa (10^7lb/in.^{2}), $\rho=2.67\times10^3$kg/m^3(2.5×10^{-4}lb$\cdot$sec^2/in.^{4}), $K=10^6$sec^{-1}, and impact velocity $V=15$ m/sec (600 in./sec). Using the preceding values and various values of K and V, we have also calculated the instantaneous distribution of strain along a bar and its time history at various stations. Thus, numerical results for constant velocity impact are shown in Figs. 1–3.

Figure 1 shows the strain distribution in a bar at various instants of time after the beginning of the impact with constant velocity of 15 m/sec. The figure clearly shows the plateau of uniform strain adjacent to the impact end. This indicates that the strain plateau can exist within Malvern's theory under both conditions of the constant velocity impact and the constitutive equation of linear rate dependence, and its appearance requires a certain time.

Figure 2 shows the strain distribution for various values of K at 2000 μsec after the impact with constant velocity of 15 m/sec. The solid line is for Karman's solution neglecting strain-rate effect. We observe that the larger the value of K, the shorter will be the time required for the appearance of a strain plateau. It should be noted that the strain-rate dependence of the material becomes smaller with increasing of the value of K. The strain-rate independent theory of Karman may be obtained as the limiting case by taking $K\to\infty$.

In Fig. 3 the effect of impact velocity on the form of strain distribution and the appearance of the strain plateau at 2000 μsec after impact is illustrated for the case of $K=5\times10^6$ sec^{-1}. The figures shows that the magnitude of the plastic strain near the impact end increases with increasing impact velocity, but conversely, plateau length decreases. The latter indicates that the strain plateau appears much faster as the impact velocity becomes lower.

References

1 Karman, T. V., and Duwez, P., "The Propagation of Plastic Deformation in Solids," *Journal of Applied Physics*, Vol. 21, 1950, pp. 987–994.

2 Taylor, G. I., "The Plastic Wave in a Wire Extended by an Impact Load," British Official Report RC429, 1942.

3 Duwez, P. E., and Clark, D. S., "An Experimental Study of the Propagation of Plastic Deformation Under Conditions of Longitutinal Impact," *Proceedings of the American Society for Testing Materials*, Vol. 47, 1947, pp. 502–532.

4 Malvern, L. E., "The Propagation of Longitudinal Waves of Plastic Deformation in a Bar of Material Exhibiting a Strain-Rate Effect," ASME Journal of Applied Mechanics, Vol. 18, 1951, pp. 203–208.

5 Kolsky, H., and Douch, L. S., "Experimental Studies in Plastic Wave Propagation," *Journal of the Mechanics and Physics of Solids*, Vol. 10, 1962, pp. 195–223.

6 Malvern, L. E., "Experimental Studies of Strain-Rate Effects and Plastic-Wave Propagation in Annealed Aluminium," *Behavior of Materials Under Dynamic Loading*, ASME, New York, 1965, pp. 81–92.

7 Wood, E. R., and Phillips, A., "On the Theory of Plastic Wave Propagation in a Bar," *Journal of the Mechanics and Physics of Solids*, Vol. 15, 1967, pp. 241–254.

8 Suliciu, I., Malvern, L. E., and Cristescu, N., "Remarks Concerning the Plateau in Dynamic Plasticity," *Archives of Mechanics*, Vol. 24, 1972, pp. 999–1011.

9 Cristescu, N., "A Procedure for Determining the Constitutive Equations for Materials Exhibiting Both Time-Dependent and Time-Independent Plasticity," *International Journal of Solids and Structures*, Vol. 8, 1972, pp. 511–531.

An Efficient Method for Computing the Critical Damping Condition

D. J. Inman[1] and I. Orabi[2]

Introduction

Recently several authors [1–4] have defined the concept of critical damping for linear lumped parameter systems with n degrees of freedom. The intent of this Note is to compare the difinitions given in [1] and [3] and to derive a method for

[1]Assistant Professor, Department of Mechanical and Aerospace Engineering, State University of New York at Buffalo, Buffalo, N.Y. 14260. Assoc. Mem. ASME.

[2]Graduate Student, Department of Mechanical and Aerospace Engineering, State University of New York at Buffalo. Currently at Department of Mechanical and Industrial Engineering, Clarkson College, Potsdam, N.Y. 13676. Student Mem. ASME.

Manuscript received by ASME Applied Mechanics Division, August, 1982; final revision, December, 1982.

material, Malvern [4] could account for these contradictions, but his calculations did not exhibit the strain plateau. This appeared to be the main weakness of Malvern's strain-rate dependent theory [5]. Later, Malvern [6] and Wood and Phillips [7] pointed out that a strain plateau might be obtained with Malvern's theory. It should be remarked, however, that while in Malvern's earlier paper a constant velocity boundary condition was used, in his later paper and reference [7] a constant stress boundary condition was applied. Further, Suliciu, Malvern, and Cristescu [8] demonstrated that Malvern's linear overstress law could not predict a true plateau $\partial\epsilon/\partial x=0$ over any finite distance; an asymptotic plateau could occur. In addition, Cristescu [9] showed the existence of a stress plateau (asymptotic) under a constant velocity boundary condition.

However, the existence of strain plateau has still not explicitly showed within Malvern's theory under the condition of constant velocity impact and his constitutive equation of linear rate-dependence.

In this paper, we show that the existence of the strain plateau (asymptotic) can be predicted by Malvern's strain-rate dependent theory even under the foregoing conditions and its appearance is governed not only by the strain-rate dependence of the material but also the impact velocity at the end of a bar.

Numerical Analysis and Discussion

The strain-rate dependent theory of Malvern for plastic wave propagation along a bar results in the following system of three quasi-linear partial differential equations:

$$\left.\begin{aligned} \frac{\partial\sigma}{\partial x} &= \rho\frac{\partial v}{\partial t} \\ \frac{\partial\epsilon}{\partial t} &= \frac{\partial v}{\partial x} \\ E_0\frac{\partial\epsilon}{\partial t} &= \frac{\partial\sigma}{\partial t} + g(\sigma,\epsilon) \end{aligned}\right\} \tag{1}$$

where σ and ϵ are the nominal stress and strain, v is the particle velocity, E_0 is Young's modulus, ρ is the density, t is the time, and x is the initial distance from the impact end. Malvern has assumed that the strain rate is proportional to the excess stress over the stress at the same strain in a static test, namely

$$g(\sigma,\epsilon)=K\{\sigma-f(\epsilon)\} \tag{2}$$

where $f(\epsilon)$ is the static stress-strain relation, and K is a multiplicative constant that determines the magnitude of the dependence of the stress-strain curve on the strain-rate. The system of equations (1) and (2) is hyperbolic, which can be solved numerically by the method of characteristics.

For hardened aluminum specimins, Malvern used $f(\epsilon)=6.89(20-0.01/\epsilon)\mathrm{MPa}((2\times10^4-10/\epsilon)\mathrm{lb/in.}^2)$ together with the constants $E_0=68.9$ GPa (10^7lb/in.^{2}), $\rho=2.67\times10^3$kg/m^3(2.5×10^{-4}lb•sec^2/in.^{4}), $K=10^6$sec^{-1}, and impact velocity $V=15$ m/sec (600 in./sec). Using the preceding values and various values of K and V, we have also calculated the instantaneous distribution of strain along a bar and its time history at various stations. Thus, numerical results for constant velocity impact are shown in Figs. 1–3.

Figure 1 shows the strain distribution in a bar at various instants of time after the beginning of the impact with constant velocity of 15 m/sec. The figure clearly shows the plateau of uniform strain adjacent to the impact end. This indicates that the strain plateau can exist within Malvern's theory under both conditions of the constant velocity impact and the constitutive equation of linear rate dependence, and its appearance requires a certain time.

Figure 2 shows the strain distribution for various values of K at 2000 μsec after the impact with constant velocity of 15 m/sec. The solid line is for Karman's solution neglecting strain-rate effect. We observe that the larger the value of K, the shorter will be the time required for the appearance of a strain plateau. It should be noted that the strain-rate dependence of the material becomes smaller with increasing of the value of K. The strain-rate independent theory of Karman may be obtained as the limiting case by taking $K\to\infty$.

In Fig. 3 the effect of impact velocity on the form of strain distribution and the appearance of the strain plateau at 2000 μsec after impact is illustrated for the case of $K=5\times10^6$ sec^{-1}. The figures shows that the magnitude of the plastic strain near the impact end increases with increasing impact velocity, but conversely, plateau length decreases. The latter indicates that the strain plateau appears much faster as the impact velocity becomes lower.

References

1 Karman, T. V., and Duwez, P., "The Propagation of Plastic Deformation in Solids," *Journal of Applied Physics*, Vol. 21, 1950, pp. 987–994.

2 Taylor, G. I., "The Plastic Wave in a Wire Extended by an Impact Load," British Official Report RC429, 1942.

3 Duwez, P. E., and Clark, D. S., "An Experimental Study of the Propagation of Plastic Deformation Under Conditions of Longitutinal Impact," *Proceedings of the American Society for Testing Materials*, Vol. 47, 1947, pp. 502–532.

4 Malvern, L. E., "The Propagation of Longitudinal Waves of Plastic Deformation in a Bar of Material Exhibiting a Strain-Rate Effect," ASME Journal of Applied Mechanics, Vol. 18, 1951, pp. 203–208.

5 Kolsky, H., and Douch, L. S., "Experimental Studies in Plastic Wave Propagation," *Journal of the Mechanics and Physics of Solids*, Vol. 10, 1962, pp. 195–223.

6 Malvern, L. E., "Experimental Studies of Strain-Rate Effects and Plastic-Wave Propagation in Annealed Aluminium," *Behavior of Materials Under Dynamic Loading*, ASME, New York, 1965, pp. 81–92.

7 Wood, E. R., and Phillips, A., "On the Theory of Plastic Wave Propagation in a Bar," *Journal of the Mechanics and Physics of Solids*, Vol. 15, 1967, pp. 241–254.

8 Suliciu, I., Malvern, L. E., and Cristescu, N., "Remarks Concerning the Plateau in Dynamic Plasticity," *Archives of Mechanics*, Vol. 24, 1972, pp. 999–1011.

9 Cristescu, N., "A Procedure for Determining the Constitutive Equations for Materials Exhibiting Both Time-Dependent and Time-Independent Plasticity," *International Journal of Solids and Structures*, Vol. 8, 1972, pp. 511–531.

An Efficient Method for Computing the Critical Damping Condition

D. J. Inman[1] and I. Orabi[2]

Introduction

Recently several authors [1–4] have defined the concept of critical damping for linear lumped parameter systems with n degrees of freedom. The intent of this Note is to compare the difinitions given in [1] and [3] and to derive a method for

[1] Assistant Professor, Department of Mechanical and Aerospace Engineering, State University of New York at Buffalo, Buffalo, N.Y. 14260. Assoc. Mem. ASME.

[2] Graduate Student, Department of Mechanical and Aerospace Engineering, State University of New York at Buffalo. Currently at Department of Mechanical and Industrial Engineering, Clarkson College, Potsdam, N.Y. 13676. Student Mem. ASME.

Manuscript received by ASME Applied Mechanics Division, August, 1982; final revision, December, 1982.

calculating a critical damping condition that is more computationally efficient than the conditions given in [1, 3, 4].

The systems of interest here are those that can be successfully modeled by a vector differential equation of the form

$$M\ddot{x}+C\dot{x}+Kx=0 \tag{1}$$

Here, M, C, and K are real n x n symmetric positive-definite matrices, $\mathbf{x}=\mathbf{x}(t)$ is a vector of generalized coordinates, and $\dot{\mathbf{x}}$ and $\ddot{\mathbf{x}}$ are the velocities and accelerations, respectively. The eigenvalue problem resulting from (1) is

$$(\lambda^2 M+\lambda C+K)\mathbf{q}=0 \tag{2}$$

where λ is complex scalar called an eigenvalue of (2) and $\mathbf{q}$ is a nonzero vector of constants called the eigenvector of (2).

Previous Work

In [1], Beskos and Boley define critical damping for the system (1) by requiring the value of the damping coefficients c_i to be a minimum such that the eigenvalues of (2) are negative real numbers. This is shown to correspond to those values of c_i such that

$$\frac{d}{db}[\det(b^2M-bC+K)]=0 \tag{3}$$

where b is a positive real number and where det(.) indicates the determinant of the enclosed matrix.

In [3], Inman and Andry defined a critically damped multidegree-of-freedom system as one in which each mode of vibration is a critically damped motion. That is, each solution of the eigenvalue problem (2) is a pair of repeated negative real numbers. This is then shown to be the case if and only if the coefficient matrices of (1) are such that $C=2(M^{-1/2}KM^{-1/2})^{1/2}$. Here the exponent 1/2 indicates the unique positive-definite square root of the positive-definite matrices M^{-1} and $M^{-1/2}\ KM^{-1/2}$, and M^{-1} denotes the inverse of the nonsingular matrix M. This expression defines the critical damping matrix, denoted $C_{\rm cr}$.

In [4], Gray and Andry developed a computationally more efficient method of calculating $C_{\rm cr}$ as defined in [3]. Namely they pointed out that $C_{\rm cr}$ can be calculated by $C_{\rm cr}=2M\phi\Lambda^{1/2}\phi^TM$ where ϕ is the modal matrix of K i.e., the matrix whose columns are the eigenvectors of K). The matrix $\Lambda^{1/2}$ is a diagonal matrix whose nonzero elements are the positive square roots of the eigenvalues of K. This method of calculating $C_{\rm cr}$ requires the computation of one less square root than the method used in [3] requires. Thus only one eigenvalue-eigenvector problem need be solved to find $C_{\rm cr}$.

Both of the methods used to calculate $C_{\rm cr}$ require the computation of one or more sets of eigenvectors. The method presented here yields $C_{\rm cr}$ without having to calculate any eigenvectors as in [3] and [4] and defines critical damping without having to calculate derivatives as in [1, 2].

Main Result

It is desired to find a method of calculating the critical damping matrix that would avoid having to calculate the square root of a matrix or its eigenvectors. The following result provides such a method.

Theorem: There exist n constants. β_j, such that the damping matrix

$$\tilde{C}=\sum_{j=0}^{n-1}\beta_j\tilde{K}^j \tag{4}$$

causes the system

$$\ddot{y}+\tilde{C}\dot{y}+\tilde{K}y=0$$

to be critically damped in each mode. Here, $\tilde{K}=M^{-1/2}KM^{-1/2}$, and (1) and (5) are related by the eigenvalue preserving transformation $y=M^{1/2}x$.

This result follows from the Cayley-Hamilton theorem which yields the following representation of a function of a matrix.

$$f(A)=\sum_{j=0}^{n-1}\beta_iA^i \tag{6}$$

where the function f is such that $f(\omega_i)$ and its derivatives exist for each eigenvalue, ω_i, of Λ (see for instance [5]). For critical damping we require $C_{\rm cr}=2\tilde{K}^{1/2}$. Application of (6) then yields

$$2\tilde{K}^{1/2}=\sum_{j=0}^{n-1}\beta_j\tilde{K}^j \tag{7}$$

since $\tilde{K}$ is positive definite.

Let S denote the modal matrix for $\tilde{K}$ such that $S^TS=I$. Let Λ denote the diagonal matrix of eigenvalues $\tilde{K}$. Pre and post multiplying (7) by S^T and S respectively, yields

$$2\Lambda^{1/2}=\sum_{j=0}^{n-1}\beta_j\Lambda^j. \tag{8}$$

This follows since

$$S^T K^j S=S^T KK\ldots KS$$
$$=S^TKSS^TKS\ldots S^TKS=\Lambda\Lambda\ldots\Lambda=\Lambda^j.$$

Equation (8) is diagonal and may be rewritten in the form

$$2\begin{bmatrix}\omega_1^{1/2}\\ \omega_2^{1/2}\\ \cdot\\ \cdot\\ \cdot\\ \omega_n^{1/2}\end{bmatrix}=\begin{bmatrix}1&\omega_1&\omega_1^2&\cdots&\omega_1^{n-1}\\ 1&\omega_2&\omega_2^2&\cdots&\omega_2^{n-1}\\ \cdot&&\cdot&&\cdot\\ \cdot&&\cdot&&\cdot\\ \cdot&&\cdot&&\cdot\\ 1&\omega_n&\omega_n^2&\cdots&\omega_n^{n-1}\end{bmatrix}\begin{bmatrix}\beta_0\\ \beta_1\\ \cdot\\ \cdot\\ \cdot\\ \beta_{n-1}\end{bmatrix} \tag{9}$$

where ω_i are the eigenvalue of $\tilde{K}$. If each of the ω_i are distinct then the matrix in (9) has an inverse and the β_j are uniquely given by

$$\begin{bmatrix}\beta_0\\ \beta_1\\ \cdot\\ \cdot\\ \cdot\\ \beta_{n-1}\end{bmatrix}=2\begin{bmatrix}1&\omega_1&\omega_1^2&\cdots&\omega_1^{n-1}\\ 1&\omega_2&\omega_2^2&\cdots&\omega_2^{n-1}\\ \cdot&\cdot&\cdot&\cdot&\\ \cdot&\cdot&\cdot&\cdot&\\ \cdot&\cdot&\cdot&\cdot&\\ 1&\omega_n&\omega_n^2&\cdots&\omega_n^{n-1}\end{bmatrix}^{-1}\begin{bmatrix}\omega_1^{1/2}\\ \omega_2^{1/2}\\ \cdot\\ \cdot\\ \cdot\\ \omega_n^{1/2}\end{bmatrix} \tag{10}$$

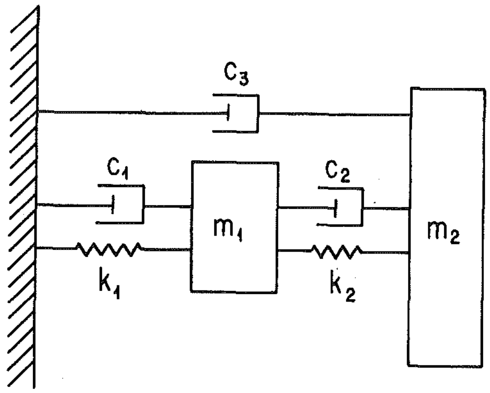

Fig. 1

If $\tilde{K}$ has repeated eigenvalues, these constants are still uniquely determined by examing the derivatives with respect to ω_i of equations (9) to obtain a set of n linearly independent equations (see for example [6]). The critical damping matrix can then the written as

$$C_{\mathrm{cr}} = \sum_{j=0}^{n-1} \beta_{j_{\mathrm{cr}}} \tilde{K}^j$$

where $\beta_{j_{\mathrm{cr}}}$ are the solutions given in (10). The result then follows from [3].

Example

The example shown in Fig. 1 with $c_3 = 0$ is a two degree-of-freedom system considered in Example 3 of reference [1]. Briefly, Beskos and Boley's method defines critical damping as the smallest values of c_1 and c_2 such that the system will not oscillate. These are calculated by differentiating the characteristic equation with respect to the eigenvalue that is constrained to be real and negative (i.e., equation (3), the details are given in [2]). The process yields an infinite number of possibilities. As given in [1, 2] for the case with $k_1 = 3000$ lb/ft $= 43{,}779.528$ N/m, $k_2 = 4000$ lb/ft $= 58{,}372.703$ N/m, $m_1 = m_2 = 2$ lb-sec^2/ft $= 29.186$ N sec^2 m, and $c_3 = 0$ the minimization yields two critical damping curves. One curve separates a region of complete underdamping from a region of partial underdamping. The second curve separates the region of partial underdamping from a region of complete overdamping. A point on this second curve $c_1 = c_2 = 279.6$ lb-sec/ft $= 4080.202$ N sec/M. The equation of motion (1), becomes

$$\begin{bmatrix} m_1 & 0 \\ 0 & m_2 \end{bmatrix} \ddot{x} + \begin{bmatrix} c_1 & 0 \\ 0 & c_2 \end{bmatrix} \dot{x} + \begin{bmatrix} k_1+k_2 & -k_2 \\ -k_2 & k_2 \end{bmatrix} x = 0 \tag{11}$$

With the preceeding values, the characteristic roots are given in [2] as $\lambda_1 = \lambda_2 = -69.9$, $\lambda_3 = -4.5$, and $\lambda_4 = -135.3$. Thus the application of the critical damping condition of [1] yields a system with one critically damped mode ($\lambda_1 = \lambda_2$) and one overdamped mode ($\lambda_3 \neq \lambda_4$).

Next consider applying the critical damping condition of [3] to the preceeding example. Since, $M = 2I$, the identity matrix, in this case the critical damping matrix can be found from $C_{\mathrm{cr}}^2 = 2K$. Using the appropriate matrices from (11) this becomes

$$\begin{bmatrix} c_1^2 & 0 \\ 0 & c_2^2 \end{bmatrix} = 2 \begin{bmatrix} k_1+k_2 & -k_2 \\ -k_2 & k_2 \end{bmatrix} . \tag{12}$$

This condition obviously cannot be satisfied unless k_2 and c_2 are both zero, reducing the system to one degree of freedom. Thus, the condition given in [3] indicates that the only way to make both modes of this example become critically damped is to alter the structure.

Intuitively and from examining (12) one is encouraged to add the damper c_3 into the system in an attempt to achieve critical damping in both modes. With the addition of c_3 in the (2,1) and (1,2) position of the damping matrix the equation $C_{\mathrm{cr}}^2 = 2K$ then yields three nonlinear simultaneous algebraic equalities in the c_i and k_i which must be solved. The other approach [4] is to compute the square root of the stiffness matrix K and solve the three linear simultaneous equalities given by $C = 2\theta\Lambda^{1/2}\theta^T$.

Hence, the method of [3, 4] requires either the solution of simultaneous nonlinear algebraic equalities or the computation of eigenvalues ($\Lambda^{1/2}$) and eigenvectors (θ) of the stiffness matrix K followed by the solution of a set of three simultaneous linear equations. However, use of the theorem presented in the foregoing offers a third possibility. Namely, C_{cr} can be computed by calculating just the eigenvalues of the *stiffness matrix and the coefficients given by equation (10)* and then solving three simultaneous linear equations for each of the coefficients c_i.

Recalling that in this example $M = 2I$, equation (7) yields

$$C_{\mathrm{cr}} = \beta_0 I + \beta_1 \tilde{K}. \tag{13}$$

The eigenvalues of the stiffness matrix are $\omega_1 = 613.9991$ and $\omega_2 = 4{,}886{,}0009$, so that equation (10) yields:

$$\begin{bmatrix} \beta_0 \\ \beta_1 \end{bmatrix} = 2 \begin{bmatrix} 1 & 613.9991 \\ 1 & 4{,}886.0009 \end{bmatrix}^{-1} \begin{bmatrix} 24.7790 \\ 69.8999 \end{bmatrix}$$

$$= \begin{bmatrix} 36.5878 \\ 0.02112 \end{bmatrix}$$

Substitution of these values into (13) yields the critical damping matrix. Comparing this to the desired damping structure yields

$$\begin{bmatrix} c_1+c_3 & -c_3 \\ -c_3 & c_2+c_3 \end{bmatrix} = \begin{bmatrix} 221.04 & -84.5 \\ -84.5 & 157.67 \end{bmatrix} = C_{\mathrm{cr}} \tag{14}$$

It then remains to solve the three very simple linear algebraic equalities resulting from (14) to find the value of the damping coefficient for each of the three dashpots. This yields $c_1 = 136.54$, $c_2 = 73.17$, and $c_3 = 84.5$. These values cause the motion of the system of Fig. 1 to be critically damped in each mode (the characteristic equation is $\lambda^4 + 189.3579\lambda^3 + 12{,}428.2\lambda^2 + 327978\lambda + 3{,}000{,}000 = 0$, with roots $\lambda_{1,2} = -24.78$ and $\lambda_{3,4} = -69.90$).

Comparison of Methods

The difference between the two approaches in defining critical damping for (1) can best be pointed out by considering the *definition of critical damping* for a single degree-of-freedom spring, mass, damper arrangement. For such systems the equation of motion is the scalar ordinary differential equation, $m\ddot{x} + c\dot{x} + kx = 0$. This system is critically damped if and only if either of the following statements are true: (*i*) c_{cr} is the smallest value of c such that the system does not oscillate (this yields $c_{\mathrm{cr}} = 2\,m\omega = 2\sqrt{mk}$), or (*ii*) the discriminant of the characteristic equation is zero (this yields $c_{\mathrm{cr}} = 2\sqrt{mk}$). Condition (*i*) is extended to multidegree-of-freedom systems in [1] and [2], whereas condition (*ii*) is extended in [3] and here.

When these two definitions are extended to two or more degrees of freedom they no longer agree as shown in the example. The example illustrates that the critical damping condition of [1] is satisfied but only one mode is actually critically damped, the other mode is overdamped. The condition yields a stationary point, dividing regions of oscillation from regions of nonoscillation. On the other hand, the extension of conditions (*ii*) to more than one degree-of-freedom systems is algebraic and carries through to yield systems that are critically damped in each mode.

The preceeding discussion indicates that the difference between the two basic methods lies in the difference in the definition of critical damping given in [1] and the definition presented in [3]. The definition of critical damping delineated in [3] requires each mode to be critically damped while the definition prescribed in [1] results in each mode being nonoscillatory. The method given in [1] is more general in the sense that it yields many choices of damping coefficients for producing a nonoscillatory system. Namely, any values of damping coefficients lying on the critical damping surface will yield a critically damped system as defined in [1]. On the other hand, application of the definition of critical damping given in [3] requires a very specific choice of damping coefficients. However, this choice of damping rates quarantees that each mode will be critically damped and not just nonoscillatory. Thus if one is free to make structural changes the analysis given here desirable. If dash pots cannot be added to the system, then the analysis given in [1] for critical damping or that given in [3], [7], or [8] for nonoscillation may be more useful.

It should be pointed out that the calculation of the critical damping condition is "unstable" in the sense that a small perturbation of any of the coefficients c_i, m_i, or k_i causes the system to lose its critically damped status. As is often the case with the one degree-of-freedom system, the interest in calculating the critical damping matrix is for comparison and design. As is shown in [3], the definiteness of the matrix $C - C_{cr}$ determines the oscillatory nature of (1). The matrix $C - C_{cr}$ can also be used in design work as pointed out in [7] and [8].

Conclusions

A comparison between two different methods of defining critical damping for multiple degree-of-freedom systems has been made. The distinction is made based on the nature of each mode. A more computationally efficient method of computing the critical damping condition has also been presented. This method does not require the calculation of eigenvectors or derivatives as previously presented methods do. In addition, and example has been given illustrating the difference between the various definitions.

Acknowledgment

The first author acknowledges the support of National Science Foundation grant number MEA 8112826.

References

1 Besko, D. E., and Boley, B. A., "Critical Damping in Linear Discrete Dynamic Systems," ASME Journal of Applied Mechanics, Vol. 47, 1980, pp. 627-630.

2 Besko, D. E., and Boley, B. A., "Critical Damping in Linear Discrete Dynamic Systems," Office of Naval Research Report No. 1979-2, Nov. 1979.

3 Inman, D. J., and Andry, A. N., Jr., "Some Results on the Nature of Eigenvalues of Discrete Damped Linear Systems," ASME Journal of Applied Mechanics, Vol. 47, 1980, pp. 927-930.

4 Gray, J., and Andry, A. N., Jr., "Simple Calculations for the Critical Damping Matrix of a Linear Multidegree of Freedom System," *Mechanics Research Communications*, Vol. 9, No. 6, 1982, pp. 379-380.

5 Mirsky, L., *An Introduction to Linear Algebra*, Oxford, p. 342.

6 Lin, Y. K., Discussion of "Classical Normal Modes in Damped Linear Dynamic Systems," ASME Journal of Applied Mechanics, Vol. 33, 1966, pp. 471-472.

7 Inman, D. J., and Andry, A. N., Jr., "A Procedure for Designing Overdamped Lumped Parameter Systems," *52nd Shock and Vibration Bulletin*, Part 5, 1982, pp. 49-53.

8 Ahmadian, M., and Inman, D. J., "A Computer Package for the Design of Damped Linear Multidegree of Freedom System," *Research in Structural and Solid Mechanics*, NASA Conference Publication, No. 2245, Oct. 1982, pp. 391-403.

Numerical Evaluation of Double Integrals With a Logarithmic or Cauchy-Type Singularity

J. T. Katsikadelis[1] and A. E. Armenàkas[2]

1 Description of the Numerical Procedure

In solving two-dimensional boundary value problems by the boundary integral equation (BIE) method, double improper integrals of the following form [1-3] are encountered

$$I(P) = \iint_R f(Q)K(Q,P)d\sigma_Q, \quad Q(\xi,\eta), \; P(x,y)\epsilon R \tag{1}$$

whose kernel $K(Q,P)$ exhibits a logarithmic or a Cauchy-type singularity. That is, denoting by $r = |P-Q|$ the distance between points P and Q, their kernel behaves like $ln(r)$ or $1/r$ when point $P \rightarrow Q$. The function $f(Q)$ is defined on R and it is regular. The region R is plane and may be simply or multiply connected. It is bounded by a curve C which may be piecewise smooth. The index Q in $d\sigma_Q$ indicates that the integration is performed with respect to point Q, while point P remains constant.

Integral (1) has been evaluated over triangular or rectangular regions [2-4]. Its values over these regions may be used to evaluate integral (1) over an arbitrary region R by subdividing it into triangles or rectangles. However, these shapes do not fit curved boundaries well. Consequently, to obtain accurate results the region near the curved boundary must be subdivided into many triangles or rectangles.

In this Note, a procedure is presented for the evaluation of integral (1) which can be easily programmed on a digital computer. In this procedure the integrand is transformed to polar coordinates [1] whose origin is the point of singularity of the kernel. Thus, integral (1) may be rewritten as

$$I(P) = \iint_R f^*(r,\theta)K(r)rdrd\theta = = \int_0^{2\pi}\int_0^{r_c(\theta)} f^*(r,\theta)K(r)rdrd\theta \tag{2}$$

It is apparent that $r \rightarrow 0$ when $Q \rightarrow P$ and $\lim_{r\rightarrow 0} rK(r)$ is a finite constant. Hence, the integrand of integral (2) is not singular

[1] Lecturer, Institute of Structural Analysis, National Technical University of Athens, Athens, Greece.

[2] Professor of Aerospace Engineering Polytechnic Institute of New York, New York, Brooklyn, N. Y. 11201. Also Professor and Director of the Institute of Structural Analysis, National Technical University of Athens, Athens, Greece. Mem. ASME

Manuscript received by ASME Applied Mechanics Division, December, 1982; final revision, January, 1983.

When these two definitions are extended to two or more degrees of freedom they no longer agree as shown in the example. The example illustrates that the critical damping condition of [1] is satisfied but only one mode is actually critically damped, the other mode is overdamped. The condition yields a stationary point, dividing regions of oscillation from regions of nonoscillation. On the other hand, the extension of conditions *(ii)* to more than one degree-of-freedom systems is algebraic and carries through to yield systems that are critically damped in each mode.

The preceeding discussion indicates that the difference between the two basic methods lies in the difference in the definition of critical damping given in [1] and the definition presented in [3]. The definition of critical damping delineated in [3] requires each mode to be critically damped while the definition prescribed in [1] results in each mode being nonoscillatory. The method given in [1] is more general in the sense that it yields many choices of damping coefficients for producing a nonoscillatory system. Namely, any values of damping coefficients lying on the critical damping surface will yield a critically damped system as defined in [1]. On the other hand, application of the definition of critical damping given in [3] requires a very specific choice of damping coefficients. However, this choice of damping rates quarantees that each mode will be critically damped and not just nonoscillatory. Thus if one is free to make structural changes the analysis given here desirable. If dash pots cannot be added to the system, then the analysis given in [1] for critical damping or that given in [3], [7], or [8] for nonoscillation may be more useful.

It should be pointed out that the calculation of the critical damping condition is "unstable" in the sense that a small perturbation of any of the coefficients c_i, m_i, or k_i causes the system to lose its critically damped status. As is often the case with the one degree-of-freedom system, the interest in calculating the critical damping matrix is for comparison and design. As is shown in [3], the definiteness of the matrix $C-C_{cr}$ determines the oscillatory nature of (1). The matrix $C-C_{cr}$ can also be used in design work as pointed out in [7] and [8].

Conclusions

A comparison between two different methods of defining critical damping for multiple degree-of-freedom systems has been made. The distinction is made based on the nature of each mode. A more computationally efficient method of computing the critical damping condition has also been presented. This method does not require the calculation of eigenvectors or derivatives as previously presented methods do. In addition, and example has been given illustrating the difference between the various definitions.

Acknowledgment

The first author acknowledges the support of National Science Foundation grant number MEA 8112826.

References

1 Besko, D. E., and Boley, B. A., "Critical Damping in Linear Discrete Dynamic Systems," ASME Journal of Applied Mechanics, Vol. 47, 1980, pp. 627–630.

2 Besko, D. E., and Boley, B. A., "Critical Damping in Linear Discrete Dynamic Systems," Office of Naval Research Report No. 1979-2, Nov. 1979.

3 Inman, D. J., and Andry, A. N., Jr., "Some Results on the Nature of Eigenvalues of Discrete Damped Linear Systems," ASME Journal of Applied Mechanics, Vol. 47, 1980, pp. 927–930.

4 Gray, J., and Andry, A. N., Jr., "Simple Calculations for the Critical Damping Matrix of a Linear Multidegree of Freedom System," *Mechanics Research Communications*, Vol. 9, No. 6, 1982, pp. 379–380.

5 Mirsky, L., *An Introduction to Linear Algebra*, Oxford, p. 342.

6 Lin, Y. K., Discussion of "Classical Normal Modes in Damped Linear Dynamic Systems," ASME Journal of Applied Mechanics, Vol. 33, 1966, pp. 471–472.

7 Inman, D. J., and Andry, A. N., Jr., "A Procedure for Designing Overdamped Lumped Parameter Systems," *52nd Shock and Vibration Bulletin*, Part 5, 1982, pp. 49–53.

8 Ahmadian, M., and Inman, D. J., "A Computer Package for the Design of Damped Linear Multidegree of Freedom System," *Research in Structural and Solid Mechanics*, NASA Conference Publication, No. 2245, Oct. 1982, pp. 391–403.

Numerical Evaluation of Double Integrals With a Logarithmic or Cauchy-Type Singularity

J. T. Katsikadelis[1] and A. E. Armenàkas[2]

1 Description of the Numerical Procedure

In solving two-dimensional boundary value problems by the boundary integral equation (BIE) method, double improper integrals of the following form [1–3] are encountered

$$I(P)=\iint_R f(Q)K(Q,P)d\sigma_Q, \quad Q(\xi,\eta),\ P(x,y)\epsilon R \tag{1}$$

whose kernel $K(Q,P)$ exhibits a logarithmic or a Cauchy-type singularity. That is, denoting by $r=|P-Q|$ the distance between points P and Q, their kernel behaves like $ln(r)$ or $1/r$ when point $P\rightarrow Q$. The function $f(Q)$ is defined on R and it is regular. The region R is plane and may be simply or multiply connected. It is bounded by a curve C which may be piecewise smooth. The index Q in $d\sigma_Q$ indicates that the integration is performed with respect to point Q, while point P remains constant.

Integral (1) has been evaluated over triangular or rectangular regions [2–4]. Its values over these regions may be used to evaluate integral (1) over an arbitrary region R by subdividing it into triangles or rectangles. However, these shapes do not fit curved boundaries well. Consequently, to obtain accurate results the region near the curved boundary must be subdivided into many triangles or rectangles.

In this Note, a procedure is presented for the evaluation of integral (1) which can be easily programmed on a digital computer. In this procedure the integrand is transformed to polar coordinates [1] whose origin is the point of singularity of the kernel. Thus, integral (1) may be rewritten as

$$I(P)=\iint_R f^*(r,\theta)K(r)rdrd\theta = =\int_0^{2\pi}\int_0^{r_C(\theta)} f^*(r,\theta)K(r)rdrd\theta \tag{2}$$

It is apparent that $r\rightarrow 0$ when $Q\rightarrow P$ and $\lim_{r\rightarrow 0} rK(r)$ is a finite constant. Hence, the integrand of integral (2) is not singular

[1] Lecturer, Institute of Structural Analysis, National Technical University of Athens, Athens, Greece.

[2] Professor of Aerospace Engineering Polytechnic Institute of New York, New York, Brooklyn, N. Y. 11201. Also Professor and Director of the Institute of Structural Analysis, National Technical University of Athens, Athens, Greece. Mem. ASME

Manuscript received by ASME Applied Mechanics Division, December, 1982; final revision, January, 1983.

and can be evaluated by any of the known numerical techniques of double integration [5, 6].

The numerical integration of (2) is performed by dividing the boundary C into intervals, referred to as boundary elements, by M points $q_1, q_2, \ldots q_M$, whose coordinates are known with respect to the fixed system of axes Oxy. Each boundary element can be approximated by a boundary curve (e.g., straight line, parabolic arc, etc.) The region R is then subdivided into M sectors by straight lines from point P to points $q_1, q_2, \ldots q_M$. The integral (2) can be approximated by

$$I(P) = \sum_{i=1}^{M} I_i(P) \tag{3}$$

where referring to Fig. 2

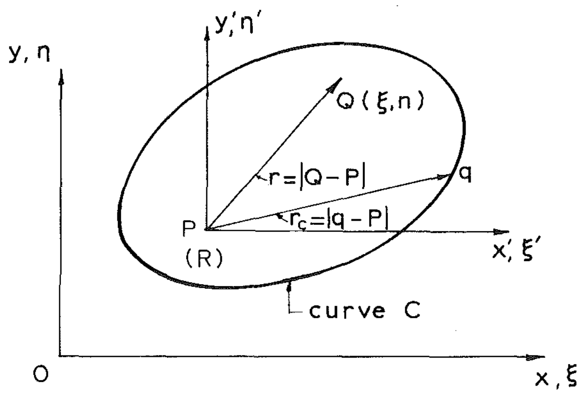

Fig. 1 The two-dimensional region R bounded by the curve C.

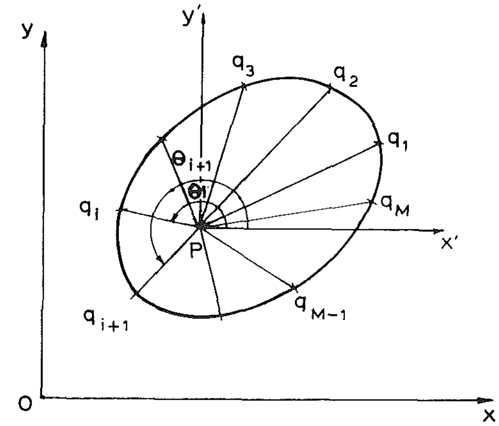

Fig. 2 The region R divided into M sectors.

Table 1 Values of the computed integrals

Number of boundary elements M	Straight line	Second-degree parabolic	Third-degree parabolic	Fourth-degree parabolic
	Approximation of the boundary element			
$I_2 = \int\int_R ln(\sqrt{x^2 + (y-\rho)^2} dxdy$, exact value $I_2 = 0.17991 + 02$				
5				0.17988 + 02
10	0.16796 + 02	0.17984 + 02	0.17988 + 02	0.17991 + 02
20	0.17691 + 02	0.17989 + 02	0.17991 + 02	
30	0.17858 + 02	0.17991 + 02		
50	0.17943 + 02			
100	0.17979 + 02			
150	0.17958 + 02			
200	0.17988 + 02			
$I_4 = \int\int_R \frac{1}{\sqrt{x^2 + (y-\rho)^2}} dxdy$, exact value $I_4 = 0.10000 + 02$				
5				0.99956 + 01
10	0.92128 + 01	0.99945 + 01	0.99967 + 01	0.99999 + 01
20	0.97732 + 01	0.99996 + 01	0.99998 + 01	
30	0.98917 + 01	0.99999 + 01		
50	0.99576 + 01			
100	0.99883 + 01			
150	0.99945 + 01			
200	0.99967 + 01			
$I_5 = \int\int_R \mathrm{ker}(\sqrt{x^2 + y^2}) dxdy$, exact value $I_5 = 0.2339 + 01$				
5				0.2340 + 01
10	0.2426 + 01	0.2340 + 01	0.2340 + 01	0.2339 + 01
20	0.2361 + 01	0.2340 + 01	0.2339 + 01	
30	0.2349 + 01	0.2339 + 01		
50	0.2343 + 01			
100	0.2340 + 01			
150	0.2340 + 01			
200	0.2340 + 01			

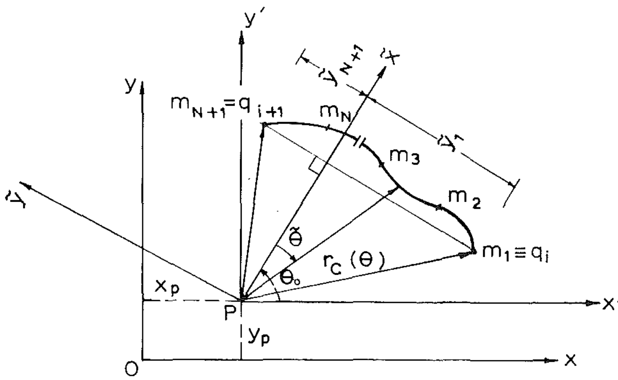

Fig. 3 Approximation of the boundary element by an *N*-degree curve

$$I_i(P) = \int_{\theta_i}^{\theta_{i+1}} \int_0^{r_c(\theta)} f^*(r,\theta)K(r)rdrd\theta \quad (4)$$

In the following, a technique is presented for evaluating the integral (4) in the general case where the boundary element is approximated by a parabola of N degree. The straight line or the second degree parabola are special cases for $N=1$ and $N=2$, respectively.

Consider a sector extending between the lines Pq_i and Pq_{i+1} and choose a system of axes of reference $P\tilde{x}\tilde{y}$ having its $\tilde{x}$ axis normal to the straight line connecting points q_i and q_{i+1}. Choose N-1 interior points $m_i(\tilde{x}_i, \tilde{y}_i)(i=2,3, \ldots N)$ on the element q_iq_{i+1}. The boundary element is approximated by an N degree curve whose equation has the following form

$$\tilde{x} = \tilde{x}(\tilde{y}) = \sum_{k=1}^{N+1} \alpha_k \tilde{y}^{k-1} \quad (5)$$

This implies that any line $\tilde{y}$ = constant intersects the curve approximating the boundary element only at one point. The coefficients α_k are obtained from the solution of the following system of linear algebraic equations

$$\sum_{k=1}^{N+1} \tilde{y}_i^{k-1}\alpha_k = \tilde{x}_i, \quad (i=1,2, \ldots, N+1) \quad (6)$$

In order that the method is also applicable to regions that are not convex, we will replace the angle θ, $\theta_1 \le \theta \le \theta_{N+1}$ in the integral (4) by the variable $\tilde{y}$, $\tilde{y}_1 \le \tilde{y} \le y_{N+1}$. Referring to Fig. 3, the relation between θ and $\tilde{y}$ is

$$\theta = \theta_0 + \tilde{\theta}, \quad \tilde{\theta} = \arctan(\tilde{y}/\tilde{x}) \quad (7)$$

Using the variable $\tilde{y}$ the integral (4) is expressed as

$$I_i(P) = \int_{\tilde{y}_1}^{\tilde{y}_{N+1}} \int_0^{r_c(\tilde{y})} \tilde{f}(r,\tilde{y})K(r)J(\tilde{y})rdrd\tilde{y} \quad (8)$$

where $J(\tilde{y})$ is the Jacobian of the transformation (7). Thus,

$$J(\tilde{y}) = \tilde{\theta}'(\tilde{y}) = (\tilde{x} - \tilde{y}\tilde{x}')/(\tilde{x}^2 + \tilde{y}^2) \quad \tilde{x},\tilde{y}\epsilon C \quad (9)$$

$$r_c(\tilde{y}) = (\tilde{x}^2 + \tilde{y}^2)^{1/2} \quad \tilde{x},\tilde{y}\epsilon C \quad (10)$$

and

$$\tilde{x}' = \frac{d\tilde{x}}{d\tilde{y}} = \sum_{k=2}^{N+1} (k-1)\alpha_k \tilde{y}^{k-2} \quad)11)$$

The integral (8) can be computed readily in the region $\tilde{y}_1 \le \tilde{y} \le \tilde{y}_{N+1}$, $0 \le r \le r_c$ using any numerical technique suitable for the evaluation of double integrals whose integrand [5, 6] is nonsingular.

2 Numerical Results and Conclusions

A computer program has been written for the numerical evaluation of integrals employing the method presented in this note. The input data of the program consists of the coordinates of the points $q_1, q_2 \ldots q_M$ chosen on the boundary of the region of integration R. The integration is performed on each sector by using six-point recursive Gaussian quadrature for multidimensional integrals (subroutine RGAUSS of the CERN Computer Program Library is used). The program has been run on a CDC/CYBER 171 computer and the integrals shown in Table 1 were evaluated on a circular region R of radius $\rho = 2.5$.

From the numerical results it is apparent that the approximation of a curved boundary element by a higher order parabola considerably decreases the computer time required to obtain results of a desired accuracy. In the cases considered, the same degree of accuracy was obtained when the boundary was subdivided into about 200 straight line elements, 20 second-degree parabolic elements, 10 third-degree parabolic elements, or 5 fourth-degree parabolic elements. An analogous reduction of computation time was achieved.

Finally, it should be pointed out that the proposed technique can be employed in evaluating nonsingular integrals over a region bounded by a complicated curve.

References

1 Katsikadelis, J. T., "The Analysis of Plates on Elastic Foundation by the Boundary Integral Equation Method," Ph.D. Dissertation, Polytechnic Institute of New York, June 1982, pp. 123–132.

2 Cruse, T., and Rizzo, F., ed., "Boundary-Integral Equation Method: Computational Applications in Applied Mechanics," AMD-Vol. 11, ASME, New York, 1975, pp. 47–84.

3 Brebbia, C. A., ed., *Recent Advances in Boundary Element Method*, Pentech Press, London, 1978, pp. 375–390.

4 Brebbia, C. A., *The Boundary Element Methods for Engineers*, Pentech Press, London, 1980, pp. 86–89.

5 Stroud, A. H., *Approximate Calculation of Multiple Integrals*, Prentice-Hall, Englewood Cliffs, N.J., 1971, pp. 346–348.

6 Davis, P. J., and Rabinowitz, P., *Methods of Numerical Integration*, Academic Press, New York, 1975, pp. 261–314.

Flexible Thrust Pads of Fixed Inclination

H. D. Conway[1] and M. W. Richman[1]

Introduction

As is very well known, the load supported by a rigid thrust-bearing pad varies markedly with its angle of inclination. At first the load increases rapidly with increase in inclination, reaches a maximum at a certain optimum angle, and then falls off quite precipitously as the inclination is further increased. The optimum angle for rigid pads of infinite aspect ratio was first shown by Lord Rayleigh [1] to occur when the inlet/outlet film thickness ratio is about 2.2. An extensive survey of the literature on the subject is given in the book by Cameron [2].

The object of the present investigation is to extend the work done on rigid bearings by Rayleigh [1] to take into account the elastic deformation of the bearing. Of particular interest is to determine the effect of deformation on both the total load supported by the bearing as well as on the angle of inclination at which the bearing supports the optimum load. This is done by modeling both the slider and pad as Winkler foundations [3] wherein the displacement is proportional to the local pressure.

[1] Department of Theoretical and Applied Mechanics, Cornell University, Ithaca, N.Y. 14853.

Manuscript received by ASME Applied Mechanics Division, January, 1983.

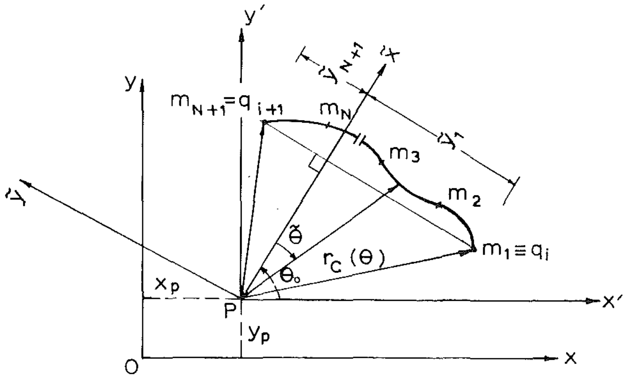

Fig. 3 Approximation of the boundary element by an N-degree curve

$$I_i(P)=\int_{\theta_i}^{\theta_{i+1}}\int_0^{r_c(\theta)} f^*(r,\theta)K(r)rdrd\theta \tag{4}$$

In the following, a technique is presented for evaluating the integral (4) in the general case where the boundary element is approximated by a parabola of N degree. The straight line or the second degree parabola are special cases for $N=1$ and $N=2$, respectively.

Consider a sector extending between the lines Pq_i and Pq_{i+1} and choose a system of axes of reference $P\tilde{x}\tilde{y}$ having its $\tilde{x}$ axis normal to the straight line connecting points q_i and q_{i+1}. Choose N-1 interior points $m_i(\tilde{x}_i, \tilde{y}_i)(i=2,3, \ldots N)$ on the element q_iq_{i+1}. The boundary element is approximated by an N degree curve whose equation has the following form

$$\tilde{x}=\tilde{x}(\tilde{y})=\sum_{k=1}^{N+1}\alpha_k\tilde{y}^{k-1} \tag{5}$$

This implies that any line $\tilde{y}=$constant intersects the curve approximating the boundary element only at one point. The coefficients α_k are obtained from the solution of the following system of linear algebraic equations

$$\sum_{k=1}^{N+1}\tilde{y}_i^{k-1}\alpha_k=\tilde{x}_i, \quad (i=1,2, \ldots, N+1) \tag{6}$$

In order that the method is also applicable to regions that are not convex, we will replace the angle θ, $\theta_1 \leq \theta \leq \theta_{N+1}$ in the integral (4) by the variable $\tilde{y}$, $\tilde{y}_1 \leq \tilde{y} \leq y_{N+1}$. Referring to Fig. 3, the relation between θ and $\tilde{y}$ is

$$\theta=\theta_0+\tilde{\theta}, \quad \tilde{\theta}=\arctan(\tilde{y}/\tilde{x}) \tag{7}$$

Using the variable $\tilde{y}$ the integral (4) is expressed as

$$I_i(P)=\int_{\tilde{y}_1}^{\tilde{y}_{N+1}}\int_0^{r_c(\tilde{y})}\tilde{f}(r,\tilde{y})K(r)J(\tilde{y})rdrd\tilde{y} \tag{8}$$

where $J(\tilde{y})$ is the Jacobian of the transformation (7). Thus,

$$J(\tilde{y}) = \tilde{\theta}'(\tilde{y})=(\tilde{x}-\tilde{y}\tilde{x}')/(\tilde{x}^2+\tilde{y}^2) \quad \tilde{x},\tilde{y}\epsilon C \tag{9}$$

$$r_c(\tilde{y}) = (\tilde{x}^2+\tilde{y}^2)^{1/2} \quad \tilde{x},\tilde{y}\epsilon C \tag{10}$$

and

$$\tilde{x}'=\frac{d\tilde{x}}{d\tilde{y}}=\sum_{k=2}^{N+1}(k-1)\alpha_k\tilde{y}^{k-2} \qquad)11)$$

The integral (8) can be computed readily in the region $\tilde{y}_1 \leq \tilde{y} \leq \tilde{y}_{N+1}$, $0 \leq r \leq r_c$ using any numerical technique suitable for the evaluation of double integrals whose integrand [5, 6] is nonsingular.

2 Numerical Results and Conclusions

A computer program has been written for the numerical evaluation of integrals employing the method presented in this note. The input data of the program consists of the coordinates of the points $q_1, q_2 \ldots q_M$ chosen on the boundary of the region of integration R. The integration is performed on each sector by using six-point recursive Gaussian quadrature for multidimensional integrals (subroutine RGAUSS of the CERN Computer Program Library is used). The program has been run on a CDC/CYBER 171 computer and the integrals shown in Table 1 were evaluated on a circular region R of radius $\rho=2.5$.

From the numerical results it is apparent that the approximation of a curved boundary element by a higher order parabola considerably decreases the computer time required to obtain results of a desired accuracy. In the cases considered, the same degree of accuracy was obtained when the boundary was subdivided into about 200 straight line elements, 20 second-degree parabolic elements, 10 third-degree parabolic elements, or 5 fourth-degree parabolic elements. An analogous reduction of computation time was achieved.

Finally, it should be pointed out that the proposed technique can be employed in evaluating nonsingular integrals over a region bounded by a complicated curve.

References

1 Katsikadelis, J. T., "The Analysis of Plates on Elastic Foundation by the Boundary Integral Equation Method," Ph.D. Dissertation, Polytechnic Institute of New York, June 1982, pp. 123-132.

2 Cruse, T., and Rizzo, F., ed., "Boundary-Integral Equation Method: Computational Applications in Applied Mechanics," AMD-Vol. 11, ASME, New York, 1975, pp. 47-84.

3 Brebbia, C. A., ed., *Recent Advances in Boundary Element Method*, Pentech Press, London, 1978, pp. 375-390.

4 Brebbia, C. A., *The Boundary Element Methods for Engineers*, Pentech Press, London, 1980, pp. 86-89.

5 Stroud, A. H., *Approximate Calculation of Multiple Integrals*, Prentice-Hall, Englewood Cliffs, N.J., 1971, pp. 346-348.

6 Davis, P. J., and Rabinowitz, P., *Methods of Numerical Integration*, Academic Press, New York, 1975, pp. 261-314.

Flexible Thrust Pads of Fixed Inclination

H. D. Conway[1] and M. W. Richman[1]

Introduction

As is very well known, the load supported by a rigid thrust-bearing pad varies markedly with its angle of inclination. At first the load increases rapidly with increase in inclination, reaches a maximum at a certain optimum angle, and then falls off quite precipitously as the inclination is further increased. The optimum angle for rigid pads of infinite aspect ratio was first shown by Lord Rayleigh [1] to occur when the inlet/outlet film thickness ratio is about 2.2. An extensive survey of the literature on the subject is given in the book by Cameron [2].

The object of the present investigation is to extend the work done on rigid bearings by Rayleigh [1] to take into account the elastic deformation of the bearing. Of particular interest is to determine the effect of deformation on both the total load supported by the bearing as well as on the angle of inclination at which the bearing supports the optimum load. This is done by modeling both the slider and pad as Winkler foundations [3] wherein the displacement is proportional to the local pressure.

[1] Department of Theoretical and Applied Mechanics, Cornell University, Ithaca, N.Y. 14853.

Manuscript received by ASME Applied Mechanics Division, January, 1983.

Analysis

The model to be investigated is shown in Fig. 1. The lower surface moves with a velocity U with respect to the upper one, the two surfaces being inclined to one another by a small angle A. Both are assumed to deform as Winkler foundations [3], and are separated from one another by a fluid of viscosity η.

Assuming a long bearing so that the pressure varies only with x, Reynold's equation for the calculation of the pressure p is [2]

$$\frac{d}{dx}\left(h^3\frac{dp}{dx}\right)=-6U\eta\frac{dh}{dx}, \tag{1}$$

whence on integrating

$$\frac{dp}{dx}=6U\eta\left(\frac{\bar{h}-h}{h^3}\right) \tag{2}$$

where $\bar{h}$ is the film thickness at the place where the pressure gradient vanishes.

The initially undeformed surfaces are assumed to be inclined at a small angle A to one another. Modeling the surfaces as Winkler foundations [3], the film thickness takes the form

$$h=Ax+(\lambda_1+\lambda_2)p \tag{3}$$

where λ_1 and λ_2 are the foundation moduli for the slider and pad surfaces, respectively. As an approximation, these may be taken as the particular thickness divided by the appropriate modulus of elasticity. For convenience, then define the effective foundation modulus of the two surfaces, λ, as the sum $\lambda_1 + \lambda_2$. Substituting equation (3) in equation (2) yields

$$\frac{dh}{dx}=6U\lambda\eta\left(\frac{\bar{h}-h}{h^3}\right)+A. \tag{4}$$

The exact closed-form solution of equation (4), from which h and hence $p = p(x)$ can be calculated, is given in the Appendix. The force per unit length, W, of bearing is then obtained by integrating the pressure.

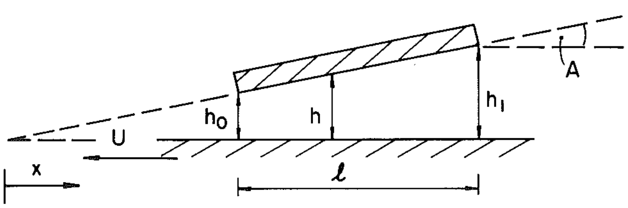

Fig. 1 Thrust-bearing geometry

Results and Conclusions

Figure 2 shows graphs of normalized load $W^* = Wh_0^2/\eta Ul^2$ plotted against the normalized initial angle of inclination $Q_1 = Al/h_0 = (h_1-h_0)/h_0$ for various values of the bearing flexibility parameter $Q_2 = 6U\eta l\lambda/h_0^3$. The solution for the rigid case ($Q_2 = 0$) is well known [2], and is given, in terms of notation used here, by

$$W^*=\frac{1}{Q_1^2}\ln(1+Q_1)-\frac{2}{Q_1(2+Q_1)}. \tag{5}$$

As expected, it is observed that the load decreases markedly with increase of Q_2 and hence an accompanying increase in bearing deformation. The decrease of load is seen not to occur so precipitously, however, as the flexibility of the surfaces increase. Moreover, as compared with the rigid ($Q_2 = 0$) and nearly rigid cases, the effect on load of increasing inclination to an optimum value also appears to be much less dramatic as flexibility of the surfaces increases. These effects are similar to those obtained [2] by plotting $W^* = Wh_0^2/U\eta l^2$ versus $Q_1 = Al/h_0 = (h_1-h_0)/h_0$ for various values of bearing aspect ratio on the assumption that the bearing surfaces are rigid.

The optimum load for a rigid bearing ($Q_2 = 0$) is found to occur at a value of $Q_1 = Al/h_0 = (h_1-h_0)/h_0$ of 1.2 as was first observed by Rayleigh [1]. The optimum value of Q_1 corresponding to maximum load increases with increase of

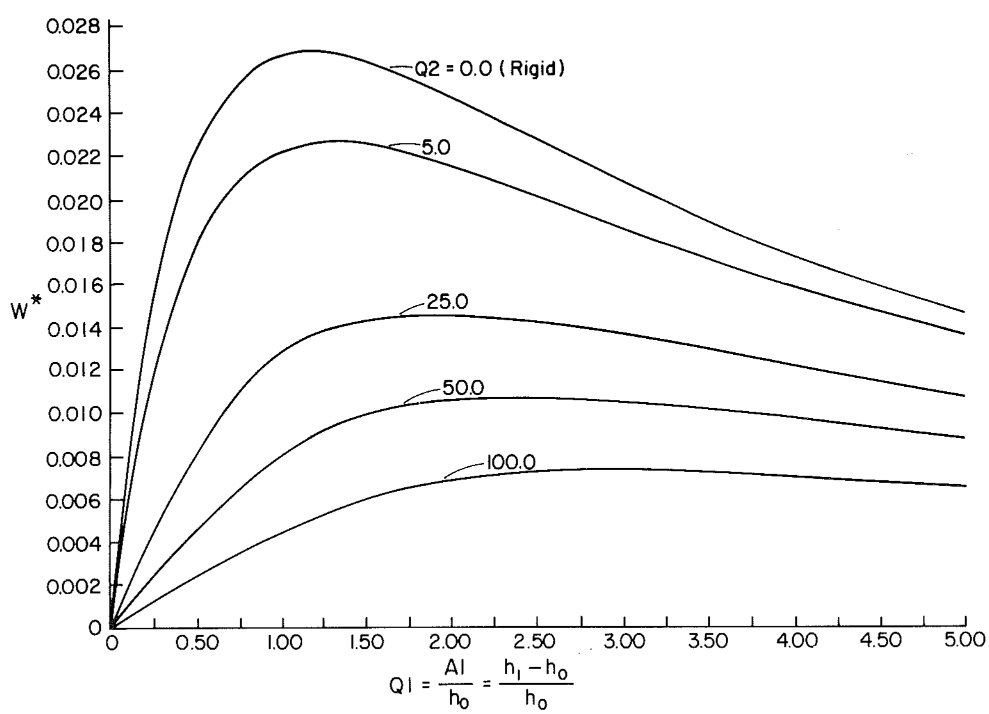

Fig. 2 Graphs of normalized load $W^* = Wh_0^2/\eta Ul^2$ versus normalized slope $Q_1 = Al/h_0$ for various values of normalized flexibility parameter $Q_2 = 6U\eta l\lambda/h_0$

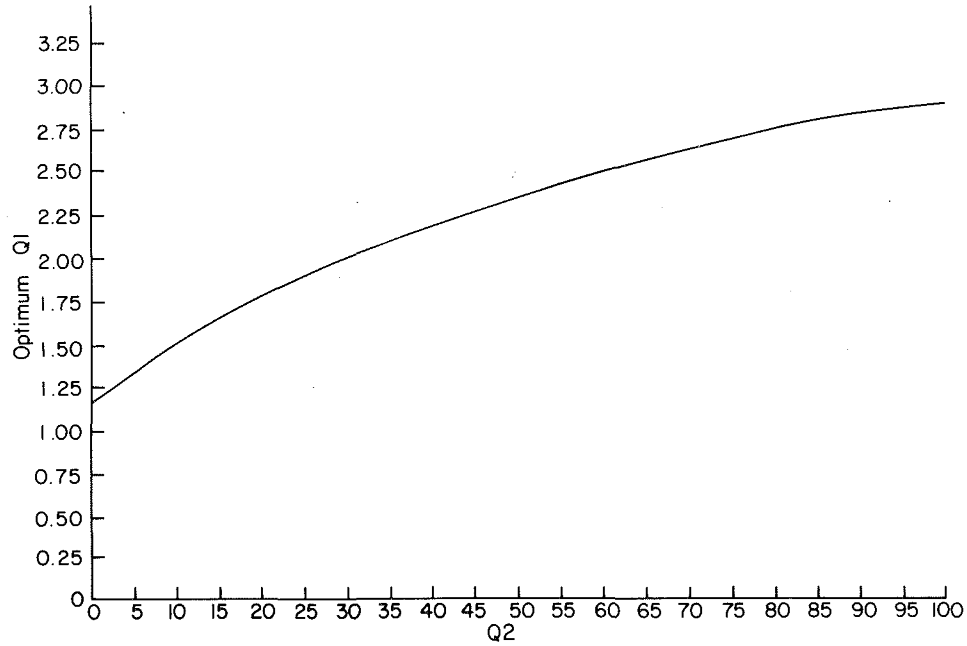

Fig. 3 Graph of normalized flexibility parameter $Q_2 = 6U\eta l\lambda/h_0^3$ versus optimum normalized slope $Q_1 = Al/h_0$ for maximum load

Q_2, as shown in Fig. 3. Again it is seen that the effect of increasing Q_2 on the optimum value of Q_1 diminishes with increasing flexibility.

Acknowledgments

This study grew out of an investigation of elastofluid dynamics of contact lenses sponsored by Bausch & Lomb, Inc. Rochester, N.Y. The authors are grateful for this sponsorship and for the stimulating discussion with Professor J. T. Jenkins and M. Shimbo of the Department of Theoretical and Applied Mechanics, Cornell University. Thanks are also due to Dr. Walter Mendenhall for pointing out that equation (4) can be integrated in closed form.

References

1 Lord Rayleigh, "Notes on the Theory of Lubrication," *Phil. Mag.*, Vol. 35, 1918, pp. 1-12.

2 Cameron, A., *Principles of Lubrication*, Wiley, New York, 1966, Chapter 6.

3 Volterra, E., and Gaines, J. H., *Advanced Strength of Materials*, Prentice-Hall, Englewood Cliffs, N.J., 1971, pp. 379-428.

APPENDIX

To solve equation (4), first write it in a form

$$\frac{dx}{dh} = \frac{1}{A}\left(1 + B\,\frac{h-\bar{h}}{Ah^3 - Bh + B\bar{h}}\right) \qquad (A1)$$

where $B = 6U\eta\lambda$. The second term on the right-hand side may be expressed in partial fractions by factoring the denominator in the form

$$Ah^3 - Bh + B\bar{h} = A(h-r)(h^2 + rh + 2b/r) \qquad (A2)$$

where $a = -B/3A$, $b = -B\bar{h}/2A$, $c = b^2 + a^3$, $r = (b+c^{1/2})^{1/3} + (b-c^{1/2})^{1/3}$ and all roots are chosen real. Equation $(A1)$ may now be integrated to give

$$x = -C + \frac{h}{A} + \frac{B}{12A^2(b-ar)}\left[r(r-\bar{h})\log\frac{(h-r)^2}{(h^2+rh+2b/r)} + \frac{4b+r^2(r+3\bar{h})}{(2b/r-r^2/4)^{1/2}}\tan^{-1}\frac{h+r/2}{(2b/r-r^2/4)^{1/2}}\right] \qquad (A3)$$

where C is a constant of integration. From the boundary condition $p(x=h_0/A) = 0$ and equation (3), it is found that

$$C = \frac{B}{12A^2(b-ar)}\left[r(r-\bar{h})\log\frac{(h_0-r)^2}{(h_0^2+rh_0+2b/r)} + \frac{4b+r^2(r+3\bar{h})}{(2b/r-r^2/4)^{1/2}}\tan^{-1}\frac{(h_0+r/2)}{(2b/r-r^2/4)^{1/2}}\right], \qquad (A4)$$

which gives C as a function of $\bar{h}$. To determine $\bar{h}$, use the secondary boundary condition $p(x=(h_1/A) = (h_0/A) + l) = 0$, equation (3), and equation $(A4)$ to obtain

$$r(r-\bar{h})\log\left[\frac{(h_0-r)^2(h_1^2+rh_1+2b/r)}{(h_1-r)^2(h_0^2+rh_0+2b/r)}\right] + \frac{4b+r^2(r+3\bar{h})}{(2b/r-r^2/4)^{1/2}}\tan^{-1}\left[\frac{(h_0-h_1)(2b/r-r^2/4)^{1/2}}{2b/r+h_0h_1+\frac{r}{2}(h_0+h_1)}\right] = 0 \qquad (A5)$$

Equation $(A5)$ is the transcendental equation for $\bar{h}$.

Thus, the film thickness variation is obtained implicitly and the pressure distribution is found from equation (3). Finally, the load, W, is obtained by integrating the pressure distribution. The results may then be expressed in normalized form, and plots of $W^* = Wh_0^2/\eta Ul^2$ versus $Q_1 = Al/h_0 = (h_1-h_0)/h_0$ are obtained for various values of $Q_2 = 6U\eta l\lambda/h_0^3$, as shown in Fig. 2.

Vibrations of Suspended Cables

J. G. Gale[1] and C. E. Smith[2]

An analytical investigation of the small, normal-mode motions of a homogeneous, inextensible, perfectly flexible cable suspended in a gravitational field was made. With cable arc length as the independent variable, the differential equations that govern the mode shapes have irrational coefficients. A transformation of the independent position variable yields equations that have polynominal coefficients, which then lend themselves to power series solutions. Natural frequencies of oscillation and corresponding mode shapes are determined from these solutions. Figures showing the natural frequency ratios for a variety of cable support geometries are presented for both in-plane and out-of-plane motion.

Nomenclature

a = catenary size parameter; arc length-measured from the cable apex to a position where the cable makes an angle of $\pi/4$ with the horizontal plane

b = horizontal distance between cable support points

g = gravitational acceleration

h = vertical distance between cable support points

l = total length of the cable

s = arc length from the apex of the cable to any point on the cable

u = in-plane, tangential displacement of a point on the cable from its equilibrium configuration

v = in-plane, normal displacement of a point on the cable from its equilibrium configuration

w = out-of-plane displacement of a point on the cable from its equilibrium configuration

$\alpha, \bar{\alpha}$ = angle that the cable makes with the horizontal plane in its equilibrium and displaced configurations

$\tilde{\gamma}$ = angle between the vertical plane of the equilibrium and displaced cable configuration at a point

σ = nondimensional arc length: s/a

τ = nondimensional cable tension

ω = nondimensional natural frequency of oscillation

Slash $'$ = partial derivative with respect to σ

Dot $\dot{}$ = partial derivative with respect to θ

[1] U.S. Department of Energy, Argonne National Laboratory, Idaho Falls, Idaho 83401.

[2] Professor, Department of Mechanical Engineering, Oregon State University, Corvallis, Ore. 97331. Mem. ASME

Manuscript received by ASME Applied Mechanics Division, June, 1982; Final revision, February, 1983.

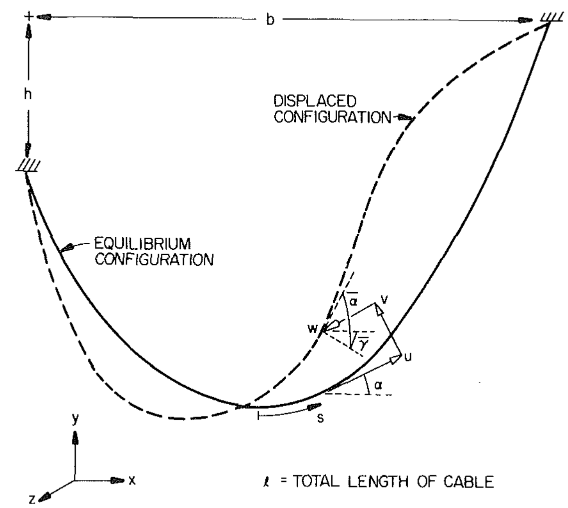

Fig. 1 Displaced configuration of hanging cable showing displacement vectors and angles

Introduction

Until the early 1970s, all attempts to solve the equations of motion for a uniform cable suspended from two points were approximations. Routh [1] presented the equations of motion and solved them for a nonuniform cable that hangs in the shape of a cycloid. Pugsley [2] performed some experimental work and developed an empirical equation for determining the natural frequencies of a symmetrically supported cable. Saxon and Cahn [3], and Goodey [4] developed approximate solutions to Routh's cable equations. In 1971, Smith and Thompson [5] presented the solution to the cable equations in the form of a power series and obtained the natural frequencies of vibration for symmetric and unsymmetric supports. The results in [5] were limited to in-plane modes of motion and depth-to-span ratios of less than 0.76. This paper extends the work reported in [5] to include out-of-plane modes and depth-to-span ratios up to 1.09.

Analysis

Figure 1 shows the relationship between the equilibrium configuration and the displaced configuration of a point on the cable. The nondimensional, linearized equations of motion for the three displacement components of the undamped cable are given by

$$\frac{\ddot{u}}{a}+\frac{1}{a}\left[\frac{v'}{(1+\sigma^2)^{1/2}}+\frac{u}{(1+\sigma^2)^{3/2}}\right]-\tau'=0 \tag{1}$$

$$\frac{\ddot{v}}{a}-\frac{\tau}{1+\sigma^2}-\frac{v''}{a}(1+\sigma^2)^{1/2}-\frac{v'}{a}\frac{\sigma}{(1+\sigma^2)^{1/2}}+\frac{u}{a}\frac{\sigma}{(1+\sigma^2)^{3/2}}-\frac{u'}{a}\frac{1}{(1+\sigma^2)^{1/2}}=0 \tag{2}$$

$$\frac{\ddot{w}}{a}-\frac{w''}{a}(1+\sigma^2)^{1/2}-\frac{w'}{a}\frac{\sigma}{(1+\sigma^2)^{1/2}}=0 \tag{3}$$

The linearized constraint of inextensibility of the cable is given by

$$u'=\frac{v}{1+\sigma^2} \tag{4}$$

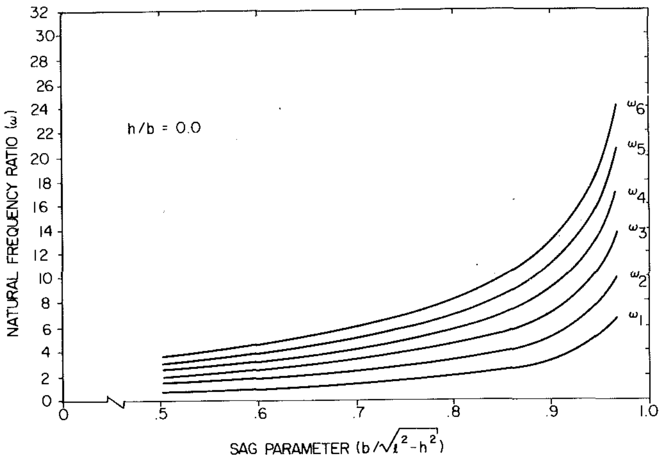

Fig. 2 Natural frequency ratios for in-plane normal mode motion versus sag parameter for $h/b = 0.0$

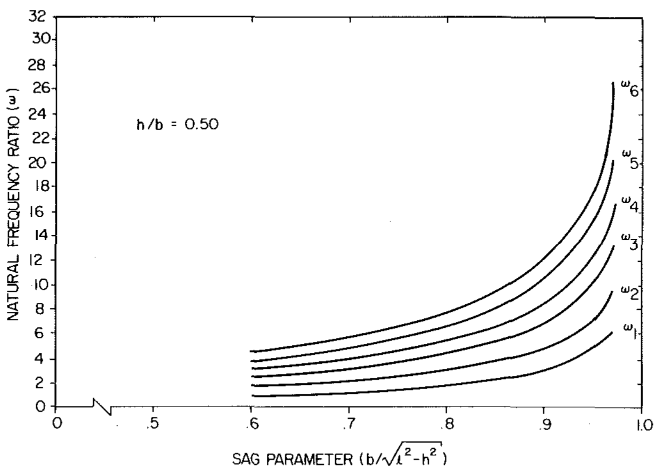

Fig. 3 Natural frequency ratios for in-plane normal mode motion versus sag parameter for $h/b = 0.50$

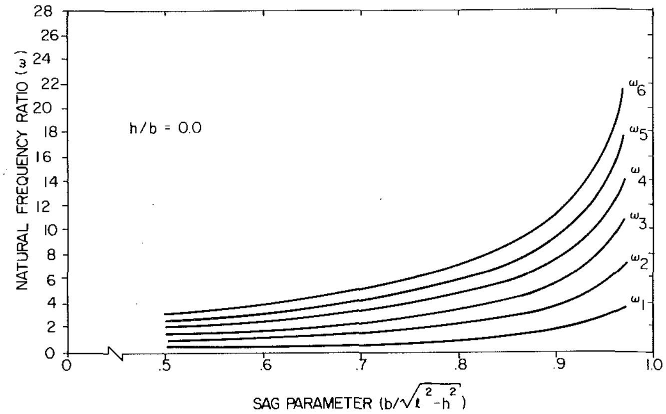

Fig. 4 Natural frequency ratios for out-of-plane normal mode motion versus sag parameter for $h/b = 0.0$

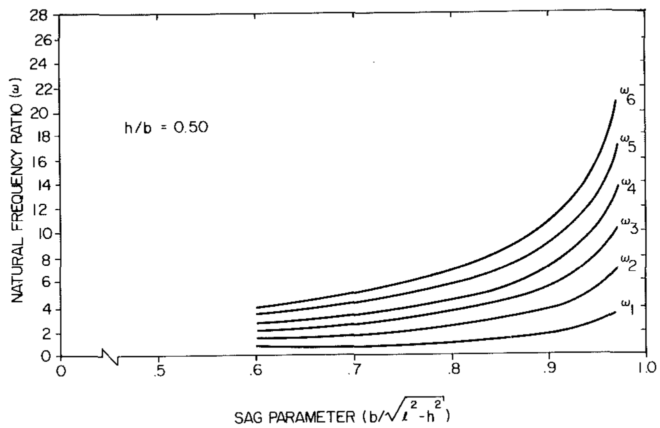

Fig. 5 Natural frequency ratios for out-of-plane normal mode motion versus sag parameter for $h/b = 0.50$

Equations (1)–(4) complete the set of equations that describe the four unknowns u, v, w, and τ. Note that equation (3), governing the out-of-plane motion of the cable, is independent of the equations governing the in-plane motion of the cable. Actual coupling is reflected in nonlinear terms which are lost upon linearization.

By assuming a normal-mode motion solution along with an appropriate independent variable change, the differential equations can be expressed as ordinary differential equations with rational coefficients. These equations can then be solved using power series solution techniques. The restriction that the displacements are zero at the support points will lead to the development of the standard eigenvalue problem for which the natural frequency ratios are the eigenvalues. Details of the equation development and solution technique are available in references [5] and [6].

Results

A FORTRAN IV program was written that generates the power series expressions for the displacement of any point on the cable. A Newton-Raphson root-finding technique was then incorporated into the program to find values of the natural frequencies of oscillation which yielded zero displacements at the two fixed ends of the cable. Figures 2 and 3 show curves of the first six natural frequencies of oscillation for in-plane motion of the cable for different values of the sag parameter $(b/(l^2-h^2)^{1/2})$ and support parameter (h/b). Figures 4 and 5 show curves of the first six natural frequencies of oscillation for out-of-plane motion of the cable for different sag and support parameters.

Conclusions

Having developed an exact solution for the small oscillations of an unsymmetrical cable, general statements regarding the behavior of cable systems may be made which could prove useful in their design. Typically in design of mechanical systems, an attempt is made to assure that the natural frequencies of oscillation of the system are not "close" to possible exciting frequencies which may be imposed on the system and could cause a resonance condition. Should resonant states appear imminent, several things can be done to the system to circumvent their possible occurrence. The system configuration (i.e., geometry, material, or structure) could be modified or damping could be introduced into the system. Damping may not significantly affect the natural frequencies of oscillation of the system, but it will attenuate its response at the resonant frequency.

Since the work presented herein is for perfectly flexible, undamped cable systems, statements regarding natural frequency behavior may be made in reference to cable support position changes and cable length changes only. Inspection of the natural frequency curves will provide insight as to how cable geometry changes will affect the natural frequency ratios.

1. For both in-plane and out-of-plane motion at any one support parameter value (h/b ratio), the natural fre-

quencies increase for increasing values of the sag parameter $(b/\sqrt{l^2-h^2})$. It should be observed that increased values of the sag parameter infer a "tightening" of the cable system.

2. For both in-plane and out-of-plane motion at any one sag parameter value, the natural frequencies decrease for increasing values of the support parameter. The natural frequencies are not as sensitive to changes in the support parameter as they are to changes in the sag parameter (i.e., a 50 percent increase in the support parameter may only reduce the natural frequency by 3 percent, whereas a 50 percent increase in the sag parameter may increase the natural frequency by 75 percent). Thus, if one is interested in modifying the natural frequencies significantly, the overall cable length, l, is the parameter that produces the most effect.

The natural frequencies shown in Figs. 2–5 are nondimensional. To make the conversion to dimensional (radian) frequencies, it is necessary to multiply the nondimensional frequencies (ω's) by $\sqrt{a/g}$. The cable parameter a is related to the cable geometry by the transcendental equation:

$$\frac{b}{\sqrt{l^2-h^2}}=\frac{b/2a}{\sinh(b/2a)}.$$

Solution to the preceding equation for a, can be easily accomplished using standard numerical root-finding techniques.

1. For both in-plane and out-of-plane motion at any one support parameter value (h/b ratio), the natural frequencies increase for increasing values of the sag parameter $(b/\sqrt{l^2-h^2})$. It should be observed that increased values of the sag parameter infer a "tightening" of the cable system.

2. For both in-plane and out-of-plane motion at any one sag parameter value, the natural frequencies decrease for increasing values of the support parameter. The natural frequencies are not as sensitive to changes in the support parameter as they are to changes in the sag parameter (i.e., a 50 percent increase in the support parameter may only reduce the natural frequency by 3 percent, whereas a 50 percent increase in the sag parameter may increase the natural frequency by 75 percent). Thus, if one is interested in modifying the natural frequencies significantly, the overall cable length, l, is the parameter that produces the most effect.

The natural frequencies shown in Figs. 2–5 are nondimensional. To make the conversion to dimensional (radian) frequencies, it is necessary to multiply the nondimensional frequencies (ω's) by $\sqrt{a/g}$. The cable parameter a is related to the cable geometry by the transcendental equation:

$$\frac{b}{\sqrt{l^2-h^2}}=\frac{b/2a}{\sin(b/2a)}.$$

Solution to the preceeding for a, can be easily accomplished using standard numerical root-finding techniques.

References

1 Routh, E. J., "Motion of a String or Chain," *Advanced Rigid Dynamics*, 6th Ed., Macmillan, New York, 1905, Chapter XIII.

2 Pugsley, A. G., "On the Natural Frequencies of Suspended Chains," *The Quarterly Journal of Mechanics and Applied Mathematics*, Vol. II, Part 4, Dec. 1949, pp. 412–418.

3 Saxon, D. S., and Cahn, A. S., "Modes of Vibration of a Suspended Chain," *The Quarterly Journal of Mechanics and Applied Mathematics*, Vol. VI, Part 3, Sept. 1953, pp. 273–285.

4 Goodey, W. J., "On the Natural Modes and Frequencies of a Suspended Chain," *The Quarterly Journal of Mechanics and Applied Mathematics*, Vol. XIV, Part I, Feb. 1961, pp. 118–127.

5 Smith, C. E., and Thompson, R. S., "The Small Oscillations of a Suspended Flexible Line," ASME Journal of Applied Mechanics, Vol. 40, 1973, pp. 624–626.

6 Gale, J. G., "Vibrations of Suspended Cables," Ph.D. Dissertation, Oregon State University, 1976.

The Effect of Plastic Deformation on the Acoustoelastic Response of Metals

G. C. Johnson[1]

Introduction

The use of an ultransonic technique called acoustoelasticity for the nondestructive measurement of residual stress has received considerable attention recently. Acoustoelasticity is based on the observation that the speeds at which waves propagate in a structure depend on the stress in that body. To effectively determine the residual stress, the quantity being measured, in this case velocity, should be a function of the stress alone. Unfortunately, there are data that indicate that the velocity is dependent on prior plastic deformation in certain materials [1]. Given this observation, we seek to develop a continuum theory that allows for changes in wave speed as a function of plastic deformation. The work presented in this Note follows an earlier theoretical development along these lines [2]. However, the present approach employs different measures of the elastic and plastic deformation and so results in a set of velocity relations that may be more usable than those in [2].

The Elastic-Plastic Continuum

The developments discussed here are based on the continuum description of elastic-plastic response proposed by Green and Naghdi [3]. For simplicity, only the isothermal response of an isotropic material is considered.

In deriving expressions for the propagation velocities of plane waves, an analysis of the motion of an infintesimal disturbance superposed on a finite, elastic-plastic deformation will be performed. As such, it is convenient to introduce three configurations of the body. Let the vectors $\mathbf{X}$, $\mathbf{x}$, and $\mathbf{x}^*$ denote the undeformed reference state, the state of finite elastic-plastic deformation (called the deformed state), and the current state (which includes the superposed wave), respectively. We take the deformed state to be in static equilibrium so that $\mathbf{x} = \mathbf{x}(\mathbf{X})$ and the total deformation gradient and Lagrange strain are

$$\mathbf{F}=\frac{\partial \mathbf{x}}{\partial \mathbf{X}},\quad \mathbf{E}=\frac{1}{2}(\mathbf{F}^T\mathbf{F}-\mathbf{I}). \tag{1}$$

The deformation gradient may be decomposed into elastic and plastic parts as [4, 5]

$$\mathbf{F}=\mathbf{F}^e\mathbf{F}^p. \tag{2}$$

This decomposition has been used by Lee and his coworkers in their development of a finite deformation plasticity theory and has been discussed by Green and Naghdi [6] as it relates to their theory. In this regard, we recall that this decomposition is not unique since

$$\mathbf{F}=\hat{\mathbf{F}}^e\hat{\mathbf{F}}^p,\quad \hat{\mathbf{F}}^e=\mathbf{F}^e\hat{\mathbf{Q}},\quad \hat{\mathbf{F}}^p=\hat{\mathbf{Q}}^T\mathbf{F}^p \tag{3}$$

for all orthogonal $\hat{\mathbf{Q}}$.

Elastic and plastic strains are defined as

$$\mathbf{E}^e=\frac{1}{2}(\mathbf{F}^{eT}\mathbf{F}^e-\mathbf{I}),\quad \mathbf{E}^p=\frac{1}{2}(\mathbf{F}^{pT}\mathbf{F}^p-\mathbf{I}), \tag{4}$$

so that

$$\mathbf{E}=\mathbf{E}^p+\mathbf{F}^{pT}\mathbf{E}^e\mathbf{F}^p \tag{5}$$

and we assume the free energy ψ to be a function of these

[1]Assistant Professor, Department of Mechanical Engineering, University of California, Berkeley, Calif. 94720. Assoc. Mem. ASME.

Manuscript received by ASME Applied Mechanics Division, March, 1982; final revision, February, 1983.

quencies increase for increasing values of the sag parameter $(b/\sqrt{l^2-h^2})$. It should be observed that increased values of the sag parameter infer a "tightening" of the cable system.

2. For both in-plane and out-of-plane motion at any one sag parameter value, the natural frequencies decrease for increasing values of the support parameter. The natural frequencies are not as sensitive to changes in the support parameter as they are to changes in the sag parameter (i.e., a 50 percent increase in the support parameter may only reduce the natural frequency by 3 percent, whereas a 50 percent increase in the sag parameter may increase the natural frequency by 75 percent). Thus, if one is interested in modifying the natural frequencies significantly, the overall cable length, l, is the parameter that produces the most effect.

The natural frequencies shown in Figs. 2–5 are nondimensional. To make the conversion to dimensional (radian) frequencies, it is necessary to multiply the nondimensional frequencies (ω's) by $\sqrt{a/g}$. The cable parameter a is related to the cable geometry by the transcendental equation:

$$\frac{b}{\sqrt{l^2-h^2}}=\frac{b/2a}{\sinh(b/2a)}.$$

Solution to the preceding equation for a, can be easily accomplished using standard numerical root-finding techniques.

1. For both in-plane and out-of-plane motion at any one support parameter value (h/b ratio), the natural frequencies increase for increasing values of the sag parameter $(b/\sqrt{l^2-h^2})$. It should be observed that increased values of the sag parameter infer a "tightening" of the cable system.

2. For both in-plane and out-of-plane motion at any one sag parameter value, the natural frequencies decrease for increasing values of the support parameter. The natural frequencies are not as sensitive to changes in the support parameter as they are to changes in the sag parameter (i.e., a 50 percent increase in the support parameter may only reduce the natural frequency by 3 percent, whereas a 50 percent increase in the sag parameter may increase the natural frequency by 75 percent). Thus, if one is interested in modifying the natural frequencies significantly, the overall cable length, l, is the parameter that produces the most effect.

The natural frequencies shown in Figs. 2–5 are nondimensional. To make the conversion to dimensional (radian) frequencies, it is necessary to multiply the nondimensional frequencies (ω's) by $\sqrt{a/g}$. The cable parameter a is related to the cable geometry by the transcendental equation:

$$\frac{b}{\sqrt{l^2-h^2}}=\frac{b/2a}{\sin(b/2a)}.$$

Solution to the preceeding for a, can be easily accomplished using standard numerical root-finding techniques.

References

1 Routh, E. J., "Motion of a String or Chain," *Advanced Rigid Dynamics*, 6th Ed., Macmillan, New York, 1905, Chapter XIII.

2 Pugsley, A. G., "On the Natural Frequencies of Suspended Chains," *The Quarterly Journal of Mechanics and Applied Mathematics*, Vol. II, Part 4, Dec. 1949, pp. 412–418.

3 Saxon, D. S., and Cahn, A. S., "Modes of Vibration of a Suspended Chain," *The Quarterly Journal of Mechanics and Applied Mathematics*, Vol. VI, Part 3, Sept. 1953, pp. 273–285.

4 Goodey, W. J., "On the Natural Modes and Frequencies of a Suspended Chain," *The Quarterly Journal of Mechanics and Applied Mathematics*, Vol. XIV, Part I, Feb. 1961, pp. 118–127.

5 Smith, C. E., and Thompson, R. S., "The Small Oscillations of a Suspended Flexible Line," ASME Journal of Applied Mechanics, Vol. 40, 1973, pp. 624–626.

6 Gale, J. G., "Vibrations of Suspended Cables," Ph.D. Dissertation, Oregon State University, 1976.

The Effect of Plastic Deformation on the Acoustoelastic Response of Metals

G. C. Johnson[1]

Introduction

The use of an ultransonic technique called acoustoelasticity for the nondestructive measurement of residual stress has received considerable attention recently. Acoustoelasticity is based on the observation that the speeds at which waves propagate in a structure depend on the stress in that body. To effectively determine the residual stress, the quantity being measured, in this case velocity, should be a function of the stress alone. Unfortunately, there are data that indicate that the velocity is dependent on prior plastic deformation in certain materials [1]. Given this observation, we seek to develop a continuum theory that allows for changes in wave speed as a function of plastic deformation. The work presented in this Note follows an earlier theoretical development along these lines [2]. However, the present approach employs different measures of the elastic and plastic deformation and so results in a set of velocity relations that may be more usable than those in [2].

The Elastic-Plastic Continuum

The developments discussed here are based on the continuum description of elastic-plastic response proposed by Green and Naghdi [3]. For simplicity, only the isothermal response of an isotropic material is considered.

In deriving expressions for the propagation velocities of plane waves, an analysis of the motion of an infintesimal disturbance superposed on a finite, elastic-plastic deformation will be performed. As such, it is convenient to introduce three configurations of the body. Let the vectors $\mathbf{X}$, $\mathbf{x}$, and $\mathbf{x}^*$ denote the undeformed reference state, the state of finite elastic-plastic deformation (called the deformed state), and the current state (which includes the superposed wave), respectively. We take the deformed state to be in static equilibrium so that $\mathbf{x} = \mathbf{x}(\mathbf{X})$ and the total deformation gradient and Lagrange strain are

$$\mathbf{F}=\frac{\partial \mathbf{x}}{\partial \mathbf{X}}, \quad \mathbf{E}=\frac{1}{2}(\mathbf{F}^T\mathbf{F}-\mathbf{I}). \tag{1}$$

The deformation gradient may be decomposed into elastic and plastic parts as [4, 5]

$$\mathbf{F}=\mathbf{F}^e\mathbf{F}^p. \tag{2}$$

This decomposition has been used by Lee and his coworkers in their development of a finite deformation plasticity theory and has been discussed by Green and Naghdi [6] as it relates to their theory. In this regard, we recall that this decomposition is not unique since

$$\mathbf{F}=\hat{\mathbf{F}}^e\hat{\mathbf{F}}^p, \quad \hat{\mathbf{F}}^e=\mathbf{F}^e\hat{\mathbf{Q}}, \quad \hat{\mathbf{F}}^p=\hat{\mathbf{Q}}^T\mathbf{F}^p \tag{3}$$

for all orthogonal $\hat{\mathbf{Q}}$.

Elastic and plastic strains are defined as

$$\mathbf{E}^e=\frac{1}{2}(\mathbf{F}^{eT}\mathbf{F}^e-\mathbf{I}), \quad \mathbf{E}^p=\frac{1}{2}(\mathbf{F}^{pT}\mathbf{F}^p-\mathbf{I}), \tag{4}$$

so that

$$\mathbf{E}=\mathbf{E}^p+\mathbf{F}^{pT}\mathbf{E}^e\mathbf{F}^p \tag{5}$$

and we assume the free energy ψ to be a function of these

[1] Assistant Professor, Department of Mechanical Engineering, University of California, Berkeley, Calif. 94720. Assoc. Mem. ASME.

Manuscript received by ASME Applied Mechanics Division, March, 1982; final revision, February, 1983.

strains and a work-hardening parameter κ. The constitutive equation for the symmetric Piola-Kirchoff stress $\mathbf{S}$ is given through ψ as

$$\mathbf{S}=\rho_0\frac{\partial\psi}{\partial\mathbf{E}},\quad \psi=\bar{\psi}(\mathbf{E}^e,\mathbf{E}^p,\kappa). \tag{6}$$

Since the decomposition of $\mathbf{F}$ is unique only up to the rotation $\hat{\mathbf{Q}}$, we have the condition that

$$\bar{\psi}(\mathbf{E}^e,\mathbf{E}^p,\kappa)=\bar{\psi}(\hat{\mathbf{Q}}\mathbf{E}^e\hat{\mathbf{Q}}^T,\mathbf{E}^p,\lambda) \tag{7}$$

which requires that the free energy be an isotropic function in the elastic strain.

Let us now examine the relation between the Cauchy stress $\mathbf{T}$ and the elastic portion of the motion. Recall that the Cauchy stress may be written in terms of the symmetric Piola-Kirchoff stress as

$$\mathbf{T}=J^{-1}\mathbf{F}\mathbf{S}\mathbf{F}^T,\quad J=\det\mathbf{F}. \tag{8}$$

Using equations (5) and (6) this becomes

$$\mathbf{T}=\rho_0 J^{-1}\mathbf{F}^e\frac{\partial\psi}{\partial\mathbf{E}^e}\mathbf{F}^{eT}. \tag{9}$$

If the plastic deformation is taken to be volume preserving, then $\det\mathbf{F}=\det\mathbf{F}^e$ and the Cauchy stress is written in terms of the elastic deformation alone.

Wave Propagation at Finite Deformation

As indicated in the preceding section, the velocity expressions sought will be obtained by considering an infintesimal deformation superposed on a finite state of elastic-plastic deformation. The position of a material point in this current state is given by

$$\mathbf{x}^*=\mathbf{x}+\mathbf{u}(\mathbf{X},t). \tag{10}$$

In this analysis, only superposed motions that are elastic will be examined, the ultrasonic waves not being of sufficient magnitude to cause plastic loading. Under these circumstances the quantities associated with the plastic part of the deformation are unchanged under the superposed motion, so that

$$\mathbf{F}^{p*}=\mathbf{F}^p,\mathbf{E}^{p*}=\mathbf{E}^p,\kappa^*=\kappa. \tag{11}$$

The quantities associated with the elastic part of the motion depend on the disturbance $\mathbf{u}$, but since this is taken to be an infinitesimal deformation, all such quantities will be taken to be linear in $\mathbf{u}$ and its derivatives.

The equation of motion for the disturbance is

$$\frac{\partial T^*}{\partial\mathbf{x}^*}=\rho^*\ddot{\mathbf{u}} \tag{12}$$

where $\mathbf{T}^*$ and ρ^* are the Cauchy stress and mass density in the current state. The linearization of this equation (see [2] for example) involves expanding each of the starred quantities about the deformed state. The resulting equation in component form is

$$\frac{\partial}{\partial x_i}\left[(C^e_{ijkl}+T_{il}\delta_{jk})\frac{\partial u_k}{\partial x_l}\right]=\rho\ddot{u}_j \tag{13}$$

where

$$C^e_{ijkl}=\rho F^e_{im}F^e_{jn}F^e_{kp}F^e_{lq}\frac{\partial^2\psi}{\partial E^e_{mn}\partial E^e_{pq}}. \tag{14}$$

This expression for the equations of motion for the disturbance $\mathbf{u}$ is identical in form to that for a small deformation superposed on a finite elastic deformation. Further, the quantities in equation (13) are computed by taking derivatives of the strain energy with respect to the elastic strain. The plastic deformation is then seen to act primarily in the role of modifying the coefficients of the elastic strain.

To obtain a characteristic equation from which the propagation velocities can be evaluated, the usual assumptions made in developing an acoustoelastic theory are made here. These are that the finite deformation is homogenous and that the superposed disturbance has the form

$$\mathbf{u}=\mathbf{A}e^{ik}(\mathbf{n}\cdot\mathbf{x}-Vt),\quad k=\omega/V \tag{15}$$

which represents the motion of a plane wave propagating in the $\mathbf{n}$ direction with amplitude $\mathbf{A}$, speed V, and frequency ω. Using this equation (13) leads to the characteristic equation

$$\det[(C^e_{ijkl}+T_{il}\delta_{jk})n_i n_l-\rho V^2\delta_{jk}]=0. \tag{16}$$

This equation has the usual symmetry properties so that the eigenvalues, ρV^2, are real and the eigenvectors, A_k, are mutually orthogonal.

Acoustoelastic Response

We now propose a simple form for the strain energy which represents the constitutive relation for an isotropic material,

$$\psi=\alpha_1 I_1^2+\alpha_2 I_2+\beta_1 I_1^3+\beta_2 I_1 I_2+\beta_3 I_3 \tag{17}$$

where

$$I_1=\mathrm{tr}\mathbf{E}^e,\quad I_2=\mathrm{tr}\mathbf{E}^{e^2},\quad I_3=\mathrm{tr}\mathbf{E}^{e^3} \tag{18}$$

and the α's and β's are functions of the κ and the invariants of $\mathbf{E}^p$.

To evaluate the acoustoelastic response we consider the case of a plane wave propagating along one of the principal directions of elastic deformation, taken to be the x_1 direction. The computation of velocities is carried out by evaluating the stiffness and stress terms in equation (16) through differentiation of ψ and noting that the elastic strain is sufficiently small that the velocities may be taken as linear in the strain. The velocities are found to be

$$\begin{aligned}
\rho_0 V_1^2 =\ & 2\alpha_1+2\alpha_2+(2\alpha_1+6\beta_1+2\beta_2)E^e_{kk}\\
&+(8\alpha_1+10\alpha_2+4\beta_2+6\beta_3)E^e_{11}\\
\rho_0 V_2^2 =\ & \alpha_2+(2\alpha_1+\beta_2+\tfrac{3}{2}\beta_3)E^e_{kk}+4\alpha_2E^e_{11}\\
&+2\alpha_2E^e_{22}-\tfrac{3}{2}\beta_3E^e_{33}\\
\rho_0 V_3^2 =\ & \alpha_2+(2\alpha_1+\beta_2+\tfrac{3}{2}\beta_3)E^e_{kk}+4\alpha_2E^e_{11}\\
&+2\alpha_2E^e_{33}-\tfrac{3}{2}\beta_3E^e_{22}
\end{aligned} \tag{19}$$

where V_1 is the velocity of a longitudinal wave, and V_2 and V_3 are the velocities of pure shear waves with particle motions in the x_2 and x_3 directions, respectively.

We observe here that these equations are identical to those given by Hughes and Kelly [7] for elastic deformation if the parameters used here are identified with the Lamé and Murnaghan constants as

$$\begin{aligned}
\alpha_1 &= \lambda/2,\quad \alpha_2=\mu\\
\beta_1 &= (2l-2m+n)/6,\quad \beta_2=m-n/2,\quad \beta_3=n/3
\end{aligned} \tag{20}$$

The parameters used in this work, the α's and β's, were deliberately chosen as different symbols than the Lamé and Murnaghan constants to emphasize that here the coefficients in the velocity expressions are functions of the plastic deformation.

The most significant feature of this development is that when the coefficients are taken to be constants, the velocities may be directly related to the stress, be it active or residual. The corresponding expressions for acoustoelastic response in elastic-plastic bodies developed in [2] indicate a change in acoustoelastic response with plastic flow regardless of the form taken by the coefficients. This undesirable aspect arises from the fact that in [2] the fundamental constitutive equation relates the strain to the sysmmetric Piola-Kirchoff stress while the equations of motion are written in terms of the Cauchy stress. Thus the plastic flow enters the velocity through the transformation between these measures of stress. In the present work, we were able to get an expression for the Cauchy stress in terms of the elastic strain, equation (9), so that we did not have to involve the plastic strain in the equations of motion.

Acknowledgment

This material is based on work supported by the National Science Foundation under Grant No. MEA-8116376.

References

1 Johnson, G. C., "On the Applicability of Acoustoelasticity for Residual Stress Determination," ASME JOURNAL OF APPLIED MECHANICS, Vol. 48, 1981, pp. 791-795.
2 Johnson, G. C., "Acoustoelastic Theory for Elastic-Plastic Materials," *J. Acoust. Soc. Am.*, Vol. 70, 1981, pp. 591-595.
3 Green, A. E., and Naghdi, P. M., "A General Theory of an Elastic-Plastic Continuum," *Arch. Rat. Mech. Anal.*, Vol. 18, 1965, pp. 251-281.
4 Lee, E. H., "Elastic-Plastic Deformation at Finite Strains," ASME JOURNAL OF APPLIED MECHANICS, Vol. 36, 1969, pp. 1-6.
5 Lee, E. H ., "Some Comments on Elastic-Plastic Analysis," *Int. J. Solids Struct.*, Vol. 17, 1981, pp. 859-872.
6 Green, A. E., and Naghdi, P. M., "Some Remarks on Elastic-Plastic Deformations at Finite Strain," *Int. J. Eng. Sci.*, Vol. 9, 1971, pp. 1219-1229.
7 Hughes, D. S. and Kelly, J. L., "Second-order Elastic Deformation of Solids," *Phys. Rev.*, Vol. 92, 1953, pp. 1145-1149.

Flexural Vibrations of Clamped Polygonal and Circular Plates Having Rectangular Orthotropy

Y. Narita[1]

Introduction

In the present Note, a series-type method previously developed [1-3] is applied to the free vibration of clamped polygonal and circular plates having rectangular orthotropy, and the natural frequencies and mode shapes of these plates are calculated with good accuracy. The effects of varying the geometric and orthotropic parameters on the vibration characteristics are examined in detail.

Application of the Method

As explained in references [1-3], frequency equations are obtained for plates of the desired shape by the appropriate location of some straight or curved clamping segments on the original plate. The major axes of the orthotropic material are taken to coincide with x, y axes in rectangular coordinates. Regular polygons have a finite number of geometrically symmetric axes and some of them coincide with the major axes of orthotropy. Vibration mode shapes in that case can be classified as symmetric mode or antisymmetric mode with respect to each axis. That is, two types of vibration modes (S-type, and A-type) exist for pentagonal and septangular plates, and four types (SS-type, SA-type, AS-type, and AA-type) exist for hexagonal and octagonal plates. The resulting frequency equations for the polygons take the same form as those given in reference [1] except for ω_{mn}.

For the circular plate, elements of the frequency matrix are expressed as

$$I^{(1)}_{mn,i}=\frac{2}{a}\int_0^{\pi/2}\sin\frac{m\pi}{2}(1+\cos\phi)\sin\frac{n\pi}{2}(1+\sin\phi)\sin 2i\phi\, d\phi$$

$$J^{(1)}_{mn,i}=\frac{\partial}{\partial r}I^{(1)}_{mn,i}=\frac{2\pi}{a^2}\Big[m\int_0^{\pi/2}$$

$$\times\cos\frac{m\pi}{2}(1+\cos\phi)\sin\frac{n\pi}{2}(1+\sin\phi)\sin 2i\phi\cos\phi\, d\phi$$

$$+n\int_0^{\pi/2}\sin\frac{m\pi}{2}(1+\cos\phi)\cos\frac{n\pi}{2}(1+\sin\phi)\sin 2i\phi\sin\phi\, d\phi\Big]$$

where ϕ is an angle of the line between a point on the circular boundary and the center of the circle. Definite integrals in the preceding equations are numerically evaluated by the Gauss-Legendre quadrature with 24 points, while the integrals given in the case of polygons are exactly calculated [1].

[1] Lecturer, Computer Center, Hokkaido Institute of Technology, Teine, Sapporo 061-24, Japan.

Manuscript received by ASME Applied Mechanics Division, January, 1983; final revision, March, 1983.

Table 1 Comparison of the fundamental frequency parameters Ω of isotropic polygonal plates

Number of sides	5	6	7	8
Present method	14.48	12.97	12.12	11.67
Shahady et al. [4]	14.44	12.85	12.03	11.54
Walkinshaw et al.[5]	14.32	12.80	11.99	11.53
Laura et al. [6]	14.37	13.08	12.8	---

Table 2 Comparison of the lowest four frequency parameters Ω of isotropic and orthotropic circular plates

	[0,0]	[1,0]	[2,0]	[0,1]
(a) Isotropic case				
Present method	10.23	21.25	34.97	39.81
Exact values	10.216	21.260	34.877	39.771
Asai [7]	10.22	21.22	---	---
(b) Orthotropic case	($D_x/H=1.469$, $D_y/H=0.735$)			
Present method	10.59	20.09	---	---
Asai [7]	10.59	20.05	---	---

Table 3 Fundamental frequency parameters for orthotropic polygonal and circular plates clamped at the edges

Number of sides	(D_x/H, D_y/H)			
	(0.5,0.5)	(0.5, 2)	(2,0.5)	(2, 2)
5	11.44 (11.30)	15.57 (15.74)	15.59 (15.59)	19.14 (19.10)
6	10.25 (10.27)	14.05 (14.4)	13.97 (14.27)	17.15 (17.33)
7	9.574	13.10	13.11	16.04
8	9.276	12.73	12.73	15.53
∞ (circle)	8.090	11.05	11.05	13.51

( ): Values from reference [6]

form taken by the coefficients. This undesirable aspect arises from the fact that in [2] the fundamental constitutive equation relates the strain to the sysmmetric Piola-Kirchoff stress while the equations of motion are written in terms of the Cauchy stress. Thus the plastic flow enters the velocity through the transformation between these measures of stress. In the present work, we were able to get an expression for the Cauchy stress in terms of the elastic strain, equation (9), so that we did not have to involve the plastic strain in the equations of motion.

Acknowledgment

This material is based on work supported by the National Science Foundation under Grant No. MEA-8116376.

References

1 Johnson, G. C., "On the Applicability of Acoustoelasticity for Residual Stress Determination," ASME JOURNAL OF APPLIED MECHANICS, Vol. 48, 1981, pp. 791-795.

2 Johnson, G. C., "Acoustoelastic Theory for Elastic-Plastic Materials," *J. Acoust. Soc. Am.*, Vol. 70, 1981, pp. 591-595.

3 Green, A. E., and Naghdi, P. M., "A General Theory of an Elastic-Plastic Continuum," *Arch. Rat. Mech. Anal.*, Vol. 18, 1965, pp. 251-281.

4 Lee, E. H., "Elastic-Plastic Deformation at Finite Strains," ASME JOURNAL OF APPLIED MECHANICS, Vol. 36, 1969, pp. 1-6.

5 Lee, E. H ., "Some Comments on Elastic-Plastic Analysis," *Int. J. Solids Struct.*, Vol. 17, 1981, pp. 859-872.

6 Green, A. E., and Naghdi, P. M., "Some Remarks on Elastic-Plastic Deformations at Finite Strain," *Int. J. Eng. Sci.*, Vol. 9, 1971, pp. 1219-1229.

7 Hughes, D. S. and Kelly, J. L., "Second-order Elastic Deformation of Solids," *Phys. Rev.*, Vol. 92, 1953, pp. 1145-1149.

Flexural Vibrations of Clamped Polygonal and Circular Plates Having Rectangular Orthotropy

Y. Narita[1]

Introduction

In the present Note, a series-type method previously developed [1-3] is applied to the free vibration of clamped polygonal and circular plates having rectangular orthotropy, and the natural frequencies and mode shapes of these plates are calculated with good accuracy. The effects of varying the geometric and orthotropic parameters on the vibration characteristics are examined in detail.

Application of the Method

As explained in references [1-3], frequency equations are obtained for plates of the desired shape by the appropriate location of some straight or curved clamping segments on the original plate. The major axes of the orthotropic material are taken to coincide with x, y axes in rectangular coordinates. Regular polygons have a finite number of geometrically symmetric axes and some of them coincide with the major axes of orthotropy. Vibration mode shapes in that case can be classified as symmetric mode or antisymmetric mode with respect to each axis. That is, two types of vibration modes (S-type, and A-type) exist for pentagonal and septangular plates, and four types (SS-type, SA-type, AS-type, and AA-type) exist for hexagonal and octagonal plates. The resulting frequency equations for the polygons take the same form as those given in reference [1] except for ω_{mn}.

For the circular plate, elements of the frequency matrix are expressed as

$$I^{(1)}_{mn,\,i}=\frac{2}{a}\int_0^{\pi/2}\sin\frac{m\pi}{2}(1+\cos\phi)\sin\frac{n\pi}{2}(1+\sin\phi)\sin 2i\phi\,d\phi$$

$$J^{(1)}_{mn,\,i}=\frac{\partial}{\partial r}I^{(1)}_{mn,\,i}=\frac{2\pi}{a^2}\left[m\int_0^{\pi/2}\right.$$

$$\times\cos\frac{m\pi}{2}(1+\cos\phi)\sin\frac{n\pi}{2}(1+\sin\phi)\sin 2i\phi\cos\phi\,d\phi$$

$$\left.+n\int_0^{\pi/2}\sin\frac{m\pi}{2}(1+\cos\phi)\cos\frac{n\pi}{2}(1+\sin\phi)\sin 2i\phi\sin\phi\,d\phi\right]$$

where ϕ is an angle of the line between a point on the circular boundary and the center of the circle. Definite integrals in the preceding equations are numerically evaluated by the Gauss-Legendre quadrature with 24 points, while the integrals given in the case of polygons are exactly calculated [1].

[1]Lecturer, Computer Center, Hokkaido Institute of Technology, Teine, Sapporo 061-24, Japan.

Manuscript received by ASME Applied Mechanics Division, January, 1983; final revision, March, 1983.

Table 1 Comparison of the fundamental frequency parameters Ω of isotropic polygonal plates

Number of sides	5	6	7	8
Present method	14.48	12.97	12.12	11.67
Shahady et al. [4]	14.44	12.85	12.03	11.54
Walkinshaw et al. [5]	14.32	12.80	11.99	11.53
Laura et al. [6]	14.37	13.08	12.8	---

Table 2 Comparison of the lowest four frequency parameters Ω of isotropic and orthotropic circular plates

	[0,0]	[1,0]	[2,0]	[0,1]
(a) Isotropic case				
Present method	10.23	21.25	34.97	39.81
Exact values	10.216	21.260	34.877	39.771
Asai [7]	10.22	21.22	---	---
(b) Orthotropic case (D_x/H=1.469, D_y/H=0.735)				
Present method	10.59	20.09	---	---
Asai [7]	10.59	20.05	---	---

Table 3 Fundamental frequency parameters for orthotropic polygonal and circular plates clamped at the edges

Number of sides	(D_x/H, D_y/H) (0.5,0.5)	(0.5, 2)	(2,0.5)	(2, 2)
5	11.44 (11.30)	15.57 (15.74)	15.59 (15.59)	19.14 (19.10)
6	10.25 (10.27)	14.05 (14.4)	13.97 (14.27)	17.15 (17.33)
7	9.574	13.10	13.11	16.04
8	9.276	12.73	12.73	15.53
∞ (circle)	8.090	11.05	11.05	13.51

( ): Values from reference [6]

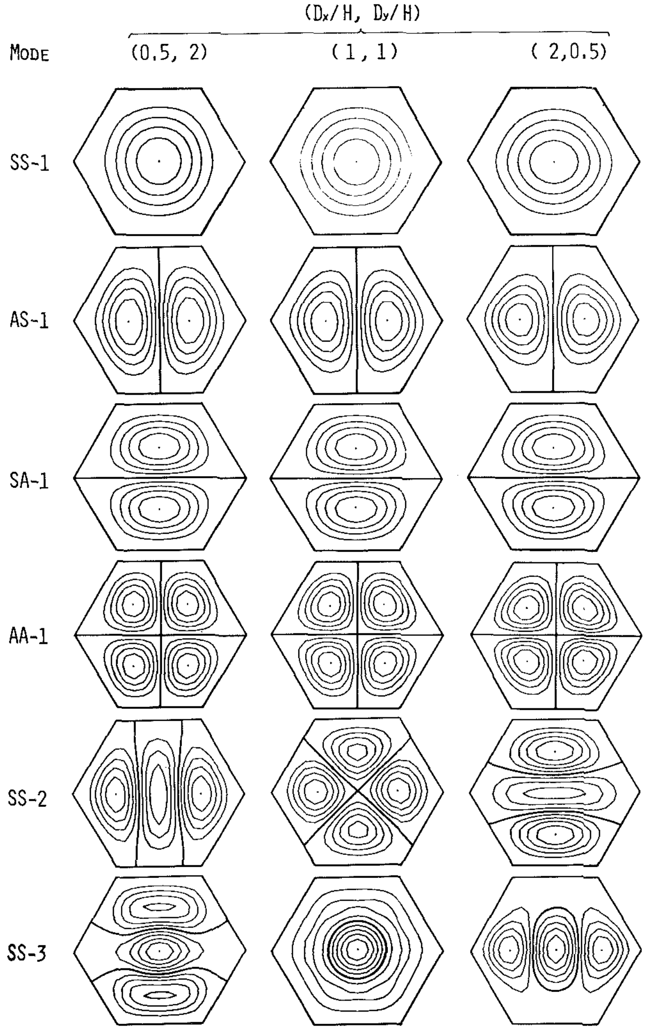

Fig. 1 Mode shapes of clamped hexagonal plates

Table 4 Frequency parameters Ω of orthotropic polygonal and circular plates for higher modes

Number of sides	mode	$(D_x/H, D_y/H)$ (0.5,0.5)	(0.5, 2)	(2,0.5)	(2, 2)
5	(A-1)	23.61	26.89	36.47	39.53
	(S-2)	23.60	36.33	26.87	39.49
	(S-3)	36.49	42.85	42.76	65.71
	(A-2)	39.81	51.65	51.61	62.03
	(S-4)	43.52	64.28	61.24	72.96
6	(AS-1)	21.24	23.88	32.76	35.35
	(SA-1)	21.21	33.50	24.37	35.73
	(SS-2)	33.08	38.82	37.84	59.91
	(AA-1)	36.22	45.24	48.03	56.04
	(SS-3)	39.42	62.27	59.83	66.20
7	(A-1)	19.86	22.58	31.03	33.29
	(S-2)	19.89	31.08	22.58	33.30
	(S-3)	30.97	35.84	35.82	56.30
	(A-2)	34.03	43.75	43.62	52.59
	(S-4)	36.96	56.89	57.26	61.99
8	(AS-1)	19.26	21.81	30.33	32.28
	(SA-1)	19.26	30.33	21.81	32.28
	(SS-2)	30.15	34.93	34.93	55.06
	(AA-1)	32.99	42.08	42.08	50.69
	(SS-3)	35.91	56.39	56.39	60.37
∞	(AS-1)	16.82	19.09	26.22	28.06
	(SA-1)	16.82	26.22	19.09	28.06
	(SS-2)	26.09	30.20	30.20	47.31
	(AA-1)	28.97	37.21	37.21	44.59
	(SS-3)	31.42	48.75	48.75	52.48

Numerical Results and Discussions

In the numerical calculations, frequency parameters were calculated by use of 15×15, 15×15, 14×14, and 12×12 matrices for pentagonal, hexagonal, septangular, and octagonal plates, respectively, and the terms of infinite series in m, n were truncated at the 40th term. Comparison is made in Table 1 with other results available for isotropic case. Nondimensional frequency parameters are expressed in the form of $\Omega = \omega R^2 \sqrt{\rho h/H}$, with R being the radius of circles circumscribing over the polygons. The present values agree well with those of Shahady et al. [4] and Walkinshaw et al. [5], but the values of reference [6] tend to be less accurate as the number of size is increased.

Table 2 also presents the comparative study of the results for the circular plate in both isotropic and orthotropic cases. Here, a 10×10 matrix was used for the calculation, with m, n truncated at 60th term. The two integers in the bracket denote the number of nodal diameters and that of internal nodal circles. On the whole, good agreement is attained throughout the results in Tables 1 and 2.

Table 3 presents the fundamental frequencies of the plates for four different combinations of the orthotropic parameters (D_x/H, D_y/H). The present values are again compared to those in reference [6], but their results for a septangular plate were eliminated because of the discrepancy of the same order as in the isotropic case. The frequency parameters for higher modes are given in Table 4. For the isotropic plates [1], the degeneracy of frequencies was found for AS-1 and SA-1 (or A-1 and S-2), and AA-1 and SS-2 (or A-2 and S-3) modes. The orthotropic plates, however, discriminate those modes as different ones, due to the bending stiffnesses varying in directions.

The effects of orthotropy on the mode shapes of the hexagonal plate are illustrated in Fig. 1, wherein the thick solid lines inside the boundary denote nodal lines, i.e., lines of zero deflection, and the thin lines are contour lines denoting deflections of 0.2, 0.4, 0.6, and 0.8 of the maximum deflection marked with a dot. The mode shapes of the isotropic plates are given in the middle column of the figure, and the bending rigidity in x direction is increased, as moving from left to right. It is clearly observed that not only the frequency values but the mode shapes are influenced by the presence of the orthotropy.

References

1 Irie, T., Yamada G., and Narita Y., "Free Vibration of Clamped Polygonal Plates," *Bulletin of the Japan Society of Mechanical Engineers*, Vol. 21, No. 162, 1978, pp. 1696–1702.

2 Narita, Y., "Application of a Series-Type Method to Vibration of Orthotropic Rectangular Plates With Mixed Boundary Conditions," *Journal of Sound and Vibration*, Vol. 77, No. 3, 1981, pp. 345–355.

3 Narita, Y., Maruyama, K., and Sonoda, M., "Transverse Vibration of Clamped Trapezoidal Plates Having Rectangular Orthotropy," *Journal of Sound and Vibration*, Vol. 85, No. 3, 1982, pp. 315–322.

4 Shahady, P. A., Passarelli, R., and Laura, P.A.A., "Application of Complex-Variable Theory to the Determination of the Fundamental Frequency of Vibrating Plates," *Journal of the Acoustical Society of America*, Vol. 42, No. 4, 1967, pp. 806–809.

5 Walkinshaw, D. S., and Kennedy, J. S., "On Forced Response of Polygonal Plates," *Ingenier Archiev*, Vol. 38, No. 6, 1969, pp. 358–369.

6 Laura, P. A. A., Luisoni, L. E., and Sarmiento, G. S., "A Method for the Determination of the Fundamental Frequency of Orthotropic Plates of Polygonal Boundary Shape," *Journal of Sound and Vibration*, Vol. 70, No. 1, 1980, pp. 77–84.

7 Asai, S., "Deflection, Natural Frequency and Supersonic Panel Flutter of the Orthotropic Elliptical Plates (in Japanese)," *Journal of the Japan Society for Aeronautical and Space Sciences*, Vol. 25, No. 280, 1977, pp. 248–256.

An Elastic Beam Contained in a Frictionless Channel[1]

D. P. Vaillette[2] and G. G. Adams[3]

An infinitely long elastic beam, contained within a frictionless and rigid channel, is subjected to axially compressive forces. It is shown that the elastica theory predicts a maximum permissible axial force that can be supported. This critical force is expressed by a very simple relationship involving the flexural rigidity of the beam and the channel width.

Introduction

When a lightweight flexible material must be pushed through a narrow guideway, it is possible for the material to fold over on itself resulting in a mechanical "jam" of the device. Typical examples of this are the feeding of paper through a copier machine and the motion of film through a movie camera. Studies related to this problem were made by Benson [1, 2] who treated the medium as a thin, incomplete, elastic ring and thus restricted his attention to the end region. In [1] the deformation and jam threshold were determined and in [2] a related stick/slip problem was studied using a perturbation analysis.

In this investigation we determine the response of an infinitely long elastic beam, contained within a frictionless and rigid channel, to axially compressive forces applied at each end (Fig. 1). The theory of the elastica is applied and a complete solution is obtained. In particular we find that there is a maximum permissible axial force that may be supported after which the beam collapses in the channel.

Solution

We consider this problem using the theory of the elastica which is well known and best described in Love [3] and Frisch-Fay [4]. From symmetry, we need only consider a one-quarter cycle of the beam that corresponds to one-half of that portion of the beam between any two contact points. The result is the equivalent cantilever beam of curved length L (Fig. 2) subjected to an axial compressive force P and the unknown transverse force R which is equal to one-half of the reaction force $2R$ at each contact point of Fig. 1. Here we define Q as the resultant of P and R which act at an angle α_1 with respect to the horizontal (Fig. 2). The known deflection at the end of the cantilever beam is δ which corresponds to one-half of the channel width. Furthermore α is the angle between the tangent at the free end and the horizontal. The moment curvature relation for the elastica becomes

$$EI\frac{d\theta}{ds} = Q(\delta - y)\cos\alpha_1 - Q(l-x)\sin\alpha_1 \tag{1}$$

where $\theta(s)$ is the angle made by the tangent to the curve and the horizontal, and s is the arc length coordinate. The boundary conditions are

$$\theta(0)=0, \quad \theta(L)=\alpha, \quad \theta'(L)=0, \quad y(L)=\delta. \tag{2}$$

[1] Based on the Master's thesis of D. Vaillette, submitted in partial fulfillment of the requirements for the degree of Master of Science in Mechanical Engineering, Northeastern University, Boston, Mass.

[2] Graduate Student, Department of Mechanical Engineering, Northeastern University, Boston, Mass. 02115. Currently at the Advanced Systems Division, Texas Instruments, Dallas, Texas.

[3] Associate Professor, Department of Mechanical Engineering, Northeastern University, Boston, Mass. 02115. Assoc. Mem. ASME.

Manuscript received by ASME Applied Mathematics Division, December, 1982; final revision, April, 1983.

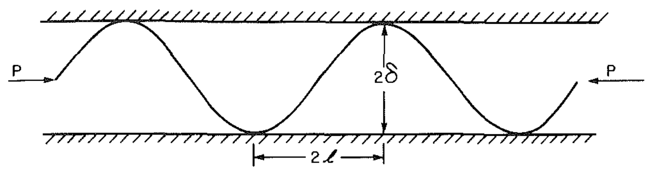

Fig. 1 An infinite beam in a frictionless and rigid channel subjected to axially compressive loads P at each end

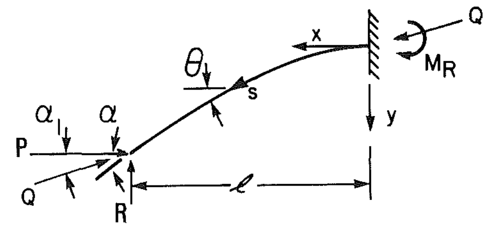

Fig. 2 An equivalent cantilever beam

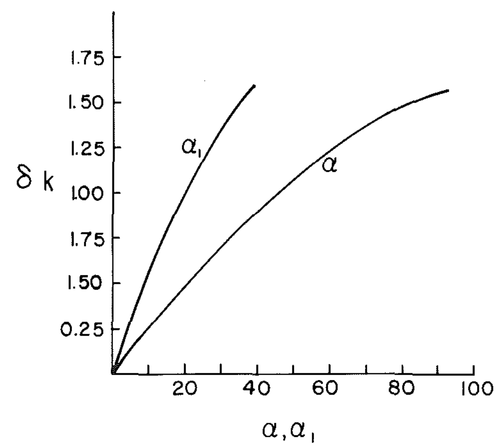

Fig. 3 Dimensionless load (δk) versus angles α and α_1

In the elastica theory it is necessary to distinguish between the curved length L and the horizontal length l.

Using the results obtained in [4, section 2.6] or [5], and omitting the details for brevity we obtain

$$Lk = \sqrt{\cos\alpha_1}\,[K(p) - F(p,\phi)], \quad kz\sqrt{P/EI} \tag{3}$$

$$p = \sin\left(\frac{\alpha-\alpha_1}{2}\right), \quad \phi = \sin^{-1}\left[\sin\left(-\frac{\alpha_1}{2}\right)/p\right] \tag{4}$$

where $K(p)$ and $F(p,\phi)$ are, respectively, the complete and incomplete elliptic integrals of the first kind given by

$$K(p) = F(p,\pi/2), \quad F(p,\phi) = \int_0^\phi \frac{d\phi}{\sqrt{1-p^2\sin^2\phi}}. \tag{5}$$

Imposing the restriction on the vertical deflection gives

$$\delta k = lk\tan\alpha_1 + 2p\cos\phi/\sqrt{\cos\alpha_1} \tag{6}$$

and relating l to L finally yields

$$(L+l)k = 2\sqrt{\cos\alpha_1}\ [E(p) - E(p,\phi)], \tag{7}$$

where $E(p)$, $E(p,\phi)$ are, respectively, the complete and incomplete elliptic integrals of the second kind defined by

$$E(p) = E(p,\pi/2), \quad E(p,\phi) = \int_0^\phi \sqrt{1-p^2\sin^2\phi}\,d\phi. \tag{8}$$

Solving for Lk in (3) and lk in (6), then substituting these expressions into (7), we eventually obtain

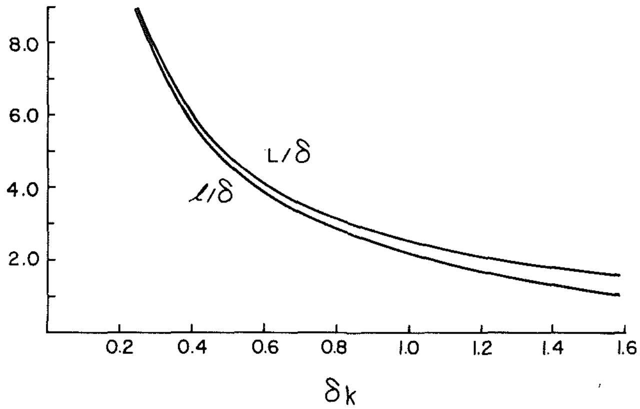

Fig. 4 Effective dimensionless lengths (L/δ, l/δ) versus dimensionless load (δk)

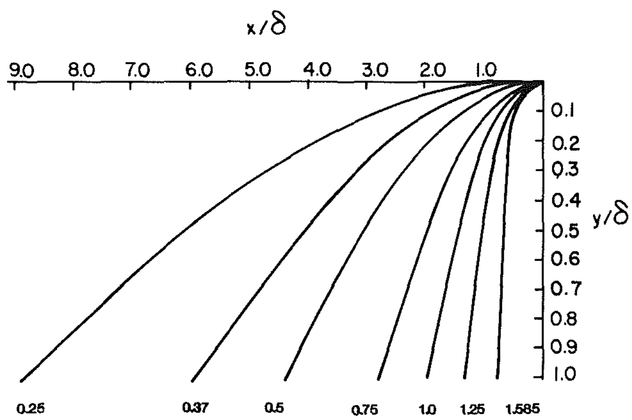

Fig. 5 Beam displacement shapes for various values of the dimensionless load (δk)

$$\delta k = \sqrt{\cos\alpha_1}\,\{2p\cos\alpha_1\cos\phi - [K(p) - F(p,\phi)]\sin\alpha_1 + 2[E(p) - E(p,\phi)]\sin\alpha_1\}. \tag{9}$$

With ϕ known explicitly by $(4)_2$, we observe that (9) has the two unknowns α_1 and p.

The restriction that the channel reaction be non-negative leads to

$$\alpha_1 \geq 0 \tag{10}$$

and the curvature requirement yields

$$\tan\alpha_1 \leq \delta/l \tag{11}$$

which can be simplified with the aid of (6) to

$$\alpha \geq 2\alpha_1 \tag{12}$$

From (10) and (12) it follows that any solution will have the Euler buckling load as a lower bound and a solution with vanishing curvature at the fixed end as its upper bound. A load greater than the Euler buckling load is possible only with the transverse force R in the opposite direction of the "buckled" configuration (Fig. 2).

Any p and α_1 satisfying (9), subject to (10) and (12) will yield a solution satisfying equilibrium. However, the actual p, α_1 combination is taken as that which will minimize the total potential energy of the system.

Notice that the beam having the minimum energy of any configuration in Fig. 2 is not necessarily that which minimizes the energy for the entire system; this is because the length of the beam is a variable and different lengths will correspond to a different number of cycles fitting into a given fixed length of beam. We therefore find the energy per unit length

$$U/L = \frac{EI}{2L}\int_0^L \left(\frac{d\theta}{ds}\right)^2 ds - P(1 - l/L) \tag{13}$$

which, in dimensionless form becomes

$$U/PL = \left\{ \frac{2(1+\cos^2\alpha_1)[E(p) - E(p,\phi)] - p\cos\phi\sin2\alpha_1}{K(p) - F(p,\phi)} - (\cos^2\alpha_1 + \cos\alpha_1 - 2p^2 + 2)\right\}/\cos\alpha_1 \tag{14}$$

after using (1) and integrating. Summarizing, for a given value of the load parameter (δk), we find the complete range of the admissible α_1,p combinations from (9), (10), and (12), and then use (14) to find the solution with the minimum energy.

Results and Discussion

Having determined α_1 and p for given δk, we can now calculate Lk from (3), α from $(4)_1$, and lk from (7). In Fig. 3 we show a graph of δk versus α and α_1, and in Fig. 4 we display a graph L/δ, l/δ versus δk. Notice that solutions are obtained only for $\delta k \leq 1.585$ ($P \leq 2.512\ EI/\delta^2$). Hence we conclude that for greater values of the dimensionless load ($\delta k \geq 1.585$) the beam becomes unstable and "folds over" on itself. We note that a solution has also been obtained using the linear theory which predicted that the beam could support an infinite force [5]. Although the elastica usually gives stiffer results, that was not the case in this problem because the elastica makes a distinction between the horizontal length and the curved length of the beam. Whereas the linear theory allowed the length of the beam (Fig. 2) to shrink to zero supporting an infinite force, the curved length L cannot shrink to zero and only a finite force can be sustained. Finally in Fig. 5 we show the deflected shape of the beam for various values of δk.

References

1 Benson, R. C., "The Deformation of a Thin, Incomplete, Elastic Ring in a Frictional Channel," ASME Journal of Applied Mechanics, Vol. 48, 1981, pp. 895–899.

2 Benson, R. C., "Stick/Slip Conditions for a Thin, Incomplete, Elastic Ring Impinging on a Frictional Barrier," ASME Journal of Applied Mechanics, Vol. 49, 1982, pp. 231–232.

3 Love, A. E. H., *A Treatise on the Mathematical Theory of Elasticity*, 4th ed., Dover, New York, Chapter 19, 1944.

4 Frisch-Fay, R., *Flexible Bars*, Butterworth, London, 1962.

5 Vaillette, D. P., "Stability of a Beam in a Rigid Channel," M.S. Thesis, Northeastern University, Boston, Mass., July 1982.

Constraint to Side Flow in Plates

J. Liss,[1] W. Goldsmith,[1] and F. E. Hauser[1]

An experimental program was conducted to determine the increase in flow stress relative to simple uniaxial compression for 2024-0 aluminum plates subjected to symmetric quasi-static compression by steel punches and to dynamic compression using the Kolsky (split Hopkinson-bar) technique. An average constraint factor of 2 was determined experimentally for a ratio of specimen thickness to bar diameter of 0.5 for the quasi-static case. This correlated well with the value predicted theoretically. Under dynamic conditions the

[1] Department of Mechanical Engineering, University of California, Berkeley, Calif. 94720. W. Goldsmith is a Fellow, ASME.

Manuscript received by ASME Applied Mechanics Division, January, 1983; final revision, April, 1983.

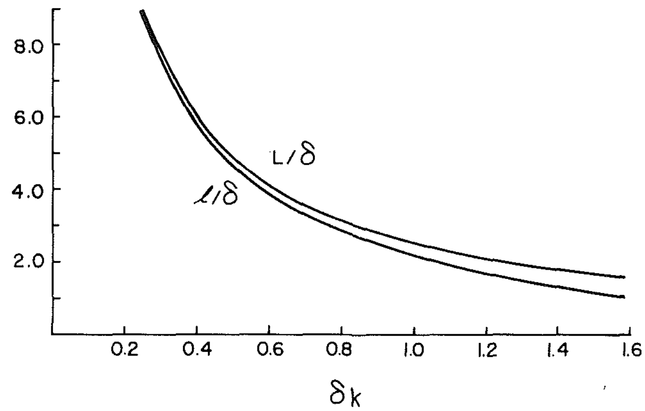

Fig. 4 Effective dimensionless lengths (L/δ, l/δ) versus dimensionless load (δk)

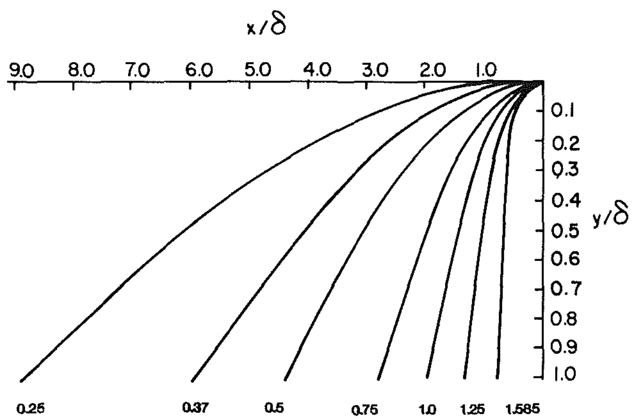

Fig. 5 Beam displacement shapes for various values of the dimensionless load (δk)

$$\delta k = \sqrt{\cos\alpha_1}\,\{2p\cos\alpha_1\cos\phi - [K(p) - F(p,\phi)]\sin\alpha_1 + 2[E(p) - E(p,\phi)]\sin\alpha_1\}. \tag{9}$$

With ϕ known explicitly by $(4)_2$, we observe that (9) has the two unknowns α_1 and p.

The restriction that the channel reaction be non-negative leads to

$$\alpha_1 \geq 0 \tag{10}$$

and the curvature requirement yields

$$\tan\alpha_1 \leq \delta/l \tag{11}$$

which can be simplified with the aid of (6) to

$$\alpha \geq 2\alpha_1 \tag{12}$$

From (10) and (12) it follows that any solution will have the Euler buckling load as a lower bound and a solution with vanishing curvature at the fixed end as its upper bound. A load greater than the Euler buckling load is possible only with the transverse force R in the opposite direction of the "buckled" configuration (Fig. 2).

Any p and α_1 satisfying (9), subject to (10) and (12) will yield a solution satisfying equilibrium. However, the actual p, α_1 combination is taken as that which will minimize the total potential energy of the system.

Notice that the beam having the minimum energy of any configuration in Fig. 2 is not necessarily that which minimizes the energy for the entire system; this is because the length of the beam is a variable and different lengths will correspond to a different number of cycles fitting into a given fixed length of beam. We therefore find the energy per unit length

$$U/L = \frac{EI}{2L}\int_0^L \left(\frac{d\theta}{ds}\right)^2 ds - P(1 - l/L) \tag{13}$$

which, in dimensionless form becomes

$$U/PL = \left\{ \frac{2(1+\cos^2\alpha_1)[E(p) - E(p,\phi)] - p\cos\phi\sin2\alpha_1}{K(p) - F(p,\phi)} - (\cos^2\alpha_1 + \cos\alpha_1 - 2p^2 + 2)\right\} / \cos\alpha_1 \tag{14}$$

after using (1) and integrating. Summarizing, for a given value of the load parameter (δk), we find the complete range of the admissible α_1, p combinations from (9), (10), and (12), and then use (14) to find the solution with the minimum energy.

Results and Discussion

Having determined α_1 and p for given δk, we can now calculate Lk from (3), α from $(4)_1$, and lk from (7). In Fig. 3 we show a graph of δk versus α and α_1, and in Fig. 4 we display a graph L/δ, l/δ versus δk. Notice that solutions are obtained only for $\delta k \leq 1.585$ ($P \leq 2.512\ EI/\delta^2$). Hence we conclude that for greater values of the dimensionless load ($\delta k \geq 1.585$) the beam becomes unstable and "folds over" on itself. We note that a solution has also been obtained using the linear theory which predicted that the beam could support an infinite force [5]. Although the elastica usually gives stiffer results, that was not the case in this problem because the elastica makes a distinction between the horizontal length and the curved length of the beam. Whereas the linear theory allowed the length of the beam (Fig. 2) to shrink to zero supporting an infinite force, the curved length L cannot shrink to zero and only a finite force can be sustained. Finally in Fig. 5 we show the deflected shape of the beam for various values of δk.

References

1 Benson, R. C., "The Deformation of a Thin, Incomplete, Elastic Ring in a Frictional Channel," ASME JOURNAL OF APPLIED MECHANICS, Vol. 48, 1981, pp. 895–899.

2 Benson, R. C., "Stick/Slip Conditions for a Thin, Incomplete, Elastic Ring Impinging on a Frictional Barrier," ASME JOURNAL OF APPLIED MECHANICS, Vol. 49, 1982, pp. 231–232.

3 Love, A. E. H., *A Treatise on the Mathematical Theory of Elasticity*, 4th ed., Dover, New York, Chapter 19, 1944.

4 Frisch-Fay, R., *Flexible Bars*, Butterworth, London, 1962.

5 Vaillette, D. P., "Stability of a Beam in a Rigid Channel," M.S. Thesis, Northeastern University, Boston, Mass., July 1982.

Constraint to Side Flow in Plates

J. Liss,[1] W. Goldsmith,[1] and F. E. Hauser[1]

An experimental program was conducted to determine the increase in flow stress relative to simple uniaxial compression for 2024-0 aluminum plates subjected to symmetric quasi-static compression by steel punches and to dynamic compression using the Kolsky (split Hopkinson-bar) technique. An average constraint factor of 2 was determined experimentally for a ratio of specimen thickness to bar diameter of 0.5 for the quasi-static case. This correlated well with the value predicted theoretically. Under dynamic conditions the

[1] Department of Mechanical Engineering, University of California, Berkeley, Calif. 94720. W. Goldsmith is a Fellow, ASME.

Manuscript received by ASME Applied Mechanics Division, January, 1983; final revision, April, 1983.

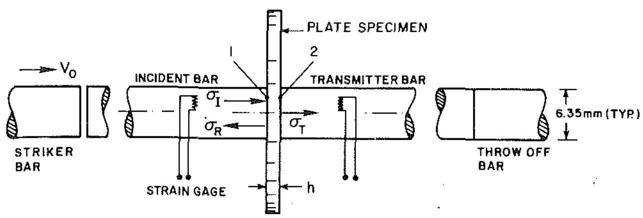

Fig. 1 Schematic of the Kolsky (split Hopkinson-bar) arrangement

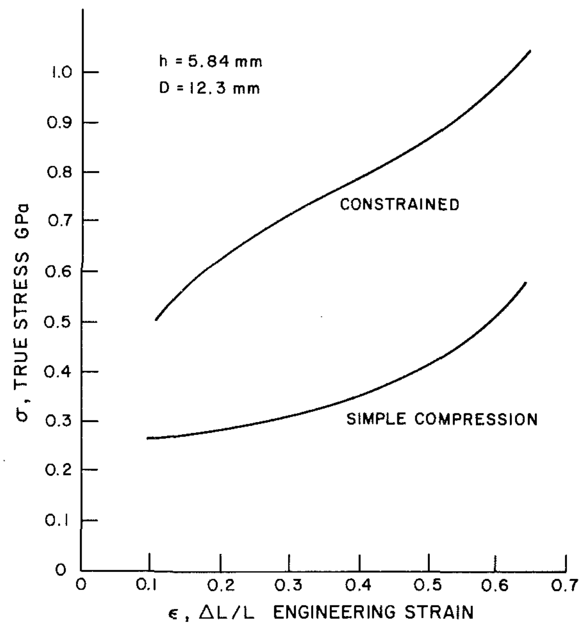

Fig. 2 True stress as a function of engineering strain for quasi-statically compressed simple and constrained specimens

constraint factor at yield stress was found to be slightly lower at a value of 1.75 and appeared to be nearly independent of strain rate over the test range from 10^3 to $1.5 \times 10^4 s^{-1}$.

Introduction

It has been recognized for many years that an increase of pressure beyond the uniaxial yield strength is required to cause plastic deformation of metallic blocks when the specimen is subjected to indentation by flat or hemispherical punches. Theoretical investigations of this phenomenon have shown that the necessary pressures under these conditions range from about $2.6Y$ to $3Y$, where Y is the yield strength in simple tension or compression, and this apparent strength increase has been substantiated experimentally [1]. The effect is attributed to the prevention of side flow by the undeformed portion of the block that gives rise to a hydrostatic stress component. This type of constraint is also present in the penetration and perforation of plates by projectiles.

To the authors' knowledge, no exact theory of continuum mechanics describing the stress distribution in the plastic zone produced by impact loading constrained by an outer elastic annulus has been developed to date. Constraint to side flow was considered by Woodward and De Morton [2, 3]; the first reference extended an analysis of the uniaxial compression of a die in the presence of friction by Johnson [4] to the symmetrical compression of a plate by two flat-ended cylinders. The resultant constraint factor was in reasonable agreement with the average value of static data. Reference [3] is concerned with the deformation of the plate and the projectile. The present approach involves both static and dynamic tests

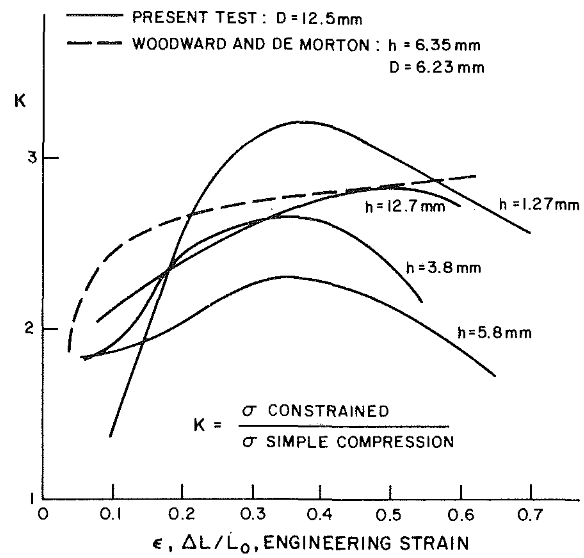

Fig. 3 Constraint factor *K* as a function of engineering strain for various specimen thicknesses *h*. Data from reference [2] represented by a dashed line

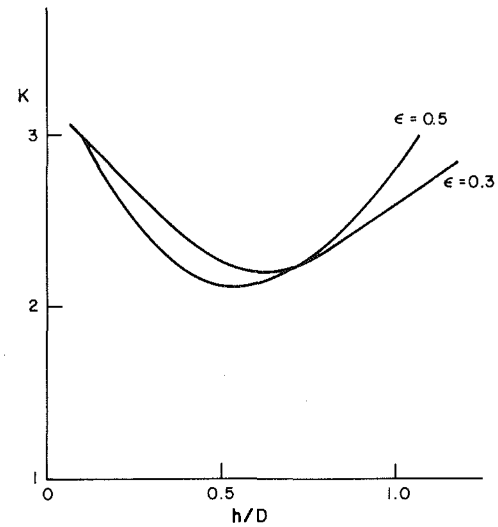

Fig. 4 Quasi-static contraint factor as a function of the ratio of specimen thickness to penetrator diameter for values of engineering strain of 0.3 and 0.5

for the determination of constraint factors and a comparison of the experimental information with predictions based on a simplified analysis. The effects of friction are neglected here since its influence cannot be independently measured. Frictional effects have been shown to be small and have generally been disregarded in problems involving ballistic penetration [5].

As indicated in reference [2] and shown in greater detail in reference [6], to plastically deform a soft plate between hard cylindrical punches, the axial stress must be twice the uniaxial yield strength Y leading to a constraint factor $K = 2$. This evaluation is based on the following assumptions: conservation of volume (neglecting elastic strains), continuity of the radial stresses across the boundary of the compressed zone in the plate, and discontinuity of the axial stresses across this boundary, the value of the axial stress in the region outside of the punch being zero.

Experiments

Two types of quasi-static experiments were conducted on a Tinius-Olson Universal Testing machine: (*i*) simple uniaxial compression of cylindrical specimens and (*ii*) constrained symmetrical compression of flat plates. All specimens consisted of 2024-0 aluminum alloy with a nominal Brinell hardness of 47; both the uniaxial specimens and the hardened steel cylinders utilized to compress the plates were 12.5 mm in diameter. The samples had initial thicknesses of 1.3, 3.8, 5.8, and 12.7 mm, respectively. Loads up to 360 kN were applied to the specimens at crosshead speeds ranging from 0.5 to 2.5 mm/min by means of two smooth dry parallel steel plates.

The same two types of tests were conducted dynamically using a Kolsky (split Hopkinson-bar) technique. A schematic of the arrangement is shown in Fig. 1. The arrangement consisted of a striker bar, an incident bar, a transmitting bar, and a throw-off bar, all 6.35 mm (1/4 in.) diameter and made from Ti-6Al-6V-2Sn alloy having a yield strength of 1.07 GPa. The striker bar had a length of 508 mm, while the other bars were each 558 mm long. The specimen was sandwiched between the incident and transmitting bars. Two 120 Ω longitudinal foil strain gages with nominal gage lengths of 1.59 mm (1/16 in.) and gage factors of 2.08 were mounted opposite each other at stations 101 mm (4 in.) from the specimen interface on each of these bars. The strain gage outputs were digitized, stored, and recorded in a two-channel digital oscilloscope with sampling rates as fast as 50 nsec per point. Each channel cold store 2048 consecutive data points.

Both cylindrical and plate specimens composed of 2024-0 aluminum were employed in the dynamic tests. The cylinders for the uniaxial compression tests were 6.35 mm in diameter with thicknesses of 1.23 and 3.17 mm. The plates had a 119 mm diameter with thicknesses of 0.5 and 1.24 mm. A pneumatic gun propelled the striker bar at speeds from 9 to about 30 m/s; the velocity was determined from the signal amplitude at the incident bar strain gages.

Results and Discussion

(a) Quasi-Static Tests. Initial and final specimen dimensions as well as load-deflection histories were recorded. Typical true stress-engineering strain curves for simple and constrained quasi-static compression are plotted in Fig. 2. The constraint factor K, defined as the ratio of the constrained to the uniaxial unconstrained true stress at the same strain, is shown in Fig. 3 as a function of engineering strain for various initial specimen thicknesses. This diagram shows a minimum constraint value when the ratio of specimen height h to punch diameter D is about one-half. For a value of unity of h/D, the present results are in reasonable agreement with those in reference [2] where a cold-rolled commercial aluminum was tested. A cross-plot for two values of engineering strain is shown in Fig. 4. The constraint factor varies substantially both with strain and h/D ratio in a manner not consistent with the currently available simple analysis. This behavior is attributed to the combined effects of the friction present between the specimen and the loading surfaces and nonuniform stress distribution in the thickness direction.

As seen in Fig. 4, a minimum value of the constraint factor $K \simeq \cong 2$ which corresponds to the value predicted by the simple analysis was determined experimentally at a strain of about 0.3 and $h/D = 0.5$. As the h/D ratio increases toward unity, the constraint factor tends toward 3 which is the theoretical value for a semi-infinite solid [1, 4].

Figure 5, which shows the variation of K with engineering

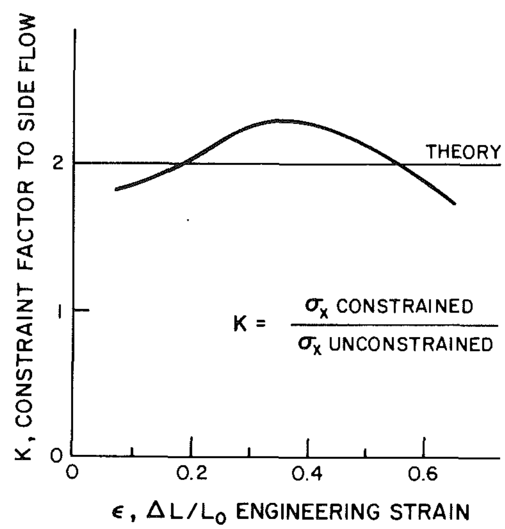

Fig. 5 Quasi-static constraint factor for an h/D ratio of 0.5 as a function of engineering strain compared with theoretical prediction

Table 1 Summary of dynamic tests

Test No.	Specimen Type	Specimen Thickness, mm	Striker Velocity, m/s	Incident Stress, MPa	Yield Stress, MPa	Relative Velocity at Yield, m/s	Strain Rate, $[s^{-1}]$
1	C+	3.17	9.3	206.6	126.6	7.2	2280
2	C	3.17	11.3	249.9	136.6	10.2	3220
3	C	1.23	11.8	261.4	190.5	6.3	5110
4	C	3.17	19.7	436.5	213.2	20.1	6360
5	C	1.23	20.6	456.1	286.6	15.3	12440
6	Px	1.24	11.7	259.9	226.6	3.0	2430
7	P	1.24	15.0	333.2	276.6	5.1	4110
8	P	1.24	20.3	449.9	366.6	7.5	6050
9	P	0.49	20.7	459.3	409.9	7.0	9120
10	P	0.50	29.3	649.9	566.5	7.5	14820

+ C - Cylinderical Specimen
x P - Plate Specimen

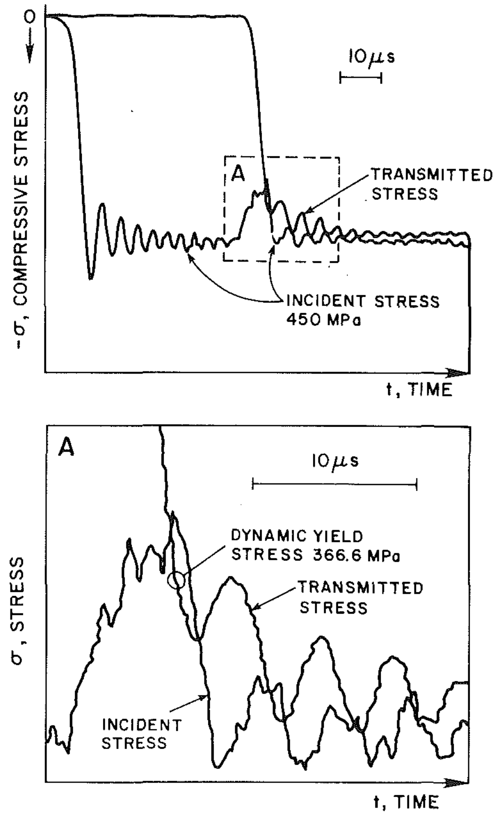

Fig. 6 Typical incident and transmitted strain records for the constrained specimens subjected to a Kolsky (split Hopkinson-bar) loading technique (run no. 8). Specimen thickness: 1.24 mm. The insert shows the enlarged yield zone.

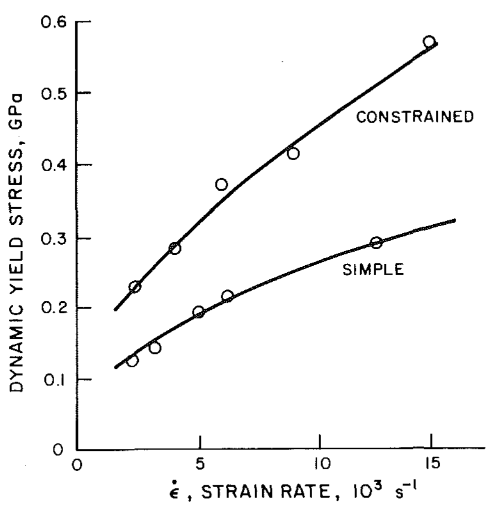

Fig. 7 Simple and constrained dynamic yield stress as a function of strain rate for specimens from 0.5-3.2 mm thick

strain for a specimen thickness to diameter ratio of 0.5, indicates that the average experimental value for this parameter is 2, with a maximum deviation of 13 percent for the strain range from 0.08 to 0.65. The corresponding values cited by reference [2] for the constraint factor in cold-rolled aluminum with $h/D = 1$ ranged from 1.9 to 2.8 as the strain increased from 3 to 50 percent. No variations in specimen thickness were reported in those test results.

(b) Dynamic Tests. The data analysis for the dynamic tests assumes that the transients produced on both sides of the test specimens propagate uniaxially without attenuation or dispersion along the elastic incident and transmitting bars.

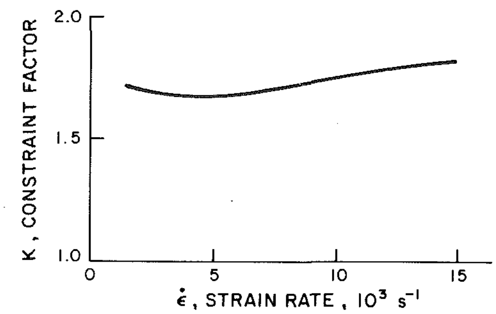

Fig. 8 Dynamic constraint factor at the yield stress as a function of strain rate for thin specimens

The stress and particle velocity conditions at the specimen interfaces can then be determined from the measurements at the strain gage locations. For a sufficiently thin test specimen, the elastic stress wave transit time is small ($<1\mu$s) compared to the test duration; dynamic equlibrium is established in a short period compared to the test duration (≈ 100 μs), and plastic deformation can be assumed to take place uniformly throughout the specimen.

For the present tests, where the deformed sample area is the same as the cross-sectional areas of the adjacent bars, the average stress and strain rates in the specimen are given by

$$\sigma_{\rm avg} = 1/2\,[(\sigma_i + \sigma_r) + \sigma_t] \tag{1}$$

and

$$\dot{\epsilon} = [(\sigma_i - \sigma_r) - \sigma_t]/\rho c_0 h \tag{2}$$

where σ is stress, subscripts i, r, and t refer to incident, reflected, and transmitted waves, ρ is the unit mass, c_0 the wave speed (ρc_0 is the acoustic impedance) of the bar material, and h the specimen thickness. These relations are approximate as the direct shear applied at the periphery of the incident bar within the plate specimen is expected to cause a difference in stress on opposite sides and thus affect the uniformity of the deformation. The frictional constraint between specimen and bars is assumed to be small compared to the lateral flow constraint due to the surrounding material in the plate samples.

Table 1 presents a summary of the results obtained on five specimens for each type of dynamic test. Figure 6 shows the strain gage records for the incident and transmitted stresses with the yield zone enlarged for the plate specimen, run no. 8. The slight difference in the stress levels on opposite sides of the specimen is due to the peripheral shear on the incident side as indicated in the foregoing. This difference became insignificant when the plate thickness was reduced to the minimum utilized in the present tests.

The transmitted stress is considered to represent the homogeneous stress in the test sample. No simple procedure exists in the present dynamic experiments to optimize the specimen thickness to minimize the factors influencing nonhomogeneous stress distribution as was effected in the quasi-static case. Attempts to reduce the effects of friction under dynamic loading conditions have resulted in the ejection of lubricants at the interfaces, leading to spurious apparent values of measured strain. However, the influence of dynamic friction is expected to be smaller than in the static case and may approach negligible proportions under ballistic conditions [3].

Figure 7 shows the results for the simple uniaxial and for the constrained dynamic yield strength as a function of strain rate, and Fig. 8 shows the variation of the dynamic constraint factor at the yield stress level. The latter was found to vary between 1.7 and 1.8 for the strain rate range from quasi-static to $1.5 \times 10^4 \text{s}^{-1}$ where the former was extrapolated to the yield strain from Fig. 3. In this domain, the influence of the loading rate appears to be negligible.

Conclusions

The present tests indicate that a constraint factor to side flow (the ratio of flow stress in a plate loaded by a flat punch to that of a simple compression specimen) in a 2024-0 aluminum plate under quasi-static conditions may be taken as 2 $\pm$ 10 percent for ratios of plate thickness to punch diameter of 0.5. This minimum value is in good correspondence with the predictions of a simple theory. Corresponding dynamic tests using a Kolsky (split Hopkinson-bar) technique provide a lower value of the contraint factor of 1.75 $\pm$ 5 percent at the yield strain over the strain rate range from quasi-static to 1.5 $\times$ $10^4 s^{-1}$ indicating a slightly smaller influence of friction and h/D ratio at low strain values. In consequence, a constraint factor of 2 appears to be a good approximation for the augmentation of the yield stress under conditions of lateral constraint regardless of loading rate or specimen geometry.

Acknowledgment

This work represents a portion of the doctoral dissertation of the first author at the University of California, Berkeley, performed under the sponsorship of the Army Office of Research, Durham on Contract No. DAAG29-80-K-0052.

References

1 Tabor, D., *The Hardness of Metals,* Clarendon Press, Oxford, 1951, pp. 37, 42, and 49.

2 Woodward, R. L., and De Morton, M. E., "Penetration of Targets by Flat-ended Projectiles," *Int. J. Mech. Sci.*, Vol. 18, 1976, pp. 119–127.

3 Woodward, R. L., "Penetration of Semi-infinite Metal Targets by Deforming Projectiles," *Int. J. Mech. Sci.*, Vol. 24, 1982, pp. 71–87.

4 Johnson, W., *Impact Strength of Materials*, E. Arnold, London, 1972, p. 151.

5 Krafft, J. M., "Surface Friction in Ballistic Penetration," *J. Appl. Phys.*, Vol. 26, 1955, pp. 1248–1253.

6 Liss, J., A Phenomenological Penetration Model of Thin Plates, Ph.D. Dissertation, University of California, Berkeley, 1982.

Journal of Applied Mechanics Discussion

Axisymmetric Elastic Waves Excited by a Point Source in a Plate[1]

J. R. Hutchinson.[2] Drs. Weaver and Pao are to be congratulated for a very thorough study of the elastic waves emanating from a transverse step load on the surface of an elastic plate. The purpose of this discussion is threefold: first, to make the reader aware of a much more simplistic approach taken by the discusser in a recent paper [1]; second, to compared this simplistic approach with the more precise approach of Weaver and Pao, and to point out both similarities and differences in the solution; and third, to suggest that perhaps consideration of even higher thickness modes might be of interest.

In reference [1] the same problem as treated by Weaver and Pao was considered. The approach used was to expand the solution in terms of the normal modes found by using Mindlin's plate theory. Instead of considering the radius approaching infinity, as Weaver and Pao did, the radius of the plate was chosen as just large enough so that for the points considered and for the time intervals of interest the wave would not have time to be reflected back from the boundary to the point considered. The transverse displacement response was found for both a step load and an impulsive load in dimensionless form. Because of the simplicity of the solution it was easy to solve the problem for the specific dimensions and physical properties used by Weaver and Pao. Results of this solution are shown in Figs. 1 and 2.

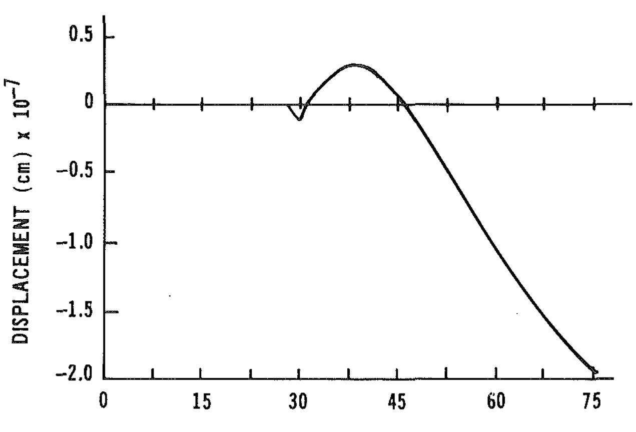

Fig. 1 Transverse displacement at a radius of 10 cm

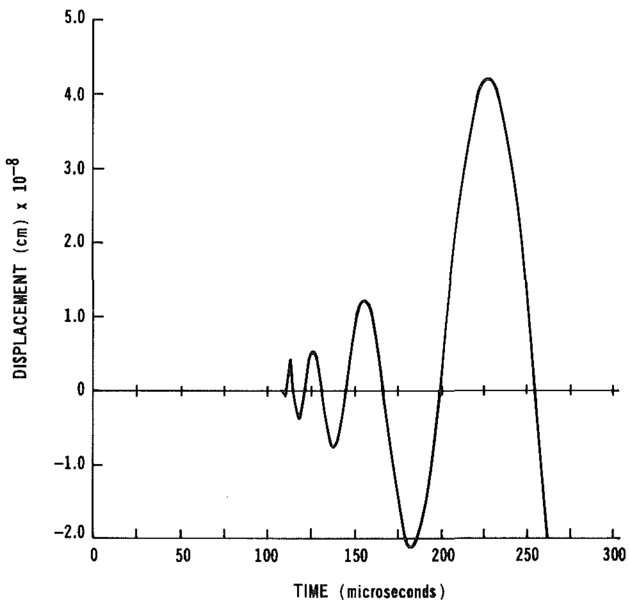

Fig. 2 Transverse displacement at a radius of 40 times the thickness ($r = 80h$)

The first thing to notice is that if Fig. 1 were inverted then both Figs. 1 and 2 would be almost identical in overall shape to Weaver and Pao's Figs. 8(*a*) and 10(*a*), respectively. The reason for the inversion on Fig. 1 is that I took my force as upward (in the same direction as positive transverse displacement) whereas Weaver and Pao took the force downward; however, by the same reasoning, Fig. 2 should also be inverted from Weaver and Pao's, which it is not. The second major discrepancy is in the magnitude of the response. My displacements are about two and half times smaller than those reported by Weaver and Pao.

The difference in sign and amplitude are too large to be ascribed to differences in solution methods, particularly when the solutions match in other important aspects. The simplicity of the method used in reference [1] also allows a very simple check on the accuracy of the modal superposition. The boundary conditions on the (finite) plate in reference [1] were clamped. Use of modal superposition of the particular solution of the modal equations of motion should, therefore, lead to the static solution for a clamped centrally loaded circular plate. This modal superposition check was performed and gave answers that were within three significant figures of the static solution as given on p. 69 of reference [2]. Unless I am misreading their physical and geometric properties I would have to conclude that Weaver and Pao have made some minor numerical error in their analysis which accounts for the sign and amplitude differences.

[1] By R. L. Weaver and Y. H. Pao and published in the December, 1982 issue of the ASME Journal of Applied Mechanics, Vol. 49, pp. 821–836.

[2] Civil Engineering Department, University of California, Davis, Calif. 95616.

Other differences to note are that the simple solution is incapable of showing the spike caused by the Rayleigh surface wave on the upper surface. The simple solution in fact looks more similar to the response found by Weaver and Pao using only the first antisymmetric branch shown in their Fig. 7(*a*). There is no doubt that their solution contains many refinements that the simple solution cannot possibly show.

In reference [3] axial wave propagation in a circular rod due to laser deposition was studied. It was found that whereas an approach similar to that used in reference [1] yielded results that matched the gross behavior extremely well, certain details were not adequately represented without consideration of the higher thickness modes of the elasticity solution. It was found for instance that modes above the forty-fifth showed group velocities that approached the dilatational velocity and further had a large component of plane-type behavior. Thus these very high thickness modes were able to explain the experimentally observed waves that arrived at the dilatational velocity. Those results would indicate that there might also be something to be learned by investigation of the higher thickness modes in a plate (Weaver and Pao stopped at the tenth thickness mode).

In this brief discussion it has not been my purpose to denigrate the excellent work done by Weaver and Pao. Their investigation goes far beyond the simplistic approach of reference [1] and their response curves show the refinements brought about by the inclusion of many thickness modes. It has only been my purpose to show that the simpler approach is capable of describing the gross response of the plate, and to comment that further study of higher thickness modes might also prove fruitful.

References

1 Hutchinson, J. R., "Wave Propagation Using Mindin Plate Theory," *Proceedings of the Second Cairo University MDP Conference*, Dec. 27–29, 1982, Cairo, Egypt.

2 Timoshenko, S., and Woinowsky-Krieger, S. *Theory of Plates and Shells*, 2nd Ed., McGraw-Hill, New York, 1959.

3 Hutchinson, J. R., and Percival, C. M., "Higher Modes of Longitudinal Wave Propagation in Thin Rods," *Journal of the Acoustical Society of America*, Vol. 44, 1968, pp. 1204–1210.

Authors' Closure

The authors thank Dr. Hutchinson for his comments and for his careful comparison of the plate response determined from Mindlin's theory of a moderately thick plate and that from the Rayleigh-Lamb theory of a plate with arbitrary thickness.

In the preprint version of the authors' paper a factor of π was missing from the denominator of equation (7.1). This error and its ramifications were corrected in the published and reprint versions. The discrepancies in magnitude are explained if Dr. Hutchinson has made his comparisons with the early version. He is undoubtedly correct in pointing out the sign error in Figs. 10. The authors regret the confusion.

Investigation of higher modes is needed if one is interested in the high frequency response of the plate. In that case, and in the near field and at early times, the method of generalized ray is more effective. Based on that method, Ceranoglu and Pao (reference [12] in authors' paper) showed that the earliest arrived signal indeed travels with the speed of dilatational wave. The amplitude of these early arrivals, however, is much less than that of the later signals.

But if the interest is in the far field and with the highest frequency details of the earliest arrivals, a normal mode expansion of far more than 10 branches, as suggested by Dr. Hutchinson, would probably be necessary. One might conjecture however, that there exist asymptotically valid closed expressions for the earliest arrivals in the far field. A normal mode expansion of hundreds of branches would be very time-consuming and possibly prone to round-off errors.

Journal of Applied Mechanics

Book Reviews

Mechanics of Solids With Applications to Thin Bodies. By G. Wempner. Martinus Nijhoff, 1982. 633 Pages. Price $79.00.

REVIEWED BY T. J. LARDNER[1]

This book was originally published by McGraw-Hill in 1973 and it has, I believe, stood the test of time well; I have had many occasions to refer to different sections in the book during the past nine years. A review of the book appeared in *Applied Mechanics Reviews* (AMR, Review No. 10535, 1976) and this reviewer agrees with the conclusions of the AMR review.

The principal goal of the book, according to the author "... is to build a bridge between the most fundamental concepts of continuous media and the practical theories of structures. Foundations are laid with a view toward their eventual role in the analysis of flexible bodies." This bridge at times appears strange when fundamental relations are derived and then applied to a simple structure; the reader new to solid mechanics may wonder if the formulation might be easier by direct approaches to the simple structure. Of course, easier methods do exist but the author stresses the importance of the general approach in his discussion. Further he does emphasize that the book "... is intended for *engineers* interested in the *applied* mechanics of solids." Chapter titles and a brief outline of some of them follows:

1. *Introduction.* A review of notation to be used in the book.
2. *Deformation.* The basic kinematic results for the deformation of a continuous solid are derived.
3. *Stress.* The basic concepts of internal forces are presented.
4. *Behavior of Materials.* The general theory of elasticity, the incremental theory of plasticity, and the linear theory of viscoelasticity are developed.
5. *Linear Theories of Isotropic Elasticity and Viscoelasticity.*
6. *Extension, Flexure, and Torsion of Rods.*
7. *Elastic Plates.*
8. *Mechanics of Curved Rods.* A useful chapter containing a number of results.
9. *Energy Principles.*
10. *Curvilinear Coordinates.*
10. *Differential Geometry of a Surface.*
12. *Theory of Shells.*

As can be seen from the chapter titles, the book covers a wide range of topics in the mechanics of solids. The derivations are carefully presented and clear. References up to the time of the original publication provide sources to the original works on a number of topics. This is a useful reference book and can be used effectively for an introductory graduate course in solid mechanics.

[1] Professor, Department of Civil Engineering, University of Massachusetts, Amherst, Mass. 01003.

Wave Propagation in Viscoelastic Media. Edited by F. Mainardi. Pitman Publishing, Marshfield, Mass. 272 Pages. Price $25.00.

REVIEWED BY T. C. T. TING[2]

This book is Volume 52 of *Research Notes in Mathematics* which contains 11 articles by lecturers who took part at the Euromech Colloquium 127 on "Wave Propagation in Viscoelastic Media," held at Taormina (Sicily, Italy) in April, 1980.

The authors and the titles of the articles are as follows: D. Graffi, "Mathematical models and waves in linear viscoelasticity," M. Hayes, "Viscoelastic plane waves," S. Zahorski, "Properties of transverse and longitudinal harmonic waves," L. Brun and A. Molinari, "Transient linear and weakly nonlinear viscoelastic waves," A. Jeffrey and J. Engelbrecht, "Waves in nonlinear relaxing media," T. B. Moodie, R. J. Tait, and J. B. Haddow, "Waves in compliant tubes," E. Strick, "Applications of linear viscoelasticity to seismic wave propagation," E. A. Trautenberg, K. Gebauer, and A. Sachs, "Numerical simulation of wave propagation in viscoelastic media with nonreflecting boundary," J. L. Sackman, "Prediction and identification in viscoelastic wave propagation," G. C. Gaunaurd, W. Madigosky, H. Überall, and L. R. Dragonette, "Inverse scattering and the response of viscoelastic and electromagnetic waves," and J. Brilla, "generalized variational principles and methods in dynamic viscoelasticity."

The problems of wave propagation in viscoelastic media are much more difficult to analyze than the associated problems in elastic media because of the history dependence nature of the stress-strain laws. The governing equations are in general in the form of integro-differential equations if the stress-strain laws are written in an integral form. If they are written in a differential form, one can obtain the governing equations in the form of differential equations but they are usually of higher order than the equations for elastic waves. Therefore, with few exceptions, only linear or one-dimensional problems can be treated analytically. This is reflected in this book in which most articles are concerned with linear and/or one-dimensional problems. With the exception of the article by Zahorsky, which deals with viscoelastic fluids and the article by Jeffrey and Engelbrecht, which discusses both fluids and solids, the articles deal with waves in viscoelastic solids. Moodie, Tait, and Haddow consider the wave propagation in

[2] Professor of Applied Mechanics, Department of Civil Engineering, Mechanics, and Metallurgy, University of Illinois at Chicago, Chicago, Ill. 60680.

a fluid-filled tube in which the tube can be elastic or viscoelastic but the fluid is assumed to be incompressible and inviscid. All articles are very mathematically and analytically oriented. Nevertheless, the articles cover a fairly wide range of wave propagation phenomena in viscoelastic media. In view of the fact that there are not many books available on viscoelasticity and even fewer on wave propagation in viscoelastic media, the appearance of this volume is welcome. It would serve as a useful reference for those who want to venture into this field.

Plane-Strain Slip-Line Fields for Metal-Deformation Processes. By. W. Johnson, R. Sowerby, and R. D. Venter. Pergamon Press, New York, 1982. 364 Pages. Price $45.00.

REVIEWED BY S. KOBAYASHI[3]

This monograph comprises the previous one *Plane-Strain Slip-Line Fields: Theory and Bibliography*, published by Edward Arnold in 1970, describes most of the advances in the field developed during the last decade, and includes references to many new papers which give results in specific problems.

The Introduction begins with a historical note on plane-strain slip-line fields, followed by a list of physical observations in working metal. In Chapter 2 certain basic aspects of the plasticity theory that are necessary for the development of the methods of solution of the two-dimensional problems are presented. Chapter 3 is concerned with the governing equations of the plane plastic flow of a rigid-perfectly plastic solid, and their solution method. It contains the method of characteristics, properties of slip-line net, hodograph, and the discussion on a complete solution. In Chapter 4 a number of boundary value problems are examined to show how solutions may be developed by a straightforward step-by-step procedure. Construction of slip-line fields, stress boundary conditions, and construction of hodographs are discussed. While Chapters 2, 3, and 4 have dealt with basic plasticity theory, Chapter 5 is devoted to the application of the theory to specific problems of plane plastic flow. Slip-line solutions to many metal deformation processes are presented. They include pressure vessels, compression, indentation, cutting, sheet drawing, extrusion, piercing, forging, machining, swaging, notched bar tension, bending, rolling, and blanking. The discussion is extended to the application of slip-line fields in the area of crack initiation and fracture. More than 500 references are listed in this chapter alone. In Chapter 6 a numerical computational procedure which is referred to as the matrix-operation method is presented in detail. The method was developed recently, and greatly facilitates the solution to problems of the indirect type where there are insufficient known starting conditions for the determination of the slip-line field (or hodograph). The procedure is based on a power series representation of the solution to the governing equations and a vector representation of slip-lines and a system of matrix operators. This chapter contains mathematical formulations for the procedure, matrix operator subroutines, and solution of direct-type and indirect-type problems. The final chapter is concerned with the plasticity problems for other than isotropic rigid-perfectly plastic materials under plane-strain conditions. The method of characteristics is described for plane stress and axisymmetric problems, and for materials such as clay, ice, and soils. Slip-line fields for anisotropic materials are given, and the problems of minimum weight frames, plastic bending of plates and the force-plane diagram for slip-line fields are shown as analogies with metal-forming operations.

This book is the most complete source book on the subject and contains the references in each chapter, totaling almost 900 references. The book indeed provides teachers and researchers with basic material and a bibliography of papers on the theory and application of plane-strain slip-line fields to metal deformation processes.

[3]Professor, Department of Mechanical Engineering, University of California, Berkeley, Calif. 94720. Fellow ASME

Impact Dynamics. By J. A. Zukas, T. Nicholas, H. F. Swift, L. B. Greszczuk, and D. R. Curran. Wiley, New York, 1982. 452 Pages. Price $47.50.

REVIEWED BY L. E. MALVERN[4]

This book grew out of a short course taught by the authors, but is more a reference book than a textbook. It covers a wide range from low-speed to hypervelocity impact of projectiles against targets, with emphasis on impacts causing damage.

J. A. Zukas wrote five of the 11 chapters. The first two introduce stress waves and some limitations of elementary theory. Chapter 5 is a well-illustrated comprehensive treatment (with some 160 references) of penetration and perforation of solids. Experimental methods and approximate analyses by force laws are discussed.

In Chapter 10, Zukas presents an authoritative discussion (with 90 references) of numerical simulation of impact phenomena. Several remarkable examples of successful calculation are reviewed, including spall prediction, ricochet, oblique impact by a long-rod penetrator, and the self-forming fragment. The last chapter catalogues available three-dimensional codes (72 references) and closes with a section on current developments. The most serious limitation is not cost or complexity of numerical simulation, but rather the inadequacy of models describing material behavior, especially failure models.

This critical problem of material behavior at high rates is addressed by T. Nicholas in Chapter 8, a comprehensive review of experimental methods (140 references) at strain rates up to about 10,000/sec. The split Hopkinson pressure bar or Kolsky aparatus is treated at length. Biaxial testing is mentioned, but few high-rate results are available. Rate-history effects and their modeling are considered.

At higher rates, inelastic wave analysis is needed to interpret the experiments, but this requires assumed constitutive properties and leads to an iterative procedure for properties determination that may not have a unique solution. Nicholas treats elastic-plastic stress waves in Chapter 4 (116 references).

Damage in composite materials, caused by low-velocity impact, is discussed by L. B. Greszczuk in Chapter 3. A theory is developed and applied for elastic impact of two bodies of revolution made of transversely isotropic and orthotropic materials, including laminated composite targets. Failure criteria are proposed, and a few experimentally observed failure modes presented.

Hypervelocity impact mechanics, at velocities where strength of projectile and target are sufficiently negligible that solids may be considered as fluid, is concisely and clearly treated by H. F. Swift in Chapter 6. Launchers include gas guns, explosive projectors, and electrical accelerators.

In Chapter 7 Swift authoritatively discusses cameras and related image-forming instruments and presents several interesting accounts of ingenious techniques.

[4]Professor, Engineering Sciences Department, University of Florida, Gainesville, Fla. 32611. Fellow ASME.

A chapter on dynamic fracture by D. R. Curran treats recent progress in the microstatistical internal state variable approach to microvoid kinetics and reports on experimental measurements and constitutive modeling of nucleation, growth, and coalescence. Applications include fragmenting rounds, fracture of geologic materials, and quasi-static ductile fracture of metals.

This is a valuable reference, which every research engineer dealing with projectile impact dynamics will want to have.

Tribological Technology, Vols. I & II. Edited by P. B. Senhalzi. Martinus Nijhoff, The Netherlands, 1982. 775 Pages. Price $109.00.

REVIEWED BY F. F. LING[5]

These volumes constitute the Proceedings of a NATO Advanced Study Institute on the subject held in Maratea, Italy, 1981. To those interested in applied mechanics, these volumes offer a broad view of the field of tribology which beckons innovative solutions to relevant, well-posed applied mechanics problems. Aside from the Introduction and three Appendices, there are 10 Chapters: "Scope of Tribology" by H. Czichos of West Germany; "Surface Interaction" by W. P. Suh of the United States; "Materials in Tribotechnical Applications" by A. W. J. de Gee of The Netherlands; "Surfaces" by M. J. Edwards of the U.K.; two chapters on "Lubrication" and "Lubricants, respectively, by W. O. Winer of the United States; "Contamination in Fluid Systems" by E. C. Fitch of the United States; "Tribological Failures and Mechanical Design" by M. B. Peterson of the United States; "Tribo-Testing" by M. Godet of France; "Monitoring" by D. Scott of the U.K.; and "Multidisciplinary Approach" by B. R. Reason of the U.K.

So far as this reviewer knows, all of the chapters are reviews. By and large they are well written and the reviews are comprehensive. One fine feature of these two volumes is that the authors have been given space to sufficiently render detailed and quantitative treatment of the subject at hand.

Returning to this reviewer's earlier claim that the field of tribology beckons, examples of solutions sought to mechanics problems are: surface mechanics problems with smooth as well as nonsmooth surfaces; rheological problems with pressure and temperature effects; problems involving complex failure mechanisms; problems of fluid flow with entrained particulates; problems in nonlinear mechanics; problems involving various forms of composites; and problems involving interpenetrating continua.

Constitutive Equations for Engineering Materials, Volume I: Elasticity and Modeling. By W. F. Chen and A. F. Saleeb. Wiley, New York, 1982, pp. xii–580. price $68.50.

REVIEWED BY G. J. DVORAK[6]

Over the past two decades, rapid advances in numerical analysis of engineering structures have stimulated extensive research in constitutive modeling of material behavior. Yet, few books are available that survey the numerous constitutive theories, their experimental verification, and their usefulness in applications. This is especially true in the case of complex materials, such as concrete and soils, which are difficult to model, but which are frequently encountered in practice.

The book fills this gap in technical literature. It is written primarily for civil engineers both as a graduate textbook and a reference book. The work comes in two volumes. The first volume deals with elastic, hyperelastic, and hypoelastic models. Plasticity will be treated in the second volume. Time-dependent behavior is not considered.

The first volume is divided into three self-contained parts. *Part One* on Basic Concepts in Elasticity provides an introduction to vectors and tensors, analysis of stress and infinitesimal strain, and to elastic stress-strain relations. This last topic is presented in an elaborate way, with extensive expositions of both linear and especially nonlinear theories. Uniqueness and stability, and their effect on elastic constitutive relations in terms of normality and convexity are discussed together with nonlinear isotropic stress-strain relations based on strain or complementary energy functions, and on modifications of linear models. Incremental (hypoelastic, secant moduli, and variable moduli based) stress-strain relations are formulated and illustrated by many examples.

Part Two on Concrete Elasticity and Failure Criteria treats mechanical behavior, linear and nonlinear elasticity theories, failure criteria, and fracture models of concrete. An extensive collection of classical and more recent results is presented. Four total stress-strain models, and five incremental models for nonlinear isotropic and orthotropic concrete materials are discussed. Applications of some of the models in finite element analysis of concrete structures are illustrated in several examples.

Part Three on Soil Elasticity and Failure Criteria is organized in a similar way as Part two. Mechanical behavior, failure criteria, and nonlinear elasticity formulations are presented. A total stress-strain model, a third-order hyperelastic model, and four incremental models are discussed and illustrated by examples of their finite element applications.

Each of the three parts is rather self-contained, and the book, although well organized, is further divided into seven separate chapters, each with its own table of contents. Thus, there are altogether eight lists of contents in different locations. The material presented is quite diverse due to both the depth of the treatment – which includes basic theories, experimental data, and examples of applications – and the wide range of modeling approaches to deformation, and failure of concrete and soils, which the book covers. The authors have mastered the difficult task of presenting the material well. For the most part, the narrative is clear, the theoretical background is reasonably rigorous, and well illustrated by many examples. Particularly useful to the reader should be the many summaries and conclusions that discuss the validity of the numerous constitutive models described in the book.

Proceedings, International Conference on Constitutive Laws for Engineering Materials, Theory and Application. Edited by C. S. Desai and R. H. Gallagher. January 10–14, 1983, Tucson, Ariz. 604 Pages. Price $40.00.

REVIEWED BY L. B. FREUND[7]

This paper-bound volume contains about 100 papers which were presented at a conference held in January of 1983, in-

[5] William Howard Hart, Professor, Department of Mechanical Engineering, Aeronautical Engineering and Mechanics, Rensselaer Polytechnic Institute, Troy, N.Y. 12181. Fellow ASME.

[6] Professor, Department of Civil Engineering, University of Utah, Salt Lake City, Utah 84112. Mem. ASME.

[7] Professor, Division of Engineering, Brown University, Providence, R.I. 02912. Fellow, ASME.

cluding summaries of 28 invited lectures. The complete texts of the invited lectures will appear in a hard-bound volume which is in preparation. The papers are divided into seven categories: General Theory, Metals and Composites, Geological Materials, Discontinuous Media, Concrete, Granular Materials and Aggregates, and Implementation and Evaluation. The objective of the conference was to stimulate interaction between researchers concerned with the theoretical and experimental aspects of developing constitutive models of deformable solids and those concerned with the implementation of constitutive laws in engineering analysis and design.

Many individuals who are active in the field of the conference contributed articles and, consequently, the volume provides a reasonably complete picture of the current state of development of models for describing the mechanical behavior of solids. Of course, the volume would be more valuable if it contained complete texts of the overview lectures as well as the contributed articles.

Theory of Laminar Flames. By J. D. Buckmaster and G. S. S. Ludford. Cambridge University Press, New York, 1982. 266 Pages. Price $49.50.

REVIEWED BY H. W. EMMONS[8]

A mixture of a gaseous fuel and oxidizer (air) will, if within the appropriate composition range, propagate a reaction that converts the reactants to products and produces heat and light: a flame. The process involves the diffusion of heat and reactive chemical specie from the reaction zone to the unignited mixture: the feedback of energy and specie.

The principal obstacle to the progress in the analysis of laminar combustion is the usually very complex series of chemical reactions needed for even very simple overall chemical reactions and the nonlinear nature of the Arrheneous relation for the chemical rate of each of the many chemical reactions actually occurring.

The book under review undertakes the task of introducing its readers to the progress that has been made in this analysis for very simple hypothetical forward reactions with an activation energy E in the Arrheneous formula which is very large ($E/R \gg T$). Under these conditions singular perturbation methods make it possible to attain solutions with considerable rigor and fair accuracy.

The book begins with a derivation of the required basic equations and continues with their application to a series of flame spread problems. The study of steady flame phenomena is followed by that of slowly varying flames (SVF's) and near equidiffusional flames (NEF's).

The study of nonsteady flames naturally leads to consider questions of flame stability under various perturbed conditions.

The calculation of flow fields is discussed in general terms but is presented at length for flames as discontinuities and for flames in a preassigned approach flow field. There is an occasional discussion of various known experimental facts, even a few flame photographs. These are used as suggestive of the kind of phenomena to be looked for in subsequent solutions. Various reasonable-looking flow fields are analytically reproduced, but no attempt is made to show their quantitative accuracy.

For anyone who desires to get started on the further development of the applied mathematics of problems of the laminar flow of multicomponent reacting gas mixtures, this book is superb. Anyone who is already familiar with combustion phenomena who desires to acquire a knowledge of the present status of the analytic understanding of what happens will find this book superior to the slow process of finding, critically reading, and absorbing the significance of the large number of papers now available. Anyone not familiar with combustion phenomena who wants to acquire that familiarity and the more physical and important intuitive understanding will find this book disappointing. The authors state (for a specific problem but generally applicable to the whole book) "...we regard the models as mathematical idealizations whose study can provide some insight into the nature of diffusion flames." And again, "..., which shows an early appreciation of activation-energy asymptotics (though not in the formal sense of this monograph)."

Needless to say, the reviewer made no attempt to check the correctness of the 819 equations printed in this book. Only an equation, which for some reason appeared to be wrong was checked and indeed the text formula for γ immediately following equation 60 is wrong ($\gamma = 1/(1 - R/mC_p)$).

Boundary Element Methods in Solid Mechanics. By S. L. Crouch and A. M. Starfield. Allen & Unwin, Winchester, Mass., 1983. 322 Pages. Price $30.00.

REVIEWED BY F. J. RIZZO[9]

The authors are of the opinion that boundary elements methods "... have not received the attention they deserve ..." compared with finite difference and finite element methods. Chief among several reasons for this, in their view, is the apparently somewhat "abstruse" character of many of the "... technical papers on boundary element methods." They suggest that the mathematics often used in these papers "... has prevented many from seeing the simple and attractive algorithm that ultimately emerges."

From this viewpoint, the authors have produced a book in which physical interpretation and intuitive reasoning are used to the utmost. Indeed, their development is so physical and so directed toward a computational scheme that the steps in their development may significantly alter whatever previous understanding the reader may have had of the terminology "boundary element methods." This terminology, which seems well on its way to supplanting the terminology "integral equation methods" or "boundary integral equation (BIE) methods," has been, since it was introduced, an understandable choice for obvious reasons. But boundary elements always seemed to this reviewer to be at least related to integral equations, i.e., as a way of numerically solving them. In this book, however, it seems that the concept of an integral equation is not at all necessary to introduce, understand, and use boundary element methods. Indeed, integral equations are hardly mentioned until the sixth chapter (of eight) where the concept is definitely less important to the authors' purpose than that of an influence function. All of this strikes thie reviewer as astonishing! Nevertheless, the whole development in this book is interesting, lucid, and, no doubt, correct for its intended audience and purpose such that the expressed astonishment is, in the end, quite pleasant. One may disagree on the degree to which physical interpretation in such detail is necessary or even helpful in understanding boundary elements for one who would not find most of the

[8] Professor, Division of Applied Sciences, Harvard University, Cambridge, Mass. 02138. Hon. Mem. ASME.

[9] Professor, Department of Engineering Mechanics, University of Kentucky, Lexington, KY. 40506.

ERRATA

Erratum on "Postbuckling Ring Analysis," by L. B. Sills and B. Budiansky, and published in the March, 1978 issue of the ASME JOURNAL OF APPLIED MECHANICS, Vol. 45, pp. 208–210.

There is a factor-of-two error in the postbuckling coefficient λ_2 calculated for the case of inverse-square loading. Equation (26) should read

$$\lambda_2 = -999/224 \qquad (IS)$$

The authors are grateful to Dr. Gaylen A. Thurston (NASA Langley) who studied the postbuckling ring behavior numerically, discovered disagreement between his results and ours, and told us about it; and to J. Mark Duva (graduate student, Harvard University) who subsequently reanalyzed the problem and found the factor-of-two error. The corrected value of λ_2 now provides excellent agreement with Thurston's numerical results.